THE UNIVERSITY OF CHICAGO

QUANTUM HALL PHYSICS WITH PHOTONS

A DISSERTATION SUBMITTED TO
THE FACULTY OF THE DIVISION OF THE PHYSICAL SCIENCES
IN CANDIDACY FOR THE DEGREE OF
DOCTOR OF PHILOSOPHY

DEPARTMENT OF PHYSICS

BY
NATHAN SCHINE

CHICAGO, ILLINOIS
DECEMBER 2019

Dedicated to my father

TABLE OF CONTENTS

LIST OF FIGURES

ACKNOWLEDGMENTS

My time in Chicago has brought me together with many warm and brilliant people—colleagues, lab-mates, and friends who have helped and supported me through graduate school. What successes I've experienced are due in no small part to this wonderful community around me.

First among the many I'd like to thank is my advisor, Jonathan Simon. He has been terrific. He has been deeply invested in my training and growth as a scientist, spending innumerable hours working with me in lab and in the office, and sending me to speak at conferences around the globe. His infectious excitement about physics and his constant investment and support during the long slogs and setbacks have been central to making this adventure fruitful, fulfilling, and fun. I have particularly valued his conversational approach, treating me even as a first-year like an intellectual partner, generously understanding half-baked ideas and keenly pushing me to clarify my thoughts and assumptions.

The experiments I've worked on are a large team effort, and I've learned and benefited greatly from all of my labmates. When I started, Alex Georgakopoulos immediately and happily showed me the ropes. Whether it was building lasers, working in the machine shop, or assembling the vacuum system, learning and working with Alex and his particular sense of humor was a pleasure. Albert Ryou developed the lab's first generation cavities with great care, determination, and precision. His work provided the intellectual and technical bedrock for the various cavities I later built. Ariel Sommer was our first postdoc, bringing constant knowledge, experience, and advice when we were all new. His careful, meticulous thought process offered a model for how to be a successful graduate student and physicist. Ningyuan Jia brought a quiet presence, indomitable work ethic, and wide ranging intellectual curiosity to the lab. Perhaps the clearest view of Jia's role in the lab came with the hole he left behind after he graduated. He more than anyone had turned every knob and knew the inner

workings of the experiment we built together.

More recently, Logan Clark and Claire Baum have joined the experiment and have made the past couple of years a great pleasure. Their optimism and good cheer has been like an earworm, spreading excitement and congeniality. Logan is our second postdoc, immediately stepping into the experiment with expertise and new ideas. His creativity, skill, attention to detail, and tenacity have been essential in making the science go. It would not have happened without him. Claire has been a great early grad student, learning rapidly, reliably building urgently needed components, and offering new questions and ideas. I am happy to be leaving the experiment in her capable hands.

The other members of the Simon lab have also helped to build a wonderful community. Clai Owens and I joined the lab in the same year, and I have greatly valued our friendship and conversation. Our projects' underlying physics is very similar, but the implementations are radically different; talking through these different perspectives has enriched my understanding in profound ways. Aziza Suleymanzade and Mark Stone have built their hybrid system from the ground up, solving one crazy, intimidating problem after another. They have greatly influenced the lab's culture, scientifically and socially, for the better. The circuit QED cadre of Alex Ma, Brendan Saxberg, and Gabrielle Roberts have been a fantastic addition to the lab, bringing welcome breadth and lively discussion to group meetings. The newest graduate students, Lavanya Taneja and Chuan Yin have already had a large impact in the lab and I look forward to hearing about their future progress.

I have also worked with several undergraduate researchers over the years, Carl Padgett, Lin Su, Michael Cervia, Leon Lu, Tahoe Schrader, Sohini Upadhyay, and Evan Mata. In particular, I worked closely with Michelle Chalupnik for around two years, building cavities, performing experiments, and even writing a paper together. I greatly enjoyed the opportunity to mentor, teach, and do science together, and in so doing learned a lot myself.

I also want to thank our theory colleagues, in particular Andrey Gromov. He came to us at the perfect time as we were struggling to understand the role of symmetries and topology in a Landau level. The gulf between the theoretical descriptions and experimental observables of quantum Hall systems is vast, and Andrey enthusiastically helped to build the necessary bridges.

The lab is itself by no means in a vacuum. We have depended enormously on the support of JFI staff. Maria Jimenez and before her, Pegg Anderson, have kept the wheels turning through their administrative support. Luigi Mazzenga in the student shop has been generous with his time, knowledge, and skills helping us to make a working apparatus. A huge debt of thanks is owed to John Phillips, our building and lab manager, who has been a constant and reassuring presence throughout the building, always checking in, fixing problems, and generally going the extra mile.

Outside of the lab, many people have kept me sane and happy here in Chicago. Clai Owens and Jungmin Cho, Thomas Videbaek, Kieran Murphy, Patrick Bryant, Aaron Mowitz, Mary Burkey and Gerwin Koolstra, Chris and Lisa Anderson—we may have met through physics, but your friendship is what I will most take with me. Not everyone I know is related to physics, though. To Duncan Price, Michael Osheroff, Catherine Berry, Emily Cook, Mattie Feder, Vanessa Harper, Dan Sullivan, Amy Levine and Sarale Ben-Asher, and Samantha Pellegrino and Zach Ralston—I love our time together and hope to see each of you soon!

Finally, I wish to thank my wonderful and supportive family. They have taught me so much and kept me grounded in what really matters. To my sister Miriam Schine Lee and brother-in-law Jonathan Lee, I am so lucky to have witnessed both your family and dreams growing over the years. I will always look up to you. To my parents Peter Schine and Andrea Barach, you have always encouraged me, supported me, inspired me, and loved me. Dad, I miss you every day and trust that you would be proud.

To my wife, Rachel Schine, every day you make me a better person and forgive me when I am not. You have put up with many late nights and frustrations all the while completing your own thesis. I love you so much, and I am excited for our next steps together.

ABSTRACT

Can quantum materials be made of light? This exciting possibility requires two primary ingredients, photons that behave like massive particles and strong interactions between those photons. This thesis describes our realization of these ingredients and our initial explorations of the resulting system.

First, we develop a synthetic magnetic field for harmonically trapped photons and observe the formation of a Landau level. This enables investigation into three distinct topological characteristics of a photonic integer quantum Hall system. Next, we turn photons into strongly-interacting cavity Rydberg polaritons, quasiparticles which inherit their motional dynamics from the optical cavity and gain strong interactions from Rydberg excitations of a cold Rubidium gas. Granting these polaritons access to a degenerate Landau level of cavity states allows them to move, collide, and order themselves into topologically nontrivial material states. Observations of strong correlations in both real space and angular momentum space certify the creation and detection of a photonic Laughlin state, a ground state of a fractional quantum Hall system. Developing synthetic quantum materials out of light provides fundamentally new experimental capabilities and opportunities and here establishes quantum many-body optics as a direct route towards breakthroughs in understanding topological order and strongly correlated materials.

CHAPTER 1

INTRODUCTION

Figure 1.1: **Victorian on Mud Heap (2011), by Mike Doyle.** Over 100,000 LEGO pieces combine to form a dilapidated Victorian mansion. Image from Ref. [1].

Anyone who has played with LEGO toys is aware of the extraordinary variety of structures that may be created by combining many pieces out of only a handful of unique types. All LEGO pieces have the same basic structure, with smooth plastic sides, sharp corners, and nubbly tops. Yet large aggregates of LEGO pieces, combined in creatively ordered ways, can evoke an entirely different style. Figure 1.1, above, shows a LEGO masterpiece that combines numerous shapes, textures, and forms out of individual blocky pieces that together

create a dilapidated Victorian mansion.

This basic idea—that combinations of a few fundamental ingredients can give rise to unexpected and qualitatively new results—also applies to scientific inquiry, as was recognized by Philip Anderson in the seminal article "More is Different" [2]. As a condensed matter physicist, Anderson applies this idea to the study of materials. Although the constituent elementary particles in chunk of diamond are completely described by the standard model of particle physics, it would be both absurd and fruitless to attempt to explain diamond's structure, not to mention its extreme hardness and thermal conductivity, through direct application of these basic laws. The study of materials, their properties and their phases, is made independent from elementary particle physics due to the great number of particles and resulting emergent phenomena that contribute to their formation*.

Since the 1930s, condensed matter physics has gone about explaining how ordinary matter can take on its enormous variety of forms through underlying symmetries and the spontaneous breaking thereof [3–5]. At the heart of this *Landau paradigm* are two interlocking ideas: the existence above the ground state of well defined electron-like quasiparticle excitations that govern material properties, and the existence of a Landau order parameter which classifies and distinguishes between phases of matter. The Landau order parameter quantifies the symmetry breaking of an ordered phase, and long wavelength fluctuations in the order parameter lead to universal critical behavior in materials that depends only on the underlying symmetries [6].

However, since the 1980s certain experiments with correlated quantum materials, i.e. those

$\star$. It is worth making this statement somewhat more precise. The low energy limit of the standard model of particle physics may justify certain approximations and simplifications into an effective theory. For instance, the Schrödinger equation is valid as long as none of the particles are moving close to the speed of light, yielding *ab initio* techniques to model real materials, such as density functional theory or the configuration interaction and coupled cluster techniques. Even when these approximations are suitably accurate, we are doing a something qualitatively different from a fundamental particle physics calculation. We do not appeal to the same objects, equations, or theories. Density functional theory and its colleagues may be justified by more fundamental theories, but describe qualitatively different systems and behaviors.

materials in which quantum mechanical interactions and correlations are dominant, have challenged this otherwise successful paradigm. In cuprate high temperature superconductors and heavy fermion metals, numerical and experimental evidence appears to show transitions between phases with different broken symmetries characterized by different order parameters. This is should not happen according to the Landau paradigm. Above zero temperature quantum critical points, critical behavior appears which is not in agreement with the Landau theory and the very existence of well defined quasiparticle excitations is in doubt [6].

1.1 The Quantum Hall Effect

Challenging the both pillars of the Landau paradigm are topological materials, the best known of which are states that appear in the quantum Hall effect [9, 10] generated in two dimensional low disorder electronic systems subject to a strong magnetic field (see Fig. 1.2). Even in the non-interacting integer quantum Hall effect, the system is characterized by a global topological invariant, the Chern number [11, 12], not any Landau order parameter quantifying a broken symmetry. In the fractional quantum Hall effect, strong Coulomb interactions between electrons drive the formation of "dancing patterns" of long range quantum entanglement [13, 14]; the resulting topological order again does not reference any sort of order parameter, while quasiparticle excitations are no longer even electron-like. Instead electrons appear to bind to magnetic flux quanta and break apart to form fractionally charged anyons [15–25]. We can understand these statements more precisely by looking at the form of the ground state wavefunction at simple filling factors $\nu^\star$. At $\nu = 1/q$ where $q > 1$ is an odd integer, the ground state wave function is given by the Laughlin wavefunction [15],

$$\Psi_L(z_1, \ldots, z_N) = C \prod_{j,k:\, j<k}^{N} (z_j - z_k)^q \prod_{j}^{N} e^{-\frac{1}{4}|z_j|^2}, \tag{1.1}$$

⋆. In figure 1.2 this is labeled i, but ν is more convenient in equations where i might be confused with the imaginary unit.

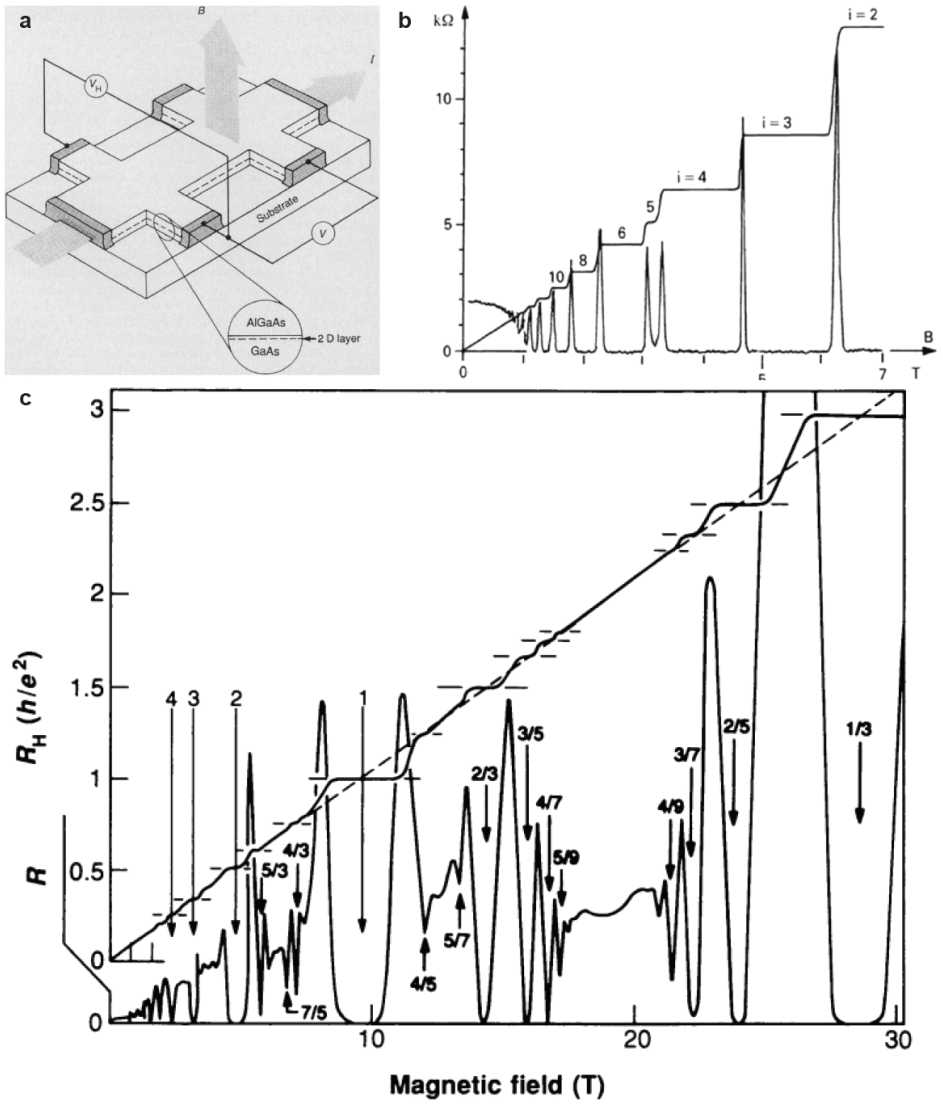

Figure 1.2: **The Quantum Hall Effect. (a)** The typical experimental apparatus for observing a quantum Hall effect is a Hall bar. Electrons flowing through this structure are confined to the interface (dotted line) between two semiconductor layers, aluminum gallium arsenide (AlGaAs) above gallium arsenide (GaAs). The structure may by subject to an external magnetic field B. The ratio of the measured longitudinal voltage (V) and transverse Hall voltage (V_H) to the current drive I then yields the longitudinal and Hall resistances R and R_H. Figure from Ref. [7] **(b)** At low fields or high temperatures the Hall resistances is linear in the applied magnetic field. However in cold clean samples, the Hall resistance increases stepwise with the magnetic field, as increasing unit fractions of the von Klitzing constant $\frac{1}{i}\frac{h}{e^2}$. Since the denominator i must be an integer, this is called the integer quantum Hall effect. The plateaus of the integer quantum Hall effect are so precisely flat that since the year 1990, measurements of the Hall resistance in such samples are the international metrological standard of resistance. The lower, sharply peaked curve is the longitudinal resistance, which vanishes at plateaus of the Hall resistance. Figure from Ref. [8]. **(c)** At higher magnetic fields, plateaus appear in the Hall resistance in between those corresponding to integers i. Instead, the great majority of features occur on regular sequences of fractional i with odd denominators. Note in particular the $i = 1/3$ plateau at the far right; this is the prototypical and most prominent fractional quantum Hall state. Figure from Ref. [7].

where $z_j = x_j + iy_j$ gives the position of particle j, and C_N is a normalization constant. There is a q-order zero as any pair of particles approach each other. This minimizes the energetic cost of two repulsively interacting particles coming close to each other; for contact interactions, this wavefunction has zero interaction energy.

Now the presence of n quasiholes at locations z_h changes the wavefunction to

$$\Psi_L^{qh}(z_1, \ldots, z_N) = C' \prod_j^N \prod_h^n (z_j - z_h) \prod_{j<k}^N (z_j - z_k)^q \prod_j^N e^{-\frac{1}{4}|z_j|^2}. \tag{1.2}$$

When $n = q$ and the quasiholes are at the same location z_H, this wavefunction looks the same as the original Laughlin wavefunction in equation 1.1, but with an extra particle located at $z_{N+1} = z_H$. Evidently q quasiholes are 'equivalent' to one particle. However, unlike a particle, these q quasiholes are not bound together in lockstep, but rather can move independently. Thus we infer that the charge of a quasihole is e/q where e is the charge of a single particle. A similar argument runs for the quantum *statistics* of a quasihole. The q-quasihole composite object is the same as a particle, so if we swap the locations of two of these composite objects and do nothing else, we have effectively swapped the location of two regular particles. If these particles are fermions, as is true for the electrons in the fractional quantum Hall effect, then the total many-body wavefunction picks up a sign of -1 or equivalently, a phase $e^{i\pi}$. However, if we take two individual quasiholes, q of which make up a particle, and swap their locations, the many-body wavefunction must pick up the reduced phase $e^{i\pi/q}$ [26].

This is very remarkable! No naturally occuring particles in nature are anything other than bosons or fermions, for which the phase upon exchange is either 0 or π, respectively[§]. Instead, in these two dimensional materials all sorts of nontrivial phases π/q are possible! Because

§. This is in fact a requirement of particles which move in three or more dimensions, since encircling paths are deformable into a trivial path without the two particles ever approaching each other. Thus it is only in two (or one) spatial dimensions that there exists the possibility of anyonic statistics [27].

the quasiparticles can have any statistical phase, they are called *anyons* [28].

There are more complicated ground state wavefunctions than the Laughlin wavefunction to explain the plateaus as less simple filling factors. Very quickly after Laughlin's proposed wavefunction, Haldane and others recognized that states at filling factors $\nu = \frac{2}{5}, \frac{2}{7}, \ldots$ could be obtained by starting with quasiparticles above the Laughlin wavefunction with a filling factor in the primary sequence $\nu = \frac{1}{3}, \frac{1}{5}, \ldots$ and allowing those quasiparticles to condense into their own fractional quantum Hall phase [29]. And quasiparticles above these states could then condense to make yet more complex fractional quantum Hall states. This construction thus produces what are, for obvious reasons, called hierarchy states. Some years later, Jain offered a different explanation of states $\nu = p/(2mp \pm 1)$ in terms of composite fermions. Magnetic flux tubes carrying $2m\phi_0$, where ϕ_0 is the quantum of magnetic flux, are attached to each particle and these particles condense into an integer quantum Hall state at filling factor p; "the FQHE of electrons is a manifestation of the IQHE of composite fermions" [16]. Yet more complicated states were observed that could not be explained by any of the preceding theories, most notably at $\nu = 5/2$ [30]. Now, despite disagreement between a large number of proposed ground state wavefunctions, this state is expected to support a degenerate manifold of ground states with non-Abelian anyons as the low energy excitations [31]. Braiding two non-Abelian anyons does not just yield a non-trivial statistical phase but also applies a unitary matrix on the ground state manifold. The Moore-Read state at $\nu = 5/2$ is an exact ground state in the presence of pure 3-body interactions (much like the Laughlin state with 2-body interactions), indicating that it may be possible to create this state by engineering the appropriate interactions. Furthermore, Read-Rezayi states generalize this to higher order k-body interactions, with the expected simplest filling factors that support them at $\nu = 12/5$ and $13/5$ [32, 33]. Unlike for Moore-Read state, excitations above the Read-Rezayi states yield non-Abelian anyons that support universal topological quantum computation [33].

The rapid discovery and initial explanations of the quantum Hall effects in the early 1980s motivated an explosion of interest in related models and topological physics more generally. In roughly chronological order, these include the Haldane model for a quantum Hall effect without Landau levels [34], topological spin liquids [35, 36], Abelian and non-Abelian Kitaev models [37] and topological string net condensation [38] with applications to topological quantum computing [14, 37, 39], the quantum spin Hall effect [40] and topological insulators [41–44], symmetry protected topological phases [45], Weyl semimetals [46], and topological superconductors [47]. This also pulled out older topological descriptions of condensed matter systems into the limelight, including the BKT transition [48, 49] and the SSH model of polyacetalene [50, 51]. Throughout this evolution, studies in topological physics continue to use the quantum Hall effect as a theoretical touchstone and exemplar of topological order.

However, there is plenty about the fractional quantum Hall effect that is not fully understood. Beyond the controversies concerning filling factors $\nu = 5/2$ and $1/2$ and developments in more complex quantum Hall systems involving bilayers [52, 53] and Moire superlattices [54], there remain basic aspects of the fractional quantum Hall effect that have not been observed or fully elucidated. For instance, although it underpins the formation of topological order in fractional quantum Hall phases, repulsive interactions between constituent particles have not been directly observed. As the density of particles in an interacting quantum Hall system is reduced, the system is predicted to freeze from a topologically ordered fluid into a Wigner crystal[‡]. Furthermore, new topological invariants appear in fractional quantum Hall physics which have not been extensively explored, even though the topological degrees of freedom these invariants characterize are central to the formation of topological order. These gaps in

‡. The qualitative energetics of this phase transition are straightforward. At low densities, localizing particles into a crystal costs negligible interaction energy. As the density increases, localization implies a larger kinetic energy due to the Heisenberg uncertainty principle while also no longer providing sufficient interparticle separation to zero the interaction energy. At some density, this raises the energy of the Wigner crystal above that of a correlated quantum liquid, which does not pay the kinetic energy penalty since it is not localized and which minimizes short range interaction energy through spatial anti-correlations.

evidence stem from existing fractional quantum Hall systems being restricted to electronic structures. These experiments mostly rely on charge transport measurements which cannot locally probe the fractional quantum Hall states and so cannot reveal spatial correlations. Furthermore, the new topological invariants are associated with transport measurements that are either impossible or very difficult with state-of-the-art capabilities. More broadly, electronic systems are large, in that they contain thousands to millions of particles. There are a host of interesting questions about the development of topological order as the system size grows from a few, to several, to many particles.

This indicates that new experimental probes implemented in a new experimental platform for quantum Hall physics could open the door to qualitatively new measurements, looking at manifestations of the same underlying physics that are simply inaccessible to electronic systems.

1.2 Synthetic Quantum Materials

Atomic physicists have had remarkable success using cold atoms to explore condensed matter models. Bose-Einstein condensates and degenerate Fermi gases both naturally form fascinating material systems. In combination with the deep atomic physics toolbox, they have enabled studies in Bose- and Fermi-Hubbard models, quantum magnetism, dipolar quantum liquids, bosonic Luttinger liquids and Tonks-Girardeau gases, synthetic gauge fields and spin-orbit coupling, and the BEC-BCS crossover [55]. Of particular note for the broader condensed matter community, Fermi gas microscopes are at the forefront of Fermi-Hubbard physics which underlies high temperature superconductivity [56–60].

While numerous methods have been proposed and implemented to create synthetic gauge fields for ultracold atoms [61–64], combining these methods with strong interactions between atoms has proven challenging [65, 66]. This is most often due to additional heating induced

by the off-resonant laser dressing or lattice shaking used to induced the synthetic gauge field.

A new forefront of synthetic quantum materials are optical systems in which photons are the dynamic particles. Although this is a younger field, already the necessary ingredients for an interacting quantum Hall system have been demonstrated, albeit not at the same time. Although numerous techniques have been developed to make synthetic gauge fields for light [67], before our work, these techniques induced far too much photon loss to be compatible with the tools to make photons collide.

Foundational works making materials out of photons coupled optical cavity modes to an intracavity medium to make photons behave like massive particles in a harmonic trap. This concept successfully enabled Bose-Einstein condensation of weakly interacting exciton polaritons [68–72] and dye-thermalized photons [73], while extensive theoretical work laid out numerous exciting possibilities if interactions could be made strong [74]. As a consequence of this beautiful analogy and theoretical work, there have been numerous efforts to make exciton polaritons strongly interact, but as we began our work, no one had succeeded. Now, exciton polaritons are entering this regime; the groups of Atac Imamoglu and Thomas Volz have recently engineered this system to make individual photons collide one time out of twenty within the polariton lifetime [75, 76].

Very strong interactions between microwave photons have been developed, motivated by the possibility of universal digital quantum computation based on superconducting circuits in which Josephson junctions provide an extraordinary nonlinearity at the single photon level [77–79]. Tailoring these technologies instead for many-body quantum systems has enabled the development of synthetic gauge fields [80, 81] in principle compatible with strongly interacting many-body systems [82, 83]. Despite the great nonlinearities accessible in the superconducting microwave platform, creating many identical emitters is a great technical challenge. In comparison, atomic systems scale favorably since all atoms of the same kind are identical, so it is natural to consider mediating optical photon interactions with cold

atoms. In 2005, Birnbaum, *et al.* demonstrated strong photon-photon interactions mediated by a single atom in an optical cavity [84], and in 2012 Peyronel, *et al.* established a more tractable platform for strong photon-photon interactions based on Rydberg polaritons [85].

The challenge, then, that faced us at the beginning of my Ph.D. in 2013 was how to combine these ingredients together. It was clear that adding an optical cavity around the atomic sample used to support Rydberg polaritons would only improve the atom-photon coupling and effective interaction strength while also making the theoretical treatment of the system simpler. Indeed at present, our cavity Rydberg polaritons interact very strongly, with the probability that each polariton will collide with another exceeding 98% (see Fig. 6.2d). However, prior to our work, all of the techniques then available for engineering a synthetic magnetic field for light at that time were incompatible with even moderately low-loss optical cavities.

Nevertheless, creating strongly interacting cavity Rydberg polaritons was a promising direction to pursue since it enables a rich diversity of experiments and applications, benefiting from enhanced Rydberg mediated interactions and enhanced optical read-out and light-matter coupling from the optical cavity. These range from quantum repeaters [86–92], single photon transistors [93–96], and more general quantum information processing [97–103], to blockade enhanced imaging [104, 105], quantum-enhanced metrology [102], and a spectrally narrow high-fidelity on-demand single photon source [100, 106]. Of most interest to our work, cavity Rydberg polaritons also have direct application in the formation quantum many-body systems [74, 102, 107–114] including quantum crystals [109, 115, 116] and, with a synthetic magnetic field for light, topologically ordered phases of matter [67, 116–121].

A clear and early concern when setting out to investigate fractional quantum Hall physics with Rydberg polaritons were the quantum statistics of the particles. Electrons in the traditional solid state systems are fermions, while Rydberg polaritons are bosons. Does this fundamentally affect quantum Hall physics? The answer is a qualified no. The necessary

ingredients are only a flat two dimensional band with an effective magnetic field, and strong interparticle interactions. Quantum statistics does influence the filling factors and precise wavefunctions that appear, but in apparently trivial ways. For instance, the Laughlin state with bosons first appears at $\nu = 1/2$ rather than $1/3$. The exponent q in the first term of eq. 1.1 must be even rather than odd. Similar effects occur for more complex states. The Moore-Read state predicted for electrons at $\nu = 5/2$ instead is predicted for bosons at $\nu = 1$, while bosonic Read-Rezayi states are predicted at $\nu = 3/2$ and 2 [61]*. Thus it is expected that the full richness of fractional quantum Hall physics is available to bosonic synthetic material platforms, while moving from the solid state to photonic materials offers ground-up Hamiltonian control, particle-by-particle injection and measurement, and local manipulation and probing of not just the wavefunction amplitude, but also its phase. All of this provides unique access to new observables characterizing quantum Hall systems.

1.3 Layout of the Thesis

In chapter 2, we introduce cavity quantum electrodynamics and the two primary architectures for creating effective strong interactions at the single photon level: the Jaynes-Cummings nonlinearity and Rydberg mediated interactions. This also serves to introduce theoretically cavity Rydberg polaritons which are quantum superpositions of individual cavity photons and Rydberg excitations. These are then the workhorse of all our experiments making photons interact. Chapter 3 introduces the physical apparatus necessary to make these experiments happen. We start with a discussion of the properties of optical cavities and then transition into the various atomic physics tools used to cool, trap, and manipulate the Rubidium atoms that mediate photon interactions through their Rydberg excitations.

$\star$. Modest dipolar interactions are required in addition to contact interactions, e.g. $\alpha = V_2/V_0 = 0.38$ where V_0 and V_2 are the Haldane pseudo-potentials [61]. Dipolar interactions between Rydberg polaritons may be achieved by microwave manipulation of the Rydberg state [122, 123], as described in section 7.1.2.

The breakthrough for creating a synthetic magnetic field for light that was compatible with strong interactions mediated by Rydberg excitations came early in my Ph.D. work in the form of a nonplanar cavity. Simply reconfiguring the arrangement of a standard four mirror running wave optical cavity so that the four mirrors do not lie in a single plane creates an effective magnetic field for cavity photons. Chapter 4 describes this effort and the subsequent investigations into non-interacting quantum Hall physics.

Chapter 5 demonstrates the formation of strongly interacting Rydberg polaritons, focusing on how we characterize and manipulate strong interactions in a single mode and between a pair of modes. Chapter 6 then combines the synthetic magnetic field for photons and strong interactions between photons to explore fractional quantum Hall physics. We observe the formation of a Laughlin state of photons via both angular momentum and spatial correlations. Finally, in chapter 7 we explore some of the low-hanging fruit for future work and discuss further apparatus improvements that would enable exciting new experiments in quantum Hall physics and beyond.

CHAPTER 2

NONLINEAR QUANTUM OPTICS

Figure 2.1: **In this lightsaber duel** from Star Wars, Episode V: The Empire Strikes Back (1980), strong repulsive interactions between photons make the lightsaber a formidable weapon.

Strong interactions between individual photons are a basic building block for quantum information processing and quantum many-body physics with photons. In particular, for creating a photonic fractional quantum Hall system, strong interactions are required to drive the development of topological order. While quantum optics is concerned with the properties and behaviors of single photons, strong nonlinearities in which system parameters significantly change with the addition of a single photon, are the physical basis for making photons interact. However, there are two major architectures for engineering nonlinear quantum optics.

Both architectures begin by coupling photons to an atomic (or atom-like) excitation, so this chapter begins with a discussion of cavity quantum electrodynamics. By considering a minimal model of a single atom in a single optical mode, we arrive at the Jaynes-Cummings model,

the first route toward strong photon-photon interactions. The Jaynes-Cummings interaction is fabulously useful in many quantum engineering and information processing platforms; however, it does come with some downsides. In particular making the atom-photon cooperativity sufficiently large for optical frequency photons is difficult. To circumvent this, we can place a large number of atoms into the optical mode, which ruins the Jaynes-Cummings interaction, but then we can reintroduce interactions by coupling individual photons to strongly interacting Rydberg excitations. We will discuss this second architecture, based on Rydberg polaritons, with a focus on our implementation of cavity Rydberg polaritons, limitations on their lifetime, their dependence on system parameters, and the form of their interactions. Finally, we connect the collective cooperativity directly to the total number of collisions that polaritons may undergo, a central result that has been a guiding light for our experimental goals and system design.

2.1 Cavity Quantum Electrodynamics

Photons do not interact with each other in a vacuum due to the linearity of Maxwell's equations*. This statement raises the possibility that photons can interact in a medium. While the entire field of nonlinear optics explores the manifold ways in which materials with a nonlinear optical susceptibility create interesting and useful applications, with prominent examples in second-harmonic generation, sum and difference frequency generation, optical parametric amplification and oscillation, and the optical Kerr effect and optical solitons. However, all of these effects require *many* photons. To make individual photons interact with each other, we need a qualitatively different system. To that end, an atom or atomic ensemble near resonantly coupled to an optical cavity mode can mediate photon-photon interactions. This is the realm of cavity quantum electrodynamics, which we now introduce.

$\star$. One loop QED corrections (at quartic order in the fine structure constant) do allow direct photon photon interactions via virtual electrically charged fermions or $W^\pm$ bosons. While this has been observed in accelerators, the cross section is *tiny* [124].

Deriving the Hamiltonian for the coupling of light with matter in the dipole and rotating wave approximations is hardly necessary given its many references and inclusion in basic atomic physics textbooks. However, a brief sketch of this derivation serves as a convenient place to define terms that will appear throughout this thesis. We follow closely the calculations of Scully and Zubairy [125].

The interaction of an atom with a light field may be written as

$$H = \sum_i E_i |i\rangle\langle i| + \sum_k \hbar\omega_k \left(a_k^\dagger a_k + \frac{1}{2} \right) - q\mathbf{r} \cdot \mathbf{E}. \tag{2.1}$$

Here E_i is the energy of an atom in state $|i\rangle$, $a_k^\dagger (a_k)$ is the creation (annihilation) operator for a photon in mode k with frequency ω_k, $\mathbf{r}$ is the position of the atom's relevant electron, and $\mathbf{E}$ is the electric field of the light, which we will assume is constant over the atom, i.e. the *dipole approximation*. We have included multiple atomic and optical modes for completeness, but we will now consider a two level atom interacting with a single mode mode—it is straightforward to reintroduce summations and indices later if more atomic or optical modes are needed.

Investigating the interaction part of the Hamiltonian,

$$e\mathbf{r} = \sum_{ij} q|j\rangle\langle j|\mathbf{r}|i\rangle\langle i| = \sum_{ij} d_{ij}\sigma_{ij}, \tag{2.2}$$

where $d_{ij} = q\langle j|\mathbf{r}|i\rangle$ is the electric dipole matrix element and $\sigma_{ij} = |j\rangle\langle i|$ is the atomic transition operator taking atomic state $|i\rangle$ to $|j\rangle$. Now, $d_{ii} = 0$ and $d_{ij} = d_{ji} = d$ for a two level atom. According to the dipole approximation, we evaluate the electric field at the position of the atom, so

$$\mathbf{E} = \hat{\epsilon}\mathscr{E}(a^\dagger + a), \tag{2.3}$$

where $\hat{\epsilon}$ is the polarization vector of the mode and $\mathscr{E}$ is the magnitude of the electric field

of a single photon at the location of the atom. We calculate $\mathscr{E}$ by distributing the energy of the single photon over the volume V of the mode in which the photon resides [126],

$$\mathscr{E} = \sqrt{\frac{\hbar\omega}{2\epsilon_0 V}} \tag{2.4}$$

with

$$V = \int |E(r,\theta,z)|^2 dV = \int_0^\infty 2\pi r\, dr \int_0^L dz\, e^{-2\,r^2/w_0^2} = \frac{1}{2}\pi w_0^2 L. \tag{2.5}$$

Diffraction does not play a role in calculating the mode volume because the 2D integrated energy density $\int |E(z)|^2\, 2\pi r\, dr$ is constant as the mode diffracts.

We combine the coefficients of the interaction part of the Hamiltonian into a single number,

$$g = -\frac{d\cdot\hat{\epsilon}\mathscr{E}}{\hbar}, \tag{2.6}$$

and write out the Hamiltonian as

$$H = \frac{1}{2}\hbar\omega_a\sigma_z + \hbar\omega a^\dagger a + \hbar g(\sigma_{ge} + \sigma_{eg})(a^\dagger + a), \tag{2.7}$$

where $\hbar\omega_a = E_e - E_g$ is the energy difference between the two atomic energy levels $|g\rangle$ and $|e\rangle$, $\sigma_z = \sigma_{ee} - \sigma_{gg}$, and we have dropped the constant zero point energy $\frac{1}{2}\hbar\omega$ and $\frac{1}{2}(E_g + E_e)$ terms.

Finally, we recognize that the interaction part of the Hamiltonian contains four terms. Two terms approximately conserve energy, $\sigma_{ge}a$ and $\sigma_{eg}a^\dagger$, while two terms change the energy by $\hbar(\omega + \omega_a)$, $\sigma_{ge}a^\dagger$ and $\sigma_{eg}a$. So long as atom-photon coupling $g \ll \omega$, it is reasonable to take

the *rotating wave approximation* where we drop the energy non-conserving terms[§]. Thus,

$$H = \frac{1}{2}\hbar\omega_a\sigma_z + \hbar\omega a^\dagger a + \hbar g(\sigma_{ge}a + \sigma_{eg}a^\dagger). \tag{2.8}$$

This is the famous Jaynes-Cummings Hamiltonian [129, 130]. It is straightforward to diagonalize since we begin with near-degenerate pairs of states $|e, n\rangle$ and $|g, n+1\rangle$, where the first index gives the state of the atom, and the second index gives the photon number in the optical mode (since this is by assumption an isolated mode, we will call this a cavity mode). These states are split by the detuning $\delta = \omega - \omega_a$ between the cavity photon frequency and the atomic transition frequency. When the coupling g is turned on, only pairs of near degenerate states mix and so shift to energies

$$E_{\pm,n} = \hbar\omega(n+1) + \frac{1}{2}\left(-\delta \mp \sqrt{4g^2(n+1) + \delta^2}\right). \tag{2.9}$$

For $|\delta| \gg g$, the eigenstates are approximately the original states, but each shifted apart by the cavity shift $E_{cs} = \frac{g^2}{\delta}(n+1)$, precisely like the ac Stark shift of an atom. This shift even exists for no population in the cavity mode; the coupling between the atom and *the cavity vacuum* causes a shift in the cavity photon and atomic transition frequencies of an amount g^2/δ!

For $|\delta| \ll g$, the atom-cavity eigenstates are basically the symmetric and antisymmetric superposition of the two bare states, with energies $E_{\pm,n} = \mp g\sqrt{n+1}$. Again, even the vacuum of the cavity mode causes a splitting between the coupled eigenstates, called the vacuum Rabi splitting. When the eigenstates are spectrally resolved, i.e. g is greater than

§. It is natural to wonder what happens when the atom-photon coupling g approaches or even surpasses the photon frequency ω. Clearly the rotating wave approximation is no longer valid, as all four interaction terms are relevant. These situations are described within the "ultrastrong coupling" and "deep strong coupling" regimes [127, 128], in which qualitatively new behaviors emerge. For instance, the ground state of such systems is no longer the product of a ground state atom with empty photonic modes, but rather includes virtual excitations with the mean photon number even exceeding 1, and for large enough g the ground state consists of photonic cat states entangled with the atomic state [127, 128].

the eigenstate linewidth, the only stationary states of the system are these eigenstates, superpositions of atomic and photonic excitations called polaritons.

Because the energy of an eigenstate of the Jaynes-Cummings Hamiltonian depends on the total excitation number, this Hamiltonian provides a nonlinearity which is useful for quantum computing and information processing [84, 129, 131–146] and quantum simulation‡ [83, 107, 108, 110, 113, 117, 118, 147, 148]. For example, if an external drive has energy $\hbar\omega + g$, it can excite a single symmetric polariton. But the energy needed to add a second polariton is $\hbar\omega + g(\sqrt{2}-1)$, so the external drive is off resonance for the second transition by an amount $\hbar g(\sqrt{2}-2)$. For large g, this effectively makes the single atom, single cavity mode system a two-level emitter, but where the excitation is part photonic, rather than purely atomic.

2.1.1 The Cooperativity Parameter

But what counts as 'large g'? As has already been hinted at by mentioning polaritons being spectrally resolved, or the second polariton excitation being off resonance, we need to compare g to the cavity and atomic loss rates, κ and Γ. The cavity loss rate $\kappa = \frac{\omega_{FSR}}{F} = \frac{c}{L}\frac{L_{ic}+\sum T_i}{2\pi}$ comes from finite transmission through the cavity mirrors, T_i, and intracavity scattering and absorption L_{ic}, while the atomic loss rate $\Gamma = \frac{1}{4\pi\epsilon_0}\frac{4\omega^3 d^2}{3\hbar c^3}$ arises from spontaneous emission of an atom into free space. The width of the symmetric and anti-symmetric polaritons is the average of κ and Γ, so we might consider the unitless parameter

$$\frac{2g}{\kappa+\Gamma}$$

‡. This sentence is almost certainly the largest understatement of this thesis. I have included a selection of references which is by no means exhaustive of the enormous literature using the Jaynes-Cummings Hamiltonian for various purposes. It is beyond the scope of this thesis to give a detailed review of the various platforms, techniques, schemes, and purposes represented in these works.

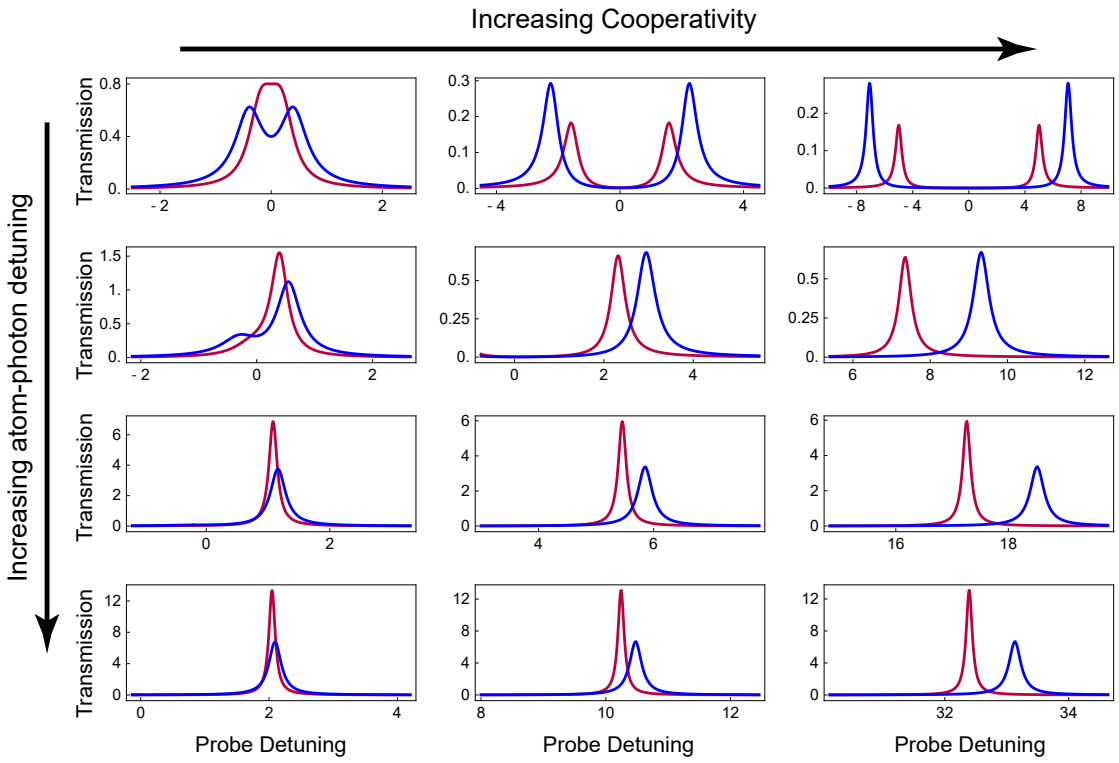

Figure 2.2: **Transmission Spectra for a Jaynes-Cummings System.** A single atom inside a cavity produces a spectrum* which is markedly different for zero (red) and one (blue) preexisting excitation. As the atom-photon coupling (here expressed as a cooperativity) increases, the nonlinearity grows. As the atom-photon detuning increases, the nonlinearity shrinks, but the polariton linewidths also shrink (in the limit $\kappa < \Gamma$), producing a local maximum in the nonlinear shift relative to polariton linewidth. This calculation is taken at parameters $\eta = \{4, 100, 1000\}$, $\delta = \sqrt{\eta} \times \{0, 1/8, 1/2, 1\}$, $\kappa = 0.1$, $\Gamma = 1$. * Interpreting the "two excitation" (blue) curves as spectra is really only valid in the detuned limit when there exists a photon-like polariton which can be doubly excited. At small detunings, the two excitation curves are better thought of as the transmission conditioned on measuring two photons, akin to a g_2. Nevertheless, these curves provide a measure of "how nonlinear" the system is.

as the relevant figure. While this parameter does determine if the polaritons are spectrally resolved, it is overly pessimistic. A more meaningful parameter is the cooperativity,

$$\eta = \frac{4g^2}{\kappa\Gamma} \tag{2.10a}$$

$$= \frac{6F}{\pi}\frac{1}{k^2 w_0^2} \tag{2.10b}$$

$$= \frac{F}{\pi}\frac{\sigma_{atom}}{\sigma_{photon}}, \tag{2.10c}$$

These equalities are quite remarkable and lie at the heart of many experimental design considerations. Equation 2.10a casts the cooperativity as the ratio of rates of coherent to incoherent processes: Since $1/g$ gives the time for a coherent Rabi oscillation of a photon into an atomic excitation and back and $1/\kappa, \Gamma$ gives the lifetime of a cavity photon or excited state atom, the cooperativity measures the average number of coherent oscillations before the excitation is lost. While all three of these quantities depend on the entire system, with both g and Γ requiring a detailed quantum mechanical derivation, plugging in the definitions of the quantities given above yields equation 2.10b where the ratio is expressed with only three geometrical system parameters, the cavity finesse F, the cavity waist size w_0, and the wavelength of light $\lambda = 2\pi/k$. In particular, the cavity length L and the electric dipole matrix element d drop out$^{\diamond}$, implying that neither the total mode volume nor the strength of the atomic transition affect the fundamental behavior of the system**. Finally, equation 2.10c recasts the cooperativity as the probability for the atom to absorb a photon, given by the ratio of the atomic cross section $\sigma_{atom} = \frac{3\lambda^2}{2\pi}$ and photonic cross section $\sigma_{photon} = \pi w_0^2$, enhanced by (twice) the number of round trips $n_{rt} = 1/(L_{ic} + \sum T_i)$. Thus the ratio which was originally quantum mechanical in definition and meaning reduces to a purely geometric classical form! This form also provides additional meaning, since $\sigma_{atom}/\sigma_{photon} \ll 1$ gives the probability P_{abs} that the atom absorbs the photon in the absence of the cavity. Although the finesse is in principle arbitrary, so η is not required to be less than one, and so η cannot simply be the cavity enhanced probability that the atom absorbs the photon, it turns out that

$$P_{abs} = \frac{\eta}{1+\eta} \tag{2.11}$$

$\diamond$. As we will see in section 2.1.2, with many atoms in the cavity, the waist size also drops out leaving only the 2D atomic density as the physically relevant parameter.

$\star\star$. Although that is not to say that they are irrelevant. Narrower features make experiments more susceptible to inhomogeneous broadening. The cavity length also directly controls the data collection rate $\propto \kappa$ and both parameters control various lineshapes, accurate measurements of which are helpful for calibration and troubleshooting.

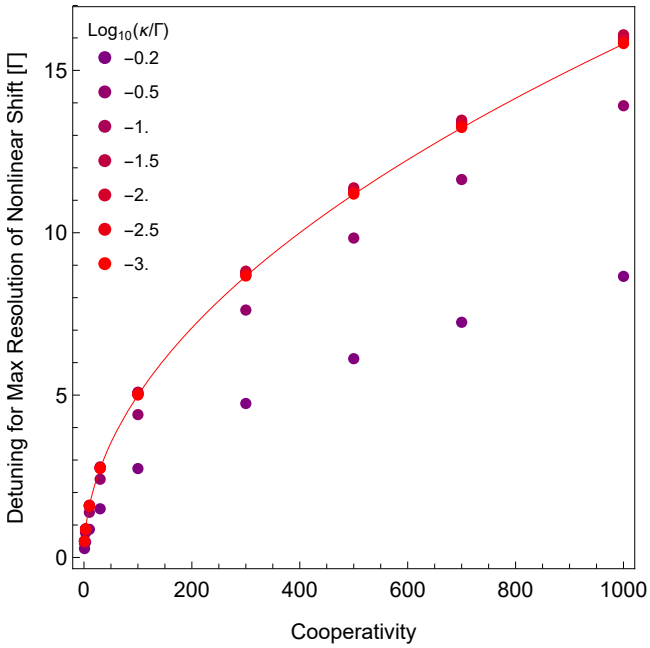

Figure 2.3: **Maximal Resolving Power of Jaynes-Cummings Nonlinearity.** As the detuning δ increases, the cavity-like polariton's linewidth reduces from $\frac{1}{2}(\kappa+\Gamma)$ to κ, so that the Jaynes-Cummings nonlinear shift χ_{JC} is easier to resolve. However, the magnitude of the shift decreases like δ^{-1} for large δ, making χ_{JC} harder to resolve. Optimizing the ratio of χ_{JC} to the polariton linewidth over the detuning δ (points) reveals that the optimal detuning is given by $\frac{1}{2}\sqrt{\eta}$ (red curve) in the limit of $\kappa \ll \Gamma$.

is the cavity enhanced probability that the single atom absorbs a single photon. Similarly, the optimal Jaynes-Cummings nonlinearity between zero and one intracavity photon, in terms of the linewidth of the polariton [136], is given *solely* by the cooperativity[§§],

$$\chi_{JC} = \frac{1}{2}\sqrt{\eta} \tag{2.12}$$

which occurs at the detuning $\delta = \frac{\Gamma}{2}\sqrt{\eta}$. This provides an example through which to understand in what sense our first guess of unitless parameter $\frac{2g}{\kappa+\Gamma}$ was pessimistic: it gives the resolving power at zero detuning where the polariton linewidth is larger; optimizing over the detuning generally improves the resolving power significantly. More generally,

$$\left(\frac{2g}{\kappa+\Gamma}\right)^2 = \frac{\eta}{2+\frac{\kappa}{\Gamma}+\frac{\Gamma}{\kappa}} \leq \frac{\eta}{4}.$$

§§. This calculation is performed in the limit $\kappa < \Gamma$.

As these considerations imply, achieving $\eta > 1$ is the essential ingredient for making use of the Jaynes-Cummings nonlinearity.

2.1.2 Many Atoms in a Cavity: Collective Enhancement

While the Jaynes-Cummings nonlinearity is useful for numerous applications, it comes with serious challenges. In particular, for a single atom trapped inside an optical cavity, achieving a sufficiently high cooperativity is quite challenging. A photon mode size of 300 nm is required to make $\sigma_{atom}/\sigma_{photon} = 1$ for the 780 nm D2 line of Rubidium; a state of the art finesse 100,000 cavity with a waist size of 10 μm provides a cooperativity of only 30. A significantly higher atom-photon coupling is available by placing many atoms in the photonic mode. As we will see, $g \to g\sqrt{N_{atom}}$ and so $\eta \to N_{atom}\eta$. Thus we can achieve a total cooperativity of 100 with ~ 1000 atoms in the waist of a finesse ~ 2000 cavity with a waist size between 12 - 20 μm.

This parameter regime is much easier to achieve and leaves room for more complex cavity designs while increasing the single photon collection rate by a couple orders of magnitude. We now calculate the effect of including many atoms in a cavity mode l by writing down the N-atom version of the Jaynes-Cummings Hamiltonian of equation 2.8, i.e. the Tavis-Cummings model [131]

$$H = \hbar\omega_l a_l^\dagger a_l + \sum_{k=1}^{N} \frac{1}{2}\hbar\omega_a \sigma_z^k + \hbar g_l^k(\sigma_{ge}^k a_l + \sigma_{eg}^k a_l^\dagger), \tag{2.13}$$

where σ_{ij}^k is the atomic transition operator for the k^{th} atom, and g_l^k is the atom-photon coupling rate for that atom to the cavity mode l excited by $a_l^\dagger$. This atom dependent coupling rate follows the cavity mode's electric field profile, ϕ_l, so that $g_l^k(\mathbf{x}) = g_0\phi_l(\mathbf{x}_k)/\phi_0(0)$, where g_0 is the rate of a single atom coupling to a single photon when centered at the peak of the

fundamental mode of the cavity, as calculated previously. We can then define the collective excitation operator

$$p_l^\dagger = \frac{1}{g_l} \sum_{k=1}^{N_{at}} g_l^k \sigma_{ge}^k \tag{2.14}$$

with $g_l = \sqrt{\sum_{k=1}^{N_{at}} |g_l^k|^2}$, so that the many atom Hamiltonian becomes

$$H = \hbar\omega_l a_l^\dagger a_l + \hbar\omega_a p_l^\dagger p_l + \hbar g_l (p_l^\dagger a_l + p_l a_l^\dagger). \tag{2.15}$$

If all atoms have the same coupling to the cavity mode, then $g_l = \sqrt{\sum_k |g_l^k|^2} = g_0\sqrt{N_{at}}$, reflecting the typical $\sqrt{N}$ *collective enhancement* due to multiple emitters [125, 149]. Indeed, this result might have been anticipated from the $\sqrt{n_{photon}}$ scaling of the atom-photon coupling in the eigenenergies of the Jaynes-Cummings model (see Eq. 2.9). Even though atoms will be distributed at uniform density across the mode profile, we will typically refer to a smaller effective atom number, each with the full coupling g_0. It is straightforward to obtain atomic densities of 10^{11} cm^{-3} with cold thermal atomic gas, while a BEC provides atomic densities above 10^{13} cm^{-3}. In a 20 μm thick cloud, this yields an atomic column density of 2 - 200 μm^{-2} and an effective atom number given a 20 μm mode waist of 1300 - 130,000 atoms.

The collective enhancement in the atom-photon coupling rate directly leads to an enhanced collective cooperativity,

$$\eta = N\frac{4g_0^2}{\kappa\Gamma} \tag{2.16}$$

indicating an accessible three to five orders of magnitude enhancement compared to a single atom system. A further advantage arises when using an ensemble of atoms since the mode size drops out of the collective cooperativity:

$$g_0^2 \propto 1/V \propto 1/w^2 \quad \text{while} \quad N \propto d\,w^2.$$

As the mode waist size increases, the reduced coupling per atom is offset by the increased number of atoms, assuming a constant atomic density d, giving a constant collective cooperativity. Only the atomic column density, cavity finesse, and atomic transition wavelength determine the collective cooperativity.

The cost of collective enhancement in the atom-photon coupling and the cooperativity is loss of the Jaynes-Cummings nonlinearity [131]. The nonlinearity arises because of the saturability of a single atom, so qualitatively, we can expect roughly N polaritons to reside in the cavity before the atomic ensemble is saturated. More precisely, one can show that collective excitation operator's commutation relation is

$$[p, p^\dagger] = 1 - 2\frac{n_e}{N}. \tag{2.17}$$

So, when the number of excited atoms n_e (roughly, the number of polaritons) is much less than the number of atoms, the commutation relation of the polariton creation and annihilation operators is that of a harmonic oscillator. As the sample becomes nearly saturated, p and $p^\dagger$ naturally switch roles, so the commutator switches sign.

Despite this loss of nonlinearity directly arising from cavity QED, collectively enhanced atom-photon coupling is still a promising ingredient for quantum nonlinear optics, since polaritons may interact directly through their atomic part. While ground state interaction energies are uselessly small given achievable polariton lifetimes, *Rydberg polaritons*—which are each a superposition of a photon in the cavity and a Rydberg excitation of the atomic sample—offer large interaction energies useful for creating nonlinearity at the single particle level [85, 100, 150–153].

2.1.3 Calculating Spectra with Non-Hermitian Perturbation Theory

It is worth pausing briefly at this point to discuss a very useful technique for calculating the transmission spectrum of a cavity coupled to atoms. While direct computation from the Schrödinger equation (typically in the Heisenberg or interaction formulation for computational simplicity) certainly works, it can become quite tedious for multilevel atoms and/or multimode cavities. However, perturbation theory allows for calculating the weakly driven steady state of the system via a single inversion of the Hamiltonian matrix, which is easy to write down and efficient to calculate. The only complication is the inclusion of optical and atomic loss. The loss rates may be calculated in several ways: the cavity loss rate can be written down classically as $\kappa = 2\pi \times \frac{c}{LF}$ while both the cavity and atomic loss rates can be calculated quantum mechanically through Fermi's golden rule or the Wigner-Weisskopf theory of spontaneous emission [125]. In any case, given these loss rates, it is a remarkable fact that they may often[‡‡] be included in the Hamiltonian as an imaginary contribution to the energy[◇◇]

$$\hbar\,\omega_l \to \hbar\left(\omega_l - \frac{i}{2}\kappa_l\right), \qquad \hbar\,\omega_a \to \hbar\left(\omega_a - \frac{i}{2}\Gamma\right). \tag{2.18}$$

Driving the cavity mode l with a laser of frequency ω and strength v corresponds to a term in the Hamiltonian $v\,e^{i\omega t}\,(a_l^\dagger + a_l)$. Thus we may write out the Hamiltonian for multiple

‡‡. Caveat emptor. If the decay leaves the system in a state from which it is likely to be re-excited, then the diagonal element of the density matrix corresponding to the decay product should increase as the decay progresses. This is relevant in highly nonlinear systems, such as a single atom coupled to a cavity mode with cooperativity $\eta > 1$. In these cases, thankfully a full master equation treatment including the appropriate Lindblad terms is available to incorporate just these effects!

◇◇. The origin of the factor of $\frac{1}{2}$ is straightforward. A hand-waving explanation goes as follows: The probability of measuring a single photon in a cavity decays as $P_c(t) = e^{-\kappa t}$, and we have freedom to add numerical factors in κ as we wish to make this true. Since the observed probability decays as $e^{-\kappa t}$, the amplitude must decay as $e^{-\frac{\kappa}{2}t}$ and $\psi = e^{iHt}$. So the diagonal element of H that yields the amplitude to be in the excited state must be $-\frac{i}{2}\kappa$.

atoms in a driven cavity in the frame rotating with the drive as

$$H = \begin{pmatrix} 0 & v & 0 \\ v & \Delta_l - \frac{i}{2}\kappa & \sqrt{N}g \\ 0 & \sqrt{N}g & \Delta_e - \frac{i}{2}\Gamma \end{pmatrix} \tag{2.19}$$

where the detunings $\Delta_l = \omega_l - \omega$, $\Delta_e = \omega_e - \omega$ and

$$\begin{pmatrix} 1 \\ 0 \\ 0 \end{pmatrix} = |0, G\rangle, \qquad \begin{pmatrix} 0 \\ 1 \\ 0 \end{pmatrix} = |1, G\rangle, \quad \text{and} \quad \begin{pmatrix} 0 \\ 0 \\ 1 \end{pmatrix} = |0, E\rangle.$$

The first index of each ket indexes the photon number in the cavity, while the second index lists the state of the atoms: $|G\rangle$ indicates all atoms in their ground state, while $|E\rangle = p^\dagger|G\rangle$ indicates the collective excited state. Note that we have truncated the Hilbert space to either zero or one excitation in the system, which is reasonable because we assume weak driving. If we also know that the system is linear, the spectrum we compute will be accurate even at higher probe strengths.

Following Ref. [116, 153, 154], the inclusion of imaginary terms in the Hamiltonian alters the structure of normal perturbation theory. It is essential that the bras $\langle\psi_n|$ and kets $|\psi_m\rangle$ satisfy $\langle\psi_n|\psi_m\rangle = \delta_{n,m}$, where $\delta_{n,m}$ indicates the Kronecker delta function. With Hermitian Hamiltonians, this is enforced by forming the bras by taking the Hermitian conjugate of the kets. With non-Hermitian Hamiltonians, this construction is insufficient. However, it is straightforward to find the set of kets that ensures $\langle\psi_n|\psi_m\rangle = \delta_{n,m}$ given the set of bras which are the eigenvectors of the Hamiltonian. Using these kets rather than the Hermitian conjugates of the bras then allows normal perturbation theory to proceed. In fact, all we will need is the single bra $\langle\psi_0|$ corresponding to the state about which we apply perturbation theory $|\psi_0\rangle$.

We write $H = H_0 + V$ where V is a small perturbation which only couples the known state $|\psi_0\rangle$ into the rest of the Hilbert space, i.e. $\langle\psi_0|V|\psi_0\rangle = 0$. In the example above,

$$H_0 = \begin{pmatrix} 0 & 0 & 0 \\ 0 & \Delta_l - \frac{i}{2}\kappa & g\sqrt{N} \\ 0 & g\sqrt{N} & \Delta_e - \frac{i}{2}\Gamma \end{pmatrix}, \quad V = v \begin{pmatrix} 0 & 1 & 0 \\ 1 & 0 & 0 \\ 0 & 0 & 0 \end{pmatrix}, \quad \text{and} \quad |\psi_0\rangle = \begin{pmatrix} 1 \\ 0 \\ 0 \end{pmatrix}.$$

Turning the crank of perturbation theory in powers of v to obtain the steady state wavefunction $|\psi_{ss}\rangle = |\psi_0\rangle + |\psi_1\rangle$, we find the correction to be

$$|\psi_1\rangle = (\varepsilon_0 \mathbf{1} - H_0)^{-1} QV|\psi_0\rangle$$

where ε_0 is the energy of the known state $|\psi_0\rangle$, $\mathbf{1}$ is the identity matrix, and $Q = \mathbf{1} - |\psi_0\rangle\langle\psi_0|$ projects onto the subspace orthogonal to $|\psi_0\rangle$. Given the Hamiltonian written above, it is not permitted to go beyond first order, since additional states in and couplings to the two excitation manifold must be included. However, with the sufficient Hamiltonian, this results at second order in

$$\begin{aligned} |\psi_{ss}\rangle &\approx (\mathbf{1} + G_0 V + G_0 V G_0 V)|\psi_0\rangle \\ G_0 &= (\varepsilon_0 N_{ex} - H_0)^{-1} Q, \end{aligned} \tag{2.20}$$

where N_{ex} is the operator that counts the number of excitations in the system.

This is now very useful as we can compute the cavity transmission spectrum given a Hamiltonian which could include multiple atomic states or optical modes via a single matrix inversion. The transmitted power ratio is $T = \frac{\kappa}{R_{in}}\langle\psi_{ss}|a^\dagger a|\psi_{ss}\rangle$, that is, we take the expectation value of $a^\dagger a$ times κ as the rate of photons leaking out of the cavity and compare that to the incident photon rate R_{in}. Comparison with a bare cavity driven by $V = v\,(a^\dagger + a)$ yields

$R_{in} = 4v^2/\kappa$. Then, to first order, we find

$$T(\omega) = \frac{\kappa^2}{4v^2}\langle\psi_{ss}|a^\dagger a|\psi_{ss}\rangle = \frac{\kappa^2}{4}\left|\langle 1|\frac{1}{\varepsilon_0\tilde{\mathbf{1}} - \tilde{H}_0}|1\rangle\right|^2. \tag{2.21}$$

where, in the second equality $a^\dagger a = |1\rangle\langle 1|$ at this order, and the superscript tildes indicate that these operators act only on the strongly coupled manifold, i.e. we have simply dropped $|\psi_0\rangle$ from the Hilbert space. The example Hamiltonian above is written in the frame rotating with the laser drive at frequency ω so the energy of the vacuum state is $\varepsilon_0 = 0$; however, including the energy offset $\varepsilon_0\tilde{\mathbf{1}}$ is essential when the utilized rotating frame sets the energy of the vacuum to be non-zero.

2.2 Cavity Rydberg Electromagnetically Induced Transparency

Having learned how to handle efficiently calculations involving more complex Hamiltonians, we now introduce our scheme for producing Rydberg polaritons. Creating a strong coupling between cavity photons and Rydberg excitations requires using three level atoms in a scheme called electromagnetically induced transparency, or EIT [155–160]. Although the direct ground to Rydberg transitions, around 297 nm for Rubidium, are much weaker than the D2 line, this is not relevant for the cooperativity. However, these transitions are very much not closed. Additionally, the UV wavelengths required are far from ideal for high efficiency optical control and detection. These considerations motivate using a two laser, three atomic level EIT scheme in which cavity photons are resonant with the 780 nm D2 line, while a strong control field near 480 nm couples the $P_{3/2}$ "intermediate" state to a Rydberg state. Ignoring Rydberg-Rydberg interactions, all levels in this system are harmonic, so we can understand the resulting level structure by considering what happens with a single excitation. The extrapolation to many excitations is then trivial. Therefore, we can write down a simple three state Hamiltonian for the coupling of a single cavity photon to a collective intermediate

state, and the coupling of that intermediate state to a collective Rydberg state ($r^\dagger|0,G\rangle$ where $r^\dagger = \frac{1}{g}\sum g^k \sigma^k_{gr}$ in exact analogy to the definition of $p^\dagger$ above*):

$$H_0 = \begin{pmatrix} \delta_c - \frac{i}{2}\kappa & g & 0 \\ g & -\frac{i}{2}\Gamma & \Omega \\ 0 & \Omega & \delta_r - \frac{i}{2}\gamma_r \end{pmatrix}. \tag{2.22}$$

This Hamiltonian is written in the frame rotating with the D2 transition frequency, $g = g_0\sqrt{N}$ is the total atom-photon coupling rate, Ω is the control field Rabi frequency coupling the intermediate state to the Rydberg state, and γ_R is the linewidth of the Rydberg state. As discussed later in section 2.2.2, this linewidth is often dominated by sources of decoherence other than the natural linewidth, for instance, laser linewidths, electric field inhomogeneities, or Doppler broadening.

2.2.1 Dark Polaritons

As a general feature and the primary use of EIT, this Hamiltonian provides for an eigenstate which is purely a superposition of the first and third states, that is, in our system, a superposition of a cavity photon and a collective Rydberg excitation. This can be seen

$\star$. While this is sufficient for the theory presented here, it is worth writing down the correct operators in a continuum limit with a atomic cloud of longitudinal length L,

$$p^\dagger(x) = \sqrt{\frac{1}{L}}\int_{-L/2}^{L/2} dz\, p^\dagger(x,z) e^{-ik_{cav}z}$$
$$r^\dagger(x) = \sqrt{\frac{1}{L}}\int_{-L/2}^{L/2} dz\, r^\dagger(x,z) e^{-i(k_{ctrl}-k_{cav})z}.$$

We have assumed that the cavity and control field are counter propagating. This z dependence will be important for understanding Doppler decoherence of dark polaritons.

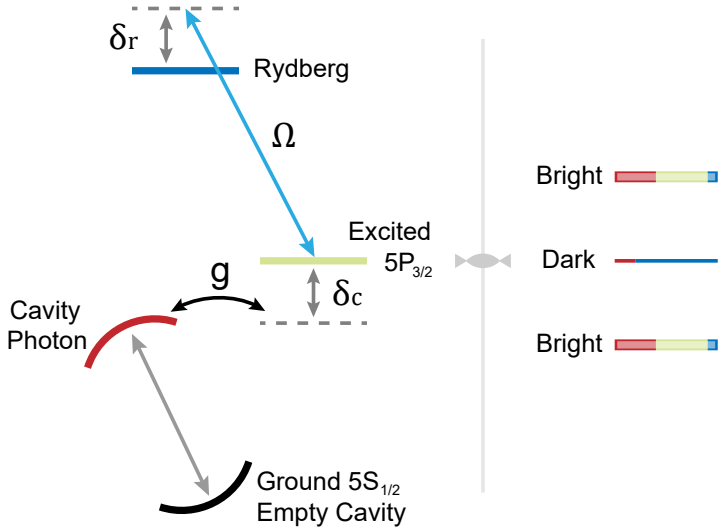

Figure 2.4: **Cavity Rydberg EIT Level Structure.** A single cavity photon is coupled with total Rabi frequency g to a collective P state which is also coupled with Rabi frequency Ω to a collective Rydberg state. The detuning of the cavity resonance frequency from the D2 atomic resonance frequency is δ_c, while the detuning of the control laser frequency from the P to Rydberg transition frequency is δ_r. These three strongly coupled states produce three polaritonic eigenstates, a dark polariton and two bright polaritons.

immediately by plugging the Hamiltonian into the Schrödinger equation

$$\begin{pmatrix} \dot{c}_c \\ \dot{c}_p \\ \dot{c}_r \end{pmatrix} = \frac{1}{i} \begin{pmatrix} \delta_c - \frac{i}{2}\kappa & g & 0 \\ g & -\frac{i}{2}\Gamma & \Omega \\ 0 & \Omega & \delta_r - \frac{i}{2}\gamma_r \end{pmatrix} \begin{pmatrix} c_c \\ c_p \\ c_r \end{pmatrix} \tag{2.23}$$

neglecting linewidths, and guessing that $\dot{c}_p = c_p = 0$,

$$\dot{c}_c = -i\delta_c c_c$$

$$\dot{c}_p = 0 = -i\left(g c_c + \Omega c_r\right)$$

$$\dot{c}_r = -i\delta_r c_r$$

If we make the further approximation that $\delta_c = \delta_r$, which corresponds to enforcing two-

photon resonance, the vector

$$\psi_D = \frac{1}{\sqrt{g^2+\Omega^2}} \begin{pmatrix} \Omega \\ 0 \\ -g \end{pmatrix} = \begin{pmatrix} \cos\theta_D \\ 0 \\ -\sin\theta_D \end{pmatrix} \tag{2.24}$$

is clearly an eigenvector of the Hamiltonian with eigenvalue δ_c. The second equality writes this eigenstate, the dark state polariton, in terms of the cosine and sine of the dark state rotation angle, $\theta_D = \tan^{-1}(g/\Omega)$. This parameter sets how photon-like and Rydberg-like the dark polariton is. Two additional bright polaritons complete the triad of eigenstates of this three state Hamiltonian (with $\delta_c = \delta_r = 0$),

$$\psi_{B\pm} = \frac{1}{\sqrt{2}} \begin{pmatrix} \sin\theta_D \\ \pm 1 \\ \cos\theta_D \end{pmatrix}. \tag{2.25}$$

In figure 2.5a, we use the methods of section 2.1.3 to calculate a typical cavity EIT spectrum. Instead of a single cavity resonance, we find three resolved resonances: a tall, narrow dark polariton resonance at laser detuning $\delta_L = 0$ flanked by two shorter broad bright polariton resonances. We operate in the limit of large dark state rotation angles, so our dark polariton is mostly Rydberg like. In contrast, in addition to their broad width, this means that the bright polaritons have little overlap with a Rydberg excitation and so have negligible interactions. While they are important for interpreting spectra and quantitative analyses of system dynamics, we will focus on understanding dark polaritons.

Since there is zero population in the intermediate state, dark polaritons are unaffected by the linewidth Γ of the intermediate state; thus dark polaritons are typically much narrower—and therefore scatter fewer photons than—the bright polaritons. The linewidth of a dark

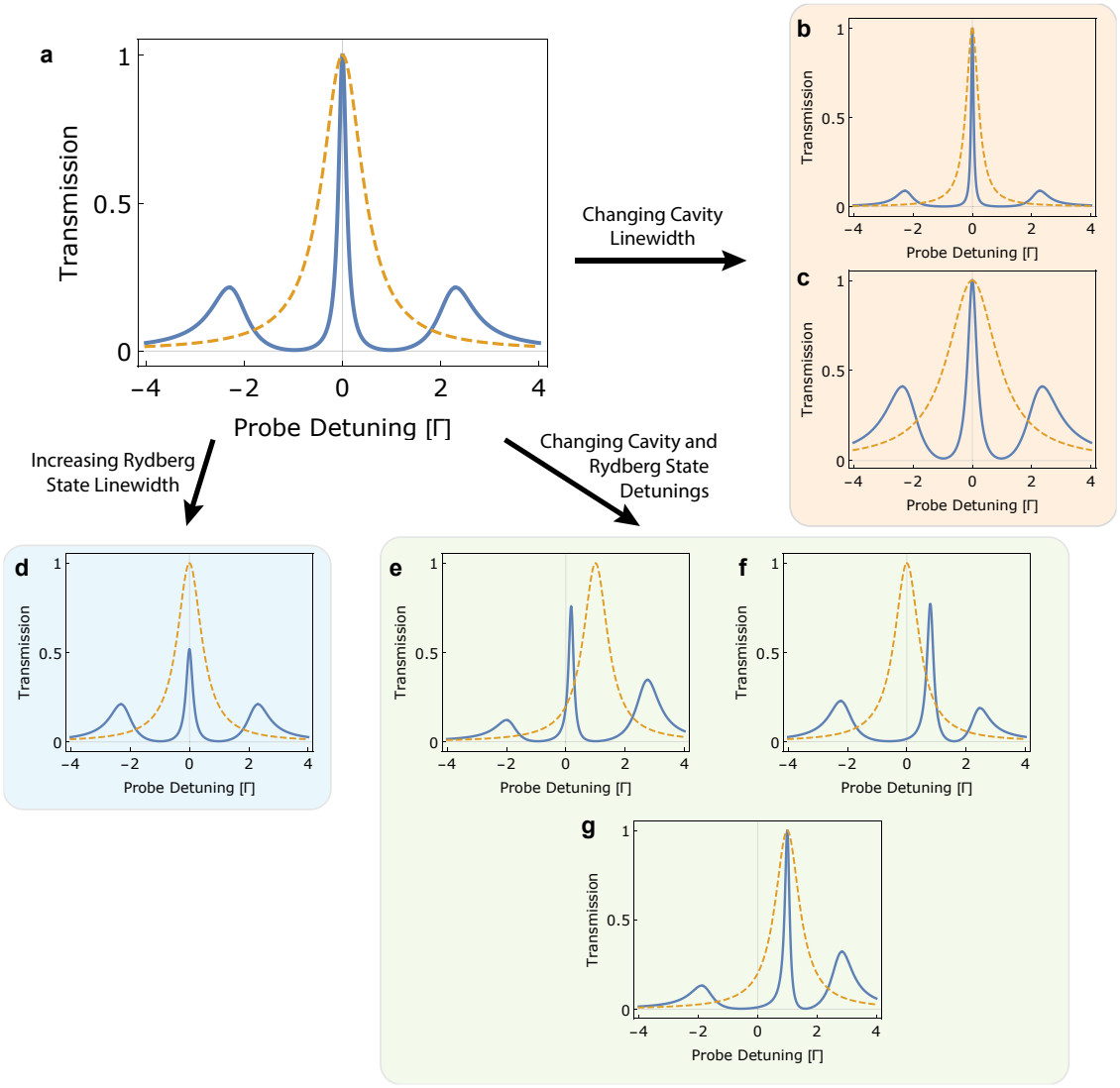

Figure 2.5: **Theoretical Dependence of Cavity Rydberg EIT Spectra on Various Parameters** **(a)** The "regular" EIT spectrum with parameters $\{g,\ \Omega,\ \kappa,\ \delta_c,\ \delta_r,\ \gamma_r\} = \{2, 1, 1, 0, 0, 0\}\ \Gamma$ is calculated using non-Hermitan perturbation theory, as described in section 2.1.3. The tall, narrow dark polariton resonance occurs at $\omega_l = 0$ and reaches the full cavity transmission rate (orange dashed line). The bright polaritons appear at $\pm\sqrt{g^2 + \Omega^2}$ and have peak transmission $(\kappa/(\kappa + \Gamma))^2$. **(b,c)** Decreasing (to $\kappa = 0.5\ \Gamma$) or increasing (to $\kappa = 2\ \Gamma$) the cavity linewidth does not change the peak dark polariton transmission rate, but it does affect the polaritons' linewidths as well as the bright polariton transmission rate. **(d)** Even a small Rydberg state loss (here $\gamma_r = 0.1\ \Gamma$) dramatically reduces the peak dark polariton transmission. **(e-g)** Detuning either the cavity or the Rydberg state causes a significant reduction of the dark polariton transmission and a increase in the dark polariton linewidth, since the two photon resonance condition is broken. However, if both the cavity and the Rydberg state are detuned by the same amount, which is equivalent to only detuning the intermediate state, then the two photon resonance condition is preserved and the full dark polariton transmission occurs.

polariton is

$$\gamma_D = \kappa \cos^2\theta_D + \gamma_R \sin^2\theta_D + a(\delta_c - \delta_r)^2, \tag{2.26}$$

where $a = 4\Omega^2 g^2 \Gamma/(\Omega^2 + g^2)^3$ is the coefficient of the second-order correction [116]. The first order term $\gamma_D = \kappa \cos^2\theta_D + \gamma_R \sin^2\theta_D$ is simply interpreted as the linewidth of each state times the probability that the dark polariton is measured to be in that state. Since Rydberg states are typically quite narrow compared to the cavity, the dark polariton is typically much narrower than the cavity mode that supports it. Thus dark polaritons are long lived-quasiparticles, with increased lifetime at larger dark state rotation angles and increased transmission at lower dark state rotation angles. This control makes them particularly attractive as the constituents of a nonlinear system, where their utility depends on the ratio of the available interaction energy (which increases as $\sin^4\theta_D$, see below) to the individual polariton linewidth.

The second order correction depends on the detuning from two photon resonance; the splitting $\delta_c - \delta_r$ which doubles the polariton decay rate is $\Delta = \frac{\Omega^2/\Gamma}{\sqrt{\eta}}/\cos^2\theta_D$. This detunes the energy of the dark polariton by $\Delta\cos^2\theta_D = \frac{\Omega^2/\Gamma}{\sqrt{\eta}}$, which is the same as the free space EIT linewidth [156]. This linewidth can be understood as a spectral window for interacting dark polaritons, in that dark polaritons stop being useful quasiparticles for detunings $(\delta_c - \delta_r) > \Delta$. In addition to broadening, dark polaritons' amplitude also shortens as the two photon resonance condition is broken by more than Δ. The peak transmission follows a squared Lorentzian profile

$$T_d \propto \frac{1}{\left(1 + \frac{(\delta_c - \delta_r)^2}{(\Gamma_w/2)^2}\right)^2},$$

so the EIT window width $\Gamma_w \approx 2\Delta$ sets the bandwidth for dark polariton dynamics and interactions [116]. More precisely, in a multimode cavity where dark polaritons have kinetic energy for their motion in the transverse plane, Γ_w sets the maximum kinetic energy. Similarly, a quantum gate reliant on detuning from EIT resonance (e.g. [97]) has a minimum

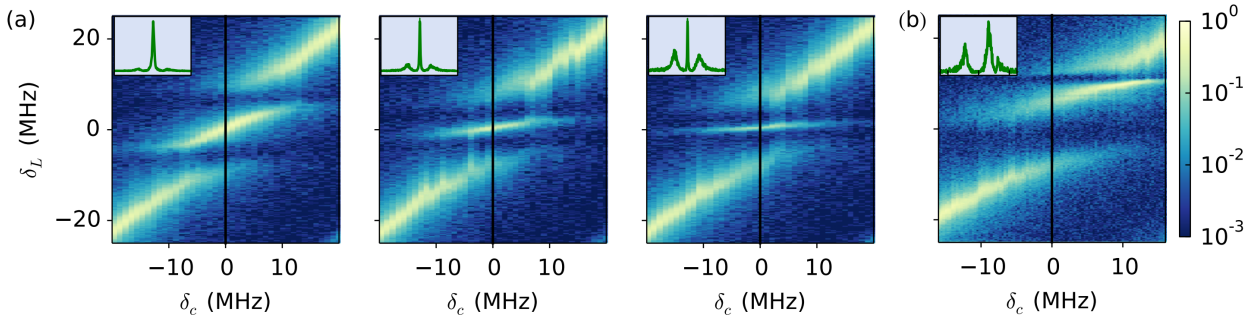

Figure 2.6: **Spectroscopy of Cavity Rydberg Polaritons.** To explore single particle properties of cavity Rydberg polaritons, the control laser is tuned to excite the weakly interacting 40S state. **(a)** Cavity transmission spectra versus cavity detuning δ_c at three values of the control field Rabi frequency, $\Omega = 13.1(1)$, 6.9(1), and 4.9(1) MHz ($g = 12.3(2)$, 13.0(1), and 14.7(1) MHz). The corresponding dark state rotation angles are $\theta_D = 43$, 62, and 72 degrees. As the dark state rotation angle increases, the dark polariton becomes more Rydberg-like, making the dark polariton peak narrower versus the probe laser frequency δ_L and reducing the slope of the dark polariton resonance frequency versus the cavity frequency δ_c. The width in δ_c over which the dark polariton has high transmission corresponds to the EIT window. **(b)** Cavity transmission spectra vs cavity detuning with significant control laser detuning $\delta_r = 9.8(4)$ MHz ($g = 16.8(3)$ MHz and $\Omega = 8.2(6)$ MHz). The colorbar indicates the transmission as a fraction of the bare cavity transmission on a logarithmic scale. Insets are spectra along the centered vertical black lines. Figure taken from Ref. [158].

gate time $\sim 1/\Gamma_w$.

2.2.2 Decoherence

Rydberg polaritons are sensitive to a variety of decoherence mechanisms. These typically increase the effective Rydberg state loss γ_r. Beyond straightforward broadening effects such as laser linewidths or cavity shaking, Rydberg polaritons are particularly sensitive to Doppler broadening and electric field inhomogeneity, compared to ground state EIT systems. Doppler broadening is enhanced because the collective Rydberg state has a phase grating written onto the atoms' excitation amplitude of $e^{i\mathbf{k}_r \cdot \mathbf{x}}$ where the wavevector of the spin wave is the difference between the wavevector of the probe and control files: $\mathbf{k}_r = \mathbf{k}_c - \mathbf{k}_p$. Since ground state EIT uses 780 nm photons that differ by 6.8 GHz, in a counter-propagating configuration, $|\mathbf{k}_r| = 2\pi/(44\text{ mm})$. However, for Rydberg EIT, the k-vectors do not nearly cancel, creating a grating with $|\mathbf{k}_r| = 2\pi/(1.2\ \mu\text{m})$. Finite temperature blurs out the phase grating of the collective Rydberg state when the thermal motion of the atoms has moved

them by about half the phase grating period. Thus the naive (it will turn out better than this!) Doppler decoherence rate is

$$\gamma_{kv} = 2\pi \times \frac{k_r}{\pi}\sqrt{k_B T/m} \tag{2.27}$$

where k_B is Boltzmann's constant, and T and m are the temperature and mass of the atoms. This a small but non-negligible rate of $2\pi \times 80$ kHz at 25 μK. Similarly, a spatially dependent spread in the ground-Rydberg energy difference due to an inhomogeneous electric field or a confining trap causes the Rydberg state phase to evolve at different rates at different locations and thus decoheres the collective Rydberg state. The coupling rate to the bath of bright states is $\gamma_{\delta E} \approx \alpha\, E\, \delta E$ where α is the DC electric polarizability of the Rydberg state, E is the magnitude of the electric field at the location of the atoms, and δE is the magnitude of the variation of the electric field across the sample.

In fact, these sources of broadening are suppressed. The phase scrambling couples the desired collective Rydberg state to a bath of other collective Rydberg states, distinguished by different phases of each element in the superposition. Each of these collective Rydberg states is coupled with Rabi frequency Ω to a corresponding collective P state, but these are *not* coupled to the cavity mode. Thus, in the rotating frame, Doppler decoherence couples dark polaritons with a rate γ_{kv} to a bath of states detuned by Ω. As long as the decoherence is smaller than Ω and Γ, this effect suppresses the additional loss rate of dark polaritons to

$$\Gamma_{Dop} = \alpha \frac{\gamma_{kv}^2 \sin^4\theta_D}{\Omega^2}\Gamma \tag{2.28}$$

where is α is a numerical factor of order unity and the bare coupling γ_{kv} is rescaled by $\sin^2\theta_D$ to reflect the fraction of the polariton which is a Rydberg excitation. For the parameters demonstrated in figure 2.6, this reduces Doppler broadening at 25 μK to less than 10 kHz. The same treatment applies for broadening due to inhomogeneous electric fields or confining

traps.

A more complete analysis of the effect of atomic motion is carried out in Georgakopoulos *et al.* [161], which further includes effects unique to multimode cavities including thermalization of atomic motion into polaritonic degrees of freedom. The analysis above reproduces the basic result that decoherence is suppressed by the detuning of the bath from resonance by Ω; physically, the presence of the control field continuously "refreshes" the spin wave back into the original configuration.

Perhaps surprisingly, an inhomogeneous control field does not broaden dark polaritons, at least for small variations in intensity, since the collective Rydberg state renormalizes its density in inverse proportion to the local control field intensity [158]. Of course, if the control field nearly vanishes anywhere, atoms at that location become two-level scatterers, greatly increasing cavity photon loss rate and greatly lowering the atom-photon cooperativity.

Finally, there are three additional sources of broadening that arise purely when considering polaritons, which we reproduce here without derivation from Georgakopoulos *et al.* [161]. The first arises as an off resonant direct coupling of dark polaritons to bright polaritons when two photon resonance is broken, resulting in

$$\Gamma_{D\to B} \approx 2\frac{(\delta_c - \delta_r)^2 \cos^4\theta_D}{\Omega^2}\Gamma. \tag{2.29a}$$

The final two sources are interaction induced broadening corresponding to collisions that take two dark polaritons to either two bright polaritons resonantly or to a single bright and single dark polariton off-resonantly:

$$\Gamma_{DD\to BB} = 2\sin^4\theta_D \cos^4\theta_D \frac{U_{eff}^2}{\Gamma} \tag{2.29b}$$

$$\Gamma_{DD\to DB} = 4\sin^8\theta_D \cos^2\theta_D \frac{U_{eff}^2}{g^2}\Gamma \tag{2.29c}$$

where U_{eff} is a phenomenological effective delta function interaction strength. In our typical limit of Rydberg-like dark polaritons, $\theta_D \rightarrow \pi/2$ and so the $DD \rightarrow DB$ process is the dominant interaction induced loss process. This inelastic process has also been investigated theoretically by Grankin, *et al.*, who show that these collisional effects are visible without correlations [162]. While the dramatic dependence on the rotation angle makes these processes weak for typical conditions, direct observation of inelastic collisions are now within reach. In combination with interaction induced blockade, this offers a route towards dissipative stabilization of photon number states.

2.2.3 Polariton-Polariton Interactions

Rydberg polaritons interact with each other through their Rydberg component. This interaction can be made quite large since the Rydberg-Rydberg interaction is a van-der-Waals interaction of the form

$$U(x - x') = c_l(\theta)\frac{C_6}{|x - x'|^6} \tag{2.30}$$

where $c_l(\theta)$ gives the angular distribution of the interaction potential (for S states, $c_l \sim 1$). The van-der-Waals coefficient C_6 grows very rapidly with principal quantum number, $C_6 \propto n^{11}$ enabling strong nonlinearities [85, 153, 163–169] for a variety of quantum applications [99, 100, 112, 116, 121, 150, 170–177].

Since this interaction strength falls rapidly with distance, there is a natural length scale within which two Rydberg atoms interact strongly and beyond which two Rydberg atoms ignore each other. This is the Rydberg blockade radius, r_b, defined by when the interaction energy equals the dark polariton linewidth,

$$r_b = \sqrt[6]{\frac{C_6}{\gamma_D}}. \tag{2.31}$$

For the 100 S Rydberg state, $C_6 = 2\pi \times 56$ THz μm^6, so with a $2\pi \times 200$ kHz wide dark polariton, $r_b = 25$ μm[§].

For a cloud that is thin compared to the blockade radius, we can project the relative coordinate onto the transverse plane of the cavity so that the interaction Hamiltonian is

$$H_{int} = \frac{1}{2}\iint d^2x\, d^2x'\, r^\dagger(x) r^\dagger(x') U(x-x') r(x') r(x). \tag{2.32}$$

Neglecting Rydberg state loss and two photon detuning and calculating to lowest order in the ratio of the interaction energy to the EIT window, the interaction Hamiltonian projected onto the dark polariton manifold is

$$\hat{P}_D H_{int} \hat{P}_D = \frac{1}{2}\sin^4\theta_D \iint d^2x\, d^2x'\, \hat{n}_D(x)\hat{n}_D(x') U(x-x') \tag{2.33}$$

where $\hat{n}_D$ is the two dimensional number density operator for dark polaritons. That is, the interaction for dark polaritons is essentially a rescaled version of the bare Rydberg-Rydberg interaction.

At short distances, the Rydberg-Rydberg interaction mixes in additional states other than the two-dark-polariton state. When projected onto the dark polariton manifold, this results in a screened effective interaction potential which becomes imaginary at short distances [116],

$$\begin{aligned} U_{eff}(x-x') &= \frac{C_6}{C_6\chi + |x-x'|^6}, \quad \text{with} \\ \chi &= \frac{\delta_{1p} - \frac{i}{2}\Gamma}{\Omega^2} - \frac{1}{\delta_{1p} - \frac{i}{2}\Gamma}, \end{aligned} \tag{2.34}$$

§. Comparison with the Rydberg blockade radius is reliable only within an order-of-magnitude. We use this to guide our apparatus design and to develop intuition. In the end, to validate qualitative statements made using the blockade radius, full atomistic numerics using non-hermitian perturbation theory is necessary until a full robust effective field theory is developed [161].

where $\delta_{1p} = \delta_c + \delta_r$ is the single photon detuning. This effective potential introduces a length scale $\xi = |C_6\chi|^{1/6}$ for the separation below which interactions are primarily imaginary and constant with magnitude $|U_{eff}|(0) = \frac{\Omega^2}{\Omega^2+(\Gamma/2)^2}\frac{\Gamma}{2}$ and above which interactions are primarily real and sharply decaying. Especially because of the saturation of the effective interaction energy, it is especially important to obtain a narrow enough dark polariton so that the interaction energy can exceed the dark polariton linewidth at *some* separation. The cavity mode waist must be smaller than the blockade radius in order to ensure strong interaction induced blockade, and the naive calculation of the blockade radius from equation 2.31 implies that a sufficiently small cavity waist can ensure strong blockade even with a broad dark polariton. However, the interaction energy saturation depends only on Ω and Γ. Increasing the Rydberg level n increases the range over which polaritons interact with their saturated interaction energy, but, counter-intuitively, reduces the maximum interaction energy since the control field Rabi frequency scales as $n^{-3/2}$. On the other hand, reducing the dark polariton linewidth is always advantageous (except on the rate of data collection). This discussion mostly serves as a caveat to experimental planners against unguided reduction in cavity mode size or increased Rydberg level. These actions are difficult and do not necessarily help increase the accessible

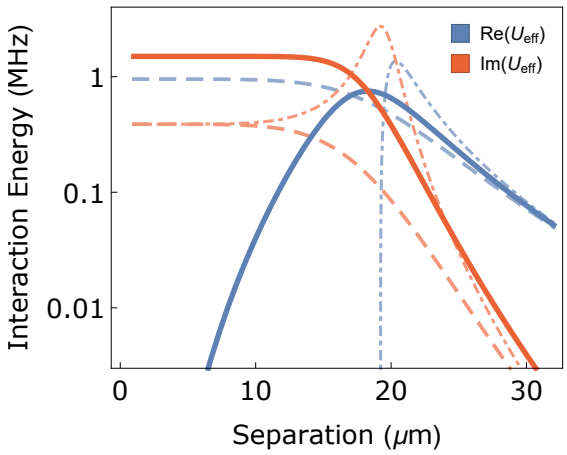

Figure 2.7: **Effective Interaction Potential for Dark Polaritons.** At large distances, dark polaritons directly inherit the real (blue curves) C_6/r^6 interaction potential of the underlying Rydberg atoms. However, at short distances, admixing of higher energy states causes interaction induced loss, which appears as an imaginary component (red curves) of the effective interaction potential. Remarkably, the short range interaction induced loss is *constant* with separation, indicating a saturation of the magnitude of the interaction energy (here, around 1 MHz for 100S Rydberg excitations). The crossover between a mostly real and mostly imaginary interaction energy occurs at the characteristic length scale $\xi \approx 18$ μm, defined in the text. A single photon detuning of one sign can make the short range potential real at the cost of reduced magnitude (dashed curves), while the other sign of single photon detuning reduces the real part of the interaction potential (dot-dashed curve). This calculation performed for the 100S state, with $C_6 = 56$ THz μm^6, $\Omega = 3$ MHz, and $\delta_{1p} = 0, \pm 9$ MHz.

polariton-polariton interactions.

For strongly interacting dark polaritons, the interaction energy approaches the dark-bright splitting and perturbation theory in the ratio of the interaction energy to the EIT window breaks down. In reference [161], Georgakopoulos, *et al.* develop an effective theory for dark polaritons in exactly this situation. Strong interactions at short range renormalized the two Rydberg state, reducing the control field coupling and the effective interaction energy. For example, in the extreme limit of strong interactions, they find that the two Rydberg excitations avoid each other enough to reduce the effective interaction strength to $\tilde{U} \approx \frac{1}{120}\frac{C_6}{w_0^6}$. The interaction energy arises primarily from Rydberg excitations separated by 2.2 w_0, more than the $1/e^2$ diameter of the available volume. Nevertheless, while this nonperturbative theory is necessary for a quantitative effective theory of strongly interacting dark polaritons, the simple model of equation 2.33 captures the essence of the system. Dark polaritons inherit polariton-polariton interactions through their underlying Rydberg-Rydberg interactions.

In a single mode cavity, the Hamiltonian for a photon is just $H_{phot}^{sm} = \delta_c - \frac{i}{2}\kappa$. We have already seen that the photonic contribution to the Hamiltonian for dark polariton is, to first order, $H_D^{phot,sm} = (\delta_c - \delta_r)\cos^2\theta_D - \frac{i}{2}\kappa\cos^2\theta_D$. This indicates that dark polaritons inherit single particle dynamics through their photonic part, rescaled by $\cos^2\theta_D$. As with the interaction Hamiltonian, higher order effects add additional broadening terms (see, for example, Eqn. 2.26).

Together, the rescaled Rydberg-Rydberg interaction Hamiltonian and single mode photonic Hamiltonian provide for a strongly interacting zero dimensional system, a polaritonic quantum dot [153], in which the transmission of photons through the cavity is strongly altered. Much like Coulomb blockade in a quantum dot [178–180], strong interactions imply only a single polariton can reside in the cavity at a time; there is no possibility of exciting a two polariton state in the cavity. Thus the transmitted light field only ever has a single photon within a time bin set by the dark polariton lifetime $\tau = \gamma_D^{-1}$ (see Ch.5).

In degenerate multimode cavities, the same behavior holds, although the photonic Hamiltonian is significantly more complex. For nearly degenerate sets of Hermite Gaussian or Laguerre Gaussian cavity eigenmodes, the dynamics of a photon in the cavity are equivalent to dynamics of a quantum harmonic oscillator potentially also subject to a constant magnetic field. As developed by Sommer, *et al.* in reference [181], by coarse-graining photons' motion over the round trip propagation, photons' transverse degrees of freedom reduce to an arbitrary quadratic Hamiltonian of the form

$$\begin{aligned} H_{phot} &= \int dx\, a^\dagger(x)\, h_{phot}\, a(x), \qquad \text{with} \\ h_{phot} &= \frac{\mathbf{\Pi}^2}{2m_p} + \frac{1}{2} m_p \omega_t^2 |x|^2 - \frac{i}{2}\kappa \end{aligned} \tag{2.35}$$

where the mechanical momentum $\mathbf{\Pi} = i\hbar\nabla - eA$, m_p is the effective transverse photon mass, and ω_t is the effective harmonic trap frequency. The available effective vector potentials eA are those corresponding to a constant effective magnetic field eB perpendicular to the transverse plane. The parameters eB, ω_t, and m_p are determined by cavity geometry: mirror positions and radii of curvature along with the nonplanar twist of the cavity mode [116, 161, 181, 182].

Following Georgakopoulos, *et al.* [161], to lowest order in $\frac{\omega_t^2}{\Omega^2+g^2}$, the polaritonic single particle Hamiltonian is identical to the Hamiltonian for cavity photons, up to a rescaling by $\cos^2\theta_D$. The dominant correction to this is a second order dark to bright polariton coupling. In the limit that the dark polariton with energy $E_D = (\delta_c - \delta_r)\cos^2\theta_D$ is well within the EIT window, this correction is primarily imaginary, increasing the dark polariton loss rate by

$$\Gamma_{D\to B} \approx 2\frac{(\delta_c - \delta_r)^2 \cos^4\theta_D}{\Omega^2}\Gamma$$

as listed above in equation 2.29a.

Combining the rescaled photonic Hamiltonian for the single particle dynamics and the

rescaled effective Rydberg interaction Hamiltonian for the two particle interactions, we arrive at the following Hamiltonian for interacting dark polaritons in a multimode cavity, in the limit that the interaction energy is small compared to the EIT window,

$$\begin{aligned} H_D &= \hat{P}_D(H_{tot} + H_{int})\hat{P}_D \\ &= \cos^2\theta_D \int dx\, \psi_D^\dagger(x) \left(\frac{\mathbf{\Pi}^2}{2m_p} + \frac{1}{2} m_p \omega_t^2 |x|^2 - \frac{i}{2}\kappa \right) \psi_D(x) \\ &+ \frac{1}{2}\sin^4\theta_D \iint dx\, dx'\, \hat{n}_D(x)\hat{n}_D(x') U_{eff}(x - x'). \end{aligned} \tag{2.36}$$

This Hamiltonian contains the basic ingredients for polaritons to form a quantum material. Polaritons can move in a continuous two dimensional space, potentially subject to a harmonic trap or a magnetic field while also strongly interacting with each other. The eigenstates of this system are therefore typically correlated quantum many body states. While the general connection between the intracavity polaritonic state and the emitted light field can be subtle, this enables the emission and detection of strongly correlated states of light, such as a Laughlin state (see Ch. 6).

Additional richness is possible via further control over the single particle and interaction Hamiltonians. Floquet engineering of atomic states offers the prospect of creating effective multilayer systems, which in the context of the fractional quantum Hall effect yield intriguing novel forms of topological order [52, 183]. Microwave driving of Rydberg states [102, 123] offers the prospect of dramatic fast manipulation of the Rydberg-Rydberg interaction energy, by enhancing the interaction strength by driving to a Förster resonance [96, 164][‡] Alternatively, microwaves may be used to zero the regular Rydberg-Rydberg interaction and

‡. These authors use static FÖrster resonances. The basic requirement is to reduce the pair state energy defect between the doubly excited Rydberg state and some other pair of Rydberg states connected by dipole matrix elements, which can be done by optimizing over the chosen Rydberg state and applying a DC electric field. However, off resonant microwave dressing allows the target pair state energy to be manipulated via the frequency and power of the microwaves, which could allow for dynamic control of the interaction energy of Rydberg polaritons.

create a pure three-body interaction [184, 185]. Either the appropriate addition of dipolar interactions through a Förster resonance or the production of pure three body interactions would in the context of the fractional quantum Hall effect produce a Pfaffian ground state and supports non-Abelian excitations [61, 186, 187].

2.2.4 Number of Collisions per Polariton Lifetime

In this section we will attempt to understand how well a polaritonic quasi-particle "holds together" in the face of forces on its photonic and and material components, with the former coming from an applied external potential and the latter from polariton-polariton collisions. We will find that, under optimal conditions, the polariton can undergo $\sim \sqrt{OD_B}$ collisions within its lifetime; this is an intuitively satisfying result because it says that our intuition that OD_B characterizes the "strength" of the coupling between the light and matter is correct.

2.2.4.1 Polariton-Confinement Collisions

The simpler story to understand is the interaction of a single polariton with a confining potential. We consider two photonic modes; a spatially even mode, and a spatially odd mode, with energy splitting Δ, and prepare our polariton in a superposition of these two modes. We would like to know how many oscillation cycles the polariton undergoes before it decays. Larger Δ means that the polariton oscillates more quickly, but will also eventually reduce its lifetime by driving one component of the superposition state out of the EIT window.

To quantitatively understand this problem, we compute the dependence of polariton linewidth and shift upon Δ, the energy of the odd-component of the polariton. We follow the derivation

in [116, 158], and find:

$$E_{pol} \approx i\frac{2\kappa\Omega^2}{4G^2+\kappa\Gamma+4\Omega^2} + \Delta\frac{16\Omega^2(G^2+\Omega^2)}{(4G^2+\kappa\Gamma+4\Omega^2)^2} + i\Delta^2\frac{32\Omega^2\Gamma(G^2+\Omega^2)}{(4G^2+\kappa\Gamma+4\Omega^2)^3}$$

Here the imaginary part of E_{pol} reflect its linewidth, and the real part its energy shift; it is thus apparent that $N_{coll} \approx \frac{Re(E_{pol})}{Im(E_{pol})}$. Writing $E_{pol} = i(\alpha+\beta\Delta^2)+\gamma\Delta$ and optimizing over Δ one finds a maximum of $N_{coll} = \frac{1}{2}\sqrt{\frac{\gamma^2}{\alpha\beta}}$ for $\Delta = \sqrt{\frac{\alpha}{\beta}}$. Substituting the full expressions for α, β and γ yields $N_{coll} = \sqrt{\frac{G^2}{\kappa\Gamma}} = \frac{1}{2}\sqrt{OD_B}$ (in the limit $\Omega \ll G$, where polaritons interact strongly and the quadratic expression for E_{pol} is valid).

2.2.4.2 Polariton-Polariton Collisions

Here we suppose that there is no limit upon the available interaction strength between Rydberg atoms, and attempt to compute how many "collisions" (how many 2π of interaction-phase) we can accumulate between a pair of polaritons within their lifetimes. At first glance, it appears that in the limit $\frac{\Omega}{g} \to 0$, $N_{coll} \to \infty$; the reasoning is that in the limit of no control field ($\Omega \to 0$), the polariton becomes infinitely long-lived (cavity leakage is reduced to nothing), with finite interaction strength. The problem with this argument is that the (infinitesimal) remaining photonic component will be unable to follow the rapidly evolving spatial mode of the Rydberg components.

Put another way, imagine a single mode optical cavity akin to the one employed in our experiments; the Rydberg-Rydberg interactions will provide an pairwise separation-dependent energy shift which rotates the two-polariton state out of the spatial mode of the cavity, thereby acting at least in part as a *decoherence* channel in the polariton basis!

To quantify this effect, we compute the perturbative impact of interactions between two dark polaritons: The "average" atomic interaction U_{rr} can be mapped onto the polariton-polariton interaction U_{DP} through the relation

$$U_{DP} = U_{rr} \sin^4 \theta_D. \tag{2.37}$$

Aside from the single polariton loss $\kappa \cos^2 \theta_D + \gamma_r \sin^2 \theta_D$ (note that we will assume $\gamma_r = 0$ for the remainder of this section), the interaction introduces two sources of decoherence: tuning of the individual polaritons out of the EIT window, and coupling to collective Rydberg/excited states that do not couple to the cavity mode. The extra loss caused by detuning is given by [158]:

$$\gamma_\Delta = \frac{2\Gamma U_{rr}^2 \sin^2 \theta_D}{(G^2 + \Omega^2)} \tag{2.38}$$

The interaction also couples the collective Rydberg state $|rr\rangle$ to another collective Rydberg state $|\tilde{rr}\rangle$ with a different Rydberg distribution (Fig. 2.8a). The control beam will then couple $|\tilde{rr}\rangle$ to a collective excited state $|\tilde{ee}\rangle$ that will not couple to the cavity mode due to symmetry. In the polariton basis (Fig. 2.8b), the Rydberg-Rydberg interaction couples the dark polariton state to the loss states detuned by Ω, and the interaction induced polariton loss can be calculated using the methods employed for collective Doppler decoherence suppression [158] as:

$$\gamma_{int} = \alpha \frac{U_{rr}^2}{\Omega^2} \Gamma \tag{2.39}$$

where α is the geometric factor of order unity reflecting the precise form of the interactions and the cavity mode.

The number of collision within a polariton lifetime can then be calculated as:

$$N_{coll} \approx \frac{U_{DP}}{\gamma_{DP}} \tag{2.40}$$

with:

$$U_{DP} = U_{rr} \sin^4 \theta_D \tag{2.41}$$

$$\gamma_{DP} = \kappa \cos^2 \theta_D + \gamma_\Delta + \gamma_{int}. \tag{2.42}$$

The optimal number of collisions is obtained by maximizing N_{coll} with respect to U_{rr} and Ω, and is given by

$$N_{max} = \sqrt{\frac{OD_B}{\alpha}} \tag{2.43}$$

where $OD_B = N\eta = N\frac{4G^2}{\kappa\Gamma}$ is the optical depth per blockade volume. This optimum occurs as the control field intensity vanishes $\Omega \to 0$, so long as the intrinsic decoherence of a single collective Rydberg excitation is ignorable $\gamma_r \approx 0$. Here we have used the fact that in our experiment all the atoms are distributed within a blockade volume.

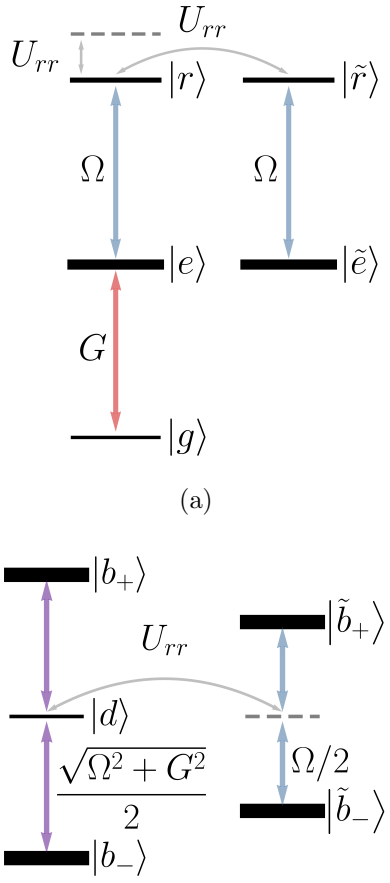

Figure 2.8: **Maximum polariton-polariton collision number. (a)** Three-level system with coupling (αU_{rr}) to another manifold of collective Rydberg $|\tilde{r}\rangle$ and excited states $|\tilde{e}\rangle$ that are uncoupled from the resonator. The Rydberg-Rydberg interaction detunes the Rydberg state and also couples the two manifolds. The extra states are coupled by the blue laser with Rabi frequency Ω. **(b)** The same system expressed in the polariton basis. The bright polaritons $|b_-\rangle$ and $|b_+\rangle$ are no longer at the same energy as the dark polariton $|d\rangle$ due to the probe and control field couplings. Similarly, the lossy manifold splits in energy because of the control field. Figure taken from Ref. [153].

CHAPTER 3

EXPERIMENTAL SETUP

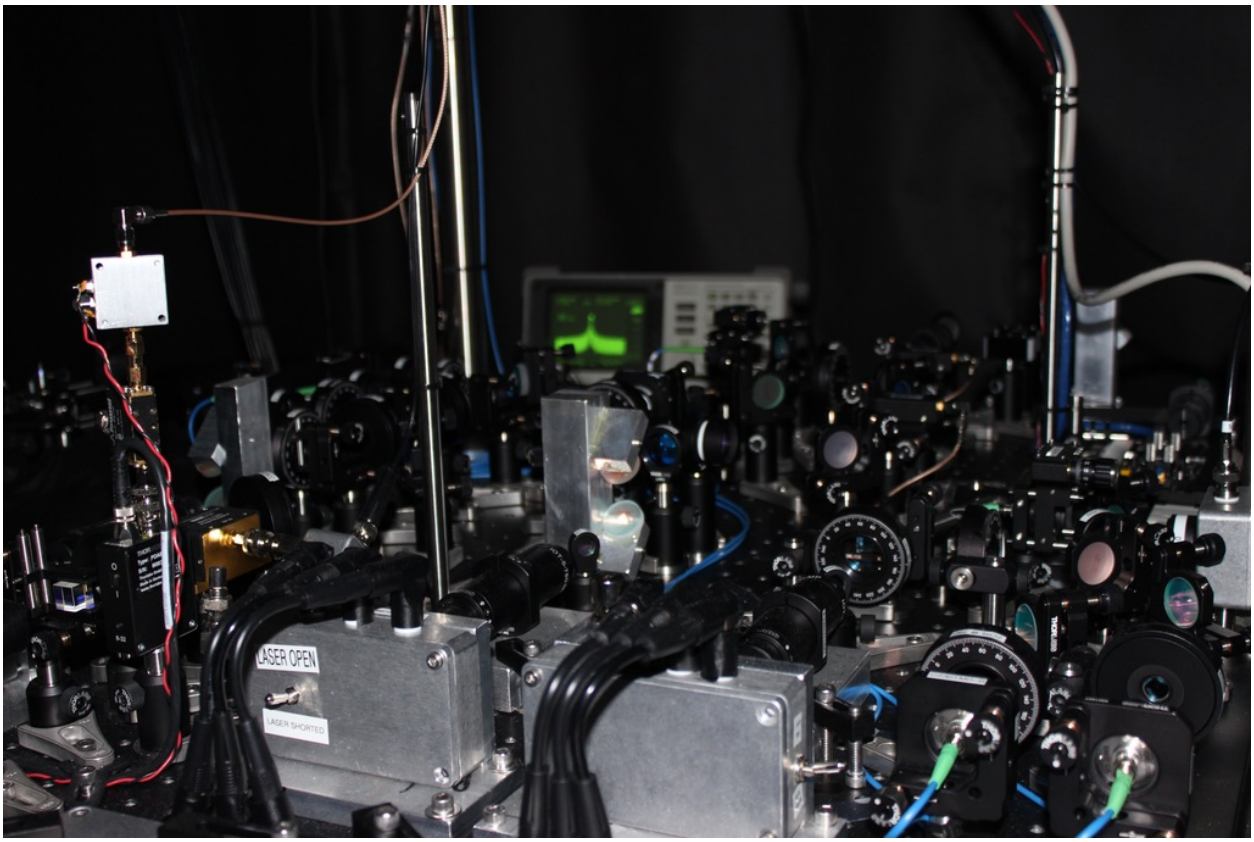

Figure 3.1: **The Laser Table.** A portion of the optical setup for the master, MOT, and repumping lasers is shown. In the background, a spectrum analyzer characterizes a beatnote lock.

In this chapter, we will introduce the hardware necessary for our experiments. Since all of our work has an optical cavity as a central element, we begin with a basic overview of optical cavities, focusing in particular on the experimental considerations which drive optical cavity design. We then move on to more nuts-and-bolts aspects of integrating an optical cavity into a useful apparatus including how to stabilize cavity length by generating an error signal and feeding back on a piezo actuator. Many of our optical cavities have multiple relevant transverse modes, and so we next introduce our primary tool for generating non-trivial optical modes: the digital micromirror device. With that, we will have introduced the necessary equipment for investigating novel optical cavities non-interacting topological

effects in light (Chapter 4).

Creating strongly interacting photons via Rydberg polaritons requires invoking the atomic physics toolbox for cooling, trapping, transporting, manipulating, and probing alkali atoms. As most of these tools are quite standard, we move rather quickly through our implementation of them. We conclude the chapter with two sections on somewhat more unusual techniques. The penultimate section discusses our procedures for atomic sample preparation, initially by 'slicing' the atomic ensemble into a thin pancake, and later upgrading to a degenerate Raman sideband cooling system followed by transfer into a shallow elliptical lattice. The final section discusses intermediate state modulation which enables redistributing the atomic density of states to bridge non-degeneracy between optical cavity modes.

3.1 Optical Cavities

At the heart of all of the experiments in my graduate work is an optical cavity. Also called an optical resonator or a Fabry-Pérot interferometer, this is an optical device of two or more mirrors pointed at each other so that the reflected light makes a closed round trip. This condition of a closed round trip implies the existence of optical resonances—the cavity only supports light which is in-phase with itself after one round trip. For a two-mirror cavity, this amounts to the condition that the cavity length is an integer multiple of half the wavelength of light. Like modes of a string, this implies that the cavity has a forest of resonances equally spaced in frequency (or, equivalently, cavity length). This frequency is called the free spectral range, which is given by $\nu_{FSR} = c/L$ where L is the total round trip length, and is the inverse of the time required for one round trip through the cavity.

We may see this mathematically by simply calculating the transmission through two reflective

surfaces as the (infinite) sum of transmitted electric fields, as shown in 3.2.

$$\begin{aligned} E_t &= E_i t^2 e^{ikL}(1 + r^2 e^{2ikL} + ...) \\ &= E_i e^{ikL} \frac{t^2}{1 - r^2 e^{2ikL}} \\ T &= \left|\frac{E_t}{E_i}\right|^2 = \frac{1}{1 + \mathcal{F}\sin^2(kL)} \end{aligned} \tag{3.1}$$

where $\mathcal{F} = 4R/(1-R)^2$ and $k = 2\pi/\lambda$. Converting the length dependence into frequency dependence and defining the finesse as $F = \frac{\pi}{2}\sqrt{\mathcal{F}}$, we have,

$$T = \frac{1}{1 + \frac{4}{\pi^2}F^2 \sin^2(\pi \frac{\nu}{\nu_{FSR}})} \tag{3.2}$$

This shows that an optical cavity's transmission is determined by two quantities, the free spectral range, which is set by the length, and the finesse, which is set by the mirror reflectivities. The arbitrary redefinition of the finesse utilized above is motivated by making F more physically meaningful. For high finesse cavities, the transmission expression Eqn.(3.2) amounts to individual Lorentzian profiles, each separated by ν_{FSR}. That is, near a resonance

$$T \approx \frac{1}{1 + (\frac{\omega - \omega_0}{\kappa/2})^2}, \tag{3.3}$$

where $\omega = 2\pi\nu$ is the angular frequency of the probe laser, ω_0 is the angular frequency of the nearby cavity resonance, and $\kappa = 2\pi\nu_{FSR}/F$ is the linewidth of the resonance. Thus, the finesse is the ratio of the spacing between neighboring resonances and their widths. Furthermore, in the high finesse limit, this definition of the finesse is given simply by the reciprocal of the round-trip loss, L_{rt}, $F = \frac{2\pi}{L_{rt}}$, with L_{rt} being the sum of all mirror transmissivities and other loss mechanisms, including scattering or absorption due to mirror surface imperfections, intracavity atoms, or just debris on the mirrors. Finally, since the round trip loss and the average number of round trips (measured until the intracavity intensity falls to $1/e^2$

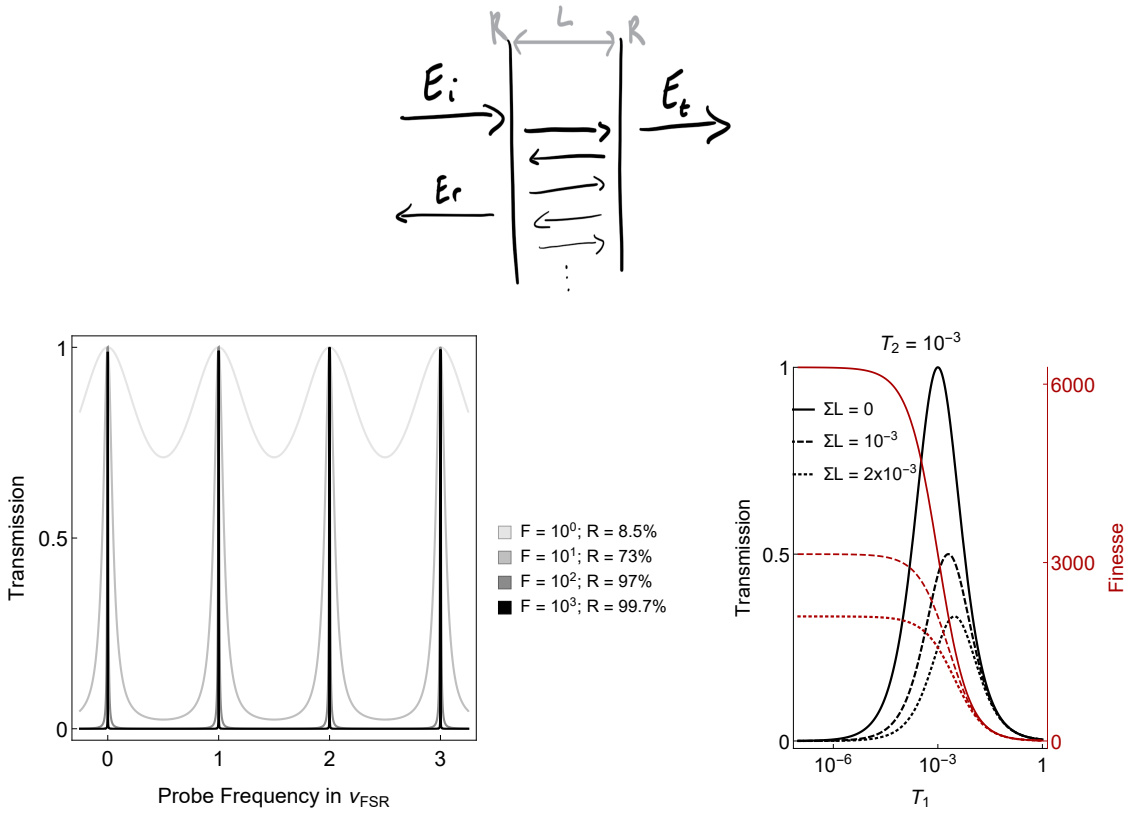

Figure 3.2: **Transmission through an optical cavity (a)** Two mirrors separated by a length L and of reflectivity R subject to an incident electric field E_i transmits an electric field E_t and reflects E_r. **(b)** The transmission through an optical cavity is plotted versus probe frequency at constant cavity length. Equivalently, the probe frequency could be held constant and the horizontal axis would then be labeled *Cavity Length L* [$\lambda/2$]. Each peak corresponds to excitation of a subsequent longitudinal mode of the cavity. **(c)** When the two mirror transmissivities are not equal, either higher or lower, the peak transmission is reduced from unity (black, solid). Given the quality of mirror fabrication, this issue is typically less severe than the presence of any loss, ΣL that is not due to the transmissivities of the in- or outcoupling mirrors (dashed or dotted). In addition to the reduction in the peak transmission, note that the optimal transmissivity of T_1 shifts upwards from the fixed T_2 by an amount ΣL.

of its initial value) quantify the same thing, we have $N_{rt} = F/2\pi$.

The transmission of the ideal optical cavity always goes to unity on each longitudinal resonance. In practice, this 'transmission dominated' regime is difficult to reach for two reasons, impedance matching and transverse mode matching. Impedance matching characterizes intracavity loss that differs from two equally transmissive mirrors. That is, if the input and output mirrors have different transmission coefficients T_1 and T_2 or if there are additional loss mechanisms, the transmission of the cavity will be less than unity. More precisely, the transmission fraction *on resonance* is $T = 4T_1T_2/L_{rt}^2$, with the standard Lorentzian frequency

dependence. In many cavities, especially those of high finesse, additional loss mechanisms are difficult to avoid and dramatically limit the cavity transmission. Therefore, in situations where total transmission efficiency is an important figure of merit, such as the cavities for the main Rydberg polariton experiments, blue light buildup, or mode sorting, extreme care must be taken to preserve mirror cleanliness, and strategic forethought must be exercised to balance the desire for higher finesse (and better ultimate physics) with realistic residual loss that limits cavity transmission.

3.1.1 Transverse Mode Structure

Further care must be taken to ensure proper matching between the incoupled field and the transverse electric field profile of the desired intracavity mode. The simplest solution for the transverse electric field profile of a cavity mode is a Gaussian in both transverse variables. Since the incoupling beam is also typically a Gaussian beam, there are therefore six beam parameters that must be well matched between the incoupling beam and the fundamental cavity mode: the waist position and orientation (x, y, k_x, and k_y) and waist size and longitudinal position (w_0 and z). These are grouped in this way since the first four are typically optimized using mirrors on the incoupling beam, while the final two are optimized by varying so-called mode-matching lenses given an incoupling beam size. The transverse modes of an optical cavity form an orthonormal basis (subject to compact support), so any mismatch in these six parameters between the incoupling beam and the cavity mode will cause the excitation not just of the lowest order mode but also higher order transverse modes, according to a standard overlap integral. That is, the amplitude $c_{n,m}$ for exciting the (n,m) transverse mode given an incident mode profile $E_{in}(\mathbf{x})$ is given by $c_{n,m} = \int E^*_{in}(\mathbf{x}) E_{n,m}(\mathbf{x})\, \mathrm{d}^2\mathbf{x}$.

The natural next question is, 'What are the transverse mode profiles of an optical cavity?' To approach this, we need to solve Maxwell's equations in a vacuum. Starting with the

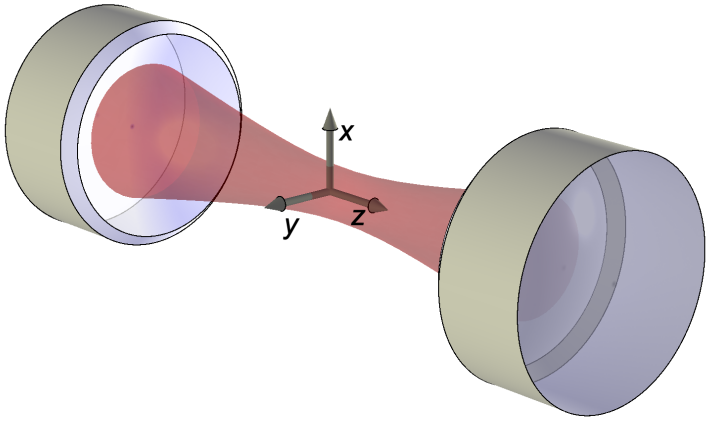

Figure 3.3: **Visualization of a two mirror cavity.** Two concave mirrors support a cavity mode with a three-dimensional electric field profile (red), which is represented as the surface where the intensity of light has fallen by $1/e^2$ relative to the axial intensity. The mirror curvature focuses circulating light so that there is a point of maximum intensity and minimum transverse extent, called the waist of the cavity, at which we define coordinate axes. By convention, the optic axis is the z direction.

scalar wave equation $\left(\nabla^2 + k^2\right) E(x, y, z) = 0$ and factoring out the fast z-dependent phase accrual e^{ikz}, we make a useful approximation, called the *paraxial approximation*, that the remaining, diffractive z-dependence in the electric field profile is slow compared to not only λ but also the transverse size of the beam. Thus we arrive at the paraxial wave equation:

$$2ik\partial_z u(\mathbf{x}) = \nabla_\perp^2 u(\mathbf{x}) \tag{3.4}$$

where $u(\mathbf{x}) = e^{ikz}E(\mathbf{x})$ and $\nabla_\perp^2$ is the Laplacian with respect to the transverse coordinates. At this point, we solve this equation by separation of variables, finding

$$HG_{n,m}(x, y, z) = N\frac{w_0}{w(z)}H_n\left(\frac{\sqrt{2}x}{w(z)}\right)H_m\left(\frac{\sqrt{2}y}{w(z)}\right)e^{-\frac{x^2+y^2}{w^2(z)}}e^{-i\frac{k(x^2+y^2)}{2R(z)}}e^{i\phi^G_{n,m}(z)}e^{ikz} \tag{3.5}$$

These are the Hermite-Gaussian electric modes for the electric field, where N is a normalization constant, $H_n(x)$ is the n^{th} Hermite polynomial, $w(z; w_0) = w_0\sqrt{1 + (z/z_R)^2}$ is the dependence of the mode waist size ($1/e^2$ intensity radius) on z, $R(z) = z\left[1 + \left(\frac{z_R}{z}\right)^2\right]$ is the dependence of the field curvature on z, $z_R = \pi w_0^2/\lambda$ is the Rayleigh range, and $\phi^G_{n,m}(z) = (1 + n + m)\arctan(z/z_R)$ is the Gouy phase. This can be generalized to allow for

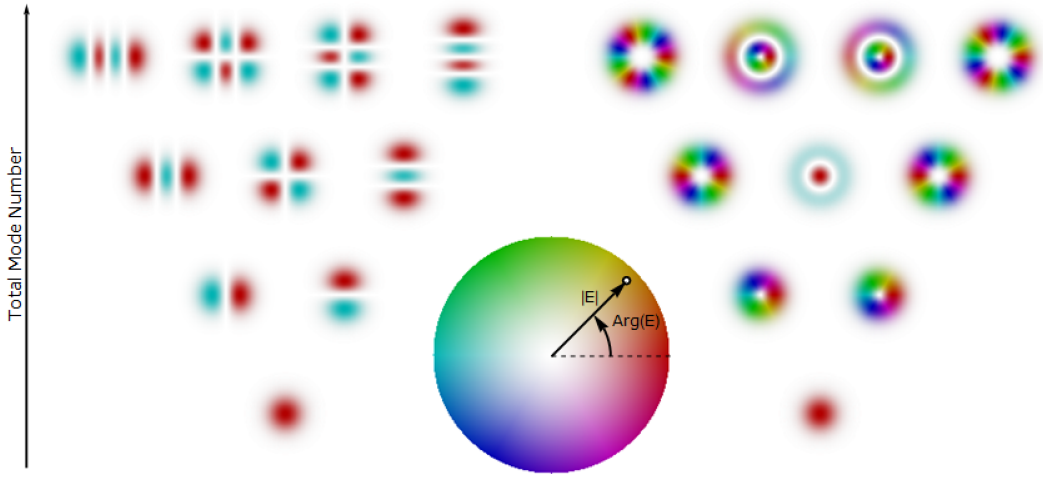

Figure 3.4: **Cavity Modes.** The Hermite-Gaussian modes (left) and Laguerre-Gaussian modes (right) are common orthonormal bases for expanding optical cavity electric field profiles due to the symmetries they respect. These are each plotted versus 'total mode number,' $n+m$ for the HG modes, and $|l|+2p$ for the LG modes. The colorscale encodes the electric field amplitude in the color saturation and the electric field phase in the hue. While the HG modes display only 0-π phase flips across nodal lines, LG modes show complex phase structure, both winding about the origin and flipping across azimuthal nodal rings.

the x and y waists to be in different locations and have different sizes.

The Hermite-Gaussian modes break azimuthal symmetry while maintaining a rectangular x, y symmetry. These modes are therefore natural for problems with cylindrical lenses or non-normal reflections off of curved mirrors. For problems that break a helical symmetry, or otherwise where a respect for azimuthal symmetry is desired, an equivalent orthonormal set of modes may be defined called the Laguerre-Gaussian modes for the electric field:

$$LG_{l,p}(r,\phi,z) = N\frac{w_0}{w(z)}\left(\frac{\sqrt{(2)}r}{w(z)}\right)^{|l|} L_p^{|l|}\left(\frac{2r^2}{w^2(z)}\right) e^{-\frac{r^2}{w^2(z)}} e^{-ik\frac{r^2}{2R(z)}} e^{-il\phi} e^{i\phi^G_{l,p}(z)} e^{ikz} \quad (3.6)$$

where p is the radial index, l is the azimuthal index, $L_p^{|l|}(r)$ are the generalized Laguerre polynomials, and $\phi^G_{l,p}(z) = (1+|l|+2p)\arctan(z/z_R)$. It is worth emphasizing that the $LG_{0,l}$ profiles may be cast as a particularly simple function of a single complex coordinate: $LG_{0,l}\left(z \equiv \frac{x+iy}{w_0/\sqrt{2}}\right) \propto z^l e^{-|z|^2/2}$. These modes are rings, the radii of which increase as $\sqrt{l}$,

and which have $2\pi \times l$ phase winding of the electric field around the ring. That is, these modes carry l units of orbital angular momentum.

3.1.1.1 Gouy phase and cavity mode degeneracy

The preceding discussion of transverse modes did not assume the presence of cavity mirrors, and was fully applicable to free space. As we turn our attention to the modes of an optical cavity, one term that deserves particular attention in both Eqn. (3.5) and Eqn. (3.6) is the Gouy phase term $\exp(i\phi^G)$. This term adds an additional pure phase due to passing through a focus, of an amount given by π times the total mode number; the arctangent factor accounts for propagation that does not both begin and end in the far-field of the focus. When propagating inside an optical cavity, this phase also shifts the resonant frequencies of higher-order transverse modes. When the fundamental mode accrues a round-trip phase of zero modulo 2π, the higher-order modes accrue an additional phase of $\phi^G_{n,m} - \phi^G_{0,0}$ which in general is *not* zero modulo 2π. That is, the frequency of the light must be adjusted so that additional propagation phase compensates for the different Gouy phase. Since the Gouy phase only depends on the total mode number, we naturally find families of degenerate higher-order modes, unless something comes along to break this degeneracy.

Two-mirror standing wave optical cavities intrinsically do not break any rectangular or rotational symmetry, so one might expect the degeneracy of higher-order modes to remain. However, it is typical for cavities of even moderate finesse (several hundreds to thousands) to show a slight mode splitting between otherwise degenerate Hermite-Gaussian modes, presumably due to minor mirror imperfections.

More exotic optical cavity geometries can lead to a dramatic breaking of the total mode number based degeneracy and even the formation of new degenerate sets of modes. For instance, a four mirror running-wave cavity in a planar bowtie configuration naturally breaks an x,

y symmetry, picking the in-plane (or *tangential*) and out-of-plane (or *sagittal*) transverse directions as special. This arises because non-normal reflection off of a curved mirror leads to effectively different radii of curvature, with the tangential curvature increased (shorter radius of curvature) and the sagittal curvature reduced (longer radius of curvature). Such astigmatic reflections make the mode waists different for the tangential and sagittal directions, producing different Rayleigh ranges, and thus different Gouy phases for round-trip propagation. Therefore we write down the expression for the cavity-round-trip Gouy phase as a sum of two terms:

$$\phi^G_{n,m} = \left(n + \frac{1}{2}\right)\phi^G_t + \left(m + \frac{1}{2}\right)\phi^G_s, \tag{3.7}$$

where $\phi^G_(t, s)$ are the additional Gouy phase accrued by a single transverse mode excitation in the tangential and sagittal directions, respectively. That is, $\phi^G_t = \phi^{G,r.t.}_{1,0} - \phi^{G,r.t.}_{0,0}$ and $\phi^G_s = \phi^{G,r.t.}_{0,1} - \phi^{G,r.t.}_{0,0}$, where the superscript $r.t.$ refers to calculating the full Gouy phase through a cavity round trip, which may include passage through multiple waists. The Gouy phase directly influences the resonant frequency of the cavity, such that a phase shift by 2π implies a shift in the resonant frequency by ν_{FSR}. So, we then have a simple expression for the resonances of all modes of an optical cavity in terms of only three quantities, the free spectral range and two round trip Gouy phases:

$$\nu_{n,m,q} = \left[q + \left(n + \frac{1}{2}\right)\frac{\phi^G_t}{2\pi} + \left(m + \frac{1}{2}\right)\frac{\phi^G_s}{2\pi}\right]\nu_{FSR} \tag{3.8}$$

for transverse mode indices n and m and axial mode index q. In most calculations, it is fine to drop the $+\frac{1}{2}$ terms as these provide mode number independent frequency shift, and we almost always only care about the frequency difference between modes.

Given a set of mirror locations and radii-of-curvature, it is thus possible to compute the spectrum of the resonator. However, the formalism presented above requires a tedious algebra

of Gaussian optics in order to compute cavity mode positions, sizes, and thus Gouy phases. There is a much simpler and more elegant approach, using so-called ABCD or ray transfer matrices, in which one calculates the *ray* optics round trip propagation around an optical cavity. Perhaps remarkably, *wave* optics quantities such as the waist sizes (at a reference plane) and round trip Gouy phases may then be obtained from the round trip ABCD matrix [188]. The round trip Gouy phases are calculated from the log of the eigenvalues of the round trip ABCD matrix, while the waists are computed from the eigenvectors. Furthermore, there is no requirement that the transverse modes of an optical cavity be either Hermite-Gaussian or Laguerre-Gaussian; these are just two well studies points in a large family of possible mode bases. The ABCD matrix eigenvectors further allow the construction of raising operators $a^\dagger_{1,2}$ for constructing the higher-order cavity mode profiles $\psi_{\alpha,\beta}(x,y) = \frac{1}{\sqrt{\alpha!\beta!}} a_1^{\dagger\alpha} a_2^{\dagger\beta}$. One subtlety with this mode construction is that the meaning of mode indices may be different than standard usage. For example, in cavities that support Hermite-Gaussian modes, the α and β indices have the same meaning as n and m, but for cavities that support Laguerre-Gaussian modes, $\alpha = p + \frac{|l|+l}{2}$ and $\beta = p + \frac{|l|-l}{2}$ correspond to adding $+1$ or -1 units of angular momentum. See appendix A.1.2 for details on these calculations.

Now knowing how to compute the mode spectra of cavities, we can introduce the various forms of cavity mode degeneracy. The 'default' mode degeneracy shown in Fig. 3.4 occurs because, by default, the two round trip Gouy phases are equal. A more general kind of degeneracy can form whenever $r\phi_1^G = s\phi_2^G$ for arbitrary integers r and s. These degeneracies are always between a finite number of modes.

A richer, infinite degeneracy occurs when $\phi_i^G = r/s$, so that increasing the i^{th} mode index by s and reducing the axial mode index by r produces another degenerate mode. For instance, when $\phi_i^G \to 1^-$ the cavity approaches the *concentric* limit, so named because in a two mirror cavity with equal radii-of-curvature, this occurs when the cavity length equals twice the radius-of-curvature and the mirrors are two caps of the same sphere. At this

limit, the cavity also becomes unstable, as every ray through the common sphere's center is equivalent and so there is no confinement of a circulating ray from walking to ever larger angles, eventually walking off the sides of the finite mirrors.

When $\phi_i^G = 1/2$ the cavity reaches the *confocal* limit. This name is given because when the cavity length equals the mirrors' radius-of-curvature, the mirrors share a common focal point ($f = R/2$). Here, the cavity supports only two distinct families of degenerate modes, the even and odd modes. This means that *any* electric field profile may circulate in the cavity so long as it possesses either even or odd symmetry. For many applications, such as using a scanning Fabry-Pérot cavity to analyze the spectrum of a laser, this is advantageous since mode matching is hardly necessary; any offcenter, poorly matched profile couples into two superposition states, the its symmetric reflection and anti-symmetric reflection, and strong transmission peaks occur every $\nu_{FSR}/2$.

Higher order degeneracies, such as $\phi_i^G = 1/s$ for $s \geq 3$, called s-fold degeneracies for lack of a better name, in general do not have such nice symmetry properties. That is, coupling an arbitrary off-center mode into a cavity where all $HG_{0,0}, HG_{s,0}, HG_{2s,0}, ...$ modes are degenerate does not produce an output that is trivially related to the input. However, these types of degeneracy are more interesting if Laguerre-Gaussian modes are used. Just as a confocal cavity supports an arbitrary offcenter mode subject to a reflection symmetry, a s-fold degenerate cavity supports an arbitrary offcenter mode subject to a s-fold rotational symmetry.

3.1.1.2 Multimode nonplanar cavities

It is interesting (and indeed fruitful! See chapters 4 and 6) to wonder how any cavity can break a right-left rotational symmetry so that Laguerre-Gaussian modes will be split out at different frequencies, much like the Hermite-Gaussian modes of an astigmatic cavity.

Physically spinning an intracavity dielectric medium could do it, but rotation frequencies above $\sim 10^8$ rpm would be required!* The answer comes from considering a four mirror running-wave *nonplanar* cavity. The nonplanarity causes a geometric rotation of all vectors perpendicular to the optic axis, including the polarization vector as well as the position vector of the transverse mode profile; this is a real-space manifestation of Berry's phase [189]. It is easy to position the mirrors so that the round trip rotation angle is significant, and this round trip rotation breaks the left-right rotational symmetry, splitting out circularly polarized Laguerre-Gaussian modes based on their total orbital angular momentum [190]. Of course time reversal symmetry is not broken by making the cavity nonplanar—the round trip rotation direction is flipped for the counter propagating mode, so the forward propagating $LG_{1,0}$ mode is degenerate with the backward propagating $LG_{0,1}$ mode. Application of a magnetic field on an intracavity medium or a spin polarized atomic ensemble is then required to break time reversal symmetry [191, 192]. Single mode nonplanar cavities are certainly not new, having found applications in laser design [191, 193], ring laser gyroscopes [194, 195], and even future gravitational wave detectors [196].

It is therefore reasonable to consider engineering a cavity which supports a degeneracy between multiple Laguerre-Gaussian modes. A cavity with all Laguerre-Gaussian modes degenerate is the same as a cavity with all Hermite-Gaussian modes degenerate, and is unstable because it is a fully concentric cavity. The confocal cavity ($s = 2$) with Laguerre-Gaussian modes is not stable for subtler reasons. Any nonplanar cavity must have some non-normal mirror reflections, and so must have some x-y astigmatism. The energy scale of this astigmatism can be small compared to the rotational splitting so that the eigenmodes are very nearly exact Laguerre-Gaussian modes; however, even small astigmatism can affect cavity stability at degeneracy. To see this, we note that the general astigmatic potential has the form of $\hat{x}^2 - \hat{y}^2$ for some choice of perpendicular axes x and y. This potential can be rewritten in

$\star$. Clever tricks involving slow light techniques inside a rotating atomic cloud might work, but that is definitely more difficult than our solution.

terms of rotational ladder operators:

$$\hat{x} = \sqrt{\frac{\hbar}{2m\omega}}(\hat{a}_x + \hat{a}_x^\dagger),\ \hat{a}_R = \frac{1}{2}(\hat{a}_x + i\hat{a}_y),\ \hat{a}_L = \frac{1}{2}(\hat{a}_x - i\hat{a}_y)$$
$$\hat{x}^2 - \hat{y}^2 = \frac{\hbar}{4m\omega}(\hat{a}_R^2 + \hat{a}_L^2 + 2\hat{a}_R\hat{a}_L^\dagger) + h.c. \tag{3.9}$$

where $\hat{a}_{(R,L)}^\dagger$ adds $+1$ and -1 units of angular momentum, respectively. Written in this form, it is clear that an astigmatic potential directly couples states that differ by two units of angular momentum. Therefore, as the confocal limit is approached, the energy splitting between modes that differ by two units of angular momentum becomes small compared to astigmatism, and so astigmatism couples photons to states of ever higher angular momentum. Since these high angular momentum modes have large spatial extent, this coupling quickly guides photons out past the edge of the cavity mirrors, causing dramatic loss.

Therefore, the lowest order degeneracy that results in a stable cavity with Laguerre-Gaussian modes is the 3-fold degenerate cavity, although higher $s \geq 4$ degeneracies are certainly possible.

3.1.1.3 Formal analogy between paraxial wave equation and the quantum harmonic oscillator

The transverse mode solutions for the paraxial wave equation are suggestively similar to the solutions to a massive quantum particle in a harmonic trap. This arises because of the formal equivalence between the paraxial wave equation and the Schrodinger equation for a quantum harmonic oscillator.

This is perhaps most intuitive in the near planar limit, i.e. the mirrors' radii-of-curvature are much larger than their separation. In this limit, in the ray-optics picture, bounce between the mirrors quickly, while only slowly oscillating in the transverse plane due to mirror curvature.

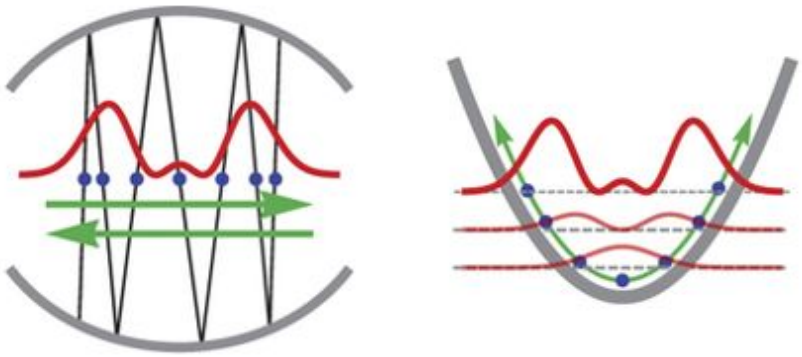

Figure 3.5: **Stroboscopic Evolution of a Near Planar Cavity.** As a photon bounces back and forth between two mirrors, mirror curvature causes side-to-side oscillation (black lines). This oscillation appears stroboscopically as a Poincare hit pattern at the transverse plane of the cavity (blue dots). Coarse-graining over the longitudinal degree-of-freedom provides effective dynamics in the transverse plane corresponding to harmonic motion (green arrows). In the wave optics picture, this results in Hermite-Gaussian mode profiles (red curve). In the right panel, the objects from this story reappear in the coarse-grained effective theory. Figure adapted from Ref. [182].

As the distance between the cavity mirrors decreases away from the optic axis, there is a corresponding phase shift $\Delta\phi = k_z \, \Delta L$, and a phase shift $\Delta\phi$ causes a frequency shift $\delta\nu = -\nu_{FSR}\Delta\phi/(2\pi)$. Thus, the frequency of a photon must increase in proportion with the decreasing separation between the mirrors. Since this is to lowest order quadratic, we conclude the transverse motion of a photon in this resonator is harmonically trapped [73, 116].

This intuitive picture remains valid near any appropriate degeneracy of the cavity (e.g. concentric, confocal, or higher order). For instance, near the concentric limit, the angle of the photon ray passing through the waist will slowly oscillate over many cavity round-trips. Position and angle have effectively swapped roles, and coarse-graining over the longitudinal motion yields an effective harmonic trap for the transverse motion of a cavity photon.

This story was formalized by Sommer and Simon in reference [181]. From the general 4×4 ABCD matrix $\mathbf{M}$, they calculate the effective Hamiltonian for transverse dynamics as

$$H = \nu_{FSR} \left[\frac{1}{2} \mu^{\mathsf{T}} \boldsymbol{G} \left(\log \boldsymbol{\beta} \boldsymbol{M} \boldsymbol{\beta}^{-1} \right) \mu \right], \tag{3.10}$$

where $\mu^{\intercal} = (\mathbf{x}\ \mathbf{p})$ is the phase-space state-vector, $\boldsymbol{G} = \begin{pmatrix} 0 & \mathbf{I_2} \\ \text{-}\mathbf{I_2} & 0 \end{pmatrix}$ and $\boldsymbol{\beta} = \begin{pmatrix} \mathbf{I_2} & 0 \\ 0 & \hbar k \mathbf{I_2} \end{pmatrix}$. This Hamiltonian may then be recast into a general quadratic Hamiltonian of the form

$$H = \frac{1}{2\boldsymbol{m}_{eff}} \left(\boldsymbol{p} + \frac{i}{2} B\, \boldsymbol{\sigma}_y \cdot \boldsymbol{x} \right) + \frac{1}{2} \boldsymbol{m}_{eff} \boldsymbol{\omega}_t^2 \boldsymbol{x}^2. \tag{3.11}$$

In this form, we have gauged away spherical and rotated differential defocus terms and suppressed the astigmatic, i.e. matrix, forms for the effective mass and harmonic trapping. The complete form of this decomposition is available in appendix A.1.4 and reference [181].

The breakdown of this treatment away from degeneracy only comes about because members of other sets of harmonic modes intersperse with the appropriate modes. For instance consider a one dimensional degeneracy between every third mode, so that $E_{0,0}$, $E_{3,0}$, $E_{6,0}$, ... are nearly degenerate. Nearby in energy are another similar set of modes distinguished by a different, but constant, second index. For nearly flat mirrors, this would correspond to $E_{0,1}$, $E_{3,1}$, $E_{6,1}$, ... but in general could be the energy of a higher mode aliased down by an integer multiple of the free spectral range. Regardless, as the cavity degeneracy is broken, higher modes in the desired set move away while modes from other non-desired sets move in, so that the effective Hamiltonian becomes woefully incomplete. In practice, when coupling atoms to these cavity modes, the dominant limitation on the mode non-degeneracy is that all relevant modes must reside within the EIT window. Since this is more stringent, we are well within the nearly degenerate limit of the bare cavity mode structure, and the effective quadratic Hamiltonian for the transverse degrees of freedom of cavity photons is valid.

3.1.2 Achieving Small Waists

To use Rydberg-Rydberg interactions to make effective strong interactions between individual cavity photons, it is important that the Rydberg blockade radius, r_B be similar to or

larger than the radial size of the cavity photon. As the smallest cavity mode available is the fundamental mode, the least stringent condition is $r_B \gtrsim w_0$. While the blockade radius may be increased by using a higher principal quantum number or reducing the dark polariton linewidth, it is generally advantageous to use as as small a waist size as possible.[§]

The simplest method for this is to use smaller radius-of-curvature mirrors spaced more closely together. However, this only slowly reduces the waist size; the waist size of a confocal cavity is $w_{cf} = \sqrt{\lambda R/2\pi}$. It is also challenging to super-polish and coat strongly curved mirror substrates, so high finesse mirrors with radii-of-curvature much shorter than 10 mm are not available. This would limit waists to $\sim$ 35 μm using 780 nm light. Of course, near the concentric limit, the waist size shrinks to zero, but one must approach very close to this limit to win a waist size reduction that is more than a factor of a few (see Fig. 3.6a, inset).[‡] Technically this is quite challenging as it is limited by even weak astigmatism, and more fundamentally precludes exploring physics in a degenerate, multimode cavity. This final constraint motivates us to employ more involved methods to shrink the cavity waist size.

3.1.2.1 Bowtie cavities and convex mirrors

A relatively easy way to shrink the waist size of a cavity without using short radius-of-curvature mirrors or moving close to the concentric limit is to use two additional flat mirrors to form a running-wave bowtie cavity (see Fig. 3.6b). A bowtie is preferable over a rectangular configuration as it significantly reduces astigmatism due to non-normal reflections off of the curved mirrors. An intuitive argument for the reduction in waist size due to a bowtie configuration proceeds as follows: A round trip through a bowtie cavity of small angle and

§. Note that a smaller waist size is *not* helpful for increasing our atom-cavity coupling. The increased single atom-cavity coupling is precisely offset by the reduced number of atoms interacting with the cavity mode.

‡. The near planar limit similarly provides a strong reduction in waist size only as the cavity length becomes very small compared to the radii-of-curvature, and this is additionally made difficult by the requirement that we have optical access to transport cold atoms into the cavity waist.

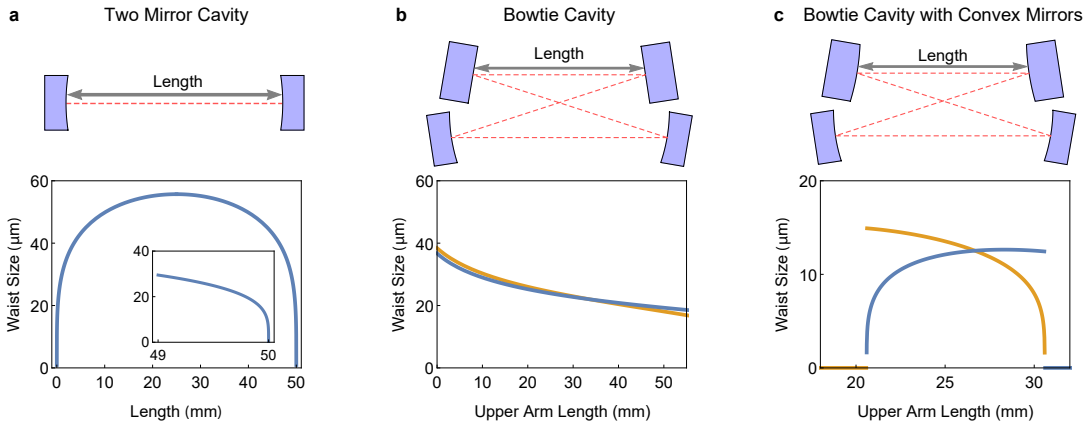

Figure 3.6: **Comparison of Cavity Modes.** We compare the transverse mode size at the waist of three different cavity geometries. **(a)** A two mirror cavity with 25 mm radius-of-curvature mirror has a nearly constant mode size over most stable lengths. The cavity length must be within a few hundred microns (0.4% of total length) of the concentric limit to shrink the waist size be even a factor of three (inset). **(b)** The addition of two flat mirrors to create a bowtie cavity significantly reduces the waist size, with a longer upper arm reducing the waist size further, at a constant near-confocal lower arm length of 28 mm. The non-normal incidence on the curved mirrors results in the lower waist have different tangential (orange) and sagittal (blue) waists. Note that the upper arm length $\to 0$ limit does not match the confocal waist size in panel (a) since this limit corresponds to a triangular cavity, not the two mirror cavity of panel (a). **(c)** A further reduction in waist size is achieved by replacing the upper, flat mirrors with convex mirrors. The cavity has dramatically increased astigmatism and is stable over a significantly smaller range of upper (and also lower) arm lengths; however, a full factor of five reduction in waist size has been achieved compared to the two mirror cavity formed by the lower mirrors at the same separation.

equal radii-of-curvature is equivalent to two round trips through a two mirror cavity. There are four equal waists, one between each pair of mirrors. Then, by making the upper two mirrors flat, the waist between the two flat, upper mirrors becomes much larger, and the intermediate waists between the upper and lower mirrors disappear. A larger mode is then incident on the lower mirrors, and so the focal spot between the lower mirrors is correspondingly smaller. This effect can be amplified by making the distance between the flat, upper mirrors larger than the distance between the curved, lower mirrors, since then diffraction serves to increase the mode size on the lower mirrors further.

One downside to increasing the distance between the upper mirrors is the overall increase in cavity length, which decreases the atom-photon coupling g and the linewidth κ. While this does *not* affect the cooperativity, this reduces transmission signal rates at fixed intracavity photon numbers, especially in the presence of fixed additional loss (e.g. the Rydberg state linewidth for dark state polaritons). While this may be compensated by reducing the cavity finesse, do so does reduce the cooperativity. As such it is always preferable to shorten the cavity, all other things being equal.

The intuition introduced above suggests a way forward: make the upper cavity mirrors convex! While it may seem odd to use convex defocussing mirrors inside an optical cavity, such mirrors allow the upper arm to be shorter, while providing defocus otherwise provided by diffraction over a long distance. Or, put another way, a smaller waist may be achieved for the same bowtie cavity length (see Fig. 3.6c).

3.1.3 Locking Optical Cavities

Most applications of optical cavities require stabilizing the absolute length of the cavity or locking the frequency of a laser to a cavity resonance. There are a variety of methods and guides for accomplishing these goals. Very generally, this requires generating an 'error signal',

a voltage that is proportional to the difference between the setpoint (e.g. the desired cavity length or laser frequency) and the actual value of the controlled variable (e.g. the actual, measured cavity length or laser frequency). Then a standard proportional-integral, or PI,[◇] filter converts the error signal into a control signal to actuate and stabilize the controlled variable via negative feedback. In the preceding examples, this control signal may drive (through an amplifier) a piezo actuator to vary the length of the optical cavity or might modulate the laser diode current to vary the frequency of the laser. The general problem of servoing may then be broken down into two halves, (1) the generation of the error signal, and (2) its filtering and implementation for negative feedback. We now turn to the first of these two problems.

3.1.3.1 Generating an error signal

Whether stabilizing a cavity length or locking a laser frequency to a cavity resonance, the techniques for generating an error signal are identical; these objectives only differ by what is then controlled by the error signal. In what follows I will focus on intuition and physical meaning rather than the math, since the math is somewhat tedious and easily found in standard references, e.g. [197, 198]. Also for concreteness in building intuition, I will assume a cavity length is being stabilized by locking to a stable reference laser.

The simplest source for an error signal is the transmission signal of a laser through an optical cavity, as collected by a sufficiently fast photodiode. As discussed above, the transmission signal displays a narrow peak near resonance. The peak location itself is not useful, since a drift of the cavity length in either direction corresponds to a decrease in the putative error signal voltage. However, we can use the side of the transmission peak as an error signal, in what is called 'side-of-fringe' locking. While quick and easy, side-of-fringe error signals suffer

◇. More generally, a differential term is added, making this a PID filter, but we rarely find the differential term beneficial.

from several drawbacks. The cavity is not locked on the reference laser resonance, which is often desirable. Additionally, fluctuations of more than the cavity linewidth ($\frac{\lambda}{2F}$) cause the error signal to jump 'over the top' of the peak and flip sign, causing the system to unlock. Most critically, any intensity fluctuations of the reference laser correspond to fluctuations of the length setpoint, and so intensity noise in the laser directly limits the stability of the cavity length.

Frequency modulation/demodulation techniques provide an answer to these limitations, in addition to typically providing a lower noise error signal. The laser incident on the optical cavity is phase modulated at a frequency ω_m, typically by an EOM or by directly modulating the laser current. Demodulating the transmission signal at also at ω_m then produces a signal which, in the limit of weak sidebands, is the sum of two terms, the interference of the lower sideband with the carrier, and of upper sideband with the carrier. If the laser carrier is on resonance, the lower sideband will transmit with a relative phase of $-\phi$, while the upper sideband will transmit with a phase of ϕ, where ϕ tends to zero for $\omega_m \ll \kappa$ and to $\pi/2$ for $\omega_m \gg \kappa$. The sum of these terms will be a sinusoid with a phase offset of zero and will thus provide a demodulated error signal value of zero. However, if the carrier frequency is offset from resonance, the phases of the two interference terms will no longer be equal and opposite; in the limit of large ω_m the phases become $-\pi/2+\phi_c$ and $\pi/2+\phi_c$, for the carrier phase shift ϕ_c relative to its phase on resonance. Thus the sum of the two terms provides a sinusoid with a non-zero phase offset, and the demodulated error signal will be non-zero. Importantly, if the carrier then fluctuates to the opposite side of the cavity resonance, the two terms' phases both shift in the opposite direction, and the phase of their sum as well as the value of the demodulated error signal will have the opposite sign.

All this implies that the demodulated error signal is an odd function about the laser-cavity resonance. This makes it ideal for controlling the length of the cavity to maintain resonance. Furthermore, the optical laser power, rf amplifiers, and the cavity linewidth all set the slope

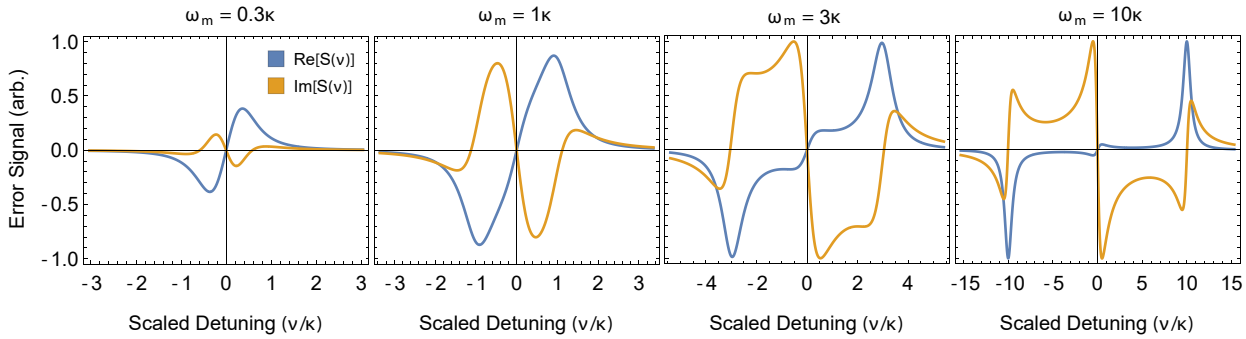

Figure 3.7: **Pound-Drever-Hall Error Signals.** The two quadratures of the demodulated reflection of a modulated laser off of a finesse 500 cavity are plotted versus the detuning of the carrier from resonance (ν, in units of the cavity linewidth κ) for several modulation frequencies ω_m. For $\omega_m \ll \kappa$, the real quadrature is dominant, although the overall signal is small. For $\omega_m \gg \kappa$, only the imaginary quadrature provides a significant signal near resonance, which become large and constant as ω_m increases.

of the error signal which then determines the effective proportional gain of the lock. This means that fluctuations of the optical laser power only make the proportional gain of the lock fluctuate, not the set point. Since it is straightforward to make the lock stability insensitive to small fluctuations in the gain parameters, this removes optical intensity fluctuations as a noise source. Although any *amplitude* modulation of the incident laser can cause effective reference phase fluctuations that correspond to setpoint fluctuations, amplitude modulation of the laser is typically much easier to eliminate.

There is one significant remaining downside to locking with the demodulated transmission signal which is that this signal responds to length fluctuations of frequency $\omega > \kappa$ as ω^{-2}. This limits the bandwidth of the resulting lock since the unity gain bandwidth must then be kept less than κ. While this is not relevant for broad cavities such as our main physics cavities with typical linewidths above 1 MHz, this is relevant for locking to a narrow stable cavity where high-bandwidth feedback for narrowing laser linewidths is desired. This motivates demodulating the *reflection* off of the optical cavity to create a Pound-Drever-Hall error signal [197, 199].

The Pound-Drever-Hall error signal is derived from demodulating the reflection off of a cavity of a phase modulated laser. That is, the incident laser has an electric field time dependence

$E(t) = E_0 e^{i(\omega t + \beta \sin(\omega_m t))} \approx E_0 \left[J_0(\beta) e^{i\omega t} + J_1(\beta) \left(e^{i(\omega+\omega_m)t} - e^{i(\omega-\omega_m)t} \right) \right]$, where ω_m is the modulation frequency, J_n is the n^{th} Bessel function, and β is the modulation depth. The reflection of this laser off the cavity must be collected on a photodiode with a bandwidth greater than ω_m.** The photodiode signal is then given by

$$\begin{aligned} P(\omega) = {} & V_0 J_0^2(\beta) |R(\omega)|^2 + V_0 J_1^2(\beta) \left(|R(\omega+\omega_m)|^2 + |R(\omega-\omega_m)|^2 \right) \\ & + 2V_0 J_0(\beta) J_1(\beta) \left[\mathrm{Re}\left(S_1(\omega)\right) \cos(\omega_m t) + \mathrm{Im}\left(S_1(\omega)\right) \sin(\omega_m t) \right] \\ & + (2\,\omega_m \text{ terms}) \end{aligned} \tag{3.12}$$

where $S_1(\omega) = R(\omega)R^*(\omega+\omega_m) - R^*(\omega)R(\omega-\omega_m)$ is the term oscillating at ω_m, R^* indicates the complex conjugate of R, and $R(\omega) = \frac{r\left(e^{i\omega/\nu_{fsr}}-1\right)}{1-r^2 e^{i\omega/\nu_{fsr}}}$ is the reflection coefficient of an ideal cavity. A particular quadrature of the term oscillating at ω_m is picked out by sending the reflection signal to the RF port of a phase detector (e.g. Minicircuits ZRPD-1+) with the modulation tone $V_{LO}\cos(\omega_m t + \phi_{LO})$ at the LO port. Empirically varying the relative phase ϕ_{LO} of the LO relative to the RF while looking at the demodulated signal from the IF port on an oscilloscope then allows selection of the correct quadrature. This is identifiable in particular by maximizing the magnitude and slope of the error signal near resonance, and, for $\omega_m > \kappa$ balancing the sideband features at $\pm\omega_m$. Selecting the correct phase is quite forgiving, since a small error primarily shrinks slightly the central locking feature while skewing the sideband features. Figure 3.7 plots the two quadratures of the Pound-Drever-Hall error signal for several modulation frequencies. For $\omega_m > \kappa$, the full width between extrema of the error signal near resonance goes to κ, while the full range is set by available laser power, intracavity loss, and the photodiode quality; typically the full range is easily several volts, providing a sharp error signal with high signal-to-noise. The lock capture range with this error signal is also quite large, being set by the modulation

$\star\star$. The only real requirement is that the photodiode respond at frequencies $\omega_m - \Delta\omega < \omega < \omega_m + \Delta\omega$ where $\Delta\omega$ is greater than the desired lock bandwidth.

frequency rather than κ.

3.1.3.2 System control given an error signal

The preceeding section discussed three ways of generating an error signal to lock a cavity to laser, or vice-versa. For other applications other methods must be used for the generation of an error signal, such as heterodyned saturated absorption spectroscopy for locking a laser to an atomic transition. In any case, the error signal must be converted into a control signal that actuates the device being locked in a way that implements negative feedback. There are many tutorials and papers concerning this broad topic [198, 200–202]; here I only mention a couple concerns that recurred over the course of this work.

Increasing the bandwidth of a lock is a central goal of many locking systems. The unity gain bandwidth directly sets the noise frequencies $\omega_n < \omega_{G=1}$ that are controlled and suppressed by the feedback, and since the system gain typically falls like $1/\omega_n$ and the noise suppression is inversely proportional to the system gain, increasing the unity gain bandwidth also increases the noise suppression at low frequencies. Thus the total noise suppression grows *at least* as the square of the unity gain bandwidth, with the possibility of further suppression at low frequencies through the use of a double integrator.

Optimizing the feedback loop involves first matching the corner of the PI lockbox to the corner frequency of the system under lock. This can be tricky since the easiest characterization of the system uses network analysis once the system is already in lock! However, reasonable guesses are typically sufficient to obtain an initial lock. Once the PI corner is set, increasing the overall lock gain increases the unity gain bandwidth. This should be continued until either of two things happens:

First, the phase at unity gain can increase significantly past 90°. This initially causes a *servo*

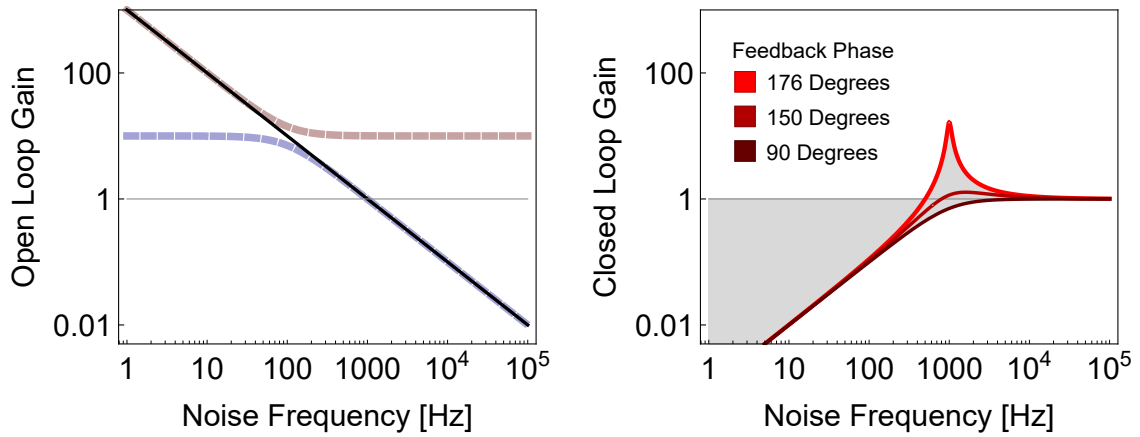

Figure 3.8: **Feedback and Control. (a)** A system to be controlled ideally responds to a periodic drive as a low pass filter (blue dashed line) with a corner frequency (10^3 shown). A suitably tuned PI filter adds $1/\omega$ gain out to the corner frequency, with a flat response beyond (red dashed line). Together, these produce a smooth $1/\omega$ open loop gain (black line). **(b)** The suppression of noise (gain < 1) in closed loop is the reciprocal of one plus the open loop gain. For an ideal $1/\omega$ open loop gain, this results in a phase at unity gain of 90° and a smooth crossover from suppressing noise at low frequencies to no response at high frequencies (black). If any other component in the system provides additional phase, e.g. a resonance, additional filter, or delay, the phase at unity gain increases. As this phase approaches 180° negative feedback switches to positive feedback, causing oscillations at the unity bandwidth frequency (bright red).

bump in the noise suppression curve, where feedback weakly amplifies noise around the unity gain frequency. Additional phase at unity gain will then cause the system simply to oscillate, and typically unlock (see Fig. 3.8b). This arises either from a time delay τ, which adds a phase linear in frequency $\omega\tau$ or additional filters. A finite time delay can only be reduced by physically shortening the closed loop path length. For example, to limit the path length delay at 10 MHz to less than 30°, the path length (at the speed of light), must be less than 2.5 m. So the optical and electronic system must be optimized for minimal path length. If the additional phase arises due to the presence of a higher order filter so that the transfer function is falling steeper than $1/\omega$, this may be fixed by simply removing or replacing the offending filter, or if that is not possible, the addition of a lead-lag filter.

The second possibility is that a resonant peak, at a frequency well beyond the unity gain frequency, approaches and exceeds unity gain. This can come from the primary actuator-mass system (e.g. piezo mirror resonance) or from a mount resonance (e.g. the piezo drives a

secondary resonance through its mounting structure). These appear as a peak or a peak-zero pair in the magnitude of the transfer function. In either case, the phase of the transfer function rapidly winds through at least an additional π phase, ensuring that the total feedback gain hits 180° at some point on the resonance thus causing positive feedback and oscillation. While a single isolated resonance may be carefully measured, inverted, and canceled by an appropriate notch-filter, this is typically difficult, and resonances are often not isolated, but rather appear in a forest of peaks. Thus these effects are best dealt with during the design stage, where the goal is to push resonances to higher frequency and to spoil their quality factor. Using shorter, stiffer piezos, lighter mirrors, and thinner, harder glue all contribute to pushing the piezo-mirror resonance up, while, if possible, roughing the surface of the piezo can help lower the quality factor of resonances [203]. The mount design is similarly important and often more flexible. Ensuring the piezo is attached to a relatively heavy block reduces coupling to other mass-spring systems, while ensuring that that block is securely and symmetrically mounted to the main structure removes low frequency "tuning fork" mount resonances. Finally, making the entire structure as monolithic as possible greatly aids in reducing low frequency resonances.

Finally, a very helpful technique for locking lasers to a reference has been the addition of fast feedback. Laser frequency may be rapidly modulated via the diode current (through either a bias-tee or a MOSFET current diversion circuit), enabling high-frequency feedback only limited by time delay. Thus it is reasonable to attempt to electronically narrow the laser frequency, so long as it starts below 1 MHz[§§]. Our standard PI lockboxes do not have the bandwidth for this feedback; however, a fast feedback path in parallel with the slow feedback PI path can be optimized for this purpose. The basic idea is to split off a portion of the error signal[‡‡], send it through a simple filter and possibly an amplifier, and use the

§§. As a rule of thumb, 10× the laser bandwidth is required to narrow the laser.

‡‡. In practice, it has been helpful to split off the signal *before* demodulation, and have a separate mixer to generate the fast feedback error signal. This ensures that optimizing the fast feedback gain does not affect the slow PI path error signal, and vice-versa.

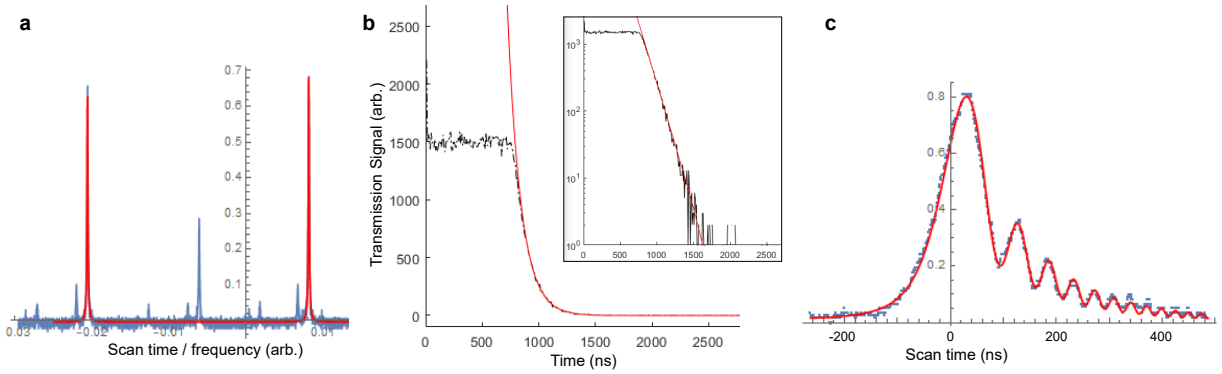

Figure 3.9: **Determining cavity finesse.** **(a)** We fit the transmission of the 480 nm build-up cavity used in chapter 6 to the sum of two Lorentzians, finding the finesse to be 200. **(b)** We observe cavity ringdown with the 780 nm experimental cavity used in chapter 6. Plotting the data on a logarithmic scale (inset) reveals a linear slope, providing the decay constant and corresponding linewidth $\kappa = 2\pi \times 1.35$ MHz. **(c)** We sweep a laser across the cavity resonance of the 780 nm experimental cavity used in chapter 6, producing a complicated oscillating decay (see Eq.3.13). This fits to a linewidth of $\kappa = 2\pi \times 1.3$ MHz. These measurements are not as reliable as the exponential ringdown measurements of panel **b**, since the fit parameters are highly correlated, and multiple measurements of the same cavity tend to yield more divergent results. Nevertheless, this is a useful quick diagnostic for obtaining cavity finesses accurate to the several percent level.

result to actuate the laser current. This is typically left always on, so that the PI lockbox is optimized to stabilize the laser to the reference in the presence of fast feedback. This appears as a characteristic flattening of the error signal, as the fast feedback attempts to maintain the error set point even as the laser scans away (see Figs. 3.13b and 3.17c).

3.1.4 Measuring Cavity Parameters

Measuring the free spectral range of a cavity is typically straightforward. When accuracy of only a few percent is required, simply measuring the round trip cavity length L and computing $\nu_{fsr} = c/L$ is sufficient. For more precise measurements, a cavity may be probed with a laser which is phase modulated by a fiber coupled EOM. The modulation frequency can then be ramped until particular laser lines overlap, e.g. the $+1$ and -1 sidebands from neighboring FSRs overlap. The appropriate modulation frequency can be determined to a reasonably small fraction of $\kappa/(2\pi)$ and the free spectral range is easily determined from there.

There are several useful techniques for measuring a cavity linewidth or finesse. If the finesse is relatively low, a transmission spectrum of the cavity that covers a full free spectral range may be fit to a sum of Lorentzians—the ratio of the separation to the width yields the finesse (see Fig. 3.9a). If the finesse is high so that the acquisition of spectra is difficult (because a scan that covers a full FSR does not provide enough resolution on each peak), the linewidth may be determined via cavity ringdown. This yields the finesse if the free spectral range is already known. The conceptually simplest ringdown measurement proceeds by probing the cavity on resonance, and then quickly (fast compared to κ^{-1}) extinguishing the probe. The intracavity field then relaxes exponentially, with time constant $\tau = 1/\kappa$ where κ is the linewidth in rad/s, (see Fig. 3.9b). In practice, such a ringdown measurement requires a sophisticated apparatus that stabilizes the cavity length and laser frequency and modulates the laser intensity quickly. In order to quickly measure cavity linewidths without these complications, it is sufficient to sweep quickly the cavity length or the laser frequency across the cavity resonance. While a slow sweep produces a Lorentzian line, the sweep axis is typically uncalibrated and anyway laser and cavity jitter typically broaden the Lorentzian significantly. If the sweep is very fast, then the cavity is "pinged"—light effectively only enters on resonance and the relaxation is exponential, but very little light enters to begin with. The intermediate regime of moderate sweep speed (time to sweep the probe frequency by κ is comparable to κ^{-1}) provides a large signal but at the cost of a significantly more complicated lineshape. In fact the transmission profile is given by [204]

$$A\, e^{-\frac{t-t_0}{\tau}} \left| \mathrm{erfc}\left[\frac{1-i}{2\sqrt{2}} \frac{\pi}{F} \sqrt{\frac{\lambda \nu_{fsr}}{2\pi v}} - \frac{1+i}{2\sqrt{2}} \left(4\pi \frac{v}{\lambda} \sqrt{\frac{\lambda \nu_{fsr}}{2\pi v}} (t-t_0) - \sqrt{\frac{2\pi v}{\lambda \nu_{fsr}}} \right) \right] \right|^2, \quad (3.13)$$

where A is an overall amplitude, t_0 is an offset time, $\tau = \kappa^{-1}$ is the decay time, v is the velocity of the cavity length sweep, and $\mathrm{erfc}(x)$ is the complementary error function of x. We can qualitatively understand the source of the oscillations as the interference of light at different frequencies: some light enters on resonance and continues to decay for a time τ.

Meanwhile, the probe frequency has shifted and so excites the cavity with light that differs significantly in frequency. Even though that light is somewhat off resonance, some enters and leaks out of the cavity, and that light can interfere with the original resonant decay. The full form then comes from the continuous distribution of decaying light fields at different frequencies. Despite the complexity of Eq. 3.13, these lineshapes are easily measured and fit to provide the cavity linewidth (see Fig. 3.9c) The nonlinear model fit to this form has a very non-monotonic χ^2 minimization landscape, so the initial guess must be quite close to the data.

Finally, the intracavity loss may be estimated by measuring either the total transmission efficiency or the reflection dip on resonance of a well mode-matched cavity and combining that information with the measured finesse. The power transmission efficiency is $T = (T_m F/\pi)^2$ from which the transmission of a single mirror T_m and the additional cavity loss may be inferred.

3.2 Digital Micromirror Device

For mode injection into higher order transverse modes of our various experimental cavities, we employ DLP LightCrafter Modules using the DLP3000 digital micromirror device (DMD). This device, manufactured by Texas Instruments, consists of an array of 608 by 684 square aluminum mirrors, 7.6 μm on a side, that fill the approximately 6.6 mm by 3.7 mm active area with a filling factor of 92 %. A computer uploads 608×684 binary bitmap to the DMD, which then tilts its mirrors by $\pm$ 12° depending on the binary values of the corresponding bitmap pixels. The DMD is not flat across its surface; typically we find several λ of smooth variation or ripple. Following techniques described by Zupancic, et al. [205] we image the diffraction off the DMD into a Fourier plane and calculate a phase map correction to reduce observed aberrations (see Fig. 3.10a).

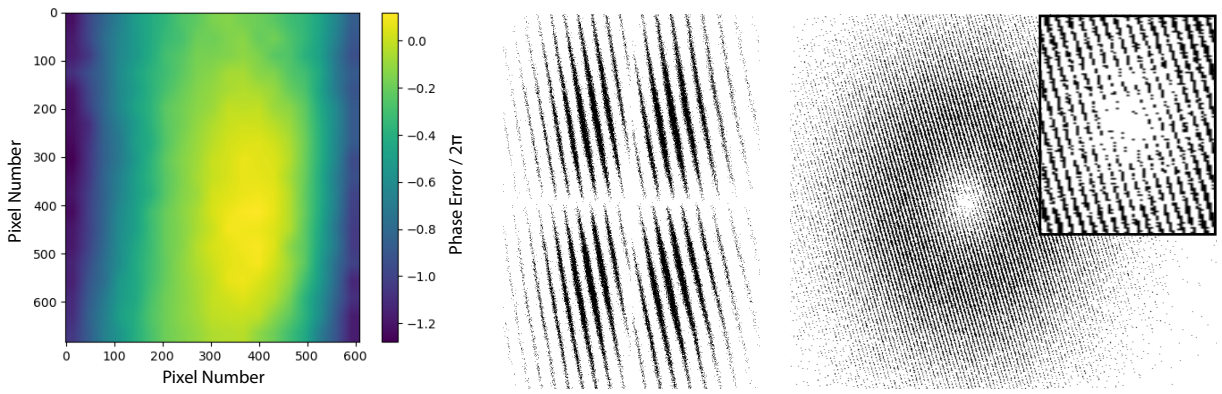

Figure 3.10: **DMD holography.** **(a)** The DMD and its imaging system display significant phase errors across the DMD plane. We experimentally determine and subsequently subtract off these phase errors using a phase mask; a sample mask is shown. The colorbar units are height in wavelengths, or equivalently phase/2π. **(b)** A sample hologram for a Hermite Gaussian (1,1) mode is shown. The hologram period is expanded by a factor of six to show detail. Note that the phase shifts of π across the nodal lines appear as a shift in the position of the hologram fringes. **(c)** A sample hologram for a Laguerre Gaussian (0,1) mode is shown. The 2π phase winding associated with the orbital angular momentum of this mode appears as a fork in the interference fringes at the center (inset).

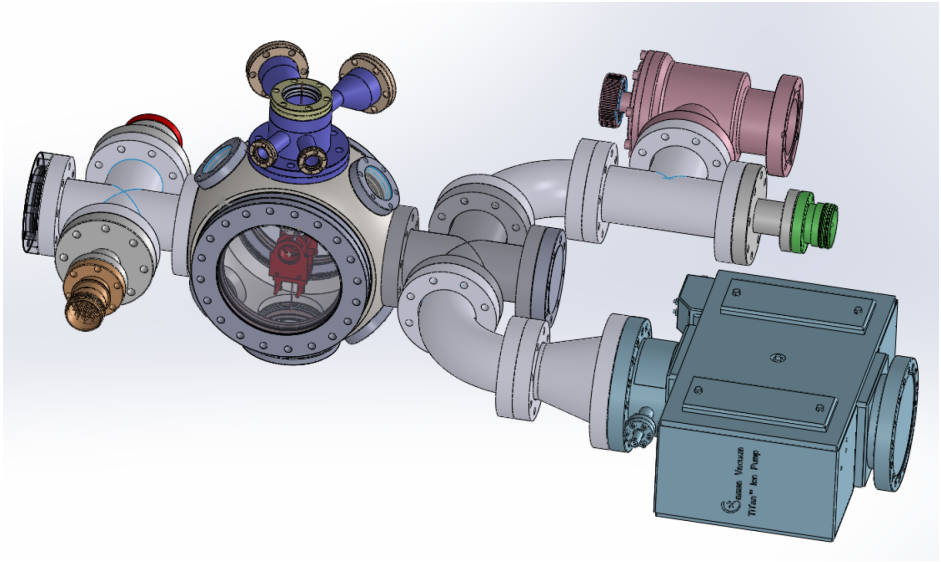

Figure 3.11: **The Vacuum System.** The main chamber is an octagonal square, which contains the primary experimental setup, including the MOT coils (dark red) and experimental cavity (not visible). The main chamber has two large 8" windows and four 4.5" flanges that define the principal axes of the system. The two vertical 4.5" flanges provide vertical optical access via windows, although the upper window is displaced upward from the main chamber by a custom flange (dark blue) that includes a mounting structure and instrumentation feedthroughs for the experimental cavity system (see Appendix B.2). The two remaining 4.5" flanges connect to four-way-crosses, with windows along the common axis. This provides optical access for fluorescence imaging at the MOT location. The four additional flanges from the four-way crosses provide (1) an instrumentation feedthrough (orange) for the MOT coils and four Rubidium dispensers, (2) an ion gauge (red), (3) an ion pump (light blue), and (4) a Ti-sub pump (green) and gate valve (pink) for a roughing pump. Four additional 2.75" windows on the main octagonal square provide diagonal access along axes perpendicular to the 8" window direction.

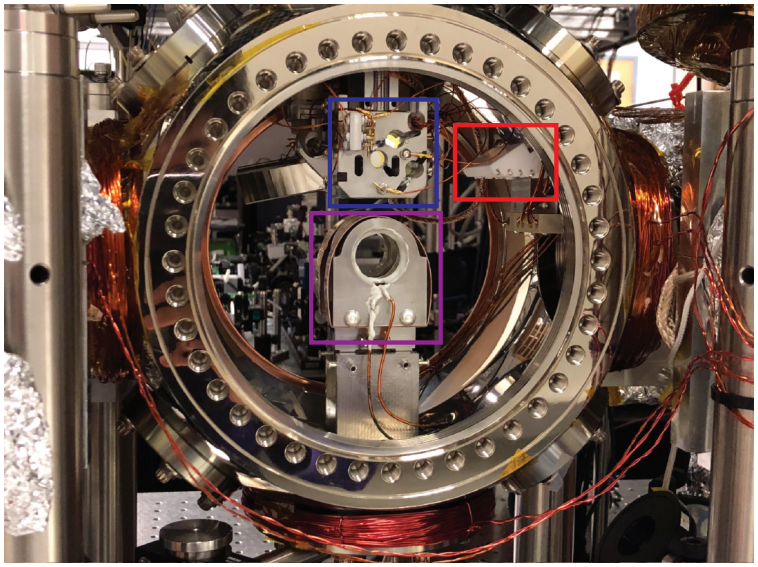

Figure 3.12: **The Main Chamber.** Rubidium atoms from a dispenser (red box) are captured by the MOT (coils in purple box). After cooling, atoms are transported vertically into the waist of the experimental cavity (blue box). Numerous electrode and piezo control wires are connected to elements on the cavity mounting structure via pins. Also visible are three of six ~ 100 turn magnetic field bias coils; the third axis is installed around the 8" windows which are removed in the photo.

To couple into arbitrary modes of a=n optical cavity, we need control over both the amplitude and phase of the electric field. This is accomplished by computing the product of the desired electric field profile with a sinusoid of relatively short period—we typically use a period of four pixels, and rotate the k-vector by 10° to avoid aliasing effects. We normalize the maximum value to one, and then interpret the result at a location as the probability for that pixel to be turned on (see Fig. 3.10b,c). This reduces aliasing effects compared to a fixed threshold. From Fourier analysis, we know that the sinusoid makes two copies of the desired complex field, shifted by $\pm\ k$, that is, the full desired electric field profile appears in the diffraction off the DMD pattern. An iris then picks out one diffracted order and additional mirrors and lenses couple this mode into the cavity.

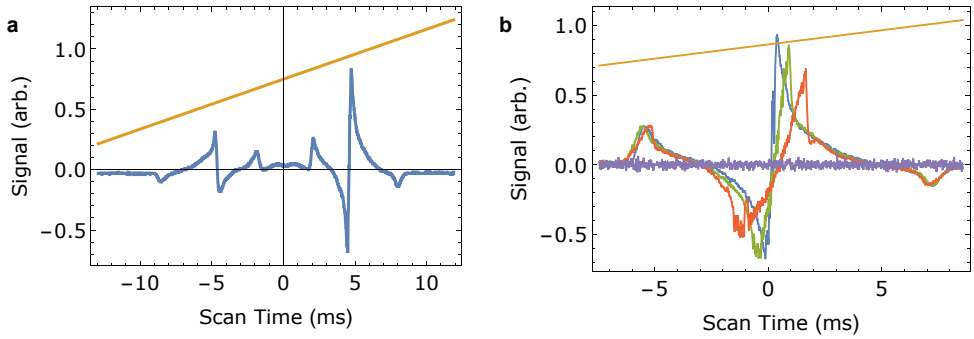

Figure 3.13: **MOT Laser Frequency Lock Error Signals. (a)** The error signal of the MOT laser shows several potential locking features when laser is scanned over $\sim$ 0.5 GHz; we lock to the largest feature, on the right, which may be swept in frequency by adjusting the beatnote reference DDS frequency. **(b)** Zooming in, we see a sharp $\sim$ 10 MHz wide locking feature (blue), set by the bandwidth of the helical filter used for frequency to voltage conversion. Adding fast feedback via an SR560 preamplifier (to break ground loops, filter, and add gain) into a bias tee on the laser diode current flattens the error signal slope (green) and increases the maximum slew rate of the MOT laser sweep. Increasing the gain from 5x to 20x on the preamplifier enhances this effect (red) and shows the error signal used in practice.

3.3 Vacuum System and Magneto-optical Trapping

Now we turn to the atomic physics apparatus necessary for the formation of cavity Rydberg polaritons. All of these experiments begin with a cold, trapped sample of ^{87}Rb atoms produced by a magneto-optical trap (MOT) inside of our vacuum chamber. The entire vacuum system is shown in figure 3.11. The ion pump maintains a pressure in the main chamber of several nTorr. The Ti-sub pump can reduce this to half a nTorr but saturates over the course of a few days. Since our experimental duty cycle is 4-12 Hz, we are much less sensitive than typical BEC experiments to atomic loss due to collisions with background gas, making our several nTorr pressure acceptable. While increasingly large and complicated in vacuum cavity structures have caused working pressures to increase, we remain at pressures < 5 nTorr.

A custom Macor ceramic mount holds four Rubidium dispensers (see Appendix B.3). By continuously running 2.5 - 3.5 A through one of these dispensers, atomic Rubidium is emitted toward the MOT coil structure. This structure holds two 36-turn coils that, in an anti-Helmholtz configuration, produce a field gradient of 22 $\frac{G}{\text{cm}\cdot\text{A}}$. To cool and trap atoms, we

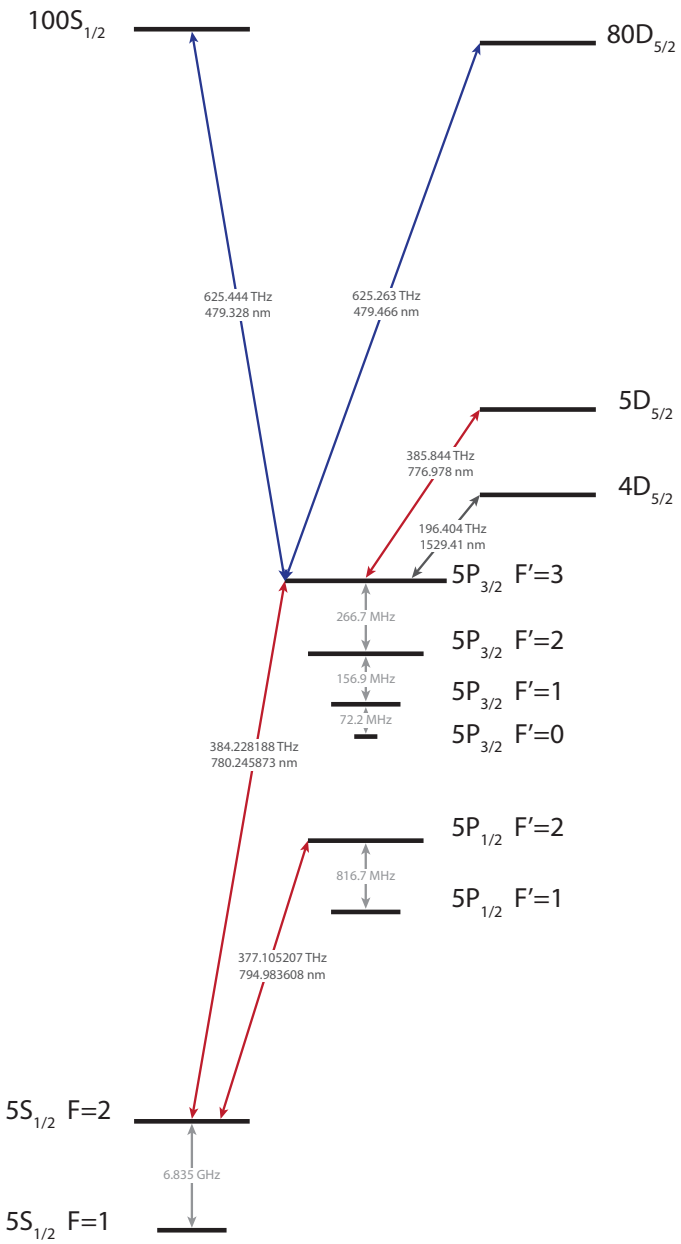

Figure 3.14: **Rubidium Energy Levels.** A sampling of relevant Rubidium energy levels are shown, not to scale, along with the relevant transition frequencies. The MOT and probe lasers are near the $5S_{1/2}(F = 2) \rightarrow 5P_{3/2}(F' = 3)$ 780 nm transition, while the repump laser is on $F = 1 \rightarrow F' = 2$. The vertical transport lattice is red-detuned from these transitions at 784 nm to produce optical dipole potential to trap and transport atoms. The control laser addresses a transition from $5P_{3/2}(F' = 3)$ to a high lying Rydberg state, such as $100S_{1/2}$ or $80D_{5/2}$. We modulate the P-state energy by intensity-modulating an off resonant laser near the $5P_{3/2} \rightarrow 4D_{5/2}$ or $5P_{3/2} \rightarrow 5D_{5/2}$ transition.

employ a standard six beam $\sigma+/\sigma-$ MOT. The light for this comes from our MOT laser system described below.

The MOT laser system begins with a distributed feedback laser (DFB, from Eagleyard) at 780 nm. This 'Master' laser is locked with an enriched Rubidium vapor cell to the $F = 2 \rightarrow 2'$, $F = 2 \rightarrow 3'$ crossover point using heterodyned saturated absorption spectroscopy*. The primary MOT laser is a distributed Bragg reflector laser (DBR, from Photodigm) at 780 nm, and the repumping laser is a second DFB. Each of these lasers is combined with the reference laser into single mode fibers which are then sent on to photodiodes, producing an rf beatnotes[§]. Each laser's frequency is stabilized by locking the beatnote frequency to an rf standard, produced by a computer controlled direct digital synthesizer (DDS, see Appendix D)[‡]. Sweeping a DDS frequency thus allows the laser frequency to be swept while maintaining lock. To improve the maximum sweep rate, we additionally inject an appropriately filtered version of the beatnote-derived error signal directly into the laser diode current to provide fast feedback (see Fig. 3.13b).

The MOT laser, thus stabilized, provides the seed for a tapered amplifier (TA, Thorlabs TPA780P20) which provides approximately 1 W of power. This combined with the stabilized repump laser is the source of MOT light which is split into three equal-intensity beams for

$\star$. This was a poor choice. Locking to a ^{85}Rb feature would allow all desired DDS frequencies to be in the GHz range, ensuring that the desired lock feature is well isolated. Locking to the ^{87}Rb feature requires using an additional double-passed 200 MHz AOM to shift the reference point outside of the $F = 2 \rightarrow P_{3/2}$ band, and results in relatively low DDS frequencies causing the resulting error signal profiles to be complicated.

§. Combining the lasers in a single mode fiber is very helpful compared to free space or a multimode fiber. A small change in relative alignment between the two lasers creates a set of fringes that travels across the photodiode at the beatnote frequency. Very quickly, this greatly reduces the strength of the ac photodiode signal, while still suffering from the shot noise of the full power. In comparison, the single mode fiber enforces that both lasers are copropagating, and a misalignment at the input only reduces the incoupled power. This is not so bad because the optical beatnote amplitude goes as the geometric mean of the two laser amplitudes, so the photodiode signal drops only slowly with a reduced input power of one laser.

‡. The frequency to voltage conversion is accomplished by forming an rf Mach-Zehnder interferometer with a reflection off of a helical filter at 100 MHz in one arm. This compares favorably with a delay line in one arm by providing only a few narrow features to lock to, as opposed to a forest of broad features which allow for significant frequency drift and undesired relocks of the laser.

the 6 beam MOT.

The MOT light is also used for various other purposes throughout the sequence, most notably as a depumper, for efficiently pumping $F = 2$ ground state atoms into $F = 1$. This accomplished by tuning the MOT to the $F = 2 \rightarrow 2'$ resonance 266 MHz below the cycling transition. To prevent pumping atoms into a dark state in the $F = 2$ manifold of magnetic sublevels, we send this beam through a cats-eye double pass AOM, keeping both orders, to produce a second frequency component at -157 MHz that drives the $F = 2 \rightarrow 1'$ transition.

The MOT is on between experimental sequences, while the control computer is saving data and sending instructions to hardware for the next sequence. The sequence then begins by ramping the MOT -200 MHz from resonance and turning off the MOT coils to begin polarization-gradient cooling (PGC). The vertical transport lattice is also turned on, so that the PGC will cool atoms into the lattice.

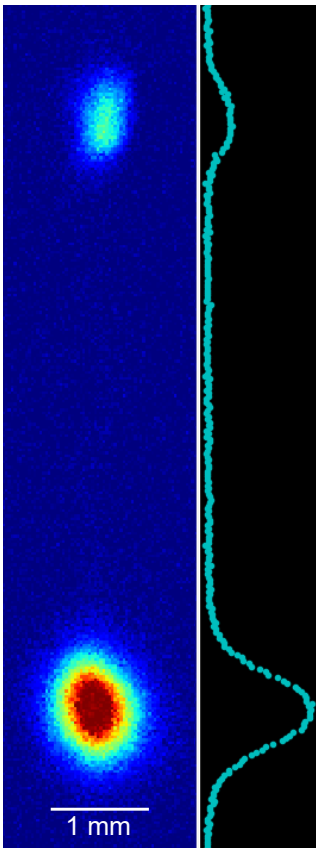

Figure 3.15: **Atom Transport in Fluorescence.** A fluorescence image taken mid-transport shows the atomic sample 6 mm above the remaining MOT. The MOT is recaptured after every run of the experiment to maximize the transported atom number despite little MOT loading time.

3.4 Transport Lattice

After PGC, 10% – 30% of the MOT atoms are loaded into a retroreflected 784 nm optical lattice using ~ 0.2 W into a ~ 85 μm waist. The optical system producing this light was initial sourced by a Photodigm DBR locked and frequency-narrowed by a Pound-Drever-Hall

error signal derived from a high finesse invar cavity. More recent experiments have instead used a Topica 780 DL-Pro tuned to 784 nm, locked and narrowed by a Pound-Drever-Hall error signal derived from our ultrastable reference cavity (see section 3.5.1). In either case, the locked and narrowed seed light is directed into a Sacher Lasertechnik tapered amplifier. The $\sim$ 1 W output of this TA is the light source of the vertical transport lattice.

The atoms are *transported* in this lattice when the retroreflected beam of the lattice is frequency shifted relative to the downward path. The two beams start a the same frequency resulting in stable antinode locations, but as the relative frequency is increased, the antinodes accelerate upwards, carrying the trapped atoms with them (see Fig. 3.15). The frequency offset is produced by using two orthogonal acousto-optic modulators (AOM) in a cats-eye double pass configuration, one AOM shift cancelling the other. By ramping one AOM relative to the other, the atoms are accelerated at 100 g up to 4 m/s (10 MHz shift).

At the end of transport, one to several thousand atoms are released in the waist of the optical resonator in a $\sim$ 40 μm radius cloud.

3.5 Probe and Control Lasers

The details of the optical cavity and atomic sample preparation varied between experiments. Here, we continue with the final common aspects of all cavity Rydberg polariton experiments, namely the probe and control lasers.

The experimental cavity is probed by a narrow stable 780 nm laser, near resonant with the $5S_{1/2}\,(F=2) \rightarrow 5P_{3/2}\,(F'=3)$ transition of ^{87}Rb. This probe laser is produced by a 1560 nm frequency doubled laser system beginning with an Orbits Lightwave Ethernal seed laser at 1560.49 nm. This laser is only tunable over $\sim$ 40 GHz, but is intrinsically very stable, with a tested FM noise of 37 Hz/$\sqrt{\text{Hz}}$ at 100 Hz and a flat sub 1/$\sqrt{\text{Hz}}$ spectrum. This is

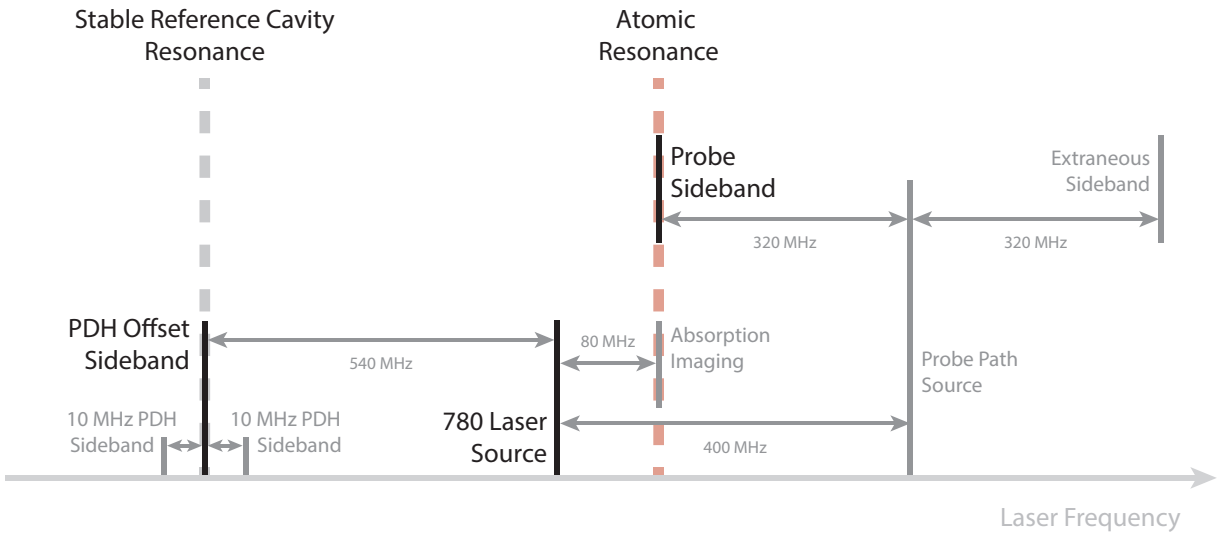

Figure 3.16: **The 780 nm Probe Laser System.** A sideband of the 780 nm laser is locked to a resonance of the stable reference cavity, which lies at an arbitrary–but stable–frequency offset from the atomic resonance. The Pound-Drever-Hall (PDH) locking sideband offset is chosen so that the 780 nm carrier lies 80 MHz from the atomic resonance, making a resonant absorption imaging source easy to produce via an 80 MHz AOM. For probing, the 780 nm source is shifted with a double passed 200 MHz AOM and sent through an EOM to produce the probe sideband. This AOM and EOM frequency pair is arbitrary and chosen to ensure that the probe path source and extraneous sidebands do not accidentally hit any higher-order cavity modes.

amplified up to $\sim$ 2 W by a Nufern 10 W fiber amplifier. This is then directed through a MgO doped periodically poled Lithium Niobate crystal for frequency doubling in single pass. This produces $\sim$ 50 mW of 780.24 nm light. A small fraction of the remaining 1560 nm light is picked off and used for stabilizing experimental cavities. The 780 nm light is then divided for various purposes including the cavity probe, the probe laser frequency locking system, and absorption imaging.

The light probing the experimental cavity needs to be frequency-swept rapidly (typically 10-1000 MHz/ms) and switched on an off very rapidly ($\tau_{switching} \ll 100$ ns). These capabilities are provided by using a sideband frequency produced by a fiber-coupled electro-optic modulator (EOSpace PM-0K5-10).

The control laser near 480 nm is a Toptica TA-SHG pro. This laser system is an external cavity diode laser at 960 nm which is amplified by a TA and frequency doubled inside a

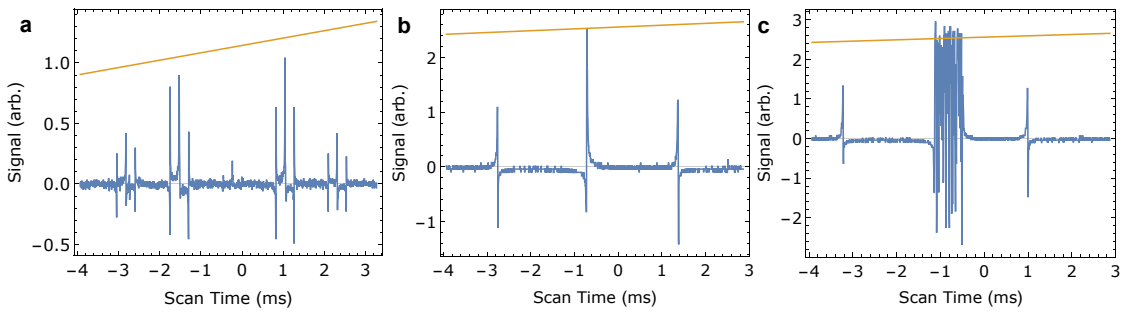

Figure 3.17: **PDH Error Signal of the 960 nm Laser. (a)** The PDH error signal is observed by scanning the 960 laser carrier frequency across an ultrastable cavity resonance. The offset sideband frequency is 90 MHz and is strong enough to cause the carrier feature nearly to vanish while second order sidebands appear prominently. This scan is perturbed by the finite sampling of the digital oscilloscope used; there are 1700 samples in this scan over 500 MHz, while each feature locking feature has a width set by the linewidth of the ultrastable cavity, $\kappa_{pdh} = 40$ kHz. **(b)** Zooming in on a single feature, we find the standard PDH lineshape with the typical sharp locking feature in the middle. The full width of the locking feature is just over one sample wide. **(c)** Adding fast feedback helps stabilize the laser frequency. Here a small amount of fast feedback is enabled while scanning the laser; we see that the laser dwells on the locking feature with the correct slope, while rushing across the two flanking features with the opposite slope.

resonant second harmonic generation cavity. The cavity automatically locks to the input 960 nm light and provides ~ 400 mW of 480 nm power. A few mW of 960 light is also picked off for the laser frequency locking and stabilization system. At various times, we have wished to drive different Rydberg states, from as low as $40S_{1/2}$ up to $121S_{1/2}$. This requires tuning the 960 nm seed laser by several nanometers, which is easily accomplished by fine rotation of the laser grating; only minimal realignment is then necessary.

3.5.1 Pound-Drever-Hall Lock to Ultrastable Cavity

While absolute frequency stability for the MOT and Repump lasers is derived from a Rubidium cell, the $\Gamma = 2\pi \times 6$ MHz wide 780 nm transition is too broad to stabilize our narrow, $\sim$ kHz-wide lasers. Instead, the day-to-day frequency reference for our probe and control lasers is a Stable Laser Systems ultra-low thermal expansion high-finesse cavity. We pick off a piece of both the 780 nm probe and 960 nm control (before SHG cavity) and send each of these through a fiber coupled EOM. Each EOM is driven at two tones, a PDH offset sideband frequency generated by a DDS and a modulation tone around 10 MHz. The output

of the EOM is mode matched to a fundamental mode of the dual-coated cavity (Finesse $\sim 30,000$ at both 780 nm and 960 nm). The reflection off of the cavity is separated with an optical isolator and directed onto a photodiode. Demodulation with a phase-shifted copy of the 10 MHz tone provides a Pound-Drever-Hall (PDH) error signal. The offset sideband modulation creates optical sidebands at integer multiples of the offset sideband modulation frequency, typically optimized to maximize the first order; this results in prominent PDH locking features at the carrier and first order offset sideband frequencies (see Fig. 3.17). To find a desired atomic line, the lasers are first coarsely tuned to the correct free spectral range of ultrastable cavity, and then locked to a PDH feature on an offset sideband. Varying the offset sideband modulation frequency provides fine adjustment of the laser frequency onto the atomic line.

Beyond removing frequency drift, we also use the PDH lock to remove high-frequency laser noise on the control laser via fast feedback. The regular PDH locks operate by adjusting a piezo voltage in the laser, which is limited in bandwidth to the kHz range. Higher bandwidth is available by modulating the laser diode current directly. To that end, we take the demodulated PDH error signal, send it through amplifiers and passive filters, and direct that result to the laser diode current modulation port of the laser. The characteristic drop in the slope of the PDH feature at moderate gain indicates that this fast feedback is working. Once the slow lock is operational, the gain of the fast feedback may be increased to remove high-frequency laser noise and reduce the laser linewidth.

3.6 Sample Preparation

In order to ensure that Rydberg polaritons interact strongly, it is essential that the relevant atomic sample hosting Rydberg excitations is small compared to the blockade radius $r_B = (C_6/\gamma_R)^{1/6}$, where C_6 is the van-der-Waals interaction coefficient and γ_R is the ef-

fective linewidth of the Rydberg state, which is, in practice, 100 times broader than the natural linewidth. Helpfully, the optical mode interacting with the atoms provides effective confinement in the transverse directions, since the spatial polariton distribution follows that of the cavity mode. Once a cavity with a suitably small waist size is installed, special effort to manipulate the atomic sample is only required to reduce the *longitudinal* extent of the cloud. While different experiments have differing cavity parameters and principle quantum numbers for the Rydberg excitation, it has generally been the goal to reduce the longitudinal extent of the cloud to around 10 μm.

We have implemented two basic techniques for achieving longitudinal confinement of the cloud. For initial experiments (see Ch. 5), we "sliced" the cloud by depumping all atoms not in a thin strip into a transparent bystander ground state (see Sec. 3.6.1). Due to the temperature of the atoms, this strip would then diffuse over a few hundred μs, requiring that it be repeated many times over even 1 ms of probing. This 1 ms probe time was limited by the atoms' free fall out of the mode of the cavity; leaving the transport lattice on could hold the atoms, but introduce $\sim$ MHz inhomogeneous broadening of the dark polaritons.

Recent experiments (see Ch. 6) upgraded our sample preparation scheme by cooling the atoms with degenerate Raman sideband cooling (dRSC, see Sec. 3.6.3) to around 1 μK [206]. This allows trapping the atoms with a much weaker trap, adding inhomogenous broadening of only around 20 kHz, less than the narrowest observed effective Rydberg linewidth of 50 kHz. This enables implementing an elliptical lattice to hold the atoms after cooling, resulting in a longitudinal atomic cloud radius of 11 μm, smaller than the transverse mode size of our cavity. Our degenerate Raman sideband cooling scheme also naturally spin polarizes the atoms into the $F = 2, m_F = -2$ magnetic sublevel. Along with an applied magnetic field and the driving only of stretched transitions (requiring Rydberg D-states, rather than S-states), optical pumping makes the atoms truly three level systems by removing coupling of the collective Rydberg state to additional collective P states, and thereby reducing effective

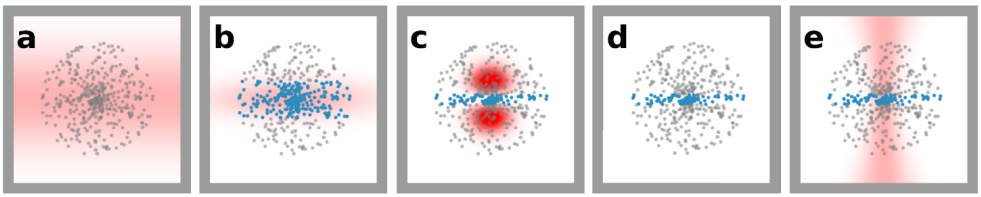

Figure 3.18: **Slicing Beam Sequence. (a-e)** shows the beam setup and the atomic state of one slice-probe cycle. In **a**, all atoms are depumped to $F = 1$. Then (**b**), atoms near the center of the cloud are repumped back into $F = 2$. The repumped atoms are then sliced (**c**) with a TEM_{10} shaped depumper. There is a short wait time (**d**) before probing the atoms in the experiment (**e**). Atoms color coded with blue are in the $|F = 2\rangle$ ground state, and those in gray are depumped to $|F = 1\rangle$ ground state. Figure taken from Ref. [153].

Rydberg state loss from several hundred kHz to 50-80 kHz.

3.6.1 Slicing

To reduce the longitudinal extent of the cloud, we first shine a large global depump beam (Fig. 3.18a) with a waist size of 500 μm. The laser is on resonance with the $|F = 2\rangle \rightarrow \left|F' = 2\right\rangle$ transition and depumps all of the atoms into the $|F = 1\rangle$ ground state. Without this beam, we would typically find the at-the-cavity-waist-equivalent of one atom in the $F = 2$ ground state due to stray atoms beyond the spatial extent of the subsequent beams. Such stray atoms significantly broaden the EIT feature and dramatically reduce blockade effects. A vertical local repump beam (Fig. 3.18b) tuned to the $|F = 1\rangle \rightarrow \left|F' = 2\right\rangle$ transition is then switched on for 2 μs. The beam is narrow in the cavity axis in order to only repump the atoms in the center of the cloud. Finally, another slicing beam with a TEM_{10}-like beam profile (Fig. 3.18c) is turned on and tuned to $|F = 2\rangle \rightarrow \left|F' = 2\right\rangle$ transition. The node of the mode is aligned to the center of the cloud which coincides with the cavity waist. After the final slicing, the longitudinal size of the atomic cloud is reduced to $\sim$10 μm. The probe and control beams are then turned on after the slicing. To avoid creating shelved Rydberg atoms, a 2 μs gap time is set between the slicing and probing processes.

During 1 ms of probe time, 10 slice-probe cycles are implemented to maintain the confinement

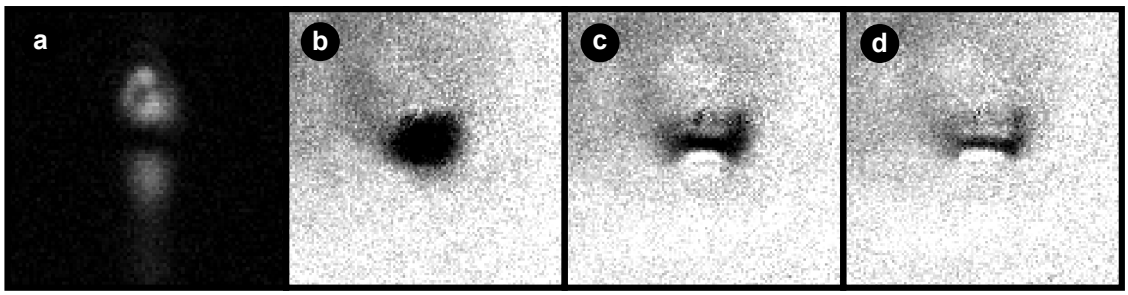

Figure 3.19: **Slicing Beam and the sliced cloud. (a)** A nodal line is produced in the slicing beam by transmission through a π step phase plate. The slicing beam depumps atoms out of $F = 2$ so that they become transparent. **(b-d)** The unsliced cloud (panel **b**) is reduced in size along the vertical axis—corresponding to the direction of the experimental cavity mode—by illumination with the slicing beam (panel **c**). Increasing the duration of the slicing beam shrinks the cloud further (panel **d**), at the cost of reduced remaining atomic density, due to imperfection in the slicing node. Note that the time is increased, not the power, to avoid saturating the depumping transition away from the node. All panels image the same plane with the same imaging system. The resolution is approximately 3 μm per pixel. The large background in the upper half of panels **b-d** is the MOT out of focus below the atomic sample.

of the atomic cloud. The lattice is turned off throughout the process primarily to avoid broadening the Rydberg level, and thus the location and size of the cloud change due to gravity and finite temperature. The free fall limits the total probe time to less than 1.5 ms, during which time the cloud falls by 11.5 μm; within this same interval the cloud also expands to $\sim$100 μm, larger than the slicing beam. As such, a global depump is performed at the beginning of each slicing sequence to remove all of the atoms in the tails, as they would not be depumped effectively by the slicing beam. To maintain constant atom number in the sliced cloud over all 10 slicing cycles in spite of cloud expansion, we repump more weakly in first cycle, and increasingly strongly over subsequent cycles. In so doing we trade peak density for atom number uniformity.

It bears mentioning that the magnetic field is zeroed at the cavity waist in order to minimize the dark-polariton linewidth, without necessitating optical pumping into a single Zeeman sublevel m_F. The $|F = 2\rangle \rightarrow \left|F' = 2\right\rangle$ beams will thus optically pump some of the atoms into a dark state before depumping them to the $|F = 1\rangle$ ground state. To break this dark-state, the global depumping beam is sent through an electro-optical modulator (EOM) with the polarization 45° off of the EOM axis; the EOM is then driven at a frequency of $2\pi \times$

390kHz, producing polarization modulation of the output light. Unfortunately this method is inapplicable to the slicing beam, because it passes through a polarizing beam splitter downstream in the optical path. To rotate the atoms out of the dark state in the slicing process, a weak polarization scrambling beam on $|F = 2\rangle \rightarrow \left|F' = 3\right\rangle$ transition with linear polarization is applied along with the slicing beam.

3.6.2 Stray Atom Removal

If a fraction of the transported atomic cloud is improperly decelerated, atoms may spray upwards in a sort of fountain. The atoms may then intersect the cavity mode near the upper waist, or even in the intermediate arms. Such atoms behave as an absorbing medium, broadening an EIT feature and reducing any blockade effect. To remove these residual atoms, a "blasting" beam from the side which is tuned to $|F = 2\rangle \rightarrow \left|F' = 3\right\rangle$ is aligned between the lower waist and the crossing point. The power of this beam is set to push the atoms away before they reach higher portions of the cavity mode.

3.6.3 Degenerate Raman Sideband Cooling

Degenerate Raman sideband cooling is an efficient and quick scheme to cool atoms trapped in a 3D optical lattice [206]. Our implementation cools our atomic sample from around 25 μK to less than 1 μK (see Fig. 3.21), with the exact final temperature slightly dependent on the atomic density. The basic concept is relatively simple: thermal atoms trapped in a 3D optical lattice live in some highly excited state vibrational state n of a harmonic trap in each of the three directions.

With no applied magnetic field, the vibrational energy levels (for us spaced by $\sim$ 220 kHz with 3 MHz total trap depth) are equal between each magnetic sublevel m_F. By rotating

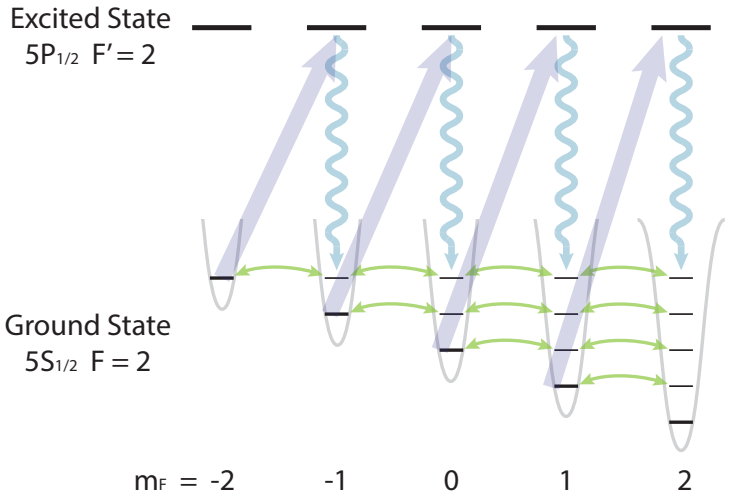

Figure 3.20: **Degenerate Raman Sideband Cooling Scheme.** Our degenerate Raman sideband cooling scheme operates on the D1 line. A magnetic field counterpropagating with the quantization axis produces a Zeeman shift in the ground states; the Zeeman shift of the excited states are not shown because of their large linewidth. When the ground state Zeeman shift equals the vibrational energy level spacing within each harmonic trap, lattice beams drive Raman transitions between degenerate states. Optical pumping on the D1 line serves to spin polarize the atoms in the $m_F = 2$ ground state. Since spontaneous emission does not affect the vibrational energy of each atom, Raman transitions and optical pumping together cool atoms into the lowest vibrational level of the $m_F = 2$ ground state.

retroreflected lattice polarizations slightly, two counterpropagating lattice beams can drive Raman transitions between magnetic sublevels, so long as the connected sublevels are degenerate (since the two lattice beams have the same frequency), that is $|n, m_F\rangle \leftrightarrow |n, m_F - 1\rangle$. Applying a magnetic field naively breaks this degeneracy between sublevels due to the Zeeman effect, and thus stops the Raman transitions. However, when the applied magnetic field produces a Zeeman shift between adjacent magnetic sublevels that equals the harmonic trap spacing, Raman transitions resume, but couple states by trading one harmonic trap quantum for one magnetic quantum. That is, $|n, m_F\rangle \leftrightarrow |n - 1, m_F - 1\rangle$.

Now, we apply an optical pumping beam by driving with σ^+ light on the D1 line $|F = 1\rangle \rightarrow |F' = 2\rangle$ transition, with a weak sideband off-resonantly driving the $|F = 2\rangle \rightarrow |F' = 2\rangle$ transition. If this beam is *both* well polarized and copropagating along the magnetic field axis, it efficiently pumps atoms into the $|F = 2, m_F = 2\rangle$ ground state.

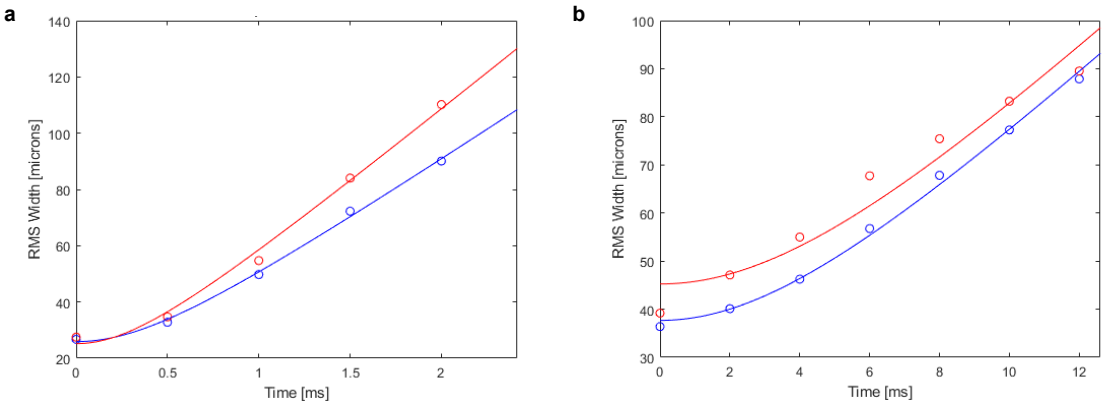

Figure 3.21: **Degenerate Raman Sideband Cooling Results. (a)** Before dRSC, the width of the atomic cloud increases rapidly as it falls (measured by absorption imaging after controlled time-of-flight). This fits to temperatures of 20 μK and 29 μK along the x and y axes. **(b)** After dRSC, the atomic cloud expands much more slowly (note the scale on both axes), corresponding to a temperature of 500 nK along both axes.

Together, the Raman transitions and optical pumping cool the atoms. Raman transitions drive atoms out of the $|F = 2, m_F = 2\rangle$ and reduce the atoms' vibrational state, while the optical pump puts atoms back in $|F = 2, m_F = 2\rangle$ without (in the Lamb-Dicke regime) changing the atoms' vibrational state. This process only stops when the atoms are in the harmonic trap ground state and $|F = 2, m_F = 2\rangle$, which is dark to both the Raman transition and optical pump.

We implement this scheme as follows:

- Our 3D lattice is made from the 1D vertical transport lattice at 784 nm, along with a 2D horizontal lattice using $\sim$ 15 GHz detuned 780 nm light from a free running Eagleyard DFB laser which is split into two inputs. One input beam is retro-reflected while a second beam intersects the retroreflected beam at a 47° angle at the location of the atoms; together these interfere to produce a horizontal 2D lattice orthogonal to the vertical 1D lattice. The horizontal lattice is near detuned to the D2 line, and so heats trapped atoms. However, this lattice is only used while dRSC is operating. Since the cooling provided by dRSC is much stronger than the heating from off-resonant scattering, the heating from the horizontal lattice is irrelevant.

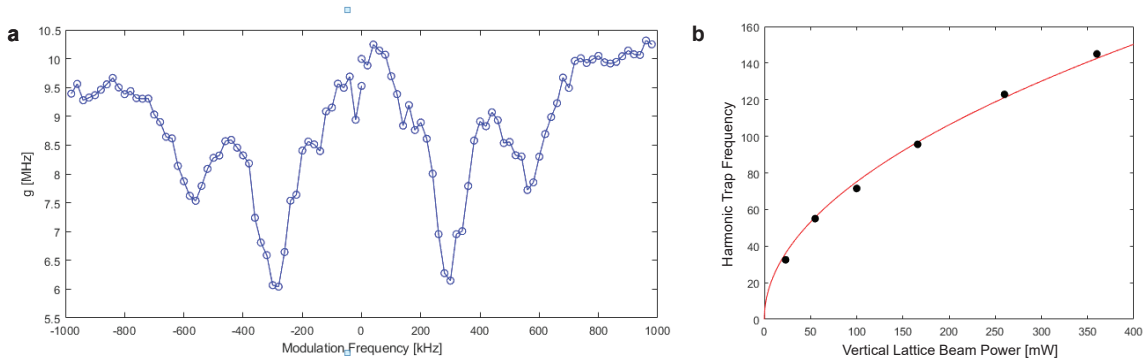

Figure 3.22: **Calibration of Vertical Lattice Trap Frequency via Parametric Resonant Heating.** **(a)** After transport, we hold atoms in the vertical lattice and modulate the lattice depth. When the modulation frequency is *twice* the axial harmonic trap frequency of the lattice, parametric resonance causes rapid heating and loss of atoms, as seen through the resulting vacuum Rabi splitting $g \propto \sqrt{N}$ of the cavity mode. Lattice depth modulation via intensity modulation of the lattice beam is implemented by adding a second RF tone near the 80 MHz carrier of the main lattice AOM; when this second tone is weak, its primary effect is to amplitude modulate the lattice beam at the frequency difference between the tone and the 80 MHz carrier. As the second tone increases in intensity, it also introduces frequency modulation, which causes the appearance of an atom loss feature at the modulation frequency. To avoid this, we operate with the second tone 28 dB smaller than the 80 MHz carrier. The modulation–and the atom loss–is equivalent whether the detuning is positive or negative. **(b)** The measured harmonic trap frequency (half of the detuning of the first atom loss feature) increases with the square root of the lattice power, as expected.

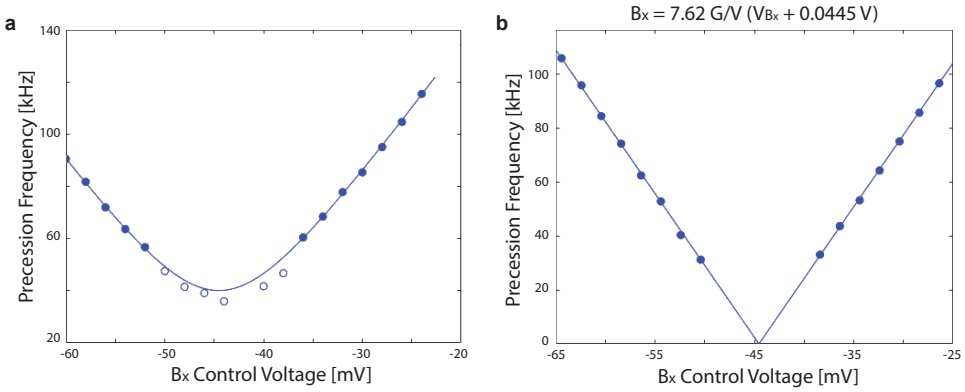

Figure 3.23: **Calibration of Magnetic Field via Larmor Precession.** Atoms are optically pumped in the cavity mode, resulting in vacuum Rabi splitting of the σ^+ polarized cavity mode. An applied magnetic field causes the magnetic spin of the atoms to Larmor precess. Since the Clebsch-Gordon factor relevant for the atom-cavity coupling g depends on the initial magnetic sublevel of the atoms, as the atoms precess, the atom-cavity coupling g oscillates. Probing just outside of a vacuum Rabi peak causes the cavity transmission signal to oscillate at the frequency of the atomic Larmor precession. **(a)** In a background magnetic field, sweeping an applied field minimizes the Larmor precession frequency at zero field along that axis. The fit form $\sqrt{a(V-V_0)^2 + B_{off}^2}$ is applied to the solid points, which are chosen based on the confidence of extracting the Larmor precession frequency, which becomes poor at low frequencies. **(b)** Doing this for all three field directions results in a sharp zeroing of the Larmor precession frequency at zero field. This provides direct calibration of the magnetic field offset and magnitude along all three field directions; the zero is accurate to ~ 3 mG, limited by the orthogonality of the bias field coils (only B_x is shown).

- Our optical pumping beam is produced by a Photodigm DBR at 795 nm locked to a vapor cell via heterodyned saturated absorption spectroscopy on the $F = 2 \rightarrow 1', F = 2 \rightarrow 2'$ crossover feature. It is sent through two 80 MHz AOMs (red sideband) for switching and then sent through a fiber coupled EOM, providing several mW of power to be directed at the atoms. A sideband near 570 MHz drives the $F = 2 \rightarrow 2'$ optical pumping transition, while a sideband near 7.4 GHz provides repumping on the $F = 1 \rightarrow 2'$ transition.

- Matching the Zeeman energy and harmonic trap frequencies requires calibration of all three magnetic field bias coils and the three harmonic trap frequencies. We calibrate lattice trap frequencies by modulating the lattice intensity which parametrically heats (and causes loss of) atoms when the modulation frequency is twice the lattice trap frequency (see Fig. 3.22). We calibrate the magnetic field at the location of the atoms versus magnetic bias coil control voltages by utilizing Larmor precession of a spin polarized atomic sample. As the atoms precess in a magnetic field, they couple more and less strongly to the cavity mode; the frequency of the oscillation of this coupling is the Larmor frequency which provides the absolute magnitude of the magnetic field (see Fig. 3.23).

- While the powers of all three beams forming the horizontal lattice can be controlled to match a horizontal lattice trap frequency to the vertical lattice trap frequency, our horizontal lattice configuration (third beam intersecting at 47°) prohibits exactly matching the two horizontal lattice trap frequencies–they differ by at least $\sim 20\%$. In practice, as shown in figure 3.24, we find that the efficacy of the dRSC is quite insensitive to exactly matching the Zeeman energy and the vibrational energy level spacing, so the $\sim 20\%$ difference in trap frequencies does not matter.

- Pure σ^+ polarization of the optical pump is required to ensure that the $|F = 2, m_F = -2\rangle$ state remains dark, since any π or σ^- light will resonantly drive allowed transi-

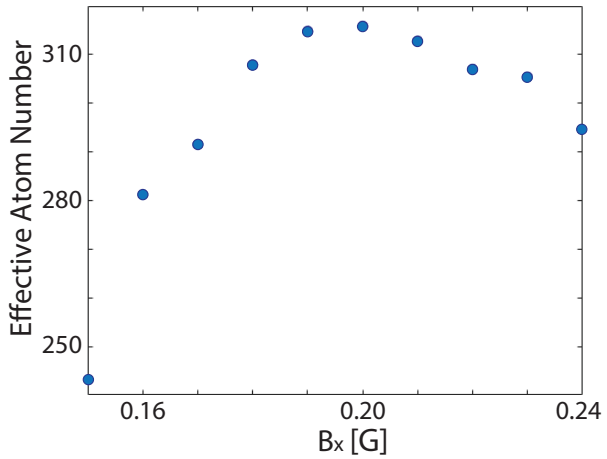

Figure 3.24: **dRSC vs Applied Magnetic Field.** The effectiveness of dRSC is measured by the total number of atoms remaining in the cavity after a hold time of 5 ms; hot atoms are untrapped and fall away within this time. We find that the atom number changes by $< 10\%$ over a broad range of applied fields.

tions. This required special attention to the quality of our waveplates, as well as using uncoated metal mirrors, rather than standard dielectric mirrors that have significant birefringence. We found that day-to-day temperature drifts of the system caused minor polarization drift in the pump due to temperature dependence of birefringence of remaining, particularly in-vacuum, optics. These small polarization drifts would limit the quality of the atomic polarization during experiments, and must be compensated for regularly by maximizing atom number while pumping hard. This same procedure can be used to ensure proper alignment of the pump and magnetic field, although we did not observe drifts in the alignment, so this was only necessary initially.

Once the atoms are cold, they may be transfered and held in a shallow lattice that is then left on throughout the experiment. We replace the slicing procedure described above by making this lattice highly elliptical, so that the depth of the cloud along the cavity axis is similar to or smaller than the fundamental mode waist size. The elliptical lattice is produced using the same light as the transport lattice. The light is diverted into a separate path, reshaped by a cylindrical telescope and sent vertically into the chamber copropagating with the transport lattice. While in principle alternating cycles of cooling and free evolution in the harmonic

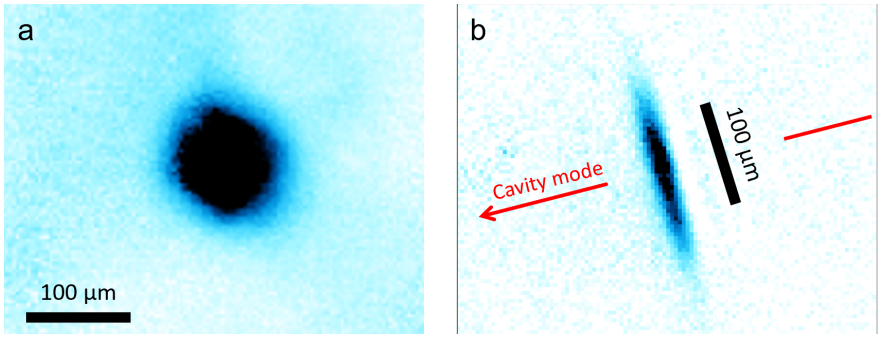

Figure 3.25: **Transfer into the Elliptical Lattice. (a)** The cold dense cloud of atoms after degenerate Raman sideband cooling is shown via absorption imaging. **(b)** A smooth ramp of lattice powers transfers atoms into the shallow elliptical lattice.

trap should enable cloud compression and enhanced final atomic density in the elliptical lattice, we were unsuccessful in achieving greater atom number than provided by a single adiabatic ramp up of the elliptical lattice.

The elliptical lattice has a lifetime in excess of 200 ms, and we wish to probe for around 100 ms to achieve a total data collection duty cycle approaching 50%. To keep atom number constant throughout the probe time, we initially depump a small proportion of the atoms into the $F = 1$ ground state. Every 10 ms, we repump a small fraction of these atoms to replace the atoms lost during the preceeding 10 ms. We then also apply a pure optical pumping pulse (with no repump sideband!) with the D1 laser. This procedure stabilizes the collective coupling g to within 5% over the entire 100 ms probe time.

3.7 P-state Modulation

As discussed in the second half of chapter 5 and in 6, we enable Rydberg polaritons in separate, non-degenerate spatial modes to interact by bridging the frequency difference between modes via frequency modulation of the intermediate $5P_{3/2}$ state. We achieve this goal using a multichromatic field near the $5P_{3/2} \rightarrow 5D_{5/2}$ transition at 776 nm (Fig. 3.26b), or, after an upgrade, near the $5P_{3/2} \rightarrow 4D_{5/2}$ transition at 1529 nm. The field contains red-detuned

(lower frequency than resonance) and blue-detuned (higher frequency) components, each approximately 1 GHz away from resonance on opposite sides of the transition, so that there is no average Stark shift of the $5P_{3/2}$ state. Then, we intensity modulate the blue-detuned component to cause the energy of the $5P_{3/2}$ state to oscillate around zero with controllable frequency f and amplitude η. We tune the modulation amplitude by adjusting the total intensity of the 776 nm laser.

To generate the multichromatic field, we begin with a single frequency source with a total power of 20 mW which is red-detuned from the transition, locked at detuning $\delta = -\Delta$ (where $\Delta \equiv 1$GHz) relative to the resonance frequency. We then generate the blue-detuned component using a fiber electro-optic modulator (EOM), driven with two RF tones at 2Δ and $2\Delta + f$. This modulation generates a variety of sidebands, most of which are farther detuned from the resonance than the original beam. The sidebands which eventually produce the greatest shifts of the $5P_{3/2}$ state are the blue-detuned bands at $\delta = \Delta, \Delta + f$ which have similar detuning to the original beam and are first order in the RF power. These two frequency components are equivalent to a single component at $\Delta + f/2$ which is intensity modulated at frequency f. Therefore, our scheme can be understood simply as producing a red-detuned component with constant intensity and a blue-detuned component with modulated intensity. Finally, in order to enable large shifts of the $5P_{3/2}$ state, the entire modulated beam is sent through a tapered amplifier to achieve a maximum power of about 1 W before illuminating the atomic

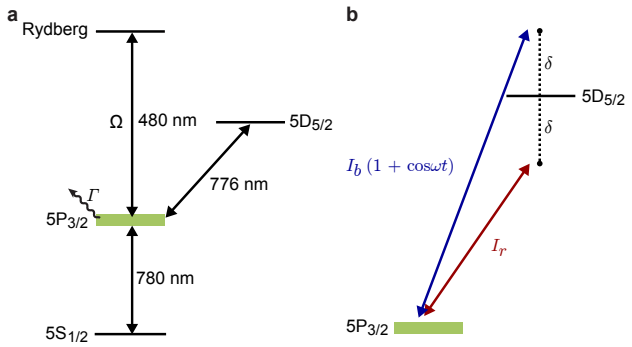

Figure 3.26: **Atomic level diagram. (a)** Three key electronic transitions of ^{87}Rb atoms enable the formation of Floquet polaritons. First, cavity photons near 780 nm couple with the $5S_{1/2} \rightarrow 5P_{3/2}$ atomic transition. Second, a beam near 480 nm drives the $5P_{3/2} \rightarrow nS_{1/2}$ transition to the Rydberg level with principal quantum number n at strength Ω. Third, a multichromatic field near the $5P_{3/2} \rightarrow 5D_{5/2}$ transition modulates the energy of the $5P_{3/2}$ state. **(b)** The multichromatic field has two components with approximately opposite detunings $\mp\delta$: a red-detuned component with constant intensity I_r, and a blue-detuned component with sinusoidally modulated intensity $I_b(1 + \cos\omega t)$. Figure taken from Ref. [207].

sample. We experimentally adjust the exact detunings and RF powers in order to achieve the largest possible $5P_{3/2}$ modulation for a given total laser power while also ensuring that the average Stark shift of the $5P_{3/2}$ state is zero.

We have designed our setup to avoid a few detrimental side effects of frequency modulation. First, we have attempted to make the average Stark shift of the $5P_{3/2}$ state as small as possible, such that the $j = 0$ band always remains at the same energy as the unmodulated $5P_{3/2}$ state. This choice is important because it ensures that the $5P_{3/2}$ band frequencies are not varying spatially due to to inhomogeneity in the modulation laser beam intensity profile, nor do they fluctuate over time due to total intensity instability. Moreover, canceling the average Stark shift also ensures that we do not have to tune the cavity length to match a new $j = 0$ band frequency every time we adjust the modulation amplitude. Note that, in this setup, the largest remaining source of temporal drift in the average Stark shift of the $5P_{3/2}$ state seems to come from the tapered amplifier, whose relative amplification of the various EOM sidebands exhibits very small fluctuations due to temperature instability. We suspect that this comes from a weak etalon effect in the amplifier chip; we observe that the $5P_{3/2}$ energy oscillates as we steadily increase the amplifier temperature. We believe that we mitigated this effect somewhat by choosing an amplifier temperature which is at an extremum of the oscillation, making the system quadratically insensitive to temperature fluctuation around the extremum.

A second detrimental side effect comes from the off-resonant shift of the $5S_{1/2}$ state. The multichromatic field is only 4 nm detuned from the strong $5S_{1/2} \rightarrow 5P_{3/2}$ transition at 780 nm. In principle, this shift could also be canceled, for example by using a copropagating beam at approximately 784 nm, but in practice cancellation was not practical in this case. We minimized the inhomogeneity of this shift, which would otherwise cause broadening of the dark polariton lines, by ensuring that beam was large (approximately round with a waist of 70 μm) compared to the horizontal cavity mode waist of 12 μm. Moreover, the 776 nm

beam propagates along the vertical axis (the long axis of the TEM_{40} mode), ensuring that its intensity is approximately homogeneous across the sample along that axis without needing to increase the waist size. With sufficiently small inhomogeneity, we are able to slightly adjust the cavity length to account for the net shift of the $5S_{1/2}$ state without any deterioration of the performance in our system.

Subsequent experiments (see chapter 6) benefit from an upgrade our apparatus to use a modulation field near the $5P_{3/2} \rightarrow 4D_{5/2}$ transition at 1529 nm instead of the 776 nm field. This substitution has three key advantages. First, the $5P_{3/2} \rightarrow 4D_{5/2}$ transition is stronger than the $5P_{3/2} \rightarrow 5D_{5/2}$; switching transitions makes the energy modulation approximately 40× larger for similar beam intensity. Second, the new detuning from the $5S_{1/2} \rightarrow 5P_{3/2}$ transition is nearly 100× greater, dramatically reducing the off-resonant shift of the $5S_{1/2}$ state. Finally, fiber EOMs operating at 1529 nm can operate with much higher total powers, even exceeding 1 W, enabling us to put the modulator after the amplifier and thus preventing the amplifier from causing instability in the intensity ratios of the various frequency components in the field.

CHAPTER 4

INTEGER QUANTUM HALL PHYSICS WITH PHOTONS

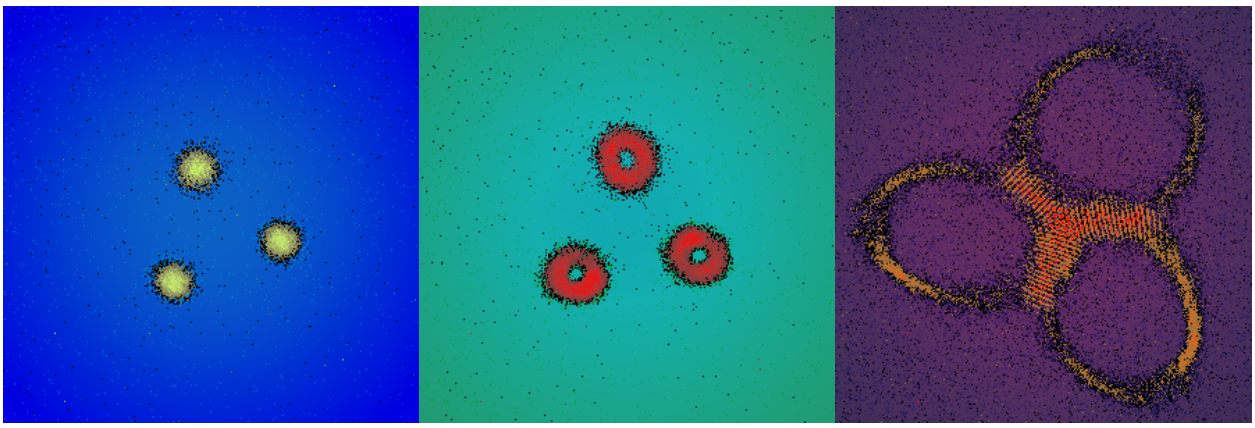

Figure 4.1: **Photonic states in a Landau level on a cone.**

In this chapter, we implement a novel cavity design supporting degenerate sets of Laguerre-Gaussian modes and link the corresponding two dimensional dynamics for photons to those of a massive charged particle in a magnetic field and, potentially, a harmonic trap. To maintain cavity stability, we impose a threefold rotational symmetry on nearly degenerate cavity modes. We can then identify these nearly degenerate sets of modes as Landau levels for photons and observe their formation as the length of the experimental cavity is adjusted. The effect of the threefold rotational symmetry is to effectively place the Landau level on the surface of a cone, since a one-third wedge of real space contains complete information and has periodic boundary conditions.

The link between the presence of Landau levels and non-interacting quantum Hall systems is straightforward: an integer quantum Hall material is formed when particles occupy each state in a Landau level with equal population. Thus we can observe properties associated with integer quantum Hall physics, including a build up of state density at the cone tip due to the singularity of spatial curvature. This is linked to the underlying topological structure of a Landau level. To explore this further, we measure the three topological invariants that

characterize a general quantum Hall system, the Chern number, the mean orbital spin, and the chiral central charge. The buildup of state density and its spatial extent around the cone tip provide direct access to the latter two, while the Chern number is measured via a real space projective scheme which reveals the underlying chiral structure of single particle states. Together, these experiments develop new observables and techniques of their measurement to access topological effects of quantum Hall physics.

This chapter is based on Ref. [182]

> Nathan Schine, Albert Ryou, Andrey Gromov, Ariel Sommer, and Jonathan Simon. Synthetic Landau levels for photons. *Nature*, **534**, 671 (2016).

and Ref. [208]

> Nathan Schine, Michelle Chalupnik, Tankut Can, Andrey Gromov, and Jonathan Simon. Electromagnetic and gravitational responses of photonic Landau levels. *Nature* **565**, 173 (2019).

4.1 Landau Levels for Photons

Synthetic photonic materials are an emerging platform for exploring the interface between microscopic quantum dynamics and macroscopic material properties[74, 85, 209–213]. Photons experiencing a Lorentz force develop handedness, providing opportunities to study quantum Hall physics and topological quantum science[214–216]. Here we present an experimental realization of a magnetic field for continuum photons. We trap optical photons in a multimode ring resonator to make a two-dimensional gas of massive bosons, and then employ a non-planar geometry to induce an image rotation on each round-trip[190]. This results in photonic Coriolis/Lorentz and centrifugal forces and so realizes the Fock-Darwin Hamiltonian

for photons in a magnetic field and harmonic trap[61]. Using spatial- and energy-resolved spectroscopy, we track the resulting photonic eigenstates as radial trapping is reduced, finally observing a photonic Landau level at degeneracy. To circumvent the challenge of trap instability at the centrifugal limit[61, 62, 65, 217], we constrain the photons to move on a cone. Spectroscopic probes demonstrate flat space (zero curvature) away from the cone tip. At the cone tip, we observe that spatial curvature increases the local density of states, and we measure fractional state number excess consistent with the Wen-Zee theory, providing an experimental test of this theory of electrons in both a magnetic field and curved space[218–221]. This work opens the door to exploration of the interplay of geometry and topology, and in conjunction with Rydberg electromagnetically induced transparency, enables studies of photonic fractional quantum Hall fluids[116, 119] and direct detection of anyons[222, 223].

4.1.1 Synthetic Magnetic Field

The Lorentz force on a charged particle moving in a magnetic field leads to the unique topological features of quantum Hall systems, including precisely quantized Hall conductance, topologically protected edge transport, and, in the presence of interactions, the predicted anyonic and non-abelian braiding statistics that form the basis of topological quantum computing[14]. To controllably explore the emergence of these phenomena, efforts have recently focused on realizing synthetic materials in artificial magnetic fields, and in particular, upon implementations for cold atoms and photons. Successful photonic implementations have employed lattices with engineered tunneling[214, 216, 224–226]. However, it is desirable to realize artificial magnetic fields in the simpler case of a continuum (lattice-free) material[120, 215, 227], where strong interactions are more easily accessible and the theory maps more directly to fractional quantum Hall systems. In this work, we develop a new approach and demonstrate the first continuum synthetic magnetic field for light.

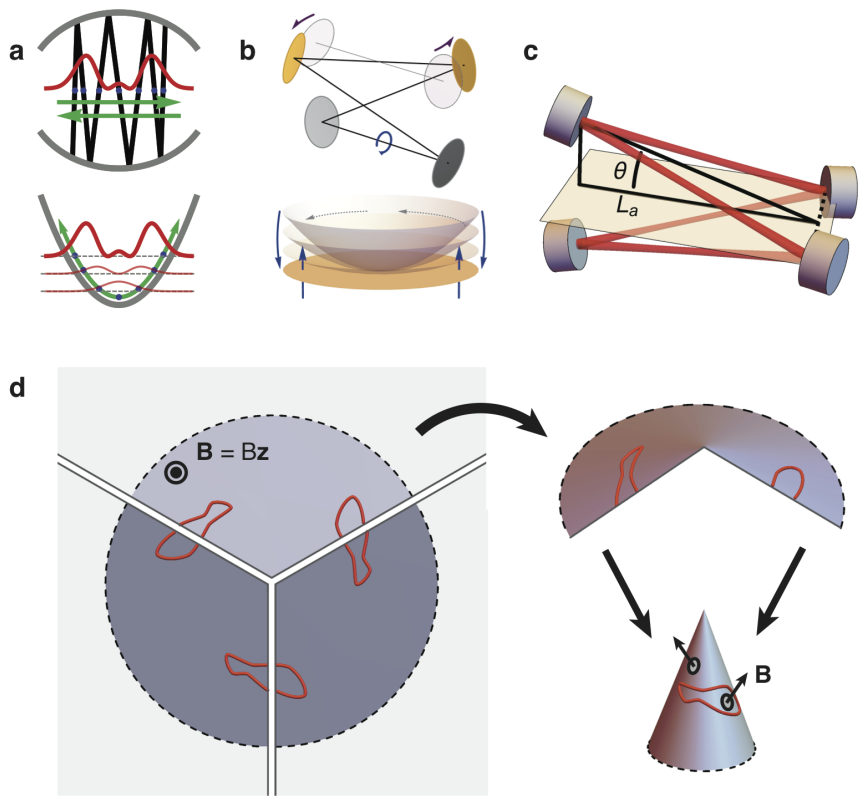

Figure 4.2: **Resonator structure and transverse manifold geometry. a,** Top, ray trajectories (black lines) in a curved mirror resonator oscillate transversely (green arrows). In a particular transverse plane, the stroboscopic time evolution of the ray-positions samples a harmonic oscillator trajectory (blue points). In paraxial optics, the solutions for the transverse modes are Hermite-Gauss profiles (red curve). The transverse degrees of freedom of a resonator are precisely those of a 2D quantum harmonic oscillator (below). **b**, Top, as a four mirror resonator is made non-planar (purple arrows), the light rays are induced to rotate (blue arrow) about the optic axis. In the transverse plane (represented below), this corresponds to flattening the 2D harmonic potential (centrifugal force) and the introduction of an effective magnetic field (Coriolis force). **c**, Our non-planar resonator consists of four mirrors (blue and purple) in a stretched tetrahedral configuration of on-axis length L_a and opening half-angle θ. The image rotates about the optic axis (red) on every round trip. **d**, We depict the transverse plane at the resonator waist pierced by a uniform perpendicular (along $\hat{\mathbf{z}}$) magnetic field $\mathbf{B}$ of magnitude B, and show a generic profile (red curve) with threefold symmetry. When the plane is cut arbitrarily into three equal sections, the entire profile is fully determined within any one-third section of the plane: when a trajectory leaves one side of a section, it reappears on the other side. Each section may be wrapped into a cone on which the original profile appears once (this would be true for any discrete rotational symmetry). The effective magnetic field is everywhere perpendicular to the cone's surface. Figure taken from Ref. [182].

To achieve photonic Landau levels we harness the powerful analogy between photons in a near-degenerate multimode cavity and massive, trapped 2d particles[73, 181]. Owing to mirror curvature, the transverse dynamics of a running wave resonator are equivalent to those of a 2D quantum harmonic oscillator (Fig. 4.2a). Non-planar reflections cause the

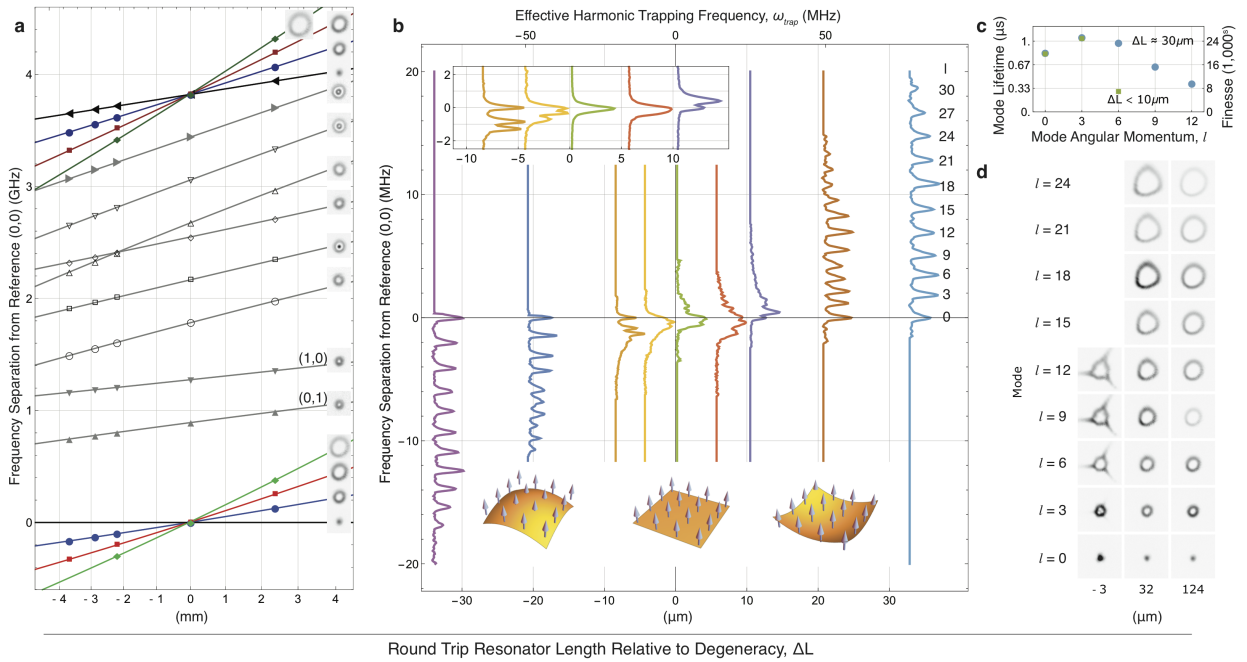

Figure 4.3: **Building a Landau level.** The modes of our resonator follow the Fock-Darwin Hamiltonian of a massive, harmonically trapped particle in magnetic field: the magnetic field creates a ladder of Landau levels uniformly spaced by the cyclotron frequency, ω_c, while the harmonic trap of frequency ω_{trap} uniformly splits levels within each Landau level by ω_{trap}^2/ω_c (see Appx. A.1.4). We probe this spectrum versus resonator length L_{rt}, and demonstrate that, for each L_{rt}, the spectrum is determined by two energies $\nu_{(1,0)}$ and $\nu_{(0,1)}$ according to $\nu_{(\alpha,\beta)} = \alpha\nu_{(1,0)} + \beta\nu_{(0,1)} \mod \nu_{FSR}$, where $\omega_c = 2\pi \times \nu_{(1,1)}$ gives the cyclotron frequency and $\omega_{trap}^2/\omega_c = 2\pi \times \nu_{(3,0)}$ provides the harmonic trapping frequency. Furthermore, fine-tuning L_{rt} drives ω_{trap} to zero, bringing specific sets of angular momentum eigenmodes into degeneracy, thereby forming Landau levels. **a,** The frequency separations between several modes and a reference $l = 0$ mode are plotted as the harmonic confinement is coarsely tuned relative to an approximately degenerate reference length $L_{rt} = 78.460$ mm (corresponding free spectral range $\nu_{FSR} = 3.8209$ GHz). Solid lines are obtained as integer linear combinations of fits to the modes labeled (1,0) and (0,1) and the free spectral range. **b,** Main panel, we plot the transmission spectrum of the first ~ 10 modes in the lowest Landau level against small deviations from nominal degeneracy. Top inset, low order modes become degenerate to within a resonator linewidth, $\kappa \approx 200$ kHz, while in the main panel, we observe weak level repulsion (approximately equal to the resonator linewidth) in the higher order modes consistent with mode mixing due to mirror imperfections of $\sim \lambda/5000$. ω_{trap} is presented on the upper horizontal axis. **c,** The lifetimes (and corresponding finesses) of representative modes decrease for higher mode numbers both away from degeneracy (blue circles) and near degeneracy (green squares). Here ΔL is the offset of the round trip resonator length from nominal degeneracy. **d,** With significant residual harmonic trapping ($\Delta L = 124$ μm), angular momentum modes are simple rings. As the trapping is reduced ($\Delta L = 32$ μm), high angular momentum modes begin to mix due to local disorder. When the trapping is precisely cancelled ($\Delta L = -3$ μm), mirror imperfection consistent with a single nanoscopic scratch dramatically alters the modes' shape away from the predicted near-Laguerre-Gauss profiles. Even the first resonator mode is noticeably triangular, indicating at least a mixing of Laguerre-Gauss $l = 0$ and $l = 3$ modes. Overcoming this disorder necessitates only ~MHz photon-photon interactions to explore strongly correlated physics. Figure taken from Ref. [182].

transverse properties of the light field—for example, field profile (image) and polarization vectors—to rotate by an angle ϕ upon a round trip (Fig. 4.2b). Polarization rotation splits the energy of circularly polarized eigenmodes, while image rotation, in analogy to a rotating

frame, introduces Coriolis and centrifugal forces. As the anti-confinement from the rotation compensates the confinement from the mirror curvature, we are left primarily with a Coriolis force, or equivalently, a Lorentz force. When dynamics are coarse-grained over many-round trips, we arrive at the Fock-Darwin Hamiltonian (see Appx. A.1.4) $H_{FD} = \frac{1}{2m}(\vec{\mathbf{p}} - \frac{(qB)^{syn}}{2}\hat{\mathbf{z}} \times \vec{\mathbf{r}})^2 + \frac{1}{2}m\omega_{trap}^2 r^2$, where m is the dynamical particle mass, $\vec{\mathbf{p}}$ is the particle's transverse momentum vector, $\vec{\mathbf{r}}$ is the particles transverse position vector, $\hat{z}$ is the longitudinal unit vector, and $\omega_{trap}/2\pi$ is the (residual) harmonic trapping frequency. The synthetic magnetic field is[181] $(qB)^{syn}/\hbar = \frac{2\pi}{\lambda L_a}\phi \approx \frac{8\pi}{\lambda L_a}\theta^2$ for small angles θ, where L_a and θ are the on axis resonator length and opening half angle (Fig. 4.2c), and λ is the wavelength of light. When the resonator length is tuned to eliminate residual harmonic trapping, only a Lorentz force remains, and the Hamiltonian describes massive particles in Landau levels, where the nth Landau level has energy $\hbar\omega_c(n + \frac{1}{2})$, with ω_c being the cyclotron frequency, and consists of states with angular momentum $l = -n, -n+1, \ldots$ in units of the angular momentum quantum $\hbar$. The synthetic magnetic field is then equivalently given by $(qB)^{syn}/\hbar = 4/w_0^2$, that is, one flux quantum per area $\pi w_0^2/4$, where w_0 is the resonator $l = 0$ mode waist ($1/e^2$ intensity radius). The magnetic length l_B may therefore be identified as $w_0/2$.

4.1.2 Reaching Degeneracy: Landau Levels on a Cone

Although Landau levels exhibit 'topological protection' against localized disorder, long-range potentials may guide the particles to infinity, inducing loss[63, 217]. In our system, the dominant source of long-range disorder is trap asymmetry (astigmatism) that arises from mirror imperfections and off-axis reflection and drives $\Delta l = \pm 2$ transitions (see Sec. 3.1.1.2). We circumvent this by imposing an additional discrete threefold rotational symmetry on our Landau levels. To achieve this, we carefully balance transverse and longitudinal energy scales by making the Gouy phase for one transverse mode exactly one third, so that only every third angular momentum state is degenerate (see Sec. 3.1.1.1).

The threefold symmetry of the Landau levels induces a conical geometry on the 2D space for transverse photon dynamics. To see this, consider a particle which leaves the edge of a particular 120° wedge of the plane; the discrete rotational symmetry requires it to appear on the other side, which is equivalent to wrapping this wedge into a cone (Fig. 4.2d). Working away from the apex of the cone gives access to flat space Landau levels with every angular momentum state accessible, while working near the apex allows experimental investigation of particle dynamics near a singularity of spatial curvature.

Our experimental resonator consists of four mirrors with nominal radii of curvature $R = (2.5, 5, 5, 2.5)$ cm arranged as shown in Fig. 4.2c, and has an $l = 0$ mode finesse of $2. \times 10^4$. The on-axis length $L_a = 1.816$ cm and the opening half-angle $\theta = 16°$ were chosen to create a photonic Landau level while minimizing residual astigmatism. Varying the resonator length by ~ 20 μm adjusts the splitting between states by ~ 1 MHz (see Appx. A.1.2). Tuning this splitting to zero results in a free spectral range at degeneracy of $\nu_{FSR} = 3.8209(2)$ GHz. The resonator has an $l = 0$ waist size $w_0 = 43$ μm and a cyclotron frequency $\omega_c = 2\pi \times 2.1671(2)$ GHz, which together yield a photon dynamical mass of $m_{dyn} = \frac{4\hbar}{\omega_c w_0^2} = 1.84 \times 10^{-5}$ m_e where m_e is the electron mass.

We perform mode-dependent cavity spectroscopy using two narrow 780 nm laser probes. The first is the output of a digital micromirror device (DMD, see Sec. 3.2) for arbitrary mode injection. The second is the output of a fiber-coupled electro-optic modulator (EOM) that is coupled only to the $l = 0$ cavity mode. We track the energy spectrum and spatial profiles of resonator modes by observing the transmission signal of circularly polarized light on an avalanche photodiode while sweeping the cavity length and tuning the EOM modulation frequency until the $l = 0$ sideband overlaps the desired mode; we may read off the mode spacing as precisely that modulation frequency. This avoids the need to calibrate the nonlinear scan of the cavity piezo.

In practice, we tune our resonator to degeneracy by varying its length, which primarily

changes the harmonic trapping without changing the effective magnetic field. Figure 4.3a shows the evolution of a number of mode energies in numerous Landau levels as we adjust the resonator length over almost a centimeter. Using the observed mode-profiles (shown as insets), we identify the four lowest modes in the figure as those comprising the lowest conical Landau level, and centre the graph on their approximate degeneracy point. Figure 4.3b shows high-resolution spectroscopy of a larger number of modes in the lowest Landau level near the length where the harmonic confinement is cancelled. We precisely extract the change in resonator length from the spectroscopically measured free spectral range and compensate the residual harmonic trapping to zero. At this point, the residual non-degeneracy comes from local disorder, which causes an observed level repulsion for high angular momentum states (Fig. 4.3b, main panel) that is not observed at lower angular momentum (Fig. 4.3b, top inset) as well as a significant reduction in mode lifetime (Fig. 4.3c). Away from degeneracy the modes are nearly ideal rings with $2\pi \times l$ phase winding (experimentally determined by varying the phase profile of the injected light); at degeneracy these modes mix due to local disorder potentials (Fig. 4.3d). This effect is apparent because of the long particle lifetime (high finesse of our resonator) and, in only causing mode distortion, is qualitatively different from global potentials such as astigmatism that cause mode deconfinement. The local disorder merely creates chiral, localized states; it does not break topological protection so long as it only mixes modes within a single Landau level and, in an interacting system, is weaker than the interactions. This insensitivity to weak disorder is a notable advantage of our setup as compared to, e.g. injecting angular momentum modes into a two mirror resonator.

4.1.3 Structure of a Landau Level

4.1.3.1 Magnetic Translations

To demonstrate our system's stability out to large displacements from the cone tip, figures 4.5a-b show large angular momentum orbits. Figure 4.5a presents a large displaced state composed of modes with angular momentum up to $l \approx 60$, which exhibits threefold symmetry and interferes with itself, producing a strongly fringed pattern due to the rapid phase winding of each ring. Figure 4.5b unwraps another large angular momentum mode showing that if an orbit encircles the cone tip, then it must do so three times, as a consequence of the threefold symmetry.

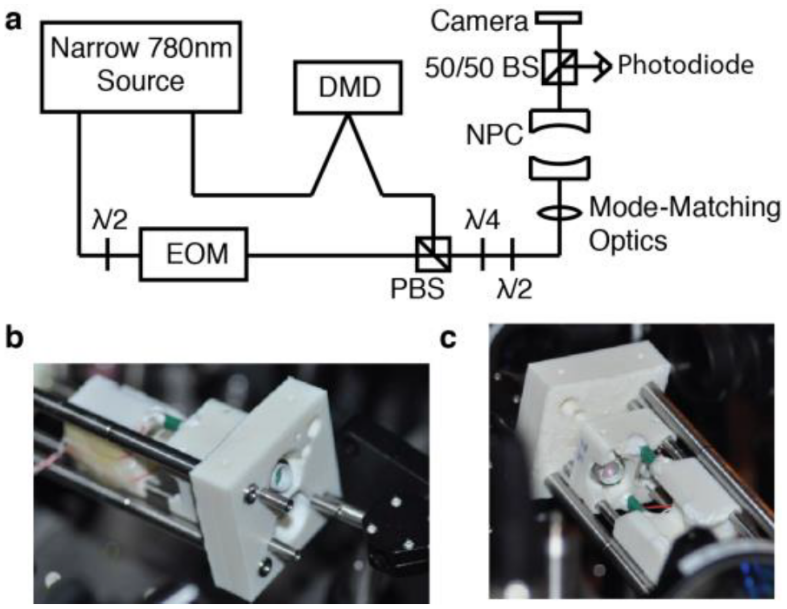

Figure 4.4: **Experimental Apparatus. (a)** A schematic of the experimental setup is shown. Two beams from a 780 nm laser with a $\sim 10\ kHz$ linewidth are used. One reflects off a digital micromirror device while a second passes through an electro-optic modulator before being combined on a polarizing beam splitter. Two waveplates and mode matching optics allows coupling into a single circularly-polarized mode of the resonator; the reference beam couples into the (0,0) mode while the DMD beam couples into any mode as determined by the hologram projected onto the DMD surface. The transmitted light is collected on a camera and a photodiode. **(b,c)** Photographs of the front and back of the experimental cavity structure show mirrors in stainless steel holders embedded in two 3D printed plastic mounts. Two piezos (green) move the smaller, back mount along rails to vary the resonator round trip length. Figure taken from Ref. [182].

Remarkably, photons in our resonator may live on three distinct cones, distinguished by additional magnetic flux threaded through their tips. To understand this, note that the planar lowest Landau level may be spanned by angular momentum states $\psi_l(z = \frac{x+iy}{w_0}) \propto z^l e^{-|z|^2}$ for $l = 0, 1, 2, \ldots$, with the transverse position vector $\vec{\mathbf{r}} = (x, y)^\mathsf{T}$. In our resonator these are partitioned into three separately degenerate sets corresponding to lowest Landau levels on different cones. These sets are the $l = 0, 3, 6, \ldots$ modes, the $l = 1, 4, 7, \ldots$ modes, and the $l = 2, 5, 8, \ldots$ modes and satisfy the angular symmetry condition $\psi_l(\theta + \frac{2\pi}{3}) = e^{2\pi i c/3}\psi_l(\theta)$, where $c = 0, 1$, or 2 is the lowest angular momentum state in the set and serves

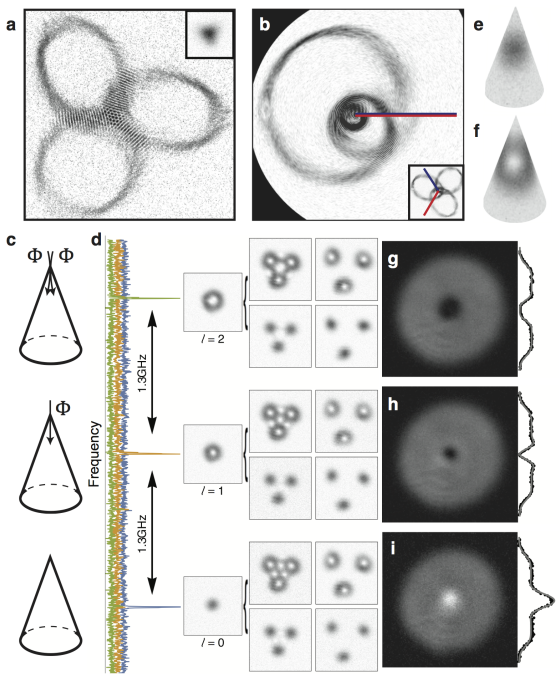

Figure 4.5: **Photonic lowest Landau levels on a cone. a,** At degeneracy, all resonator modes display three-fold symmetry. We present a very large displaced angular momentum mode with radial extent up to 8 times the mode waist, w_0, implying that ∼20 modes must be degenerate. The rapid phase winding for large l modes causes the strong fringing pattern when the mode self-interferes. Inset, an $l = 0$ mode at the same scale. **b,** We project another large angular momentum mode onto a cone and view it from above the apex. We observe a general property that circular orbits must encircle the cone apex either zero or three times. Inset, the original image of the mode. The pair of rays overlaying the inset image corresponds to the cut in the main image. **c,** The twisted resonator corresponds to Landau levels on three cones with differing quantities of magnetic flux threaded through the tip. The cone built out of $l = 0, 3, 6, \ldots$ has no flux threading; the cone built out of $l = 1, 4, 7, \ldots$ is threaded by $\Phi_0/3$; and the cone built out of $l = 2, 5, 8, \ldots$ is threaded by $2\Phi_0/3$, where Φ_0 is the magnetic flux quantum. **d,** With the resonator tuned to degeneracy, we identify the energies of the $l = c$ modes for $c = 0, 1$, or 2 by the transmission peaks (blue, orange, and green curves, respectively) that correspond to the correct observed transmitted mode's profile (single images, labelled). The degenerate sets starting with these modes each form a lowest Landau level on different cones. Except at the apex, each cone is flat, so away from the tip each lowest Landau level supports modes of—and therefore the dynamics of—a planar lowest Landau level with $l = 0, 1, 2, \ldots$ defined about a displaced point. On each cone, we show displaced $l = 0$ (bottom two) and $l = 1$ (top two) modes. For large displacements (right two), these modes are undistorted; however, for small displacements (left two), where there is significant mode amplitude at the tip, we observe distortions due to self-interference, similar to panel **a**. **e,f,** Displaced $l = 0$ and $l = 1$ modes from **d** are projected onto a cone to show how observed mode images may be interpreted on a conical surface. **g-i,** We explore the effects of curvature and flux threading near the tip by measuring the local density of photonic states. For the $c = 0$ cone (**i**), we find an approximately threefold increase in local state density near the cone apex above a constant background plateau of density. This corresponds to an additional one-third of a state localized near the apex. For the cones with $c = 1$ and 2 (**h** and **g**, respectively), we find a vanishing local density of states near the apex, reflecting the negative magnetic flux threading through the cone apex. Each unit of flux removes one-third of a state local to the apex so that the $c = 1$ cone has no additional states, and the $c = 2$ cone is missing one-third of one state. The data to the right display a slice through the middle of each image; the gray curves are fits to the expected analytic form (see Appx. A.1.9). Figure taken from Ref. [182].

as the cone's label. c = 0 defines the symmetry relation that describes an unthreaded cone; with $c \neq 0$, the cone has an additional Aharanov-Bohm phase arising from $c/3$ magnetic flux quanta threaded through its tip (Fig. 4.5c). Angular momentum states encircling the cone tip enclose this flux three times, so states experience integer flux, reflected in their $\sqrt{l}$ radial extension.

Away from the apex, photons on each cone behave as in a flat space lowest Landau level. In Fig. 4.5d, we identify each cone by the lowest angular momentum state supported around its apex. Then, on each cone, we show that we can create arbitrary angular momentum states ($l = 0, 1$) about displaced points so long as the displaced mode does not self intersect or encircle the cone tip. Beyond reflecting the invariance of our system under magnetic translations, this permits the creation of canonical fractional quantum Hall states in a future interacting system, in addition to novel Laughlin states accessible at the cone tip (see Appx. A.1.7). As a visualization, figures 4.5e-f project these displaced $l = 0$ and $l = 1$ modes onto a cone, further demonstrating that, away from the apex, modes on the cone closely resemble modes on a regular plane.

4.1.3.2 Probing Topology

Particles living in a Landau level directly realize an integer quantum Hall material if the population of each state in the Landau level is equally populated. In this first investigation of an integer quantum Hall fluid of photons, we investigated an effect of the singularity of spatial curvature at the cone tip on the particle density as a function of space (local density of states, or LDOS). In particular, although the LDOS is typically uniform in a quantum Hall state, the LDOS develops remarkable structure when the space in which the quantum Hall state resides is curved. This response to geometric deformation (sometimes called a *gravitational response*), is topological in origin.

The topological numbers that characterize quantum Hall phases are predicted to specify the response of the photonic local density of states to magnetic field and spatial curvature, as described by the Wen-Zee theory[218–221] (see Appx. A.1.8). We perform an experimental test of this theory by measuring the LDOS (Figs. 4.5g-i) via transmission images of each state in the relevant weakly split Landau level and summing these images (see Appx.A.1.9). We then compare the LDOS near the cone tip with the flat space density away from the tip (within each panel Fig. 4.5g-i) and compare the LDOS with different quantities of flux threaded (between panels Fig. 4.5g-i). We clearly observe a density buildup for the $c = 0$ cone; however, we find a vanishing LDOS on the other two cones, reflecting additional magnetic flux threaded through their tips equal to $-\Phi_0/3$ and $-2\Phi_0/3$, where Φ_0 is the magnetic flux quantum (Fig. 4.5c). According to the Wen-Zee effective theory, the expected excess state number is given by $\delta N = \frac{2}{3}\bar{s} - \frac{c}{3}$, where $c/3$ is the number of flux quanta threaded through the cone tip and $\bar{s}$ is a parameter called the mean orbital spin that characterizes particles' coupling to spatial curvature and is predicted to be $1/2$ for the lowest Landau level[218]. We therefore expect $\delta N = 1/3, 0,$ and $-1/3$ of a state near the tips of the $c = 0, 1,$ and 2 cones, respectively. By integrating the measured LDOS excess or deficit near the apex, we measure the state number excess to be $0.31(2)$ on the $c = 0$ cone, $-0.02(1)$ on the $c = 1$ cone, and $-0.35(2)$ on the $c = 2$ cone, yielding the experimentally measured value $\bar{s} = 0.47(1)$. We find quantitative agreement between our measured results and the Wen-Zee theory.

We can extend our test of the Wen-Zee theory by measuring fractional state number excess in higher Landau levels, where radial structure in the constituent modes causes dramatic oscillations in the local state density. Beyond the mean orbital spin, there are two additional topological invariants that characterize a quantum Hall state. The same LDOS measurements could provide access to the chiral central charge through the second moment of the excess particle density; however, the experimental apparatus used so far displayed too much residual astigmatism to permit this measurement. Additionally, the Chern number could

be measured through local real-space projective measurements in which, like a scanning-tunnelling microscope, we raster a weak, local probe and monitor the cavity response. In order to access these additional topological invariants, we rebuilt the experimental apparatus with several upgrades in mind. To reduce astigmatism, the mirror curvature was significantly reduced to 100 *mm* radii-of-curvature for all four mirrors, while special care was taken in aligning the imaging system. To enable a stable raster scan, the experimental cavity also needed to be locked, so the structure was machined out of steel and a locking piezo integrated behind one of the cavity mirrors. Finally, we developed the heterodyne imaging necessary to measure the projector matrix elements.

4.2 Measuring Electromagnetic and Gravitational Responses of Photonic Landau Levels

The topology of an object describes global properties that are insensitive to local perturbations. Classic examples include string knots and the genus (number of handles) of a surface: no manipulation of a closed string short of cutting it changes its "knottedness"; and no deformation of a closed surface, short of puncturing it, changes how many handles it has. Topology has recently become an intense focus of condensed matter physics, where it arises in the context of the quantum Hall effect [9] and topological insulators [228]. In each case, topology is defined through invariants of the material's bulk [11, 40, 229], but experimentally measured through chiral/helical properties of the material's edges. In this work we measure topological invariants of a quantum Hall material through local response *of the bulk*: viewing the material as a many-port circulator, the Chern number manifests as the spatial winding of the circulator phase; excess density accumulation near spatial curvature quantifies the curvature-analog of charge known as mean orbital spin, while the moment of inertia of this excess density reflects the chiral central charge. We observe that the topological invari-

ants converge to their global values when probed over a few magnetic lengths l_B, consistent with intuition that the bulk/edge distinction exists only for samples larger than a few l_B. By performing these experiments in photonic Landau levels of a twisted resonator [182], we apply quantum-optics tools to topological matter. Combined with developments in Rydberg-mediated interactions between resonator photons (see [153, 207] and Ch. 6), the following sections provide a roadmap for precision characterization of topological matter in strongly correlated fluids of light.

Topological phases of matter, which cannot be characterized by the spontaneous breaking of a local symmetry, have revolutionized modern condensed matter physics and materials science [230, 231]. Such phases are so named because they possess global invariants which are insensitive to material imperfections. These invariants have found applications from the redefinition of the unit of electrical resistance to error-resilient spintronics [42] and quantum computation [37].

Constructed as integrals of a "curvature" over a closed parameter space, these invariants are each defined as a *global* property resulting from the integral of a *local* property, akin to the relationship between the (local) Gaussian curvature of a surface and the (global) Euler characteristic which determines the number of handles of the surface. In the integer quantum Hall effect, integration of the Berry curvature over the Brillouin zone (momentum space) defines an invariant called the first Chern number [11, 12]. Two additional topological invariants, the mean orbital spin and chiral central charge (hereafter central charge), are defined similarly to the Chern number, but over even more abstract parameter spaces [233–235][⋆§].

Understanding the physical significance of the invariants characterizing topological matter

⋆. An attractive alternative approach is to employ a topological quantum field theory. Although unnecessary for integer quantum Hall, this allows to argue the quantization and invariance of ν, $\bar{s}$, and c on simpler principles and applies equally well to integer and fractional states.

§. We use central charge and chiral central charge interchangeably.

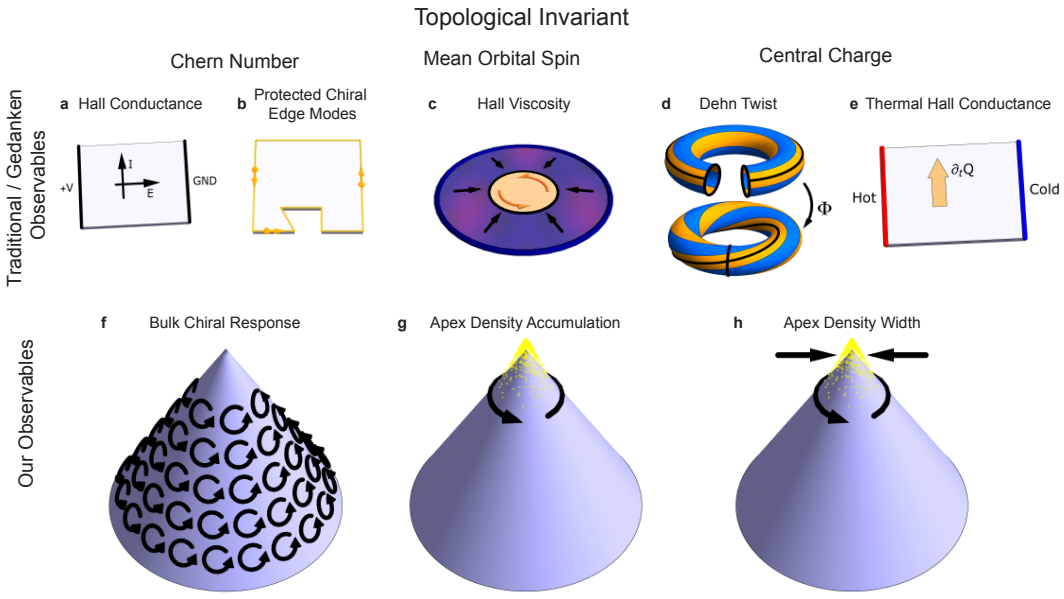

Figure 4.6: **Topological Invariants and their Associated Observables. (a)** In solids, a band's Chern number is typically obtained through a measurement of the Hall conductance, σ_H, which quantifies the current, I, induced perpendicular to an applied electric field, E. **(b)** The precise quantization of the Hall conductance arises from the presence of chiral disorder-protected edge-channels. **(c)** The mean orbital spin is the orbital angular momentum carried by particles in a quantum Hall fluid; it gives rise to Hall viscosity, a dissipationless transverse diffusion of momentum. It is most easily understood as the force (black arrows) on a rotating disk (orange) applied by a surrounding fluid (purple): even viscosity produces an azimuthal drag force along the disk's edge that counters the rotation, while odd viscosity produces a radial force normal to the disk's edge [232]. **(d)** The central charge is the third topological invariant characterizing quantum Hall fluids; it is most simply understood as a geometric phase Φ picked up by the many-body ground state wave function in response to a "Dehn twist" of the torus on which the fluid lives, and most directly measured through **(e)** the thermal Hall conductance, where the heat flow, $\partial_t Q$, is perpendicular to a temperature gradient. **(f-h)** In our system, we measure all three topological invariants through newly accessible observables. **(f)** Working in flat space away from the cone apex, we measure a bulk chiral phase response (Fig. 4.8), to extract the Chern number (Fig. 4.9). **(g)** We measure the accumulation of particles at the cone apex and **(h)** associated orbital angular momentum (via the moment of inertia of the apex density), to extract the mean orbital spin and central charge (Fig. 4.10). Figure taken from Ref. [208].

remains a challenge. What is known is that each topological invariant is connected to a family of physical phenomena. In quantum Hall materials, the transverse (Hall) conductance is an experimentally quantized invariant, corresponding in the integer quantum Hall case to the Chern number [11, 12]‡. Explorations of synthetic quantum matter composed of ultracold atoms has resulted in new experimental observables connected to the Berry curvature [237–240], the anomalous velocity [241], quantized charge transport in a Thouless pump [242–244],

‡. In the interacting case, the Hall conductance is given by a related many body Chern number and the degeneracy of the ground state. See [236].

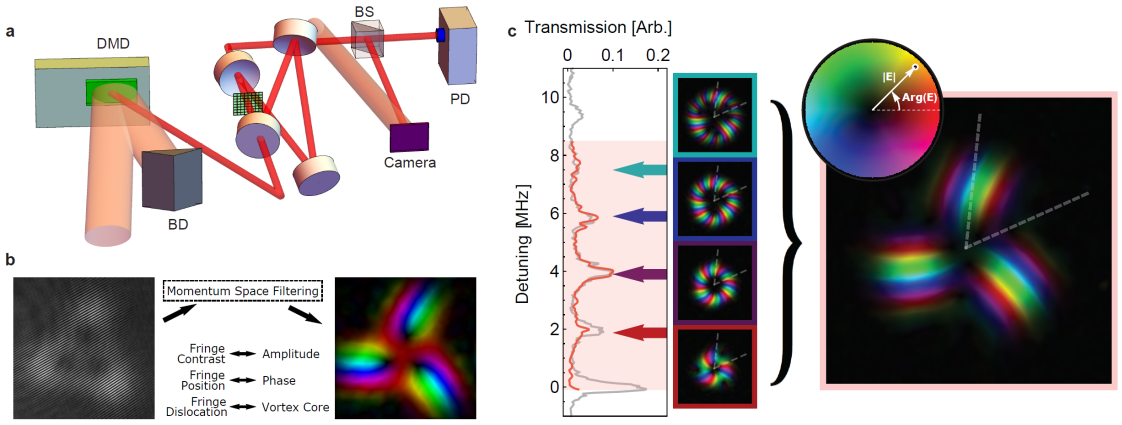

Figure 4.7: **Holographic Reconstruction of Band-Projectors.** Holographic beam shaping allows injection of arbitrary light fields into our photonic quantum Hall system, while heterodyne imaging of the cavity leakage field enables full complex-valued electric-field reconstruction of the system's response. **(a)** A 780 nm laser field is directed onto a digital micromirror device (DMD, green) and diffraction off of the DMD's hologram is directed into the non-planar resonator. The direct reflection is absorbed by a beam dump (BD, black). Light leaking from the resonator through one of its mirrors is split on a 50:50 beamsplitter (BS, grey) and directed to a photodiode (PD, blue) and camera (purple) that images the transverse plane at the waist of the cavity (green grid). A few percent of the initial input light forms a reference beam that is also directed onto the camera but at a significant angle relative to the resonator output to enable heterodyne imaging akin to optical holography. **(b)** The plane wave reference beam interferes with the cavity output to produce an image (left) where the fringe contrast provides field amplitude information, and fringe position provides field phase information. A dislocation in the fringe pattern identifies an optical vortex core, about which the phase of the electric field winds by an integer multiple of 2π. This amplitude and phase information is extracted from the images via a filtering scheme in momentum space (see Appx. A.1.12), providing the cavity mode electric field profile (right). **(c)** The projectors used to extract the Chern number are measured by injecting a magnetically translated Gaussian beam (see Appx. A.1.15) and integrating (via long camera exposure) the heterodyned cavity response while sweeping the laser frequency across the Landau level. This procedure is robust to potential disorder that broadens the Landau level so long as the disorder is not strong enough substantially admix other Landau levels. While it is difficult to controllably introduce such disorder, we demonstrate this robustness by applying weak harmonic confinement: the Landau level broadens into spectrally resolved Laguerre-Gaussian rings (small boxes & gray trace). A displaced Gaussian beam has significant overlap with only a few of these modes (red trace), but integrating across the relevant frequency band (pink) yields a *localized* response (pink box) from which we extract the projector; this is because the holographic reconstruction effectively integrates the complex electric *field* leaking from the cavity, rather than its *intensity*, resulting in constructive interference of the various modes along the vertical dashed lines, and destructive interference along the diagonal lines (see Appx. A.1.12). This field-integration is insensitive to potential disorder that broadens the band. In the electric field profiles, the brightness of each pixel corresponds to the amplitude $|E|$ of the electric field, while the hue corresponds to the phase, $\arg(E)$, of the electric field. Figure taken from Ref. [208].

and linking number [245]; amazingly, all of these observations relate directly back to the Chern number, all are global measurements, and each teaches us something different about its fundamental character in determining material properties. Meanwhile, understanding the physical significance of the mean orbital spin and central charge has remained challenging because the transport coefficients they impact are notoriously difficult to measure [246],

and there exists no experimental work investigating the locality of any of these topological invariants.

Observing phenomena associated with new topological invariants is as provocative as it is useful; such manifestations provide deep insight into the significance of otherwise opaque quantum numbers, and are real-world tools that characterize topological matter. Photonic topological materials offer especially promising routes to new experimental probes of topological invariants [81, 214, 216, 224, 247, 248], as they offer the time-, energy-, position-, and momentum-resolved control available in cold-atom experiments [66, 237–241, 243, 244, 249], plus spectroscopic tools unique to electromagnetic systems [247, 250, 251].

In a prior effort [182] we demonstrated photonic Landau levels in curved space; this platform provides us new tools including (1) *spatially-arbitrary excitation via holographic beam shaping*, and (2) a *conical singularity of spatial curvature* that perturbs the Landau levels. In this work, we introduce (3) *complex-valued tunneling spectroscopy using holographic reconstruction of the system response* to access topological invariants through spatially localized observables: harnessing a holographic reconstruction of the band projector, we measure the Chern number [37, 250] without relying on edge modes or non-local measurement; using the conical defect in the photonic Landau level, we measure the mean orbital spin and the central charge through the gravitational response, that is, the response to geometric deformation–curvature or shear–via the amount of density build-up, and its structure, at a singularity of spatial curvature.

We begin with a brief description of the local character of these topological invariants, connecting them to new observables. We then describe our measurement of the Chern number via a quantized bulk chiral phase response, and measurements of the mean orbital spin and chiral central charge from precision measurements of density oscillations near singularities of spatial curvature and magnetic flux. Finally, we conclude with a brief discussion of extensions of this work to interacting quantum Hall materials.

4.2.1 New Probes of Topology

While the Chern number $\mathcal{C}$ is traditionally defined as an integral over the Brillioun zone [11], the "bulk boundary correspondence" connects a non-zero $\mathcal{C}$ to robust chiral edge channels that extend around the boundary of the material [43]; indeed the presence of these channels is often taken as *proof* that the bulk is topological [214, 216, 224, 225]. Accordingly, a conceptually simple local measure of the bulk Chern number results from cutting the system down to a patch a few magnetic lengths across and surrounding it with vacuum. The number and chirality of these edge modes directly reflects the Chern number.

In practice, it is challenging to cut the system; Kitaev proposed a recipe to extract equivalent information from triple-products of spatial projectors onto a spectrally isolated band [252]. We implement this approach using spatially-resolved complex-valued tunneling spectroscopy of a patch within the bulk of the lowest Landau level, thereby measuring a non-zero Chern number [250]$^{\diamond}$.

Two additional topological invariants appear in quantum Hall physics: the mean orbital spin $\bar{s}$ is a bulk invariant quantifying a particle's magnetic-like coupling to curvature and is related to the Hall viscosity and Wen-Zee shift (see Appx. A.1.19); the chiral central charge [255], c, which is related to the gravitational anomaly, is equal to the total number of edge modes (neutral and charged) in integer quantum Hall and Laughlin states and gives rise to the thermal Hall conductance [235, 256, 257] (see Fig. 4.6). To date, these invariants have been understood in terms of gedanken experiments requiring topological gymnastics, and measured through their connection to exotic transport coefficients. We are able to access them because they govern the coupling of several local observables, namely particle- and angular-momentum- densities, to spatial curvature.

$\diamond$. After we developed this theory and were experimentally well underway, we learned of a series of papers building off of Kitaev's formulation as a 'real space Chern marker' [253, 254]. This represents a separate and fundamentally equivalent theoretical development of a local observable quantity given by the Chern number.

Generically, the competition between phases in a topological fluid can be sensitive to microscopics—lattice structure, inter-particle interaction strength and form, number of filled bands, and disorder can each bias the system between competing ground-states. Perhaps surprisingly, a quantum Hall fluid near its manybody ground state may be described by a low energy "effective theory" that is fully characterized by a few parameters that incorporate all of the aforementioned microscopics. In [220, 258], it was shown that the effective action describing this theory is $W(B, R) = f(B, R; \nu, \bar{s}, c)$, where $B(x, y)$ is the magnetic field and $R(x, y)$ is the spatial (Ricci) curvature. $\nu \frac{e^2}{h} = \sigma_H$ is the Hall conductance, which specifies the current induced perpendicular to an applied electric field and is precisely quantized in the famous plateaus of the integer and fractional quantum Hall effects; for integer quantum Hall physics, ν is equal to the Chern number $\mathcal{C}$. The mean orbital spin and central charge complete the triplet of topological invariants that appear in quantum Hall systems. These five quantities fully specify the effective action, whose derivatives are a host of physical observables including densities and transport coefficients.

While one could potentially calculate the topological invariants from first principles, doing so has proven computationally challenging and depends upon microscopic parameters which are often unknown. From the effective action, however, it can be shown that introducing a conical geometry and threading the cone tip with a small tube of magnetic flux produces a localized density response that depends sensitively upon both the mean orbital spin [220] and central charge (see Appx. A.1.17). As such, we employ a curvature $R(x, y) = \frac{8\pi}{3}\delta^{(2)}(x, y)$ and vary a magnetic field $B(x, y) = B_0 + \Phi_B \delta^{(2)}(x, y)$, where $\delta^{(2)}(x, y)$ is the two dimensional dirac delta function and $\Phi_B/2\pi = 0, -1/3, -2/3$ are possible values for the additional magnetic flux threading, to measure the localized density response and thereby provide a window into these topological invariants.

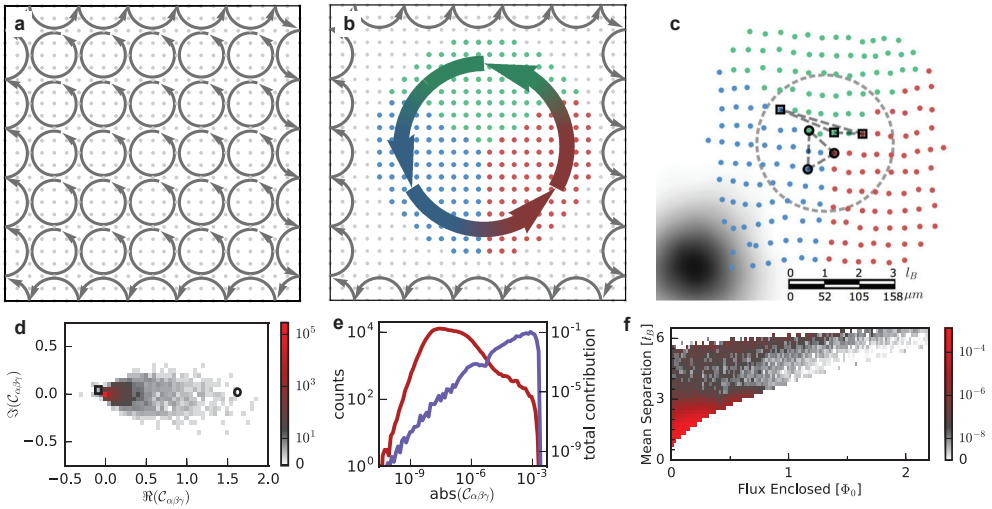

Figure 4.8: **Chern Number Measurement in Real Space.** **(a)** A 2D system with a perpendicular applied magnetic field forms a bulk insulator because particles far from system edges undergo cyclotron orbits rather than linear motion. Associated with these bulk orbits are counter-orbiting ("skipping") edge-trajectories. Existence of these topologically-protected 1D chiral edge channels is often the simplest-to-detect signature of a topological bulk. **(b)** Direct measurement of bulk topology requires a disorder-insensitive probe of bulk chiral non-reciprocity. We split the bulk into three adjacent but otherwise arbitrary regions and sum, for all sets of three points α, β, γ with one selected from each region, the non-reciprocity of the transmission amplitude $\alpha \to \beta \to \gamma$ vs $\gamma \to \beta \to \alpha$. **(c)** To employ this approach to measure the Chern invariant, we inject a TEM_{00} (bottom left, at the same scale in size and position) magnetically displaced to points α, β, γ spaced by less than a magnetic length (in the first quadrant, to avoid the cone tip located at the TEM_{00} mode location) into a degenerate Landau level. The injected beam size is matched to the resonator waist size of $w_0 = 105$ μm that also sets the magnetic length $l_B = w_0/2$. A dashed gray circle of radius $2l_B$ is included for comparison to Fig. 4.9. **(d,e)** Historams of all $\sim$ 285,000 terms $C_{\alpha\beta\gamma} \equiv 12\pi i \left(P_{\alpha,\beta}P_{\beta,\gamma}P_{\gamma,\alpha} - P_{\alpha,\gamma}P_{\gamma,\beta}P_{\beta,\alpha}\right)$, from triples of points in **c** are presented. The sum of these provides a single (complex) Chern number measurement of $\mathcal{C} = 1.01 + 0.01i \pm 0.027(\text{sys})$ (averaging ten such measurements yield $\text{Re}(\mathcal{C}) = 1.00 \pm 0.02(\text{stat}) \pm 0.027(\text{sys})$). Bins with zero counts are separated from the logarithmic histogram and are colored white. The histogram in **d** displays a large concentration of $C_{\alpha\beta\gamma} \approx 0$. These are better visualized in **e**, showing that the increase in the number of $C_{\alpha\beta\gamma}$ with small magnitude does not result in appreciable contribution from these terms. Indeed, truncating all $|C_{\alpha\beta\gamma}| < 10^{-5}$ changes the sum by $< 1\%$. **(f)** Triples that enclose more magnetic flux and have separations of $\sim$ one magnetic length (two sites) give the largest contributions (example circled in **c** & **d**), while triples that are far apart or do not enclose much flux provide a small contribution (example boxed in **c** & **d**). This behavior is confirmed quantitatively by plotting the mean contribution to $\mathcal{C}$ versus enclosed flux (in units of the flux quantum Φ_0) and mean separation of triples. The presence of non-zero imaginary components of $C_{\alpha\beta\gamma}$ reflects imperfect alignment of injection and measurement grids and cancel in $\mathcal{C}$. Figure taken from Ref. [208].

4.2.2 Electromagnetic Response — The Chern Number

To extract the Chern number we measure a quantized bulk chiral response [252, 259](Fig. 4.6f). Particles inhabiting multiple Landau levels exhibit cyclotron orbits creating a bulk circulating current. While particles in a single Landau level do not display orbital dynamics, they still accrue a chiral (Aharanov-Bohm) phase when forced to travel in a closed path (Fig.

4.8a). While this chiral phase is not apparent from the momentum-space definition of the Chern number [11, 260], it is highlighted by an alternate expression [252]:

$$\mathcal{C}^{\mu} = 12\pi i \sum_{\alpha\in A,\beta\in B,\gamma\in C} P^{\mu}_{\alpha,\beta} P^{\mu}_{\beta,\gamma} P^{\mu}_{\gamma,\alpha} - P^{\mu}_{\alpha,\gamma} P^{\mu}_{\gamma,\beta} P^{\mu}_{\beta,\alpha} \tag{4.1}$$

where the area probed is split spatially into thirds labeled A, B, and C, as shown in Fig. 4.8b and the band projector $P^{\mu}_{\alpha,\beta} = \langle \mathbf{x}_\beta | \left[\sum_{j\in\mu} |j\rangle\langle j| \right] |\mathbf{x}_\alpha\rangle$ maps eigenstates $|j\rangle$ residing in band μ to themselves and all other eigenstates to zero. Intuitively, this means injecting a tiny probe (transverse size $\ll l_B$) $|\mathbf{x}_\alpha\rangle$ at some desired location $\mathbf{x}_\alpha = (x_\alpha, y_\alpha)$ and energy-integrating the resulting complex cavity response (leakage field) at another location $\mathbf{x}_\beta = (x_\beta, y_\beta)$ across the band/Landau level [250, 261] (see Fig. 4.7c and appendix A.1.13); for a Landau level/Chern band, this response is exponentially localized with a characteristic scale l_B/magnetic unit cell respectively.

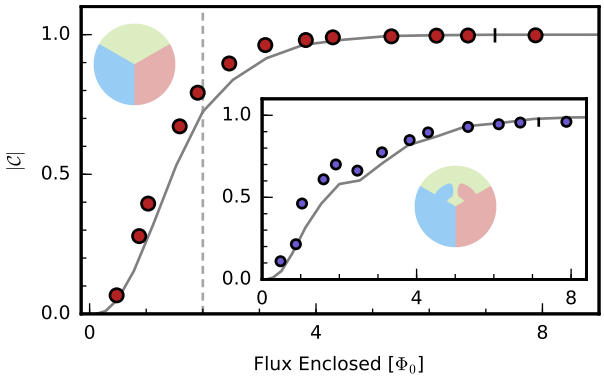

Figure 4.9: **Measuring the Chern Number.** The sole length scale for physics in the lowest Landau level is the magnetic length, l_B, so it is reasonable to expect that the Chern number will converge once the measurement area extends beyond this scale. Indeed, as the sum in Eqn. 4.1 is taken out to larger radii on a grid as in Fig. 4.8, the measured Chern number data (red points) rapidly converges to one, in agreement with first-principles theory (gray curve) with no adjustable parameters. The derivation of this theory curve is provided in appendix A.1.14.1. A vertical dashed line at an enclosed flux of 2 Φ_0, where Φ_0 is the magnetic flux quantum, indicates the area enclosed by a circle of radius 2 l_B as shown in Fig. 4.8c. Errorbars are calculated from the standard deviation from 10 repetitions of the experiment and are all smaller than the points; a typical one-standard-deviation statistical error of ± 0.02 is plotted in place of the penultimate point. **(inset)** The Chern number is invariant to distortions of the boundaries between the three summation regions, even when the three regions approach each other at a second location. Figure taken from Ref. [208].

We may then assemble triple products of these complex responses into a measurement of

$\mathcal{C}^\mu$ from what are essentially chirality measurements: for any triplet of points $(\mathbf{x}_\alpha, \mathbf{x}_\beta, \mathbf{x}_\gamma)$, the first term $P^\mu_{\alpha,\beta} P^\mu_{\beta,\gamma} P^\mu_{\gamma,\alpha}$ measures particle current in a trajectory with one handedness, $\mathbf{x}_\alpha \to \mathbf{x}_\beta \to \mathbf{x}_\gamma \to \mathbf{x}_\alpha$, while the second term measures the reverse trajectory. In magnitude, the currents are equal; however, due to the vector potential providing an Aharanov-Bohm phase for particles traversing in a closed loop, their phases are opposite. Each term in the sum is then the net non-reciprocity for that trajectory, and summing over all possible trajectories provides the Chern number (Fig. 4.8b-d).

We experimentally implement this protocol using a digital micromirror device (DMD) to excite each $|\mathbf{x}_\alpha\rangle$ on a chosen grid (Fig. 4.7a). Holographic reconstruction of the transmitted resonator electric field (Fig. 4.7a,b) while sweeping the excitation laser frequency across the Landau level then provides matrix elements of the band projector $P^\mu_{\alpha,\beta}$ from $\mathbf{x}_\alpha$ to all $\mathbf{x}_\beta$ (Fig. 4.7c). We obtain all projector matrix elements are obtained by iterating the excitation location over all points on the chosen grid, and the Chern number is then computed via Eqn. (4.1).

The terms in the sum of Eqn. (4.1) fall off rapidly as the points $\mathbf{x}_\alpha$, $\mathbf{x}_\beta$, and $\mathbf{x}_\gamma$ stray from one another since $P^\mu_{\alpha,\beta} \propto e^{-|\mathbf{x}_\alpha - \mathbf{x}_\beta|^2/4l_B^2}$, so the dominant contributions to the sum come from trios of points near the meeting point(s) of the three sectors: the contribution from terms that contain any point several magnetic lengths away from the center is negligible. Accordingly, the sum in Eqn (4.1) can be easily truncated, as is apparent in Fig. 4.9, where the Chern number is evaluated as the radius of the circular summation region is increased. Beyond a total enclosed flux of $\sim 4\ \Phi_0$, the physically-meaningful real-part of the Chern number (see Appx. A.1.14.4) saturates to $\mathcal{C} = 1.00 \pm 0.02(\text{stat}) \pm 0.027(\text{sys})$, with the systematic error arising from finite summation region and sample-spacing, plus sampling-lattice distortion (see Appx.. A.1.14.2). Eqn. (4.1) may thus be considered a spatially localized definition of the Chern number, in the sense that an independent measurement may be made by choosing a different center of the sectors.

The quantity so-measured is *indeed* an invariant, highly robust to imperfections in both the the Landau level and the measurement apparatus: nanoscopic mirror imperfections give rise to a disorder potential that weakly couples modes within the Landau level, and the excitation locations deviate from a perfect grid by $\sim 20\%$ (Fig. 4.8c), yet the Chern number converges smoothly to 1 (Fig. 4.9). In Fig. 4.9, inset, we intentionally distort the summation regions to produce a second, off-center location where all three regions approach each other (as this is where the triple-product of projectors may be largest). While the summation region must now fully enclose this new "defect" before the sum converges, the Chern number remains invariant to this distortion.

4.2.3 Gravitational Response — the Mean Orbital Spin and Chiral Central Charge

The response of a quantum Hall fluid to manifold curvature is controlled by two topological invariants, the mean orbital spin and the central charge, specific to the particular Hall state under consideration. Our platform, consisting of Landau levels on a cone with additional flux of $\Phi_B = -2\pi a/3$, $a = 0, 1$, or 2 threaded through the tip, provides an idealized source of manifold curvature localized precisely at the cone tip. In what follows, we connect variations in the Local spatial Density of States (LDOS) at this curvature singularity directly to the mean orbital spin and central charge (see Appx. A.1.17).

In flat space the LDOS of a Hall fluid is uniform, providing few signatures of the fluid's properties; in curved space, however, the LDOS displays oscillations about its flat-space background that depend on the local curvature and threaded flux, a: the excess particle number localized to the cone tip, defined as the spatial integral of the excess density there, directly reflects the mean orbital spin (Fig. 4.6g), while the width of this excess particle density reflects the orbital angular momentum attached to the curvature singularity, and

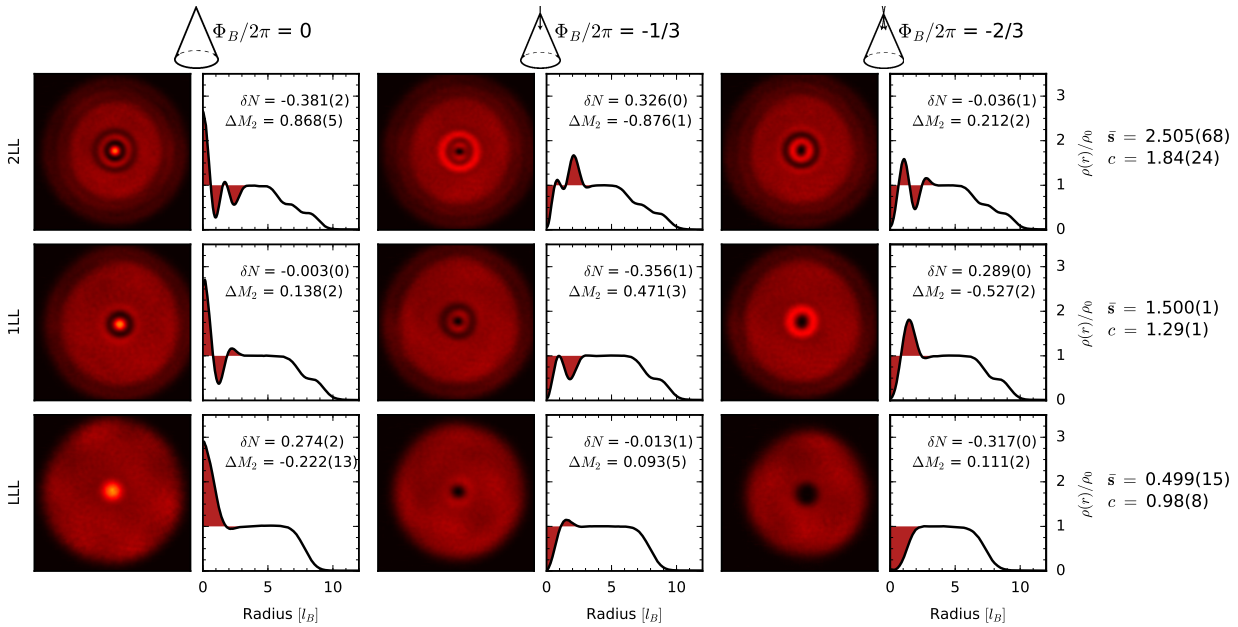

Figure 4.10: **Response to Manifold Curvature.** A quantum Hall fluid's response to spatial curvature is governed by two additional topological invariants, the mean orbital spin and central charge. Injecting, imaging, and summing several (~ 10) single particle states provides high-precision measurements of the local state density in nine different Landau levels (red images), from which azimuthally averaged radial profiles, $\rho(r)$, are extracted (black curves, errorbars negligible). These data display the characteristic local density oscillations at the cone tip; a region of uniform density at larger radii; and a smooth decrease to zero due to the finite number of states measured. The uniform density region is averaged over all levels to define a background density, ρ_0, from which excess local state density (red filling) may be defined. For each Landau level, the excess local state density near the cone tip is integrated to measure the total excess state number, δN, from which the mean orbital spin, $\bar{s}_n$, is extracted. The shifted second moment, ΔM_2, (see text) is also computed, which then provides a higher-precision measurement of the mean orbital spin as well as the central charge, c_n. We benchmark the connection between these topological invariants and the local density oscillations by performing the same experiment in nine situations: the lowest (LLL), first excited (1LL), and second excited (2LL) Landau levels on a cone with three possible values of magnetic flux threading its apex (left to right, flux specified at top). Errorbars estimate systematic uncertainty in the upper bound of the integration region for moment analyses, and, in $\bar{s}_n$ and c_n, additional variation from averaging over flux threading. Figure taken from Ref. [208].

thus the central charge (Fig. 4.6h). We derive these connections in appendix A.1.17. In the n^{th} Landau level, the particle density near the cone-tip ρ and excess angular momentum L_{tip} obey (appendix Eqn's A.30 and A.49, respectively):

$$\rho = \frac{\nu e B}{2\pi\hbar} + \frac{\nu \bar{s}_n}{4\pi} R$$
$$L_{tip}^{(n)} = \frac{c_n - 12\nu\bar{s}_n^2}{24}\left(s - s^{-1}\right) + \frac{1}{2}a\left(2\bar{s}_n - \frac{a}{s}\right)$$

Here R is the the spatial (Ricci) curvature, and s is the number of unwrapped cones required to cover the plane (in our case $s = 3$), providing an alternate parameterization of the curvature. The preceding expressions indicate that while more curvature/B-field (B) increase the particle density, the density *distribution* depends non-monotonically upon the curvature/B-field. The proportionality constants depend upon the orbital spin and central charge in the n^{th} Landau level, $\bar{s}_n$, and c_n, respectively; disentangling these quantities will require exploring dependence of density upon *both* curvature and magnetic field (parametrized by the number of excess flux quanta a threading the cone tip).

Technical improvements to the apparatus since prior lowest Landau level LDOS experiments of [182] (see Fig. A.1.4) enable undistorted, high-precision access to the LDOS oscillations, thereby extending measurements of the mean orbital spin to excited Landau levels where the invariant takes on new values, expected to obey $\bar{s}_n = n + \frac{1}{2}$, where $n = 0, 1, 2, ...$ specifies the lowest, first excited, and second excited Landau levels. This further provides a new and independent probe of the mean orbital spin and, most importantly, permits measurements to verify that the central charge, $c = 1$ in all Landau levels [220, 262–264].

In Fig. 4.10, we present the LDOS of lowest, first excited, and second excited Landau levels on three cones differentiated by effective magnetic flux threading the cone tip, following the same procedure as above (section 4.1.3.2, Ref. [182]). Near the cone tip, we observe characteristic oscillations LDOS radial profile $\rho(r)$, which settles to a uniform background level by $r \sim 4l_B$. At large radii, the LDOS drops to zero only because a finite number of single particle states were included, the number being limited by the size of the DMD used for mode injection. The background level is equal for all nine LDOS measurements (see Appx. A.1.16.1), and their average is used to define the background local state density ρ_0 for all measurements. We then compute the total excess particle number, $\delta N = \int (\rho(\mathbf{r}) - \rho_0)\, \mathrm{d}^2\mathbf{r}$, and a measure of the excess density's width, the shifted second moment, $\Delta M_2 = \int (\rho(\mathbf{r}) - \rho_0) \left(r^2/2 - (2n+1)\right) \mathrm{d}^2\mathbf{r}$. These quantities then provide the mean orbital spin and central charge (as the primary

theoretical result of this article, see Appx. A.1.17 and A.1.18)

From the excess particle number, we measure the mean orbital spin and average the result over flux threading in the lowest three Landau levels, finding $\bar{s}_n = \{0.44(4), 1.46(2), 2.44(2)\}$ for $n = 0, 1$, and 2, respectively. We can also use measurements of ΔM_2 to extract the mean orbital spin, as the linear component of the dependence of ΔM_2 on the flux a is exactly $(\bar{s}_n - n)a$ (see Appx. A.1.17). This provides a significantly more precise determination of $\bar{s}_n = \{0.499(15), 1.500(1), 2.505(68)\}$. We then use these measurements of $\bar{s}_n$ along with measurements of ΔM_2 to calculate the central charge in each Landau level, finding $c_n = \{0.98(8), 1.29(1), 1.84(24)\}$. While the precision of the central charge measurement drops in higher Landau levels due to finite field of view and increased sensitivity to error in the mean orbital spin, all mean orbital spin measurements and the lowest Landau level central charge measurement are in agreement with theoretical expectations for the integer quantum Hall fluid.

4.2.4 Outlook

We have demonstrated the first synthetic magnetic field for continuum photons. Furthermore, we have created an integer quantum Hall system in curved space, a long-standing challenge in condensed matter physics. This has stimulated new theoretical studies of both interacting and non-interacting photonic quantum Hall systems [265–270].

We have developed and measured local observables that characterize bulk invariants of topological materials, providing the first measurement of the central charge and mean orbital spin of an integer Hall system in the lowest- and excited- Landau levels, respectively. Our approach elucidates the physical significance of these invariants and relaxes the non-physical sensitivity of the standard definitions to experimental imperfections like disorder. Indeed, the TKNN formulation of the Chern number assumes discrete translational symmetry [11],

whereas our approach is applicable even to systems composed of spatial domains separated by topological phase boundaries, where spatial resolution would provide a "Chern map."

While Hall conductance, mean orbital spin, and central charge do not fully characterize a *generic* quantum Hall state, they often provide sufficient information to distinguish between candidate phases in the lab. In the case of the electronic $\nu = 5/2$ fractional quantum Hall plateau, a measurement of *either* the mean orbital spin or central charge would suffice to choose amongst the more-than nine candidate states [271, 272]. The photonic analog is bosonic, so similar physics is expected at $\nu = 1$, permitting the exploration of and differentiation between Pfaffian and parafermion states [61, 273, 274].

Generalizing the measurements performed here to interacting systems is certainly non-trivial, however. The real space projector measurements do not directly map onto the many body Chern number; indeed, with an isolated ground state, it is not obvious onto what space to project. Furthermore, while the mean orbital spin is linked fundamentally to conservation of angular momentum and thus generally connected to the excess density at the cone tip, the same is not generally accepted as true for the central charge, which is defined in a significantly more general context. Connecting the second moment of the excess density at the cone tip to the central charge in general, interacting quantum Hall states would require significant new theoretical advances.

Investigating interacting topological phases of photons [213] will require combining Landau levels of light in twisted resonators [182] with Rydberg-mediated interactions between photons [85, 153]. Such phases may be assembled particle-by-particle [270, 275, 276] or by dissipative stabilization [267, 277, 278]; in either case, quantum state tomography or fidelity to a target state will be a poor diagnostic of a topologically ordered phase of matter, particularly as the particle number grows. Rather than investigating the $2^N \times 2^N$ density matrix, the relevant topological order is better demonstrated through a handful of observables with

more general physical meaning**. One of these meaningful observables is the gravitational response, measurement of of which will be an essential tool for characterization of the resulting topological phase [265]. Furthermore, extension of the bulk circulation measurement to the strongly interacting regime has the potential to permit direct observation of anyon braiding statistics. More broadly, this work highlights the power of photon fluids for exploration of topological and quantum matter, and demonstrates unique tomography and state reconstruction tools inaccessible to other platforms.

$\star\star$. This point was made well by Cooper, in reference [61] "While a large wavefunction overlap is encouraging, this is not necessarily the best way to characterize a phase of matter. In the thermodynamic limit, owing to the exponential increase in the size of the Hilbert space, the wavefunction overlap with any trial state will surely vanish, even if the two wavefunctions describe the same topological phase. A robust characterization of the topological phase is provided by the ground state degeneracy on the torus [279]; this degeneracy is expected to survive (and even improve) in the thermodynamic limit, provided the wavefunction is in the same topological phase as the trial state". This "ground state degeneracy on the torus" is related to the topological phase of matter rather than a particular wavefunction, much like the topological invariants discussed here.

CHAPTER 5

INTERACTING PHOTONS

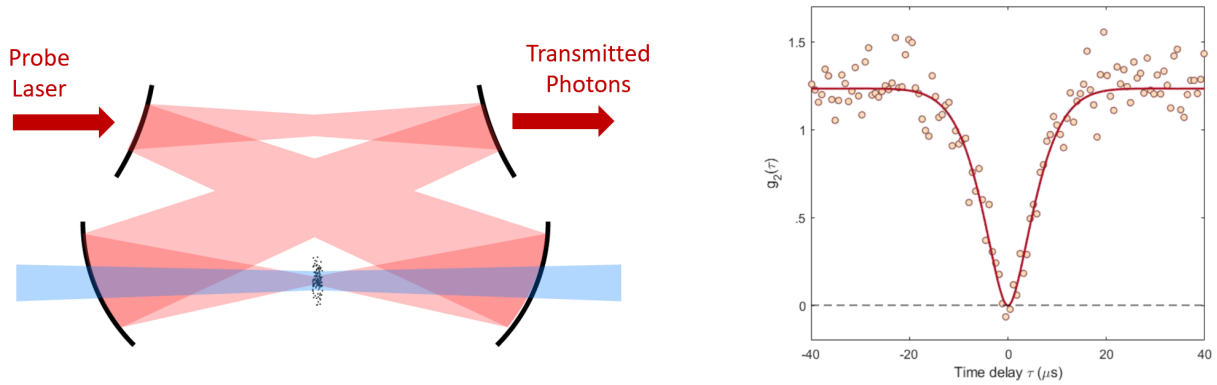

Figure 5.1: **Intracavity atoms illuminated with a control field mediate strong photon-photon interactions.** This is best revealed through the transmitted photon temporal antibunching, meaning that photons leak out of the cavity separated by a minimum time delay. This implies that the the cavity (a 10 cm long macroscopic object!) supports at most a single photon at a time, which is only possible in the presence of strong quantum mechanical interactions.

Photons do not naturally interact. However, effective strong interactions between photons may be engineered by coupling photons to atoms. This arises either through the Jaynes-Cummings interaction which depends on the saturability of a single emitter, or through direct interactions between the atoms which may be greatly enhanced with Rydberg excitations (see Ch. 2). In this chapter, we describe the formation of Rydberg polaritons in a single mode cavity, in which individual cavity photons are strongly hybridized with Rydberg excitations of a cold atomic gas. We then observe the resulting strong interactions between cavity photons through the sharply sub-Poissonian statistics of the transmitted light field. That is, transmission of photons through the atom-cavity system proceeds one-at-a-time due to Rydberg blockade. The dynamics of a single Rydberg polariton showing Rabi oscillations followed by saturation at an average population of one-half due to decay further validates treating this atom-cavity system as a single two-level emitter with exaggerated properties.

Strongly nonlinear oscillators are the building blocks of quantum information processors and quantum many-body systems. But engineering such devices or investigating such materials

requires combining many nonlinear oscillators together. As the first step in this direction, we perform a two mode collider experiment involving counter propagating optical modes with orthogonal spatial structure. Nevertheless, Rydberg polaritons still collide and induce cross blockade between the two modes. This experiment is enabled by Floquet engineering, in which modulation of the intermediate state energy bridges the non-degeneracy between the optical modes. Future degenerate cavities will not require this technique, but Floquet engineering will remain a powerful addition to our nonlinear quantum optics toolbox.

This chapter is based on Ref. [153]

> Ningyuan Jia, Nathan Schine, Alexandros Georgakopoulos, Albert Ryou, Logan W. Clark, Ariel Sommer, and Jonathan Simon. A strongly interacting polaritonic quantum dot. *Nature Physics*, 14:550, (2018).

and Ref. [207]

> Logan Clark, Ningyuan Jia, Nathan Schine, Claire Baum, Alexandros Georgakopoulos, and Jonathan Simon. Interacting Floquet polaritons. *Nature* (2019).

5.1 A Strongly Interacting Polaritonic Quantum Dot

Polaritons are promising constituents of both synthetic quantum matter [74] and quantum information processors [99], whose properties emerge from their components: from light, polaritons draw fast dynamics and ease of transport; from matter, they inherit the ability to collide with one another. Cavity polaritons are particularly promising as they may be confined and subjected to synthetic magnetic fields controlled by cavity geometry [182], and furthermore they benefit from increased robustness due to the cavity enhancement in light-matter coupling. Nonetheless, until now, cavity polaritons have operated only in a

weakly interacting mean-field regime [150, 280]. Here we demonstrate strong interactions between individual cavity polaritons enabled by employing highly-excited Rydberg atoms as the polariton's matter-component. We assemble a quantum dot composed of approximately 150 strongly interacting Rydberg-dressed ^{87}Rb atoms in a cavity, and observe blockaded transport of photons through it. We further observe coherent photon tunneling oscillations, demonstrating that the dot is zero-dimensional. This work establishes the cavity Rydberg polariton as a candidate qubit in a photonic information processor and, by employing multiple resonator modes as the spatial degrees of freedom of a photonic particle, the primary ingredient to form photonic quantum matter [116].

Recent years have seen a growing effort to create matter from light [74, 281]. The speed of the photon may be employed to realize reduced-dimensional models with near-arbitrary single particle dynamics, and recent breakthroughs have even enabled the creation of synthetic gauge fields which impose a Lorentz-like force on the photon [224, 225, 282]. While a number of groundbreaking experiments have probed the physics of photon condensation[73, 280], emergent crystallinity from long-range interactions [210, 211, 283], and opto-mechanics [284], the challenge of achieving strong interactions between individual photons for exploration of entangled photonic quantum matter persists. The demonstration of a single-photon nonlinearity mediated by a single atom coupled to a Fabry Pérot cavity [84] spurred an outpouring of theoretical work exploring Hubbard physics in coupled nonlinear resonators [108, 117], but the severe technical challenges associated with the deterministic preparation of individual atoms in resonator arrays remain.

Two major efforts have begun to address the technical challenges of mediating strong photonic interactions using atoms. In the first, researchers successfully demonstrated the loading of an individual atom into the near-field of a photonic crystal cavity [285], and this capability was subsequently extended to the coupling of atomic ensembles to waveguides [286]. In the second, the challenges associated with trapping and cooling single atoms within opti-

cal resonators are eliminated by using Rydberg Electromagnetically Induced Transparency (EIT) [157]. With Rydberg EIT, an entire thermal gas of atoms may act as a single "super atom" which has the cross section of the ensemble and the nonlinearity of a single atom [85, 95, 96, 167, 287]. Nonetheless, the propagation of these free-space excitations complicates their application to quantum information processors or materials compared to their cavity-confined counterparts.

In this work, we pioneer a new approach combining Rydberg EIT and optical resonators [159, 288], which benefits from the best aspects of each previous approach: Rydberg EIT provides a robust atomic-ensemble-mediated single-photon nonlinearity, while the resonator enhances the light-matter coupling and allows us to work at substantially lower atomic densities while maintaining a high optical depth per blockade volume (OD_B). This quantity is crucial, because OD_B determines the number of collisions per polariton lifetime in a synthetic quantum material and the gate fidelity in a photonic quantum information processor [100] (see Sec. 2.2.4). Perhaps most significantly, in the future a quantum nonlinear resonator may be tuned near a mode-degeneracy point where interactions couple the transverse modes and the system behaves as a continuum-equivalent of an array of tunnel-coupled resonators. This approach would enable the creation of a strongly interacting quantum fluid *within an individual, multi-mode cavity*. Furthermore, the fluid can be trapped and subjected to strong magnetic fields [182], providing access to the physics of photon crystals and Laughlin puddles [116].

Here, we use this platform to demonstrate the first strongly interacting polaritonic quantum dot. We create a discrete mode-spectrum by confinement of the photon in a cavity and strong interactions by tight confinement of the assembled atom cloud. In what follows, we describe the quantum dot in more detail and show that it exhibits the characteristic features of strong nonlinearity at the single-photon level, in contrast to related works exhibiting only weak nonlinearities [150, 158]. First, we demonstrate strong light-matter coupling by measuring a well-resolved dark-polariton resonance in the transmission spectrum. We next

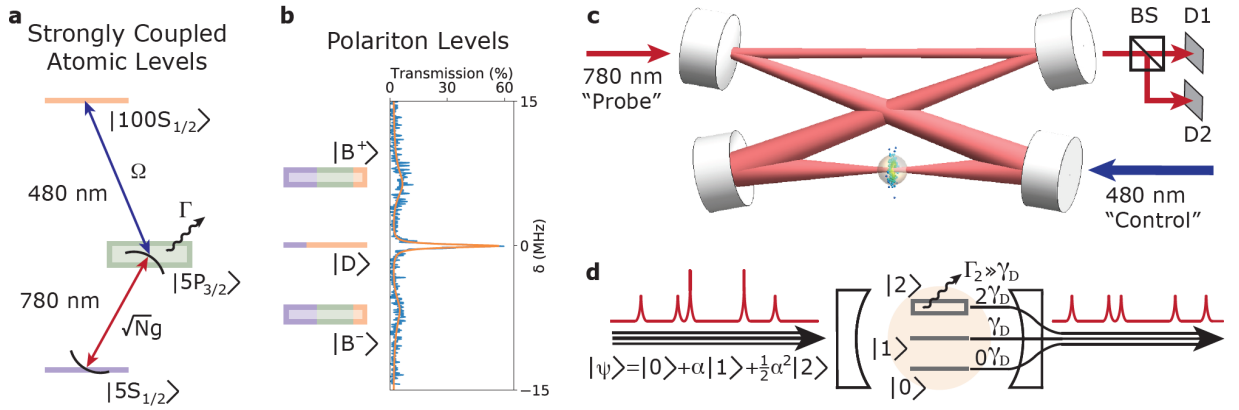

Figure 5.2: **Rydberg Polariton Blockade in an Optical Resonator.** Photons in an optical resonator are hybridized with Rydberg excitations via electromagnetically induced transparency, inducing strong photon-photon interactions. The coupled atom-cavity system thus becomes a single two-level emitter. **(a)** Because photons do not naturally interact with one another, we employ atoms to mediate interactions. An optical resonator couples 780 nm photons (red) to a sample of $N \approx 150$ ^{87}Rb atoms, creating a collective $\sqrt{N}g$ enhancement in the single atom-photon Rabi frequency, g. A 480 nm "control" laser (blue) coherently couples excited atoms to the $n = 100$ Rydberg state with Rabi frequency Ω. Rydberg atoms interact strongly with one another, and the light-matter coupling imprints these interactions on the 780 nm photons. **(b)** When we probe the spectrum of this strongly-coupled light-matter system, we observe three distinct peaks corresponding to the three quasi-particle eigenstates, called polaritons: two broad "bright" polaritons, with a linewidth set by the excited state spontaneous decay rate Γ, and one narrow, tall "dark" polariton in the middle, with a loss rate γ_D independent of Γ. The dark polariton is the longest-lived and most Rydberg-like quasi-particle, so it provides the best platform for mediating interactions between photons. **(c)** Atoms are loaded into the smallest waist of the resonator and "sliced" (see Sec. 5.7.1) so that the Rydberg components of the polaritons all reside within a single blockade volume and thereby strongly repel each other. Signatures of this interaction are then observed in the 780 nm photons that leak out through one of the resonator mirrors, pass through a 50:50 beam-splitter (BS) and are measured by single photon detectors (D1 and D2). **(d)**. The system behaves as a zero-dimensional strongly interacting quantum dot. The weak probe field is in a coherent state $|\alpha\rangle$, represented by the red curve which consists primarily of zero photons, occasionally one photon, and infrequently two photons, when counts are binned into a time $1/\gamma_D$. Each photon enters the cavity as a dark polariton, and strong Rydberg-Rydberg interactions cause the first polariton to broaden and shift the dark polariton resonance sufficiently to preclude simultaneous injection of a second polariton; accordingly, only isolated photons emerge from the cavity. Figure taken from Ref. [153].

explore transport via the statistics of photons tunneling through the cavity, observing deep anti-bunching indicative of blockade due to strong interactions between individual polaritons. We further demonstrate that our polaritonic dot is zero-dimensional by detecting coherent Rabi-oscillations between an empty dot and a dot containing a single polariton, as well as saturation of the intracavity dark polariton number at 0.47(3). We conclude with a discussion of applications in quantum information and strongly-correlated, topological phases of matter.

Our quantum dot is formed from a sample of 2600(500) atoms loaded into the 12μm×14μm

waist of a high finesse single mode optical resonator (Fig. 5.2a,c, and Appx. A.2.1 for details), at a peak density of $1 \times 10^{11}\text{cm}^{-3}$ (see Methods, Sec. 5.7). These atoms are distributed over a 35 μm RMS axial length which may be reduced to 10 μm RMS by spatially selective optical depumping, or "slicing" (see Sec. 5.7.1). Due to strong light-matter coupling ($OD_B \approx 13$), the modes of the system hybridize, forming polaritons (Fig. 5.2b): composite states of a resonator photon with an atomic excitation. Two of the hybridized modes are "bright" polaritons, composed primarily of an admixture of a resonator photon and a short-lived P-state excitation; they are weakly interacting and due to their small Rydberg component and short lifetime. The third polariton, called the "dark" polariton, is composed of a coherent superposition of a Rydberg excitation and a resonator photon, with the mixing ratio set by the dark-state rotation angle [156]: $\tan\theta = \sqrt{N}g/\Omega = 2.9(5)$, for our typical conditions. The Rydberg component of the dark polariton enables it to strongly repel other dark polaritons within a surrounding "blockade volume," which scales with $n^{\frac{11}{2}}$ (for Van der Waals interactions) where n is the Rydberg level's principal quantum number. It is for this reason that we typically employ $n = 100$ Rydberg state, as their extreme properties make this blockade volume comparable to the sample size. Confining the region of overlap between the resonator mode and the atomic gas to be smaller than the blockade volume gives rise to a zero-dimensional, strongly interacting polaritonic quantum dot; like its solid-state counterpart, the electronic quantum dot [289], it is expected to exhibit blockaded transport (Fig. 5.2d).

5.2 Nonlinear Spectroscopy

To investigate the polaritonic excitations of our quantum dot, we first probe the transmission spectrum of the laser-dressed cavity-atom system. In Fig. 5.2b we plot the quantum dot's transmission spectrum on the $\{5S_{1/2},\ F = 2\} \rightarrow \{5P_{3/2},\ F = 3\} \rightarrow \{100S_{1/2}\}$ transition, without slicing the cloud. We observe two broad resonances which we identify as bright

polaritons, whose spectral separation is an indication of strong light-matter coupling. The central feature is the spectrally narrow dark polariton. As we increase the probe power, the fractional transmission on the dark polariton resonance drops, as shown in Fig. 5.3, indicating that the repulsion between these polaritons suppresses their simultaneous injection into the dot.

5.3 Photon Blockade

In order to demonstrate that *individual* dark polaritons interact strongly with one another within the quantum dot, we explore transport dynamics. We test transport by injecting photons into the resonator at the energy of the dark polariton, such that most photons become dark polaritons upon entering. The strong repulsion between polaritons shifts the energy and reduces the lifetime of a second polariton in the dot, thereby precluding its injection. In an electronic quantum dot the analogous Coulomb-blockade physics is typically ascertained from the dependence of transport upon bias-voltage [289]; by contrast, we directly observe suppression of simultaneous polariton transit by detecting *when* photons tunnel through the dot. We characterize the tunneling times via the temporal intensity autocorrelation function, $g_2(\tau)$ where τ is the delay time, of the cavity transmission. This function compares the rate of photon pairs leaking

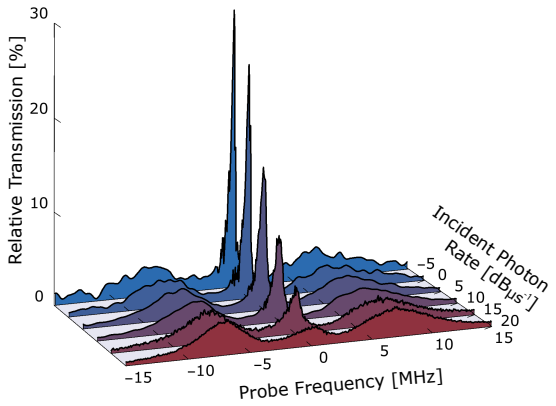

Figure 5.3: **Nonlinear Spectroscopy of a Polaritonic Quantum Dot.** The quantum dot's transmission versus probe frequency is plotted for increasing incident photon rates. Here, the sample is unsliced and thus contains several (~ 3) blockade volumes, resulting in weak, nearly mean-field interactions. We thus observe smooth broadening and transmission suppression of the dark polariton peak (at $\delta = 0$ MHz). The bright polariton resonances at $\delta = \pm 7$ MHz are not suppressed at high probe rate, because bright polaritons have little Rydberg admixture and are thus essentially non-interacting. The data for the three lowest powers are Gaussian filtered (with $\sigma_{filter} = 481$ kHz) outside of the interval (-1.5 MHz, 1.5 MHz); all data are normalized to the bare cavity transmission. Figure taken from Ref. [153].

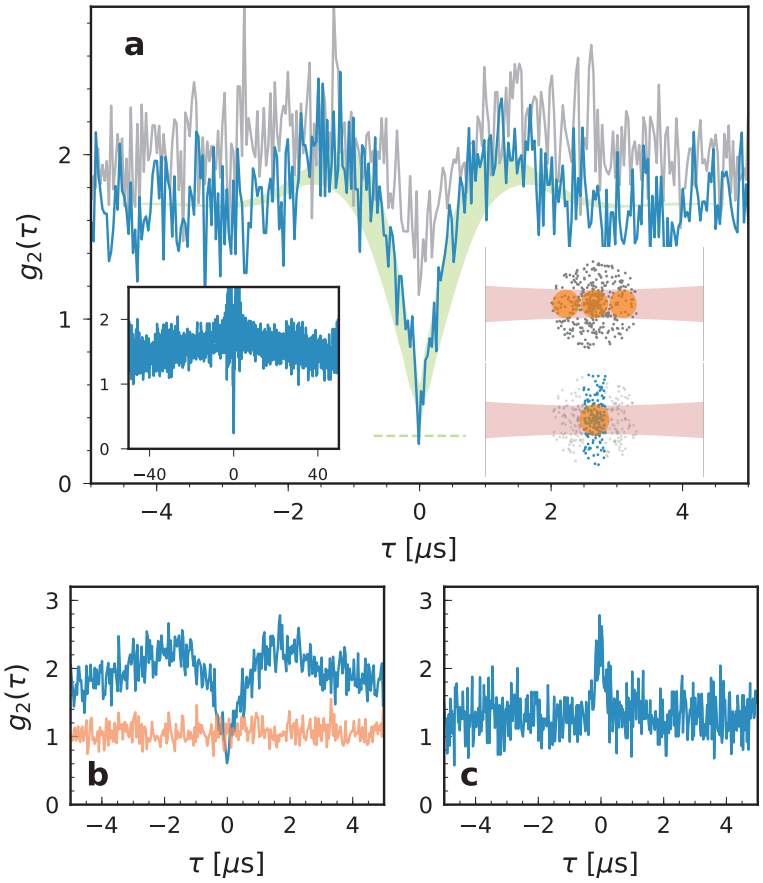

Figure 5.4: **Transport Blockade of Cavity Rydberg Polaritons.** The photons transmitted through cavity exhibit a strong anti-bunching/bunching effect, showing an interaction on the single quantum level. **(a)** A smoking gun of strong interactions in a quantum dot is blockade: the suppression of near-simultaneous particle transmission. The temporal intensity autocorrelation function $g_2(\tau)$ on the dark polariton resonance with a sliced atomic cloud reveals strong blockade: a ∼5x suppression of two-photon events relative to the long-time value shown in the inset (blue curve, $g_2 = 0.27(8)$ near $\tau = 0$ compared to $g_2 = 1.3$ at long times). The green dashed line and band are the theoretically predicted minimum value and time-dynamics, respectively (see Appxs. A.2.7, A.2.8, and Ref. [153] SI L). The unsliced cloud contains numerous blockade volumes; accordingly it provides a weaker suppression of g_2 near $\tau = 0$ (gray). In the inset, the time-bins for $|\tau| > 0.8$ μs are larger by a factor 4 to reveal large τ trends. **(b)** On the dark polariton resonance of the $85S_{1/2}$ Rydberg state (blue), the suppression of g_2 is reduced because multiple blockade volumes fit in the transverse plane. On the bright polariton resonance at 100S with a sliced cloud (orange), polaritons are very weakly interacting, resulting in uncorrelated transmission. **(c)** We observe bunching ($g_2(0) > 0$) when probing near a two-polariton resonance, achieved by shifting the cavity resonance by −5 MHz, increasing the control frequency by 5 MHz and probing −1 MHz from the single-polariton resonance. In each panel, the large-τ value of g_2 exceeds 1 due to atom number fluctuations, which lead to a variation in the on-resonance transmission. Figure taken from Ref. [153].

out of the resonator separated by a time τ to a Poisson-process with the same average rate. A reduction near zero delay ($\tau = 0$) indicates interaction-driven suppression of double-occupancy of the dot, while the rise-time back to steady-state is dominated by the injection Rabi frequency.

After slicing the cloud so that it can hold only a single polariton at a time, we observe almost complete suppression ($g_2(0) = 0.27(8)$) of simultaneous tunneling through the dot, indicative of transport blockade due to strong interactions (Fig. 5.4a). Indeed, strong anti-bunching at zero-time separation validates a model where a single intra-cavity polariton shifts and broadens the energy for the injection of the next polariton by more than the polariton linewidth, strongly suppressing its tunneling into the resonator until the first polariton tunnels out. The observed $g_2(\tau)$ is consistent with a master-equation effective theory bootstrapped by a full model of interacting 3-level atoms coupled to a single resonator mode (see Appx. A.2.7). Note that the linear growth of $g_2(\tau)$ near zero delay, as opposed to the quadratic growth anticipated from a single-mode theory, arises from virtual excitation of bright polaritons.

We verify that the observed transport blockade results from strongly interacting polaritons by comparing to transport with weaker interactions. First we test the unsliced cloud (Fig. 5.4a), which exhibits only weak suppression of g_2 near $\tau = 0$ because the cloud is large enough to hold multiple polaritons along the resonator axis simultaneously. Similarly, a sliced sample with Rydberg atoms in the smaller $85S$ state can fit multiple excitations transversely and also exhibits weak suppression of g_2 (Fig. 5.4b). Furthermore, we find that transport of bright polaritons is not blockaded at all (Fig. 5.4b), as these polaritons are essentially non-interacting [130]. The blockade of the dark polaritons can even be "reversed" by detuning from the atomic 5P state to make the polariton-polariton scattering more elastic and probing transport on the two-polariton resonance (Fig. 5.4c). In this case we observe photon bunching, $g_2 > 1$, reflecting the preferential transit of photon pairs [290].

5.4 Dark Polariton Dynamics

To investigate the dimensionality of the polaritonic dot, we probe the cavity with pulses of substantially higher intensity and observe the transmitted light as the intracavity field

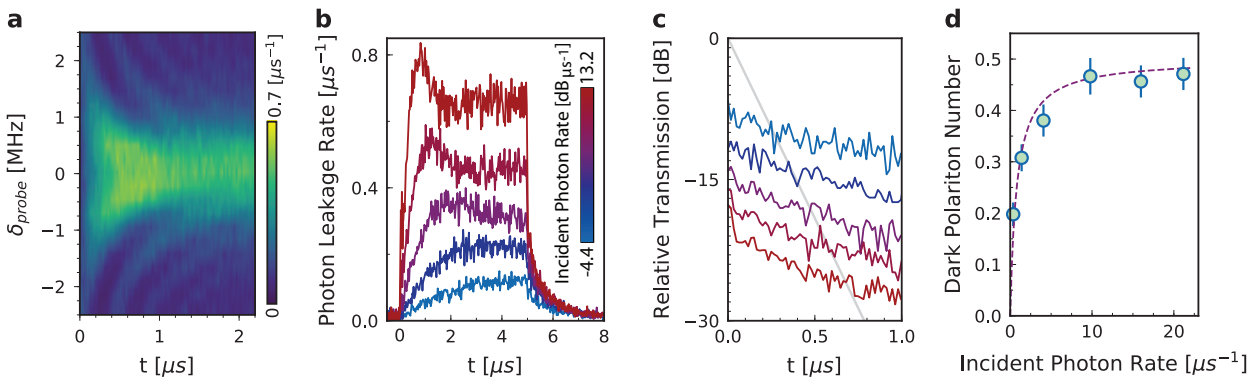

Figure 5.5: **Dynamical Evolution of a Polaritonic Quantum Dot: Ring-up and Ring-down.** When the dot is simultaneously excited with many photons within the dark polariton lifetime, these photons stimulate coherent tunneling of a polariton into and out-of the dot until the dot finally equilibrates. **(a)** We drive the resonator near the dark polariton resonance for 2.5 μs and record the transmitted intensity during the equilibration process. As probe frequency is tuned away from the resonance, the oscillation frequency increases and the visibility decreases, resulting in a "chevron" of damped Rabi oscillations. **(b)** With increasing probe strength, the overall transmitted power increases as well as the frequency of the occupation oscillation. The slow dynamics ($\sim \mu$s timescale) reflect the tunneling oscillations between zero and one dark polaritons, while the fast dynamics (on a ~ 100 ns timescale) reflect off-resonant excitation of the broad bright polaritons. Bright polaritons are weakly interacting and do not saturate with increasing probe power. Accordingly, they produce a dominant background at the highest probe powers (nearly 50% of the observed signal). **(c)** To isolate the physics of the dark polariton saturation from the bright polariton background, we explore the ring-down of the polaritons once the probe field is removed. The first ~ 100 ns of ringdown is dominated by the fast decay of bright polaritons. At later times, the cavity leakage is dominated entirely by the dark polaritons, with a lifetime substantially longer than the bare resonator (gray curve). The color-code is the same as panel **b**; the relative transmission drops as the incident photon rate increases due to the blockade. **(d)** We extract the steady-state dark polariton number by extrapolating the slow decay of cavity emission to the beginning of the ring-down. The dark polariton number saturates strongly at the highest probe power to $n_D = 0.47(3)$ (see Appx. A.2.5). Figure taken from Ref. [153].

rings up and then down. A zero-dimensional system may be coherently excited and then *de-excited* by the drive field, exhibiting Rabi oscillations, while in a one dimensional system the excitation would propagate away before it can be removed. Figure 5.5a shows the detuning dependence of the ring-up process, exhibiting rapid, detuned Rabi oscillations away from the dark-polariton resonance, and slower oscillations on-resonance. Figure 5.5b shows the ring-up dynamics on the dark polariton resonance for various probe intensities. We observe Rabi oscillations between zero and one dark polaritons at the highest intensities, indicative of a strongly blockaded, zero-dimensional dot interacting with many photons within the polariton lifetime. The dark polariton oscillations exhibit a Rabi frequency of $\Omega_{polariton} = 2\pi \times$ 245 kHz, in agreement with a first-principles calculation based upon the probe power

(see Appx. A.2.4). Note that the fast ∼100 ns oscillations arise from off-resonant excitation of non-interacting bright polaritons.

Strong interactions should cause the number of dark polaritons in the dot to saturate at large probe powers. However, the off-resonant excitation of bright polaritons does not saturate, resulting in a high steady-state leakage rate of bright polaritons which overwhelms the dark polariton signal at high probe powers. To disentangle the bright and dark contributions to the cavity transmission, Fig. 5.5c shows the ring-down of the dot once the probe beam is turned off. At each probe intensity, the ring-down consists of slow and fast exponential decays; the slow feature (with a time constant of 730(40) ns) reflects the dynamics of the dark polariton, while the fast feature reflects the decay of the interfering bright polaritons. We isolate the steady-state dark polariton number, shown in Fig. 5.5d, by extrapolating the slowly-decaying tail of the ring-down to its zero-time population. The strong saturation of dark polariton number with drive power again indicates blockade, while the saturation value of $n_d = 0.47(3)$ reflects the behavior of a single zero-dimensional two-level emitter, as described by the optical Bloch equations. This stationary, strongly coupled, two-level emitter is an excellent candidate qubit for a photonic quantum information processor [89]. To verify saturation, we measure the g_2 of the slowly-decaying tail of the ring-down, after the bright polaritons have all decayed away. We find $g_2 = 0.31(7)$, confirming that the dot rarely hosts multiple dark polaritons. Moving forward, blockade-enhanced detection of dark polaritons will directly boost the dark-polariton detection signal-to-noise above the bright-polariton background [291], while enhanced control field and light-matter coupling will suppress the background (see appendix A.2.5), enabling the dot to act as an on-demand single photon source.

Cavity Rydberg polaritons are now ripe for applications in synthetic quantum materials; recent experiments have demonstrated synthetic magnetic fields for resonator photons [182] and in conjunction with strong photon-photon interactions here presented, there is now

a clear path to topological many-photon states [116, 121]. More broadly, the numerous proposals to study synthetic quantum matter in cavity arrays and continua [74] can now be explored in the modes of an individual, multi-mode optical cavity, employing Rydberg atoms to mediate strong photon-photon interactions. Achieving stronger light-matter coupling will require only additional atomic density, rather than increasingly challenging advances in optical super-mirror technology necessary for single-emitter approaches. Indeed, densities routinely achieved in free-space experiments ($\rho \approx 10^{12}/\mathrm{cm}^3$) [85] and finesses of single atom experiments ($F \approx 10^5$) would provide $OD_B \approx 88000$, more than sufficient for few-particle synthetic materials [116]. Upcoming challenges therefore center upon harnessing these developments to answer questions in dissipative preparation of many-body quantum states [187, 278] and in the exploration of the resulting phase diagrams [292] using the quasi-particle manipulation and detection tools unique to quantum optics [223, 293–295].

5.5 Toward Multimode Collisions

So far we have explored single photon effects and two photon blockade in a single mode. In order to study materials, it is necessary to introduce interactions between photons in *multiple* spatial modes such that repulsive interactions or collisions cause ordering of photons among those modes.

Strong interactions between photons are narrow-band in the photon frequency, since these interactions arise through resonant coupling of photons with atomic excitations, with typical linewidths in the kHz to MHz range. However without special effort, the kinetic energy scale which is set by the spacing between cavity spatial mode energies is typically much larger. While special degenerate cavities may be designed to bring a family of spatial modes into degeneracy, challenges in engineering these systems have thus far allowed studies of strongly interacting photons in a single transverse mode [84, 153, 285, 296]. In parallel with developing

cavity structures that provide suitable spaces for polariton propagation in multiple modes (see Chs. 4, 6 and Refs. [181, 182, 208, 251]), we developed an alternative technique using Floquet engineering [297, 298] to bridge energy offsets of 10^s to 100 MHz between spatial modes and thereby enable strongly interacting polaritons to access multiple spatial modes of an optical cavity. First, while the atomic transitions available are normally restricted to those prescribed by nature, we show that periodically modulating an excited state of Rubidium splits its spectral weight to generate new lines separated by multiples of the modulation frequency. We next use this capability to simultaneously generate spectral lines resonant with two chosen spatial modes of a non-degenerate optical cavity, enabling "Floquet polaritons" to exist in both modes. Because both spectral lines correspond to the same Floquet-engineered atomic state, adding a single frequency field is sufficient to subsequently couple both modes with a Rydberg excitation. We demonstrate that the resulting polaritons interact strongly in both cavity modes simultaneously.

5.6 Floquet Polaritons

One approach for creating multi-mode polaritons is Floquet engineering – the periodic modulation of parameters to generate desirable new properties in quantum mechanical systems. Floquet engineering has proven to be a powerful tool for studying quantum many-body physics with ultracold atoms [298], where it has enabled tests of quantum phase transitions [299–301], the creation of new interaction processes [302–304], and the development of synthetic gauge fields [66, 305–309] for studies of topology [241, 245, 310, 311].

Frequency modulation, the periodic variation of the energy of a quantum state, is a prolific form of Floquet engineering [297]. Periodically modulating a state splits it into multiple bands at different energies, analogous to frequency modulation in signal processing [312]. Frequency modulation has enabled faster manipulation [313] and efficient random access

architectures [314] for superconducting quantum processors via first-order sideband transitions [315]. In ultracold atoms, many shaken lattice experiments can be viewed as frequency modulation [297, 298], which has also been employed to bind diatomic molecules [316, 317].

In what follows, we frequency modulate an atomic state to customize the coupling between atoms and photons, demonstrating that the "Floquet polaritons" which emerge behave as strongly interacting quasi-particles with spatial wavefunctions inherited from the chosen optical cavity modes. After loading a gas of cold atoms at the waist of the cavity, we use an intensity-modulated off-resonant laser to sinusoidally vary the energy of an excited atomic state. This modulation splits the state into bands separated by multiples of the modulation frequency. We choose a frequency that creates bands whose energy difference matches the separation between two transverse modes of the cavity. This choice enables photons in both modes to couple with the atomic ensemble and form polaritons, which we verify by measuring the transmission spectrum. Finally, we demonstrate that Floquet polaritons have strong interactions, which in these particular modes hinder multiple polaritons from entering the cavity simultaneously. We conclude by discussing the bright prospects of Floquet polaritons for many-body physics and, more broadly, customized atomic spectra for quantum science.

Our experiments begin by controllably loading a sample of 300–1800 cold ^{87}Rb atoms at the waist of a four-mirror optical cavity (Fig. 5.6a), the same cavity as used in the prior sections of this chapter. The cavity has modes near-detuned to the atomic transition between the $5S_{1/2}$ ground state and the $5P_{3/2}$ excited state at 780 nm. In order to modulate the energy of the excited state, we expose the atoms to a multichromatic optical field tuned near the $5P_{3/2} \rightarrow 5D_{5/2}$ transition at 776 nm. This multichromatic field simultaneously cancels the constant component of the Stark shift and produces a time-varying component of the Stark shift that oscillates with tunable frequency f (MHz-GHz scale) and amplitude η (Fig. 5.6b). We tune the modulation amplitude by adjusting the total intensity of the 776 nm beam; amplitudes are reported in units of the arbitrarily defined $\eta_0 = h \times 17(1)$ MHz, which

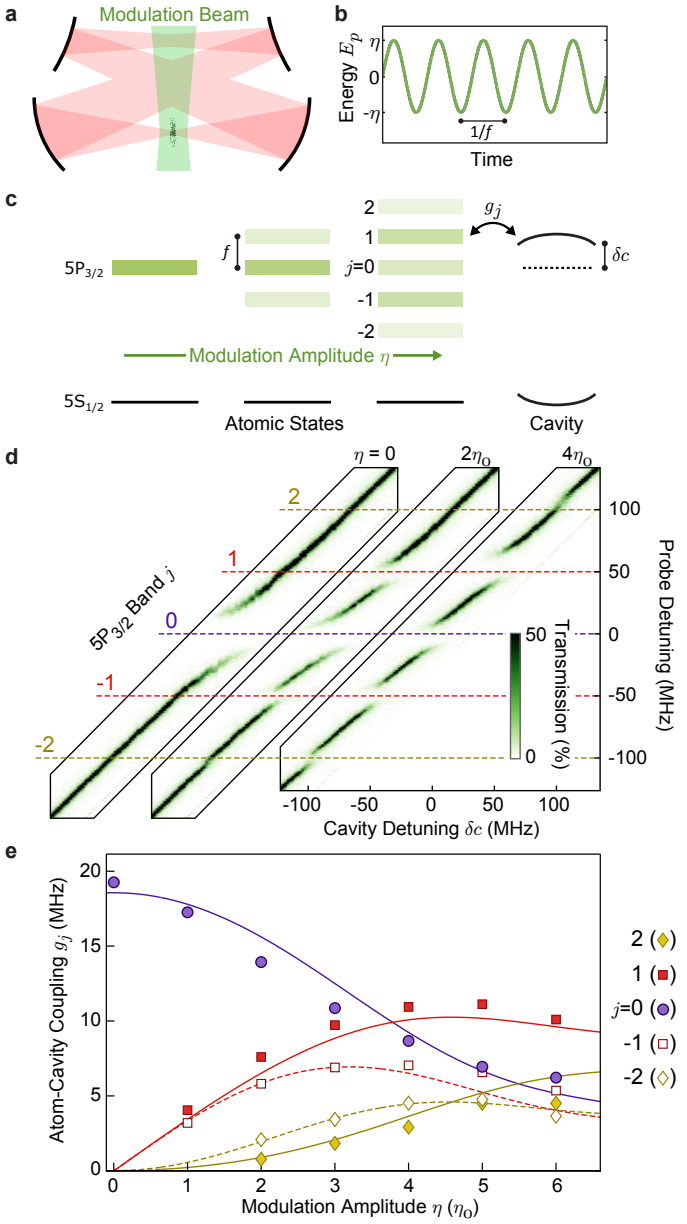

Figure 5.6: **Redistributing the spectral density of atoms coupled to a cavity.** **(a)** Photons in a four-mirror optical cavity are strongly coupled with excitations of a cloud of ultracold atoms. **(b)** To customize the atomic spectrum, an off-resonant laser (green) sinusoidally modulates the energy E_p of the $5P_{3/2}$ atomic state with amplitude η and frequency f. **(c)** As the modulation amplitude increases, the $5P_{3/2}$ state progressively splits into bands at energies $E_j = jhf$ for integer j. Each band has a collective coupling strength g_j to the cavity. **(d)** Transmission spectra measured while scanning the cavity length exhibit avoided crossings, indicative of atom-cavity coupling, for up to five different bands depending on the modulation amplitude. The frequencies of the cavity mode and probe laser are shown as detunings relative to the unmodulated $5S_{1/2} \rightarrow 5P_{3/2}$ atomic transition. Transmission is reported relative to an empty cavity. **(e)** The coupling strengths g_j extracted from transmission spectra are shown for the bands indicated on the right. Errorbars are smaller than the symbol heights. Curves (solid for positive bands, dotted for negative) show a global fit accounting for inhomogeneity and slightly asymmetric modulation. Figure taken from Ref. [207].

corresponds to a beam intensity of approximately 5 W/mm^2 determined by the polarizability at 1 GHz detuning from the $5P_{3/2} \rightarrow 5D_{5/2}$ transition. For more details on the experiment setup, see section 5.7.2 and appendices A.3.1 and A.3.2.

5.6.1 Redistributing the Spectral Density of Atoms

Periodic modulation splits the excited state into bands at energies $E_j = E_0 + jhf$, for integer j, relative to its unmodulated energy E_0 (Fig. 5.6c). For sinusoidal modulation, the collective atom-photon coupling strengths g_j at each band should take the form,

$$g_j(\eta, f) = gJ_j\left(\frac{\eta}{hf}\right), \tag{5.1}$$

where g is the unmodulated coupling and J_j is the j'th Bessel function of the first kind (see appendix A.2.10). Note that modulation does not create any new states, but rather redistributes the spectral weight of a *single state* between multiple energies; this fact is reflected in the constraint that the total coupling strength $g = \sqrt{\sum_j |g_j(\eta, f)|^2}$ is unchanged).

To test for the redistribution of the excited state into bands, we measure the transmission spectrum of a single mode of the cavity while scanning the cavity length (Fig. 5.6d). Whenever the mode energy approaches the energy of an atomic band, we observe an avoided crossing in the spectrum. Without modulation only a single avoided crossing is observed, corresponding to the original band $j = 0$. With sufficient modulation additional avoided crossings become clearly visible for the first-order bands at $j = \pm 1$ and the second-order bands at $j = \pm 2$. The frequencies of the observed features deviate slightly from $E_j = jhf$ due to shifts from off-resonant couplings with the other bands (see Appx. A.2.11).

We extract the coupling strengths $g_j(\eta)$ for each modulation amplitude from the widths of the avoided crossings in figure 5.6d, according to the fit function While the observed coupling

strengths are qualitatively similar to the prediction of Eq. (5.1), the Bessel functions are distorted by inhomogeneity of the modulation beam and slight asymmetry due to higher order Stark shifts. Accounting for these two factors through a global fit to all 29 values of $g_j(\eta)$ for all bands $j = 0, \pm 1, \pm 2$ by following a theoretical treatment in Ref. [207] SI. B1 nicely captures the observed behavior in figure 5.6e.

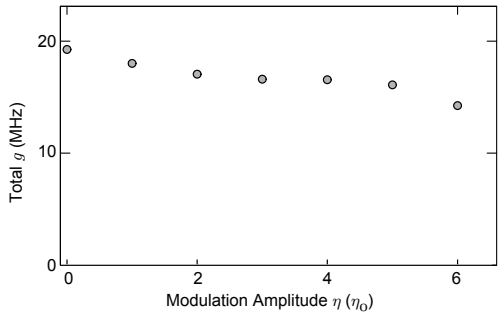

Figure 5.7: **Total atom-cavity coupling strength** The total atom-cavity coupling strength $g = \sqrt{\sum_j |g_j|^2}$ is nearly constant as the modulation amplitude is increased, consistent with the theoretical prediction (see Appx. A.2.10). We attribute the slight decrease in the total g to the admixture of the $5D_{5/2}$ state, which does not couple to the cavity photons, into the $5P_{3/2}$ bands. Figure taken from Ref. [207].

Regardless of the modulation waveform, we expect the observed band strengths to satisfy $g(\eta) = \sqrt{\sum_j |g_j(\eta)|^2}$ because we are merely redistributing the original coupling g among multiple bands.The experimentally observed total coupling strengths are shown in Fig. 5.7. While the total strength is indeed nearly constant, it is lowered by about 25% at the maximum modulation amplitude $\eta = 6\eta_0$ that we have tested. This slight decrease can be attributed to a variety of effects. First, the high intensity of the modulation beam, which leads to nonlinear effects discussed in [207] SI. B8, also causes a significant admixture of the $5D_{5/2}$ state into the $5P_{3/2}$ bands. Since the dipole matrix element between $5S_{1/2}$ and $5D_{5/2}$ is essentially zero, this admixture should indeed reduce the atom-cavity coupling strength. It is also possible that scattering or antitrapping caused by the 776 nm beam are reducing the number of atoms near the waist of the cavity.

Frequency modulation of the $5P_{3/2}$ state is also expected to affect the Rydberg coupling Ω. Here, the theory predicts that *the effective* Ω *should be the same for every feature*, because regardless of the band which resonantly couples to each cavity mode, the collective Rydberg states are all degenerate and only a single frequency blue beam couples each collective $5P_{3/2}$

state to the corresponding collective Rydberg excitation. In this work, the blue beam resonantly drives the transition from the $j = 0$ band to the Rydberg state, and therefore we expect every feature to exhibit Rydberg coupling strength of approximately $\Omega_0 = \Omega J_0(\eta/hf)$ (see Appx. A.2.10).

Similar to our treatment of the vacuum Rabi splitting features as a function of modulation amplitude in figure. 5.6d-e, we present the electromagnetically-induced transparency (EIT) features as a function of modulation amplitude in Fig. 5.8a. All of the conditions are the same as figure 5.61d-e, except that we have turned on the Rydberg coupling beam. We fit the spectroscopic features observed at each band with the total atom-cavity coupling strength fixed based on the values shown in figure 5.6e, and the Rydberg loss rate $\gamma_R = 2\pi \times 1.0$ MHz fixed to better reveal the trend of Ω with modulation amplitude η. Without constraining γ_R, there is quite a bit of spurious fluctuation in the fitted values of Ω which masks the overall trend. The results are not very sensitive to the exact value of γ_R chosen: for example, increasing γ_R by 30% shifts the entire Ω curve for $j = 0$ upward, by amounts ranging from 3%–5% across all η.

From fits to each feature we extract the effective Rydberg coupling strengths $\tilde{\Omega}$ for the features at each band, which are plotted in Fig. 5.8b. For small modulation amplitudes (especially $\eta = 2 \sim 3\ \eta_0$) the observed Rydberg coupling strengths at each band are indeed quite similar, as expected. However, there are clear deviations between the coupling strengths at $\eta = \eta_0$ and $\eta \geq 4\eta_0$. Note that, when $\eta = 0$, there is no atom-cavity coupling on bands $j = \pm 1$, so we do not observe any EIT feature and cannot extract $\tilde{\Omega}$.

We attribute the differences in the Rydberg coupling strengths between bands to the inhomogeneity of the modulation amplitude throughout the sample. As discussed above, inhomogeneity can arise from both the 776 nm beam profile and the unpolarized atomic sample. Qualitatively, inhomogeneity can cause Ω to deviate between bands because it causes each atom's $5P_{3/2}$ state to be distributed differently. For example, for small amplitudes such as

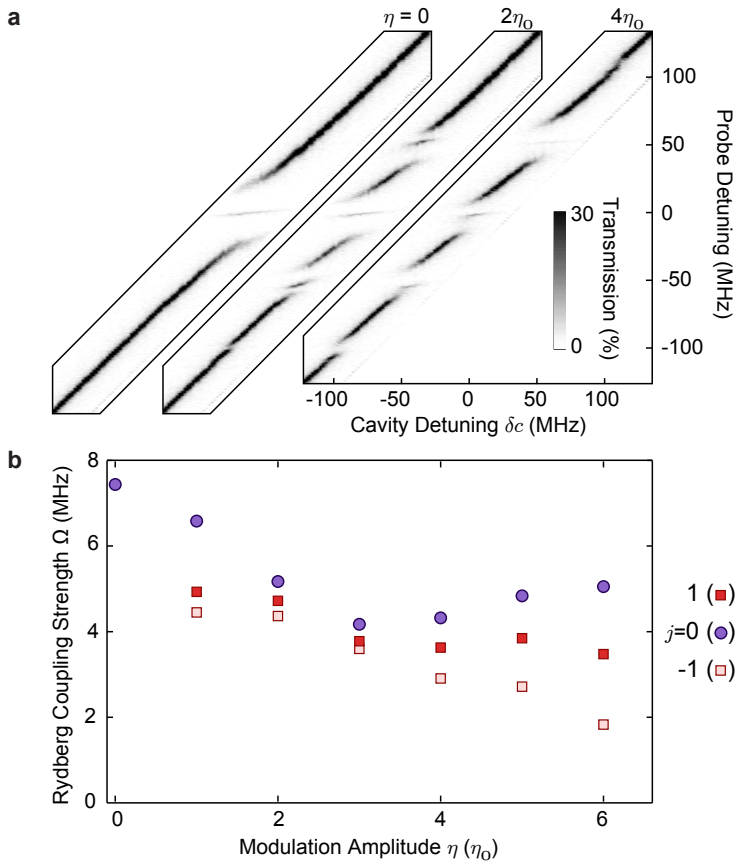

Figure 5.8: **Rydberg coupling strengths with frequency modulation.** **(a)** Electromagnetically-induced transparency spectra observed while probing the atom-cavity system for a range of cavity lengths in the presence of the Rydberg coupling field (compare to figure 5.6d). Even though the Rydberg coupling field contains only a single frequency, resonant with the unmodulated transition $5P_{3/2} \rightarrow 39S_{1/2}$, dark polariton peaks appear at each of the $5P_{3/2}$ bands in the presence of modulation. Off-resonant shifts cause the spectra to be asymmetric (see Appx. A.2.11). **(b)** Rydberg coupling strengths Ω extracted from the observed spectroscopy features for the bands indicated at the right. In the idealized theory, each feature would exhibit the same Ω; we attribute the deviations from this prediction to effects from the unpolarized atomic sample. Figure taken from Ref. [207].

$\eta = \eta_0$, the contributions to g_1 come primarily from those atoms which are being modulated more than the average, while the contributions to g_0 come primarily from atoms whose modulation is weaker than the average. Then, the Rydberg coupling Ω *for the atoms contributing the most to* g_1 will be smaller, because the same strong modulation which makes their contribution to g_1 greater makes their Ω smaller. Conversely, the coupling Ω for the atoms contributing most to g_0 will be higher than expected, because their modulation is weaker than the average. Thus, inhomogeneity leads to weaker Ω for the sidebands, in qualitative agreement with the trend observed in Fig. 5.8b.

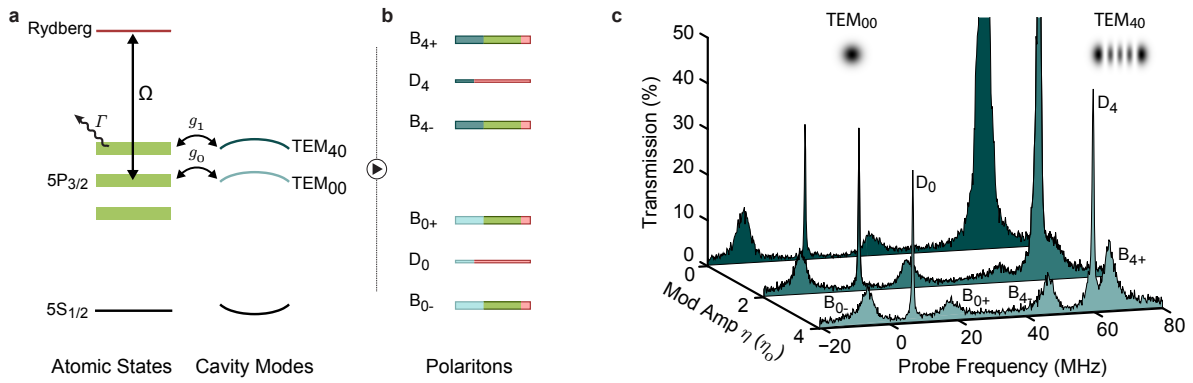

Figure 5.9: **Forming Floquet polaritons in a customized space. (a)** To form Rydberg polaritons we add a field at 480 nm to couple the $5P_{3/2}$ state to a Rydberg state with strength Ω. When the modulation frequency f matches the energy spacing between the TEM_{00} and TEM_{40} cavity modes, photons in both modes are resonantly coupled to excitations of the atoms with strengths determined by the resonant bands. **(b)** The eigenstates of this atom-cavity system are sets of three polaritons in each spatial mode TEM_{m0}, consisting of two bright polaritons $B_{m\pm}$ composed primarily of a cavity photon and a collective $5P_{3/2}$ excitation, and one dark polariton D_m composed of a cavity photon and a collective Rydberg excitation. The bright polaritons are broad due to rapid decay of their $5P_{3/2}$ component at rate $\Gamma = 2\pi \times 6$ MHz. **(c)** With the cavity length fixed, we probe the transmission spectrum of the combined atom-cavity system. Here, we use the weakly interacting $39S_{1/2}$ Rydberg level, with blockade radius 4 μm small compared to the 12 μm cavity waist, to avoid blockade effects. The probe laser is in an equal superposition of the TEM_{00} and TEM_{40} modes, and we simultaneously monitor photons output from both modes on a single detector. Without modulation, we observe the predicted polariton features in TEM_{00}, but TEM_{40} exhibits only an ordinary cavity transmission line. With sufficient modulation, we detect all six polariton features predicted in panel b. Additional frequency shifts and asymmetries in the polariton spectra result from couplings to off-resonant bands (see Appx. A.2.11). Figure taken from Ref. [207].

5.6.2 Coupling to Multiple Cavity Modes

When the atomic transition is split into bands, it can couple resonantly to multiple transverse modes of the cavity simultaneously (Fig. 5.9a). In our cavity, the fundamental TEM_{00} mode is conveniently close to the TEM_{40} mode, which is only 52 MHz away. By modulating the atoms at a frequency near that mode separation, we simultaneously couple the TEM_{00} mode with the atoms through the $j = 0$ band and the TEM_{40} mode with the atoms through the $j = 1$ band. The choice of two nearby modes minimizes the necessary modulation frequency. Note that each cavity mode couples to a unique *collective* atomic excitation, in which all of the atoms share one excitation with relative amplitudes following the electric field of the mode at each atom's location, such that different modes remain orthogonal to one another [86, 318, 319] (see Ref. [207] SI. B2).

To progress toward providing photons with the strong interactions of highly excited Rydberg atoms, we now add a 480 nm field to couple the $5P_{3/2}$ state with a Rydberg state. Because every band is part of the same $5P_{3/2}$ state, a single frequency field is sufficient to provide this Rydberg coupling. For instance, a cavity mode can couple to a $5P_{3/2}$ excitation through the $j = 1$ band, and that same $5P_{3/2}$ excitation can still be subsequently coupled to a Rydberg excitation via a different band, such as $j = 0$. In this work, we use a single frequency field tuned to create Rydberg coupling via band $j = 0$ regardless of the resonant bands used for atom-cavity coupling.

The eigenstates of this atom-cavity system are superpositions of collective, modulated atomic excitations with cavity photons, which we name "Floquet polaritons" (Fig. 5.9b). Each cavity mode TEM_{m0} yields three types of polaritons [158]: two bright polariton states $B_{m\pm}$ and one dark polariton state D_m. The bright polaritons are primarily composed of a photon in the corresponding cavity mode and a collective $5P_{3/2}$ excitation. Their $5P_{3/2}$ components with rapid decay rate $\Gamma = 2\pi \times 6$ MHz make them short-lived. We are primarily interested in the dark polaritons, superpositions of a cavity photon with a collective Rydberg excitation. Dark polaritons are useful for studying quantum many-body physics because they are long-lived and strongly interacting, as long as the Rydberg blockade radius is comparable to the mode size of the cavity [153].

To detect these polaritons we measure the transmission spectrum of the atom-cavity system for a fixed cavity length (Fig. 5.9c). We choose a length which makes the TEM_{00} mode resonant with the $j = 0$ band and the TEM_{40} mode resonant with the $j = 1$ band. Without modulation, we observe the predicted polariton features in the TEM_{00} mode, including two bright polaritons widely split due to strong light-matter coupling, as well as a dark polariton in the middle. The bright polaritons are broad due to the rapid decay of the $5P_{3/2}$ component, while the dark polariton's slow decay at rate $\Gamma_d = 2\pi \times 0.3$ MHz makes its transmission feature much narrower. However, without modulation there is no weight in the

$j = 1$ band and the atoms do not resonantly couple with the TEM_{40} mode; thus, we observe a transmission feature in that mode equivalent to an empty cavity.

Increasing the modulation amplitude couples the atoms with the TEM_{40} mode by increasing the sideband strength g_1 at the expense of the original feature strength g_0. This leads to the division of the bare TEM_{40} feature into the three polaritons $B_{4\pm}$ and D_4 as the mode becomes coupled to the atoms, while also narrowing the separation between the $B_{0\pm}$ bright polaritons due to weaker light-matter coupling in that mode. While the primary features come from the $5\mathrm{P}_{3/2}$ bands that are resonantly coupled to each cavity mode, the other bands also couple with the cavity modes off-resonantly, inducing small shifts of the polariton energies. These off-resonant couplings cause the observed asymmetry between the B_{m+} and B_{m-} features (see Appx. A.2.11). Moreover, even though their spectroscopic features remain separated, a Floquet treatment reveals that the dynamics of the two dark polariton modes is governed by an effective Hamiltonian in which they are nearly degenerate, with relative energies controlled by the modulation frequency (see Appx. A.2.12).This effect cannot be achieved by frequency modulating the Rydberg coupling field: this would enable additional modes to host dark polaritons satisfying two-photon resonance, but with an unacceptably large mismatch between the cavity photons and the $5S_{1/2} \rightarrow 5P_{3/2}$ transition. This mismatch effectively reduces the optical density of the atomic sample, making the dark polaritons very fragile (for more on this, see Sec. 5.6.4).

5.6.3 Multimode Collisions

We next test for interactions between the Floquet dark polaritons (Fig. 5.10a) by exploring the transport dynamics, as before in section 5.3. We couple to the $100\mathrm{S}_{1/2}$ Rydberg state which has a blockade radius of 25 μm, larger than the cavity mode waist of 12 μm, which is expected to make the polaritons interact strongly (see Secs. 5.3, A.3.2, and Ref. [153]). With

sufficient modulation to support dark polaritons in both modes, we simultaneously probe the cavity on the D_4 feature in the forward direction and the D_0 feature in the backward direction. We then monitor the photons leaking out of the cavity in each mode, and test for photonic interactions via the correlation function $G_{mn}(\tau)$ between photons from TEM_{m0} and photons from TEM_{n0}, separated by time τ (see Appx. A.2.9). In this system, correlations arise *exclusively* from strong interactions between individual polaritons due to their Rydberg components [153].

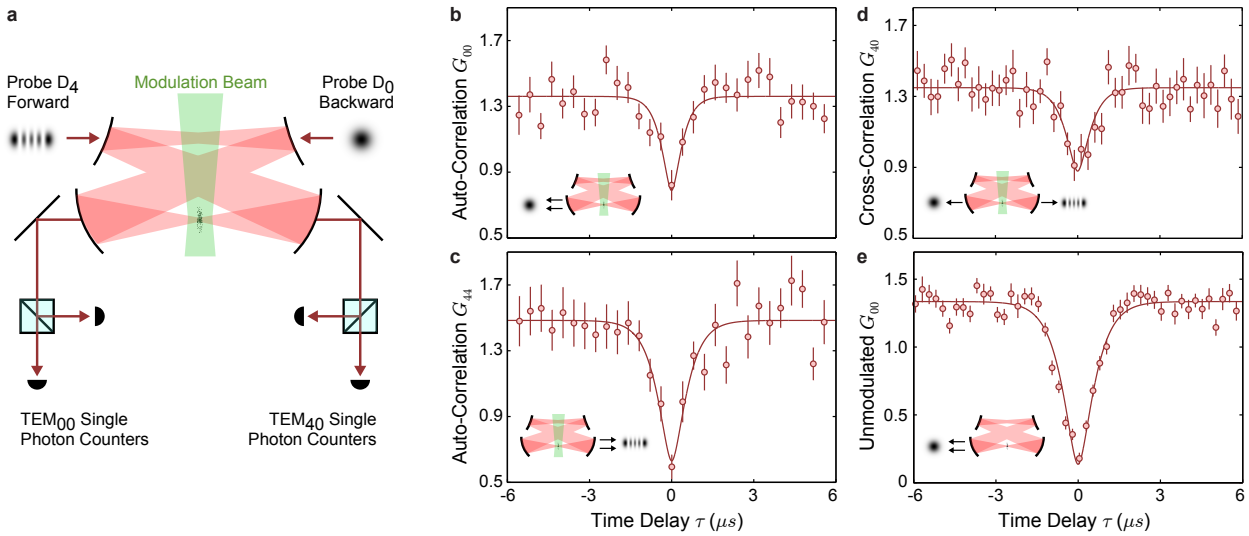

Figure 5.10: **Strong interactions between Floquet dark polaritons. (a)** We use the highly excited $100\mathrm{S}_{1/2}$ Rydberg state to make dark polaritons interact strongly with each other, such that the presence of a single polariton in the cavity hinders the entry of others. To test for this blockade effect, we probe the atom-cavity system simultaneously with one laser tuned to the dark polariton D_4 resonance in the forward direction and a second laser tuned to the D_0 resonance in the backward direction. Single photon counters monitor the cavity emission in each mode. **(b,c)** With frequency modulation at $\eta = 2.7\ \eta_0$, photons in the TEM_{00} (panel **b**) and TEM_{40} (panel **c**) modes blockade further transmission in the same mode, as indicated by the correlation minima at $\tau = 0$. **(d)** Strong interactions between polaritons in different modes lead to cross-blockade. **(e)** Under conditions optimized for single-mode blockade without modulation, the correlation minimum is close to zero. In panels (b)-**e**, the solid curves show fits to a generalization of the optical Bloch equations which allows one polariton to occupy either of the two modes (see Appx A.2.9). Error bars indicate one standard error. Figure taken from Ref. [207].

Photon antibunching in the correlation functions reveals strong interactions between Floquet polaritons (Fig. 5.10b-d). Antibunching appears as a minimum in the correlation functions $G_{mn}(0)$ at zero time delay, which can be interpreted as the relative likelihood of a second photon being present compared to the non-interacting case. A significant suppression indicates that the presence of just a single dark polariton in any mode of the cavity impedes

the entry of a second dark polariton. In particular, the depth of the correlation minima $G(0)/G(\infty) = \gamma^2/(U^2 + \gamma^2)$ reveals the strength of the interactions U relative to the polariton lifetime γ; suppression of the zero-time correlation by half would indicate interaction strength equal to the polariton lifetime. The polariton lifetime also determines the correlation time over which multiple photon events are suppressed (see Appx. A.2.9). In contrast, perfect coherent light without interactions, such as a laser beam, would exhibit a flat correlation function $G(\tau) = 1$. Classical fluctuations, such as intensity instability, cause the correlation function to rise above one. In our system, the background correlation values result primarily from trial-to-trial fluctuations in the atom number.

Future applications of this system to quantum information, such as for multimode photon-by-photon switching, would benefit from Floquet polaritons performing at the level of polaritons optimized for blockade in a single mode (Fig. 5.10e). Simulations using non-Hermitian perturbation theory indicate that the observed difference in performance between these two cases results from straightforwardly surmountable technical limitations (see Appx. A.2.9). In particular, modulation splits the coupling strengths g and Ω between multiple bands, weakening the resonant light-matter coupling for any particular mode. Upgrading this apparatus to achieve the atomic densities typical of free space experiments [85] would increase g by an order of magnitude, and the use of a buildup cavity for the Rydberg coupling beam would similarly enhance Ω. These modifications would enable the multimode performance with frequency modulation to reach or surpass the performance shown in Fig. 5.10e (see chapter 6).

We have created and characterized interacting Floquet polaritons. These polaritons live in a completely customizable space whose modes and energetic structure (see Appx. A.2.12) are controlled by frequency modulation of an atomic gas in an optical cavity. Floquet polaritons can be used to study many-body physics with features that are extremely challenging to realize in any other platform, including physics in spaces with wormholes and the non-Abelian

topological phases of multilayer fractional quantum hall systems [52, 183]. Such schemes are enabled by illuminating an atomic sample in a degenerate cavity with a patterned Floquet beam to create arbitrary potentials—and even non-local couplings—for polaritons with only a few, often one, modulation frequency (see Ref. [207] SI. B6). Along with improvements to polaritons lifetimes, these structures may even be rapidly tuned via temporal adjustments to the modulation, raising the prospect of inducing and studying polariton dynamics [269, 270, 320]. Thus, Floquet polaritons are suitable for studying strongly-correlated materials made of photons, including crystals and Laughlin states [67, 116, 269, 270] as well as for quantum information science [314, 321]. More broadly, this Floquet engineering scheme has a variety of other prospective applications, for example the matching of atomic spectra with the spectra of other physical systems for quantum information applications [99] or the tuning of spectra to enable new laser cooling schemes [322].

5.6.4 Comparison to Other Modulation Schemes

In this chapter, we have demonstrated that frequency modulation of the intermediate $5P_{3/2}$ state enables the formation of effectively-degenerate Floquet polaritons in multiple, non-degenerate transverse modes of an optical cavity. Here, we briefly discuss a variety of seemingly plausible alternative schemes which turn out to be either inferior or entirely ineffective for achieving this goal.

The easiest, plausible scheme from a technological standpoint would be to simply frequency modulate the 480 nm field used for Rydberg coupling (using an electro-optic modulator, for example). However, this scheme is ineffective because it only satisfies the two-photon resonance condition for dark polaritons, while leaving a very large single-photon detuning that makes the dark polaritons extremely short-lived.

To see this problem more explicitly, consider the scenario in which, before modulation,

photons in the TEM_{40} mode are resonant with the $5S_{1/2} \rightarrow 5P_{3/2}$ transition and thus also the combination of a TEM_{40} photon and the 480 nm field satisfy the two-photon resonance condition for the $5S_{1/2} \rightarrow nS_{1/2}$ Rydberg transition. In this scenario, the TEM_{00} mode would be detuned by $\Delta = 2\pi \times 50$ MHz from the single photon $5S_{1/2} \rightarrow 5P_{3/2}$ transition, and thus also from the two-photon $5S_{1/2} \rightarrow nS_{1/2}$ Rydberg transition. One could then frequency modulation the 480 nm field at Δ to generate first order sidebands at $\pm\Delta$. The combination of a TEM_{00} photon and a photon from the appropriate sideband would now satisfy the two-photon resonance condition, but the single-photon detuning for that mode remains large (Δ).

A large single-photon detuning causes the dark polaritons to decay rapidly before undergoing any non-trivial dynamics. For example, consider the dynamics of dark polaritons in a trapping potential, which can be created either by having a near-degenerate cavity or by slightly adjusting the Floquet modulation frequency to create a small offset in the polariton quasienergies. The trapping potential inevitably induces both the desired single-polariton dynamics and causes decays of dark polaritons. To study many-body physics with such polaritons, one would like them to undergo as many cycles N_{osc} of oscillation in the trap potential as possible before decaying. In the absence of a single-photon detuning, the number of oscillations scales with the optical depth (which could also be called the collective cooperativity) $OD = \frac{4G^2}{\kappa\Gamma}$ as $N_{osc} = \frac{\sqrt{OD}}{2}$ (see Sec. 2.2.4). The Floquet scheme is only sensible when the high frequency approximation holds ($\Delta/G \gg 1$, see Appx. A.2.11), so the effective collective atom photon coupling G should be greatly reduced due to being far from resonance. This then implies a significant penalty in the optical depth and the number of trap oscillations, so frequency modulation of the 480 nm field is not a useful alternative to modulation of the $5P_{3/2}$ state.

The above discussion emphasizes the importance of a scheme which actually creates overlap between the spectral densities of the $5S_{1/2} \rightarrow 5P_{3/2}$ atomic transition and the desired cavity

mode, which simultaneously creates the appropriate two-photon and single-photon detunings for the dark polaritons. This requirement leaves three possibilities: modulation of the energy of the cavity mode to create sidebands that match the atomic transition, or modulation of either the $5S_{1/2}$ or $5P_{3/2}$ state, which splits the $5S_{1/2} \rightarrow 5P_{3/2}$ transition into bands as discussed in this work.

In principle one could modulate the cavity mode energy by modulating the position of a mirror, but it is technologically prohibitive to shake traditional coated-glass mirrors at the necessary frequencies (50 MHz). One could also consider using an intracavity electro-optic modulator for the same purpose, but these have not yet been shown to have sufficiently low loss to be compatible with high-finesse cavities. Moreover, even if one could properly modulate the cavity modes, another problem is likely to emerge: the Floquet polaritons are no longer protected from undesired couplings due to cavity disorder (see Sec. A.3.5).

In an idealized setting, modulating either of the $5S_{1/2}$ or $5P_{3/2}$ states would be equivalent. However, in reality, the cancellation of the average energy shift of the modulated state is unlikely to be perfectly temporally stable or spatially homogeneous. For modulation of the $5S_{1/2}$ state, both of those errors would directly cause decoherence of the dark polaritons by broadening the two-photon resonance condition; therefore, the performance would be harmed by errors at the scale of our typical effective Rydberg linewidth $\gamma = 2\pi\times$ 200 kHz. When modulating the $5P_{3/2}$ state, only errors at the scale of its linewidth $\Gamma = 2\pi\times$ 6 MHz are relevant, making this scheme approximately 30 times easier to implement technically, under our present conditions. Furthermore, as the rest of our apparatus continues to improve and our Rydberg coherence times get longer, the homogeneity and temporal stability requirements for modulating the $5S_{1/2}$ would become even stricter, while the requirements for modulating the $5P_{3/2}$ remain the same. Therefore, among the schemes we have thus far considered for creating Floquet polaritons, modulation of the $5P_{3/2}$ is the most effective and easiest to achieve technologically.

5.7 Methods

Our experiments begin with a magneto-optical trap (MOT) of 10^7 ^{87}Rb atoms which is polarization-gradient-cooled to a temperature of 15 μK, and loaded into a 1D (vertical) optical conveyor belt (with waist 85 μm). It is then transported 32.1 mm in 13 ms into a four-mirror optical resonator, by detuning one of the lattice beams by up to 5 MHz, with a maximum acceleration of $\sim 1000\text{m/s}^2$. This cavity is non-degenerate with a free spectral range of 2204.6 MHz and a transverse mode spacing along the vertical axis of 564.05 MHz; as such, there is a TEM_{40} mode 4.05 MHz -2204.6 MHz $= 51.6$ MHz higher than the fundamental mode. Each cavity transverse mode contains a pair or nearly degenerate orthogonal polarization modes, which are nearly linear. We use only the modes which are approximately horizontally polarized. The resonator has a TEM_{00} waist size of $12\mu\text{m}\times14\mu\text{m}$, located at the position of the atomic sample, and a finesse of $\mathcal{F} = 1480(50)$ at 780nm, together yielding a total atom-cavity coupling strength of $g = 8 - 19$ MHz on the Rb D2 line for each cavity mode (see Appx. A.2.1). Individually, this corresponds to a maximal single-atom cooperativity on the cavity axis of $\eta = 0.26$ [126], a resonator linewidth $\kappa = 2\pi \times 1.6$ MHz, and single-atom single-quantum Rabi frequency $g = 0.78$ MHz on the $|F = 2, m_F = 2\rangle \rightarrow |3', 3\rangle$ transition of the ^{87}Rb D2 line, on the resonator axis, for a circularly-polarized TEM_{00} running-wave mode. The total optical depth per blockade volume after the slicing process (see Sec. 5.7.1) is $OD_B = N_{atom}\eta = 13$. Although the cavity mode is linearly polarized, using the maximal Clebsch-Gordan coefficient provides a well-defined notion of effective atom number.

After transport, a sample of 300-1800 atoms arrive in the region spanned by the TEM_{40} mode of the optical cavity. This atomic cloud has dimensions $35\mu\text{m}\times41\mu\text{m}\times37\mu\text{m}$, at a density of $1.1 \times 10^{11}\text{cm}^{-3}$; to realize a strongly interacting 0-D quantum dot, the sample must be smaller than the blockade radius of in the 100S Rydberg state [99]. The optical resonator waist defines a $\frac{1}{e^2}$ sample of radius $\sim 13\mu$m along two axes; unlike free-space

experiments [85], our 0-D resonator-defined dot must be smaller than a blockade radius even along the resonator axis in order to enter the strongly interacting regime. To achieve this longitudinal confinement, we employ super-resolution slicing: the atoms are locally repumped into the $|F = 2\rangle$ hyperfine state (which couples strongly to the resonator mode) with a beam whose waist is 81 μm, and then depumped with a $\sim$ TEM$_{10}$ beam whose line-node is located within the atomic cloud, leaving a sample with RMS length $\approx 10\mu$m (see below). Extra attenuation using a double pass acousto-optic modulator (AOM) is required to avoid creating shelved Rydberg atoms during the slicing process (see Appx. A.2.6). Since we are only weakly driving the cavity, the Rydberg blockade radius follows [99]

$$r_B = \left(\frac{C_6}{\gamma_R}\right)^{1/6} \tag{5.2}$$

where the effective Rydberg-Rydberg interaction potential $V(r) = C_6/r^6$ becomes equal to the Rydberg decay rate $\gamma_R \approx h \times 200$ kHz. For the 39S Rydberg state the coefficient $C_6^{39} = h \times 730$ MHz$\cdot\mu$m^6 corresponds to a radius of only $R_B^{39} = 4$ μm, whereas the much more strongly interacting 100S Rydberg state has coefficient $C_6^{100} = h \times 56$ GHz$\cdot\mu$m^6 for a blockade radius of $R_B^{100} = 25$ μm. Note that this difference in blockade radius corresponds to a blockade *volume* which is 240 times smaller for the weakly interacting state.

The enormous DC electric polarizability of the 100S Rydberg state, $\alpha \sim 6$ GHz/(V/cm)^2, makes it very easy for small electric field drifts or inhomogeneities to decohere the collective Rydberg states. A detailed theoretical treatment of this effect in the context of our system can be found in Ref. [161]. We have taken care to design our cavity and its mounting structure to keep all surfaces as far away from the atoms as possible (the closest surface is 12 mm away), so that any patch potentials or dipoles that build up due to Rb adsorbates have minimal effect on the atoms. Moreover, we use active electric field control with eight intracavity electrodes in order to zero the electric field at the location of the atoms, maximizing the Rydberg coherence time. Our effective Rydberg decay rate of $\gamma_R \approx 2\pi \times 200$ kHz at 100S is

not presently limited by the background electric field. For more detail on our experimental efforts to control the electric field, please see section A.2.1.

Two single photon counter modules are used to detect the photons leaking out of the cavity. There are two narrow line filters in a sandwich setup to block the fluorescence/parametric down-conversion 780nm photons (see Appx. A.2.2) in order to reduce the background count rate. To capture photon arrival times for correlation experiments, we employ a home-built 8-channel photon time-tagger with 8 ns resolution on each channel, based upon an Opal Kelly XEM6001 field-programmable gate array. A similar device is employed to store histogram data for ring-down and spectroscopy experiments.

5.7.1 Atom Slicing

The atom cloud that is moved into the cavity has dimensions of $35 \times 41 \times 35$ μm^3 which are much larger than the Rydberg blockade radius. The small cavity waist defines a small sample along the directions transverse to the resonator axis, but the cloud is still extended longitudinally. To reduce the longitudinal extent of the cloud we "slice" the cloud as described in section 3.6.1.

The size of the cloud depends on the power of the TEM_{10} beam and the depumping time. In figure 5.4a, we change the size of the cloud by reducing the slicing power, and the weaker suppression in g_2 shows that we have a good control of the cloud size. The fluctuation of the atom number and cloud size is mainly caused by laser power drifting and random net polarization of the atomic sample due to the lack of optical pumping. However, these small changes do not affect the blockade of transport since the cloud size is always smaller than the blockade radius during the data acquisition time. The drifting of atom number and cloud size after slicing is also very small from day-to-day running, and only small realignment is needed to maintain performance. A good agreement of the rotation angle and interaction

strength (U) between the transport blockade and ring-up/down data (which was taken over two months later) indicates a stable slicing process.

5.7.2 Frequency Modulation Setup

The goal of our frequency modulation setup is to sinusoidally vary the energy E_p of the $5P_{3/2}$ state. We achieve this goal using a multichromatic field near the $5P_{3/2} \rightarrow 5D_{5/2}$ transition at 776 nm as explained in section 3.7.

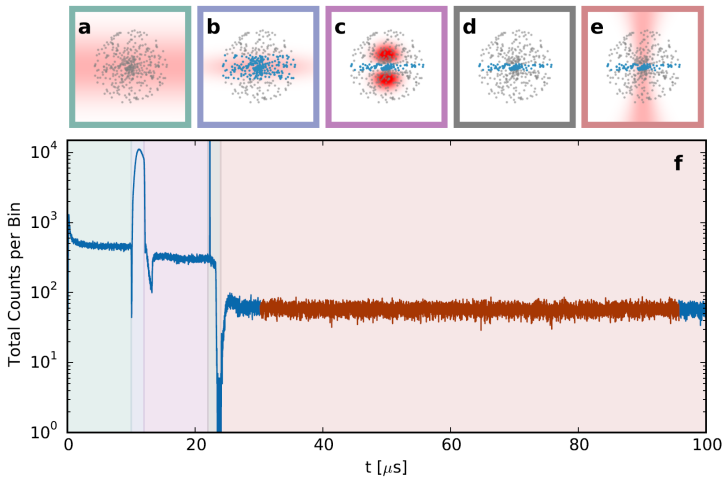

Figure 5.11: **Slice-probe sequence beam setup and histogram of single photon events for the g_2 measurement. (a-e)** shows the beam setup and the atomic state of one slice-probe cycle, reproducing the sequence shown in figure 3.18. The atoms color coded with blue are in the $|F = 2\rangle$ ground state, and those in gray are depumped to $|F = 1\rangle$ ground state. The histogram of photons detected by the single photon counter is shown in **f**. The events colored in red are used to obtain the time correlation shown in Fig. 5.4. To obtain the ring down measurement, we turn on and off the probe beam 8 times during the probe stage (red background). The histogram for the modulated probe is shown in Fig. A.2.6. Figure taken from Ref. [153].

Throughout this chapter, we report modulation amplitudes in units of the arbitrarily defined η_0, which is defined as the peak energy E_p of the $5P_{3/2}$ state in each modulation cycle for a total 776 nm beam intensity of approximately 5 W/mm^2. Based on the fit result of figure 5.6e, detailed in the next section, we estimate that $\eta_0 = h \times 17(1)$ MHz.

Note that the three sets of experiments reported in the second half of this chapter each employ a slightly different modulation frequency. In figure 5.6 we use a frequency of $f = 53$ MHz, for figure 5.9 $f = 58$ MHz, and for figure 5.10 $f = 54$ MHz. Each of these frequencies is close to the bare cavity mode spacing of 52 MHz between the TEM_{00} and TEM_{40} modes,

but differs slightly to compensate for the shifts which come from coupling to off-resonant bands, see appendix A.2.11.

CHAPTER 6

FRACTIONAL QUANTUM HALL PHYSICS WITH PHOTONS

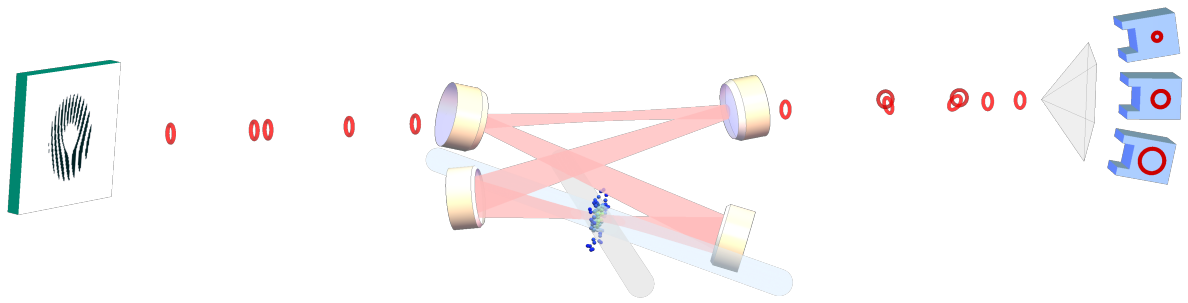

Figure 6.1: **A visualization of our experiment** shows the atom-cavity system filtering two photon states into Laughlin states, represented here as topologically linked photons.

In this chapter, we combine the ingredients previously developed and presented—strong interactions between photons and a synthetic magnetic field for photons—to create a fractional quantum Hall system for photons. A new near-degenerate non-planar experimental cavity is crossed with a non-planar buildup cavity for the control field, and these together support interacting Rydberg polaritons in multiple modes of a Landau level. Elastic and angular momentum conserving collisions between photons induce multi-photon states to develop quantum correlations. The real-space repulsive interactions between polaritons drive real-space anti-bunching, this corresponds to the formation of a particular superposition of two-photon angular momentum states. Observing both of these effects puts strong constraints on the state of the system, indicating the production of two-photon Laughlin states. As the cavity is continuously driven and continuously dissipates, we understand the role of the atom-cavity system as a 'Laughlin state filter' which lets a single photon transmit normally and projects a two photon state onto the Laughlin state. We conclude with a brief

outlook on the route towards larger fractional quantum Hall states and the observation of the hallmarks of long-range topological order including the braiding statistics of anyons.

This chapter is based off of Ref. [121]

> Logan Clark, Nathan Schine, Claire Baum, Ningyuan Jia, and Jonathan Simon. Observation of Laughlin states made of light. *arXiv preprint* (2019).

The simplest recipe for realizing topologically ordered many-body states is to place strongly-interacting particles in an effective magnetic field. The magnetic field quenches the kinetic energy of the particles, so that they order themselves solely to minimize their interaction energy, forming intricate patterns of long-range entanglement [13]. These states exhibit fascinating properties largely unseen in other forms of matter; for example, in addition to the robust quantized edge transport which also appears in weakly-interacting systems [323], topologically ordered phases can host excitations with fractional charge and anyonic exchange statistics [324]. More exotic phases can even host non-Abelian anyons, a promising constituent for fault-tolerant quantum computers thanks to their insensitivity to local perturbations [14].

Few experimental systems have been found to host topologically ordered states. All definitive observations of such order have been made in two-dimensional electron gases subjected to magnetic fields, originally in semiconductor heterojunctions [10], as well as more recently in graphene [54, 325, 326] and van der Waals bilayers [25].

The scarcity of physical platforms hosting topological order has spurred great interest in elucidating its exotic properties using the wide tunability, particle-resolved control, and versatile detection capabilities afforded by synthetic quantum matter [67, 74, 217, 327]. The constituents of typical synthetic matter are atoms and photons, which do not experience a Lorentz force in ordinary magnetic fields because they are charge neutral. Therefore, the key

challenge is to implement a synthetic magnetic field which creates an effective Lorentz force and is compatible with strong interactions between particles. A classic approach employed the Coriolis force in rotating ultracold atomic gases [61], and such systems approached the few-body fractional quantum Hall regime [65]. More recent efforts in ultracold atoms focused on Floquet engineering of synthetic magnetic fields [298] combined with strong atomic interactions thanks to tight confinement in an optical lattice [66]. Furthermore, coupling atomic gases with multiple modes of optical resonators provides exciting opportunities for studying many-body physics [210, 281, 328–331]. Photonic systems have also demonstrated a variety of synthetic magnetic fields [67] compatible with strong interactions via coupling to superconducting qubits in the microwave domain [248, 332] and cold atoms [84, 85, 153, 285] or quantum dots [333] in the optical domain. Because these ingredients have yet to be effectively combined and scaled, the formation of topologically ordered synthetic matter has remained elusive. Here, we use a multimode optical cavity to generate a synthetic gauge field for light [67, 182, 208, 224, 225, 251]. Making photons interact strongly in this cavity enables us to study strongly correlated fractional quantum Hall states of light [107, 108, 110, 113, 117–119, 213].

6.1 Combining Ingredients

In this chapter, we describe the formation of optical photon pairs in a Laughlin state. To this end, we construct a photonic system analogous to an electronic fractional quantum Hall fluid by combining two key ingredients: a synthetic magnetic field for light induced by a twisted optical cavity [182] and strong photonic interactions mediated by Rydberg atoms [153]. We first observe that photons in this system undergo collisions which satisfy conservation laws and have density-dependence characteristic of two-body processes. A closer examination of the resulting two-body correlations reveals a two-photon angular momentum distribution consistent with a Laughlin state. Moreover, characterizing these photon pairs in real space

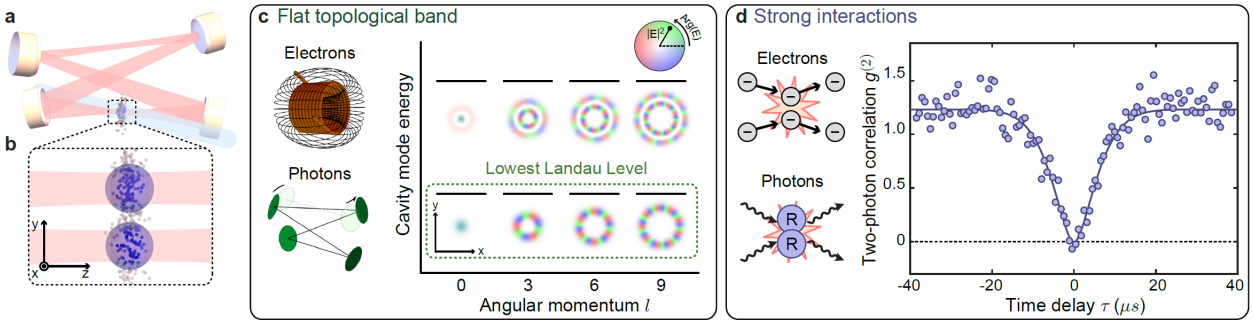

Figure 6.2: **Combining two key ingredients for topologically ordered light. a,** Our experiment couples optical photons (red) with a gas of Rubidium atoms at the waist of a twisted, four mirror optical cavity. **b,** This coupling turns each photon entering the cavity into a *polariton*, a quasiparticle combining the photon with a collective Rydberg excitation of the atomic gas. Polaritons can move around in the transverse modes available to their photonic component, and a pair of polaritons (depicted) strongly interacts because of their Rydberg components (blue spheres). **c,** Two key ingredients enable this system to explore topological order. First, we form a flat topological band of single-photon states using a twisted optical cavity, which hosts a set of degenerate photonic modes that are equivalent to the states in the lowest Landau level available to electrons in a strong magnetic field. **d,** Second, the strong polaritonic interactions are analogous to the Coulomb interactions between electrons in a traditional fractional quantum Hall system. Polaritons confined to a single cavity mode reveal their strong interactions via transport blockade, in which a single polariton present in the cavity prevents a second photon from entering. Blockade results in antibunched correlations of photons exiting the cavity, shown here for $l = 0$. Figure taken from Ref. [121].

reveals that they strongly avoid being in the same location. Together, these results indicate the formation of photon pairs with 76(18)% overlap with a pure Laughlin state.

Our typical experiment begins by loading a gas of 6000(1000) laser-cooled Rubidium-87 atoms at the waist of an optical cavity (Fig. 6.2a; Methods 6.4.1). We then continuously shine a weak probe laser beam on the cavity for 100 ms. The initially uncorrelated photons from the probe laser which enter the cavity are strongly coupled to a resonant atomic transition; in the presence of an additional Rydberg coupling field the photons are converted into polaritons, quasi-particles consisting of a superposition between a photon and a collective Rydberg excitation of the atomic gas (Fig. 6.2b) [85, 153]. Photons emerge on the other side of the cavity in a state which is highly correlated in both real space and angular momentum space, whose structure reflects the steady state formed by the intracavity polaritons.

6.1.1 Photons Become Polaritons

This section and the one immediately following provide a quick technical introduction to the synthetic photonic material platform used in this chapter to explore fractional quantum Hall physics. While these sections describe techniques central to the experimental effort, the credulous reader may skip directly to section 6.1.3.

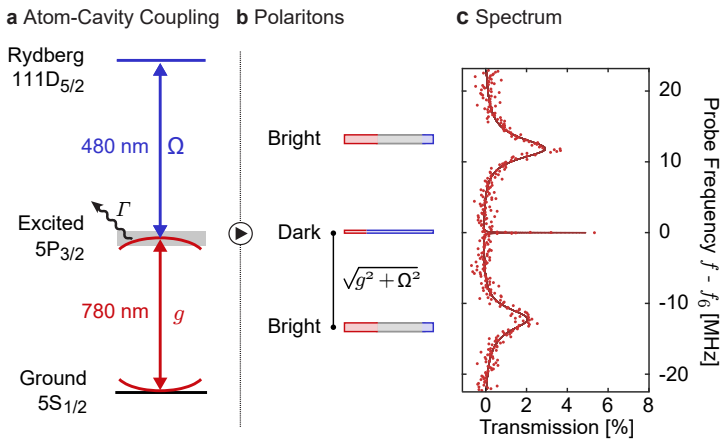

Figure 6.3: **Polariton Spectrum. (a)** Photons at the waist of our optical cavity (red) couple with strength g to the $5S_{1/2} \rightarrow 5P_{3/2}$ transition of a gas of ultracold Rubidium atoms, which is subsequently coupled with strength Ω to the highly excited $111D_{5/2}$ Rydberg state using an additional laser (blue). **(b)**These couplings cause excitations of the atom-cavity system to propagate as polaritons, quasiparticles combining photons with collective atomic excitations. **(c)** The transmission spectrum of the cavity with atoms present directly reveals the narrow dark polariton flanked by two broad bright polariton peaks. Figure taken from Ref. [121].

In our system photonic interactions are mediated by Rydberg atoms in a scheme called cavity Rydberg electromagnetically induced transparency [85, 153, 155, 156]. First, we couple cavity photons with the $5S_{1/2} \rightarrow 5P_{3/2}$ transition of the gas of Rubidium atoms at the waist of our primary cavity, which we name the "science" cavity, with coupling strength g (Fig. 6.3a). The $5P_{3/2}$ state is subsequently coupled to a highly excited Rydberg level ($111D_{5/2}$) by an additional 480 nm field with coupling strength Ω. As detailed below and in appendix A.3.2, we use a buildup cavity crossed with the science cavity in order to achieve sufficient intensity of that Rydberg coupling field.

As a result of these couplings, photons no longer propagate in the cavity on their own. Instead each cavity mode hosts three kinds of polaritons – quasiparticles comprised of hybrids between a photon and a collective excitation of the atomic gas [158] (Fig. 6.3b). The nature of these collective excitations is detailed in appendix A.3.3. The two "bright" polaritons are largely comprised of a photon and a collective $5P_{3/2}$ excitation; we do not utilize bright polaritons in this work because they are short lived due to rapid decay of the $5P_{3/2}$ state

at $\Gamma = 2\pi \times 6$ MHz. We utilize dark polaritons throughout the main text of this work. Dark polaritons are purely a superposition of a cavity photon and a collective Rydberg excitation. Because they do not have any $5P_{3/2}$ component, they are long-lived. Moreover, dark polaritons inherit strong interactions from their large collective Rydberg component [99, 153].

A typical scan of the polariton features corresponding to a single cavity mode is shown in Fig. 6.3c. That spectrum, taken with the $l = 6$ cavity mode, directly reveals the narrow dark polariton excitation at frequency f_6 with a linewidth of 60 kHz, flanked by the two bright polariton resonances which are $\pm\sqrt{g^2 + \Omega^2}$ separated in frequency and have linewidths of about 3.7 MHz. For the displayed data, the coupling strengths are $g = 2\pi \times 13$ MHz and $\Omega = 2\pi \times 1.3$ MHz and the effective Rydberg state linewidth (including decoherence effects) is $\Gamma_R = 2\pi \times 50$ kHz.

6.1.2 Floquet Polaritons

This section explains our scheme for forming the Landau level with Floquet polaritons, which provides a number of crucial features that made this work possible. Most importantly, Floquet polaritons helped us mitigate the effects of intracavity aberrations. As detailed in appendix A.3.2, aberrations prevented us from making the bare cavity modes with angular momenta $l = 3$, 6, & 9 degenerate. At the cavity length which would otherwise make them degenerate, aberrations mix the modes together, splitting them apart in energy and causing them to decay rapidly. Thankfully, Floquet polaritons are protected from the broadening caused by intracavity aberrations, as detailed in appendix A.3.5. The Floquet scheme also provides the ability to efficiently measure angular correlation functions as detailed in section 6.4.3.2 and enables frequency discrimination to improve the selectivity of our angular momentum sorters discussed in section 6.4.2.

The essence of our Floquet scheme is depicted in Fig. 6.4 and detailed in Ref. [207]. Briefly, a sinusoidal modulation of the energy of the intermediate $5P_{3/2}$ state splits it into three bands which exist at energies separated by the modulation frequency f_{mod}. Cavity photons can excite the atom through any of these bands, thereby enabling the atoms to couple with modes whose energies are also split by f_{mod}. In the previous chapter, we used 776 nm light near the $5P_{3/2} \rightarrow 5D_{5/2}$ transition. For this work, we upgraded this system to use 1529 nm light near the $5P_{3/2} \rightarrow 4D_{5/2}$ transition, which allows using 40 times less laser intensity for the same modulation strength while also reducing undesired ground state modulation by nearly a factor of 100.

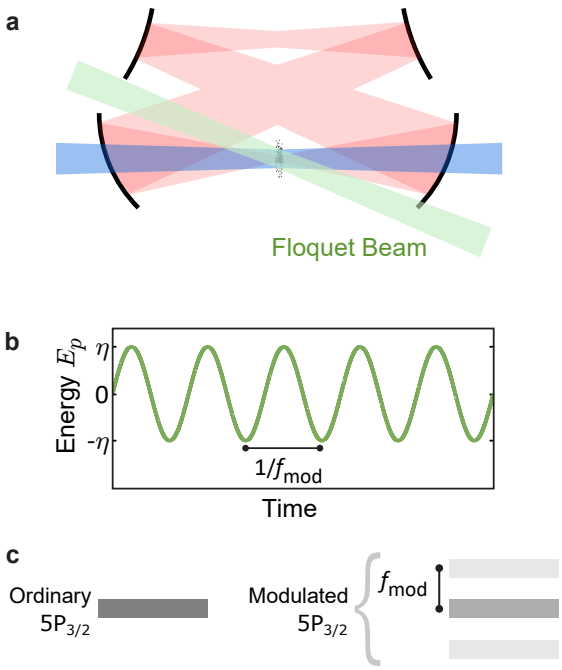

Figure 6.4: **Essential features of the Floquet scheme. (a)** Our Floquet scheme utilizes an additional laser beam (green) incident upon the atoms with a wavelength of $\lambda = 1529$ nm close to the $5P_{3/2} \rightarrow 4D$ transition. **(b)** This beam induces a sinusoidally modulated AC Stark shift $E_p = \eta \sin(2\pi f_{\mathrm{mod}} t)$ of the $5P_{3/2}$ state with amplitude η and frequency f_{mod}. **(c)** As a result of this modulation, the ordinary $5P_{3/2}$ state is split into three bands with energies separated by the modulation frequency. The additional bands enable the atoms to couple with cavity photons at frequencies shifted by $\pm f_{\mathrm{mod}}$ from the ordinary $5S_{1/2} \rightarrow 5P_{3/2}$ resonance frequency. For more details on the Floquet scheme see Ref. [207]. Figure taken from Ref. [121].

To implement the Floquet scheme, we first used temperature and piezo tuning to increase the length of the science cavity and induce a splitting of $f_{\mathrm{cav}} \approx$ 70 MHz between every third angular momentum mode (Fig. 6.5a). Then, to enable the $l = 3$, 6, & 9 modes to simultaneously support dark polaritons, we fine-tuned the cavity length to make the $l = 6$ mode degenerate with the bare $5S_{1/2} \rightarrow 5P_{3/2}$ transition and modulated the intermediate state at $f_{\mathrm{mod}} \approx$ 70 MHz to create sidebands resonant with the $l = 3$ & 9 states (Fig. 6.5b). By making it possible for the atoms to strongly couple with each of the cavity modes, the

Floquet scheme enables all three modes to host polaritons (Fig. 6.5c). Note that the splitting f_{cav}, and therefore the required modulation frequency f_{mod}, varied over a couple of MHz from day to day due to variation in the cavity temperature.

Cavity spectroscopy reveals the polariton eigenmodes in all three modes simultaneously (Fig. 6.6a). Because the cavity modes are separated by $f_{\mathrm{cav}} \approx 70$ MHz, the photonic components of the polaritons also remain separated by approximately f_{cav}. Therefore, to spectroscopically characterize the set of polaritons for mode l, we scan the probe frequency near the frequency f_l of that mode and simultaneously use a digital micromirror device to spatially mode match the probe laser with the cavity mode [205], producing the spectra shown in Fig. 6.6a. The asymmetric heights and frequency splittings of the bright polaritons relative to the dark polariton for $l = 3$ & 9 are caused by shifts due to coupling with off-resonant bands of the $5P_{3/2}$ state. Moreover, the smaller splitting of the bright polaritons with $l = 3$ & 9 (the "sideband" modes) relative to $l = 6$ (the "carrier" mode) results from smaller atom-cavity couplings $g_3 \approx g_9 = 0.35\, g_6$ on those modes relative to the central mode. The relative strengths of these couplings are determined by the modulation amplitude; here, we chose to make the sideband couplings weaker in order to make the corresponding dark polaritons more photon-like, see Methods. A.3.4 for details.

While the spectroscopic features are all clearly separated in the scan of the probe frequency f, the dark polaritons can be tuned to have equal quasi-frequency $\tilde{f}$, where $\tilde{f} = (f \mod f_{\mathrm{mod}})$ is the probe frequency modulo the modulation frequency. In a Floquet model the energy is only defined up to multiples of the modulation energy; thus, two states with the same quasi-energy (equivalently, quasi-frequency) behave as if they are degenerate [298]. In the example shown in Fig. 6.6a, the dark polaritons are separated in probe frequency by an amount equal to the modulation frequency $f_{\mathrm{mod}} = 73.3$ MHz; thus, their quasi-frequencies are identical.

It is not trivial to find conditions at which the quasi-frequencies of the dark polaritons are

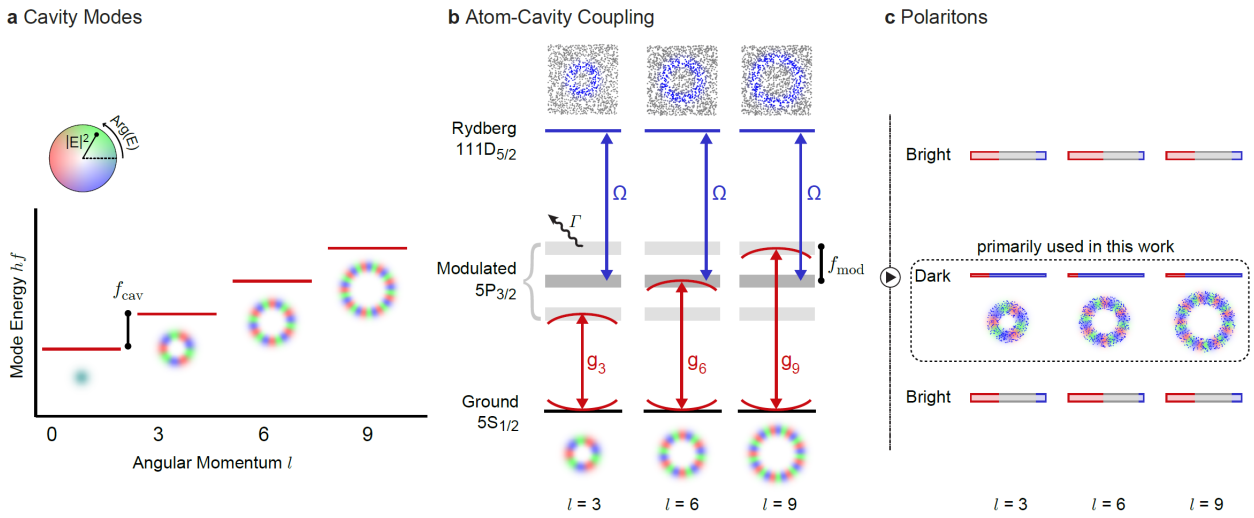

Figure 6.5: **Scheme for forming Landau level of Floquet polaritons.** **(a)** For the work described in this chapter the bare cavity modes are not degenerate, but instead the length of the cavity is increased so that there is a $f_{\mathrm{cav}} \approx 70$ MHz splitting between every third angular momentum mode. **(b)** In order to form polaritons in three modes, even though only the $l = 6$ mode is resonant with the un-modulated $5S_{1/2} \rightarrow 5P_{3/2}$ transition, we utilize the Floquet scheme depicted in Fig. 6.4 [207]. Modulating the $5P_{3/2}$ state at $f_{\mathrm{mod}} \approx 70$ MHz splits it into three bands (gray), each of which is resonant with one of the three chosen cavity modes. The coupling strengths g_l to each mode l are controlled by the modulation amplitude; in this work, $g_3 = g_9 = 0.37(4)g_6$. Note that each mode couples to a unique collective atomic excitation, as depicted at the top (blue atoms are included in the corresponding collective excitation, while gray atoms are not). (c) This scheme produces polaritons in the $l = 3,\ 6,\ \&\ 9$ modes. The dark polaritons can be made effectively degenerate (see Fig. 6.6) without making the corresponding cavity modes degenerate, which protects the polaritons from intracavity aberrations (see Appx. A.3.5). Figure taken from Ref. [121].

equal. The primary challenges are the anharmonicity in the cavity mode spectrum and the off-resonant shifts caused by weak couplings to non-resonant Floquet bands. These effects typically prevent the dark polariton energies from matching under conditions which might naively seem suitable; in particular, when $f_{\mathrm{cav}} = f_{\mathrm{mod}}$, the quasi-frequency $\tilde{f}_9$ ($\tilde{f}_3$) of dark polaritons with $l = 9$ ($l = 3$) will typically be too large (small) due to the off-resonant shifts [207].

The dark polariton quasi-frequency $\tilde{f}_l = \tilde{\delta}_c^l \cos^2\theta_l + \tilde{\delta}_r \sin^2\theta_l$ in each mode is a weighted average of the cavity mode quasi-frequency $\tilde{\delta}_c^l$ with the Rydberg quasi-frequency $\tilde{\delta}_r$; the weight is determined by the dark-state rotation angle θ_l, which satisfies $\tan\theta_l \equiv g_l/\Omega$ (see SI. B5 in Ref. [207]). A smaller ratio g_l/Ω increases the contribution from the cavity photon and thus makes the polariton more "photon-like"; in the opposite case, the polariton is more

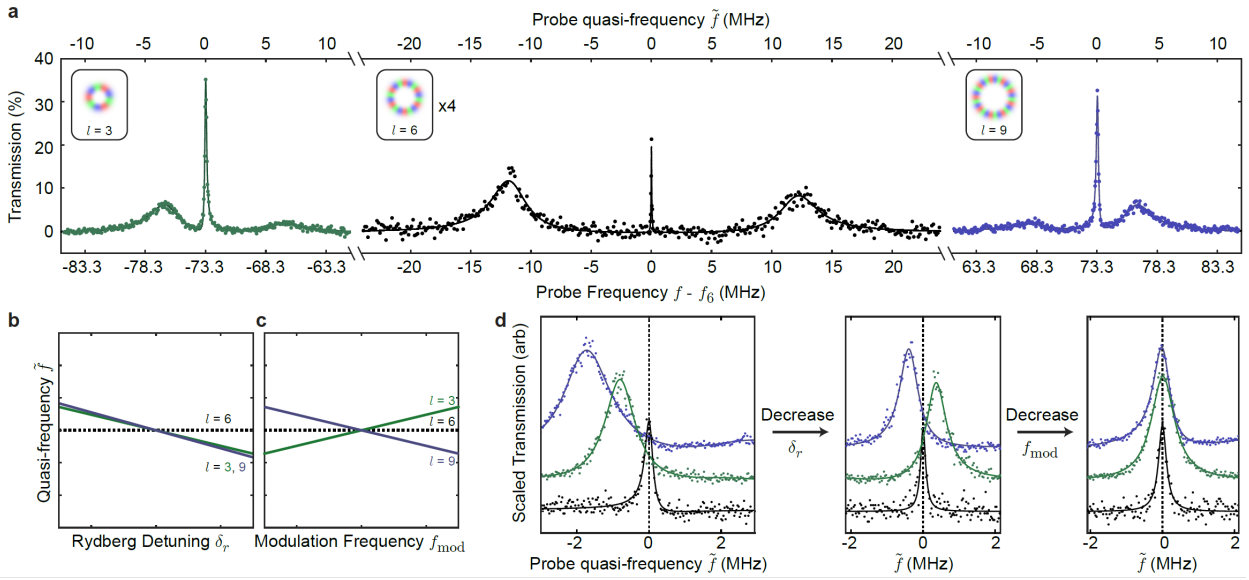

Figure 6.6: **Understanding and controlling polariton spectra with the Floquet scheme. (a)** Cavity transmission spectrum in the presence of the modulated atoms (see Fig. 6.5). The spectrum was collected in three parts, corresponding to injection of photons into $l = 3$ (left, green), $l = 6$ (middle, black), and $l = 9$ (right, violet). The transmission of $l = 6$ is multiplied by four to improve visibility. The lower x-axis indicates the frequency f of the probe laser relative to the $l = 6$ dark polariton resonance at f_6. The top x-axis indicates the quasi-frequency $\tilde{f}$, proportional to the quasi-energy of the polaritons from a treatment using Floquet theory; $\tilde{f}$ is equal to f modulo the modulation frequency f_{mod}. **(b,c)** Illustration of the theoretical dependence of the quasi-frequencies of the three dark polariton features on the Rydberg beam detuning (panel **b**) and the modulation frequency f_{mod} (panel **c**). **(d)** Example transmission spectra for the $l = 6$ (black, lower), $l = 3$ (green, middle), and $l = 9$ (violet, upper) dark polaritons as a function of quasi-frequency. The scans are scaled to make their heights equal and have additional vertical offsets for clarity. Shortly before performing each of the experiments reported in the main text, we collect a sequence of plots similar to those displayed here and adjust the Rydberg detuning and modulation frequency to make all three dark polaritons have the same quasi-frequency (right-most plot). The only experiments reported in the main text which did not use this sequence are those shown in Fig. 2b, where instead we varied δ_r to intentionally vary the energy mismatch between the polaritons. Figure taken from Ref. [121].

"Rydberg-like" [158].

We adjust the Rydberg quasi-frequency $\tilde{\delta}_r$ and the modulation frequency f_{mod} in order to tune the dark polaritons into degeneracy. The Rydberg quasi-frequency is controlled by the frequency of the Rydberg coupling laser. Because the $l = 6$ polaritons are more Rydberg-like than the $l = 3$ & 9 polaritons, their quasi-frequency increases more rapidly with $\tilde{\delta}_r$, leading to the dependence illustrated in Fig. 6.6b. Note that, in Fig. 2b of the main text, we varied the Rydberg quasi-frequency $\tilde{\delta}_r$ in order to scan the energy mismatch. Adjusting the modulation frequency f_{mod} shifts the cavity mode quasi-frequencies $\tilde{\delta}_c^3$ and $\tilde{\delta}_c^9$ oppositely,

because they couple to the atoms through opposite modulation sidebands of the $5P_{3/2}$ state (Fig. 6.5c).

These two adjustment parameters are sufficient to tune the three dark polariton features into degeneracy, as demonstrated in Fig. 6.6d. In practice, to reach degeneracy we repeatedly measure the quasi-frequency spectrum of the dark polaritons while adjusting parameters. We modify the frequency of the Rydberg laser until the average of the sideband quasi-frequencies matches the carrier, i.e. $(\tilde{f}_3 + \tilde{f}_6)/2 = \tilde{f}_6$. Similarly, we vary f_{mod} until $\tilde{f}_3 = \tilde{f}_9$. In the end, we are able to satisfy these conditions to an accuracy well within the linewidths of the dark polaritons.

6.1.3 Polaritons in the Lowest Landau Level

Key properties of the polaritons, inherited from both their photonic and Rydberg components, make them behave like particles in a fractional quantum Hall system. First, the motion of individual polaritons is determined by the cavity modes accessible to their photonic part [181]. The large energy spacing between longitudinal mode manifolds restricts the polaritons to a single manifold, confining them to undergo two-dimensional motion among the transverse modes. We utilize a twisted optical cavity whose transverse mode spectrum forms sets of degenerate orbital angular momentum states that are equivalent to the Landau levels accessible to electrons in a magnetic field [182] (Fig. 6.2c). Thus, we create a synthetic magnetic field for polaritons, realizing the first key ingredient of topological order.

To form ordered states, polaritons must also interact with one another (Fig. 6.2d). Polaritons in our system inherit the strong interactions of their Rydberg components [99], causing them to avoid each other. When confined to a single transverse mode, polaritons can only avoid each other by exhibiting blockade, wherein the presence of a single polariton in the cavity prevents a second polariton from entering [153]. Effects like blockade can be characterized

via the two-photon correlation function $g^{(2)}(\tau)$, which quantifies the likelihood of seeing two photons emerge from the cavity separated by a time τ relative to completely uncorrelated photons (Methods 6.4.3). Blockade manifests strikingly through antibunching; the same-time correlation $g^{(2)}(0)$ falls to zero because there are never two polaritons present in the cavity at the same time.

When polaritons have access to multiple transverse modes, in our case in the lowest Landau level, new physics emerges: it becomes possible for two polaritons to enter in the cavity at the same time while still avoiding one another. In this case, interactions do not always lead to blockade, but can instead drive collisions between polaritons which cause them to move among the states of the Landau level. To test for these collisions, we provide the polaritons access to exactly three states in the lowest Landau level– those with orbital angular momentum $l = 3, 6$, and 9– using a Floquet scheme [207] (section 6.1.2). Next, utilizing a digital micromirror device for wavefront shaping, we shine a laser on the cavity which only injects photons with angular momentum $l = 6$. After the photons have interacted with one another as polaritons in the cavity, they emerge from the other side, where we sort them and count how many emerge in each angular momentum state (Fig. 6.7a).

6.2 Photons Collide

Despite the exotic nature of these quasiparticles, we find that polaritons undergo collisions much like ordinary particles. In particular, collisions between polaritons must conserve the total energy, as well as angular momentum thanks to the rotational symmetry of the system. Therefore, when we inject photons into the cavity with angular momentum $l = 6$ (as we will do throughout this chapter), the only collision process which conserves angular momentum converts two input polaritons with $l = 6$ into one output polariton with $l = 3$ and another with $l = 9$. Similarly, as we tune the relative energy between the different angular momentum

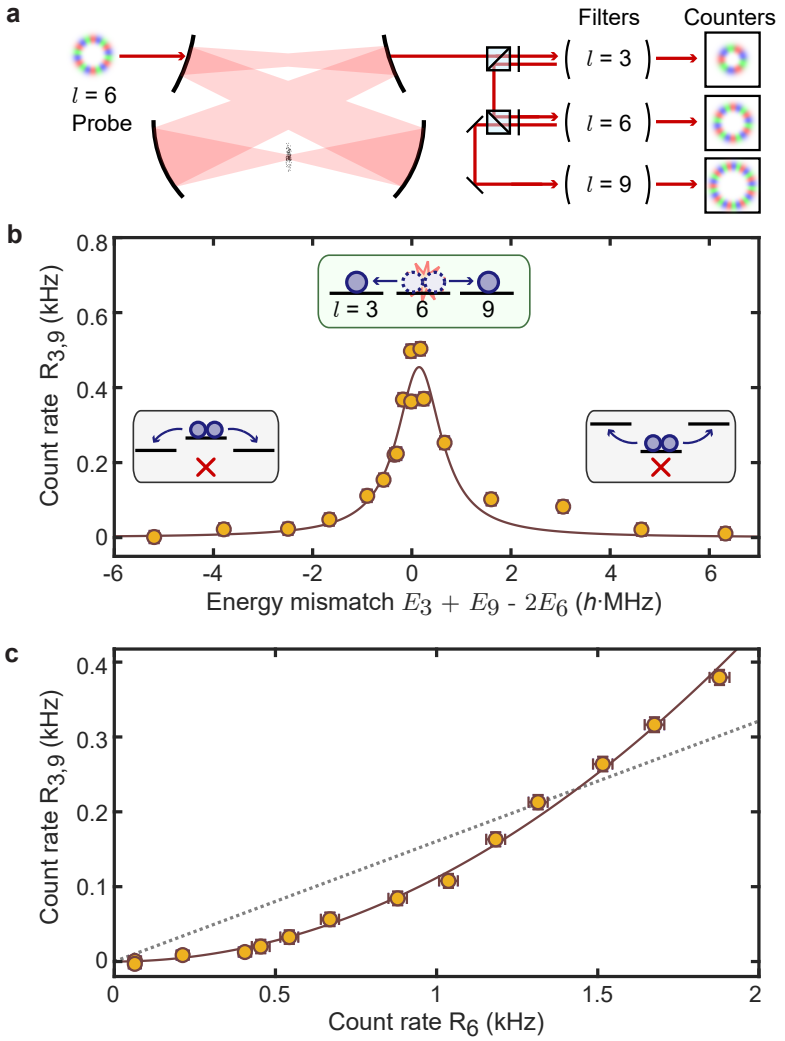

Figure 6.7: **Collisions between polaritons in a Landau level. (a)** To test for mode-changing collisions between polaritons, we inject photons with orbital angular momentum $l = 6$ and then count the photons which emerge from the cavity in each angular momentum state (Methods 6.4.2). **(b)** The total rate $R_{3,9}$ at which photons emerge from the cavity with angular momenta $l = 3$ & 9 exhibits a peak when the collision process depicted in the insets conserves energy; E_l is the energy of a polariton with angular momentum l. The data are well fit by a lorentzian peak (solid curve). **(c)** When all three states are degenerate and we vary the power of the probe laser, the count rate $R_{3,9}$ grows quadratically (solid curve) rather than linearly (dotted line) with the count rate R_6 of $l = 6$ photons, consistent with the production of $l = 3$ & 9 polaritons in collisions between two $l = 6$ polaritons. All error bars indicate standard error. Figure taken from Ref. [121].

states, we only observe photons emerging with $l = 3$ or 9 when the aforementioned collision process can conserve energy (Fig. 6.7b).

Multiple particles must encounter one another in order to collide. This requirement generically manifests in a collision rate which is nonlinear in the density of particles present in the system, much like reaction rates in chemistry. Indeed, we find that increasing the probe beam power raises the density of polaritons and thereby makes them more likely to collide (Fig. 6.7c). The rate at which collision products appear $R_{3,9} \propto R_6^2$ is quadratic in the rate R_6 at which photons emerge in the initial angular momentum state. Since the cavity never contains more than two polaritons, this behavior signals that collisions only occur when precisely two polaritons are present.

6.3 A Laughlin State of Photons

Ordered states emerge as a result of these collisions between polaritons. To better understand the ordered states accessible to polaritons in our system, we consider the energy spectrum of zero, one, and two polariton states in Fig. 6.8a & b. We focus on the case in which all of the single-polariton states $|l\rangle$ are degenerate with energy E_{pol}. When only a single cavity mode, for instance $l = 6$, is accessible, the interactions between polaritons cause the state $|66\rangle$ with two polaritons in that mode to have a shifted energy and a much shorter lifetime than it would without interactions. Thus, a probe laser which resonantly excites $|6\rangle$ from the vacuum state $|vac\rangle$ does not subsequently excite the $|6\rangle \rightarrow |66\rangle$ transition, leading to blockade like that shown in Fig. 6.2f. Such blockade precludes the formation of multi-photon states.

When three modes in the lowest Landau level are accessible, a long-lived Laughlin state $|L\rangle$ emerges in the two-particle sector (Fig. 6.8b). Our experiments offer a unique opportunity to connect the mathematical form of this Laughlin state to observations of its microscopic

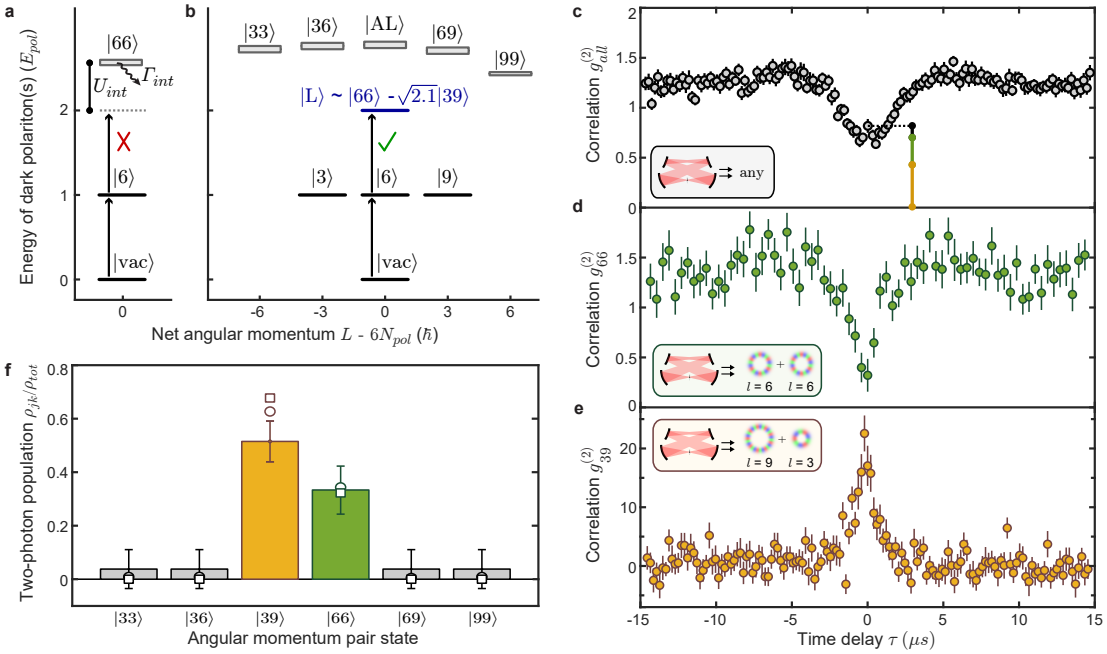

Figure 6.8: **Laughlin state characterization in angular momentum space.** Schematic of the many-body energy levels for states containing polariton numbers (N_{pol}) up to two with access to a single mode (**a**) or all three modes (**b**). In a single mode (here $l = 6$), the two polariton state $|66\rangle$ has its energy shifted (U_{int}) and rapidly decays (Γ_{int}) due to interactions; these effects induce the blockade discussed above. With three modes accessible, most two-polariton states are still shifted by interactions. However, a Laughlin state $|L\rangle$ arises in which the interference between $|66\rangle$ and $|39\rangle$ suppresses the interaction energy (to zero in the limit of contact interactions). This pair state remains long-lived and can be resonantly excited by the $l = 6$ probe laser (black arrows). **(c)** When all emitted photons are included regardless of angular momentum, photons with access to all three modes exhibit weak blockade. **(d)** Correlations between photons exiting the cavity in the probed angular momentum mode ($l = 6$) exhibit stronger blockade, with remnant nonzero correlation $g_{66}(0) = 0.32(3)$ at zero delay. **(e)** Correlations between photons with angular momenta $l = 3$ and $l = 9$ exhibit a large positive correlation because they are produced together in collisions. **(f)** Relative populations in the two-photon manifold determined from coincidence events (bars) are comparable to the Laughlin state (squares) and an atomistic numerical model [207] (circles). The contributions of each pair state to $g^{(2)}_{all}(0)$ are represented by the colored, vertical bars in panel (c), see Methods 6.4.3.1 for details. All error bars indicate standard error. Figure taken from Ref. [121].

structure. For the particular modes used in this work, the two-particle Laughlin wavefunction in real space is $\psi_L(z_1, z_2) \propto z_1^3 z_2^3 (z_1^3 - z_2^3)^2 \exp(-|z_1|^2/4 - |z_2|^2/4)$ where $z_k \equiv x_k + iy_k$ is a complex number reflecting the position (x_k, y_k) of particle k. Expanding the quadratic factor makes it possible to write this state in angular-momentum space as $|L\rangle = \frac{1}{\sqrt{3.1}}|66\rangle - \sqrt{\frac{2.1}{3.1}}|39\rangle$, where $|mn\rangle$ is the state with two polaritons of angular momenta $m\hbar$ and $n\hbar$ (Appx. A.3.7). Because the wavefunction goes to zero when the particles are at the same position ($\psi_L(z_1 = z_2) = 0$), residing in the Laughlin state enables two particles to avoid each other while remaining in the lowest Landau level. From the perspective of angular momentum states, this same property arises from destructive interference between the $|66\rangle$ and $|39\rangle$ two-photon amplitudes for particles at the same location. Similar two-particle Laughlin states can be formed among any set of three modes with evenly spaced angular momenta (see Appx. A.3.7).

The spatial anticorrelation of photons in the Laughlin state suppresses the interaction energy shift and interaction-induced decay experienced by the other two-particle states. Thus, when we shine an ordinary laser into this atom-cavity system, we anticipate that a two-photon Laughlin state will emerge from the other side, because all other two-particle states are blockaded (including the "Anti-Laughlin" superposition state $|AL\rangle = \sqrt{\frac{2.1}{3.1}}|66\rangle + \frac{1}{\sqrt{3.1}}|39\rangle$). From this perspective, the collisions observed in Fig. 6.7 are in fact the first hint of the formation of Laughlin states.

To test for the formation of Laughlin states we characterize the correlations of the photon pairs emerging from the cavity [119]. When we detect all output photons regardless of their spatial mode, the "all-mode" correlations $g^{(2)}_{all}(\tau)$ reveal only a weak blockade effect and in fact have a local maximum at time zero (Fig. 6.8c). This weak blockade confirms that photon pairs are now able to traverse the cavity, but determining their state requires more detailed measurements.

We gain deeper insight by examining the correlations $g^{(2)}_{jk}$ between photons with angular

momenta $l = j$ and $l = k$, using the same setup as shown in Fig. 6.7a. The correlations $g^{(2)}_{66}$ between photons with $l = 6$ have a nonzero value $g^{(2)}_{66}(0) = 0.32(3)$ at zero time delay, indicating substantial population in the state $|66\rangle$ (Fig. 6.8d). However, their blockade is still much deeper than that of the all-mode correlations $g^{(2)}_{all}$, indicating that $g^{(2)}_{all}$ has a large contribution from other pairs which are not in the state $|66\rangle$. Most of the remaining pairs are accounted for by examining $g^{(2)}_{39}$, which exhibits a prominent peak at time zero (Fig. 6.8e). The peak height indicates that photons are $g^{(2)}_{39}(0) = 22(2)$ times more likely to appear in both modes simultaneously than we would expect for uncorrelated photons arriving at the same individual rates. This bunching arises because photons in these modes are predominantly produced together in collisions and almost never injected independently.

In order to compare these results to the Laughlin state, we calculate the two-photon populations ρ_{jk} with angular momenta j and k by extracting the rates of coincidence events, in which two photons are observed nearly simultaneously (Fig. 6.8f; Methods 6.4.3.1). Coincidence events corresponding to $|66\rangle$ and $|39\rangle$ account for 85(15)% of all observed photon pairs, consistent with angular momentum conservation. Moreover, the ratio $\rho_{39}/\rho_{66} = 1.5(5)$ of the pair populations is compatible with the expected ratio of 2.1 for the Laughlin state. Note that, as a result of our Floquet scheme, polaritons with angular momentum $l = 3$ & 9 are more photon-like than those with $l = 6$, such that the observed photonic pair populations are related but not equivalent to the polaritonic pair populations, as detailed in appendix A.3.4; as such we are assembling *photonic* Laughlin states, not *polaritonic* ones.

We next test for the remaining essential physical feature of Laughlin states: the particles should avoid each other in real space. This spatial anticorrelation is what minimizes the interaction energy, causing Laughlin-like states to arise in fractional quantum Hall systems; however, it has not been observed directly in existing (electronic) systems.

To measure spatial correlations we filter the photons exiting the cavity with a single-mode optical fiber (Fig. 6.9a). This fiber only admits photons at the location of its tip. Thus, to

count photons at a particular position, we simply translate the fiber tip to that position. Since the average density in a state composed of $|39\rangle$ and $|66\rangle$ forms a smooth annulus, we translate the fiber to the radius with the highest density (Fig. 6.9b). A natural method for measuring angular correlations $g^{(2)}(\phi, \tau = 0)$ between photons separated by the angle ϕ around the annulus would be to use two fibers at different positions; our Floquet scheme enables an equivalent measurement using a single fiber, whilst inducing a mode-dependent phase shift between polaritons and photons that we compensate using a linear optical transformation before the fiber (Methods 6.4.3.2).

After phase compensation, two photons that simultaneously exit the cavity rarely appear at the same position (Fig. 6.9c). The spatial correlations oscillate with the angle ϕ between the photons, with a periodicity of 120° arising because our Landau level only includes every third angular momentum state. The observed correlations are compatible with the expected form of this Laughlin state, $g_L^{(2)}(\phi) \propto |\psi_L(z_2 = e^{i\phi} z_1)|^2 \propto \sin^4(3\phi/2)$ (Methods 6.4.3.2). Thus, we see that while the average density exhibits no angular structure, photon pairs are extremely likely to be separated by about 60° (equivalently,

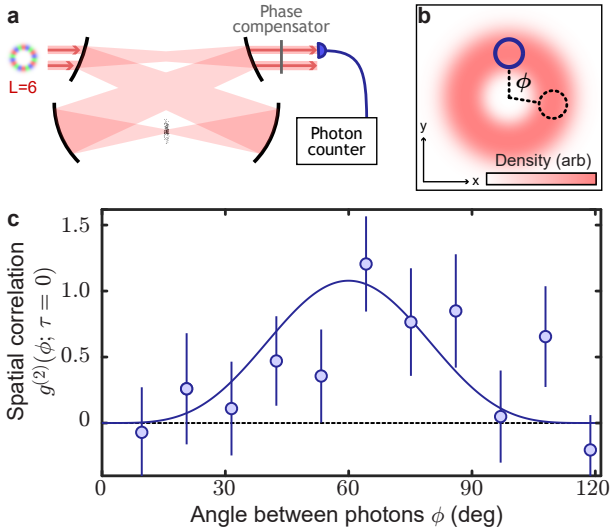

Figure 6.9: **Spatial anticorrelation of photon pairs. (a)** A single-mode fiber (purple) admits only photons at its location, enabling us to filter photons by their real-space position. A mode-dependent phase compensator counteracts the phase difference between polaritons and photons which results from our Floquet scheme (Methods 6.4.3.2). **(b)** The average density of photons forms a smooth annulus with no angular structure. We place the fiber off-center (solid circle) at the radius with the highest density and measure correlations as a function of the angle ϕ to a second location (dashed circle) around the annulus. **(c)** The angular correlations (circles) for zero time delay exhibit a periodic structure consistent with the expected form $g_L^{(2)}(\phi) \propto \sin^4(3\phi/2)$ for a Laughlin state (solid curve). The minimum of correlation near $\phi = 0$ reveals that photons avoid being in the same location. Error bars indicate standard error. Figure taken from Ref. [121].

180° or 300°), and very unlikely to be in the same location.

In addition to directly revealing an important physical property of Laughlin states, the observed spatial correlations are essential for tomographically confirming that the photon pairs have formed Laughlin states: While the detected pair-populations in angular momentum space are suggestive of Laughlin physics, they are insensitive to the phase, or even the purity, of the superposition between $|39\rangle$ and $|66\rangle$. On the other hand, the observed spatial anticorrelation only occurs for a coherent superposition with a minus sign, verifying the formation of a Laughlin state. Taken together, these data indicate that the photon pairs have 76(18)% overlap with the pure Laughlin state, limited primarily by our conservative assumptions about the unmeasured momentum-non-conserving pair populations. Alternatively, if we assume angular momentum conservation, these data indicate a photon pair overlap with the Laughlin state of 90(18)% (see 6.4.4).

We have produced the paradigmatic fractional quantum Hall ground state, the Laughlin state, and measured for the first time the constitutive quantum correlations in two conjugate bases. This work establishes quantum many-body optics as a critical route to breakthroughs in strongly-correlated materials, enabled by the unique microscopic control of our photonic platform in which system parameters are highly controllable, particles can be injected on-demand with particular spatial modes and energies, and intricate correlations can be characterized in almost any measurement basis using straightforward linear optics. Realizing novel state-preparation schemes [269, 276] such as dissipative stabilization [83, 187, 267, 277] will enable the formation of larger topologically ordered states and thus the exploration of fascinating physics including direct-measurement of the statistical phases of anyons [270, 293, 294] accessible directly from density profile measurements [295] or even non-Abelian braiding in the Moore-Read state [334].

6.4 Methods

6.4.1 Experiment Setup

The primary cavity used in these experiments, which couples with the $5S_{1/2} \rightarrow 5P_{3/2}$ transition, is the so-called "science" cavity, which consists of four mirrors in a twisted configuration [182]. The cavity finesse is $\mathcal{F} = 1950$ yielding a linewidth of $\kappa = 2\pi \times 1.4$ MHz. The modes are approximately Laguerre-Gaussian, particularly in the lower waist where they intersect with the atomic cloud; the fundamental mode has a lower waist size of 19 μm. These parameters yield a peak coupling strength with a single atom of $g_{\text{single}} = 2\pi \times 0.58$ MHz, corresponding to a cooperativity of $\eta = 0.16$ per atom [126]. The science cavity is crossed with a buildup cavity for increasing the intensity of the Rydberg coupling beam; the buildup makes it possible to achieve a sufficient intensity over the wide area spanning the science cavity modes up to $l = 9$ in which we create polaritons. Note that the polarization eigenmodes of both cavities are circular. For more details on the cavity structure, see appendix A.3.2.

The science cavity was designed to be tuned to a length at which every third angular momentum state would be degenerate, forming a photonic Landau level [182]. However, as detailed in appendix A.3.2, we found that intracavity aberrations destabilized the cavity modes when the length was tuned to this degeneracy point. Therefore, we instead tuned the cavity length far enough from degeneracy to create a 70 MHz splitting between every third angular momentum state and utilized the Floquet scheme described above in section 6.1.2 to create polaritons which are protected from the effects of intracavity aberrations (as proven in Appx. A.3.5).

We mediate interactions between the photons in the science cavity modes using a gas of 6000(1000) cold Rubidium atoms loaded at the lower waist of the cavity; this atom number covers the first ten modes of the science cavity. The gas is cooled to a temperature below

1 μK and polarized into the lowest energy spin-state $|F = 2, m_F = -2\rangle$ within the hyperfine manifold F using degenerate Raman sideband cooling [206]. For more details on the atom trapping configuration, atomic polarization, and experiment procedure, see appendix A.3.1.

6.4.2 Angular Momentum Mode Sorting

To perform detection of photons in angular momentum space we utilize the mode sorting setup depicted in Fig. 2a. The key elements in this setup are the mode filters, each consisting of a tunable two mirror non-degenerate cavity. These filter cavities are independently locked to a 795 nm laser with tunable frequency offsets, such that we can match the frequency of the filter cavity mode with angular momentum l to the frequency of the photons exiting the science cavity with the same angular momentum. The three cavities differ slightly in their parameters, but the typical cavity is composed of two identical mirrors with 98.7% transmission and radii of curvature $R = 10$ m at a separation of 15 cm, yielding a linewidth of $\kappa_{filt} = 4$ MHz and a transverse mode spacing of 55 MHz. Because the science cavity angular momentum modes are separated by $f_{\text{cav}} \approx 70$ MHz much greater than the filter cavity linewidth, the filters are able to discriminate between the science photons using both their spatial mode structure and their frequency. The typical mode sorting/filter cavity has a net transmission of 40% for photons with the desired angular momentum and suppresses transmission of photons with the wrong angular momentum by a factor of 2000. Semrock laser line filters transmit only the desired 780 nm photons, which are then collected by a multimode fiber and directed into single photon counting modules.

The experiments reported in Fig. 6.7 were performed using all three mode sorting cavities simultaneously, with each cavity tuned to transmit a different angular momentum mode. The experiments reported in Fig. 6.8 were performed before the third mode sorting cavity was constructed. Therefore, the data shown in Fig. 6.8d were collected in separate experiment

runs from the data in Fig. 6.8e; in between, the two mode sorters were adjusted to transmit the relevant angular momentum modes.

6.4.3 Two-Photon Correlations

We characterize the light exiting the science cavity using two-photon correlation functions,

$$g^{(2)}_{jk}(\tau) = \frac{\left\langle n_j(t) n'_k(t+\tau) \right\rangle_t}{\left\langle n_j \right\rangle \left\langle n'_k \right\rangle}, \tag{6.1}$$

between the photons $n_j(t)$ in mode j counted at a first detector and $n'_k(t)$ in mode k counted at a second detector, where the angle brackets denote time averaging and τ is the time delay between the detection events. The mode labels j and k may represent angular momentum modes with $l = j$ and $l = k$, or they may represent the spatially localized mode of the single-mode fiber. When $j = k$, we typically use a beam splitter to divide the photons between two separate single photon counting detectors. For many of our measurements the background count rates in the absence of the probe are comparable to the signal rates in the presence of the probe; the correlation functions presented in this work correspond to the correlations of signal photons with the backgrounds removed, as detailed in SI. A2 of Ref. [207].

6.4.3.1 Angular Momentum Correlations

The correlation functions presented in the main text Fig. 6.8c-e were collected during three separate runs of the experiment. In the first run (Fig. 6.8c), a multi-mode fiber splitter was used to collect all of the photons exiting the science cavity, regardless of mode, and split them evenly between two single photon counters. In the second run (Fig. 6.8d), the first mode sorting filter was tuned to transmit half of the photons in $l = 6$, while the second mode sorting filter transmitted the remaining half of photons with $l = 6$. In the third run

(Fig. 6.8e), the first mode sorting filter transmitted photons with $l = 9$ and the second filter transmitted photons with $l = 3$. Note that the local maximum at $g^{(2)}_{all}(0)$ in Fig. 6.8c appears because the peak in $g^{(2)}_{39}$ is somewhat narrower than the dip in $g^{(2)}_{66}$, as polaritons with $l = 3$ & 9 have shorter lifetimes than polaritons with $l = 6$ due to our Floquet scheme (see Appx. A.3.4).

The two-photon population fractions shown in Fig. 3f of the main text for $j = k = 6$ and $j = 3$, $k = 9$ are calculated by comparing the observed coincidence rates as,

$$\frac{\rho_{ij}}{\rho_{tot}} = \frac{\left\langle n_j(t) n'_k(t) \right\rangle_t}{\langle n_{mm}(t) n'_{mm}(t) \rangle_t} \frac{2}{(1+\delta_{jk})\xi_j \xi'_k}, \tag{6.2}$$

where n_{mm} (n'_{mm}) is the signal at the first (second) output port of the multimode splitter used to measure $g^{(2)}_{all}(\tau)$, ξ_j (ξ'_k) is the mode-sorted detection efficiency for mode j (k) on the first (second) detector relative to the efficiency of a single output port of the multimode splitter, and δ_{jk} is the Kronecker delta. Each of the detection efficiencies is independently calibrated by probing on the relevant dark polariton resonance and comparing the count rate after the mode-sorting filter to the count rate after the multimode splitter. Let $N_{jk}(\tau) = \left\langle n_j(t) n'_k(t+\tau) \right\rangle_t$ be the observed rate of two-photon events separated by time τ. For the mode-sorted cases we estimate $N_{jk}(0)$ by fitting the observed delay-time-dependent $N_{jk}(\tau)$ and extracting the zero-delay value from the fit; empirically, we find that $N_{39}(\tau)$ is well fit by a Lorentzian and $N_{66}(\tau)$ is well fit by the solution to the optical Bloch equations for a two-level system (see Ref. [207] SI. A2). For the multimode case we do not have a suitable fitting function, and therefore we directly use the observed value $\int_{-\Delta/2}^{\Delta/2} d\tau N_{mm}(\tau)$ averaged over a time bin with width $\Delta = 600$ ns around zero delay.

We find that the observed populations ρ_{39} and ρ_{66} may not fully account for the observed coincidences in the multimode data, with $\frac{\rho_{39}+\rho_{66}}{\rho_{tot}} = 0.85(15)$. Since we do not directly measure the correlations in any other combinations of angular momentum modes, Fig. 3f

uses the estimate that the remaining population fraction of 0.15(15) is split evenly among the remaining mode pairs. The actual distribution of this additional population among the four possible mode pairs does not affect any of our conclusions, including the density matrix and the overlap of the observed state with the Laughlin state as discussed in Methods 6.4.4. Physically, we note that angular momentum conservation should prevent these other mode pairs from being populated at all; however, we are not able to place any further constraints on their populations based on our measurements. Note also that our use of a weak probe beam, as well as the strong interaction-induced blockade of all three polariton states among these three modes, should make the effect of three-photon states on these results negligible.

6.4.3.2 Spatial Correlations

We perform measurements in real space using a single mode fiber. To properly align the fiber to detect photons in the Landau level at the desired position, we first choose an asphere as well as the position and angle of the fiber which maximizes the coupling of $l = 0$ photons from the cavity into the fiber. Once that coupling is optimized, we use a four-axis stage (two-dimensional translation, tip, and tilt) to perform a "magnetic translation" of the fiber tip [182]. In particular, we send $l = 6$ photons through the cavity and repeatedly adjust the position and angle of the fiber until the fraction of $l = 6$ photons entering the fiber is maximized. This process matches the fiber to a magnetically-translated Gaussian in our lowest Landau level at a radius near the peak in the average density of photons that are exiting the cavity in pairs (as depicted in Fig. 6.9b).

Ordinarily, a single fiber would only be able to reveal the correlations at that single location. However, as discussed in appendix A.3.4, immediately after a first photon is detected through the single mode fiber, the Floquet scheme used in this work causes the second photon to rotate one third of the way around ring with a temporal period of $T_{mod} = 1/f_{\mathrm{mod}} = 14$ ns which is

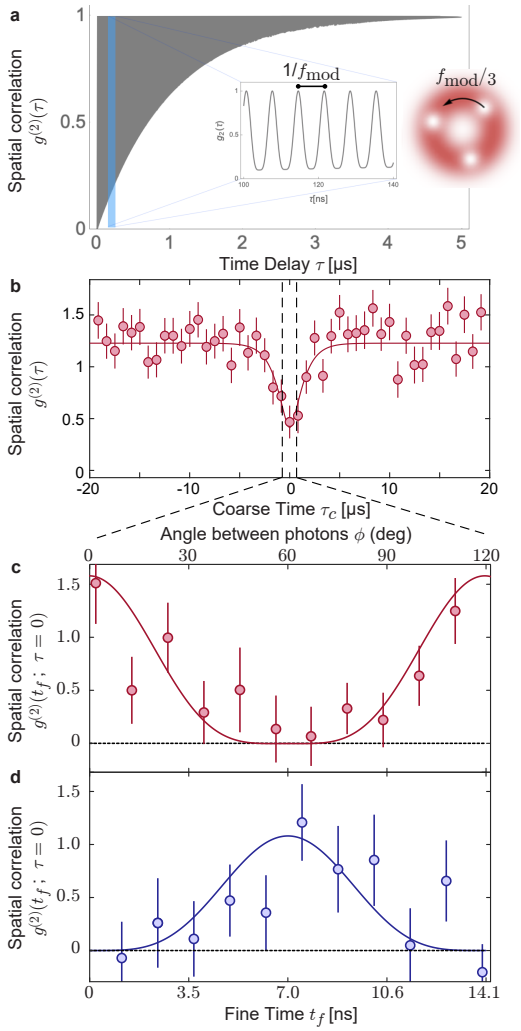

Figure 6.10: **Extracting angular correlations from rapid rotation of the second photon. (a)** Illustration of the correlation function measured through a single mode optical fiber. Rapid oscillation in the signal at f_{mod} arises from the wavefunction of the second photon, which has three holes whose positions are determined by that of the first detected photon and which rotate at $f_{\mathrm{mod}}/3$ (inset). The rotation signal decays over a microsecond timescale containing hundreds of rotation periods. **(b)** When viewed in coarse time τ_c with averaging over a timescale much longer than the rotation period, the correlations through the single mode fiber exhibit ordinary antibunching. **(c)** Breaking up the central data point into 11 parts based on their fine time t_f within the rotation period reveals the oscillation of the correlations. The instantaneous correlation ($t_f = 0$) corresponds to the same-location correlation ($\phi = 0$), while half a period later we see the correlations between locations separated by $\phi = 60°$. Without the phase compensator, we observe photon bunching at $t_f = 0$. **d,** With the phase compensation cavity implemented (see Methods 6.4.3.2), photons are anticorrelated at $t_f = 0$. Figure taken from Ref. [121].

much faster than other dynamical timescales of the system. Note that any wavefunction in our Landau level has an azimuthal periodicity of $2\pi/3$, and therefore rotating one third of the way around the ring is sufficient to map the wavefunction back on to itself. Therefore, the correlations between photons in the single mode fiber separated by a "fine time" $t_f = \tau$ mod T_{mod} are equivalent to the angular correlations that would be observed between photons at equal time with angular separation $\phi_f = \frac{2\pi}{3}\frac{t_f}{T_{mod}}$,

$$g^{(2)}(\phi_f; \tau = 0) = g^{(2)}_{ff}(t_f). \tag{6.3}$$

An illustration of this behavior is provided in Fig. 6.10a.

Therefore, to characterize the angular correlations, we perform high resolution measurements of photon arrival times through the single optical fiber. After entering the single-mode fiber, we split the field into two halves and send each to a single photon counting module. We use a home-built FPGA-based photon time tagger with 1.4 ns resolution to characterize the photon arrival times. We convert the temporal correlations $g^{(2)}_{ff}(t_f)$ into the correlation function $g^{(2)}(\phi, \tau = 0)$ using Eq. 6.3. Since we are unable to collect sufficient statistics to characterize correlations during a single rotation period, we instead average data corresponding to the same fine time t_f over many rotation periods within a large "coarse time" bin of total duration 1.2 μs. The result of this process is depicted in Fig. 6.10b & c. To calibrate any additional time offset due to time delay differences in the two detection paths, we perform a separate set of measurements sending rapidly intensity modulated coherent light directly into the fiber splitter; we extract the time delay as the difference in measured arrival times for peaks and troughs of that signal along the two detection paths. That time delay calibration has been accounted for in Fig. 6.10c & d, such that the correlation signal at $t_f = 0$ properly corresponds to photons arriving at the fiber tip at the same time.

As explained in appendix A.3.4, our Floquet scheme induces a shift of π in the relative

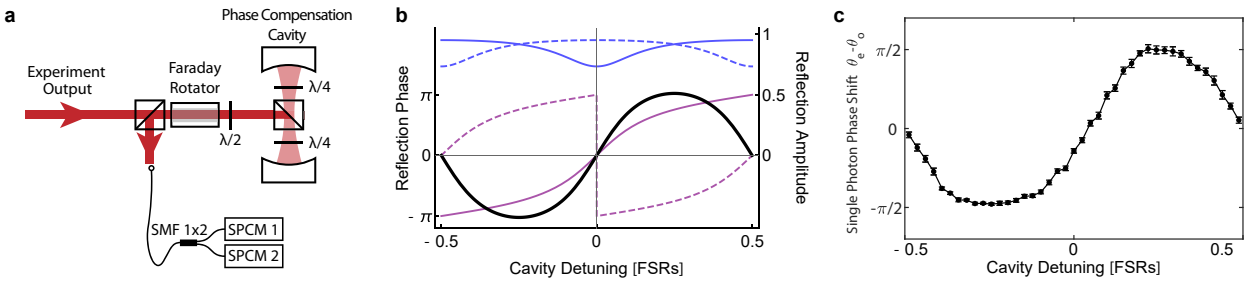

Figure 6.11: **Phase compensation cavity for spatial correlation measurements. (a)** To compensate for the additional phase shift of the photons relative to the polaritons which is induced by the Floquet scheme, we send the light emitted from the main science cavity ("experiment output") to a phase compensation cavity (PCC), which contains two quarter waveplates and a polarizing beam splitter cube that can be used to tune its finesse. Almost all of the light is reflected from the PCC after experiencing the desired phase shift. It subsequently travels to the single mode fiber, where it is split and sent to two separate single photon counting modules (SPCM) for correlation measurements. **(b)** The PCC is a confocal cavity with 82% effective transmission of the first mirror (determined by the waveplate angle), 0% transmission of the second, and 12% intracavity loss. While all modes experience relatively little loss (blue, top), even modes (solid) reflected from the cavity experience a different phase shift (purple) than odd modes (dashed). The net phase shift for the two-photon states $|66\rangle$ relative to $|39\rangle$ (black solid) can be tuned over 2π by changing the cavity length. **(c)** Experimental calibration in the *single-photon sector* verifies a tunable phase shift of up to $\pm\pi/2$ for even modes relative to odd modes. Figure taken from Ref. [121].

phase between $|66\rangle$ and $|39\rangle$ in the photonic state relative to the polaritonic state. As a result, a spatial correlation measurement performed directly after the science cavity reveals photon bunching at $t_f = 0$ ($\phi = 0$), as shown in Fig. 6.10c. While this phase shift can be compensated with a linear optical transformation, it is not affected by diffraction, single lenses, or single mirrors, and thus must be manipulated a slightly more sophisticated "optical element".

In order to compensate for this phase and produce a photonic Laughlin state, we implement the phase compensation cavity (PCC) depicted in Fig. 6.11a. The PCC consists of two curved mirrors with an intracavity polarizing beam splitter and quarter waveplates which can be used to tune the effective reflectivity of the mirrors. We adjust the waveplates to make the PCC behave as a single-ended cavity with 82% transmission on the input coupler, maximum reflection on the output coupler, and 12% intracavity loss; this corresponds to an overall finesse of 3. Moreover, we adjust the length of the cavity to be near-confocal, so that all even modes are degenerate and all odd modes are degenerate. While nearly all of

the light incident upon the PCC is reflected regardless of its parity or frequency, the PCC induces a tunable, parity-dependent phase shift (Fig. 6.11b). We chose the finesse of the cavity so that the phase shift per photon for even modes relative to odd modes is $\pi/2$ over a wide range of cavity detunings (Fig. 6.11c), and we then lock the cavity in the center of that range.

Because $|66\rangle$ contains two even phsotons and $|39\rangle$ contains two odd photons, reflecting from the PCC induces a total relative phase shift of π between them. Therefore, it exactly compensates for the extra phase induced by the Floquet scheme. As a result, when we reflect the light exiting the science cavity off of the PCC before performing the spatial correlation measurement, we observe the antibunching at time $t_f = 0$ ($\phi = 0$) which is characteristic of the Laughlin state.

6.4.4 Density matrix reconstruction

Here we combine the results of our measurements in angular momentum space and real space to calculate the density matrix among the two-photon states in our system, which has the elements,

$$\rho_{ij,i'j'} = \langle ij|\rho|i'j'\rangle. \qquad (6.4)$$

The calculation of the diagonal elements $\rho_{39} \equiv \rho_{39,39}$ was discussed in Methods 6.4.3.1 with the results shown in the main text Fig. 3f.

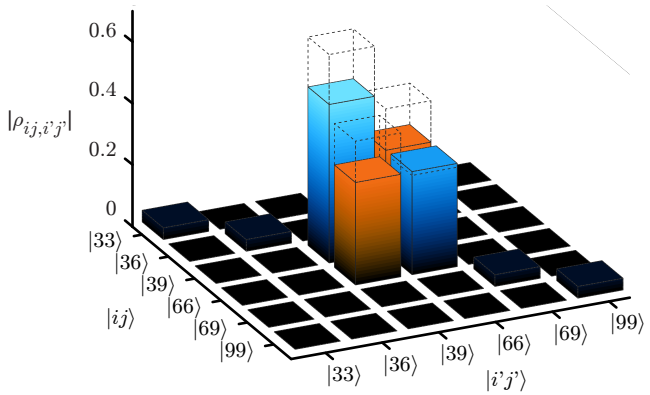

Figure 6.12: **Density matrix in the two-photon sector.** Combining our results in real space (Fig. 6.9) and angular-momentum space (Fig. 6.8) enables us to reconstruct the density matrix of the two-photon state which exits our system (solid bars). Blue bars are positive, orange bars are negative. Dashed bars correspond to the pure Laughlin state. Figure taken from Ref. [121].

We determine the relevant off-diagonal density-matrix element $\rho_{39,66}$ based on the observed spatial correlations. The angular correlation function of the ideal Laughlin state is,

$$\begin{aligned} g^{(2)}(\phi) &= \frac{8\bar{g}}{3}\sin^4(3\phi/2) \\ &= \bar{g}\left(1+\frac{1}{3}\cos 6\phi - \frac{4}{3}\cos 3\phi\right), \end{aligned}$$

where $\bar{g}$ is the time-averaged correlation. With an arbitrary density matrix among the states $|39\rangle$ and $|66\rangle$, the correlation function takes the form,

$$g^{(2)}(\phi) = \bar{g}\left(\frac{651}{260}\rho_{66} + \frac{155}{546}\rho_{39}(1+\cos 6\phi) - \frac{124}{\sqrt{1890}}\mathrm{Re}(\rho_{39,66})\cos 3\phi\right). \tag{6.5}$$

This form is independent of the radius at which the single mode fiber is placed. We fit the spatial correlation data shown in Fig. 6.10d with Eq. 6.5 and use the separately measured populations ρ_{66} and ρ_{39} to extract the coherence $\rho_{39,66} = -0.33(16)$.

Note that Eq. 6.5 neglects the additional possible contributions to the average value which come from the population in other angular momentum pair states ($|33\rangle$, $|36\rangle$, etc.). Because these contributions depend more sensitively on the position of the fiber, and because we do not know how the additional 15% of the population is distributed among these pair states, we take the most conservative approach and neglect their contributions entirely. This approach is conservative because it yields the smallest magnitude of $\rho_{39,66}$ and therefore the smallest inferred overlap with the Laughlin state. Note also that because only the real part of the coherence $\mathrm{Re}(\rho_{39,66})$ contributes to the observed correlations, we cannot distinguish between a loss in magnitude of $\rho_{39,66}$ and the presence of an imaginary component. We treat our results as if there is no imaginary component; however, this choice does not affect the inferred overlap with the Laughlin state below.

Our final result for the density matrix based on these conservative assumptions is shown in Fig. 6.12. This density matrix has a "Laughlin fidelity", its overlap with the pure Laughlin

state, of,

$$F = \langle L|\rho|L\rangle = 76(18)\%, \tag{6.6}$$

as reported in the main text.

Alternatively, we can calculate the Laughlin fidelity under an optimistic set of assumptions. In particular, because this system should satisfy angular momentum conservation, we can assume that there is actually no population in the other angular momentum pair states; in that case we set $\rho_{33} = \rho_{36} = \rho_{69} = \rho_{99} = 0$, and we re-scale the populations in the remaining two states such that their ratio matches our experimental observations but their sum is $\rho_{66} + \rho_{39} = 1$. If we also recalculate the off-diagonal coherence under those assumptions, then the resulting density matrix corresponds to an optimistic Laughlin fidelity of 90(18)%.

CHAPTER 7

OUTLOOK AND FUTURE WORK

This thesis has detailed the development of a strongly nonlinear quantum optical platform and its application to studies of fractional quantum Hall physics. Harnessing the powerful analogy between the transverse degrees of freedom of a cavity photon and a massive quantum harmonic oscillator, we use cavity photons as the dynamical particles of a material system. We developed and implemented a synthetic magnetic field for cavity photons through a careful nonplanar arrangement of cavity mirrors. This enabled the formation and observation of photonic Landau levels on the surface of a cone. Using the unique spatial and spectroscopic probes of our optical platform, we developed new local, real-space observables in the resulting integer quantum Hall system to measure three topological invariants. We observed that they converge to their bulk value when probed over a few magnetic lengths, consistent with the intuition that the distinction between the bulk and edge exist only for samples larger than several magnetic lengths. We also discussed how such measurements of topological invariants can be critical to characterize interacting quantum Hall phases of matter.

We introduced how cavity photons can be made to interact via cavity Rydberg EIT. In comparison with the dominant competing method using a Jaynes-Cummings nonlinearity, our cavity Rydberg polaritons are more robust and strongly interacting at accessible experimental parameters *. We characterize the effective photon-photon interactions through

$\star$. This strong claim needs to be backed up. Our current optimized g_2 curve (Fig. 6.2d) gives a minimum g_2 upper-bounded at one standard deviation by 0.015, which we can use to compare our system to a single two level emitter coupled to a cavity. The g_2 minimum in that case is simply given in terms of the anharmonicity U and the polariton linewidth γ as $g_2(0) = \gamma^2/(\gamma^2 + U^2)$. As developed in section 2.1.1, the resolving power of a Jaynes-Cummings system (that is, the highest ratio of the anharmonicity to the polariton linewidth after optimizing over the detuning) is given by the cooperativity $U/\gamma = \frac{1}{2}\sqrt{\eta}$. We combine these equalities to calculate the minimum cooperativity that a Jaynes-Cummings system needs in order to observe a particular g_2 minimum, $\eta = 4(1 - g_2(0))/g_2(0)$. Plugging in our upper bound for the minimum g_2 yields a required Jaynes-Cummings cooperativity of 260. For a single atom in an optical cavity, this is at the edge of technologically possible, requiring a cavity mode waist below 4 μm at a finesse of 1×10^5. Both of these parameters are near the limit of material properties and fabrication techniques for optical microcavi-

transport blockade, the suppression of a second transmitted photon given the presence of the first. Using a novel Floquet redistribution of the atomic density of states, we extended our observation of high-probability photon collisions to a two mode photon collider.

Finally we combined these ingredients, a magnetic field for photons and strong interactions between photons, to create a fractional quantum Hall system and to observe the resulting ground state, a $\nu = 1/2$ Laughlin state of two photons. In our state-of-the-art apparatus, photons in a single mode collide with a probability above 98%, driving photons to order within the larger space of available modes. When these modes are states in a Landau level, a Laughlin state emerges. The quality of this state is quantified via angular momentum correlations and spatial anti-bunching; a particular superposition of two photon angular momentum states interferes to ensure photons avoid each other in space. This opens the door to the creation of larger photonic quantum many-body states and the investigation of topological order. In combination with dissipative stabilization techniques, large Laughlin puddles may be prepared with quasi-holes in order to directly manipulate and characterize anyons. With the addition of partially dipolar interactions enabled by microwave dressing of the Rydberg state, non-Abelian fractional quantum Hall states may be prepared, allowing access to some of the most intriguing open questions in condensed matter systems.

In addition to fractional quantum Hall physics, there are numerous additional experiments

ties [335, 336]. Meanwhile, our apparatus is far from optimized on this axis. The experimental cavity finesse, blue build-up cavity finesse, and atomic density all have at least an order of magnitude of relatively easy improvement, while Rydberg interaction energies may be dramatically increased by microwave manipulation. The inquisitive reader may wonder though about alternative Jaynes-Cummings systems. For example superconducting qubits in microwave cavities regularly achieve cooperativities in excess of 10^{10} with another five orders of magnitude within reach. This makes superconducting quantum circuits a leading platform for universal digital quantum computers. However, there are numerous applications for nonlinear quantum optical systems that operate with optical photons, typically involving the transport of quantum information over large distances. Free space optical cavities are limited to mode areas much larger than the wavelength of light. However nanophotonic cavities offer the ability to confine light with a length scale much less than the wavelength. This has motivated several efforts with nanophotonic cavities coupled to atoms [286, 337, 338] or embedded solid state emitters [339, 340] to achieve high-cooperativity quantum optical systems. Such systems currently have cooperativities up to or around ten, have demonstrated single photon nonlinearities, and have much room for further improvement. Thus these systems provide strong competition for Rydberg polariton based nonlinear quantum optics.

and applications available for future work. Relaxing our efforts on strong interactions enables the creation of weakly interacting photonic materials including mean-field Abrikosov lattices and Bose-Einstein condensation of photons in the lowest Landau level. Keeping strong interactions but removing the magnetic field, e.g. in a near confocal cavity, would open investigations of quantum crystallization of photons. More generally, our strongly interacting quantum optics platform has powerful applications in quantum information processing, including quantum non-demolition measurements of single photons, the production of optical cat states, and the building of a quantum repeater.

There is no limit to the work I did not do. However, in an attempt to focus and structure the discussion of future work to the most relevant topics, the remainder of this chapter is split into three sections. First are those experiments which may be completed in the existing apparatus. Some of these experiments are naturally optimized in a future single mode apparatus, so this section continues with those considerations. Second, we discuss improvements to the existing apparatus that would enable further experiments in fractional quantum Hall physics. In the final section, we frame the description of these further experiments around a central question of how to explore a topological phase of matter and discuss recent theoretical proposals applicable to this goal.

7.1 Immediate Experiments

7.1.1 Mean Field Physics in the Lowest Landau Level

Although we have so far focused on strongly interacting physics with our current cavity (as in Ch. 6), weakly interacting or mean-field physics is also accessible, and in many ways easier to explore. By going to a lower principal quantum number, we reduce the range of the effective Rydberg-Rydberg interactions (see Sec. 2.2.3 and Fig. 2.7), increase the control field Rabi

coupling, and greatly increase the signal strength. While coupling very many modes remains difficult due to the loss of g in our Floquet scheme, several-mode mean field physics in a Landau level should enable observations of spontaneous crystallization of vortices into an Abrikosov lattice (see Fig.7.1). The non-degeneracy of each mode from the Floquet scheme will cause the entire output field to undergo rigid rotation; the vortices will not move relative to each other. This can be observed either by injecting the appropriate optical vortex lattice and observing that the output is a steady state, or by injecting a different state, for instance a single Laguerre-Gaussian mode, and watching the system decay into a lattice of vortices by splitting apart the multiply charged central vortex.

A related idea using mean field interactions in a lowest Landau level would be to observe Bose-Einstein condensation of photons by tuning the relative decay rates of polaritons in different angular momentum modes. When the $l = 0$ mode is long lived, the $l = 3$ mode has intermediate lifetime, and the $l = 6$ mode is short lived, driving on the $l = 3$ mode should yield a steady state population that is strongly peaked at $l = 0$. This compares directly with evaporative cooling techniques, since the higher energy modes have larger linewidth.

7.1.2 Microwave Manipulation of Rydberg-Rydberg Interactions

There are also several experiments that make use of only a single mode of the cavity. One of the most exciting experiments would be to use microwaves to manipulate the Rydberg component of a dark polariton. In particular, off-resonant driving of a target pair state could create a Förster resonance, dramatically enhancing the Rydberg-Rydberg interaction energy (see Fig. 7.2).

Observing this effect should be straightforward. After picking the microwave frequency from comparison with the atomic level structure, the microwave power may be ramped while monitoring the dark polariton transmission. Since the system is initially weakly interacting,

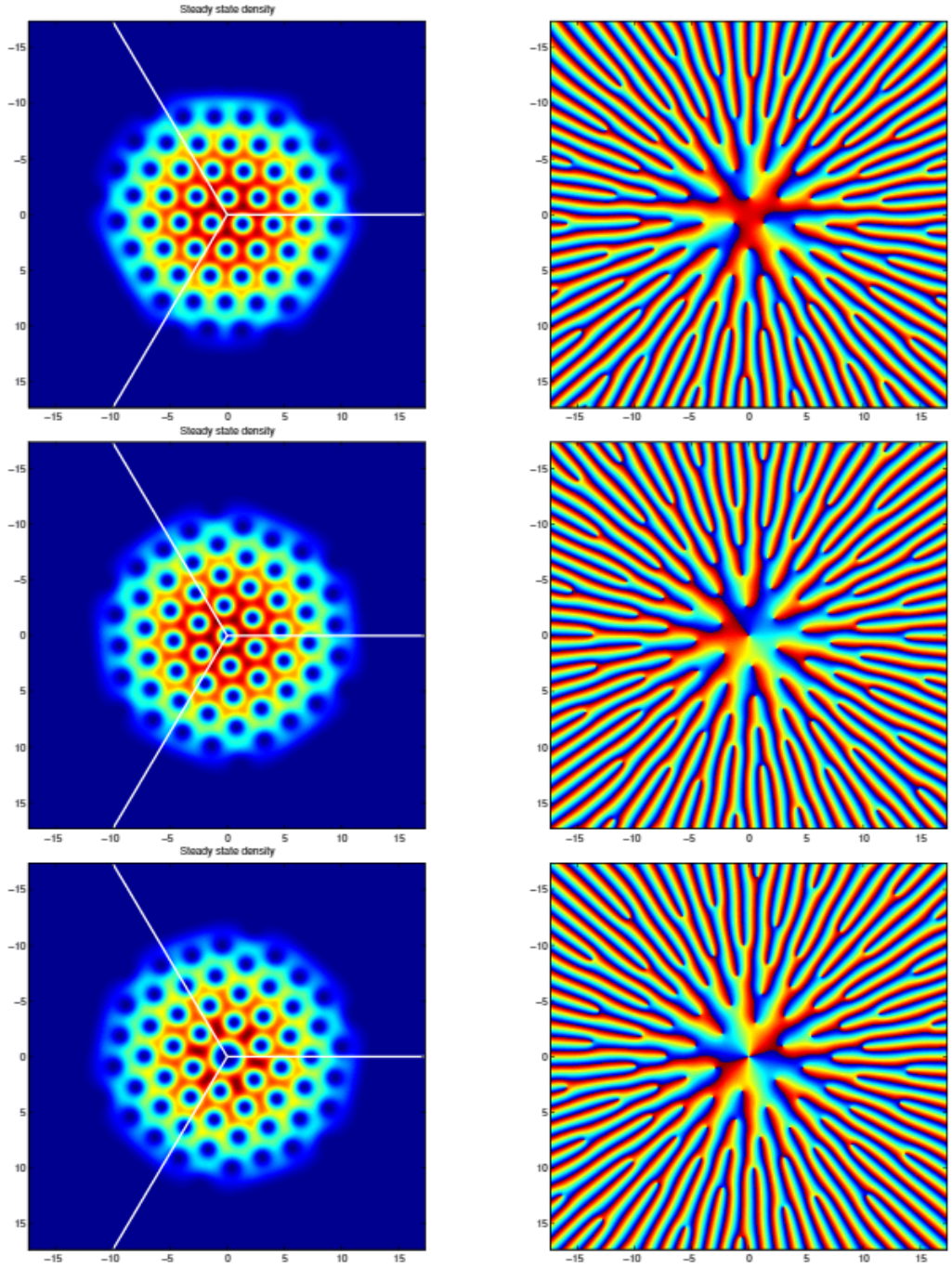

Figure 7.1: **Mean Field Physics in the Lowest Landau Level.** The density (left) and wavefunction phase (right) show the formation of a triangular Abrikosov lattice of vortices for mean field interacting photons in a lowest Landau level on a cone. The structure at the cone tip is restricted by the lowest angular momentum state available ($l = 0$ top, $l = 1$ middle, and $l = 2$ bottom); however, since the three-fold symmetry is compatible with the triangular lattice, this is a relatively minor restriction. These calculations assume effective contact interactions between photons free to order within the lowest 100 modes. Figure and supporting calculation by Logan W. Clark, personal communication, Sept. 25, 2017.

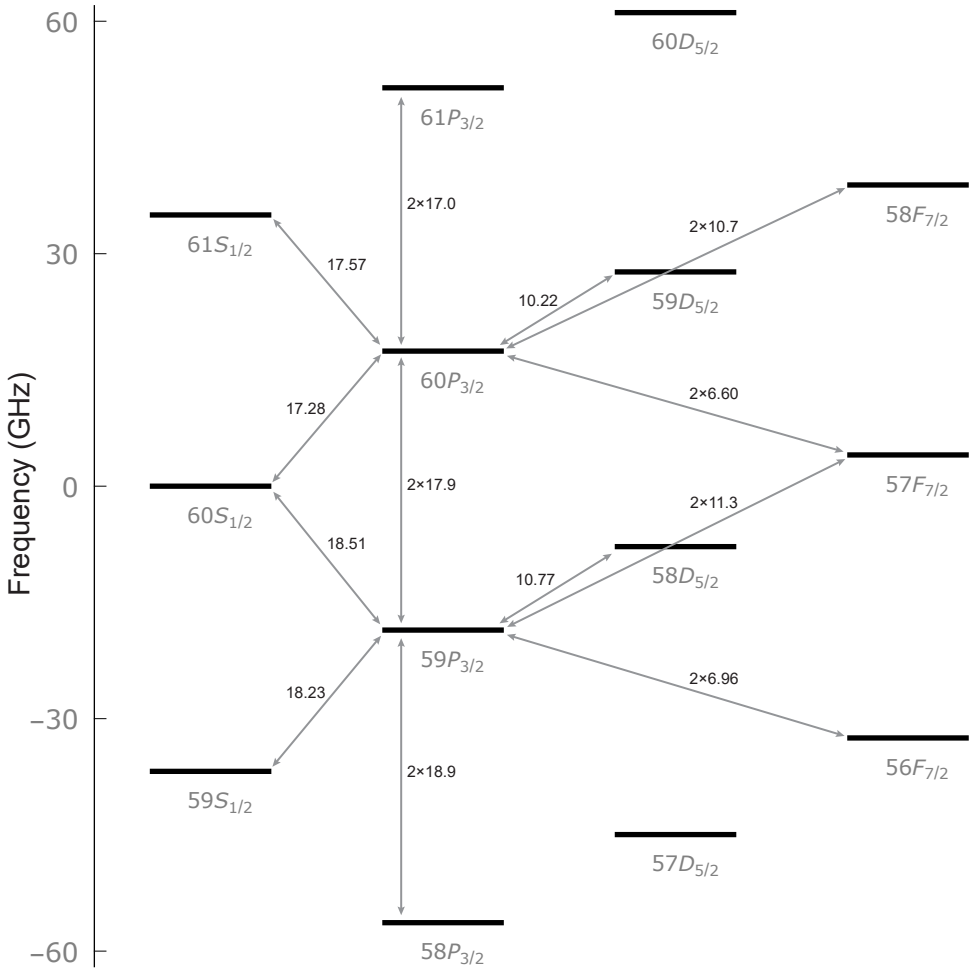

Figure 7.2: **Partial Grotrian Diagram for Rydberg Levels Near 60S.** Energy levels near and transitions under 20 GHz to $59P_{3/2}$ and $60P_{3/2}$ are listed in units of GHz. For Rydberg-Rydberg interactions at 60S, the $|60S_{1/2}, 60S_{1/2}\rangle$ pair state primarily couples to the $|59P, 60P\rangle$ pair state, off-resonance by 1.23 GHz. A microwave tone between 12 and 14 GHz will primarily act off resonantly on the $|59P_{3/2}\rangle \leftrightarrow |58D_{5/2}\rangle$ and $|60P_{3/2}\rangle \leftrightarrow |59D_{5/2}\rangle$ transitions by increasing the P states' energies. The desired shift of each P state is around 600 MHz to bring the $|59P_{3/2}, 60P_{3/2}\rangle$ pair state into resonance; the large detuning of several GHz ensures that this may be accomplished without significantly altering the P states. Ramping up the microwave power at a fixed frequency should therefore smoothly push the $|59P_{3/2}, 60P_{3/2}\rangle$ into and then past a Förster resonance. We have neglected fine structure in this diagram; for the P states, this is around 500 MHz and is an order of magnitude smaller for D states. While this will affect the required microwave power, it should not change the chosen microwave frequency or the resulting qualitative behavior. Numerics using Weber, *et al.*'s pair interaction tool [341] indicate that the $|59P_{3/2}, 59P_{3/2}\rangle$ pair state mixes at larger distances and stronger than the $|59P_{3/2}, 59P_{1/2}\rangle$, $|59P_{1/2}, 59P_{3/2}\rangle$, and $|59P_{1/2}, 59P_{1/2}\rangle$ pair states.

the cavity may be driven reasonably hard. But as the pair state defect reduces, the C_6 van der Waals coefficient will increase, causing increased polaritonic interactions and a reduced transmission signal. Measurement of a g_2 dip can then confirm enhanced interactions.

One challenge with this approach is the residual shift of the Rydberg S state. While the tone may be chosen to be reasonably far detuned from the S→P transitions and these two transitions mostly cancel, the shift of the S state is still large compared to the dark polariton linewidth. For example, using the configuration laid out in figure 7.2, choosing a 12 GHz tone requires a 670 MHz Rabi frequency to Stark shift the $P_{3/2}$ state by 600 MHz. This same tone then also Stark shifts the 60S state by 3 MHz. As such, as the microwave power increases, the Rydberg state may be followed; this also serves to calibrate the microwave drive power.

This result would be very exciting for two broad reasons. First, this indicates going forward that we could use lower principle quantum numbers and the correspondingly greater control field Rabi frequency (2.6× greater at 60S than 100S) at the minor cost of a microwave tone. Substantially all applications of our platform are improved by increasing our interaction energy and control Rabi frequency, while reducing sensitivity to electric fields! Switching of the microwave tone also allows for defined interaction times in pulsed experiments. Second, as the pair state comes into resonance, the Rydberg-Rydberg interaction becomes significantly dipolar. Creating a combination of short range (ideally contact, but van der Waals probably counts) and dipolar interactions enables the formation of non-Abelian fractional quantum Hall phases such as the Moore-Read state [61].

This scheme works well for S states, but is probably difficult to implement for D states. The scheme functions because of an asymmetry in the level structure, so that there is a spectrally isolated Rydberg-Rydberg transition. In contrast, D pair states strongly couple to PF pair states which are then sensitive to a much broader number of transitions.

A different, but potentially easier and more powerful technique would involve weak off-resonant coupling directly between the target Rydberg state and a nearby state. For instance, at 60S, rather than manipulating the pair state energy, we could directly admix some $60P_{3/2}$ by driving 100 MHz detuned from the 17.43 GHz transition. With a Rabi frequency of 10

MHz, we shift the 60S state by 1 MHz, and mix in 1% of the $60P_{3/2}$ state by population. This hybrid Rydberg state then has a permanent dipole moment, so should experience a direct a dipole-dipole interaction. It is important to maintain a significant detuning so that the orthogonal admixture (to which we may directly couple via the control field) is outside the EIT window. However, we may make this detuning much smaller than in the previous scheme since we do not need (or want) a large Stark shift. The small Rabi frequency makes the system simpler since only the single nearly-resonant transition is relevant. Since the resulting interactions are no longer a second order, van der Waals interaction, they may be much stronger. However, our available numerical tools are not able to calculate what the interaction potential of such a hybrid state would look like. Nevertheless, the experiment would be quite easy to attempt, and if this scheme works, it is easily extended to D states. This would be preferable since coupling to Rydberg D states increases the control Rabi frequency and enables using stretched transitions.

7.1.3 Dark-Bright Collisions and Autonomous Cavity Stabilization

As discussed at the end of section 2.2.2 on decoherence processes of Rydberg polaritons, interactions may cause inelastic collisions taking two dark polaritons to a dark and a bright polariton [161, 162]. This effect could be directly observed in our system by collecting only the light that transmits through a narrow analysis cavity (linewidth significantly smaller than the dark polariton). Numerical modeling will need to guide the choice of analysis cavity linewidth, since the necessary rejection of dark polariton transmission will be set by the ratio of the regular transmission rate to the inelastic scattering rate, and making the cavity any narrower than necessary slows down data collection and increases sensitivity to technical noise.

This basic idea is also potentially very powerful for autonomously stabilizing a single non-

linear cavity mode. If we drive the cavity with photons midway between a bright polariton and the dark polariton, we cannot excite either polariton, or inject a single photon into the cavity. However, we can, in principle, inject two photons at the drive frequency if they then collide into a dark and a bright polariton. The bright polariton quickly decays, leaving a single dark polariton in the cavity. Strong interactions then prevent the injection of a second dark polariton. Thus, just by driving at the appropriate frequency, we can ensure that there is always a single dark polariton in the cavity.

This scheme requires several conditions to be met simultaneously. Dark and bright polaritons must be able to collide, so both must have some Rydberg state component. Thus this process will scale as $\sin^2\theta_D \cos^2\theta_D$. However, to ensure strong blockade, this process must be weaker than the dark polaritons' interactions between themselves, which scale as $\sin^4\theta_D$. This indicates a careful tuning of the dark state rotation angle. The small intrinsic rate of the dark-bright collisions can be compensated by a strong the drive until off-resonant single particle excitation of the dark or bright polaritons becomes significant; this is improved by increasing the collective cooperativity (at constant rotation angle) which sets the dark-bright splitting.

More generally, this fits into a large family of schemes to autonomously stabilize quantum states. Already, broadly similar strategies have been developed and implemented in superconducting microwave circuits [83, 342–346], along with several proposals for optical photons [278, 347–350]. These schemes rely on engineered dissipation to the environment* with stabilization potentially enabled or enhanced by strong interactions between particles. While these are in a general sense applicable to our system, it is desirable to use only a single

$\star$. For instance, in our proposed scheme, it is the much larger linewidth of the bright polariton compared to the dark polariton which enables stabilization of fixed dark polariton number states. In contrast, in Lebreuilly, *et al.* a sharp (compared to the interaction energy), square shaped emission profile provides an effective chemical potential for photons [278]. Such an emission profile may be created with Floquet engineering. Instead of modulating the atomic energy level at a single frequency, it may be driven by a continuum of frequencies, from near DC up to a cutoff. This should produce an emission spectrum that is uniform up to the cutoff frequency and that falls to zero with a width set by the bare linewidth. Additional manipulation with EIT may enable narrowing the bare linewidth and sharpening the emission edge.

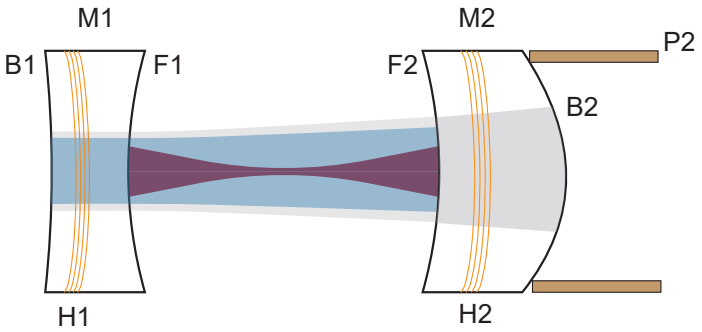

Figure 7.3: **A Two Mirror Single Mode Cavity Rydberg Polariton System.** To optimize future single mode cavity Rydberg polariton experiments, it is desirable to combine the probe and control build-up cavities into a single apparatus so that misalignment is strongly reduced. In a two mirror cavity setup, the central problem is to ensure that the atoms all experience a strong control field despite nodes in the build-up cavity. This may be accomplished by trapping the atoms at 960 nm, so that the trapping lattice overlaps with the control field lattice. The coatings are as follows. B1:PR(480,960)+AR(780,1560); F1:HR(780)+PR(1560)+AR(480,960); F2:PR(480,780,960,1560); B2:HR(960)+AR(480,780,1560). The 780 nm cavity (red) is all in-vacuum and therefore may be made low loss. As shown, the cavity is single-ended with the over-coupled port on M2; this can be varied depending on application. The piezo P2 (tan) locks this cavity to resonance with the atomic resonance. The 480 nm cavity includes the bulk of mirror M1, limiting the finesse and build-up factor. Heating the mirror M1 with heating wires H1 locks this cavity to the desired atomic resonance. The same reflective surfaces also define a 960 cavity for trapping the atoms. While the 960 trapping frequency may be varied over a free spectral range in order to assure resonance with this cavity; however, the phase of reflection off surface F2 must be controlled to ensure that antinodes 960 align with antinodes of the 480 cavity. The 960 reflection phase is controlled by heating the mirror M2 with heating wires H2 to control the resonance of a single ended 960 cavity that resides entirely within M2.

atomic ensemble for both stabilization and strong interactions.

7.1.4 Quantum Information Processing

7.1.4.1 Quantum Non-demolition Measurement

Microwave manipulation of Rydberg states offers several intriguing experiments relevant for quantum information processing and quantum control. A simple protocol for quantum non-demolition measurement [351, 352] of a single photon begins with optically π-pulsing into the cavity a single dark polariton. Adiabatically extinguishing the control field converts the polariton into a pure Rydberg excitation that a microwave π-pulse can then transfer into a similar collective state of a different Rydberg level. That ancillary Rydberg excitation

will then be quite long lived compared to dark polaritons. Turning back on the original control field (which does not affect the ancillary Rydberg state) and probing on the dark polariton resonance then allows many photons to attempt to transmit through the cavity at a mean photon rate much less than one per polariton lifetime. These photons will not transmit if the ancillary Rydberg state is present due to blockade, while they will if the original probe pulse did not excite a dark polariton. Thus Rydberg blockade can enhance the detection probability of a single cavity photon. Having detected the presence or absence of the initial excitation, the control may be extinguished, another microwave π-pulse can convert the ancillary Rydberg excitation back into the primary collective Rydberg state, and the control field adiabatically turned back on, so that the original dark polariton is read out as a cavity photon. If this second step is completed, principally limited by dephasing of the ancillary Rydberg state, then this protocol corresponds to Rydberg enhanced quantum non-demolition measurement of a single photon. This protocol may be improved by the detection polaritons accessing a lower principal quantum number so that the mean photon number during this probe may be higher. This requires the addition of a second control laser. The stored probe polariton will blockade the sample less well, but this may be offset by the increased rate of detection photons improving discrimination between the blockaded and non-blockaded cavity. This is particularly likely to be helpful if dephasing of the stored probe polariton strongly limits the detection time to only a few polariton lifetimes.

In a future over-coupled single-ended cavity (see Fig. 7.3 for an ambitiously efficient implementation), this protocol easily extends to the production of Schrödinger cat states of light [353], simply by initializing an equal superposition of an empty cavity and a single Rydberg state, i.e. performing an initial optical $\pi/2$-pulse and extinguishing the control field. If the Rydberg enhanced detection fidelity is better than the *pi*-pulse fidelity, the non-demolition measurement protocol may be continued until the microwave π-pulse, which is then replaced by a microwave $\pi/2$-pulse to prepare an equal superposition of a primary Rydberg excitation and the ancillary Rydberg excitation. A control field pulse then removes

the primary excitation, leaving the system in an equal superposition of an empty cavity and a Rydberg excitation which blockades the cavity. However it the system is prepared, immediately reflecting a single photon off of the over-coupled cavity mirror then produces a Schrödinger cat state since the reflection phase depends on the presence or absence of the auxiliary Rydberg excitation.

7.1.4.2 Rydberg Spin Squeezing

Squeezed atomic states, displaying quantum correlations between multiple atoms, are a promising resource for precision measurement, metrology, and sensing. Standard interferometric techniques achieve an increased sensitivity with the number of atoms N that grows as $\sqrt{N}$ due to the quantum projection noise associated with independent atoms. This limit corresponds to shot noise and is often in these contexts called the standard quantum limit. Quantum correlations between the atoms enable more sensitive measurements that beat the standard quantum limit [354, 355]. Ultimately, measurement sensitivity is limited by the Heisenberg limit, at which it grows with the atom number N. Saturating the Heisenberg limit requires highly entangled states such as Schroedinger cat or GHZ states [356]. Such states are difficult to prepare for large atomic ensembles and decohere rapidly, while less highly entangled squeezed states of many atoms may be prepared with a relatively accessible Hamiltonian, $H = \Omega_t \hat{J}_x + V_{OAT} \hat{J}_z^2$. The first term describes a transverse field which drives the atomic transition, a rotation of the collective Bloch vector about the x axis of the Bloch sphere, while the second 'squeezing' term shears the Bloch vector about the equator. The application of this second term is called one-axis twisting (OAT) [357]. While a more complicated two-axis twisting Hamiltonian can produce states that directly saturate the Heisenberg limit [357], simply applying the transverse field, either constantly or in pulses, along with the OAT Hamiltonian appears to produce states that very nearly approach the Heisenberg limit [358, 359].

Rydberg atoms are a promising route towards the implementation of the OAT Hamiltonian in metrologically relevant systems [360, 361]. Although developed for use in precision measurement and metrology, Rydberg based OAT presents a quantum many-body problem due to the finite range of the Rydberg-Rydberg interaction. This is made yet more fascinating by the addition of a transverse field which serves to suppress quantum fluctuations as squeezing proceeds.

In our system, we can explore this physics, although we do not make use of Rydberg polaritons. Instead, this would be a more standard atomic physics system where atoms play the central role, and the cavity serves to enhance read-out. We prepare our cold trapped atomic gas in a superposition of two ground hyperfine ground states. These are the effective spin states. An off-resonant two photon transition to the Rydberg state dresses the $F = 1$ hyperfine ground state[§] while the cavity monitors the number of atoms in the $F = 2$ hyperfine ground state. Meanwhile microwave driving (or Raman transitions) provide the transverse field. At high principal quantum numbers, critical radius around $R_c = |C_6/\Delta|^{1/6} = 10$ μm are available using our full control field Rabi frequency $\Omega = 2\pi \times 2$ MHz and a detuning $\Delta = 20\Omega$. The soft-core interaction energy $V(r) = V_0 R_c^6/(r^6 + R_c^6)$ then saturates at $V_0 = \Omega^4/\Delta^3 = 2\pi\times250$ Hz[‡]. Spin squeezing requires a product of interaction time and soft-core energy $V_0\tau < 1$ indicating that spin squeezing should occur within approximately half a millisecond [360]. This compares favorably to the lifetime of the resulting dressed state, which is set by the lifetime of the Rydberg state reduced by $(\Omega/\Delta)^2$. At an atomic density of $\rho = 10^{-11}$ cm^{-3}, 100 atoms lie within the 10 μm critical radius, which yields an optimal squeezing parameter of $\xi^2 = N(\Delta J_{\perp,\mathrm{min}})^2/\langle\vec{J}\rangle^2 = 0.03$ as the atomic sample grows in size [360]. In the limit of strong squeezing, this directly reduces the distribution of the

§. A single UV laser near 297 nm could also provide this dressing.

‡. Intuitively, this maximum shift arises because at far distances, the Rydberg state is ac Stark shifted by the detuned laser by an amount Ω^2/Δ. When the two atoms come close, their Rydberg lines move away in energy causing the detuning Δ to increase, until the ac Stark shift is effectively zero. The Rydberg dressing of the ground state admixes Ω^2/Δ^2 of the Rydberg state into the ground state, to the full shift of the dressed ground state is $V_0 = \Omega^4/\Delta^3$.

collective Bloch vector along the z direction, corresponding to uncertainty in the atomic in the upper hyperfine manifold versus the lower hyperfine manifold. Thus the fluctuations in the dispersive cavity shift should reduce by a factor of ξ.

The probability for an atom to scatter a photon into the cavity versus free space is the single atom cooperativity η_0. In our system, this is less than one, so many photons must be scattered into free space in order to measure the atomic population. As long as the cavity is on the cycling $|2,2\rangle \rightarrow |3,3\rangle$ transition, each atom can scatter around 10,000 photons before falling into the lower hyperfine manifold. Thus we can easily measure the populations in the upper hyperfine manifold at the cost of destroying any coherence between the atoms. A future cavity with a single atom cooperativity greater than one would enable projective measurement into correlated states.

There are several interesting directions to take this investigation. First, it would be fascinating to see Rydberg induced spin squeezing continue to drop as the atomic sample size increases beyond the critical radius, as this indicates a non-trivial propagation of entanglement over several interaction events. Secondly, this enables exploring the role of a transverse field in suppressing quantum fluctuations and enhancing the spread of entanglement [358, 359]. In small samples with effectively infinite range interactions, a constant transverse field is predicted to produce strong periodically structured squeezing [358]. In larger samples, the combination of the finite range OAT interaction with a transverse field has not been explored theoretically. Does transverse driving help to increase the effective range of the soft-core interactions? Are there multiple regimes in the time dynamics of the resultant squeezing? The combination of these ingredients is natural in our platform and presents a rich quantum many-body problem.

7.1.4.3 Quantum Repeater

We can also build a quantum repeater [86–89, 91, 362, 363], a device for long range entanglement generation which is a necessary requirement for quantum key distribution and quantum secure communication. The basic problem is the generation of entanglement between particles that are spatially separated. Entangled photons pairs may be produced and distributed with optical fibers, but inherent loss in optical fibers limits the probability that these photons reach their destinations. For instance, state-of-the-art optical fibers in the telecom band have an attenuation of 0.2 dB/km, implying an attenuation of 900 dB for a transmission from New York to Los Angeles. Quantum state purification and distillation schemes require minimum state fidelities, and so do not directly enable long distance communication [363]. Replacing a single long fiber with an array of fiber-linked repeaters with fixed separation promises to reduce the exponentially poor scaling of entanglement distribution fidelity with distance to polynomial scaling. This operates by successive operations of entanglement swapping [364]. The question then is transfered onto the choice of repeater nodes and transmission protocol that optimizes this entanglement distribution.

There are numerous schemes for realizing quantum repeaters. Many of these rely on probabilistic entanglement generation and probabilistic entanglement swapping which together greatly lower the efficiency of entanglement swapping. In contrast, Han, *et al.* offer a quantum repeater protocol based on deterministic Rydberg-blockade-mediated entanglement swapping operations [87, 88]. Although these proposals use free space coupling of the traveling photons to the atomic gas, a well impedance matched moderate finesse optical cavity promises to increase the atom photon coupling dramatically. These ingredients naturally come together in our system, where our cavity enhanced optical depth exceeds 100, and Rydberg excitations provide strong deterministic interactions.

7.1.4.4 Rydberg Based Quantum Computation with Cavity Enhanced Read-out

With further developments to improve a single mode cavity, these applications in quantum information processing could be optimized. Reducing the cavity length by moving to a two mirror cavity allows the finesse to be increased at constant cavity linewidth, which sets the data collection rate. Incorporating a variable transmission low loss mirror[◇] allows for in-situ optimization of impedance matching and the flexibility to convert between a conventional two port cavity at moderately high finesse (e.g. 40,000) and a single-ended cavity at lower finesse (e.g. 4,000) depending on the application.

More generally, these discussions suggest a new architecture for quantum information processing, somewhat similar to existing neutral atom systems using Rydberg excitations for fast multiqubit gates. A perennial challenge in these systems is efficient read-out of the quantum state. Wrapping the neutral atom array with a moderate finesse optical cavity offers a dramatic enhancement in readout efficiency. A significant challenge is that since single atoms form the computational qubits, the light-matter coupling does not obtain a collective enhancement.

This suggests implementing a two species experiment, with an atom array for quantum computing collocated with a dilute gas for cavity enhanced readout, depicted in figure 7.4. Cross-species Rydberg-Rydberg interactions cause blockade in the read-out species and a resulting reduction in the effective read-out species atom number. The tweezer wavelength for trapping the computational species can be chosen to repel the read-out species to maintain qubit coherence.

◇. This is an exciting ongoing research project in which a short additional cavity plays the role of a mirror in a standing wave cavity. Tuning the length of this cavity within a few linewidths of resonance controls the transmission from complete transmission down to $\sim 1/F$. Effectively, this cavity acts as a variable transmission mirror.

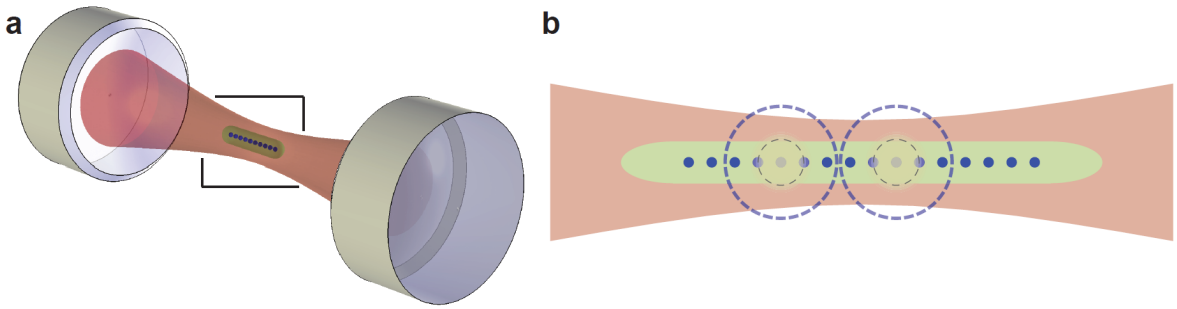

Figure 7.4: **Cavity Enhanced Rydberg Array Quantum Computation.** **(a)** A two mirror cavity defines an optical mode coupled to a two species ensemble, e.g. Rubidium and Cesium. One of these mirror is variable transmission (not shown) to optimize impedance matching. (**b**) A tweezer array supports a 1d line of Rubidium qubits (blue) which spatially overlap with a cigar shaped ensemble Cesium atoms (green). Multi-qubit gates are enabled by long-range Rydberg-Rydberg interactions (blue dashed circles). Shorter range cross-blockade with the Cesium ensemble (yellow shading) allows high-fidelity, fast, non-destructive read-out of the qubit $\langle \sigma_z \rangle$ operator.

Alternatively, a collocated 2d tweezer array and read-out species pancake could be combined with a *confocal* cavity perpendicular to the atom plane. Placing the array significantly off-center enables cavity enhanced cross-blockade imaging of the entire array or subsections down to a single atom simply by probing with a larger or smaller beam.

7.2 Apparatus Upgrades

To continue studies of fractional quantum Hall physics with photons, it will be necessary to upgrade the experimental apparatus. There are two critical pieces to this. The first critical upgrade is to make a threefold degenerate 780 nm cavity without the disorder-induced instability that the current cavity experienced. Otherwise, the new cavity can have similar parameters (waist size, finesse). The second critical upgrade is an improved blue build-up cavity. We will discuss each of these in turn.

A major limitation of the current experimental cavity is that it cannot achieve degeneracy to form a Landau level of photons without a prohibitive increase in loss. This is due astigmatism within the cavity which arises from the non-normal incidence of the cavity mode on

curved mirrors. It is therefore a very intriguing future direction to replace all curved mirrors with flat mirrors and to use two intracavity lenses to provide transverse confinement*. The nonplanar arrangement of flat mirrors provides the same round trip rotation, but the focusing from perpendicular propagation through lenses produces no astigmatism. We did not consider this option previously because our belief that intracavity optics would introduce unacceptable additional intracavity loss. However, using super-polished plano-convex fused-silica substrates with state-of-the-art IBS anti-reflection coatings, preliminary tests indicate only 0.02% additional round trip loss from this configuration. This additional loss would therefore be small to negligible for an experimental cavity with finesse less than 10,000. Beyond enabling degeneracy of the Landau level only limited by the spherical aberration of the lenses, removing astigmatism also ensures that the cavity modes are everywhere clean Laguerre Gaussian modes. Although I believe this to be a very promising approach that the next iteration of the experiment should employ, a significant challenge will be obtaining super-polished and AR coated lenses with a sufficiently short focal length. For the same radius of curvature, a glass lens (index of refraction 1.5) is approximately four times weaker than a mirror. While the available physics improves with a smaller waist size since a lower principal quantum number can be used, making the waist size much smaller than the existing 19 μm causes the mode size on the mirrors (or lenses) to become comparable to the optics' radii, thus causing additional loss. Without shortening the distance between the atoms and the closest optics, which has serious electric field implications, we are therefore already at something of a sweet spot for the cavity waist size.

The lower mirrors of the 780 cavity have been high reflectors, one with the fast locking piezo and the other with the long throw piezo. It would be useful to have optical access along this axis, but it is unclear how to make this compatible with the piezos (since a ring piezo's

$\star$. Two intracavity lenses at either end of the lower arm make the resulting cavity like a bowtie cavity with a small waist in the shorter arm, and a large waist in the longer arm. A single lens placed exactly opposite the desired waist location would behave like a two mirror cavity, in which it is quite challenging to achieve a small waist size.

center bore is at a significant angle to the cavity mode). We worked hard to manage (and it remains a major concern) the buildup of charges on the lower 780 cavity mirrors. If we cannot use intracavity lenses, we may be able to mitigate this charge build up by placing below the IBS coating a metal layer which is grounded to the cavity structure. This would provide image charges to greatly reduce the electric field produced by charge buildup (by a ratio of the IBS coating thickness to the mirror radius, or between 100 and 1000). The main question here is whether the metallic coating can be coated in fused silica, super-polished, and finally IBS coated without delaminating.

Whichever route we take, it is worthwhile to make the cavity single ended by a ratio of around 9:1, so that 90% of intracavity photons leak out a single port. A much larger ratio will make probing the cavity hard difficult, which is useful for initial alignment, but going to a nearly single-ended configuration can increase our total detection rate by almost a factor of two or permit a similar increase in finesse[§].

The blue buildup cavity had several issues. First, we aimed too high for the finesse resulting in a last minute switch to a non-IBS coated eBay mirror. This is easily solved by purchasing an appropriate IBS coated high transmitter along with HR coated mirrors. Second, ensuring relative alignment between the two cavities is quite challenging, especially due to the thermal cycle involved in baking the chamber. A promising option is to use a two mirror single ended ($\sim$ 10:1) confocal cavity driven off center to obtain a running wave mode. Since the cavity is confocal, a displaced spot will propagate through the cavity in a bowtie-like pattern no matter the input location, solving the major issue of aligning the 780 and 480 cavities. This is limited by the requirement that the spot be sufficiently displaced (more than $3w_0$, see Fig. 7.5) from the optic axis that the crossing beams do not interfere with the desired

§. This is cast as a tradeoff since increasing the reflectivity of the input port decreases the linewidth but does not change the rate of photons leaking out the output port (assuming a constant single intracavity photon). The linewidth reduction is offset by the increased fraction that emits through the output port. So taking the win in finesse by increasing the input port reflectivity does not improve the data rate. Alternatively, the cavity could be made single ended at constant finesse, and then the detection rate would be improved.

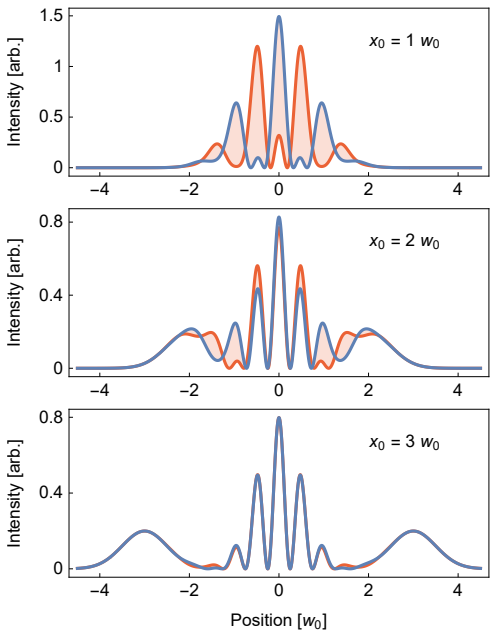

Figure 7.5: **Confocal Buildup Cavity Intensity.** A confocal cavity driven off-center has a bowtie running wave mode with two straight arms and two crossing arms. For small drive displacements, all four beams interfere to produce fringes perpendicular to the optic axis as well as along the optic axis (shaded curves plotted at extrema along the optic axis to reveal z dependent interference). As the drive displacement increases, the interference along the optic axis disappears.

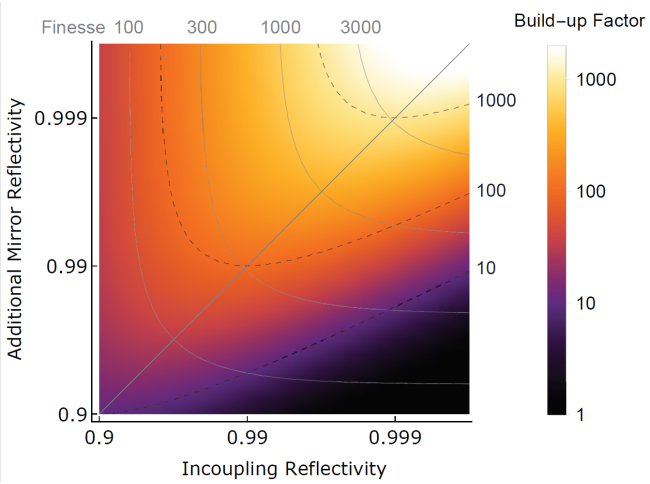

Figure 7.6: **Buildup Factor.** As the reflectivities of the two mirrors of a buildup cavity are the intensity buildup factor I_{circ}/I_{inc} changes nontrivially. Increasing the reflectivity of the non-incoupling mirror always improves the build-up factor, while whe reflectivity of the incoupling mirror creates an optimum in the build-up factor when the two reflectivities are equal. This indicates that a single ended buildup cavity driven through the higher transmission port is the ideal form for the buildup cavity, although past a reflectivity ratio of a few ($\sim$ 5:1) the benefit saturates. The dashed lines correspond to buildup factors of 10, 100, and 1000, while the gray curves overlay contours of constant finesse. These contours are, of course, symmetric between the two reflectivities.

straight beam to produce a rapidly changing blue intensity along the cavity axis. Spherical aberration will also limit the maximum allowed spatial translation of the drive before the confocal degeneracy is broken and the displaced spot is no longer a stationary state. Finally, we wish to use a circularly polarized control field, but birefringence in the mirror surface could split out linearly polarized eigenmodes. Although these last two limitations are made less serious by designing a relatively low finesse (several hundred) buildup cavity, these could prevent this design from being ideal. Both mirrors of the confocal cavity will need piezos, one fast locking piezo and a second long throw piezo to ensure confocality. To reduce the effect of charge buildup on the mirror surfaces, the cavity mirrors should be recessed by more than their diameter to provide passive electric field shielding. This recess may also allow

for the angle between the two cavity modes to be reduced. While not essential, this would certainly help maximize the Clebsch-Gordons of our relevant transitions and ensure that the transitions stay closed. Since two reflections are off the same mirror, this cavity will behave like a four mirror cavity

If the confocal blue cavity is not a good option, we should use a single ended four mirror twisted cavity to have circularly polarized eigenmodes. We can ensure good alignment between the two cavities by replacing the custom flange with a new version that incorporates a vertical translation feedthrough that actuates an inner concentric tube. Then we mount the 780 cavity from flange and the 480 cavity on the concentric tube, so that we adjust the vertical alignment between the two cavities via the external translation stage.

The existing electrode system worked well, so a future cavity structure should replicate that (see Appx. B.1.2). The future structure should also enable appling a voltage to the entire cavity structure, as this was essential for stabilizing our electric field environment. Similarly, the heating wire system worked well and have been very useful. The future structure should incorporate a similar heating wire, twisted so that no magnetic field is produced.

More optical access, particularly copropagating with the cavity modes, is always useful. Making the extra access slots bigger and horizontal would provide easier access to the atoms. As long as these slots are deeper than they are wide, they will effectively shield any electric field from outside the cavity, e.g. piezo wires, electrode wires, or charge buildup on the chamber windows. While providing access through the 780 cavity mirrors is difficult due to the presence of the piezos (although perhaps the fast piezo can be short enough to provide access), the blue mirrors should be AR coated except at 480 nm so that various beams can propagate along the blue cavity axis. In particular, it has been very helpful in the existing apparatus to have the control field, magnetic field, and optical pumping beam all copropagating.

To improve the experimental duty cycle, it would be a great improvement to be able to reapply degenerate Raman sideband cooling during probing—we currently only reapply the optical pumping beam. Doing so requires ramping down and back up the magnetic field, since the dRSC magnetic field is relatively small but the magnetic field is kept large while probing to maintain the atomic polarization. In-vacuum magnetic field coils would be very helpful for this, since they would not excite eddy currents in the steel chamber and copper gaskets and therefore could much more quickly change the magnetic field. To produce a relevant field, these coils must be rather bulky and so well integrated into the cavity structure design. Thicker wire with more current flowing through fewer turns combined with a suitable driver will help ensure that the speed of these coils is maximized.

7.3 Future Experiments in Fractional Quantum Hall Physics

As discussed in section 7.1.3, autonomous stabilization of a strongly interacting cavity mode is a near term goal. A major motivation for this effort is the resulting ability to stabilize strongly interacting many-body states. The principle requirement is that the stabilized state be incompressible with respect to atom number, i.e. adding an extra particle costs a significant amount of energy [344]. A Laughlin state with a finite number of accessible modes is just such a system, and so may be stabilized by such a scheme. This is one of the most promising routes towards the creation of larger Laughlin states of ~ 10 particles that are then necessary to explore topological order and detect anyons.

One immediate question is then, how can we limit the number of accessible modes. In chapter 6, we were able to do so since the mode degeneracy was entirely engineered through our Floquet scheme. However, this becomes a problem in a degenerate cavity. Adding a real space potential, either via mirror deformation or ac Stark shifts on the atomic sample, offer one route to limiting the available mode space. However, even a step potential yields a

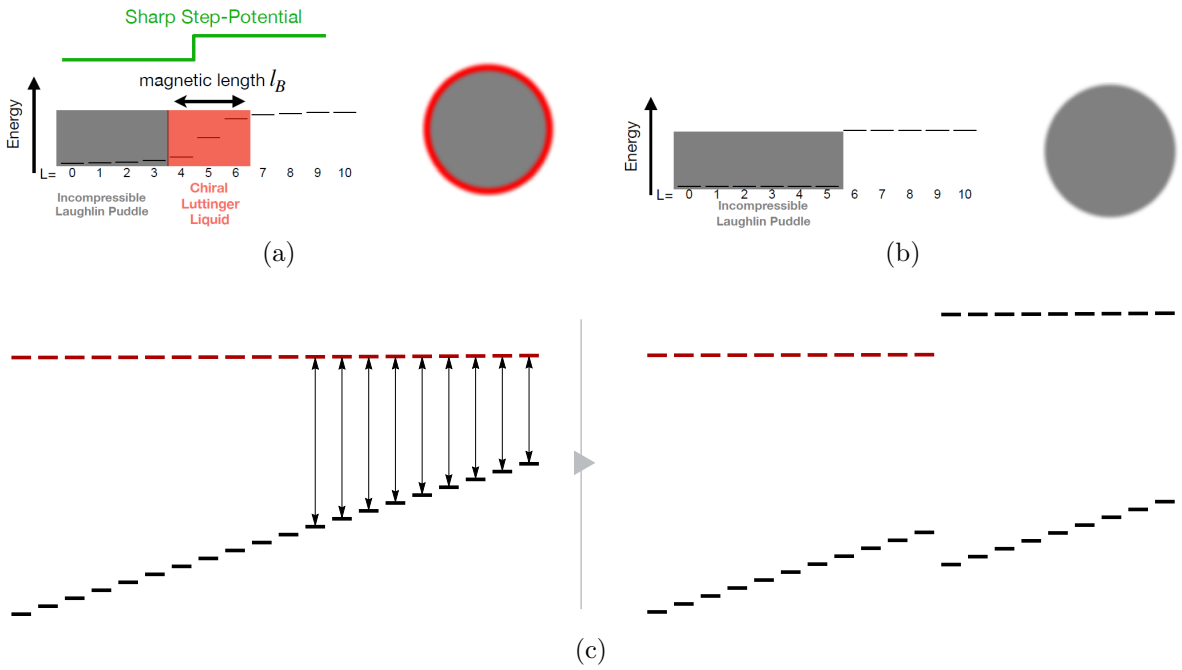

Figure 7.7: **Manipulation of a Landau Level for Future Manybody Experiments.** **(a)** Adding a real-space potential for dark polaritons confines particles to a finite Laughlin puddle. However, several angular momentum states reside at intermediate energies, even for a step potential (see Ref. [365]). This introduces a chiral Luttinger liquid at the edge into which particles may be injected for with little energetic cost. **(b)** Non-local couplings can shift *angular momentum states* and thus create a finite incompressible Laughlin puddle without a compressible chiral Luttinger liquid at the edge. This eases requirements for dissipative stabilization of a many particle Laughlin state. **(c)** An implementation of this level scheme is provided by off-resonantly coupling the science cavity Landau level to a second, non-degenerate Landau level of an auxilliary cavity. An EOM in the auxilliary cavity can make up the non-degeneracy between cavity modes selectively, shifting target modes while leaving others unaffected.

smooth variation in angular momentum mode energies due to their large spatial amplitude overlap (see Fig. 7.7a). This produces an incompressible Laughlin puddle coupled to a chiral Luttinger liquid at the edge*. This corresponds to the zero energy (and thus compressible) edge modes on a Harper-Hofstadter lattice. Can this system be stabilized? If the atomic sample used to stabilize them were small, i.e. well within the Laughlin puddle with little overlap to the chiral Luttinger liquid, it seems likely to be successful. Atoms probably need to overlap at least with mode $l = l_{max}/2$ so that particles can collide and reach a large angular momentum. But, to ensure effective stabilization we probably need a large sample. On the other hand, it may not matter much if we pump the Luttinger liquid. It is compressible,

$\star$. Note that Ref. [366] indicates that this picture may be incomplete.

so we can keep putting photons in at the edge, but they will interact and therefore decay rather rapidly. There might be an increased photonic density at the edge, but we could just ignore that in future experiments measuring density (for instance, to measure anyon statistical phase via Ref. [294, 295]).

Should we be concerned about scattering of photons from the Laughlin state into the Luttinger liquid? This scattering should presumably take place much like scattering of photons within the dilute Landau level that fills the Laughlin state in the first place. So then we have an additional loss channel out of the Laughlin state; however it is not at all clear that this is qualitatively different or worse than the outcoupling through the mirrors, with perhaps the exception that it is localized. The Laughlin state fills states $l = 0$ to $l = l_{max}$, while the edge occupies states $l = l_{max} + 1$ to $l = l_{max} + \delta l_{edge}$, with $\delta l_{edge} \sim \sqrt{l_{max}}$ as the size of the Laughlin state becomes large. So the coupling between the Laughlin state and the chiral Luttinger liquid primarily adds additional loss for the Laughlin state orbitals within δl_{edge} of l_{max}. That is, the outer annulus of approximately the edge width *within* the Laughlin state experiences added loss due to the coupling with the edge. Since the edge width is constant as the Laughlin state grows in size, this effect can be made relatively small, indicating that dissipative stabilization should be compatible with a real-space step potential provided the system size is large enough.

Intriguingly, spatially nonlocal coupling of states can provide a sharp discontinuity in angular momentum space, resulting in an incompressible Laughlin puddle *with no edge*. Such a state can be stabilized regardless of system size since it costs significant energy to add additional particles everywhere. As an example of what 'spatially nonlocal coupling' might mean, we have only to look at the Floquet scheme we already implemented. However, this does not scale well with system size. The basic goal is to find an operation that acts directly on angular momentum states rather than real space. Coupled cavities are one place where this is possible. Coupling the physics cavity to a second nonplanar cavity that is

far from degeneracy with the physics cavity offers angular momentum selective coupling. For instance, if the second cavity's non-degenerate Landau level passes through degeneracy with the physics cavity's Landau level at a finite mode number, the two cavities will couple and split out their modes near this crossing. This can sharply remove one or two modes from the physics cavity Landau level, but does not provide a sharp feature that can remove $\sim \sqrt{l_{max}}$ modes. Instead a low modulation depth EOM inside the additional cavity can provide mode dependent couplings controlled by the drive frequencies and amplitudes (see Fig. 7.7c). While this is thought provoking possibility, it should not be necessary in order to stabilize and study a larger Laughlin state.

The prospect of an autonomously stabilized several particle Laughlin state raises general questions. What is the steady state emission from such a system; what information does the emitted light field contain? From a condensed matter point of view, we want to measure quantities associated with a topological phase of matter rather than a particular model state in that phase. What are the right quantities to measure?

The first of these questions is only clear conditioned on measuring a number of photons equal to the number of polaritons, in which case the emitted field straightforwardly follows the state of the system (see Appx. A.3.4). However, the emitted field will often contain fewer than the maximum number of particles. This may be avoided by designing future experiments around pulsed procedures, where a state is prepared and then quickly read-out by, e.g. rapidly decreasing the dark state rotation angle to convert polaritons into photons and turn off interactions.

The second of these questions gets at the heart of what topological order is. Given the great difficulty of measuring particular patterns of entanglement, the most direct probes of a particular topological phase of matter are topological invariants and quasiparticle statistics. We can measure the filling factor through density of states away from the cone tip, and mean orbital spin from the build up of state density at the cone tip, much like in chapter 4.

In fact, this technique generalizes not just to Laughlin state, but also non-Abelian phases described by e.g. the Moore-Read state [265]. It is generically unclear if the width of state density excess at the cone tip relates to central charge generally, though future theoretical work may provide guidance.

Anyon statistics may be measured by braiding them, but while quasiholes may be pinned to defects which may be manipulated, this is certainly a daunting task. In fact, much simpler protocols are available. Quasiholes may be injected by tightly focused ac Stark shifts on the atomic sample without negatively affecting the state stabilization scheme. Subsequent observations of density depletion at the quasihole locations allow measurements of braiding phases of Abelian anyons [294] and fusion channels of non-Abelian anyons [295].

It could furthermore be fascinating to look in detail at a topological phase transition. The basic construction of hierarchy states [29] implies that at critical extrinsic number of quasiholes in a Laughlin state, the quasiholes will condense into a different state at the new filling factor with a new kind of topological order. With relatively few particles, this physics may be hard to observe. One place to look initially seems to be the N particle $\frac{1}{2}$-Laughlin state with $2(N-1)$ quasiholes, since that has the same number of particles and states as the N particle $\frac{1}{4}$-Laughlin state[§]. With true contact interactions, both of these states have zero interaction energy, and so nothing will drive the transition. However, as the range of interactions increases, the $\frac{1}{2}$-Laughlin state with quasiholes raises in energy. Although presumably dependent on the locations of the quasiholes (e.g. a regular lattice as opposed to all centered at the origin), this should then transition into the $\frac{1}{4}$-Laughlin state. The van der Waals $1/r^6$ interaction range may be long enough to drive this, but if not, microwave dressing to add a $1/r^3$ dipole-dipole interaction may then be sufficient to drive the transition. Numerical simulation should guide future implementations of this idea.

The tools necessary to implement and observe this are within our capabilities. Quasiholes

§. The N particle ν-Laughlin state extends up to $l_{max} = \frac{1}{\nu}(N-1)$.

may be generated and pined by an ac Stark shifting beam on the atoms controlled by a DMD. Imaging the single particle density would show depletions at the quasihole locations, but releasing the pins allows them to move and condense, so that the single particle density becomes uniform. By itself, this is not conclusive. However, initializing the system with two additional quasiholes and *not* releasing them (or potentially injecting them after condensation) should produce the $\frac{1}{4}$-Laughlin state with two quasiholes. Then the statistical phase of these quasiholes may be measured according to the procedure of Umucalilar, *et al.* [294]. This could then confirm the topological phase transition into the $\frac{1}{4}$-Laughlin state, and enable exploration of the dynamics of a topological phase transition.

Developing a new physical quantum Hall system with new probes and observables has helped to stimulate great excitement and optimism that previously unaccessible phenomena may be brought into reality. In the time between now and when these experiments are considered, I am sure that new proposals and schemes will have been developed, and I hope they greatly extend the realm of possibility for future experiments in our system. It has been a great pleasure to have struggled with these questions and to have had a small role to play in their elucidation.

APPENDIX A

SUPPLEMENTARY INFORMATION REGARDING EXPERIMENTAL RESULTS

A.1 Integer Quantum Hall Physics with Photons

A.1.1 A Brief Introduction to Magnetic Fields, Rotating Systems, and Landau Levels

Electrons confined in two dimensions and subjected to a constant perpendicular magnetic field $\mathbf{B} = B\hat{z}$ experience the minimal coupling Hamiltonian, which may be written in terms of the particle momentum $\mathbf{p}$, electron charge e and mass m, as well as the angular momentum $\mathbf{L}$ and vector potential $\mathbf{A}(\mathbf{r})$ defined according to $\nabla \times \mathbf{A} = \mathbf{B}$:

$$\begin{aligned} H &= \frac{1}{2m}\left(\boldsymbol{p} - e\boldsymbol{A}\right)^2 \\ &= \frac{\boldsymbol{p}^2}{2m} - \frac{eB}{2m}\boldsymbol{L}_z + \frac{(eB)^2}{8m}r^2 \end{aligned} \tag{A.1}$$

where the second equality follows from utilizing the symmetric gauge for the vector potential of a uniform magnetic field. In continuum systems, such a magnetic field gives rise to flat bands(Landau levels) and the quantum Hall effect [367], while in periodically modulated systems the generically chaotic Hofstadter butterfly spectrum results [54, 368]. In both cases the system exhibits topologically protected mid-gap edge-channels characteristic of the broader family of topological insulators [323]. While an actual magnetic field only acts in this way on a charged particle, synthetic magnetic fields have been realized in charge-

neutral systems; employing Raman couplings for cold atomic gases [369] and by 'spinning up' superfluids of helium and cold atoms [63, 370, 371]. The latter approach makes use of the fact that in a frame rotating with angular velocity $\mathbf{\Omega}$, there arises an $\mathbf{\Omega} \cdot \mathbf{L}$ term in the Hamiltonian [372]:

$$\begin{aligned} H &= \frac{\mathbf{p}^2}{2m} - \mathbf{\Omega} \cdot \mathbf{L} \\ &= \frac{(\mathbf{p} - e\mathbf{A})^2}{2m} - \frac{|2A|^2}{2m} \end{aligned} \tag{A.2}$$

Thus the rotating frame Hamiltonian is equivalent to a magnetic field $\mathbf{B} = \nabla \times \mathbf{A} = \frac{e\mathbf{\Omega}}{2m}$ plus a centrifugal anti-confining potential in the plane orthogonal to $\mathbf{\Omega}$: $V_{rot} = -\frac{1}{2} m \Omega^2 r_\perp^2$ [61]. It has thus been possible to stir a superfluid and observe the appearance of quantized vortices [63, 371] that crystallize into Abrikosov lattices. Such lattices are predicted to melt into fractional quantum Hall states as the particle density drops in a 2D system [373], but it has thus far been impossible to realize sufficiently strong interactions at sufficiently low densities.

A.1.2 Computing the Mode Spectrum of a General Nonplanar Cavity

The mode spectrum of an arbitrary n-mirror cavity may be computed by employing a 4x4 generalization of the ABCD or ray transfer matrix formalism [374]. We assume spherical mirrors but do account for astigmatism from non-normal incidence. The essential addition beyond the calculation for planar systems is the necessity to carry along a coordinate-system with us as we traverse the resonator. While coordinate transformations can be gauged away within a round-trip, we must start the next round-trip in the same coordinate system that we concluded the prior, so the rotation induced by non-planar reflections cannot be gauged

away. This is analogous to a Berry/Aharanov-Bohm phase acquired upon hopping around a plaquette in an optical lattice [307, 308] or the geometric rotation of a vector upon parallel transport along a closed path in curved space [375].

In our cavity the mirrors are all spherical but are rendered effectively astigmatic by non-normal reflections [374]. Because the astigmatism is (by definition) diagonal in the sagittal-tangential basis, it is convenient to employ this as a coordinate system at each mirror reflection, and perform coordinate rotations to remain in this basis for each mirror as we traverse the cavity.

For a cavity whose n mirrors are at locations $\boldsymbol{x}_j$, with radius of curvature ROC_j, we define the following quantities (assuming that the beam propagates through the resonator in increasing order of mirror index j, and for simplicity that the indices repeat at $j = n$). We further assume that the mirrors have themselves been oriented so that the axis of the cavity passes through the $\boldsymbol{x}_j$.

The vectors connecting sequential mirrors are

$$\boldsymbol{M}_{ij} = \boldsymbol{x}_i - \boldsymbol{x}_j, \quad \boldsymbol{m}_{ij} = \frac{\boldsymbol{M}_{ij}}{|\boldsymbol{M}_{ij}|}.$$

A vector normal to the plane of propagation in the plane of the mirror surface is

$$\boldsymbol{n}_j = \frac{\boldsymbol{m}_{j,j-1} \times \boldsymbol{m}_{j,j+1}}{|\boldsymbol{m}_{j,j-1} \times \boldsymbol{m}_{j,j+1}|}.$$

From these we define a propagation coordinate system before (IN) and after (OUT) the reflection off of mirror j, normal to the direction of propagation.

$$\begin{aligned} \boldsymbol{x}_j^{IN} &= \boldsymbol{n}_j & \qquad \boldsymbol{x}_j^{OUT} &= \boldsymbol{n}_j \\ \boldsymbol{y}_j^{IN} &= \frac{\boldsymbol{n}_j \times \boldsymbol{m}_{j,j-1}}{|\boldsymbol{n}_j \times \boldsymbol{m}_{j,j-1}|} & \qquad \boldsymbol{y}_j^{OUT} &= \frac{\boldsymbol{n}_j \times \boldsymbol{m}_{j,j+1}}{|\boldsymbol{n}_j \times \boldsymbol{m}_{j,j+1}|} \end{aligned}$$

We are now prepared to compute the rotation matrix that transforms from the coordinate system after mirror j to that before mirror $j+1$.

$$\boldsymbol{R}_j = \begin{pmatrix} \boldsymbol{x}_j^{OUT} \cdot \boldsymbol{x}_{j+1}^{IN} & \boldsymbol{y}_j^{OUT} \cdot \boldsymbol{x}_{j+1}^{IN} \\ \boldsymbol{x}_j^{OUT} \cdot \boldsymbol{y}_{j+1}^{IN} & \boldsymbol{y}_j^{OUT} \cdot \boldsymbol{y}_{j+1}^{IN} \end{pmatrix}$$

We can compute the angle on incidence at mirror j according to

$$\cos 2\theta_j = \boldsymbol{m}_{j,j-1} \cdot \boldsymbol{m}_{j,j+1}.$$

In a ray-matrix basis of the form $\begin{pmatrix} \text{x position} \\ \text{y position} \\ \text{x slope} \\ \text{y slope} \end{pmatrix}$, the propagation operator to move (half of the distance) between mirror $j-1$ and mirror j may be written independently for the x and y axes as

$$\boldsymbol{PROP}_j = \begin{pmatrix} 1 & 0 & |\boldsymbol{M}_{j-1,j}|/2 & 0 \\ 0 & 1 & 0 & |\boldsymbol{M}_{j-1,j}|/2 \\ 0 & 0 & 1 & 0 \\ 0 & 0 & 0 & 1 \end{pmatrix}.$$

The basis transformation from the coordinates from after mirror j to the coordinates before mirror $j+1$ is

$$\boldsymbol{ROT}_j = \begin{pmatrix} \boldsymbol{R}_j & 0 \\ 0 & \boldsymbol{R}_j \end{pmatrix}.$$

The matrix for reflection off of a mirror j, including astigmatism from non-normal reflection,

is

$$\boldsymbol{MIRROR}_j = \begin{pmatrix} 1 & 0 & 0 & 0 \\ 0 & 1 & 0 & 0 \\ \frac{-2}{ROC_j}\cos\theta_j & 0 & 1 & 0 \\ 0 & \frac{-2}{ROC_j}\frac{1}{\cos\theta_j} & 0 & 1 \end{pmatrix}.$$

Referenced to the plane midway between the $j = 1$ and $j = n$ mirror, the round-trip 4x4 ABCD matrix may now be written as

$$\boldsymbol{M}_{rt} = \prod_{j=1}^{n} \mathbf{PROP}_j \cdot \mathbf{ROT}_j \cdot \mathbf{MIRROR}_j \cdot \mathbf{PROP}_j \tag{A.3}$$

To compute the mode spectrum, we make use of techniques developed in Ref. [188]. The eigenvalues and corresponding eigenvectors of $\boldsymbol{M}_{rt}$ are computed numerically, and labeled ϵ_k and $\boldsymbol{V}_k$, respectively. When the resonator is stable, all of the eigenvalues have unit magnitude and come in conjugate pairs. We choose these pairs to be $k = 1, 3$ and $k = 2, 4$ so that we analyze $k = 1, 2$ as the two independent eigenmodes. The transverse mode spacings are

$$\nu_k = \frac{c}{L_{rt}} \frac{\log \epsilon_k}{2\pi i}, \tag{A.4}$$

where c is the speed of light and $L_{rt} = \Sigma_j |\boldsymbol{M}_{j,j+1}|$ is the round-trip cavity length.

To compute the TEM_{00} mode wavefunction and corresponding raising operators, we require

a few more definitions.

$$\boldsymbol{G} = \begin{pmatrix} 0 & 0 & 1 & 0 \\ 0 & 0 & 0 & 1 \\ -1 & 0 & 0 & 0 \\ 0 & -1 & 0 & 0 \end{pmatrix}$$

$$\boldsymbol{N}_k = \boldsymbol{V}_k^{\dagger} \cdot \boldsymbol{G} \cdot \boldsymbol{V}_k$$

$$\tilde{\boldsymbol{V}}_k = \boldsymbol{V}_k / \sqrt{\boldsymbol{N}_k / 2}.$$

Finally, we define the 2x2 matrices $\boldsymbol{B}$ and $\boldsymbol{K}$ as

$$\begin{pmatrix} \mathbf{B} \\ \mathbf{i\ K} \end{pmatrix} = \begin{pmatrix} \tilde{\mathbf{V}}_1 & \tilde{\mathbf{V}}_2 \end{pmatrix}.$$

The TEM_{00} mode may be written, up to a normalization constant (with $\mathbf{r} = \begin{pmatrix} x \\ y \end{pmatrix}$) as

$$\psi_{00}(\mathbf{r}) \propto e^{-\frac{\pi}{\lambda}\mathbf{r}^{\intercal} \cdot \mathbf{B}^{-1} \cdot \mathbf{K} \cdot \mathbf{r}}. \tag{A.5}$$

In the plane midway between mirrors 1 and n, the mode waists along the two (orthogonal) principle axes are thus given in terms of the eigenvalues d_i of the inverse complex beam parameter matrix $\mathbf{Q}^{-1} = i\mathbf{B}^{-1} \cdot \mathbf{K}$ by

$$w_k = \sqrt{\frac{\lambda}{-\pi Im(d_i)}}, \tag{A.6}$$

where λ is the wavelength of light propagating in the resonator.

The higher order transverse modes may be generated by using raising operators, given by

$$\hat{a}_k^\dagger = -i\sqrt{\frac{\pi}{\lambda}}\tilde{\mathbf{V}}_k^\dagger \cdot \mathbf{G} \cdot \begin{pmatrix} x \\ y \\ \partial_x \\ \partial_y \end{pmatrix}. \tag{A.7}$$

Therefore we calculate any transverse mode of the resonator as

$$\psi_{\alpha\beta}(\mathbf{r}) = \frac{1}{\sqrt{\alpha!\beta!}}\hat{a}_1^{\dagger\alpha}\hat{a}_2^{\dagger\beta}\psi_{00}(\mathbf{r}). \tag{A.8}$$

One must take care to interpret the mode indices α and β appropriately, as they may or may not correspond to a 'normal' choice of mode indices that naturally appear as parameters of a special function.

A.1.3 Understanding Twisted Resonators in the Ray Optics Picture

A twisted resonator composed of planar mirrors exhibits only round-trip image rotation, about the resonator axis, by small angle Θ [181], thus making each plane transverse to the resonator axis behave as a stroboscopically evolving non-inertial reference frame with Coriolis- and centrifugal- forces. To make the resonator stable, we must add mirror curvature, which provides confinement that competes with the centrifugal force. Exploring the Poincaré hit-patterns that result from plotting out round-trip ray trajectories is instructive for understanding the interplay of harmonic trapping and rotation that gives rise to both the lowest Landau level physics and the degeneracy that gives rise to Landau levels on a cone.

In Figure A.1.1a, we display a typical round-trip ray trajectory (henceforth "hit-pattern") in a twisted optical resonator with planar mirrors: the hit-location simply orbits the resonator

axis. The round-trip rotation angle Θ determines to the coarseness of the sampling of this circular orbit—we plot for a rotation angle $\Theta \sim 2\pi/60$.

In Figure A.1.1b, we display what happens when the mirrors induce harmonic trapping with a frequency equal to the rotation frequency – when the real-space rotation per round trip Θ induced by the resonator twist is equal to the phase-space rotation per round trip ϕ induced by mirror curvature. Under these conditions we are left with cyclotron orbits, corresponding to Landau level physics in the wave/quantum regime. These cyclotron orbits are not centered on the resonator axis, as a particle in only a magnetic field has no preferred axis (the gauge employed to compute dynamics may have a preferred axis, but this is a non-physical computational tool); the cyclotron orbits circulate around guiding centers $\mathbf{r}_c = \mathbf{r}_0 - \frac{\hat{\mathbf{z}} \times \mathbf{p}_0}{qB}$, where $\mathbf{r}_0$ and $\mathbf{p}_0$ are the initial ray position and (canonically conjugate) momentum, respectively. In our case the conjugate momentum has a physical significance: it is the ray slope relative to the resonator axis, times the total photon momentum $\hbar k$.

If the harmonic confinement is not perfectly compensated, as in Figure A.1.1c, the system again has a preferred axis given by the center of the trap, and there is a slow magnetron precession of the cyclotron orbit about this axis.

Thus far we have considered the situation of small real- and phase-space rotations per resonator round-trip, Θ, $\phi \ll 1$; this seemed appropriate, as we wanted to coarse-grain away the fact that our rays are repeatedly traversing the resonator structure. One can achieve such coarse graining in other limits, however: in Figure A.1.1d we consider the situation where the rays return near their initial locations after three round-trips: $|\Theta| + |\phi| \approx 2\pi/3$; alternatively, this situation may be viewed as setting the magnetron frequency to one third of the round-trip (axial) frequency. Under such conditions, we get three copies of the cyclotron dynamics—three copies of a photon in a magnetic field, rotated by 120 degrees with respect to one another. The coarseness of the coverage of the cyclotron orbit (and hence cyclotron frequency) is now determined by how commensurate either Θ or ϕ is with 2π. This is the

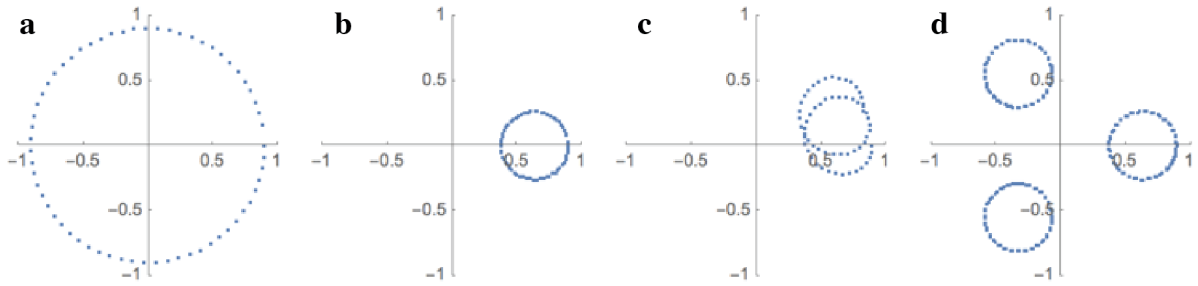

Figure A.1.1: **Round-trip hit pattern for rays in various twisted resonator configurations. (a)** For a twisted resonator without any harmonic confinement (mirror curvature), rays orbit the resonator axis. **(b)** When the harmonic confinement precisely cancels the twist-induced centrifugal anticonfinement, closed cyclotron orbits result. **(c)** A small amount of residual (anti)confinement produces a slow magnetron precession of the cyclotron orbit. **(d)** When this magnetron precession occurs at one third of the resonator round-trip frequency, we return to the zero-confinement configuration, with three identical copies oriented at 120 degrees from one another, corresponding to a cone such as in our system. Figure taken from Ref. [182].

configuration that we employ in the present experimental work. Note that neither Θ nor ϕ is individually constrained to be $\sim 2\pi/3$; only their sum (or difference) is constrained.

A.1.4 Extracting Hamiltonian Parameters for the Twisted Cavity

In order to extract from the ABCD matrix the parameters of our longitudinally coarse-grained dynamics, we employ techniques developed in a theoretical work on engineering photonic Floquet Hamiltonians [181]. We summarize the key results below:

1. For a system with ABCD matrix $\mathbf{M}$ describing round-trip propagation through the cavity, the effective Floquet Hamiltonian may be written as:

$$H = \frac{c}{L_{rt}} \left[\frac{1}{2} \begin{pmatrix} \boldsymbol{p}^{\mathsf{T}} & -\boldsymbol{x}^{\mathsf{T}} \end{pmatrix} \log(\boldsymbol{\beta M \beta^{-1}}) \begin{pmatrix} \boldsymbol{x} \\ \boldsymbol{p} \end{pmatrix} \right] \tag{A.9}$$

where $\boldsymbol{\beta} = \begin{pmatrix} 1 & 0 \\ 0 & \hbar k \end{pmatrix}$ converts between ray slope and ray transverse momentum,

which is the quantity which is canonically conjugate to ray position. L_{rt} is the round-trip propagation distance through the cavity.

2. Because our cavity requires $s = 3$ round trips to generate a low-energy manifold, the above result is employed with $\boldsymbol{M} \to \boldsymbol{M}^s$, $L_{rt} \to sL_{rt}$. This means that all frequencies are defined only modulo a third of the resonator free spectral range.

3. This Hamiltonian may then be completely decomposed according to:

$$H = \frac{1}{2}\left(\boldsymbol{p} - \beta_k \boldsymbol{\sigma}^k \cdot \boldsymbol{x}\right)^{\mathsf{T}} \boldsymbol{m}_{eff}^{-1}\left(\boldsymbol{p} - \beta_k \boldsymbol{\sigma}^k \cdot \boldsymbol{x}\right) + \frac{1}{2}\boldsymbol{x}^{\mathsf{T}}\boldsymbol{\omega}_{trap}^{\mathsf{T}}\boldsymbol{m}_{eff}^{-1}\boldsymbol{\omega}_{trap}\boldsymbol{x}, \qquad \text{(A.10)}$$

where

$$\boldsymbol{m}_{eff}^{-1} = \frac{1}{m} R_{\theta_m} \cdot \begin{pmatrix} \frac{1}{1+\epsilon_m} & 0 \\ 0 & \frac{1}{1-\epsilon_m} \end{pmatrix} \cdot R_{-\theta_m} \qquad \boldsymbol{\sigma}^k = (\boldsymbol{I}, \boldsymbol{\sigma}^x, \boldsymbol{\sigma}^y, \boldsymbol{\sigma}^y)$$

$$\boldsymbol{\omega}_{trap} = \omega R_{\theta_t} \cdot \begin{pmatrix} 1+\epsilon_t & 0 \\ 0 & 1-\epsilon_t \end{pmatrix} \cdot R_{-\theta_t} \qquad \beta_k = \left(\delta, \Delta_\times, \frac{i}{2}B_z, \Delta_+\right)$$

$$R_\phi = \begin{pmatrix} \cos\phi & \sin\phi \\ -\sin\phi & \cos\phi \end{pmatrix}$$

and the Pauli matrices operate on the real space vector $\boldsymbol{x}$.

This prescription enables us to extract the photon mass, residual trapping, and effective magnetic field. It also allows us to determine the extent to which mirror astigmatism produces tensor mass, trap astigmatism, and scalar and tensor defocus; the last of these (defocus) may be gauged away.

Applying this technique to the resonator structure of section 4.1 yields the following physical

parameters:

$$m \approx 1.06 \times 10^{-4}\, m_e \qquad \epsilon_m \approx 1.8 \times 10^{-2} \qquad \theta_m \approx -47.1^\circ$$

$$\omega_{trap} \approx 2\pi \times 180\,\mathrm{Hz} \qquad \epsilon_t \approx -4.2 \times 10^{-2} \qquad \theta_t \approx -42.8^\circ$$

$$l_B = \sqrt{\frac{\hbar}{qB}} \approx 22\,\mu\mathrm{m}$$

The key point is that while trap astigmatism persists all the way to the degeneracy point, the trap frequency itself goes to zero (and indeed changes sign), meaning that there is not residual astigmatism that persists at 'degeneracy' to destroy the Landau levels.

We employed $\boldsymbol{M}^3$ for the Floquet formalism since it is only on three round trips that rays return to the same cyclotron orbit in which they started (see Fig. A.1.1d), thus intuitively corresponding to a planar geometry. However, creating a single cyclotron orbit without threefold symmetry requires mixing the three flux-threaded cones. This aliases frequencies by one third the free spectral range rather than simply the free spectral range and is further manifested through an increased photon *mass*. The magnetic length is unaffected, as it is set by the cavity waist size and does not depend on the photon mass.

Therefore, to compare to experiment, we may have to add a multiple of one third of the free spectral range to the calculated cyclotron frequency. Quantitatively, the calculated $\nu_{FSR}/3 \approx 1.274$ GHz, so the predicted (bare) cyclotron frequency before aliasing is $\nu_{cyc}^{bare} = \nu_{cyc} + \frac{2}{3}\nu_{FSR} \approx 2.178$ GHz, which agrees with the measured cyclotron frequency of 2.167 GHz listed in section 4.1, up to corrections arising from imperfect knowledge of mirror curvature and geometric uncertainty from machining imperfections.

The aliasing of the cyclotron frequency directly causes an apparent discrepancy between the mass derived from the Floquet theory and that which we experimentally measure. Recalling the expression for the photon mass $m = \frac{4\hbar}{\omega_c w_0^2}$, we can see that the ratio of aliased to

actual cyclotron frequencies will give the inverse of the increased to actual photon mass: $\left(\frac{\omega_{cyc}}{\omega_c}\right)^{-1} = \left(\frac{0.370}{2.167}\right)^{-1} = 5.86$ while $\frac{m_{Floq}}{m_e xp} = \frac{10.6}{1.84} = 5.8(3)$.

Within a Landau level, the effective harmonic trapping is given by $\frac{1}{2}m\omega^2 r^2 \approx \frac{\omega^2}{\omega_{cyc}}(\hat{a}_R^\dagger \hat{a}_R + \hat{a}_L^\dagger \hat{a}_L)$ where $\hat{a}_{R,L}^\dagger$ adds a quantum of angular momentum within a Landau level, and promotes to the next higher Landau level, respectively. Thus the harmonic trapping induces a splitting between angular momentum states of $\frac{\omega^2}{\omega_{cyc}}$. We find that the harmonic trapping frequency ω goes as the square root of the axial resonator length defect, so the splitting between states in a nearly degenerate Landau level is linear in the length as observed experimentally.

A.1.5 Landau Levels on Flux Threaded Cones

Our system breaks apart the traditional lowest Landau level, which includes all non-negative angular momentum states, into three separate sets. These are $\{(0,0);(3,0);(6,0);\ldots\}$, $\{(1,0);(4,0);(7,0);\ldots\}$, and $\{(2,0);(5,0);(8,0);\ldots\}$. In our system, each of these sets is itself the lowest Landau level on one of three *cones*, which may be labeled by an integer $c = 0$, 1, or 2, respectively.

First we show that the $\{(0,0);(3,0);(6,0);\ldots\}$ set, or the $(0,0)$-Landau level may be said to be the lowest Landau level on a cone. This arises from a symmetry of these modes, namely that $\psi(\theta + 2\pi/3) = \psi(\theta)$. As depicted in figure 4.2d, this symmetry allows the identification of two rays from the center separated by an angle $2\pi/3$. The full plane is then three identical images of this cone. In the reduced space of this cone, the quantum of angular momentum is naturally three times larger than in the full plane, so the $(0,0)$-Landau level contains all allowed angular momentum states within this cone.

The other two sets are similarly lowest Landau levels on two other cones. The symmetry for

these is more complicated:

$$\psi(\theta + 2\pi/3) = e^{2\pi ic/3}\psi(\theta), \tag{A.11}$$

where c identifies on which cone the modes reside. We may then apply a different local gauge transformation to the modes of each set depending on c. If we write $\varphi(\theta) = \psi(\theta)e^{-ic\theta}$, then we recover the symmetry of a cone for all c, namely that $\varphi(\theta + 2\pi/3) = \varphi(\theta)$. Therefore, we justify the claim that each of the sets is a lowest Landau level on a different cone by appealing to symmetry condition of the modes of each set *after applying a different local gauge transformation for each set.*

The extra phase factor in the symmetry condition Eqn. (A.11) has an intriguing interpretation: these cones are threaded through the cone tip by a narrow tube of magnetic flux. The extra phase factor $e^{2\pi ic/3}$ appears like an Aharanov-Bohm phase from circling the cone tip if a magnetic flux of $-\frac{c}{3}\Phi_0$ were at the cone tip, where Φ_0 is the magnetic flux quantum. The possibility of extra magnetic flux reflects an inherent ambiguity in the definition of the $2\pi/3$ rotation operator $\hat{R}_3$, which is required to satisfy $\left(\hat{R}_3\right)^3 = 1$. Thus the three operators $\hat{R}_3$, $e^{2\pi i/3}\hat{R}_3$, and $e^{4\pi i/3}\hat{R}_3$ are equally good rotation operators, but physically they differ by the presence of an extra 1/3 and 2/3 units of the flux quantum. Interestingly, our system does not pick one of these cases, but realizes all of them, leaving it up to us which case to study.

A.1.6 Invariance Under Magnetic Translations of Lowest Landau Level Modes in the Laguerre Gaussian Basis

The wavefunctions of the lowest Landau level may be represented in the convenient form $\psi_l \propto z^l e^{-z\bar{z}/2}$, where $z \equiv \frac{x+iy}{w_0/\sqrt{2}}$ is a complex representation of the 2D particle position, with w_0 being the fundamental cavity mode's $1/e^2$ intensity radius. These modes are also the Laguerre Gaussian solutions to the paraxial wave equation [374].

It is not immediately obvious how the ψ_l translate, as each ψ_l seems to have a well defined center location at $z = 0$. Here we show that in fact any of the these levels arbitrarily translated in the x-y plane may be represented, up to an additional phase, by a sum over the states of the lowest Landau level. This phase reflects that the system is invariant under magnetic translations, not simple translations.

Suppose that the state we would like to represent is ψ_α centered at (x_0, y_0). We first define $z_0 = \frac{x_0+iy_0}{w_0/\sqrt{2}}$; we are inclined to see if $\psi'_\alpha = (z - z_0)^\alpha e^{-|z-z_0|^2/2}$ may be represented as a linear of the ψ_l. In fact, this is not possible, but the correct wave function differs by a spatially varying phase: $\phi = (z - z_0)^\alpha e^{-|z-z_0|^2/2} e^{(z\bar{z}_0 - \bar{z}z_0)/2}$, where the exponent in the second term is imaginary by construction. We now expand the first exponential, rearrange terms, and Taylor expand in powers of z

$$\begin{aligned}
\phi &= (z - z_0)^\alpha e^{z\bar{z}_0} e^{-\frac{|z|^2-|z_0|^2}{2}} \\
&= e^{-\frac{|z|^2-|z_0|^2}{2}} \sum_{n=0}^{\infty} \frac{\bar{z}_0^n}{n!} z^n \sum_{k=0}^{\alpha} \binom{\alpha}{k} z^k \, (-z_0)^{\alpha-k} \\
&= e^{-\frac{|z|^2-|z_0|^2}{2}} \sum_{n=0}^{\infty} \sum_{k=0}^{\alpha} \binom{\alpha}{k} (-z_0)^{\alpha-k} \frac{\bar{z}_0^n}{n!} z^{n+k} \\
&= \sum_{l=0}^{\infty} \left(e^{-|z_0|^2/2} \sum_{k=0}^{\min(l,\alpha)} \binom{\alpha}{k} (-z_0)^{\alpha-k} \frac{\bar{z}_0^{l-k}}{(l-k)!} \right) z^l e^{-|z|^2/2}
\end{aligned} \tag{A.12}$$

The final expression is clearly a sum over lowest Landau level wavefunctions, demonstrating the desired magnetic translational invariance. The additional phase required for the translation reflects that the translation operator in a magnetic field is not the simple translation $T = e^{-\frac{i}{\hbar}\hat{\boldsymbol{p}}\cdot\hat{\boldsymbol{r}}}$ but is instead the magnetic translation operator, $T_m = e^{-\frac{i}{\hbar}(\hat{\boldsymbol{p}}+e\hat{\boldsymbol{A}})\cdot\hat{\boldsymbol{r}}}$ in the symmetric gauge. The apparent preferred center of Laguerre Gaussian modes does not imply a preferred center for dynamics; in fact, the dynamics are translationally invariant and the

Laguerre Gaussian mode basis is ideal for writing the Laughlin wavefunction fo the fractional quantum Hall effect [15].

It is straightforward to extend this to our lowest Landau level consisting of modes $(\alpha, 0)$ with $\alpha = 0, 3, 6, \ldots$ under the requirement that we do not displace a mode alone, but rather create two additional displaced copies rotated to preserve threefold rotational symmetry. That is, we send $z_0 \to z_a = \hat{R}_3^a(z_0)e^{2\pi iab/3}$ for $a = 0, 1, 2$ and introduce the sum $\sum_{a=0}^{2}$. Without the presence of b in final exponent, we would only be expanding displaced modes of arbitrary angular momentum on the $c = 0$ cone; proper choice of $b = (c - \alpha) \mod 3$ will permit expanding a displaced arbitrary mode α on an arbitrary cone c, as will be justified below. Therefore we consider modes profiles of the form

$$\phi = \sum_{a=0}^{2}(z - z_a)^{\alpha}e^{-|z-z_a|^2/2}e^{(z\bar{z}_a - \bar{z}z_a)/2}e^{2\pi iab/3}$$

We perform Taylor expansion as before, so that

$$\phi = \sum_{n=0}^{\infty} e^{-|z_0|^2/2}\sum_{a=0}^{2} e^{\frac{2\pi ia}{3}(\alpha - n + b)}\left(\sum_{k=0}^{\min(l,\alpha)}\begin{pmatrix}\alpha\\ k\end{pmatrix}(-z_0)^{\alpha-k}\frac{\bar{z}_0^{n-k}}{(n-k)!}\right)z^n e^{-|z|^2/2}$$

Now, the sum over a yields 3 if $(n - \alpha) \mod 3 = b$ and 0 otherwise. This crucial condition justifies the original choice of b. If we want to expand our desired mode on the c cone, then $n \mod 3 = c$. Thus the equation above takes the form

$$\phi = \sum_{p=0}^{\infty} C(p, \alpha, c, z_0)z^{3p+c}e^{-|z|^2/2} \tag{A.13}$$

A displaced version of *any* angular momentum state about the origin may be constructed on a cone with only one third of the angular momentum states. For large displacements, on the cone the mode lives in flat space, so this expansion is exact, while in physical space (three

images of the cone) the only penalty is the addition of two copies with an appropriate relative phase. For smaller displacements, on the cone, the curvature at the cone tip significantly distorts the mode, while in physical space, the three copies interfere with each other. Only as the displacement goes to zero ($|z_0| \ll l_B$) and the three copies fully overlap and interfere does the restriction to one third of the angular momentum states prevent the construction of arbitrary states.

A.1.7 The Form of the N-particle Bosonic Laughlin State on a Cone

One a plane, the bosonic Laughlin wavefunction takes the celebrated form [15]

$$\psi_L \propto e^{-\sum_k |z_k|^2/2} \prod_{k<i} (z_k - z_i)^2 \quad \text{(A.14)}$$

This wavefunction takes the form of an exponential in all particle locations times a polynomial, known as the Jastrow factor, which for this state provides a second-order zero whenever two particles are in the same location, thereby minimizing the interaction energy. Variations to Laughlin states at other filling factors change the exponent in the Jastrow factor, while additions of quasiholes or quasiparticles correspond to additional terms, e.g. $\prod_k (z_k - z_{qh})$. To see that the Laughlin wavefunction is made up entirely of single particle states within the pla-

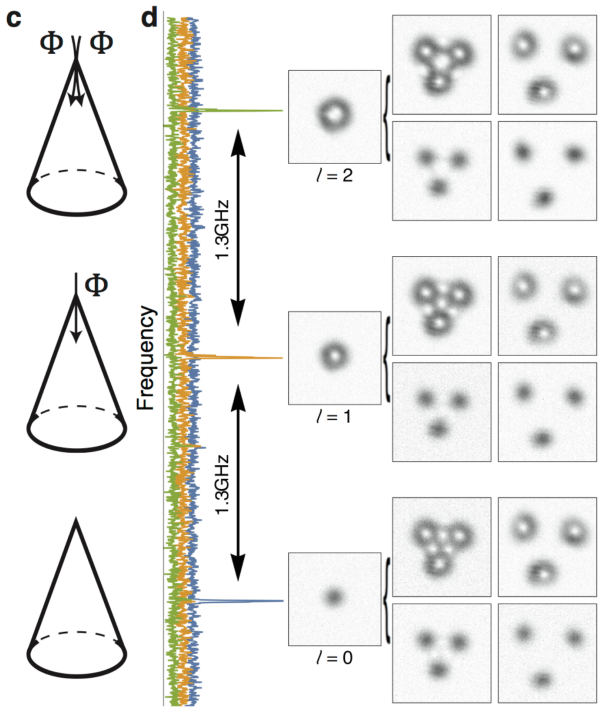

Figure A.1.2: **Displaced Modes on All Three Cones.** Panels c and d from Fig. 4.5 are reproduced. Note that displaced versions of $l = 0$ and $l = 1$ modes are formed all all three cones. For large displacements, the three copies appear identical; they differ only by a relative phase. For smaller displacements, the copies interfere. The relative phases between the copies then produces cone-dependent interference patterns. Figure taken from Ref. [182].

nar lowest Landau level $\psi_l \propto z^l e^{-|z|^2/2}$, we write the Jastrow factor in the N-particle Laughlin state as a polynomial with coefficients j on single particle wavefunctions:

$$\prod_{k<i}(z_k - z_i)^2 = \sum_{\{a_1,\ldots,a_N\}} \left(j_{a_1,\ldots,a_N} \prod_{p=1}^{N} z_p^{a_p} \right)$$
$$\psi_L \propto \sum_{\{a_1,\ldots,a_N\}} \left(j_{a_1,\ldots,a_N} \prod_{p=1}^{N} \psi_{l=a_p}(z_p) \right) \tag{A.15}$$

where the sum is taken over all possible sets $\{a_1, \ldots, a_N\}$ such that $\sum_{p=1}^{N} a_p = L = N(N-1)$ is the total angular momentum of the Laughlin state.

It is interesting to note that the Jastrow factor in this form is a Jack polynomial $J^{-2}_{1010101\ldots}(z_1, \ldots, z_N)$, the decomposition of which in terms of monomials is known [376]. The partition $\lambda = \{n_l\}$ can be read as specifying the number of particles in each angular momentum state, e.g. $[1010101\ldots]$ specifies one particle each in $l = 0, 2, 4, 6, \ldots$. This partition can be obtained given the total number of particles $N = \sum_l n_l$ and the filling factor r^{-1} as the partition corresponding to the minimum total angular momentum $L = \sum_l l n_l$ with the restriction that r consecutive angular momentum states contain no more than $k = 1$ particles. A 'squeezing rule' on the specified partition corresponds to particular collisions that conserves angular momentum, increasing a first particle's angular momentum by one and decreasing a second particle's angular momentum by one, subject to the restriction that the first particle start with less angular momentum than the second. The terms in Eqn. (A.15) correspond occupation number states obtained by repeated application of this squeezing rule, providing an explicit conversion from the first quantization particle state basis to the second quantization orbital occupation basis. To make this point less abstract, we work through the example of the $N = 3$ particle Laughlin state:

$$(z_1-z_2)^2(z_1-z_3)^2(z_2-z_3)^2 = \underset{z1,z2,z3}{\mathbf{P}} z1^4z2^2z3 - z1^3z2^3z3 - z1^4z2z3 + 2z1^3z2^2z3 - z1^2z2^2z3^3$$

where the operator $\mathbf{P}_{z1,z2,z3}$ sums over all permutations of $z1, z2, z3$. This form explicitly provides the coefficients j_{a_1,a_2,a_3}. Converting from the monomials to particle state basis first requires taking the $(l!)^{-1/2}$ normalization into account. Then assuming indistinguishable particles, we account for the multiplicity of the state vector due to permutations of the particle labels by multiplying the coefficient of the state vector by the square root of the multiplicity. Thus we have

$$\begin{aligned}\psi_L^{N=3} &= \frac{1}{\sqrt{11}}\Big(\sqrt{2}|0,2,4\rangle - \sqrt{3}|0,3,3\rangle - \sqrt{2}|1,1,4\rangle + \sqrt{2}|1,2,3\rangle - \sqrt{2}|2,2,2\rangle\Big) \\ &= \frac{1}{\sqrt{11}}\Big(\sqrt{2}|1,0,1,0,1\rangle - \sqrt{3}|1,0,0,2,0\rangle - \sqrt{2}|0,2,0,0,1\rangle \\ &\qquad + \sqrt{2}|0,1,1,1,0\rangle - \sqrt{2}|0,0,3,0,0\rangle\Big) \qquad \text{(A.16)}\end{aligned}$$

The first line lists expresses which angular momentum state each of the three particles is in, while the second line expresses the occupation number of each angular momentum state.

One might naturally ask, 'How can we make a Laughlin state in our reduced Hilbert space where we are only allowed every third angular momentum state $\psi_{3l} = z^{3l}e^{-|z|^2/2}$?'

Physically speaking, a cone looks like flat space away from its tip, with curvature only at the tip itself. Consequently, a Laughlin puddle that neither encircles nor overlaps the cone tip will behave as though it inhabits a plane. On the other hand, a Laughlin puddle that touches or encircles the cone tip is a different story: its *physical form* should be changed due to the Wen-Zee coupling to manifold curvature. We treat these two cases separately.

Away from the cone tip

Away from the cone tip, space is flat, so we should expect that the discussion above implies that a regular Laughlin state (up to additional exponential factors arising from *magnetic* translation) is supported. The only question is whether this state lives within the lowest Landau level on the cone. Since all angular momentum states may be defined on the cone so long as they are suitably displaced from the cone tip (see section A.1.6), this is straightforward.

$$\psi_L^{Tr} = \sum_{\{a_1,\ldots,a_N\}} \left(j_{a_1,\ldots,a_N} \prod_{p=1}^{N} \left(\sum_q C(q, a_p, c, z_0) z_p^{3q+c} e^{-|z_p|^2/2} \right) \right) \tag{A.17}$$

The Laughlin wavefunction looks like three copies of a Laughlin puddle, since, so long as these copies do not touch one another (meaning they are far from the cone tip), there will be no self-interactions or interference and the short range behavior (order of the zeros, etc.) will be identical to the standard planar Laughlin state. It is important to note that we do not have three independent Laughlin puddles; the copies have no dynamical degrees of freedom, just as a person's reflection in a mirror is entirely constrained by the persons motion.

At the cone tip

The story at the cone tip is more complex, as the Laughlin puddle couples to the manifold curvature directly and is thereby deformed. Taking the limit $\lim_{z_0 \to 0} \psi_L^{Tr} = 0$; the three copies of the planar Laughlin puddle destructively interfere with one another. We therefore propose an ad-hoc Laughlin wavefunction motivated by the $z \to z^3$ mapping from the plane to the cone:

$$\psi_L^{conetip} \propto e^{-\sum_k |z_k|^2/2} \prod_{k<i} (z_k^3 - z_i^3)^2 \tag{A.18}$$
$$\propto e^{-\sum_k |z_k|^2/2} \prod_{k<i} (z_k - z_i)^2 \prod_{p<q} (z_p^2 + z_p z_q + z q^2)^2$$

This wavefunction bears similarities to the Laughlin wavefunction, but with an additional post-factor. Because the post-factor is a symmetric polynomial of z, it does not influence the order of the zero when two particles approach each other or any other anti-symmetry property. Instead, it changes the angular momentum of the 'center of mass' of the particle distribution, from $L_{CM} = 0$ for the canonical Laughlin state to $L_{CM} = 2N(N-1)$ for the N-particle Laughlin state around the cone tip.

A.1.8 Measurable Quantities of Quantum Hall Systems: Topological Shift and Trapped Fractional Charge

This subsection is the intellectual work of Andrey Gromov, and in included here as theoretical background for other sections.

In this section we explain the relation between the local density and quantum Hall transport coefficients. The shortest way to access this relation is through the effective action technique. The effective action $W[A]$ is an extremely compact way to encode linear response functions, i.e. ground state expectation values of density ρ, electric current j_i and stress tensor T_{ij}. In a gapped system such as quantum Hall state the effective action depends only on external probes, namely the external electromagnetic field and space geometry.

We start with dependence of the density on external magnetic field B. The effective action describing electromagnetic response must satisfy two properties: (i) it has to be gauge in-

variant, this reflects particle number conservation and (ii) it must be "assembled" only from the vector potential A_μ, and space and time derivatives $\partial_\mu = (\partial_0, \partial_i)$. There term with the lowest number of derivatives is the so-called Chern-Simons term

$$W[A] = \frac{\ni}{4\pi} \int dt d^2x \epsilon^{\mu\nu\rho} A_m u \partial_\nu A_\rho = \frac{\nu}{4\pi} \int dt d^2x (\epsilon^{ij} A_i \dot{A}_j + 2A_0 B) \tag{A.19}$$

where $\epsilon^{\mu\nu\rho}$ and ϵ^{ij} are absolutely anti-symmetric tensors with $\epsilon^{0xy} = 1$ and $\epsilon^{xy} = 1$. The coefficient ν is known in the fractional quantum Hall effect as the filling fraction; it determines the Hall conductivity as will become clear shortly. To obtain charge density, we differentiate the effective action with respect to A_0

$$\rho = \frac{\partial W}{\partial A_0} = \nu \frac{B}{2\pi}$$

This relation is used to determine the number of background states on a planar manifold. To obtain the x-component of the electric current, j_x, we differential W with respect to A_x

$$j_x = \frac{\partial W}{\partial A_x} = \frac{\nu}{2\pi} E_y$$

This is the Hall current with Hall conductance $\sigma_H = \nu \frac{e^2}{h}$ (restoring units). For the integer quantum Hall state with one filled Landau level, the filling factor ν is one. Since both density and electric current come from the same term in the effective action (namely, the Chern-Simons term) measuring one determines the other.

Next we wish to introduce non-trivial ambient geometry. We encode the geometry into an object that is called the spin connection ω_μ. This object is directly analogous to a vector potential in that its curl gives the (Ricci) curvature

$$\nabla \times A = B \qquad\qquad \nabla \times \omega = \frac{1}{2} R$$

The term in the effective action that contains the lowest number of derivatives and depends on both A and ω is the so-called Wen-Zee term [377]

$$W[A,\omega] = \frac{\nu\bar{s}}{2\pi}\int dtd^2x\epsilon^{\mu\nu\rho}A_m u\partial_\nu\omega_\rho = \frac{\nu\bar{s}}{4\pi}\int dtd^2x\left(\epsilon^{ij}A_i\dot{\omega}_j + \frac{1}{2}A_0R + \omega_0 B\right) \quad \text{(A.20)}$$

Now we compute the density again [378]

$$\rho = \nu\frac{B}{2\pi} + \nu\bar{s}\frac{R}{4\pi}$$

This relation is completely general and holds even in any interacting system. The numbers ν and $\bar{s}$ characterize the topological phase of matter. Generally $\bar{s}$, called the mean orbital spin, contains extra information about the topological phase of matter. To illustrate this point, we consider how ν and $\bar{s}$ depend on which Landau level is filled. For all Landau levels, the filling fraction is the same constant (for us, it is one), but $\bar{s} = n + \frac{1}{2}$, where n labels which Landau level is populated, with the lowest Landau level corresponding to $n = 0$. In condensed matter system, it is difficult to create a substantial enough source of curvature to observe a change in density (although there are intriguing developments in this direction [379]), but in our optical system, it is done with ease.

Measurement of the excess state density derived from a local density of states therefore measures the mean orbital spin. The latter allows us to calculate the value of a dissipationless, quantized transport coefficient known as the Hall viscosity, η_H, which we now describe [380]. Similarly to how the Chern-Simons term encoded Hall conductivity σ_H, the Wen-Zee term encodes the Hall viscosity. Formally, it comes from the variation in the last term in the Wen-Zee action. The Hall conductivity is defined from an off-diagonal two-point function of electric currents

$$\langle j_x j_y\rangle = i\omega\sigma_H$$

while the Hall viscosity is defined from an off-diagonal two-point function of the stress tensor

$$\langle T_{xx} T_{xy} \rangle = i\omega\eta_H$$

The Hall viscosity is a non-dissipative transport coefficient that describes transport of momentum transverse to applied shear. If follows from the Wen-Zee action that (in flat space)

$$\eta_H = \frac{\bar{s}}{2}\rho$$

Thus, in order to determine the Hall viscosity in flat space, it is sufficient to measure $\bar{s}$ through a density measurement in curved space.

A.1.9 The Local Density of States and Flux Threaded Cones

In order to measure the geometry of the manifold for transverse photon dynamics, we look at the local density of states. Because at degeneracy, the density is a series of delta functions in energy, one for each Landau level, we may fix energy at the energy of a Landau level of interest, and treat the local density of states at that energy as a measure solely of the spatial density of states for that Landau level: $\rho(\boldsymbol{x}) = \sum |\psi(\boldsymbol{x})|^2$ where the sum is taken over all single particle states in the Landau level of interest. This is easily measured by injecting each single particle state, i.e. each resonator eigenmode, and collecting the transmitted light on a camera. The images are normalized to equal area and then summed, producing figures 4.5g-i.

As discussed in the preceding subsection, the density of electrons in an integer ($\nu = 1$) quantum Hall system on a curved manifold is given by,

$$\rho(\boldsymbol{x}) = \frac{1}{2\pi l_B^2} + \bar{s}\frac{R(\boldsymbol{x})}{4\pi}$$

where $l_B = \sqrt{\frac{\hbar}{eB}}$ is the magnetic length, $\bar{s}$ is the mean orbital spin, and $R(\boldsymbol{x})$ is the local curvature of the manifold. The mean orbital spin is predicted to take values $\bar{s} = n + \frac{1}{2}$, where n indexes the Landau levels with the lowest Landau level being $n = 0$. For the $c = 0$ cone, the effective magnetic field is constant everywhere, so $\rho_0 = \frac{1}{2\pi l_B^2}$ is a constant. A delta function of curvature at the cone apex provides the only deviation from constant density, and in the lowest Landau level, $\bar{s}$ should be one half, so $\delta\rho(\boldsymbol{x}) = \frac{1}{2}\frac{s-1}{s}\delta(\boldsymbol{x})$ where $s = 3$ is the symmetry parameter that defines the cone. By integrating, we therefore expect to find one third of an extra state localized to the tip due to manifold curvature.

We may explore this behavior alternatively by looking at the known mode profiles of the lowest Landau levels ψ_l. We then construct the lowest Landau level local density of states on the c^{th} cone as

$$\rho_c = \sum_n |\psi_{3n+c}|^2$$

As represented in figure A.1.3, this predicts a threefold increase in state density near the cone tip; the increase is a Gaussian, and is in fact nothing more than the l = 0 mode. This matches the prediction from curvature, as the delta function there only suggests an increase localized to around the origin to approximately the magnetic length, and the waist size, w_0 is twice the magnetic length. Upon integrating the excess density, we find $\delta N = 1/3$, in agreement with the prediction. However, setting c to 1 or 2 immediately presents a problem, as the local density vanishes at the cone tip. This reflects that the lowest angular momentum states on these cones are $l = 1$ and $l = 2$, respectively, both of which vanish at the origin. Furthermore, when we integrate the excess density we find $\delta N = 0$ and –1/3 respectively.

We resolve this by looking at the symmetry relation that defines these cones and noting that there appears an additional magnetic flux $\Phi = -\frac{c}{3}\Phi_0$ threading the cone tip, as developed in section A.1.5. With flux threading the magnetic field in the equation for state density above is not constant, but rather has a delta function of magnitude $-2\pi c/3$ at the tip as well. This

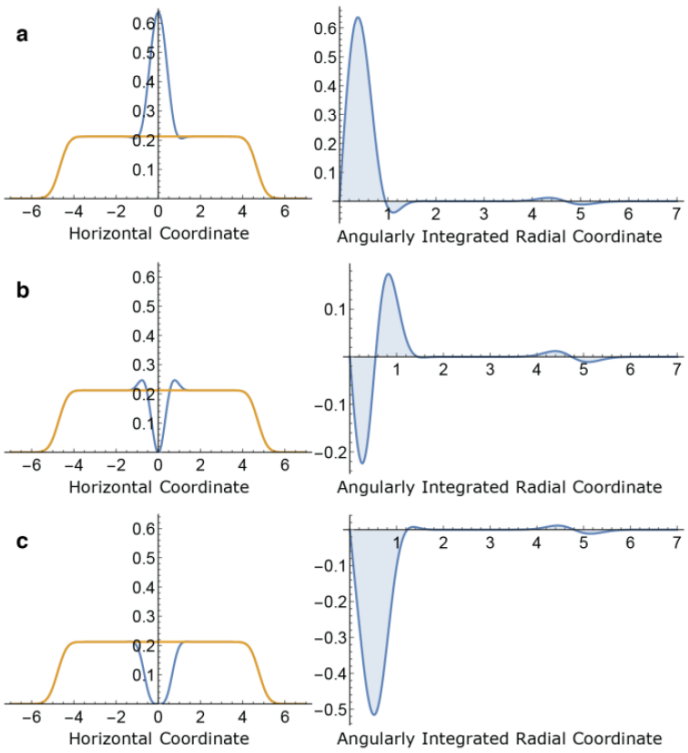

Figure A.1.3: **Expected Local Density of States. (a)** A slice through the expected local density of states for the $c = 0$ cone shows a threefold increase in density at the apex (blue) above a constant background plateau (yellow). The expected density is presented as a function of radius from the middle after having been integrated in angle. Integrating in radius then provides the total number of excess states (shaded region), which is precisely one third. **(b)**, the same expected local density of states is shown for the $c = 1$ cone. Although the slice shows a vanishing density at the tip with only a small density increase in a ring around the tip, the angularly integrated expectation shows that these two effects approximately cancel. In fact, the integral is precisely zero. **(c)**, Finally, the expectation for the $c = 2$ cone is presented, showing a broader decrease near the apex with no counterweighting rise. The integral of the density reveals a deficit of one third of one state. Figure taken from Ref. [182].

removes state density from the cone apex, resulting in the following general expectation

$$\delta\rho(\boldsymbol{x}) = \bar{x}\left(1 - \frac{1 + c/\bar{s}}{s}\right)\delta(\boldsymbol{x})$$

We may perform an integral to find the total state number excess or deficit. Doing so for the lowest Landau level, we predict $\delta N = 1/3$, 0, and –1/3 for $s = 3$ and $c = 0$, 1, and 2 respectively, matching the predictions from analytical mode profile integration. This also forms concrete predictions for integer quantum Hall systems in higher Landau levels (using $\bar{s} = n + 1/2$) as well as on cones of higher degeneracy parameters. As seen in figure A.1.3b,

the spatial dependence of the density reduction due to flux threading is not the same as the spatial dependence of the density increase due to manifold curvature, causing oscillations in the local state density. This implies that the delta-function description in the equation above is incomplete and points towards the rich interplay between curvature and topology in our system.

We measure the number of excess states on each cone directly from the data without using a fitted curve. We take the local density of states from the first six modes on each cone (Fig. 4.5g-i). The background plateau value is found as the average of pixel values over an annulus chosen to avoid both the central region and the outer limit. We then sum over pixels within a disk enclosing the central region and subsequently subtract off the average plateau value times the area of the disk. Finally, we convert this quantity to state number by using a conversion factor, which is determined from the integral of the entire image that we know corresponds to six states. We find $\delta N_{c=0} = 0.31(2)$, $\delta N_{c=1} = -0.02(1)$, and $\delta N_{c=2} = -0.35(2)$, where the uncertainty is determined from the choice of the annular background region as well as initial background subtraction.

While we have detected fractional state number excess and depletion at the cone tip, it is worth mentioning that this is unrelated to the fractional charge and fractional statistics of excitations in the fractional quantum Hall effect. True excitations in our system correspond to particle-hole pairs each of charge (state number) magnitude one. The fractional state localized to the cone tip is a defect in the integer quantum Hall state, which breaks translational invariance and is known as a disclination in solid state physics. The precise value of the state number trapped at the defect is a topological invariant determined by the filling fraction and the discrete rotational symmetry (opening angle of the cone).

Finally, it is worth mentioning another intriguing method for measuring the local density of states. In analogy to scanning tunneling microscopy experiments, we could very tightly focus a Gaussian beam at the resonator waist, and measure the total transmitted optical

power as a function of input position. This could map out the local density with a resolution given by the waist size of the incoupled light. One immediate problem presents itself in the requirement that the translated probe must also be tilted to be consistent with magnetic translations; if the tilt is not calibrated correctly, the measured density will be artificially lowered. Additionally, this method requires implementing high NA optics on the input and output of the resonator, which is technically challenging due to the presence of the resonator mirrors and mounts. Together, these considerations lead us to prefer the implemented method, which provides the same information. With interactions, though, these challenges may be offset by the unique advantages of this method, as it could enable the probing of local excited state density above a spectroscopically prepared fractional quantum Hall ground state.

A.1.10 A Note on Time Reversal Symmetry

Our system does not break time reversal symmetry—the resonator photons are analogous to electrons in a spin-hall system where the up/down spin degree of freedom is direction of propagation through the resonator. Modes traveling in opposite directions experience opposite round trip rotations and therefore opposite effective magnetic fields. So, any desired mode has a corresponding degenerate back-reflected mode. However, the polarization of the light is rotated along with the image, so the back-reflected mode has the opposite circular polarization. The identity of magnetic impurities, which in general couple the forward and backward copies of the quantum Hall physics, would be dust or defects on the mirror surface which backscatters *into the cavity* rather than into free space, and does so *while flipping the circular polarization state*. Such disorder is highly unlikely, but it is possible to energetically isolate the forward and backward propagating systems. We may exploit the atomic Faraday effect by placing a cloud of optically pumped Rubidium atoms in the resonator waist in order to split the polarization modes and the break time reversal symmetry of our system [192].

A.1.11 Measuring Electromagnetic and Gravitational Responses of Photonic Landau Levels — Methods

The experimental resonator. The four mirror, running-wave, non-planar resonator used in this work consists of four 100 mm radius-of-curvature high reflectivity mirrors coated for both 780 nm and 1560 nm mounted in two steel structures which define a stretched-tetrahedral resonator geometry characterized by an axial length of 5.1 cm and an opening half-angle of 10°. The two steel mounts are aligned via rods, and a micrometer stage controls the relative separation. This permits smooth length adjustment to tune the resonator to degeneracy. One mirror is mounted on a piezoelectric transducer, which permits stabilizing the cavity length via PI feedback based on a Pound-Drever-Hall error signal generated by the reflection 1560 nm light off a resonator mirror. The free spectral range of the resonator is 1400 MHz and the finesse for 780 nm is 8000. The cyclotron frequency is $\omega_C = 2\pi \times 900$ MHz. The $1/e^2$ intensity radius of the waist of the resonator is $w_0 = 105$ μm, and this sets the magnetic length $l_B = w_0/2$.

Digital micromirror device. To excite the resonator with light with arbitrary amplitude and phase profiles, we shine 780 nm narrowband laser light onto computer generated holograms produced by a phase-corrected digital micro-mirror device (DMD), and we direct the resulting diffracted light into the resonator. We then extract the full amplitude and phase information of the transmitted resonator field by interference with a reference beam (See Sec. A.1.12).

Projector measurement. We employ the DMD as a generalized scanning tunneling microscope, enabling us to inject light with arbitrary position, momentum, or angular momentum. Remarkably, the holographic reconstruction technique allows us to measure the (spatially localized) band projectors even when disorder or harmonic confinement breaks the degeneracy between the modes in the Landau level; it is only necessary that the probe sweep across

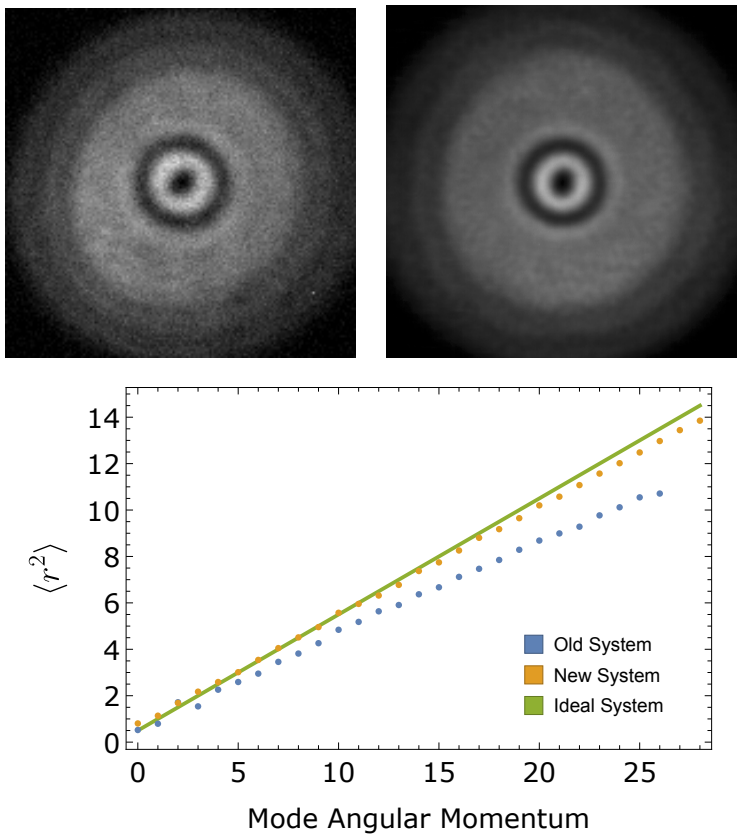

Figure A.1.4: **Resonator Imaging Comparison.** The local density of states in the second excited Landau level with effective magnetic flux $\Phi_B/2\pi = -2/3$ threading the cone tip highlights improvements in resonator design and the imaging system. The previous resonator used in [182] (top left), displays significant diagonal astigmatism, which has been removed in the current work (top right). Images of modes in the lowest Landau level provide estimations of the expectation value of r^2 (bottom), errors in which directly cause systematic errors in measurements of the shifted second moment. The significant reduction in deviations from the idealized system permits measurements of the central charge and extensions to higher Landau levels. Errorbars are calculated from uncertainty in the center location and waist size of the modes; they are all smaller than the point size. Figure taken from Ref. [208].

the band of states in the Landau level, and that the resulting resonator response be interfered with the reference beam before "integration" of the intensity on an camera. At each laser frequency in the sweep, the resonator response will be a ring carrying orbital angular momentum; these rings can interfere with one another, even if they arrive on the camera at different times, because the interference with the heterodyne beam converts phase to intensity, resulting in the desired localized mode (Fig. 4.7c). It is necessary that the sweep be sufficiently slow compared to the lifetime of photons in the resonator. For our experiments, an 8 MHz sweep is performed in 10 ms, while the linewidth is $2\pi \times 180$ kHz, resulting in

a very slow sweep of the laser compared to the cavity lifetime: 0.004 cavity linewidths per cavity lifetime.

Apparatus improvements. The current apparatus is based on that used in our previous work [182]. We rebuilt the experimental resonator with a new mirrors, mirror mounts, and in a new configuration. The resonator housing is now steel rather than plastic, and the resonator length is stabilized with a Pound-Drever-Hall error signal controlling proportional-integral feedback circuitry which actuates a piezo stack glued to a mirror. This enables the precise control of the probe laser detuning from the resonator resonance necessary for the measurement of local projectors. We image the transverse plane of the resonator by collecting light transmitted through one of the mirrors. In passing through the glass substrate of a curved mirror at significant non-normal incidence, the light is defocused by an effective cylindrical lens. This appears as an artificial breaking of rotational symmetry in the resonator modes and had previously limited LDOS measurements. In particular, it made measurements of the second moment impossible, since unlike the integrated excess density, the second moment is not invariant to astigmatic distortion. Both increasing the mirror radii of curvature from two at 25 mm and two at 50 mm to all four at 100 mm and reducing the non-planar opening half-angle from 16° to 10° serve to reduce the effect of this aberration (see Fig. A.1.4).

A.1.12 Holographic Measurement of Electric Field

Heterodyne imaging provides a phase reference for the cavity output field, allowing the extraction of not just amplitude but also phase information. The heterodyne image appears similar to an image of just the cavity output except with the addition of high frequency fringes. Much like RF modulation spectroscopy, a low noise, high quality image of the original field may be obtained by an appropriately chosen "demodulation" scheme, depicted

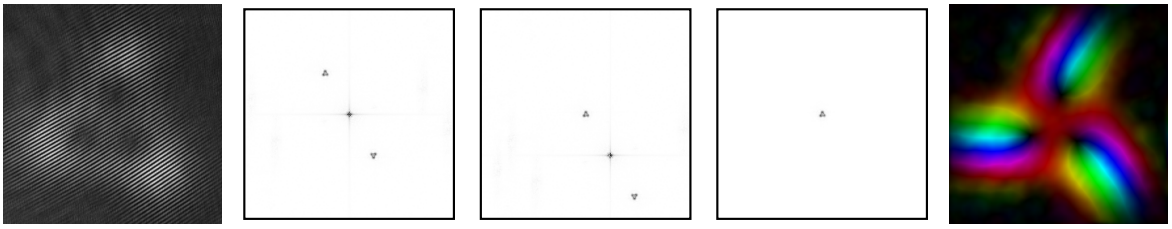

Figure A.1.5: **Holographic Electric Field Reconstruction.** A heterodyne image is obtained, (**a**), showing the cavity mode intensity with high frequency fringes superimposed. Background and cavity field images are subtracted from the heterodyne image, and a 2d spatial Fourier transform is applied, providing the momentum space image, (**b**). This reveals two copies of the unmodulated cavity mode profile shifted by plus and minus the k-vector of the heterodyne beam, with a large DC background in the middle. The momentum space image is then shifted, (**c**), and Gaussian masked, (**d**). Finally, an inverse Fourier transform provides the complex-valued electric field profile of the cavity mode (**e**). Figure taken from Ref. [208].

in SI Fig. A.1.5.

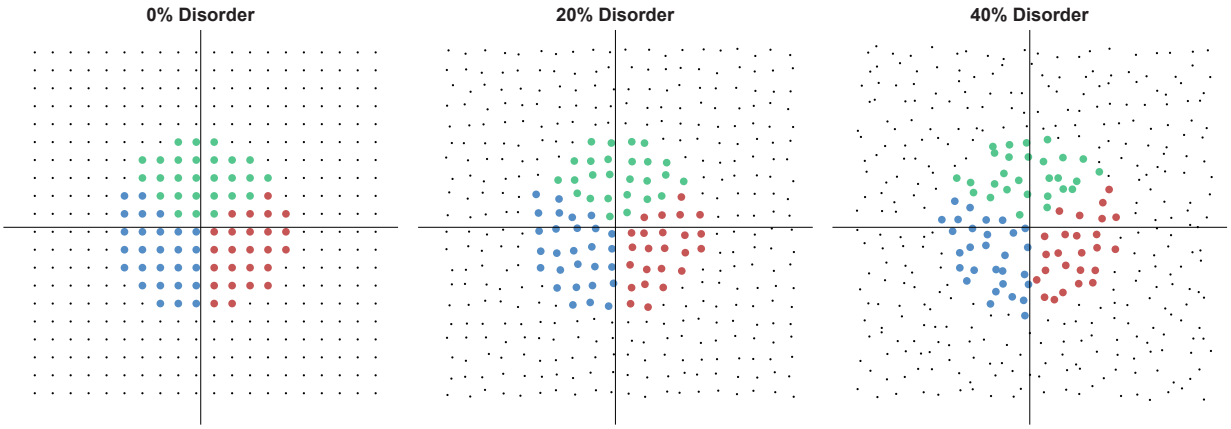

Figure A.1.6: **Numerical Evaluation Lattice.** The lattice on which the Chern number is numerically evaluated is presented for three different values of disorder. For these examples, points within a summation radius of 5 sites are included in the calculation. Figure taken from Ref. [208].

The heterodyne image is given in term of the cavity mode electric field, $E_c(\mathbf{x})$, and the heterodyne field, $E_{het}(\mathbf{x}) = E_h(\mathbf{x})\, e^{i\mathbf{k}\cdot\mathbf{x}}$, by

$$I_{het}(\mathbf{x}) = |E_c(\mathbf{x}) + E_h(\mathbf{x})\, e^{i\mathbf{k}\cdot\mathbf{x}}|^2,$$

where $E_h(\mathbf{x})$ is a slowly varying function. After subtracting off a heterodyne beam back-

ground image $|E_h(\mathbf{x})|^2$ and a cavity mode image $|E_c(\mathbf{x})|^2$, the signal is given by

$$I_{sig} = E_c(\mathbf{x})\, E_h^*(\mathbf{x})\, e^{-i\mathbf{k}\cdot\mathbf{x}} + E_c^*(\mathbf{x})\, E_h(\mathbf{x})\, e^{i\mathbf{k}\cdot\mathbf{x}}.$$

Extracting just one component of this via Fourier space filtering then yields

$$\begin{aligned} I_{demod} &= E_c(\mathbf{x})\, E_h^*(\mathbf{x}) \\ &\propto E_c(\mathbf{x}), \end{aligned} \tag{A.21}$$

where the final proportionality follows assuming the heterodyne beam was a clean plane wave with negligible variation across the cavity mode. That the demodulated signal is proportional to the square root of the intensity of the heterodyne beam indicates the suitability of this technique to the measurement of very low cavity field amplitudes, requiring in that case a camera with high dynamic range.

It is also worth noting that the subtraction of the individual heterodyne and cavity mode images is, in practice, often not necessary. To improve spatial resolution of the phase measurement, it is advantageous to make the heterodyne beam produce short wavelength fringes with a period approaching $\sqrt{2}a$, where a is the pixel size and the direction of the fringes is at 45° to the pixel axes. This also ensures that the modulated electric field is maximally separated from slowly spatially varying "DC" backgrounds. As long as the cavity modes imaged onto the camera cover many pixels, the cavity mode background $|E_c(\mathbf{x})|^2$ will appear as a slowly varying DC background. By assumption, the same holds of the heterodyne beam, so both the cavity mode and heterodyne backgrounds will be removed by the Fourier space masking (SI Fig. A.1.5c,d).

A.1.13 Connecting The Band-Projector To The Cavity Response Of A Swept Laser And Its Subsequent Normalization

The definition of the projector onto a band μ is $P^\mu \equiv \sum_{j\,in\,\mu} |j\rangle\langle j|$ for $|j\rangle$ in an orthonormal basis. From this it follows that $(P^\mu)^2 = P^\mu$.

We can then define matrix elements of the projector between localized modes injecting at $|\mathbf{x}\rangle$ and measuring at $|\mathbf{y}\rangle$ as $P^\mu(\mathbf{x},\mathbf{y}) \equiv \langle \mathbf{y}|P^\mu|\mathbf{x}\rangle$. From this definition and $(P^\mu)^2 = P^\mu$, it follows that

$$P^\mu(\mathbf{x},\mathbf{x}) = \sum_{\mathbf{y}} |P^\mu(\mathbf{x},\mathbf{y})|^2. \tag{A.22}$$

This expression forms the normalization criterion for measured matrix elements of the projector.

Measuring the projector from the cavity response

We wish to measure the projector onto a Landau level by measuring some response function of the cavity to some probe. Here, we show that matrix element of the projector between two points $\mathbf{x}$ and $\mathbf{y}$ is equal to the value of the electric field at $\mathbf{y}$ of the cavity response to an excitation at $\mathbf{x}$.

We suppose that the cavity has a Hamiltonian, H, with or without interactions, and which has complex eigenvalues $\varepsilon_j \equiv \omega_j + \frac{i}{2}\Gamma_j$. Following [250], we perform first order non-Hermitian perturbation theory to find the response of the cavity to some excitation. It is worth noting that this perturbative approach is exact for linear systems such as the one described in the main text.

A weak probe of frequency ω exciting a location $\mathbf{x}$ is described by an operator $\tilde{V}_{\mathbf{x}}$ applied to

the vacuum state $|0\rangle$. The transmitted cavity field is then given by

$$|\psi\rangle = \frac{1}{\mathbf{1}\omega - H}\tilde{V}_{\mathbf{x}}|0\rangle.$$

The value of this field at $\mathbf{y}$ is then $\langle \mathbf{y}|\psi\rangle$. When we integrate across the band of interest, the response ϕ is then

$$\phi = \langle \mathbf{y}| \sum_j \int d\omega \frac{|j\rangle\langle j|}{\omega - \varepsilon_j}|\mathbf{x}\rangle.$$

We now evaluate the integral. In practice we do not integrate over all frequencies, so we specify the limits of integration to cover a range centered at some frequency ω_0 with range Ω. Since this integral must be taken for each term in the sum, we therefore write

$$\begin{aligned}
\phi &= \sum_j \langle \mathbf{y}|j\rangle\langle j|\mathbf{x}\rangle \int_{\omega_j+\delta_j-\Omega/2}^{\omega_j+\delta_j+\Omega/2} \frac{d\omega}{\omega - (\omega_j + \frac{i}{2}\Gamma_j)} \\
&= \sum_j \langle \mathbf{y}|j\rangle\langle j|\mathbf{x}\rangle \log\left(\frac{\delta_j - \frac{i}{2}\Gamma_j + \Omega/2}{\delta_j - \frac{i}{2}\Gamma_j - \Omega/2}\right) \\
&= \sum_j \langle \mathbf{y}|j\rangle\langle j|\mathbf{x}\rangle \left(i\pi + \frac{\delta_j - \frac{i}{2}\Gamma_j}{\Omega/4} + \mathcal{O}\left(\frac{1}{\Omega^2}\right)\right)
\end{aligned} \tag{A.23}$$

where $\delta_j \equiv \omega_0 - \omega_j$ are the individual eigenstates' detunings from ω_0. In the last step we have performed a Taylor expansion in $\frac{\delta_j - \frac{i}{2}\Gamma_j}{\Omega/2}$ since we assume we sweep over a range large compared to the the individual resonances' widths and detunings from ω_0. The zeroth order term in ϕ directly provides the projector $P^\mu(\mathbf{x}, \mathbf{y})$ so long as the integration completely covers the band μ while avoiding all other states, while the first order term allows to estimate our error from finite and off-center integration over frequency.

Normalization of the measured projector

A given heterodyne image provides the electric field everywhere in the transverse plane of the cavity given a particular input location. Taking an entire scan over input locations can take ~ 10 minutes, so there could be significant drifts in the experimental apparatus between two images taken at the beginning and end of a run. This is particularly important to consider since each term in the Chern number sum compares the response of the cavity to three often well separated injection locations. As such we consider measurements of the projector matrix elements, $p^{\mu}(\mathbf{x}, \mathbf{y})$, which contain imperfections that are constant within an image, but vary between images: $P^{\mu}(\mathbf{x}, \mathbf{y}) = p^{\mu}(\mathbf{x}, \mathbf{y})\gamma^{\mu}(\mathbf{x})$. Imposing Eqn. (A.22) then determines the normalization factor.

$$\gamma^{\mu}(\mathbf{x}) = \frac{(p^{\mu}(\mathbf{x}, \mathbf{x}))^*}{\sum_{\mathbf{y}} |p^{\mu}(\mathbf{x}, \mathbf{y})|^2} \tag{A.24}$$

where z^* indicates the complex conjugate of z.

A.1.14 Evaluation of the Chern Number

A.1.14.1 First principles calculation of Chern number theory curve

In Fig. 4.9, we compare the convergence of the experimentally measured sum of terms to a numerically evaluated expectation with no free parameters. Here, we present details on the numerical procedure along with some results that inform our choice of experimental parameters.

We begin by creating a suitably large lattice of points and defining the magnetic length and summation radius in units of the lattice spacing. Uniform disorder of magnitude β is added to the lattice point locations: $x_i \to x_i(1 + \beta n_i)$, where n_i is a random variable uniformly

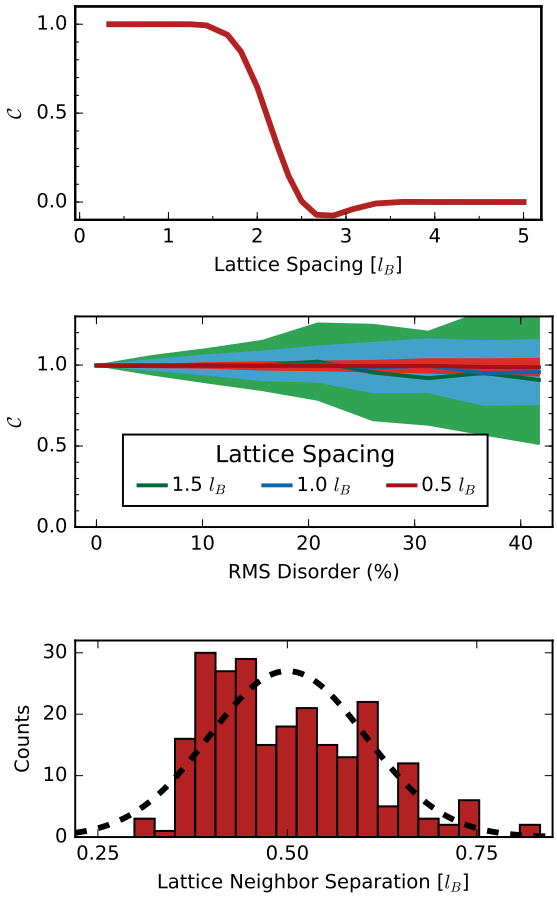

Figure A.1.7: **Chern Number Convergence.** We theoretically explore the dependence of the calculated Chern number on parameters of the underlying lattice. **(a)** If the spacing between neighboring lattice points is larger than ~ 1.5 $_B$, the sum fails to converge to the expected Chern number. **(b)** As disorder in the sampling lattice site positions is increased, the mean value of the sum remains constant while the standard deviation increases. However, the magnitude of this increase is strongly suppressed with a denser lattice. To compare with these numerical data, the experiment occurs at a lattice spacing of 0.5 l_B. The mean and standard deviations are computed on 100 independent realizations of the lattice disorder. The RMS disorder axis is obtained from independent uniform disorder in x and y values of the lattice by a simple scaling of 1.0428. **(c)** A histogram of the distances between neighboring lattice sites in the experimentally observed lattice (Fig. 4.8(c)) shows the distribution (red) with a standard deviation of 20% the mean, along with a Gaussian of the same mean and standard deviation. Since the precise form the the distribution of random disorder influences the numerical calculation of the Chern number, precise comparison of our experiment to the disorder curve is difficult. Figure taken from Ref. [208].

distributed in the interval $[-1, 1]$. We then partition the lattice points into four regions: points with a larger radius than the summation radius are excluded, and the remaining points are split into three approximately equal regions, A, B, and C by angle (see Fig. A.1.6).

Knowing the form of magnetic translations of a Gaussian spot, we define the projector from

position $\{x_\alpha, y_\alpha\}$ to $\{x_\beta, y_\beta\}$ to be

$$\begin{aligned} &P(z_\alpha \equiv x_\alpha + iy_\alpha, z_\beta \equiv x_\beta + iy_\beta) = \\ &\quad \frac{1}{2\pi l_B^2} \exp\left(-\frac{|z_\beta - z_\alpha|^2}{4l_B^2}\right) \exp\left(\frac{z_\alpha z_\beta^* - z_\alpha^* z_\beta}{4l_B^2}\right) \\ &= \frac{1}{2\pi l_B^2} \exp\left(-\frac{(x_\beta - x_\alpha)^2 + (y_\beta - y_\alpha)^2}{4l_B^2} + i\frac{x_\beta y_\alpha - x_\alpha y_\beta}{2l_B^2}\right) \end{aligned} \tag{A.25}$$

We then directly evaluate Eqn. (4.1).

By varying the set of points included in the sum, we can explore the convergence of the sum to the Chern number in a variety of contexts. In Fig. 4.9, we observe rapid convergence of the sum to the Chern number as the area of the (circular) region of summation expands, largely independent of the precise shape of the three interior partitions.

A.1.14.2 Dependence of Chern number upon sampling and disorder

In SI Fig. A.1.7, to enable us bound systematic errors in our estimate of $\mathcal{C}$, we examine the dependence of $\mathcal{C}$ upon sample-lattice spacing and disorder. We find that, for a sample lattice with a spacing of $\approx 0.5 l_B$, and r.m.s. lattice disorder of 20%, we anticipate a systematic error in $\mathcal{C}$ of ± 0.03, on par with the observed statistical error of ± 0.02 from averaging repeated measurements.

We also expect that the Chern number should be insensitive to the sample lattice spacing, so long as that spacing is less than $\sim 1.5\ l_B$. The only caveat is an increased sensitivity to lattice disorder; at a 20% lattice disorder, a lattice spacing of $1\ l_B$ yields a systematic error in the Chern number of ± 0.11. We verify the insensitivity of our Chern number measurement to the chosen lattice spacing by undersampling the regular measurement lattice. At a lattice spacing of $1\ l_B$, we measure $\mathcal{C} = 1.07 \pm 0.02(\text{stat.}) \pm 0.11(\text{sys.}) + i[0.02 \pm 0.03(\text{stat.})]$, where the

statistical uncertainty comes from averaging ten datasets. This measurement is in agreement with unity, while the increased systematic error justifies the regular use of a relatively dense lattice.

A.1.14.3 Dependence of Chern Number upon Residual Harmonic Trapping

Our "degenerate Landau level" corresponds to a set of modes with splitting between angular-momenta neighboring equal to approximately $\Delta = \frac{\omega_{trap}^2}{\omega_{cyc}} = 2\pi \times 300$ kHz, corresponding to a residual harmonic trapping frequency of $\omega_{trap} = 2\pi \times 16$ MHz (see Sec. A.1.4). For reference, the cavity-lock-broadened linewidth of each mode is $2\pi \times 300$ kHz, and we scan-and-integrate over $2\pi \times 8$ MHz (see Methods). We then increased the non-degeneracy by a factor of three so that the splitting between neighboring modes in the Landau level was $\Delta = 2\pi \times 1.0$ MHz, corresponding to a residual harmonic trapping frequency of $\omega_{trap} = 2\pi \times 30$ MHz, and observe no significant change in the measured Chern number, $\mathcal{C} = 1.03(1) + 0.11(1)i$.

Note that this test was performed prior to optimizing the measurement procedure, and in particular before we removed several sources of systematic error, such as saturation of a small subset of measured holograms due spatial-variation of the probe beam intensity on the DMD.

A.1.14.4 Imperfect cancellation of the imaginary part of the Chern number $\mathcal{C}$

As mentioned in SI A.1.12, a single $C_{\alpha,\beta,\gamma}$ measurement is derived from three images which may be taken up to about ten minutes apart. During that time, there may be significant drifts in the experimental apparatus that result in imperfect measurements of Landau level projectors and therefore imperfect $C_{\alpha,\beta,\gamma}$ values. The normalization procedure in SI A.1.12

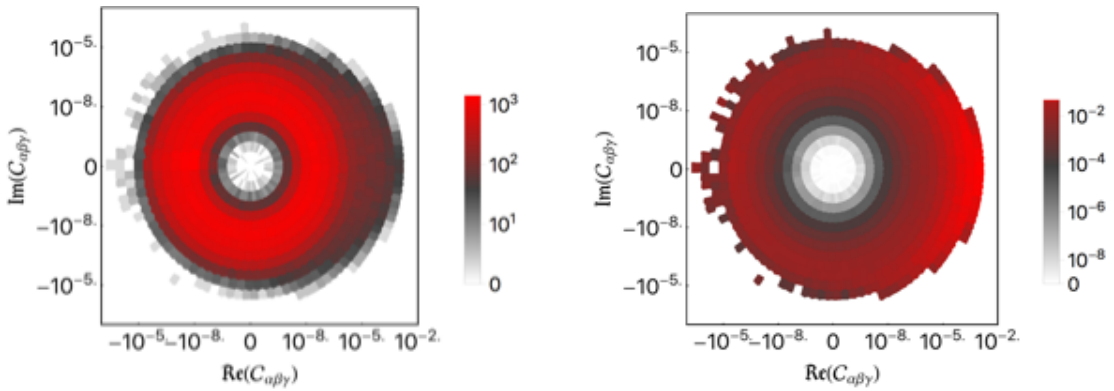

Figure A.1.8: **Logarithmic Histograms of $C_{\alpha,\beta,\gamma}$.** The distribution of $C_{\alpha,\beta,\gamma}$ as shown in Fig. 4.8d displays a large buildup of points near $|C_{\alpha,\beta,\gamma}| = 0$. (top) We present a similar logarithmic histogram of $C_{\alpha,\beta,\gamma}$ values, but with logarithmic real and imaginary axes. (bottom) We present a logarithmic density plot of the contribution to the total Chern number versus the value of the contributing $C_{\alpha,\beta,\gamma}$. Both axes cut off at 10^{-11}. As in the logarithmic histogram of Fig. 4.9d, bins with zero counts are separated from the logarithmic histogram and are colored white. Figure taken from Ref. [208].

accounts for overall brightness variation but subtler drifts remain. Such drifts (or potentially other sources such as saturation of the camera) cause the projector from $\mathbf{x} \to \mathbf{y}$ not to equal the complex conjugate of the reverse. This directly leads to an imperfect cancellation of the imaginary part of $C_{\alpha,\beta,\gamma}$, as can be seen in Fig. 4.8d and SI Fig. A.1.8. The source of the remaining imaginary component of these terms is basically random and so the terms have roughly equal contribution above and below the real axis. The resulting Chern number then becomes largely real due to a large cancellation of the imaginary components of each term. Nevertheless, the measured Chern number for each experimental run is complex.

It is also worth noting that we may be limited by the finite probe sweep range as in Eqn. (A.23). Appropriate centering of the Landau level in the sweep range makes the expected value of the imaginary component of the measured Chern number zero; however, finite sweep range may contribute to the expected error in the imaginary component. This effect could simply be reduced by increasing the probe sweep range in projector measurements.

A.1.15 Comparison to Fully Degenerate Cavities

Our measurement of the Chern number works because the number of modes in the lowest Landau level, like in a discrete system, is proportional to the area, and there is a smallest feature size (set by the magnetic length) which defines a "unit cell". This latter fact is reflected in the unusual commutator $[\hat{X}, \hat{Y}] = il_B^2$, where $\hat{X}$ and $\hat{Y}$ are the coordinates of the center of semi-classical cyclotron orbits/Landau-level projected coordinates [381, 382].

A similar Chern number measurement could be made in a resonator with all transverse modes degenerate; the cavity response would then always be determined by the size of the DMD-generated probe light. However, this would be incidental as there would be no smallest feature size and non-circulating and counter-circulating modes would be supported: the measured Chern number would sensitively-depend upon the fidelity of the DMD and would not be quantized. The present work explores a nearly-degenerate multimode resonator where the only modes in a band of near-degenerate states are precisely those comprising a Landau level, so the resonator does not support non-circulating or counter-circulating excitations (at the same energy). In fact, we need not assume anything about the mode structure of our resonator to perform the Chern number measurement: we can probe with a very tightly focused beam and find the frequency bands at which the resonator transmits. So long as the probe is spatially small enough (so that the phase profile mismatch between the probe field and cavity modes is irrelevant), it will excite chiral resonator modes from which the non-zero Chern number may be computed. In practice, making a very small probe size results in a small transmitted signal, but making the probe larger then only increases the signal if the phase profile of the probe matches the chiral modes of the cavity.

To investigate this, we excite the resonator at different locations $(x_0, 0)$ with a constant rate of tangential phase increase, $\exp ik_y y$, and with a variable rate of tangential phase increase at constant location. We observe clear maxima near $x_0/k_y = 2l_B^2$ (SI Fig. A.1.9b,

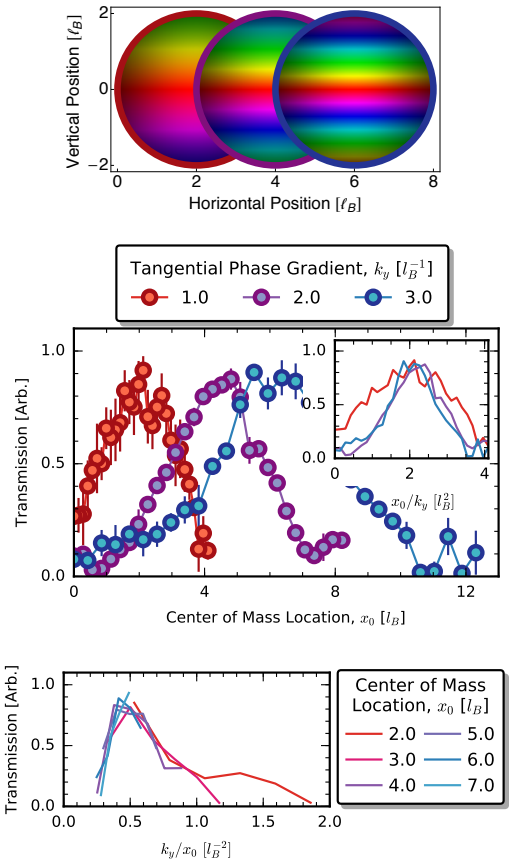

Figure A.1.9: **Chiral-Only Resonator Modes. (a)** Our photonic Landau level only supports modes of a particular chirality. As an injection point is displaced horizontally, this implies a phase gradient vertically which is proportional to the horizontal displacement. **(b)** We test the chirality of resonator modes by injecting light at various locations and tilts, with the total transmission taken as a measure for the overlap of the probing light with modes in the Landau level. The total transmission through the resonator is plotted as the radial displacement is increased with constant tangential phase gradient, k_y. When transmission is plotted versus the ratio between the tangential phase gradient and the radial displacement (inset), a distinct peak at $x_0/k_y = 2l_B^2$ is observed independent of the magnitude of the tangential phase gradient. The peaked structure of this plot indicates the chiral structure of modes supported by the resonator. Error bars represent the standard deviation of 10 identical runs of the experiment. **(c)** The same data may be re-sliced to observe transmission versus k_y at constant x_0, corresponding to cuts orthogonal to those taken in **b**. When the transmission is plotted versus the ratio k_y/w_0, we again observe a distinct peak at $k_y/x_0 = 0.5l_B^{-2}$ independent of the magnitude of the radial displacement. Figure taken from Ref. [208].

inset) and $k_y/x_0 = 0.5l_B^{-2}$ (SI Fig. A.1.9c) demonstrating that *only* modes with a particular chirality are supported. This is to say that the supported cavity modes are the TEM_{00} mode be *magnetically* translated away from the cavity axis, $E_{x_0,y_0}(x,y) = E_{00}(x - x_0, y - y_0)\exp\left(i(x_0y - y_0x)/2l_B^2\right)$. The spatial profile of the probe serves only to specify how strongly the chiral cavity modes are excited; it does not affect the measured Chern number. We have explicitly verified this insensitivity of the Chern number by operating at

$k_y/x_0 = 0.75l_B^{-2}$, away from the peaks in SI Fig. A.1.9b,c. This reduces the signal in the heterodyne images; however, the Chern number remains quantized at $C = 1$.

A.1.16 Experimental Considerations for the Local Density of States

A.1.16.1 LDOS radial profiles

In Fig. A.1.10, we show the angle-averaged LDOS for all three cones and all three Landau levels, superimposed. The large-radius asymptote is employed as the background density ρ_0.

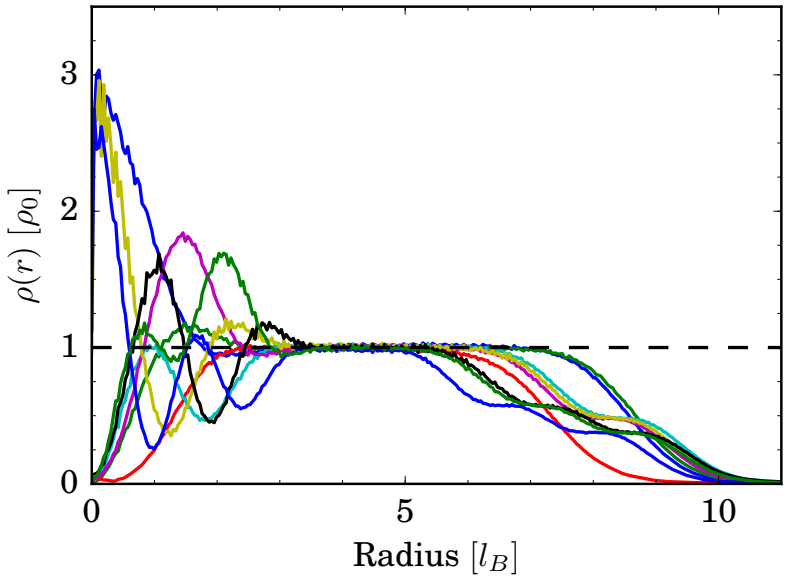

Figure A.1.10: **LDOS Radial Profiles.** All nine LDOS radial profiles are scaled uniformly and superimposed. By $\sim 4l_B$, all profiles have settled to a consistent constant value which is averaged to define the background state density ρ_0. Figure taken from Ref. [208].

A.1.16.2 Uncertainty in measurement of the shifted second moment

The primary uncertainty in the measurement of the shifted second moment comes from the upper bound of the integration region in eqn. (A.39). The integration of the excess density

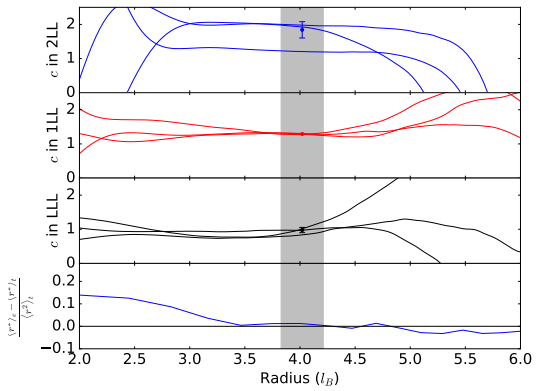

Figure A.1.11: **Dependence on the upper radial limit of integration.** The top three panels show the central charge evaluated using a variable upper radial limit of integration. The region of reasonable cutoff (gray band) is used to calculate quantities of interest and their errorbars. The quoted central charge values and errorbars are shown in the middle of this region. These curves are relatively flat through the gray band, so some additional systematic effect is presumably affecting the data, at least in the 1LL and 2LL. The bottom panel shows a potential cause for this systematic error. The expectation value of r^2 is calculated for individual modes in the lowest Landau level, and the fractional error from the theoretical value is plotted versus the theoretically expected root-mean-square radius. Figure taken from Ref. [208].

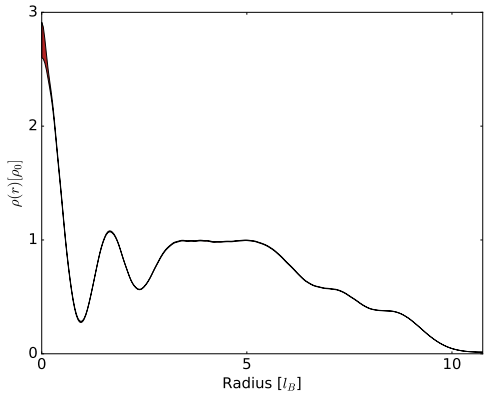

Figure A.1.12: **Radial density error band.** The azimuthally averaged radial density in the zero-flux-threaded second excited Landau level is shown as an error band. We split the density image into concentric annular regions, over which a mean and standard error of the mean is computed. The plotted band (red) fills the region between the mean minus its standard error and the mean plus its standard error. This region is smaller than the line width of the plotting except in the first few points. Figure taken from Ref. [208].

in theory extends to infinity; however finite field of view makes this impossible, and the expectation that the excess density exponentially falls to zero as the radius increases makes this unnecessary. This necessitates the introduction of an upper radial limit of integration, the choice of which is governed by a couple considerations: (1) the entire region of significant excess density must be included, and (2) the upper limit is otherwise a small as possible. This second consideration arises because the measured excess density on average falls to zero but displays some noise. As this noise is then multiplied by the square of the radius in the integrand, it may come to dominate the measurement of the shifted second moment. Motivated by inspection of data as in SI Fig. A.1.10, the chosen upper radial bound of integration is approximately $4l_B$.

We quantify this contribution to the uncertainty by varying the upper radial limit and computing the various quantities of interest. Averaging these quantities over a variation of approximately $\pm 0.2 l_B$ then provides our errorbar. We suggest that spherical aberration of the experimental resonator's mirrors (which skews the size of resonator modes) or residual aberrations in the imaging system after the resonator may cause an error dependent on the choice of radial integration upper bound, and so this procedure for errorbar estimation incorporates this potential source of error.

In the caption to Fig. 4.10, we state that the error arising from uncertainty in the azimuthal averaging is negligible. To demonstrate this, in SI Fig. A.1.12 we plot a band of the radial density of the zero-flux-threaded, second excited Landau level, from the mean minus its standard error to the mean plus its standard error. This band is very narrow except in the first few points. There, the annular regions that form the average contain sufficiently few points that the standard error is significant. However, the total contribution from this uncertainty to the error in δN or ΔM_2 is negligible compared to the previously discussed sources of error.

A.1.16.3 Full data table for mean orbital spin as extracted from excess charge

In the main text, we only present values of $\bar{s}(\delta N)$ aggregated over flux threading. This is to enable fair comparison between this method and the more precise method using the dependence of ΔM_2 on flux threading. Here, we present the full table of results for $\bar{s}(\delta N)$

Flux	0	-1/3	-2/3
LLL	0.411(3)	0.480(1)	0.524(0)
1LL	1.495(1)	1.467(1)	1.433(0)
2LL	2.428(3)	2.488(1)	2.446(1)

SI Table A.1: **Mean orbital spin** in each Landau level as extracted from the measured excess charge.

These data may be averaged over flux threading to yield $\bar{s} = \{0.44(4), 1.46(2), 2.44(2)\}$, as mentioned in the main text.

A.1.17 Local Measurements of Topological Quantum Numbers

The remaining portion of this appendix section except Fig. A.1.13 reproduces theoretical work performed by Andrey Gromov and Tankut Can. This theory connects physical observables I measured to topological indices, and so is included here to provide theoretical support to the conclusions drawn in section 4.2.

Here we show how topological quantum numbers characterizing the quantum Hall effect can be measured from the density of states. We review the response of QH states in the lowest Landau level to magnetic and geometric singularities [235], and generalize these results to higher Landau levels. For concreteness, we consider magnetic singularities as magnetic field configurations with a delta function source:

$$B = B_0 - a\phi_0\delta^{(2)}(\mathbf{r}) \tag{A.26}$$

where $\phi_0 = h/e$ is the flux quantum. Curvature singularities are geometries which have a point with a delta function curvature:

$$R = 4\pi\left(1 - \frac{1}{s}\right)\delta^{(2)}(\mathbf{r}) \tag{A.27}$$

Here $l_B^2 \equiv \hbar/(eB_0)$ defines the magnetic length. In our experiments we study cones which cover $\frac{1}{3}$ of the plane, so $s = 3$; we are further able to apply $a = \left(0, \frac{1}{3}, \frac{2}{3}\right)$ quanta of excess

flux through the cone tip [182].

The electromagnetic and geometric response of a QH state will influence both the total charge and orbital angular momentum (OAM) which accumulate at these defects. We will show how the charge and OAM are related to topological quantum numbers, and how they can be computed from the density of states.

A.1.17.1 Charge and OAM from Induced Action

The charge density and the spin density follow from the variational formula:

$$\rho = \frac{\delta W[A,g]}{\delta A_0}, \quad \rho^s = \frac{\delta W[A,g]}{\delta \omega_0} \tag{A.28}$$

where the induced action $W[A,g]$ is a functional of the gauge potential A_μ and the background metric $g_{\mu\nu}$, A_0 is the time component of the gauge field (i.e. the scalar potential), and ω_0 is the time component of the spin connection.

The induced action is given by [220, 258]

$$W = \frac{\nu}{4\pi}\int AdA + \frac{\nu\bar{s}}{2\pi}\int Ad\omega - \frac{c-12\nu\bar{s}^2}{48\pi}\int \omega d\omega. \tag{A.29}$$

This is a functional of the vector potential A_i and the background metric g_{ij}. The spin connection, ω_i, is defined through $\nabla \times \omega = R/2$ where R is the Ricci curvature. The integrands use a compressed "form" notation $Ad\omega = \epsilon^{\mu\nu\rho}A_\mu\partial_\nu\omega_\rho\,\mathrm{d}^2x\,\mathrm{d}t$ where ϵ is the absolutely antisymmetric tensor, and the indices μ, ν, and ρ cover both spatial dimensions and time.

Charge Density The charge density which follows from the the topological action is given

by the well known result

$$\rho = \frac{\nu}{2\pi}\frac{eB}{\hbar} + \frac{\nu\bar{s}}{4\pi}R = \frac{\nu}{2\pi l_B^2} + \frac{\nu\bar{s}}{4\pi}R \tag{A.30}$$

where R is the scalar curvature. Integrated over a closed surface, this yields the relation between the total number of particle N and the total flux N_ϕ through the surface (in units of the flux quantum): $N = \nu N_\phi + \nu\bar{s}\chi$, where χ is the Euler characteristic of the surface. The second term on a sphere ($\chi = 2$) defines the shift $\mathcal{S} = 2\bar{s}$. In the presence of a cone with a magnetic flux threading it, we can simply insert the singular fields (A.26 & A.27) into (A.30) and integrate to find

$$Q_{tip} = \int \left(\rho - \frac{\nu}{2\pi l_B^2}\right) dV = -\nu a + \nu\bar{s}\left(1 - \frac{1}{s}\right) \tag{A.31}$$

where $\nu/(2\pi l_B^2)$ is the value of the density far away from the cone tip.

OAM density

The spin density corresponds to the extensive part (scaling as N) of the orbital angular momentum (OAM) density, and is given by

$$\rho^s = \frac{\nu\bar{s}}{2\pi l_B^2} - \frac{(c - 12\nu\bar{s}^2)}{48\pi}R \tag{A.32}$$

Integrated over the surface this yields the Hall viscosity coeffiicent with a finite size correction [258]

$$\eta^H = \int \frac{1}{2}\rho^s dV = \frac{\nu\bar{s}}{2}N_\phi - \frac{(c - 12\nu\bar{s}^2)}{24}\chi. \tag{A.33}$$

Note that the Hall viscosity coefficient η^H generically depends upon both the mean orbital spin $\bar{s}$ *and* the central charge c; to obtain a c dependence however, requires a surface with non-zero Euler characteristic, eliminating the cylinder's sensitivity to c, as $\chi = 0$ for a cylinder.

In the presence of a magnetic and geometric singularity, the induced action will have additional contributions due to the singularities. Simply plugging in the singular field configurations will make the action infinite. For this reason, we need another approach to access the OAM due to the singular defects. This approach combines the microscopic definition of the OAM with the conformal block construction of FQH states.

A.1.17.2 OAM from moments of density

The single-particle eigenstates of the non-interacting Hamiltonian

$$H = \frac{1}{2m}\left(\Pi_x^2 + \Pi_y^2\right), \quad \Pi_i = p_i - eA_i \tag{A.34}$$

with the fields given by (A.26)and (A.27) are (in radial coordinates with magnetic length $l = 1$)

$$\Psi_k^{(n)}(r,\phi) = \frac{1}{\sqrt{\mathcal{Z}}} e^{ik\phi} r^{|k|} e^{-r^2/4} L_n^{|k|}(r^2/2), \tag{A.35}$$

$$\mathcal{Z} = \frac{2^{k+1}\pi\Gamma(n+k+1)}{s\Gamma(n+1)} \tag{A.36}$$

$$E = \hbar\omega_B \left(n + \frac{1}{2}(|k| - k) + \frac{1}{2} \right). \tag{A.37}$$

Here $n = 0, 1, ...$ labels the Landau level (LL) index, $k = sm + a$, with $m = 0, \pm 1, \pm 2, ...$, and $L_n^k(z)$ are the associated Laguerre polynomials. These wave functions are expressed in symmetric gauge to exploit the rotational symmetry of the Hamiltonian. For this reason, the orbital angular momentum commutes with the Hamiltonian and is a good quantum number. The microscopic definition of the OAM is

$$\hat{L} = \epsilon_{ij} r_i \Pi_j + \frac{\hbar}{2} r^2 \tag{A.38}$$

where ϵ_{ij} is the antisymmetric symbol, and $r = \sqrt{r_x^2 + r_y^2}$. The absolute value of the OAM in a single-particle state $\Psi_k^{(n)}$ which satisfies $\hat{L}\Psi_m^{(n)} = \hbar k \Psi_k^{(n)}$ can be expressed as a *shifted second moment* of the probability density

$$\hbar|k| = \hbar \int \left(\frac{r^2}{2} - 2n - 1 \right) |\Psi_k^{(n)}|^2 dV, \tag{A.39}$$

where the volume measure used here is $dV = \frac{2\pi}{\lambda} r dr$. This fact follows by explicit computation of the expectation value using the eigenstates (A.35).

A.1.17.3 Origin of $\hbar r^2$ in the shifted second moment

Equation (A.39) for the shifted second moment is essential for our high precision measurement of the mean orbital spin and the central charge. We give an outline of the derivation of this central result below.

The ladder operators which change the energy eigenvalue of a state are given by $a^\dagger = \frac{l}{\sqrt{2\hbar}}(\Pi_x - i\Pi_y) \equiv \sqrt{2l^2/\hbar}\,\Pi_z$ and $a = \frac{l}{\sqrt{2\hbar}}(\Pi_x + i\Pi_y)$ satisfying $[a, a^\dagger] = 1$. An independent set of ladder operators commuting with a and $a^\dagger$ are constructed from the guiding center coordinates and here denoted b and $b^\dagger$. These operators are responsible changing the OAM of the state. With these operators, it is possible to represent the wave functions (A.35) $\Psi_k^{(n)} \propto (a^\dagger)^n (b^\dagger)^{k+n} \Psi_0^{(0)}$, and the angular momentum operator as $\hat{L} = b^\dagger b - a^\dagger a$. In operator language, it becomes clear that the $\hat{L}\Psi_k^{(n)} = \hbar k \Psi_k^{(n)}$. To express this as a moment of the particle density, we return to the coordinate representation. It is convenient to introduce the notation $\Psi_k^{(n)} = \frac{1}{\sqrt{Z_n}} \Pi_z^n \Psi_{k+n}^{(0)}$. Then expressing the expectation value explicitly gives

$$\begin{aligned}
\langle \hat{L} \rangle =& \frac{1}{Z_n} \int \left(\Psi_k^{(n)}\right)^* \left(-i\bar{z}\Pi_{\bar{z}} + iz\Pi_z + \frac{\hbar}{2l^2}|z|^2\right) \Psi_k^{(n)} dV \\
=& \frac{1}{Z_n} \int \left(\Psi_{k+n}^{(0)}\right)^* \Pi_{\bar{z}}^n \left(-i\bar{z}\Pi_{\bar{z}} + iz\Pi_z\right) \Pi_z^n \Psi_{k+n}^{(0)} dV \\
&+ \hbar \int \frac{r^2}{2l^2} |\Psi_k^{(n)}|^2 dV
\end{aligned}$$

To reach the second line requires an integration by parts which makes $\Pi_{\bar{z}}^n$ act on everything to the right. The expectation value of the OAM now evidently involves the two operators

$$O_1 = \Pi_{\bar{z}}^n \bar{z} \Pi_{\bar{z}} \Pi_z^n \tag{A.40}$$

$$O_2 = \Pi_{\bar{z}}^n z \Pi_z^{n+1} = z \Pi_{\bar{z}}^n \Pi_z^{n+1} \tag{A.41}$$

To compute the integral, we must make these normal-ordered, i.e. move all $\Pi_{\bar{z}}$ to the right. The normal ordered operators (dropping the terms which appear as stuff $\times \Pi_{\bar{z}}$) are

$$: O_1 : = -i\hbar n \Pi_{\bar{z}}^n \Pi_z^n \tag{A.42}$$

$$: O_2 : = (n+1)! \left(\frac{\hbar}{2l^2}\right)^n z\Pi_z = (n+1) Z_n z \Pi_z \tag{A.43}$$

Inserting these then gives

$$\begin{aligned}\langle \hat{L} \rangle &= \hbar \int \left(\Psi_k^{(n)}\right)^* \left(\frac{|z|^2}{2l^2} - n\right) \Psi_k^{(n)} dV - \hbar(n+1) \\ &= \hbar \int \left(\frac{|z|^2}{2l^2} - 2n - 1\right) |\Psi_k^{(n)}|^2 dV = \hbar k\end{aligned}$$

which is true for $k > 0$. However, for $k < 0$, the states are described by $\Psi_{-|k|}^{(n)} = \Pi_z^{n+|k|} \Psi_n^{(0)}$, which then produces an extra factor of $2\hbar|k|$ on the RHS, and leads again to the formula (A.39) relating the second moment of the density of states to the OAM.

A.1.17.4 Many-particle states in the LLL and OAM of defects

For an N-particle state (interacting or not) in the lowest LL, this formula generalizes in the obvious way

$$\langle \hat{L}_{tot} \rangle_N = \int \left(\frac{r^2}{2} - 1\right) \langle \rho(r) \rangle dV \tag{A.44}$$

where $\hat{L}_{tot} = \sum_{i=1}^N \hat{L}_i$ and $\hat{L}_i$ acts only on the coordinate of the ith particle. This expression gives the total OAM of the many-particle state. From this, we have to assign an OAM due to the presence of the magnetic or geometric singularity at the origin. Here, we use an

important property of QH states which states that density correlations are exponentially suppressed on scales of order magnetic length l_B (which has been set to unity). This means that sufficiently far from the defect, the density will return to its mean value if the defect were not present. In the QH case, this is just $\langle\rho\rangle \to \frac{\nu}{2\pi}$, where ν is the filling fraction. Thus, the OAM of the cone tip should be captured in the moment formula

$$L_{tip} = \int \left(\frac{r^2}{2} - 1\right)\left(\langle\rho(r)\rangle - \frac{\nu}{2\pi}\right) dV \tag{A.45}$$

In Ref. [235], this was shown for Laughlin states to be equal to

$$L_{tip} = \frac{c - 12\nu\bar{s}^2}{24}\left(s - \frac{1}{s}\right) + \frac{a}{2}\left(2\bar{s} - \frac{a}{s}\right) \tag{A.46}$$

where $c = 1$ and $\bar{s} = \frac{1}{2}\nu^{-1}$. Here, $a(h/e)$ is the total flux threading the cone tip. The first term can be interpreted as the "spin" of the conical defect, while the second term (in the Laughlin case) can be interpreted as the spin of a quasihole with total charge $-\nu a/s$.

We intentionally write Eqn.(A.46) in a form which suggests generalization to arbitrary FQH states. In fact, in [383, 384], it was shown that the angular momentum due to a cone tip is a consequence of the gravitational anomaly occurring in the CFT construction of fractional QH wave functions [385, 386]. This connection is rather natural, since the gravitational anomaly controls the behavior of the wave function under scale transformations $z \to \lambda z$, while the angular momentum is read out by considering the special case $\lambda = e^{i\theta}$ which corresponds to pure rotations.

A.1.17.5 Integer quantum Hall states in Higher Landau levels

The generalization of Eqn.(A.45) to higher Landau levels is straightforward, but somewhat subtle on a conical singularity. We begin by stating the result, and proceed to unpack it in

the following section.

The OAM of a magnetic and geometric singularity in the nth Landau level is given by the moment formula

$$L_{tip}^{(n)} = \int \left(\frac{r^2}{2} - 2n - 1\right) \left(\sum_{m=0}^{\infty} |\Psi_{sm+a}^{(n)}|^2 - \frac{1}{2\pi}\right) dV \tag{A.47}$$

$$- \sum_{n'=0}^{n-1} \int \left(\frac{r^2}{2} - 2n' - 1\right) |\Psi_{-\lambda(n-n')+a}^{(n')}|^2 dV \tag{A.48}$$

$$= \frac{c_n - 12\nu\bar{s}_n^2}{24} \left(s - s^{-1}\right) + \frac{1}{2} a \left(2\bar{s}_n - \frac{a}{s}\right), \tag{A.49}$$

where $c_n = 1$ and $\bar{s}_n = n + 1/2$.

Let the energy $E = \hbar\omega_B \left(M + \frac{1}{2}\right)$. For fixed M, there will be infinitely many states at $n = M$ and $k > 0$. The density of states computed from just these eigenstates will approach a constant $1/2\pi$ away from the cone tip. This is what appears in the first integral in Eqn. (A.47), and accounts for the subtraction by the asymptotic density.

For $s = 1$ and $a = 0$, in addition to these positive k states, there will be M additional states with negative $k < 0$ which are degenerate with the $n = M$ states. These appear in the second integral in Eqn. (A.48). They will be labeled by different n indices, although they belong to the same LL.

As a consequence of the kinetics on a conical singularity, the moment formula which computes the topological contribution to the OAM of a defect will in principle involve non-degenerate states. For non-integer s, these are midgap states which exist between degenerate LLs. However, for integer s, they become degenerate with a higher LL than they started with. So for instance the state with $(n, m) = (0, -1)$ will have $M = n + s$ according to (A.37).

Nevertheless, this mixing is easily accounted for, and we can ultimately write a formula for the shifted second moment of the density of strictly degenerate states at energy $E = \hbar\omega_B(n+\frac{1}{2})$. It will read

$$\Delta M_2^{(n)} = \int \left(\frac{r^2}{2} - 2n - 1\right)\left(\rho_n - \frac{1}{2\pi}\right) dV \tag{A.50}$$

$$= L_{tip}^{(n)} + (sn - a)n - \frac{1}{2}sn(n-1) \tag{A.51}$$

$$+ \sum_{n'=0}^{n-1} (|k| + 2n' - 2n)\delta_{|k|+n',n} \tag{A.52}$$

where the the OAM of the defect is

$$L_{tip}^{(n)} = \frac{c_n - 12\nu\bar{s}_n^2}{24}\left(s - s^{-1}\right) + \frac{1}{2}a\left(2\bar{s}_n - \frac{a}{s}\right) \tag{A.53}$$

The last term accounts for the accidental degeneracy due to an itinerant level.

Fixing Experimental Parameters Here we set $s = 3$, and consider the appropriate form of the sum rule for $a \in \{0, 1, 2\}$.

For $a = 0$ and $s = 1$ the quantum numbers (n, m) which label a state at a given energy $E \sim M$ are

$$M = 0, \quad (0,0), (0,1), ... \tag{A.54}$$

$$M = 1, \quad (0,-1); (1,0), (1,1), ... \tag{A.55}$$

$$M = 2, \quad (0,-2), (1,-1); (2,0), (2,1), ... \tag{A.56}$$

$$M = 3, \quad (0,-3), (1,-2), (2,-1); (3,0), (3,1), ... \tag{A.57}$$

On a cone with $s = 3$, if we keep these original labels, the states which remain degenerate with a given Landau level are color coded below for $a = 0$, $a = 1$, and $a = 2$:

$$M = 0, \quad (0,0), (0,1), (0,2), (0,3), ... \tag{A.58}$$

$$M = 1, \quad (0,-1); (1,0), (1,1), (1,2), (1,3), ... \tag{A.59}$$

$$M = 2, \quad (0,-1), (1,-1); (2,0), (2,1), (2,2), ... \tag{A.60}$$

$$M = 3, \quad (0,-1), (1,-1), (2,-1); (3,0), (3,1), (3,2), ... \tag{A.61}$$

For example, the lowest Landau level will consist of states with $n = 0$ and $m = a + 3p$, for $p = 0, 1, ...,$. Furthermore, we can see from this graphic that for $a = 0$, the state with $(0, -1)$ becomes degenerate with the fourth LL. Evaluating the moment formula Eqn. (A.50) gives us the first few moments relevant for the experiment

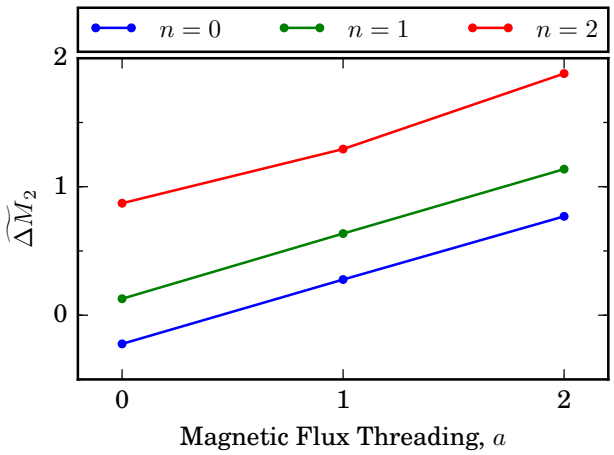

Figure A.1.13: **Extracting $\bar{s}$ from ΔM_2.** We plot $\Delta M_2(a)$ in the lowest (blue), first excited (green), and second excited (red) Landau levels. The average slope of each line provides a measurement of the mean orbital spin. Errorbars in each point are extracted from uncertainty in the radial integration cutoff and are smaller than the plotted points. Figure taken from Ref. [208].

$$\Delta M_2^{(0)} = L_{tip}^{(0)} \tag{A.62}$$

$$\Delta M_2^{(1)} = L_{tip}^{(1)} + (s-a) + \delta_{q,2}\,(s-a-2) \tag{A.63}$$

$$\Delta M_2^{(2)} = L_{tip}^{(2)} + 3s - 2a + \delta_{a,1}\,(s-a-4) \tag{A.64}$$

$$+ \delta_{a,2}\,(s-a-2)\,. \tag{A.65}$$

To extract the central charge c, we employ A.62- A.65 in conjunction with A.53.

A.1.17.6 Extracting $\bar{s}$ From Density Distribution

From the form of the previous equations, it is clear that the only piece of ΔM_2 that depends linearly on a takes the form $(\bar{s}_n - n)a$. To take advantage of this in order to make an

independent measurement of the mean orbital spin, we define

$$\widetilde{\Delta M}_2^{(n)} = \Delta M_2^{(n)} - \begin{cases} a^2/2s & n=0 \\ a^2/2s + \delta_{a,2} & n=1 \\ a^2/2s + 2\delta_{a,1} + \delta_{a,2} & n=2 \end{cases}$$

from which it follows that $\frac{\partial}{\partial a}\left[\widetilde{\Delta M}_2^{(n)}\right] = \bar{s}_n - n$. Since an integer quantum Hall state is expected to have $\bar{s}_n = n + \frac{1}{2}$, we expect the slope $\frac{\partial}{\partial a}\left[\widetilde{\Delta M}_2^{(n)}\right]$ to be independent of Landau level excitation number and equal to $\frac{1}{2}$. In SI Fig. A.1.13, we plot $\widetilde{\Delta M}_2^{(n)}(a)$ and observe a equal slopes within each Landau level. We thus measure $\bar{s}_n - n = \{0.496(4), 0.504(3), 0.505(68)\}$ for $n = \{0, 1, 2\}$.

A.1.18 Connection of δN to $\bar{s}$

Finally, we return to the charge on a cone tip in a higher Landau level. Using similar arguments as above to account for mid-gap states jumping between Landau levels and resulting in accidental degeneracies, we have that in terms of the density of degenerate states ρ_n at energy $E = \hbar\omega_B(n + \frac{1}{2})$,

$$\delta N = \int \left(\rho_n - \frac{1}{2\pi}\right) dV = Q_{tip}^{(n)} - n + \sum_{n'=0}^{n-1} \delta_{|k|+n',n} \tag{A.66}$$

where

$$Q_{tip}^{(n)} = -\frac{a}{s} + \bar{s}_n \left(1 - s^{-1}\right) \tag{A.67}$$

is what follows from the topological action according to Eqn.(A.31). For the fluxes considered in this experiment, we have

$$\delta N = Q_{tip}^{(0)} \tag{A.68}$$

$$\delta N = Q_{tip}^{(1)} - 1 + \delta_{a,2} \tag{A.69}$$

$$\delta N = Q_{tip}^{(2)} - 2 + \delta_{a,1} + \delta_{q,2} \tag{A.70}$$

The Kronecker delta functions account for the accidental degeneracies that may arise upon tuning the flux.

A.1.19 Hydrodynamic Explanation of Curvature ↔ Density Connection

There is a simple argument connecting curvature and density in hydrodynamic systems exhibiting Hall viscocity. It relies upon the intuition that positive/negative manifold curvature *must* bring with it a local deficit/excess of surface area. We will consider a cone as the paradigmatic example of a curved surface, and think about how it is constructed:

In order to create a cone, we can start with a plane, cut out a wedge (of total angle $2\pi/3$ in the case of our experiments), and glue the edges of the remaining surface together. Before performing this surgery on the geometry, however, we must get the fluid out of the way, i.e. we must remove the fluid from the removed wedge. The displacement of this fluid will create a strain in the azimuthal direction, which the Hall viscosity will respond to with a stress in the radial direction. The accumulation/depletion of charge at the tip will then depend on the sign of the Hall viscosity, as is observed.

A.2 Interacting Photons

A.2.1 Cavity Details

Our four mirror running wave resonator is arranged in a bow-tie configuration comprised of two convex mirrors and two concave mirrors in order to satisfy several opposing design constraints. To force cavity Rydberg polaritons to interact, the atomic sample size must be suitably small. The participating atomic region may be defined in two dimensions by the resonator mode cross-section, so the mode waist must be small (or radial slicing of the atomic cloud must be performed); we targeted 10-15 μm. The simplest technique for creating a stable resonator with a small waist is to use short focal length mirrors relatively close together. However, from our experience with a previous experimental cavity and its electric field filter [158], we found that any material close to Rydberg atoms, either dielectric or metallic, will build up charges or dipoles (from Rb adsorbates), the electric fields from which unacceptably broaden Rydberg lines above $n \sim 60$. This necessitates using longer focal length mirrors so that they may be placed further apart. Then, the only way to produce a small waist is a large mode size on the surface of these mirrors. For this reason, bow-tie resonators often have a longer upper arm with relatively flat mirrors so that the beam may expand due to diffraction, thereby increasing the beam size at the lower mirrors and so reducing the waist size. Having a longer upper arm, however, was unacceptable for two reasons: First, the resonator linewidth would decrease (at constant finesse), which proportionally decreases the data collection rate, (and the autocorrelation-data rate goes as the square of this rate). Second, the resonator is loaded into our vacuum chamber through a 62 mm diameter tube, which therefore sets an absolute maximum exterior size. Both of these limitations could be avoided, however, by utilizing convex mirrors in the upper arm; the defocus that they create acts, for our purposes, equivalently to diffractive expansion.

With numerical modeling, we arrived at an acceptable configuration of the resonator given

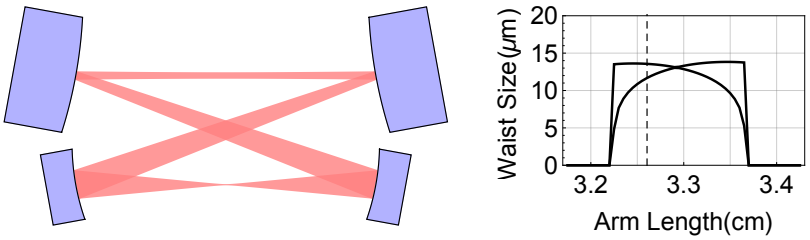

(a) (b)

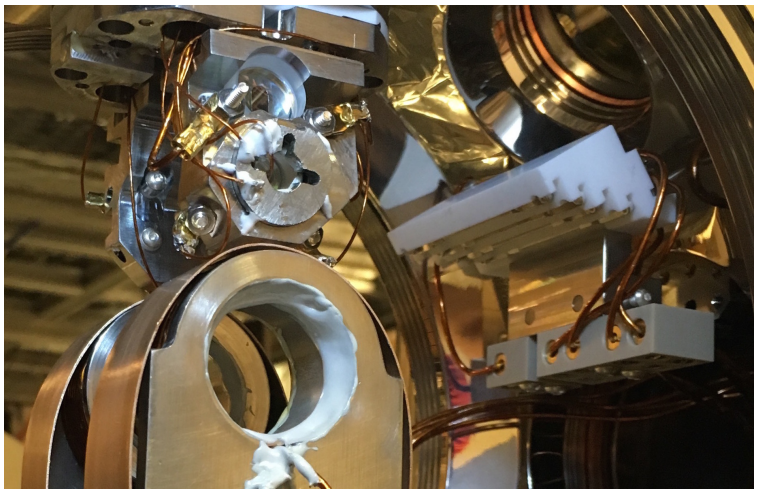

(c)

Figure A.2.1: **Cavity Views.** **(a)** A schematic of the resonator. The transverse size of the mode reflects the results of numerical calculation given the resonator geometry and is represented to scale but for a factor of 10 magnification compared to the mirror dimensions and locations. **(b)** The numerically calculated mode waist sizes are plotted as the resonator length is increased with constant aspect ratio. The cavity is stable over a 1.5 mm range, although near the edges of that range, it becomes significantly astigmatic. We set out to build the resonator at the middle where the modes waists are equal; however, assembly imperfections resulted in a somewhat shorter actual length, indicated by the dashed line. **(c)** A photograph of the in-vacuum experimental apparatus showing the resonator (top), the MOT coils (bottom), and Rubidium dispensers in their macor mount (right). The lower resonator mirror is mounted on a piezo tube which is glued to the lower circular steel disk on the resonator structure. Through the upper mirror, a narrow slot may be seen. Such slots are the only opening to the front of the mirrors and serve as a passive electric field filter to reduce the effect of charges that may build up on the mirrors' dielectric surfaces. Six out of the eight electrodes are visible: four from the outside showing their attachment to wires via gold plated crimps, and two on the inner surface of the cavity. The heads of the screws form the surface of the electrode. Figure taken from Ref. [153].

these constraints, providing a ~ 13 μm waist at least 12 mm away from the nearest surface. To provide passive electric field attenuation, the steel mounting structure fully encloses the locking piezo, which can be driven up to 1 kV, and the front surface of every mirror is covered except for small aperture at the mode location. Additionally, eight screw-head electrodes provide active electric field control, and the two separate halves of the mounting

structure may each be set to an arbitrary electric potential. In total, this provides ten degrees of freedom to control the eight independent electric field and electric field gradient components. Finite element analysis based on 3D CAD designs then provide the conversion matrix between applied electrostatic potentials and the electric field and gradients at the mode waist. Since the number of electrodes exceeds the number of controlled components, we calculate and use the 'optimal' conversion matrix which minimizes the applied electric potentials.

Figure A.2.2 shows the evolution of Rydberg linewidth with principal quantum number over two resonators: one with material $\sim$ 1.5mm [158] from the laser-cooled atomic sample, and the optimized structure employed in this work (see Fig. A.2.1c), where the closest surface is 12 mm from the atomic sample. This change produces a $\sim$ 3000-fold reduction in field-induced broadening, enabling us to enter the strongly-interacting regime.

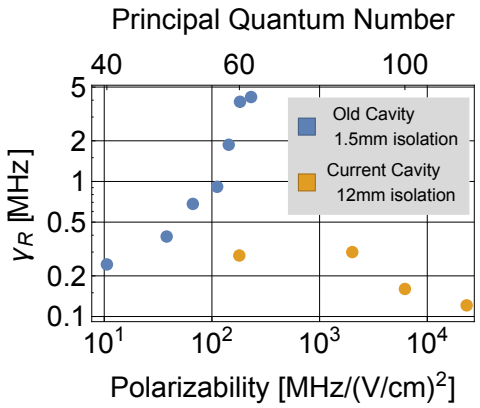

Figure A.2.2: **Improved Electric Field Environment.** The previous experimental resonator had material $\sim$1.5mm away from the atomic sample at the resonator waist. Even with eight electrodes to control the electric field environment, this led to significant electric fields and gradients at the atoms. These fields increase the Rydberg state loss, γ_R, as seen in fits to broad EIT spectra (blue). The current experimental resonator places the nearest material over 12 mm away from the atom, with most material well over 1cm away. After optimizing the electric field environment via electrodes, we find that the Rydberg state loss decreases slightly with principal quantum number. Figure taken from Ref. [153].

The resonator's upper mirrors are plano-convex with a 50 mm radius of curvature while the lower mirrors are concave with a 25 mm radius of curvature. The two upper mirrors and the non-piezo lower mirror have a custom coating provided by Layertec GmbH, specified to have a 99.9% reflectivity at both 780 nm and 1560 nm, while having >95% transmission at 480 nm. The other lower mirror has a coating by Advanced Thin Films with much higher reflectivity of 99.995%. While the optimal finesse for this resonator would be $\sim$ 2100,

contamination during resonator alignment resulted in additional loss and a cavity finesse of $F = 1480(50)$. The free spectral range is 2204.6 MHz, measured with an EOM sideband, and the polarization eigenmodes are approximately linear and split by 3.6 MHz. The measured absolute on-resonance transmission, in-coupling through one upper mirror and out-coupling through the other upper mirror, is $T_{cav} = 8.2\%$, providing an estimate of the single pass transmission through an upper mirror $T_{upper} = \sqrt{T_{cav}}\frac{\pi}{F} = 0.061\%$, and a probability of out-coupling any given intra-cavity photon through a top mirror of $P_{outcoupling} = \frac{FT_{upper}}{2\pi} = 14\%$. The detection path efficiency (after resonator out-coupling, and excluding the detector) of 92% is dominated by narrow line filters used to block external background light and down-converted 480 nm photons (see Sec. A.2.2). The output is split on a 50:50 beam-splitter, and the resulting beams are aligned (with 97% efficiency) to two single photon counting modules with a quantum efficiency of 55%. The total detection path quantum efficiency (for both detectors together) is thus $\eta_{tot} = 7.3\%$. From this, we calculate a conversion between photon detection rate and intra-cavity photon number of $708 \times 10^3 s^{-1}$ /photon.

We can lock the experimental resonator to an arbitrary detuning from the atomic resonant frequency. First we lock a frequency doubled 1560 nm laser to an ultra stable notched Zerodur cavity (Stable Laser System Model VH6020-4 with linewidths of $2\pi \times 55$ and $2\pi \times 41$ kHz at 780 nm and 960 nm, respectively), and then we lock the experimental resonator to the 1560 nm laser. The 780 nm lock to the ultra-stable cavity is accomplished via a two tone Pound-Drever-Hall technique. An EOM modulates the 780 nm light at two frequencies: one fixed at 10 MHz, and the other an arbitrary DDS-generated, computer controlled frequency between 50 MHz and 1.5 GHz. Demodulation of the reflection signal at 10 MHz provides three locking features, one at the cavity resonant frequency, one at the cavity resonant frequency plus the DDS frequency, and one at the cavity resonant frequency minus the DDS frequency. By locking to either the upper or lower sideband locking feature, this scheme allows locking the 780 nm probe (and hence the 1560 nm laser) carrier frequency to an arbitrary frequency relative to the atomic resonance.

The experimental resonator is locked to the 1560 nm laser via two tone frequency modulation spectroscopy of the resonator, with feedback controlling the length of a piezo tube on which one of the lower resonator mirrors is mounted. The error signal generation is similar to the Pound-Drever-Hall technique used with the ultra-stable cavity, except that we demodulate the transmission signal rather than the reflection because the reflection is not directed through a window of the vacuum chamber. While this in principle lowers the response of the lock above the resonator's 1560 nm linewidth (9MHz), the locking bandwidth is in practice limited much sooner by piezo-mount resonances at the few kHz level. This permits locking the resonator to an arbitrary detuning from the atomic resonance.

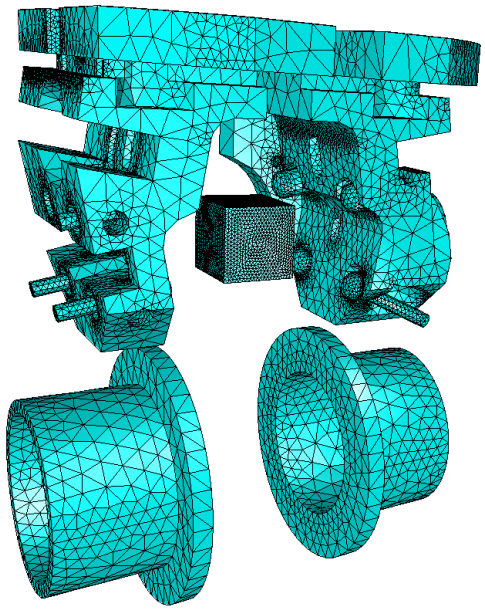

Figure A.2.3: **A 3D CAD .stl model** generated in SolidWorks is imported into ElmerGUI finite element analysis package via the Salome mesh generation software. The steel mounting structure, eight electrodes with their macor spacers, high voltage piezo, and MOT coils are included in the model; an additional fictitious cube with a finer mesh is specified near the atom location in order to increase the precision of the result. Each insulator and conductor is assigned a permittivity or voltage boundary condition respectively, with a large bounding sphere enclosing the entire model (not shown) given an 'effective infinite' boundary condition. The electric field at the atom position is calculated with each metal body set to 0V except for one set to 1V, and a python script then iterates over which metal body is set to 1V. The results provide a matrix converting electrode potentials to electric field at the atoms. This may then be inverted and used in the experimental control apparatus to convert a desired electric field (or gradient) into applied voltages. Figure taken from Ref. [153].

Slow drifts in temperature cause the resonator piezo locking voltage to drift, with a single 1560 nm free spectral range corresponding to ∼500 V on the piezo (the piezo is non-linear, so this depends on where in the 1 kV range of the piezo the FSR is measured). In particular, daily modulation of the Rubidium dispenser current and variations in the MOT coil current cause heating of the resonator. Because the resonator is thermally well isolated from the environment, the thermal relaxation time constant is ∼1 hour. The thermal impulse is also

significant: when the dispensers are turned on, the resonator drifts through 4-5 1560 nm free spectral ranges before settling. A particularly concerning effect from this voltage drift is the variable electric field experienced by Rydbergs at the mode waist. We expended considerable effort to isolate the atoms from charge buildup and the piezo voltage, but still found that, at 100S, a drift of $\sim$30 V on the piezo would shift and broaden the dark polariton significantly. At 121S, only a few volts of piezo drift are necessary to shift out of EIT resonance.

In order to remove this instability, we implement slow digital feedback on the piezo locking voltage by heating the steel resonator structure using a pulse-width modulated 980 nm laser with $\sim$1 W of power focused to a $\sim$1 mm diameter spot. This slow feedback stabilizes the locked piezo-voltage to a set-point of 60 V, with RMS error of $<$0.05 V.

A.2.2 Fluorescence/Parametric Down-conversion Background of 480nm $\rightarrow$ 780nm Photons

We employ free-space single photon counting modules (SPCMs) to improve our detection path efficiency. Careful elimination of environmental backgrounds enables us to reach the manufacturer-specified 50 Hz dark count rate of the detectors. However, in the presence of the 480nm control field, we experience 200 Hz of additional counts, even with interference filters (blocking 300-1200nm, save a $\pm \sim 1$ nm interval around 780 nm) placed in the 480nm path immediately before the vacuum chamber. Removing this background required *ultra-narrow* filtering around 780nm after the vacuum chamber, but before the SPCMs, which we achieved with two 785 nm clean-up filters (each $\pm \sim 1$ nm wide, with sub-nm edges) in the detection path, and appropriately tilted to narrow the filtering bandwidth by an order of magnitude, leaving an excess background of only 20 counts/second.

The source of this background is either fluorescence or spontaneous parametric down-conversion of 480 nm photons *within the resonator mirrors and vacuum chamber windows* to 780 nm;

this effect is not observable with single-mode fibers in the detection path, as both fluorescence and SPDC are highly multi-mode and are thus filtered out. The down-conversion almost certainly occurs within the resonator mirrors: because the control beam is focused to a tight spot at the resonator waist, the intensity of the beam in the resonator mirrors is much higher than in any other piece of glass.

A.2.3 Inhomogeneous Broadening and Performance Limitations

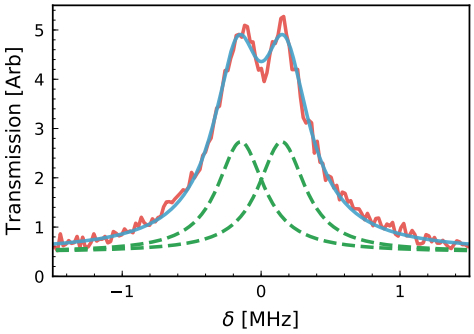

Figure A.2.4: **Structure of the EIT transmission peak.** The resonator transmission is plotted vs. probe detuning, on the $100S_{\frac{1}{2}}$ EIT feature, at zero E- and B-field. We observe a splitting of the feature, of magnitude $2\pi \times 294$ kHz. Figure taken from Ref. [153].

We observe a slight disagreement between the measured $T_1 = 590$ ns (and corresponding linewidth of $\gamma_{EIT} = 2\pi \times 270$ kHz) and the width of the EIT feature in Fig. 5.2b of $\gamma_{EIT} = 2\pi \times 400$ kHz, indicating $\sim 2\pi \times 130$ kHz of inhomogeneous broadening. This inhomogeneous broadening impacts the EIT feature by increasing its linewidth and suppressing its height, but does not substantially impact the bright polariton features due to their reduced Rydberg admixture and larger intrinsic linewidth from P-state-admixture.

Indeed, a more careful examination of the central EIT feature, shown in Fig. A.2.4, reveals a small splitting. We postulate that this arises from a weak admixture of a nearly-degenerate Rydberg state, potentially by a weak Zeeman field, or Hyperfine coupling. Another possibility is a near-degenerate ultra-long-range Rydberg molecular state, explored recently by the Hofferberth group [387] at slightly lower principal quantum numbers.

A.2.4 Calculation of Dark Polariton Rabi Oscillation Frequency

To extract the measured Rabi oscillation frequency between zero and one polaritons from the highest probe power data in figure 5.5b, we fit the ring-up curve with the solution of the optical Bloch equation starting with $\rho(t=0) = |0\rangle\langle 0|$:

$$\rho_{ee}(t) = \frac{1}{2} - \frac{\gamma^2}{\gamma^2 + 8\omega^2}\left[1 + \frac{4\omega^2}{\gamma^2}e^{-3\gamma t}\left(\cos\chi t + \frac{3\gamma}{\chi}\sin\chi t\right)\right] \tag{A.71}$$

Here $\chi \equiv 2\sqrt{\omega^2 - \gamma^2/4}$; the fit to the data yields $\omega = 2\pi \times 245$ kHz, corresponding to the observed π-pulse time of approximately 0.65μs, corrected for the rapid decay $\gamma = 2\pi \times 325$ kHz.

This ω should be compared to the Rabi frequency Ω_p predicted based on the cavity driving, which we extract from the incident photon rate, R_{inc}:

$$\Omega_p = \sqrt{\frac{R_{inc}}{4\tau}\sqrt{T_{EIT}/T_{CAV}}}. \tag{A.72}$$

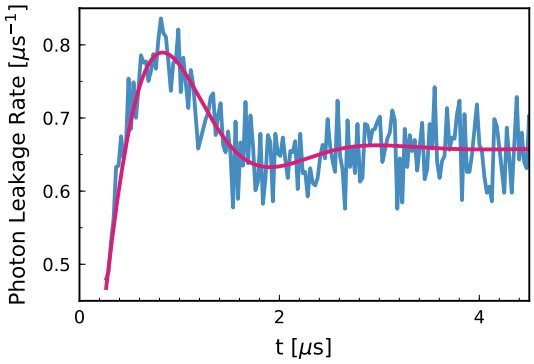

Figure A.2.5: **Polariton Rabi Oscillation and Optical Bloch Equation Fit.** The Rabi oscillation between 0 and 1 dark polaritons (Fig. 5.5a, highest power) is plotted subsequent to the bright polariton dynamics of the first $\sim$ 440ns, along with a fit to the Optical Bloch equation. Figure taken from Ref. [153].

At the highest power, $R_{inc} = 21$ MHz, yielding $\Omega_p = 2\pi \times 261(40)$ kHz, within $\sim 2\sigma$ of the measured value above.

A.2.5 Calculation of Steady-state Dark Polariton Number

In the ring-up and ring-down of the dot, the contributions of dark and bright polaritons mix in the observed resonator transmission. This is because the Rydberg-like dark polariton

is only weakly coupled to the resonator field, so the resonator drive-power necessary to excite it will off-resonantly excite bright polaritons, which are then much more likely to emit into the resonator due to their light-like nature. This effect can be suppressed by increasing the control field intensity, thereby making the dark polariton more light-like and thus more efficiently generated and read-out, increasing the atom number, to increase the bright-polariton detuning, or by detecting the dark polaritons directly through blockade-enhanced imaging [291].

In the present situation, to extract the dark polariton number we first isolate the dark- and bright- polariton contributions to the cavity leakage field by harnessing the fact that the bright polariton decays more rapidly. We thus wait for the bright polaritons to decay away, and fit the remaining long-time cavity ring down tail to a decaying exponential:

$$R_P(t) = R_P(0)e^{-t/\tau_D} \tag{A.73}$$

where $R_P(0)$ is the extrapolated zero-time photon leakage rate and τ_D is the lifetime of the dark polariton. With an arbitrarily narrow Rydberg state, the dark polariton can only decay through the photon channel, and the EIT transmission should be 100% of the empty cavity transmission. However, in a real experiment, the Rydberg state has a finite lifetime which allows the dark polariton to decay without emitting a cavity photon. This results in the reduction of EIT transmission. We can then convert the photon leakage rate to polariton decay rate using

$$R_D = \frac{R_P}{\sqrt{T_{EIT}/T_{CAV}}} \tag{A.74}$$

where T_{EIT} and T_{CAV} are the EIT and empty cavity transmission at the same probe power. The steady state dark polariton number is then obtained using

$$n_D(0) = R_D(0) \times \tau_D. \tag{A.75}$$

Note that the long-time tail would not reflect the simultaneous presence of multiple dark polaritons in the cavity, which would have already decayed rapidly due to their interactions (see section 2.2.4). However, the steady state number we calculate remains valid because multiple occupation is strongly suppressed by blockade.

A second way to calculate the dark polariton number is to calculate the extrapolated zero-time *photon* number and map it onto the dark polariton number via the dark state rotation angle.

$$n_D = \frac{R_P}{\kappa \cos^2(\theta)} \tag{A.76}$$

where R_P is the steady state rate of photons emitted from dark polaritons obtained from Fig. 4(c), $\kappa = 2\pi \times 1.55$ MHz is the cavity linewidth, and $\cos^2(\theta) = \frac{\Omega^2}{G^2+\Omega^2}$ is photonic fraction of the dark polariton. However, the dark state rotation angle θ is obtained by fitting the EIT spectrum with a ideal three level system with only homogeneous broadening. The two EIT resonant peaks (see Sec. A.2.3) indicates that our system is more complicated than the simple three-level and thus the fitted rotation angle is oversimplified for calculating the dark polariton number.

A.2.6 Shelved Rydberg Atoms

To operate in the regime of well-behaved cavity Rydberg polaritons, it is crucial that the there not be any other Rydberg atoms in the vicinity of the atomic sample. We have found two common sources of such Rydbergs, and have worked hard to suppress them:

1. Stray laser fields on the Rubidium D_2 line: during the probing cycle, a high-intensity laser promotes atoms from the $5P_{3/2}$ manifold directly to the $100S_{1/2}$ Rydberg manifold. It is assumed that the only atoms in $5P$ arise from cavity excitation, of which there should be only one (or, at most two) at any given time, due to blockade. Insuf-

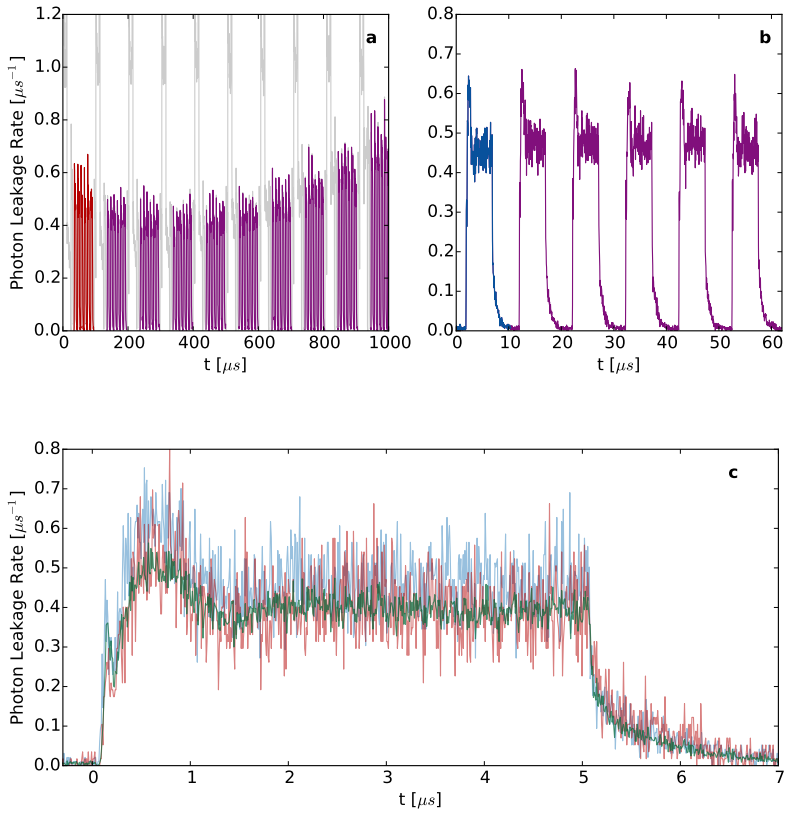

Figure A.2.6: **Ringdown Count Arrival Histogram. (a)** The entirely unfolded ringdown histogram of photon arrival times (data from Fig. 5.5a, highest power) is built up over 16,000 individual runs of the experiment. Ten 'reslicing' intervals are apparent, with the data used highlighted in purple, and the first reslicing interval in orange. The smooth and relatively minor fluctuation in the transmission rate over the course of the 1 ms total probe time indicates successful reslicing with constant atom number and the lack of shelved Rydbergs which would reduce the transmission. **(b)** The same data are folded over each reslicing interval, with the excess depump and repump photons as well as the first and last probe cycles cut out. This leaves six 10 μs probe cycles, the first of which is highlighted in blue. When all six are folded on top of each other, they yield data for Fig. 5.5. The steady transmission is constant over these cycles indicating that Rydbergs are not being shelved. **(c)** To investigate the possible buildup of stray Rydberg atoms, we plot the folded data of the first reslicing interval in orange, the folded data of the first probe cycle from all reslicing intervals in blue, the entire folded dataset (same as Fig. 5.5a, highest power) in green. If stray Rydbergs were developing during each 1 ms run or within each reslicing interval, either the orange or blue curves should saturate to a significantly higher leakage rate. Figure taken from Ref. [153].

ficient attenuation of slicing fields results in direct, unblockaded excitation of atoms to $5P$; adding additional AOMs and/or double passing existing AOMs in the slicing path resulted in a nearly two-fold increase in EIT transmission, indicating a substantial reduction in stray excitation of Rydbergs (see Fig. A.2.7a).

2. Excessive probing strength can also result in shelved Rydbergs, by breaking the block-

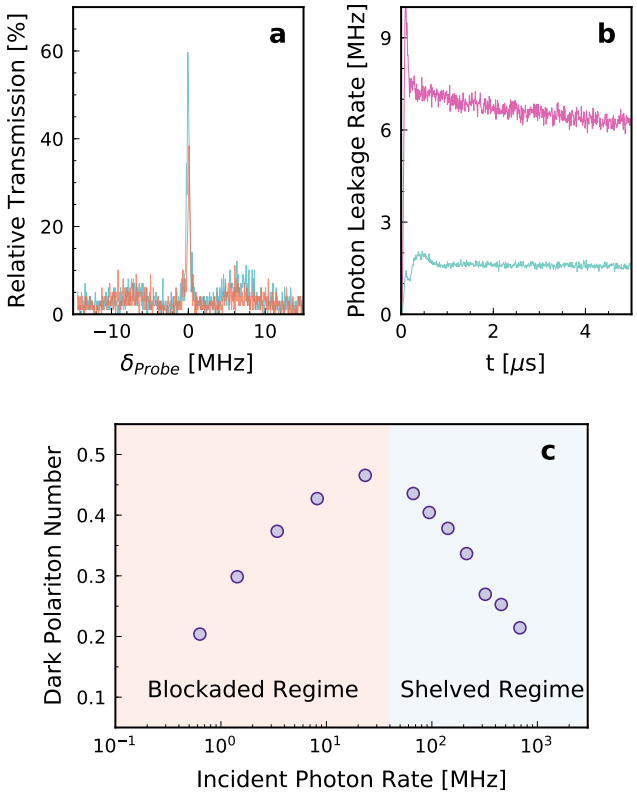

Figure A.2.7: **Sources of Shelved Rydbergs.** Rydberg atoms which are not part of a polariton may be generated either by improper sample preparation **(a)** or by overdriving the polaritonic dot with an excessively strong probe **(b-c)**. **(a)** Insufficient extinction of the slicing beam during the probe interval (when the 480 nm control field is "on") results in direct excitation of the atomic cloud to the Rydberg state. Shown is the EIT spectrum when such a process is present (red curve), contrasted with improved extinction of the slicing beam resulting in a drastically improved peak EIT transmission (blue). **(b)** At extremely high probing powers the Rydberg blockade is partially broken, resulting in Rydberg atoms irreversibly "shelved" in other principal quantum numbers. This effect is apparent in the time-dynamics of the cavity transmission; at low probe powers (blue) the transmission reaches a steady state in less than a microsecond, and remains constant thereafter. At extremely high probe powers (purple) the transmission decays over time, as "shelved" Rydbergs build up. **(c)** The (ring-down extracted) dark polariton number after 5μs of probing, versus probe power. This data shows a saturation at 0.5 dark polaritons, as explored in the main text, followed by a decay due to the shelved Rydbergs. Figure taken from Ref. [153].

ade and forcing additional photons into the resonator; these photons enter through higher-order Rydberg-collision processes which leave long-lived Rydbergs in other principal numbers. They are apparent in both the time dynamics of the Rydberg excitation process (see Fig. A.2.7b), and in the steady-state dependence of the dark polariton number on probe strength (see Fig. A.2.7c).

A.2.7 Theory Values and Curves for g_2

To arrive at the predicted g_2 at $\tau = 0$ in Fig. 5.4a, shown with a dashed line, we employ non-Hermitian perturbation theory to generate a full theory (see Ref. [153] SI L) of 360 three-level atoms which interact in their Rydberg state, coupled to a single cavity mode; the atom positions are randomly drawn from a cross-sectional area of radius 18 μm, for a cavity mode waist of 14 μm, with inhomogeneous broadening 135 kHz of the Rydberg state. This value is then multiplied by the apparent classical fluctuations near $\tau = 0$ of $g_2^{classical} \approx 1.7$, and added to the g_2 contribution from the independently measured dark-count rates of 50 Hz.

To generate a theory curve for time-dynamics of the g_2 in Fig. 5.4a, shown as a green band, we combine non-Hermitian perturbation theory as above to estimate the minimum value of the g_2 with a master-equation simulation to generate its time-dynamics (see Sec. A.2.8). This is necessary because the system is slightly over-driven, producing Rabi oscillations in the response which to include in a full theory as in Ref. [153] SI L would be computationally challenging. Accordingly we adjust the interaction strength U in the master equation of the Rydberg state to match the time dynamics predicted by full theory in the weak driving limit. The collective light-matter coupling g and control field Rabi frequency Ω are kept the same as being used in the full theory. The driving amplitude $\Omega_D = 0.52$ MHz is extracted from the photon leakage rate of an empty cavity. The error band is a result of the statistical uncertainty of the probe detuning of ± 100 kHz and driving amplitude of ± 50 kHz.

A.2.8 A Simple Master-Equation Effective Model of Cavity Rydberg Polaritons

Here we present the simple master-equation model that we employ to model the dynamics of the cavity ring-up and ring-down. Instead of employing the full model of N 3-level atoms coupled inhomogeneously to both the resonator and control field, and interacting with one another in a position-dependent manner (as in the later SI section), here we simply assume all atoms are identical, with an interaction in the Rydberg state of strength U. Accordingly, the Hamiltonian is:

$$H = \omega_c a^\dagger a + \omega_e p^\dagger p + \omega_r r^\dagger r + g\sqrt{N}(a^\dagger p + p^\dagger a) + \Omega(p^\dagger r + r^\dagger p) + \Omega_D(a^\dagger + a) + \frac{U}{2} r^\dagger r^\dagger r r \tag{A.77}$$

The evolution of the reduced density matrix ρ is given by a Lindblad master equation:

$$\dot{\rho} = -i[H, \rho] + \frac{\kappa}{2}\mathcal{L}(\rho, a) + \frac{\Gamma}{2}\mathcal{L}(\rho, p) + \frac{\gamma_r}{2}\mathcal{L}(\rho, r) \tag{A.78}$$

$$\mathcal{L}(\rho, \beta) \equiv \beta\rho\beta^\dagger - \frac{1}{2}\{\rho, \beta^\dagger\beta\} \tag{A.79}$$

The bosonic operators: $a^\dagger(a)$ creates (destroys) a resonator photon; $p^\dagger(p)$ creates (destroys) a P-state atom; and $r^\dagger(r)$ creates (destroys) a Rydberg atom. Our numerics begin at $t = 0$ with initial condition $\rho(t = 0) = |0\rangle\langle 0|$.

Here $\kappa = 2\pi \times 1.55$ MHz is the cavity linewidth, $\Gamma = 2\pi \times 6$ MHz is the atomic P-state linewidth, $\gamma_r = 2\pi \times 200$ kHz is the collective Rydberg-state linewidth [158], $\omega_c = 2\pi \times 0$ kHz is the resonator frequency in the frame rotating with the probe beam, $\omega_e = 2\pi \times 0$ kHz is the energy of the atomic P-state in the frame of the probe beam, and $\omega_r = 2\pi \times 0$ kHz is the

atomic Rydberg state energy in the frame of the probe and control beams. $g\sqrt{N} = 2\pi \times 6$ MHz is the collective light-matter coupling, $\Omega = 2\pi \times 2$ MHz is the Rabi frequency of the control field, $U = 2\pi \times 1.5$ MHz parameterizes a phenomenological Rydberg-Rydberg interaction strength that reproduces the observed blockade, and $\Omega_D = 2\pi \times 0.52$ MHz is the strength of the resonator driving field.

Note that $U = 1.5$ MHz $\ll \frac{C_6}{w_c^6} \approx 19$ MHz for the ^{87}Rb 100S van der Waals coefficient $C_6 = 56 \times 10^6 \mu\text{m}^6$, and cavity waist $w_c = 12\mu$m; this is because the two-polariton state is strongly renormalized by the blockade interaction.

A.2.9 Correlation Analysis for Floquet Polaritons

We test for interactions between polaritons by calculating the photon-photon correlation functions,

$$G_{mn}(\tau) = \frac{\left\langle n_m(t) n'_n(t+\tau) \right\rangle_t}{\langle n_m \rangle \langle n'_n \rangle}, \tag{A.80}$$

between the photons $n_m(t)$ counted at the first detector for mode TEM_{m0} and $n'_n(t)$ counted at the second detector for mode TEM_{n0}, where the angle brackets denote time averaging. Note that, for the cross-blockade measurement shown in figure 5.10d we include data from all relevant combinations of the four single photon counting modules.

To obtain correlation functions representing the cavity photons, we must account for the additional signal due to dark counts in each detector. The measured photon counts $n_m^{meas}(t)$ for detector m can be written as,

$$n_m^{meas}(t) = n_m^{cav}(t) + n_m^{dark}(t),$$

where $n_m^{cav}(t)$ are the counts coming from cavity photons and $n_m^{dark}(t)$ are the dark counts. Therefore, if we calculate the correlations between detectors m and p from the measured

photon counts naively, we actually obtain,

$$G_{mp}^{meas}(\tau) = \frac{\left\langle n_m^{meas}(t) n_p^{meas}(t+\tau) \right\rangle_t}{\left\langle n_m^{meas} \right\rangle \left\langle n_p^{meas} \right\rangle}$$

which differs from the desired correlation function of the cavity photons,

$$G_{mp}^{cav}(\tau) = \frac{\left\langle n_m^{cav}(t) n_p^{cav}(t+\tau) \right\rangle_t}{\left\langle n_m^{cav} \right\rangle \left\langle n_p^{cav} \right\rangle}.$$

Since dark counts occur at a constant rate for each detector (about 300 Hz in these experiments) and are uncorrelated with the real photon counts, we calculate the correlation functions of the cavity photons presented in the main text by using the measured counts and correcting for the average dark count rates as,

$$G_{mp}^{cav}(\tau) = \frac{\left\langle n_m^{meas}(t) n_p^{meas}(t+\tau) \right\rangle_t}{\left\langle n_m^{cav} \right\rangle \left\langle n_p^{cav} \right\rangle} - \frac{\left\langle n_p^{dark} \right\rangle}{\left\langle n_p^{cav} \right\rangle} - \frac{\left\langle n_m^{dark} \right\rangle}{\left\langle n_m^{cav} \right\rangle} - \frac{\left\langle n_m^{dark} \right\rangle \left\langle n_p^{dark} \right\rangle}{\left\langle n_m^{cav} \right\rangle \left\langle n_p^{cav} \right\rangle},$$

where the average count rate of cavity photons $\langle n_m^{cav} \rangle = \langle n_m^{meas} \rangle - \left\langle n_m^{dark} \right\rangle$ can be calculated trivially.

In these experiments, the observed correlations are affected by the strength g of the atom-cavity coupling. When the number of atoms in the cavity drops too low, reducing g, the polaritons do not blockade each other as well. Simultaneously, the reduced g causes polaritons to become more photon-like and increases the average count rate [158]. In order to eliminate experimental trials in which the coupling strength is too low, we calculate the running average of the count rate across our 340 000 total iterations of the experiment, with an averaging range of 200 trials, and remove the iterations taken at times when the average count rate was above 6.7 kHz total across all four detectors. Only the remaining 47% of datasets with a sufficiently low average count rate, indicating a sufficiently large g, were used to calculate the correlation functions shown in figure 5.10b-d.

We find that the correlations between polaritons in our atom-cavity system are well described by a three-level model in which the cavity is either empty or contains a single polariton in one of the two modes. This model simply extends the optical Bloch equations to allow excitations in either of the two possible modes. In the limit of weak driving this model predicts correlation functions of the form [388],

$$G_{mn}^{\mathrm{mod}}(\tau)/G_{mn}^{\mathrm{bkg}} = 1 + \left(1 - G_{mn}^{\mathrm{min}}\right)\left(e^{-\gamma|\tau|} - 2e^{-\gamma|\tau|/2}\right), \tag{A.81}$$

where G_{mn}^{bkg} accounts for classical fluctuations raising the apparent correlation on long timescales, G_{mn}^{min} encodes the depth of the antibunching and accounts for imperfect blockade, and γ is the lifetime of a dark polariton. The measured correlation functions shown in figure 5.10b-e are well explained by this model, as indicated by the fitted curves for which we used Eq. A.81 with G_{mn}^{bkg}, G_{mn}^{min}, and γ as the three fitting parameters.

The depth of the correlation functions at zero time delay indicates the strength of the interactions between polaritons relative to their lifetime. We can understand this using a simple model for quasiparticles with annihilation operator c_m in mode m, governed by the Hamiltonian

$$H = \sum_m \Omega_D(c_m^\dagger + c_m) + \sum_m i\frac{\gamma_m}{2}c_m^\dagger c_m + \sum_{mn}\frac{U_{mn}}{1+\delta_{m,n}}c_m^\dagger c_n^\dagger c_n c_m \tag{A.82}$$

where Ω_D is the driving strength of every mode, γ_m is the lifetime of particles in mode m, U_{mn} is the interaction strength between modes m and n, and $\delta_{m,n}$ is the Kronecker delta function. In the limit of weak driving $\Omega_D \ll \gamma_m$, non-Hermitian perturbation theory (see Ref. [207] SI. B9) can be used to calculate the correlation minimum,

$$G_{mn}^{\mathrm{min}} = \frac{(\frac{\gamma_m+\gamma_n}{2})^2}{(\frac{\gamma_m+\gamma_n}{2})^2 + U_{mn}^2}. \tag{A.83}$$

This model reveals that seeing any significant antibunching requires pairwise interactions

comparable in strength to the lifetime of the quasiparticles, $U_{mn} \gtrapprox \gamma_m, \gamma_n$. In particular, assuming equal lifetimes γ in every mode, a correlation minimum of $G^{\min}_{mn} = 0.5$ indicates interaction strength equal to the lifetime, $U_{mn} = \gamma$.

While we are confident that the correlations in this system arise exclusively from strong interactions between the polaritons, it is technically possible that the *cross-correlation* can arise from classical sources (such as probe beam intensity variation or oscillations in the atomic cloud shape). Such classical fluctuations cannot cause the zero-time dips in the autocorrelation due to the Cauchy-Schwarz inequality. Even in the case of the cross-correlation, classical sources are exceedingly unlikely: the timescale of the anticorrelation dip in comparison with the autocorrelation traces, the lack of anticorrelation when probing bright polaritons, and the agreement of the observed anticorrelations with the non-Hermitian perturbation theory all suggest that the cross-correlations arise from dark polariton interactions.

The depths of the measured correlation functions $G^{\min}_{mn}$ are consistent with our predictions using non-Hermitian perturbation theory (see Ref. [207] SI. B9). From the experimental fits we extract $G^{\min}_{00} = 0.58(8)$, $G^{\min}_{44} = 0.42(6)$, and $G^{\min}_{40} = 0.65(6)$. For comparison, our simulations predict $G^{\mathrm{sim}}_{00}(0) = 0.53(1)$, $G^{\mathrm{sim}}_{44}(0) = 0.44(1)$, and $G^{\mathrm{sim}}_{40}(0) = 0.57(1)$. The simulations were performed with the independently characterized experimental parameters of $g = 5.2$ MHz, $\Omega = 1.4$ MHz, and an average, linear P-state detuning of $\delta e = 0.6$ MHz for the TEM_{40} mode, as well as $g = 3.5$ MHz, $\Omega = 1.0$ MHz, and $\delta e = 1.0$ MHz for the TEM_{00} mode. The agreement between experiments and simulations verifies that the observed performance is consistent with our expectations based on the current experimental parameters.

In these experiments, the performance of Floquet polaritons is primarily limited by the splitting of the coupling strengths g and Ω between multiple bands due to modulation. Indeed, when the atoms are not modulated, we observe much deeper antibunching $G^{\min}_{00} = 0.11(2)$ as shown in figure 5.10e. For this optimized dataset, $g = 5.5$ MHz and $\Omega = 2.4$ MHz

on the TEM_{00} mode alone. Both of these optimized coupling strengths are less than $2.5\times$ larger than the corresponding coupling strengths achieved with the Floquet polaritons. The optimized parameters can be achieved or exceeded for the frequency modulated case with straightforward technical upgrades as discussed in the main text.

A.2.10 Redistributing a State Using Frequency Modulation

In this section we present the simplest theory of how frequency modulating the $5P_{3/2}$ state redistributes its spectral density among multiple bands.

The time-dependent Hamiltonian for a multimode cavity containing a gas of frequency-modulated three-level atoms is ($\hbar \equiv 1$),

$$H_0(t) = \sum_n^{N_{cav}} \delta_c^n a_n^\dagger a_n + \delta_e(t) \sum_m^{N_{at}} \sigma_m^{ee} + \delta_2 \sum_m^{N_{at}} \sigma_m^{rr} + \sum_n^{N_{cav}} \sum_m^{N_{at}} (g_{mn} \sigma_m^{eg} a_n + g_{mn}^* \sigma_m^{ge} a_n^\dagger) + \sum_m^{N_{at}} \left(\Omega_m^b \sigma_m^{re} + {\Omega_m^b}^* \sigma_m^{er} \right) + \frac{1}{2} \sum_{n \neq m} \sigma_m^{rr} \sigma_n^{rr} U(|x_m - x_n|). \quad \text{(A.84)}$$

This Hamiltonian is written in the rotating frame of the probe laser with frequency ω_p and the blue, Rydberg coupling laser with frequency ω_b. There are N_{cav} relevant cavity modes and N_{at} atoms in the sample. The Hamiltonian describes the dynamics among three types of excitations: cavity photons in mode n with annihilation operator a_n and energy $\delta_c^n \equiv i\frac{\kappa}{2} + E_n - \omega_p$ including leakage of photons from the cavity at rate κ, excitations of atom m to the $5\mathrm{P}_{3/2}$ state $|e\rangle_m$ with time-dependent energy $\delta_e(t) \equiv i\frac{\Gamma}{2} + E_p(t) - \omega_p$ including the decay at rate Γ, or excitations of atom m to the Rydberg state $|r\rangle_m$ with energy $\delta_2 \equiv i\frac{\Gamma_r}{2} + E_r - \omega_b - \omega_p$ accounting for decay at rate Γ_r. For convenience, we define $\sigma_m^{AB} \equiv |A\rangle_m \langle B|_m$. The coupling strength between atom m and cavity mode n is g_{mn}, which

depends on the field strength $E_n(x_m)$ of the cavity mode at the two-dimensional position x_m of the atom. The coupling from the Rydberg coupling laser is Ω_m^b, which depends on the location of atom m. Finally, $U(|x_m - x_n|) \equiv C_6/|x_m - x_n|^6$ encodes the interaction strength between two Rydberg atoms with the coefficient C_6 depending strongly on the Rydberg level [99].

We can dramatically simplify the full model above by recognizing that only a small subset of all possible atomic excitations are actually coupled to the cavity photons. In fact, the orthonormal set of cavity modes couples one-to-one with an orthonormal set of collective atomic states whose contributions from each atom match the electric field pattern of the corresponding mode.Photons in cavity mode n couple to the collective excitation created by the operator,

$$p_n^\dagger = \frac{1}{g^n} \sum_m^{N_{at}} g_{mn} \sigma_m^{eg},$$

where $(g^n)^2 \equiv \sum_m^{N_{at}} |g_{mn}|^2$ is the total atom-photon coupling strength for that mode. This operator creates an excitation in a superposition of states in which any one atom in the cavity field is in the excited state; the excitation is thus "shared" by all of the atoms at once. Similarly, the operator

$$r_n^\dagger = \frac{1}{\sqrt{g^n}} \sum_m^{N_{at}} g_{mn} \sigma_m^{rg}$$

creates a collective Rydberg excitation corresponding to the n'th cavity mode. The many other superposition states of excited atoms which do not primarily couple with one of the cavity modes can be neglected. With this we have a much simpler effective model describing the coupling of cavity modes with collective atomic excitations, governed by the Hamiltonian

[153, 161],

$$H(t) = \sum_{n}^{N_{cav}} \delta_c^n a_n^\dagger a_n + \delta_e(t) \sum_{n}^{N_{cav}} p_n^\dagger p_n + \delta_2 \sum_{n}^{N_{cav}} r_n^\dagger r_n + \sum_{n}^{N_{cav}} g^n p_n a_n^\dagger + h.c. + \sum_{n}^{N_{cav}} \Omega r_n p_n^\dagger + h.c. + \frac{1}{2} \sum_{nmpq}^{N_{cav}} U_{nmpq} r_n^\dagger r_m^\dagger r_p r_q, \quad \text{(A.85)}$$

Now, we assume that the energy of the $5P_{3/2}$ state is sinusoidally modulated $E_p(t) = \bar{E}_p + \eta \cos(\omega t)$ with amplitude η and angular frequency $\omega \equiv 2\pi f$. To put the modulated Hamiltonian in a more useful form, we transform the collective $5P_{3/2}$ excitations,

$$p_n \to \exp\left(i \frac{\eta}{\omega} \sin(\omega t)\right) p_n$$

Under this transformation and using the Jacobi-Anger expansion $e^{iz\sin(\omega t)} = \sum_{n=-\infty}^{\infty} J_n(z) e^{in\omega t}$, the Hamiltonian (dropping the interaction terms for simplicity) becomes,

$$H(t) = \sum_{n}^{N_{cav}} \delta_c^n a_n^\dagger a_n + \bar{\delta}_e \sum_{n}^{N_{cav}} p_n^\dagger p_n + \delta_2 \sum_{n}^{N_{cav}} r_n^\dagger r_n + \sum_{n}^{N_{cav}} \sum_{j=-\infty}^{\infty} g_j^n e^{ij\omega t} p_n a_n^\dagger + h.c. + \sum_{n}^{N_{cav}} \sum_{j=-\infty}^{\infty} \Omega_{-j} e^{-ij\omega t} r_n p_n^\dagger + h.c. \quad \text{(A.86)}$$

where each collective $5P_{3/2}$ state n has been redistributed among many bands, reflected by the couplings $g_j^n \equiv g^n J_j\left(\frac{\eta}{\omega}\right)$ and $\Omega_j \equiv \Omega J_{-j}\left(\frac{\eta}{\omega}\right)$ for each band j (recall that $\hbar \equiv 1$).

While chapter 5 emphasized the splitting of the atom-cavity coupling into bands, we see here

that the Rydberg coupling Ω is also split into bands with couplings Ω_j. However, unlike the many non-degenerate cavity modes which can couple resonantly to different bands, in our system all of the Rydberg states are degenerate. Therefore, the Rydberg coupling for each polariton mode comes from the same band l determined by the frequency of the coupling field, regardless of which band k is used for the atom-cavity coupling in that mode (see Fig. 5.8).

A.2.11 Floquet Polaritons in the High-Frequency Approximation

In this section we use the high-frequency approximation [298] to derive an analytical, effective Hamiltonian for our system which supports Floquet polaritons. As we have shown in the previous section, ignoring Rydberg-Rydberg interactions, the periodic Hamiltonian *for each cavity mode* n of our modulated system can be written in the form,

$$\begin{aligned} H_n(t) = &\delta_c^n a_n^\dagger a_n + \bar{\delta}_e p_n^\dagger p_n + \delta_2 r_n^\dagger r_n \\ &+ \sum_{j=-\infty}^{\infty} g_j^n e^{ij\omega t} p_n a_n^\dagger + h.c. \\ &+ \sum_{j=-\infty}^{\infty} \Omega_{-j} e^{-ij\omega t} r_n p_n^\dagger + h.c. \end{aligned} \tag{A.87}$$

In the absence of modulation, we would have $g_0 = g$, $\Omega_0 = \Omega$, $g_{j\neq 0} = 0$, $\Omega_{j\neq 0} = 0$ and recover the ordinary cavity EIT Hamiltonian. For perfect sinusoidal modulation of the P-state, we have $g_j^n \equiv g^n J_j\left(\frac{\eta}{\omega}\right)$ and $\Omega_{-j} \equiv \Omega J_j\left(\frac{\eta}{\omega}\right)$ as explained in the previous section. Here, we treat the most general form in which we allow arbitrary sideband strengths g_j^n and Ω_j.

The experimentally relevant case is the limit in which the cavity mode is near-detuned to band k of the $5P_{3/2}$ state and the Rydberg coupling laser is also near resonant for driving

$5P_{3/2} \rightarrow nS_{1/2}$ on band l for the chosen Rydberg principal quantum number n (where k and l are integers). In total, these conditions allow us to write,

$$\begin{aligned} \delta_c^n &\equiv \quad k\omega + \epsilon_c, \\ \bar{\delta}_e &\equiv \qquad \epsilon_p, \\ \delta_2 &\equiv \quad l\omega + \epsilon_r, \end{aligned} \tag{A.88}$$

with the requirement that the "quasienergies" ϵ [298] satisfy,

$$\epsilon_c, \epsilon_p, \epsilon_r \ll \omega.$$

We can then transform to the frame of this resonant coupling,

$$\begin{aligned} a_n &\rightarrow e^{ik\omega t} a_n, \\ r_n &\rightarrow e^{il\omega t} r_n, \end{aligned} \tag{A.89}$$

in which the Hamiltonian becomes:

$$\begin{aligned} H_n(t) = \epsilon_c a_n^\dagger a_n + \epsilon_e p_n^\dagger p_n + \epsilon_r r_n^\dagger r_n \\ + \sum_{m=-\infty}^{\infty} g_{m+k}^n e^{im\omega t} p_n a_n^\dagger + h.c. \\ + \sum_{m=-\infty}^{\infty} \Omega_{-m-l} e^{-im\omega t} r_n p_n^\dagger + h.c. \end{aligned} \tag{A.90}$$

Since we have stipulated that the energies ϵ are all small compared to the modulation frequency, our three states form a near-degenerate manifold. The terms with coefficients g_k and Ω_{-l} represent the near-resonant bands and are stationary, providing the primary coupling which leads to the formation of polaritons. As long as we have the additional

condition that the off-resonant couplings are small compared to the modulation frequency $g_{m\neq k}, \Omega_{m\neq -l} \ll \omega$, the rapid oscillation of the off-resonant terms enables us to use a series approximation for the Hamiltonian. In fact, the essential physics can be understood by simply dropping all of the oscillating terms. This is the typical rotating wave approximation, which is also the first order high-frequency approximation. At this level one obtains an effective Hamiltonian,

$$\begin{aligned} H_F^{(1)} = \epsilon_c a_n^\dagger a_n + \epsilon_e p_n^\dagger p_n + \epsilon_r r_n^\dagger r_n + \\ g_k^n p_n a_n^\dagger + h.c. + \\ \Omega_{-l} r_n p_n^\dagger + h.c. \end{aligned}$$

whose eigenstates are polaritons with light-matter coupling strength determined by the amplitudes of the resonant bands.

Experimentally, we often see significant shifts due to the rapidly oscillating terms, which we can understand by applying the high-frequency approximation beyond first order. The second order contribution to the effective Hamiltonian $H_F = \sum_m H_F^{(m)}$ is,

$$H_F^{(2)} = \sum_{m\neq 0} \frac{H_m H_{-m}}{m\omega},$$

where

$$H_m = \frac{1}{T}\int_0^T e^{-im\omega t} H_n(t) = H_{-m}^\dagger$$

are the Fourier components of the original Hamiltonian (Eq. A.87) and $T \equiv \frac{1}{f}$ is the Floquet

period. The total effective Hamiltonian at second order is,

$$\begin{aligned} H_F \approx & \tilde{E}_c a_n^\dagger a_n + \tilde{E}_e p_n^\dagger p_n + \tilde{E}_r r_n^\dagger r_n \\ & + g_k p_n a_n^\dagger + h.c. + \\ & + \Omega_{-l} r_n p_n^\dagger + h.c. \end{aligned}$$

with the quasienergies

$$\begin{aligned} \tilde{E}_c = & \quad \epsilon_c + \textstyle\sum_{j\neq 0} \frac{|G_{j+k}|^2}{j\omega}, \\ \tilde{E}_p = & \quad \epsilon_e + \textstyle\sum_{j\neq 0} \frac{|\Omega_{j-l}|^2 - |G_{j+k}|^2}{j\omega}, \\ \tilde{E}_r = & \quad \epsilon_r + \textstyle\sum_{j\neq 0} \frac{-|\Omega_{j-l}|^2}{j\omega}, \end{aligned}$$

shifted due to the second order terms. Note that this is the effective Hamiltonian *for each cavity mode*; since each transverse mode of the cavity couples to independent collective atomic excitations, we can perform this calculation for each mode considered on its own. The only interactions between the different polariton manifolds result from the Rydberg-Rydberg interactions, which we have neglected in this section in order to understand the behavior of single polaritons.

The additional shifts from the second order terms are relevant because the expansion parameters g_j/ω and Ω_j/ω are small but not negligible under our typical experimental conditions. For example, the shift of a cavity mode energy $\tilde{E}_c$ due to an off-resonant band with strength $g_{off} = 10$ MHz would be $g_{off}^2/\omega = 2$ MHz. These shifts have a noticeable influence on the spectrum in figure 5.9c, where the bright polariton peaks for the TEM_{40} are noticeably asymmetric. Since the TEM_{40} is near-resonant with the $j = 1$ band, the asymmetry is dominated by the off-resonant shift from the strong $j = 0$ band. For example, when $\eta = 4\eta_0$, $g_0 \approx 9$ MHz, causing the TEM_{40} energy to shift approximately 2 MHz toward higher frequency, while also shifting the corresponding collective P-state 2 MHz in the op-

posite direction. These shifts, as well as shifts from the other off-resonant bands, cause the asymmetric spectra observed in figure 5.9c.

A.2.12 Quasienergy Spectrum

In the previous section we derived the effective Hamiltonian (Eq. A.90) for each cavity mode after transforming into the frame of the near-resonant band (Eq. A.89). When considering multiple cavity modes together, we can simply extend our transformation,

$$a_n \to e^{ik_n\omega t}a_n, \tag{A.91}$$

to account for the different bands k_n of the $5P_{3/2}$ state which are near resonance with each cavity mode n. In this case, ignoring the off-resonant shifts for simplicity (that is, taking the first order High-frequency approximation), the effective Hamiltonian for the multimode system (including Rydberg interactions) is,

$$\begin{aligned} H_F = \sum_n^{N_{\text{cav}}} \Big(& \epsilon_c^n a_n^\dagger a_n + \epsilon_e p_n^\dagger p_n + \epsilon_r r_n^\dagger r_n \\ & + g_{k_n}^n p_n a_n^\dagger + \Omega_{-l} r_n p_n^\dagger + h.c. \\ & + \frac{1}{2}\sum_{nmpq}^{N_{cav}} U_{nmpq} r_n^\dagger r_m^\dagger r_p r_q \Big) \end{aligned} \tag{A.92}$$

As with typical cavity Rydberg polaritons, the dark polariton eigenstates of this Hamiltonian have quasienergies E^n_{dark} determined by the quasienergies of their constituent photon and Rydberg components [158],

$$E^n_{\text{D}} = \epsilon_c^n \cos^2\theta_n + \epsilon_r \sin^2\theta_n \tag{A.93}$$

where the dark-state rotation angles θ_n satisfy $\tan(\theta_n) \equiv g^n_{k_n}/\Omega_{-l}$.

Only the quasienergy appears in the effective many-polariton Hamiltonian (Eq. A.92), and therefore the dynamics of the Floquet system are determined by the quasienergy. That is, the specific band coupled to each cavity mode only matters to the extent that it determines the coupling strength $g^n_{k_n}$. While the coupling between the atom-cavity system and its environment, reflected for example in the spectroscopic features of figure 5.9c, may reveal "absolute" energies, the many-body dynamics governed by the effective Hamiltonian depends only on the quasienergies. Therefore, even though the measured dark polariton features in figure 5.9c for $\eta = 4\eta_0$ are detected at probe frequencies separated by 57.6(2) MHz, for the purposes of dynamics within the cavity they are nearly degenerate, with quasienergies (accounting for one unit of the modulation frequency $f = 58$ MHz) separated by only -0.4(2) MHz. Moreover, this feature can be used to control the quasienergy of each polariton mode simply by varying the modulation frequency to shift the $5P_{3/2}$ bands relative to their corresponding cavity modes.

A.3 Fractional Quantum Hall Physics with Photons

A.3.1 Experiment Setup and Typical Sequence

Our experiments begin with a gas of 10^7 cold ^{87}Rb atoms at a temperature of 15 μK prepared using a magneto-optical trap and polarization gradient cooling (Fig. A.3.1a). We transport that gas vertically into the waist of our science cavity using a moving optical lattice (Fig. A.3.1b). Previous iterations of the experiment would then release the gas from the trap in order to prevent inhomogeneous broadening of the ground to Rydberg transition due to the trapping beams [153, 207]. To improve the atomic density and experiment duty cycle for these experiments, we now cool the gas to a temperature below 1 μK and polarize the atoms into the lowest energy spin-state $|F = 2, m_F = -2\rangle$ within the hyperfine manifold F using degenerate Raman sideband cooling [206]. We then transfer the gas into an elliptical

dipole trap, which we retroreflect to form an optical lattice in order to support the atoms against gravity. This trap makes the gas at the cavity waist highly elliptical, with a very thin root-mean-squared (RMS) radius of 11 μm along the science cavity axis ($\hat{z}$) which makes the polariton interactions strong [153] while maintaining much larger transverse RMS radii of 51 μm$\times$ 120 μm in order to cover the area spanned by the desired transverse modes of the cavity (Fig. A.3.1d).

The elliptical lattice primarily traps the ground state atoms and only slightly perturbs the Rydberg state, resulting in an AC Stark shift of the two-photon resonance frequency for the $5S_{1/2} \rightarrow 111D_{5/2}$ transition of each atom. These shifts lead to inhomogeneous broadening because atoms at different positions in the trap experience different potentials. However, because the sample temperature (and therefore the spread of Stark shifts) of less than 1 μK corresponds to a frequency scale of less than 20 kHz, this inhomogeneous broadening makes a tolerably small contribution to the observed Rydberg linewidth of Γ_R=$2\pi \times$50 kHz. Therefore, we are able to leave the elliptical lattice on throughout the probe cycle in which we create dark polaritons.

We have found that careful management of the polarizations of the atoms and the light is crucial for maximizing the lifetime of our dark polaritons. In particular, while probing the system, we use a 5 G bias magnetic field directed along the Rydberg coupling beam propagation axis in order to provide a Zeeman splitting within each of the atomic state manifolds (Fig. A.3.1c). The sample is also repeatedly optically pumped along that same axis to ensure that all atoms start in the $|F = 2, m_F = -2\rangle$ state. Because the Rydberg coupling beam is coaligned with the magnetic field, and the science cavity mode axis is only $\sim 30^\circ$ away, the circularly polarized cavity photons only couple the atoms to a single spin state in each manifold. These conditions make our polarized atoms behave much more like a three-level system than an unpolarized sample; the three relevant levels are $|5S_{1/2}, F = 2, m_F = -2\rangle$, $|5P_{3/2}, F = 3, m_F = -3\rangle$, and $|111D_{5/2}, m_J = 5/2\rangle$ where we note that

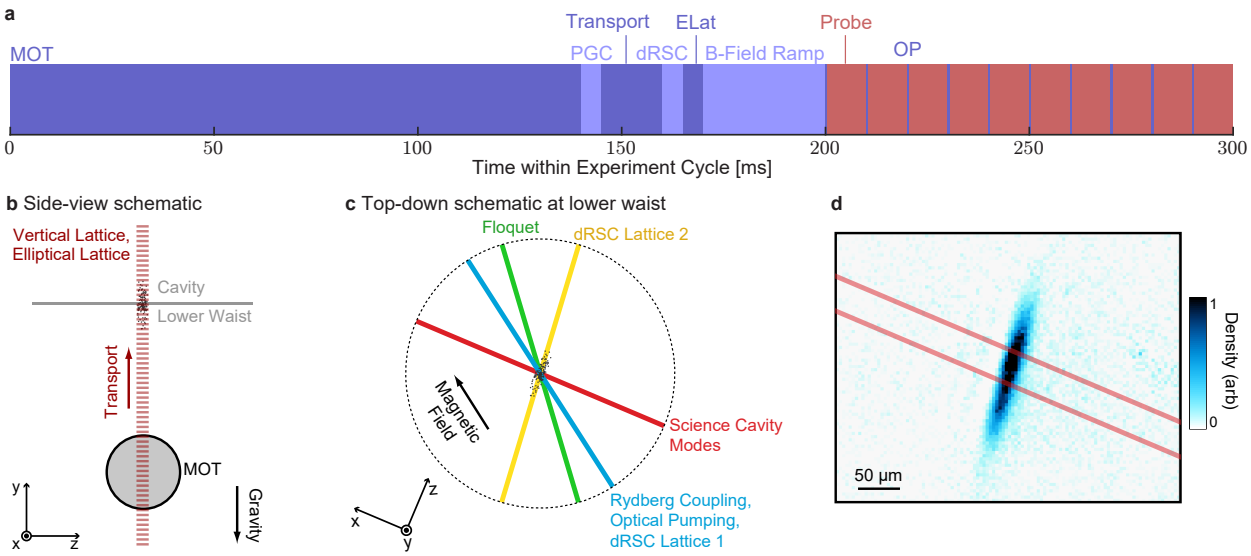

Figure A.3.1: **Experiment sequence and schematics.** **(a)** Our typical experiment sequence repeats every 300 ms. It begins with loading of the magneto-optical trap (MOT) while the electronic control system prepares to execute the rest of the sequence, followed by polarization-gradient cooling (PGC), transport of the atoms from the MOT to the cavity using a moving, vertical optical lattice (VLat), degenerate Raman sideband cooling (dRSC), transfer of the atoms into an elliptical optical lattice (ELat) to reshape the cloud, a ramp of the bias magnetic field and settling time to ensure stability, and finally ten, $\sim$ 10 ms probe cycles separated by brief pulses of optical pumping (OP) light. **(b)** A schematic of the experiment shown from the side, indicating beam alignment. **(c)** A schematic of the experiment from a top-down perspective, indicating the four beam paths which cross at the lower waist of the science cavity, as well as the beam(s) which propagate along each path. The bias magnetic field is parallel to the Rydberg coupling axis. **(d)** An example image of the atomic cloud after transfer into the ELat, which is wide transverse to the cavity mode but narrow along the cavity z-axis. The red lines indicate the edges of the fundamental mode of the science cavity. Figure taken from Ref. [121].

the hyperfine splitting of the Rydberg state is negligible. We have found that this setup maximizes the dark polariton lifetime and minimizes the creation of stray Rydberg atoms. For more details on the experiment setup, see SI. A.3.1.

The full experiment procedure is depicted in Fig. A.3.1a. Because we are able to trap the atoms while probing, we now spend approximately 200 ms preparing the sample and 100 ms performing science measurements in each trial, for a duty cycle of roughly 33%; this represents a dramatic improvement over the previous scheme, in which the duty cycle was approximately 1% [153, 207]. Note that the time spent loading the magneto-optical trap is also used by the computer to prepare the control electronics for running the next iteration of the experiment sequence.

We have also made a number of technical improvements to the Floquet setup relative to our original implementation in Ref. [207]. In this work the laser beam inducing the sinusoidally modulated AC Stark shift of the $5P_{3/2}$ state (the "Floquet beam") has a wavelength of $\lambda_f = 1529$ nm near the $5P_{3/2} \rightarrow 4D_{3/2}$ and $5P_{3/2} \rightarrow 4D_{5/2}$ transitions. This new Floquet beam has a much greater detuning from the $5S_{1/2} \rightarrow 5P_{3/2}$ at 780 nm than the old Floquet beam at 776 nm, which was used in our previous work. This increased detuning dramatically reduces the inhomogeneous broadening of the atomic ground state caused by the inhomogeneous intensity of the Floquet beam, thereby maximizing the coherence time of the dark polaritons. We set the frequency components of the multichromatic Floquet field and their relative amplitudes in order to sinusoidally modulate the energy of the $5P_{3/2}$ state while keeping its average energy constant [207]. In particular, the Floquet laser is locked at a frequency 7 GHz detuned from the $5P_{3/2} \rightarrow 4D_{5/2}$ transition, such that it has nearly equal and opposite detunings from $4D_{5/2}$ and $4D_{3/2}$ which are split by 13.5 GHz. After amplifying the beam with an erbium-doped fiber amplifier we use a fiber electro-optic modulator (EOM) to simultaneously phase-modulate the light at frequencies of 8.500 GHz and 8.573 GHz; each of the resulting first order EOM-induced sidebands has a power approximately 1/6 that of the optical carrier. We fine-tune the strength of the sidebands in order to achieve a large modulation amplitude of the $5P_{3/2}$ energy at $f_{\mathrm{mod}} = 73$ MHz while its average energy is unchanged.

A.3.2 Cavity Structure Details

The heart of this experiment consists of two crossed nonplanar cavities; a primary 'physics' cavity for 780 nm photons and a build-up cavity for 480 nm photons. The physics cavity is a 4 mirror, 3-fold degenerate nonplanar cavity modeled off of our previous work with such cavities [182, 208]. There were two primary design challenges. First we needed a smaller waist size than we had previously achieved with our degenerate nonplanar cavities, since

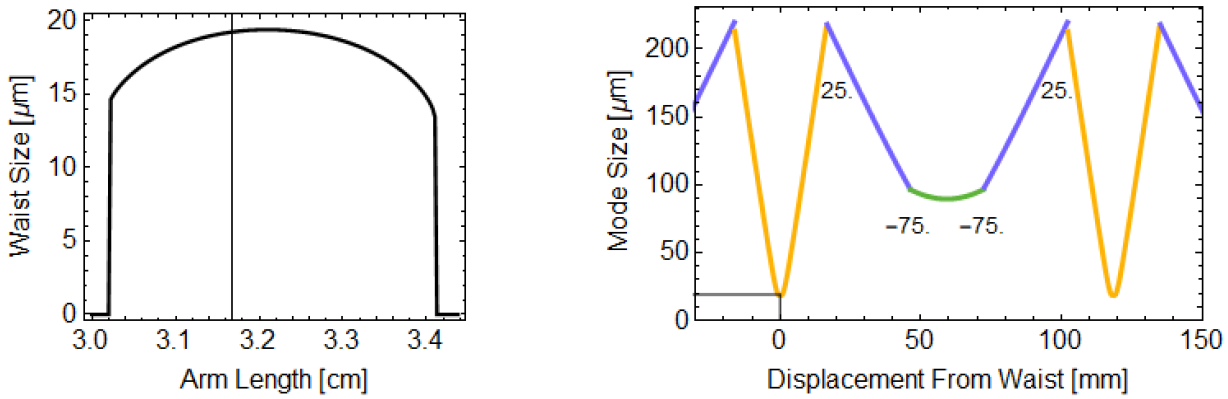

Figure A.3.2: **Physics Cavity Mode Size.** **(a)** The waist size of the cavity is plotted as the cavity size is scaled in proportion to the lower arm length. The three-fold degeneracy point we operate at is shown by the vertical line. **(b)** The mode size throughout the cavity shows the small primary waist in the lower arm (orange) along with a larger 90 μm waist in the upper arm (green). The four cavity mirrors are labelled between the arms of the cavity with their radii-of-curvature in mm. Figure taken from Ref. [121]

this cavity needed to be compatible with Rydberg mediated photon-photon interactions. This is a particular challenge because we also require Laguerre-Gaussian eigenmodes, and the standard techniques for reducing the waist such as reducing the radius-of-curvature of the cavity mirrors increases astigmatism, which then preferences Hermite-Gaussian modes. While we previously explored single and two mode blockade physics in a cavity with a 14 μm waist [153, 207], we relaxed the waist size requirement to $\sim$ 20 μm and increased the target Rydberg level accordingly. This target was then achievable by using convex, -75 mm radius-of-curvature mirrors in the upper arm along with standard 25 mm radius-of-curvature mirrors in the lower arm A.3.2.

The second design challenge for this cavity concerned reaching threefold degeneracy with the cavity in vacuum. Prior degenerate cavities were mounted in two halves separated by a micrometer stage. Adjusting this stage brought the modes into degeneracy. Since this technique is incompatible with vacuum, and the bake-out of the chamber was likely to change the cavity alignment slightly, we introduced a slow long throw piezo from Noliac (NAC2122-H40) behind one of the cavity mirrors, providing a 63 μm free stroke, corresponding to an approximately 6% change in the transverse mode frequency. Thus after aligning and gluing

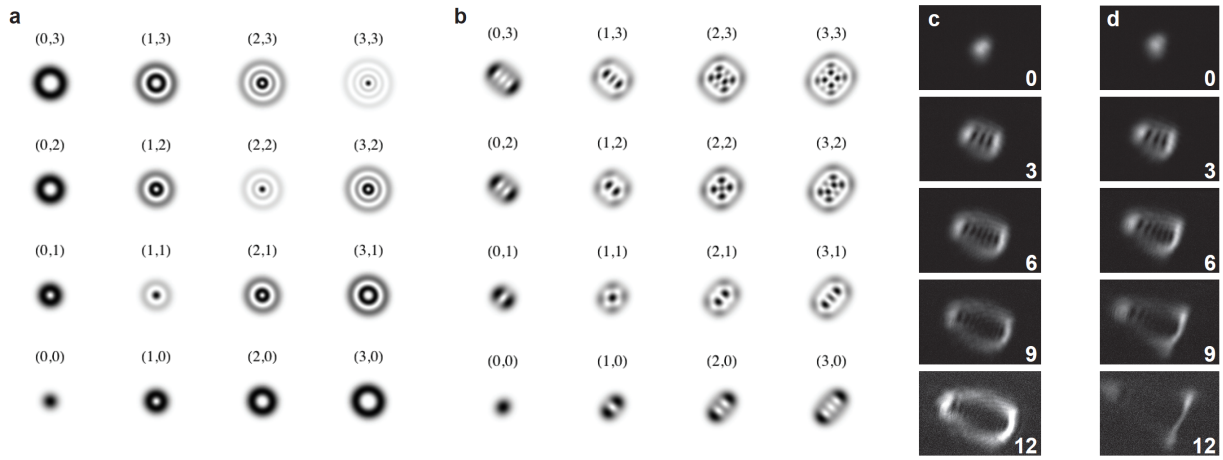

Figure A.3.3: **Comparison of Mode Profiles.** **(a)** The cavity mode at the lower waist are expected to be near-perfect Laguerre Gaussian modes. **(b)** Significant astigmatism causes the cavity modes at the upper waist to have significant Hermite Gaussian character. Since we couple into these modes with the digital micromirror device, we project the expected analytic form directly onto the DMD. **(c)** Away from degeneracy (30 MHz splitting between modes), the physics cavity's eigenmodes are as expected; however **(d)** as we approach degeneracy (13 MHz splitting) the modes couple significantly, as is evident from the strong threefold symmetry that develops. The modes also become lossy, indicating that the coupling is from long range aberration rather than local disorder. Figure taken from Ref. [121]

the cavity outside the vacuum chamber (taking into account the index of refraction of air!) and then baking out the chamber, degeneracy was within range of the long throw piezo.

Otherwise, this cavity is fairly standard. We use mirrors procured from Layertec. The two convex mirrors are coated for 99.91(1)% reflection, while the lower mirror are HR coated, so that there are effectively only two ports in this cavity. Similar coatings at 1560 nm provide for convenient cavity length stabilization, enabled by a short ring peizo (Noliac NAC2123) actuating a cavity mirror. After construction and installation, we achieve a finesse of 1900 with a free spectral range of 2500 MHz.

The presence of significant astigmatism causes several issues in this cavity. First it make the expected eigenmodes not Laguerre Gaussian in the upper waist. These modes are intermediate between Laguerre Gaussian and Hermite Gaussian and are connected to pure Laguerre Gaussian modes through an astigmatic mode converter [389]. This does not affect the physics at the lower waist, at which the cavity modes are nearly-pure Laguerre Gaussian modes. When we wish to drive a particular angular momentum mode of light,

we simply project the corresponding upper waist profile onto the DMD. More importantly however, the modes not being pure Laguerre Gaussian modes results in coupling between modes in our degenerate manifold, causing distortion and dramatically increased loss near degeneracy. Although the long throw piezo can move the cavity into degeneracy for every third mode in order to form a Landau level for cavity photons, the increased loss caused by astigmatism makes this useless. Thus we operate with Landau level modes split out by around 70 MHz (using both the long throw piezo and the heating wire), and make up the difference with Floquet modulation. As can be seen from straightforward application of the high frequency approximation, couplings between cavity modes remain off resonant when the Floquet polaritons are quasi-degenerate. Therefore we create Floquet polaritons that move in a quasi-degenerate set of Landau level states, even though direct coupling between these modes prevents the formation of a Landau level for photons.

It is necessary to use a separate build-up cavity because the 480 nm control field needs to cover all atoms and 780 nm modes used in any experiment, so it must be relatively large. To maintain sufficient control field Rabi coupling over the first five degenerate modes would then require 10 W of power in single pass. As this is significantly beyond maximum available laser power, we introduced a build-up cavity for the control field. This cavity is nonplanar to ensure circularly polarized modes, maximizing the Rabi coupling.

The science and blue build-up cavities cross at an angle of 35°, as shown in figure A.3.6. This might seem to cause several problems leading to increased loss and greater atomic level structure complexity. In fact, it does not. Doppler decoherence increases by a factor of 2.5 because the probe and control k vectors do not cancel as well and the decoherence rate goes as the inverse square of the collective Rydberg phase wavelength, but this does not qualitatively change the relative importance of this decoherence process (see Eq. 2.28). Due to our sideband cooling and repeated optical pumping occurring along the control field axis due to available optical access, the magnetic field is always along the blue build-up cavity

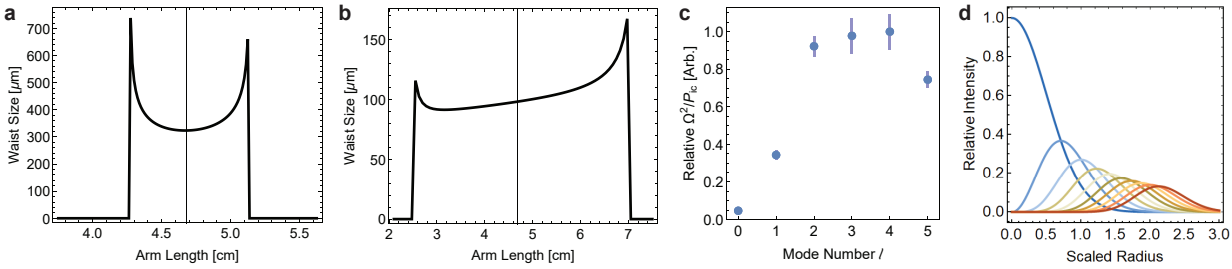

Figure A.3.4: **Buildup Cavity Modes and Relative Alignment.** **(a)** The originally intended build-up cavity mode size was more than three times larger than **(b)** the mode size of the cavity after rebuilding to include the new high transmitter. **(c)** We fit the measured control Rabi frequency from cavity Rydberg EIT transmission at 40S and plot the ratio of that frequency to the intracavity circulating power versus the LG mode injected into the build-up cavity, finding a uniform factor of ~ 20 improvement for $l = 2, 3,$or4 compared to $l = 0$. **(d)** This approximately uniform improvement indicates a relative shift in the cavity location by around 1.4 waists, or around 140 μm. Figure taken from Ref. [121]

axis. This means that the probe field, which is circularly polarized along its axis, couples with a significant π and small σ^- component along the quantization axis. The strength of the different transition components is given by

$$\{\sigma^+, \pi, \sigma^-\} = \{\frac{1}{2}(1+\cos\theta),\ \frac{1}{\sqrt{2}}\sin\theta,\ \frac{1}{2}(1-\cos\theta)\}. \tag{A.94}$$

For the relative angle of 35°, this results in a coupling of $\{0.91,\ 0.41,\ 0.09\}$. This means that additional intermediate P states will be occupied, but since the P state is broad and the shift of the transition frequency with magnetic field is weak (the difference in the Landé g factors is only 1/6), these transitions are all still resonant. The control field is well aligned to the quantization axis so this drives only σ^+ transitions. However, the hyperfine splitting is negligible for Rydberg D states, so the proper angular momentum quantum number is J not F. The stretched P state only couples to the stretched D state $|5P_{3/2}, F' = 3, m_{F'} = 3\rangle \rightarrow |nD_{5/2}, J = 5/2, m_J = 5/2\rangle|I = 3/2, m_I = 3/2\rangle$. However, the $m_{F'} = 2$ intermediate state couples to two Rydberg states, $|5P_{3/2}, F' = 3, m_{F'} = 2\rangle \rightarrow |nD_{5/2}, J = 5/2, m_J = 5/2\rangle|I = 3/2, m_I = 1/2\rangle$ and $|nD_{5/2}, J = 5/2, m_J = 3/2\rangle|I = 3/2, m_I = 3/2\rangle$. The $m_{F'} = 2$ intermediate state is also coupled back down to the ground $m_F = 1$ state by the σ^+ component of the probe field, which would serve to rapidly depolarize the atomic

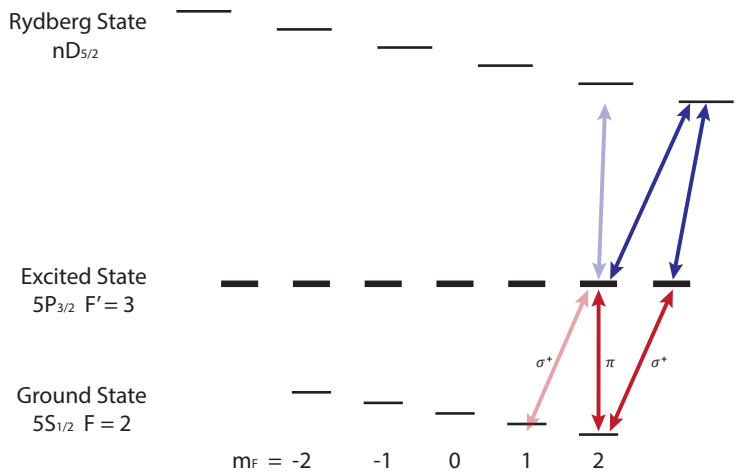

Figure A.3.5: **Level Structure and Transitions with Angle between Cavities.** The relative angle between the science and blue build-up cavities complicates the relevant atomic structure. Ideally, the atoms would act as ideal three level systems, with only the rightmost stretched transitions relevant. However, the significant angle between the two cavities creates a comparable π transition out of the ground state. This could cause another Rydberg state to become relevant and depolarization of the atomic sample. In fact, neither of these effects occur because, in the presence of a magnetic field, these processes are off-resonant. Note that the intermediate states do shift with magnetic field, but this is irrelevant due to their large linewidth.

ensemble. However, both the additional Rydberg state and ground state are off-resonance. The neighboring ground state shifts by 100 kHZ (about the dark polariton linewidth) in a 0.14 gauss field while the neighboring Rydberg state needs less than half that, so in our typical operating condition of several gauss, these processes are strongly suppressed.

Relative alignment between the two cavities is critical. Since the alignment was performed outside of vacuum before bakeout, we anticipated significant drift between the cavity modes. Communication with members of Tilman Esslinger's group indicated that misalignment at the $\sim$ 100 μm level was very possible due to the thermal cycle of the bakeout, even with robust gluing of the mirrors. As such, we aimed to produce a very large waisted build-up cavity, with a corresponding increase in desired finesse. Our standard small waist cavity tricks in reverse along with additional path length provided by adding in another pair of mirrors resulted in a broadly stable cavity design with a $\sim$ 320 μm waist.

The increased mode area along with a desire for significantly higher blue Rabi frequency

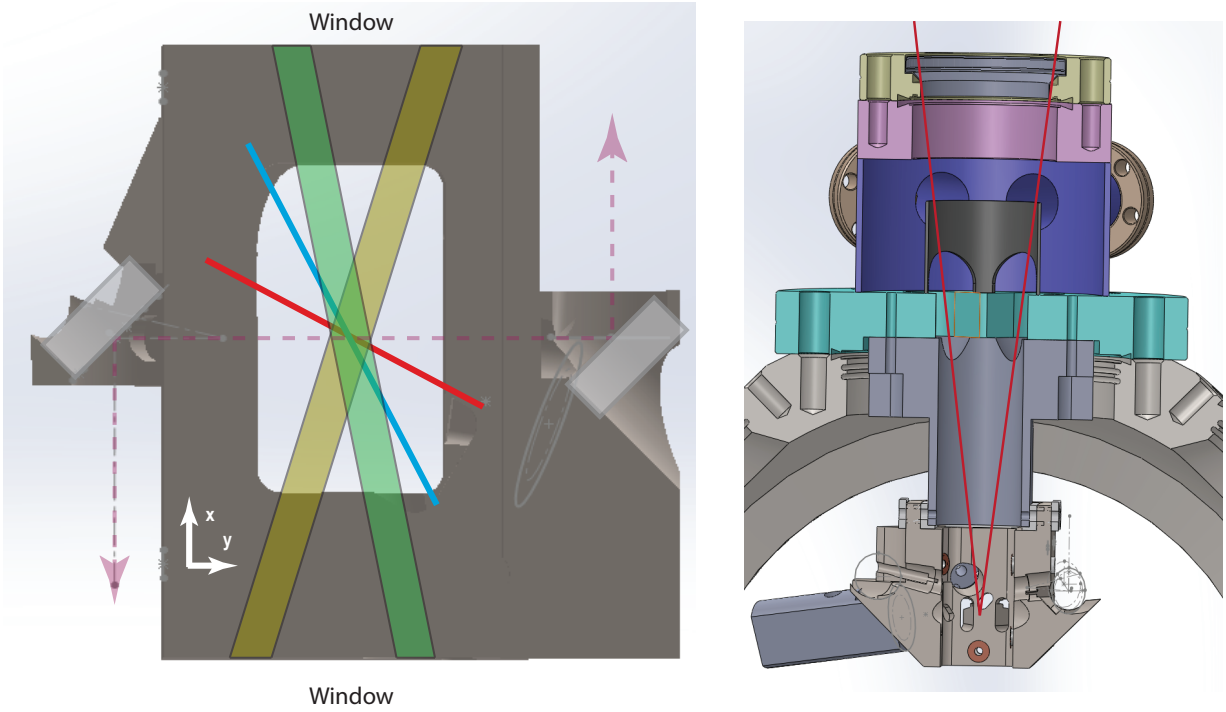

Figure A.3.6: **Cavity Structure Layout. (a)** Annotated CAD drawings of the cavity structure show the structural and optical layout. The physics cavity axis (red) is 35° from the the blue build-up cavity axis (blue), which also provides access for dRSC pumping and optical pumping since the blue cavity mirrors are AR coated near 780 nm. Two slots 51° (green) and 82° (yellow) from the physics cavity axis provide additional optical access for dRSC horizontal lattice and 1529 nm Floquet beams. The physics cavity twists towards the y direction, so that the upper arm is almost exactly along $\hat{y}$ (light red, dashed). Two aluminum redirection mirrors (gray rectangles) allow in- and out-coupling via the main windows. The blue cavity upper arm (not shown) twists towards the x direction, so in- and out-coupling is performed directly through the windows. **(b)** The cavity structure is mounted to a custom flange. This flange provides electrical feedthroughs for piezos, electrodes, and the heating wire as well as vertical optical access with NA = 0.12, limited by the upper window (red lines). See Appendix B.2 for details on the custom flange.

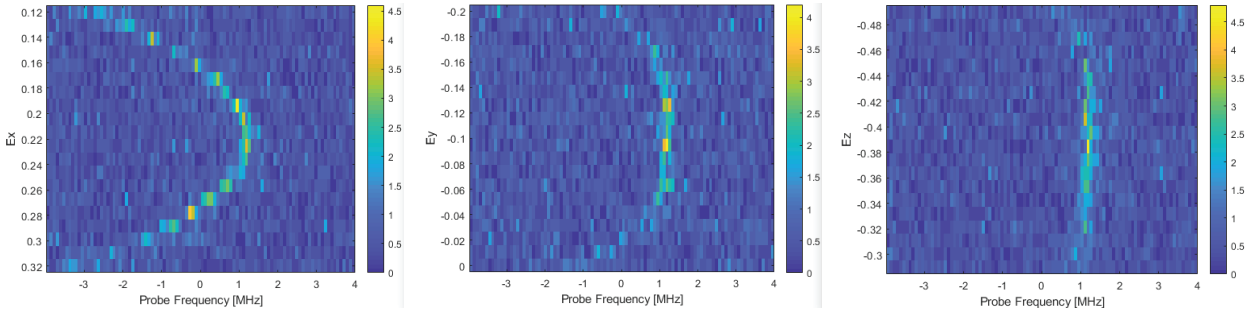

Figure A.3.7: **Electric Field Scans.** The transmission rate (colorbar) for Rydberg-like dark polaritons is plotted versus probe frequency and applied electric field (units of V/dm). To maintain an optically pumped sample, we apply a large (several Gauss) magnetic field along the blue cavity axis, which results in the x sensitivity remaining large, while suppressing the electric polarizability along the orthogonal axes. Strong orthogonal electric fields break the m_j splitting along the magnetic field axis, cause coupling to many Rydberg states, and dramatically broaden and shrink the dark polariton resonance. Figure taken from Ref. [121]

(to open up the possibility of increasing the atomic density) led to a Layertec mirror order specifying 99.97% reflectors for a finesse 10,000 cavity. In fact, the mirrors we received were 99.985% *loss dominated* reflectors. This higher than expected loss at 480 nm made these mirrors useless for the build-up cavity. Rather than wait the several months required to replace these mirrors, we bought 1.5 m radius-of-curvature mirrors off of eBay that specified a reflectivity of 97% at 480 nm. Rebuilding the cavity to include one of these mirrors produced a finesse 190 single ended cavity with a waist size of 98 μm at the location of the atoms, providing enough intensity build-up to achieve a sufficient control Rabi frequency over the first few degenerate modes of the physics cavity.

Proper alignment between the two cavities was ensured by moving a thin wire cross on a translation stage and seeing both cavity modes spoil simultaneously. After installation and bakeout, there remained significant concern about the relative alignment between the cavity modes. Initial EIT signals showed a very weak control Rabi frequency. Coupling into higher order LG modes of the build-up cavity resulted in a much greater control Rabi frequency, normalized to the intracavity circulating power (See Fig. A.3.4c). Comparison with the relative intensities of the various higher order LG modes as a function of radius (Fig. A.3.4d) indicates that the improvement in overlap between the higher order build-up

cavity modes and the physics cavity mode arose from an 140 μm shift.

In order to drive a higher order LG mode, we convert a large Gaussian beam into an $LG_{2,0}$ via a vortex half-wave retarder with $> 80\%$ efficiency. This, combined with the significant $\sim 80\%$ peak intensity reduction still leaves a factor of 5 build-up in the circulating power.

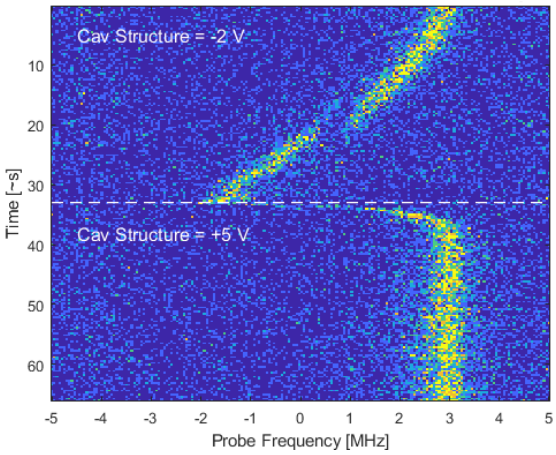

Figure A.3.8: **Stray Charge Mitigation.** The transmission spectrum near the dark polariton resonance over time; blue indicates low transmission, yellow indicates high transmission. Illumination of the cavity structure with UV light can change the build up of stray charges that cause electric field drift and thus the drift of the dark polariton resonance. Furthermore, the simultaneous application of a voltage on the cavity structure further dramatically changes the behavior of mobile charges. A substantial negative voltage appears to increase the drift rate of the electric field (above the white dashed line), while the application of a substantial positive voltage causes the field to rapidly equilibrate and strongly suppresses further drift; this suppression stabilizes the dark polariton resonance and provides the best conditions for our experiments (below the white dashed line). We make no claim as to the mechanism behind the increased stability, whether positive charges are being repelled from the relevant surfaces, or negative charges are being pinned in place. Figure taken from Ref. [121]

Special care was taken to engineer the electric field environment experienced by the Rydberg atoms. Most importantly, all surfaces, either metal or dielectric are kept at least 10 mm from the atoms, and line-of-sight between the atoms and dielectric surfaces is minimized to just the lower cavity mirrors. Piezos are shielded by grounded metal and are driven so that their surfaces that face the atoms are held at ground. In order to cancel the remaining background electric field $\mathbf{E}_{bkg}$ experienced by the atoms, the structure also supports eight electrodes which can apply additional electric fields and gradients at the location of the atomic cloud. The cavity structure itself is electrically isolated and controlled, acting as a ninth electrode. Typical scans of the dark polariton spectrum as a function of this applied electric field $\mathbf{E}$ are shown in Fig. A.3.7. These scans enable us to identify the applied field which is necessary to achieve a net electric field $\mathbf{E}_{net} = \mathbf{E}_{bkg} + \mathbf{E} = 0$ at the location of the atoms.

We observed drift of the electric field which we attribute to Rubidium (or Rubidium ion) accumulation on the cavity structure and mirrors. We mitigate this issue by pulsing a ~ 100 mW UV flashlight centered around 365 nm while jumping the set voltage of the entire cavity structure to $+10\ V$ while the MOT is loading (Fig. A.3.8). These passive mitigating factors along with active electric field control work in concert to enable our experiments with the $111D_{5/2}$ Rydberg state with negligible broadening due to electric field inhomogeneity and hours-long stability.

A.3.3 Collective Atomic Excitations

Even though thousands of atoms are present in the cavity, only a small subset of the possible atomic excitations are coupled to the cavity photons. In fact, As developed in section 2.1.2, each cavity mode couples to a unique collective $5P_{3/2}$ excitation, which is subsequently coupled by the Rydberg laser to a unique collective Rydberg excitation (see Fig. 6.5b). These collective excitations are superposition states in which one excitation is shared by many atoms with a spatial waveform that is proportional to the field of the corresponding cavity mode. In particular, photons in the cavity mode with angular momentum l (created by the operator $a_l^\dagger$) couple to the collective $5P_{3/2}$ excitation created by the operator,

$$p_l^\dagger = \frac{1}{g_l} \sum_{m=1}^{N_{at}} g_{ml} \sigma_m^{eg},$$

where $g_l^2 \equiv \sum_{m=1}^{N_{at}} |g_{ml}|^2$ is the total atom-photon coupling strength for that mode and the coupling of cavity photons to the m'th atom $g_{ml} = g_{\text{sing}} \phi_l(\mathbf{x}_m)/\phi_0(0)$ is proportional to the electric field ϕ_l (normalized such that $\int d^2\mathbf{x} |\phi_l(\mathbf{x})|^2 = 1$) at the position $\mathbf{x}_m$ of the atom as well as the peak single-atom coupling strength g_{sing}. The operator σ_m^{eg} excites atom m from the ground state to the $5P_{3/2}$ state. Similarly, the corresponding collective Rydberg

excitation is created by the operator,

$$r_l^\dagger = \frac{1}{g_l} \sum_{m=1}^{N_{at}} g_{ml} \sigma_m^{rg},$$

where the operator σ_m^{rg} excites atom m from the ground state to the Rydberg state. Because the orthonormal set of cavity modes couples one-to-one with the orthonormal set of collective atomic excitations, the atom-cavity coupling does not directly mix the cavity modes together. Therefore, only the Rydberg-Rydberg interactions cause photons to move between the modes. For more on the orthogonality of the collective excitations see SI. B2 of Ref. [207].

A.3.4 Photonic and Polaritonic States Differ in the Floquet Scheme

When forming dark polaritons in a set of near-degenerate cavity modes whose bare frequencies are all close to that of the unmodulated atomic transition, the relationship between photons and polaritons is independent of the mode. For example, because the atom-cavity coupling g_l is the same for each mode l, the dark-state rotation angle θ_l is the same for every mode, where the rotation angle satisfies $\tan(\theta_l) \equiv g_l/\Omega$ (see [158] and SI. B5 of Ref. [207]). A smaller ratio g_l/Ω increases the contribution $\cos^2(\theta_l)$ to the polaritons from the cavity photon and thus makes the polariton more "photon-like"; a larger ratio increases the contribution $\sin^2(\theta_l)$ from the collective Rydberg state, making the polariton more "Rydberg-like" [158]. Therefore, when using a set of nearly-degenerate bare cavity modes, all of the polaritons have the same fractional composition in terms of their photonic and Rydberg parts.

The Floquet scheme causes the dark-state rotation angle, and thus the polariton composition, to vary between different modes. The rotation angle varies because the so-called "sideband" features with $l = 3,\ \&\ 9$ have smaller atom-cavity coupling than the "carrier" with $l = 6$. For the parameters used in this work, the sideband dark polaritons are approximately six

times more photon-like than the carrier polaritons.

The second difference between polaritons and photons in the Floquet scheme arises from the complex phase of g_l and is more subtle to understand. Before considering the phases of the couplings, it is helpful to use a concrete example of the effect of the phase on a superposition of angular momentum states. For concreteness, consider the collective Rydberg states $|R_\pm\rangle = \frac{1}{\sqrt{2}}\left(r_3^\dagger \pm r_6^\dagger\right)|vac\rangle$. These Rydberg excitations form angular standing waves because of the interference between the $l = 3$ and $l = 6$ components; but the probability wave peaks of $|R_+\rangle$ match the troughs of $|R_-\rangle$, and vice versa, because of the flipped phase of the superposition. When utilizing ordinary polaritons with a constant $g_l \equiv g$, $|R_\pm\rangle$ couple with cavity photonic states $|a_\pm\rangle = \frac{1}{\sqrt{2}}\left(a_3^\dagger \pm a_6^\dagger\right)|vac\rangle$, where the peaks of $|a_+\rangle$ ($|a_-\rangle$) are at the same locations as the peaks of $|R_+\rangle$ ($|R_-\rangle$). Similar considerations apply for states containing multiple excitations; for ordinary polaritons, the spatial structures of the Rydberg components and the photonic components are the same.

In the Floquet scheme, the structure of the single photon state

$$|\tilde{a}_\pm\rangle \propto \left(a_3^\dagger \pm \frac{g_3}{g_6} e^{2\pi i f_{\mathrm{mod}} t} a_6^\dagger\right)|vac\rangle$$

which couples to $|R_\pm\rangle$ is different in three important ways. First, the magnitude $\left|\frac{g_3}{g_6}\right|$ of the ratio between the coupling strengths determines the relative weights of the parts of the photonic superposition. Second, the relative phase $\arg\left(\frac{g_3}{g_6}\right)$ of the couplings affects the relative phase of the photonic superposition. When using sinusoidal Floquet modulation, the phases satisfy $\arg\left(\frac{g_3}{g_6}\right) + \arg\left(\frac{g_9}{g_6}\right) = \pi$. Third, in the lab frame the phase of the superposition rotates at the modulation frequency f_{mod}. As a result, the positions of peaks and troughs in the probability wave will rotate around the center of the cavity at frequency $f_{\mathrm{mod}}/3$, where the factor of three arises because of the angular momentum difference between the modes in the superposition (equivalently, the fact that the density wave has three peaks). This

rotation can be viewed as the micromotion which is quite common in Floquet systems.

In this work, the two-Rydberg component of the polaritonic state produced by interactions is approximately,

$$|R_L\rangle \propto \left(\sqrt{\frac{21}{10}}\left|\frac{g_3 g_9}{g_6^2}\right| r_3^\dagger r_9^\dagger - \frac{1}{\sqrt{2}}\left(r_6^\dagger\right)^2\right)|vac\rangle, \tag{A.95}$$

noting that the factor $1/\sqrt{2}$ simply cancels a factor from the bosonic creation operators $\left(r_6^\dagger\right)^2$. The factor $\sqrt{21/10}$ is explained in SI. A.3.7. As a result of the Floquet scheme, this Rydberg state couples to a two-photon state,

$$\begin{aligned}|\tilde{a}_A\rangle &\propto \left(\sqrt{\frac{21}{10}}e^{i\ \arg(g_3 g_9/g_6^2)}a_3^\dagger a_9^\dagger - \frac{1}{\sqrt{2}}\left(a_6^\dagger\right)^2\right)|vac\rangle \\ &\propto \left(\sqrt{\frac{21}{10}}a_3^\dagger a_9^\dagger + \frac{1}{\sqrt{2}}\left(a_6^\dagger\right)^2\right)|vac\rangle.\end{aligned} \tag{A.96}$$

Two key features of this photonic state are worth noting: First, because the rotation factors at $\pm f_{\text{mod}}$ from the $l = 3$ and $l = 9$ photons in the first term on the right-hand side cancelled out, there is no time-dependence of the Laughlin state itself. Even though all photonic states in the Floquet scheme rotate at $f_{\text{mod}}/3$, the rotation-invariance of the Laughlin state prevents it from acquiring time-dependence. However, the net phase factors from the sideband couplings relative to the carrier do not cancel out; they contribute a factor $e^{i\ \arg(g_3 g_9/g_6^2)} = -1$ which causes the photonic superposition to have a plus sign rather than a minus sign. In Methods 6.4.3.2 we discuss the use of the phase compensation cavity to convert the state $|\tilde{a}_A\rangle$ which exits the science cavity into the photonic Laughlin state,

$$|\tilde{a}_L\rangle \propto \left(\sqrt{\frac{21}{10}}a_3^\dagger a_9^\dagger - \frac{1}{\sqrt{2}}\left(a_6^\dagger\right)^2\right)|vac\rangle. \tag{A.97}$$

While rotation-invariance makes the Laughlin state $|\tilde{a}_L\rangle$ time-independent, the rotation induced by the Floquet scheme plays a crucial role when measuring spatial correlations. The

off-center single mode fiber measures localized photons; when viewed in the angular momentum basis, the localized fiber mode has an annihilation operator corresponding to a superposition $a_f \propto c_3 a_3 + c_6 a_6 + c_9 a_9$ where c_l is the coefficient characterizing the contribution from mode l. When the fiber is translated to the radius with peak density, the coefficients are approximately $c_3 = 0.53$, $c_6 = 0.71$, and $c_9 = 0.46$. Immediately after a photon from the Laughlin state is detected through the single mode fiber, the remaining photon is in the state

$$\begin{aligned} |\tilde{a}_{rem}\rangle &\propto a_f |\tilde{a}_L\rangle \\ &\propto \left(\sqrt{\frac{21}{10}} \left(c_9 e^{-2\pi i f_{\mathrm{mod}} t} a_3^\dagger + c_3 e^{2\pi i f_{\mathrm{mod}} t} a_9^\dagger \right) - \sqrt{2} c_6 a_6^\dagger \right) |vac\rangle. \end{aligned} \tag{A.98}$$

Because the remaining photon is left behind in a state with spatial structure which is not rotation-invariant, the probability distribution of the remaining photon rapidly rotates in space. Immediately after the first photon is detected, the remaining photon has no overlap with the fiber mode and will not be observed; just half of a rotation period later the likelihood of detecting the photon is maximized. In particular, the likelihood of observing the second photon through the fiber follows,

$$\langle \tilde{a}_{rem} | a_f^\dagger a_f | \tilde{a}_{rem} \rangle \propto \sin^4 \left(2\pi f_{\mathrm{mod}} t \right). \tag{A.99}$$

A.3.5 Floquet Polaritons are Protected from Intracavity Aberrations

It is often technically challenging to form a degenerate manifold of cavity modes, because mirror defects and intracavity aberrations such as astigmatism can induce couplings between the modes which break their degeneracy. Our Floquet scheme makes it possible to form an effectively degenerate manifold of dark polaritons, in which the polaritons have the same quasi-energy, without making the bare cavity modes degenerate. Naively, it might seem that

the Floquet polaritons should inherit all of the couplings from their Rydberg and cavity photonic parts, in which case the degeneracy would still be split by the intracavity aberrations. However, as we will demonstrate below, the aberration couplings between Floquet polaritons are strongly suppressed, precisely because the large energy separation between the bare cavity modes remains.

We next demonstrate these features more formally. The behavior of Floquet polaritons is best understood in the high frequency approximation [390], as detailed in Ref. [207]. We begin with the time-dependent Hamiltonian of the system,

$$\begin{aligned} H(t) = \sum_{n}^{N_{cav}} \Bigg(& \delta_c^n a_n^\dagger a_n + \bar{\delta}_e p_n^\dagger p_n + \delta_2 r_n^\dagger r_n \\ & + \sum_{m=-\infty}^{\infty} g_m^n e^{im\omega t} p_n a_n^\dagger + h.c. + \\ & + \sum_{m=-\infty}^{\infty} \Omega_{-m} e^{-im\omega t} r_n p_n^\dagger + h.c. \Bigg) \\ & + \frac{1}{2} \sum_{nmpq}^{N_{cav}} U_{nmpq} r_n^\dagger r_m^\dagger r_p r_q \\ & + \sum_{n,q\neq n}^{N_{cav}} D_{nq} a_n^\dagger a_q + h.c. \end{aligned} \tag{A.100}$$

The first line accounts for the relative energies of the $N_{cav} = 3$ cavity modes, with energy δ_c^n for the n'th cavity mode with annihilation operator a_n, time-averaged energy $\bar{\delta_e}$ of the collective $5P_{3/2}$ states with annihilation operator p_n, and energy δ_2 for the collective Rydberg states with annihilation operator r_n. The next line denotes the atom-cavity coupling g_m^n in mode n through Floquet band m; $\omega = 2\pi f_{\text{mod}}$ is the modulation angular frequency. The third line denotes the Rydberg couplings $\Omega_m$via Floquet band m. The fourth line accounts for the Rydberg-Rydberg interactions with strength U_{nmpq} between all possible combinations of

modes. The final line represents intracavity aberrations, which couple between cavity modes n and q with strength D_{nq}.

The experimentally relevant case is the limit in which each cavity mode n is near-detuned to a band k_n of the $5P_{3/2}$ state and the Rydberg coupling laser is also near resonant for driving $5P_{3/2} \rightarrow 111D_{5/2}$ via band l. Under these conditions, we can write $\delta_c^n \equiv k_n\omega + \epsilon_c^n, \bar{\delta}_e \equiv \epsilon_p, \delta_2 \equiv l\omega + \epsilon_r$, such that the quasienergies satisfy,

$$\epsilon_c, \epsilon_p, \epsilon_r \ll \omega.$$

Transforming to the frame of this resonant coupling,

$$a_n \rightarrow e^{ik_n\omega t}a_n,$$
$$r_n \rightarrow e^{il\omega t}r_n,$$

the Hamiltonian becomes,

$$\begin{aligned} H(t) = \sum_n^{N_{cav}} \Bigg(& \epsilon_c^n a_n^\dagger a_n + \epsilon_p p_n^\dagger p_n + \epsilon_r r_n^\dagger r_n \\ & + \sum_{m=-\infty}^{\infty} g_{m+k_n}^n e^{im\omega t} p_n a_n^\dagger + h.c. + \\ & + \sum_{m=-\infty}^{\infty} \Omega_{-m-l} e^{-im\omega t} r_n p_n^\dagger + h.c. \Bigg) \\ & + \frac{1}{2}\sum_{nmpq}^{N_{cav}} U_{nmpq} r_n^\dagger r_m^\dagger r_p r_q \\ & + \sum_{n,q\neq n}^{N_{cav}} D_{nq} a_n^\dagger a_q e^{i(k_q - k_n)\omega t} + h.c. \end{aligned} \tag{A.101}$$

Since we have now transformed to this basis where the quasienergies are all similar, the dynamics of the system will be dominated by the coupling terms which are not rotating.

Two features of this Hamiltonian are worthy of particular attention. First, because all of the bare Rydberg states are degenerate, and therefore couple to the P-state through the same Floquet band, all of the Rydberg-Rydberg interaction terms remain resonant (not rotating) even after this transformation. In contrast, because the bare cavity modes were not degenerate, and each couples to the P-state through a different Floquet band, the aberration couplings between the cavity mode now have a rapidly rotating complex phase, indicating that they are off-resonant.

At lowest order in the high frequency approximation, which is equivalent to the rotating wave approximation at this order, the effective Hamiltonian is just the average of the full, time-dependent Hamiltonian above,

$$H_F^{(1)} = H_0,$$

where H_m is the m'th Fourier component of the Hamiltonian,

$$H_m = \frac{1}{T}\int_0^T e^{-im\omega t}\tilde{H}(t) = H_{-m}^{\dagger}$$

$$
\begin{aligned}
H_F^{(1)} = \sum_n^{N_{\text{cav}}} \Big(& \epsilon_c^n a_n^\dagger a_n + \epsilon_e p_n^\dagger p_n + \epsilon_r r_n^\dagger r_n \\
& + g_{k_n}^n p_n a_n^\dagger + \Omega_{-l} r_n p_n^\dagger + h.c. \\
& + \frac{1}{2} \sum_{nmpq}^{N_{cav}} U_{nmpq} r_n^\dagger r_m^\dagger r_p r_q \Big) \\
& + \sum_{n,q\neq n}^{N_{cav}} D_{nq} \delta_{k_q,k_n} a_n^\dagger a_q
\end{aligned} \tag{A.102}
$$

As expected, at this level of approximation, mirror disorder is only relevant if the bare cavity modes are degenerate, as determined by the Kronecker delta δ_{k_q,k_n} in the final line which requires that the modes couple to the P-state through the same Floquet band. The Rydberg interactions all contribute fully at the usual level because the bare Rydberg states in the absence of modulation were already degenerate.

At next order we see the effects of mirror disorder between cavity modes which are not naively degenerate. The next order contribution to the effective Hamiltonian is,

$$
H_F^{(2)} = \sum_{m\neq 0} \frac{H_m H_{-m}}{m\hbar\omega},
$$

where the relevant Fourier components are,

$$
\begin{aligned}
H_m = \sum_n^{N_{cav}} \Big(& g_{-m+k_n}^n p_n^\dagger a_n + g_{m+k_n}^n p_n a_n^\dagger \\
& + \Omega_{-m-l} r_n^\dagger p_n + \Omega_{m-l} r_n p_n^\dagger \Big) \\
& + \sum_{n,q\neq n}^{N_{cav}} D_{nq} a_n^\dagger a_q \delta_{m,k_q-k_n} + D_{nq} a_n a_q^\dagger \delta_{-m,k_q-k_n}.
\end{aligned}
$$

At this order, the effective Hamiltonian gains a variety of terms with strengths D^2/ω, Dg/ω, or $D\Omega/\omega$. As long as all of the coupling strengths $g, \Omega, D \ll \omega$ are small compared to the modulation frequency, these terms will be negligible. Overall, this treatment demonstrates how the Floquet scheme enables us to create degenerate manifolds of dark polaritons while strongly suppressing the broadening that intracavity aberrations would cause in a degenerate manifold of bare cavity modes.

A.3.6 Many-body Spectrum

The many-body spectrum for two excitations in the three modes accessible in Chapter 6 (Fig. 6.8b of the main text) is calculated as follows. When the three modes have been made degenerate with energy per particle E_{pol}, the energies of multi-particle states are only differentiated by the interaction Hamiltonian,

$$H_{\text{int}} = \frac{U}{2} \int d^2 z \psi^\dagger(z) \psi^\dagger(z) \psi(z) \psi(z), \tag{A.103}$$

where $\psi(z)$ is the field operator and we have made the approximation of contact interactions with strength U. The approximation of contact interactions is best justified when the Rydberg blockade radius is small compared to the cavity mode waist. However, even when the blockade radius and mode waist are comparable, the spectrum remains qualitatively similar. Note that the interaction strength U typically has a large imaginary component [161], but we depicted a larger real than imaginary component in Fig. 6.8a & b to make the visualization clear.

Projecting the interaction Hamiltonian into the basis of our degenerate Landau level yields,

$$H_{\text{int}} = \frac{U}{2} \sum_{ijkl \in \{3,6,9\}} \beta_{ijkl} a_i^\dagger a_j^\dagger a_k a_l, \tag{A.104}$$

where the interaction energies among modes are determined by the overlap integrals,

$$\beta_{ijkl} = \int d^2 z \phi_i^*(z) \phi_j^*(z) \phi_k(z) \phi_l(z), \tag{A.105}$$

and the wavefunction for the mode with angular momentum $\hbar l$ is,

$$\phi_l(z) = \frac{1}{\sqrt{2^l l!}} z^l e^{-|z|^2/4}. \tag{A.106}$$

Diagonalizing this interaction Hamiltonian within the two-particle manifold yields the energy spectrum of two-particle states in our system, including the Laughlin state with zero interaction energy.

A.3.7 Two-Particle Laughlin States With Quasi-holes at the Origin

Two photons in any three evenly spaced angular momentum modes can form a Laughlin state. While these Laughlin states differ in the exact form of their wavefunctions, they all enable the two particles to minimize their interaction energy while remaining in the lowest Landau level. The two particle Laughlin states in which we are interested can be expressed in real space as,

$$\psi_L(z_1, z_2; m, n) = N_{mn} z_1^m z_2^m (z_1^n - z_2^n)^2 e^{-(|z_1|^2 + |z_2|^2)/4}, \tag{A.107}$$

where $z_j \equiv x_j + i y_j$ represents the position of particle j in units of the magnetic length, m & n are positive integers, and N_{mn} is an overall normalization factor ensuring $\int \int d^2 z_1 d^2 z_2 |\psi_L|^2 = 1$. Note that these states all share the property that particles avoid each other, since $\psi_L(z_1 = z_2; m, n) = 0$.

The two particle Laughlin states $\psi_L(z_1, z_2; m, n)$ can be composed from the three angular

momentum modes with $l = m,\ m+n$, and $m+2n$. To explicitly perform the transformation to the angular momentum basis we can expand the quadratic factor, yielding,

$$\psi_L(z_1, z_2; m, n) = N_{mn} e^{-(|z_1|^2+|z_2|^2)/4} \left(z_1^m z_2^{m+2n} + z_1^{m+2n} z_2^m - 2 z_1^{m+n} z_2^{m+n} \right). \quad \text{(A.108)}$$

Comparing this form to the single particle angular momentum modes,

$$\phi_l(z) = \frac{1}{\sqrt{2^l l!}} z^l e^{-|z|^2/4}, \quad \text{(A.109)}$$

reveals that the first two terms on the right-hand side of Eq. A.108 correspond to the properly symmetrized two-particle angular momentum state ϕ_{l_1,l_2} for particles with angular momenta $l_1 = m$ and $l_2 = m + 2n$. The last term on the right-hand side of Eq. A.108 corresponds to $\phi_{m+n,m+n}$. Accounting for normalization factors of each angular momentum state, we obtain,

$$\begin{aligned} \psi_L(z_1, z_2; m, n) = N_{mn} e^{-(|z_1|^2+|z_2|^2)/4} \\ \times \big(\sqrt{2} \sqrt{2^{2n+m}(2n+m)!} \sqrt{2^m (m)!}\, \phi_{2n+m,m}(z_1, z_2) \\ - 2^{n+m+1}(n+m)! \phi_{n+m,n+m}(z_1, z_2) \big), \end{aligned} \quad \text{(A.110)}$$

or approximately in the notation of the main text (where $|uv\rangle \equiv |u, v\rangle$ means a two-particle state with the individual particles possessing angular momenta $u\hbar$ and $v\hbar$ about the origin),

$$\begin{aligned} |L\rangle_{mn} = N_{mn} \big(\sqrt{2} \sqrt{2^{2n+m}(2n+m)!} \sqrt{2^m (m)!}\, |m, m+2n\rangle \\ - 2^{n+m+1}(n+m)! |m+n, m+n\rangle \big). \end{aligned} \quad \text{(A.111)}$$

Therefore, in each Laughlin state, the ratio α_{mn} between the populations in $|m, m+2n\rangle$ and $|m+n, m+n\rangle$ is,

$$\alpha_{mn} = \frac{(2n+m)!m!}{2(n+m)!^2}. \quad \text{(A.112)}$$

For the Laughlin state with $m = n = 3$ used in this work, we find $\alpha_{mn} = \frac{21}{10} = 2.1$, as reported in the main text. Note that, for each Laughlin state $|L\rangle_{mn}$, there is a corresponding "anti-Laughlin" state,

$$|AL\rangle_{mn} = N_{mn}\big(2^{n+m+1}(n+m)!|m, m+2n\rangle + \sqrt{2}\sqrt{2^{2n+m}(2n+m)!}\sqrt{2^m(m)!}|m+n, m+n\rangle\big), \quad \text{(A.113)}$$

which exhibits spatial bunching instead of anti-bunching.

Physically, one can think of the choice of n as splitting the ordinary Landau level (containing every angular momentum mode $l = 0, 1, 2...$) into n separate Landau levels existing on cones with a spatial curvature of $R(x, y) = 4\pi\left(1 - \frac{1}{n}\right)\delta^{(2)}(x, y)$ localized at the cone tip, where $\delta^{(2)}(x, y)$ is the two-dimensional Dirac delta function [182, 208]. The n cones with the same curvature correspond to different choices of the lowest angular momentum mode m, which determines the effective magnetic flux $\frac{m \bmod n}{n}\Phi_0$ threaded through the cone tip, where Φ_0 is the magnetic flux quantum. Moreover, when m exceeds n, the Laughlin state has Floor(m/n) quasi-holes pinned at the origin, where Floor(x) denotes the largest integer less than or equal to x.

Interestingly, the azimuthal correlations $g^{(2)}_{mn}(\phi) \propto |\psi_L(z_1 = z_2 e^{i\phi}; m, n)|^2$ are independent of m and have a very simple dependence on n. Using the form of the wavefunction in Eq. A.107, it is straightforward to find that,

$$g^{(2)}(\phi)_{mn} \propto \sin^4\left(\frac{n}{2}\phi\right). \quad \text{(A.114)}$$

Moreover, when viewed in terms of the angle $\phi_{\text{cone}} = n\phi$ around the cone tip, the azimuthal correlation function is entirely independent of m and n.

Since these Laughlin states are all closely related physically, our choice of $m = n = 3$ was

made for technical reasons. First, we chose to make only every third angular momentum state degenerate to protect the Landau level from intracavity astigmatism (see Ref. [182]). In the end, because we use Floquet polaritons, this choice was likely not necessary (see SI. A.3.5); however, the length of our cavity is not sufficiently tunable to bring any other set of angular momentum modes near enough to degeneracy to be convenient for our Floquet scheme. Second, we choose $m = 3$, making $l = 3$ our lowest angular momentum mode rather than $l = 0$, because it yields $\alpha_{33} = 2.1$ much smaller than $\alpha_{03} = 10$. Smaller α_{mn} increases the contribution of $|m + n, m + n\rangle$ to the Laughlin state, improving the coupling of our coherent probe on $l = m + n$ to the Laughlin state relative to the anti-Laughlin state.

A.3.8 Three Photon Laughlin State Azimuthal Correlation

A three photon Laughlin state should display similar azimuthal correlations as derived in the previous section; however, there is no guarantee that they will be precisely the same. For simplicity, we ignore the potential for quasi-holes at the origin in this analysis. Beginning with the 3 particle Laughlin state with $n = 3$

$$\psi_L^{N=3}(z_1, z_2, z_3) \propto (z_1^3 - z_2^3)^2 (z_1^3 - z_3^3)^2 (z_2^3 - z_3^3)^2 \, e^{-\frac{|z_1|^2+|z_2|^2+|z_3|^2}{4}}$$

we assume z_1 is real (corresponding to a rotation of coordinates), set $z_2 = z_1 e^{i\phi}$, and integrate the resulting density over z_3. That is,

$$g^{(2)}(\phi) \propto \int |\psi_L(z_1, z_1 e^{i\phi}, z_3))|^2 d^2 z_3. \tag{A.115}$$

Upon evaluating this expression, we find

$$g^{(2)}(\phi) = \sin^4(3\theta/2) \left(a + b\cos(3\theta) + c\cos(6\theta)\right), \tag{A.116}$$

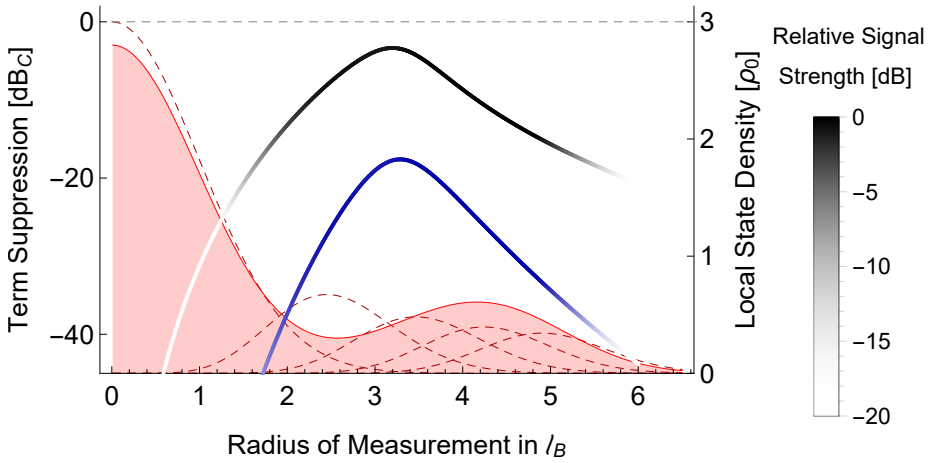

Figure A.3.9: **Relative Strength of Contributions to Azimuthal Correlation Function.** The ratios b/a (black) and c/a (blue) show that the deviations from the pure $\sin^4(3\phi/2)$ azimuthal correlation function are always small, but not entirely insignificant over a narrow range of radii. The saturation of these curves reflects the strength of the total signal a, which is peaked at intermediate radii since near the center, other photons reside at larger radii, while at the outer edge, single particle state density decreases. For reference, the single particle states (dashed) and the local density of states in the three particle Laughlin state (solid shaded) are plotted in units of the background density of states in the lowest Landau level. As the particle number increases, this should approach 1/2 over intermediate radii.

where a, b, and c are polynomials in z_1. There are two additional terms $b/a\cos(3\phi)$ and $c/a\cos(6\phi)$ beyond what appears in the two particle Laughlin state azimuthal correlation function.

In figure A.3.9 we explore the relative strength of these additional terms as a function of the radius at which the first photon is measured. While there is a significant signal over several magnetic lengths (saturation), the additional terms are always smaller than the main oscillation $\sin(3\phi/2)$; the largest correction, the $\cos(3\phi)$ oscillation at a radius of 3.2 l_B, is 46% as large as the main oscillation.

APPENDIX B

CUSTOM VACUUM COMPONENTS

B.1 Experimental Cavity

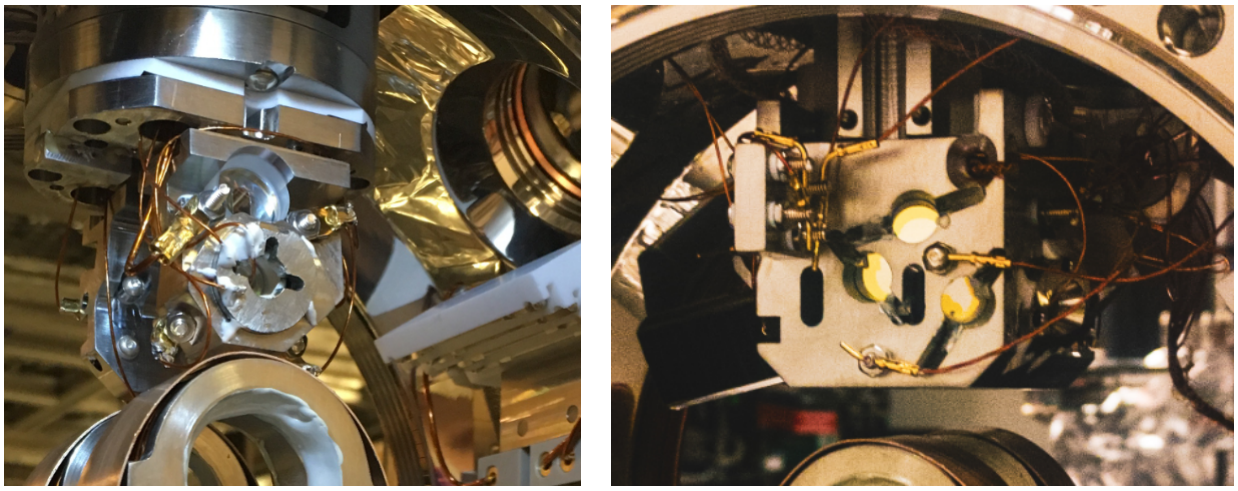

Figure B.1.1: **Photographs of Experimental Cavities.** These photographs show the two experimental cavities used for Rydberg polariton experiments hanging from their mount to the upper custom flange above the MOT coils. In both cases, mirrors are glued into 316 stainless steel structures. These structures are isolated from the main chamber by white Macor spacers. The electric field environment is controlled by eight electrodes as well as the voltage(s) applied to the cavity structure(s). The electrical connections for the electrodes and piezos were originally made with crimps and lugs, but later improved to pins and transversely pierced screws.

B.1.1 Electrodes

To control the electric field environment at the atoms, we apply voltages to eight electrodes with direct line-of-sight to the atoms. The electrodes are each the head of a screw, and, in the dual nonplanar cavity structure from chapter 6, a copper washer. These screws are isolated from the cavity structure by Macor washers. From experience with prior cavities, it is also essential that no material, conductor or dielectric, be close to the atoms, as even Rubidium deposits on the surface of steel can act like a dipole due to a differential electron affinity. As such, in all cavities, the closest material is around 10 mm away from the atoms

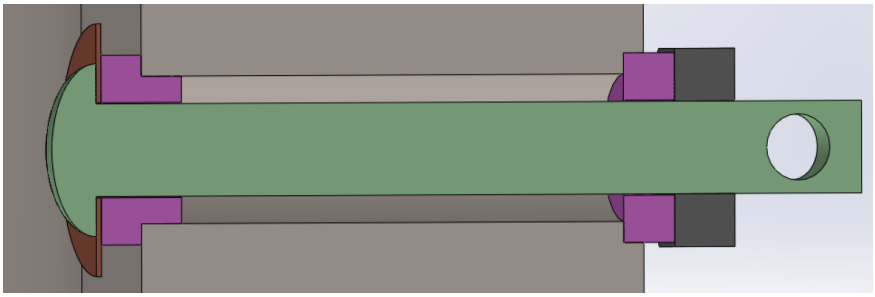

Figure B.1.2: **Electrode View.** This diagram shows the assembly of an individual electrode (green), with a copper washer (red) that increases the area of the electrode and shields the atoms (not shown, left of figure) from any charges that might build up on the Macor spacer (purple). The Macor spacers can take two forms. The inner surface of the cavity structure is very challenging to machine, so a notched Macor washer ensures proper alignment and isolation of the electrode screw. The outer surface of the cavity structure is easy to machine so a simple Macor washer may be dropped into a recess in the cavity structure. A nut (dark grey) then secures this assembly in place, and a transverse hole accepts a pin for electrical control.

and we limit line of sight from the atoms to any dielectrics. Thus, when possible, mirror surfaces are shielded from the atoms by deep slots, and other dielectrics such as the MOT coil wires and the electrode Macor washers are covered by copper.

We control eight degrees of freedom: the three electric field components and five independent electric field gradients. Thus we need to adjust at least eight voltages. In practice we have additional control because the metal cavity structure itself is also insulated from the chamber and so can be set to a voltage relative to the chamber and MOT structure nearby. For the planar cavity from chapter 5, the cavity structure came in two halves, so a relative voltage between the halves created a nearly pure electric field along the cavity axis.

To convert between applied voltages and the actual applied fields and gradients at the location of the atoms, we do not utilize symmetry, but rather perform finite element analysis. This provides a matrix transformation taking desired electric fields to necessary applied voltages. Since we can adjust more degrees of freedom than we wish to control, we restrict ourselves to the matrix which obtains the desired fields and gradients with the smallest sum of squared voltages applied. This is a somewhat arbitrary choice, and we also calculate the matrices that simply do not use any given electrode, in case that electrode breaks. We found from this analysis that good control of all gradients required that we break symmetry

between electrodes. Therefore, in the planar experimental cavity, we added additional metal spacers to some electrodes, while in the nonplanar experimental cavity, the electrodes were designed with little symmetry.

B.1.2 Electrical connections

Figure B.1.3: **In-vacuum Electrical Connections.** This photograph shows the process for drilling transverse holes in vacuum screws for making electrical connections.

Making in-vacuum electrical connections can be tricky, as vacuum compatible solder is very weak and difficult to work with. An attractive alternative is to use pressure, either from crimps or terminal blocks. This works very well for larger wires (e.g. 18 AWG), but in cases where flexibility is essential and smaller gauge wires are used (e.g. 30 AWG), the pressure from crimps or terminal blocks often causes the wires to break.

Our most recent experimental cavity improved upon the crimp-and-lug connections by instead inserting a pin into a hole drilled transversely through the electrode-screw (see Fig. B.1.2). The piezos and heating wires are connected similarly, but via a transfer screw with two transverse holes, one for the wire and one for the pin. Special tabs on the cavity structure were introduced to hold eight of these transfer screws.

The pins are attached to the free ends of a Subminiature-C cable assembly (custom, from

Accu-Glass Products, Inc.). The male Sub-C connector is glued to the cavity structure, and is connected to Sub-C feedthroughs (Accu-Glass 100012) in the upper custom flange via female-female Sub-C cables (Accu-Glass 100120). This architecture enables all electrical connections to be made and tested outside of vacuum and then strain relieved. Installing the cavity in the chamber is then relatively easy since making electrical connections to the custom flange feedthroughs requires just plugging in a couple Sub-C cables.

To machine holes transverse through the small #2-56 electrode screws, we first flatten the threads with an end-mill, start a small divot with the blunt tip of a counter-bore, and finally drill out the hole with a drill bit. This drill bit is chosen to provide a tight slip fit for the pins, and is ground short so that the chuck supports the bit very close to the end. The threads are then cleaned of chips by forcing a nut (which is then discarded) onto the screw several times.

Finally it is worth noting that for some applications silver epoxy (EPO-TEK H21D) is a great option. This is a conductive two-part epoxy that is also quite strong. It has been used to ensure that the mirror-piezo mounting structures are grounded to the cavity structure while providing additional rigidity.

B.1.3 Cavity mirrors

Our cavity mirrors are bought from Layertec, which provides both the substrates and the custom coating. To avoid the potential creation of lossy color centers due to the presence of intense blue light, we ensure that the outer layer of all coatings' dielectric stacks are SiO_2, not Ta_2O_5 [391].

Keeping mirrors clean is an obvious concern. We attempted to minimize the time between beginning a cavity assembly and installation in the vacuum system, as any dust or dirt on

the cavity mirrors would significantly impact our ultimate impedance matching and detection efficiency. Unfortunately, as each experimental cavity represented a large increase in complexity, assembly and alignment was a long process, and our cavity mirrors became dirty. I believe that this long assembly time is the primary limitation on our experimental cavity impedance matching, and future experiments would be well served by ensuring a very fast assembly and alignment procedure.

To clean or protect mirror surfaces, we often used First Contact Polymer. This method is slow and requires full access to the mirror, i.e. it is not suitable if the mirror is already installed. For these cases, lens paper with newly opened photometric grade acetone was used. As a first pass, we lightly place the paper on the mirror surface, drop a drop of acetone on the paper so that it wets to the mirror, and then drag the paper sideways until dry. For more intense cleaning of residues or films, the regular optics cleaning technique with lens paper and forceps is used but with the newly opened photometric grade acetone and a good deal of downward pressure on the mirror surface. We have had good experience with this technique cleaning off deposits that nothing else removes, at the risk that this technique can destroy mirror surfaces if there is any hard grit present.

B.1.4 Piezos and and their mounting

From prior experimental cavities, we learned that it was important to mount mirrors and piezos with a focus on stability, so that there are no low frequency mount resonances. Such resonances, from e.g. a tuning-fork mode of the mirror-piezo assembly on a suspended mounting structure, can severely limit the bandwidth of the cavity lock. As such, using wider and shorter piezos is better, along with a full mounting structure that is heavy compared to the cavity-piezo assembly and is attached to the main cavity structure at many points.

Our piezos have come from two sources, American Piezo and Noliac. The former were simple

cylinder piezos where a radial electric field created between electrodes on the inner and outer surfaces of the cylinder produces a longitudinal strain. To achieve a several micron free stroke in under a kilovolt, the piezos were sanded to 7.5 mm long. The piezos from Noliac are ring stack piezos with a significantly larger strain per applied volt. This allows a several micron free stroke with a 2 mm long piezo at a maximum voltage of 200 V. This then makes the suspended mirror more stable as the piezo then is significantly wider than it is tall.

In either case, it is important to mount the mirror, piezo, and mounting structure all concentrically with a thin layer of Torr-Seal, thin because that ensures the components are all actually concentric and not tilted and because it helps push to higher frequency flexural modes associated with the glue (see e.g. [203]). To this end, these components are first assembled in a custom jig that maintains precise alignment while giving access along two sides to glue the components together.

More generally, making a solid, monolithic cavity structure reduces the impact of mount resonances. While the primary advantage of such a design is the dramatic increase in the ease of cavity alignment, this is an important additional reason to prefer monolithic cavity structures.

B.2 Custom Flange

The experimental cavity is always mounted from the top via a custom vacuum flange. While the initial cavities in the Simon used a different custom flange design, the experiments described in this thesis all made use of a common design, albeit with minor differences.

This custom flange attaches to the top 4.5" Conflat flange of the main chamber and has a tapped hole pattern on the knife-edge side to allow the experimental cavity mounting structure to be attached. On the reverse side, a vertical tube extends up to a 2.75" flange

for a vertical window. This tube is pierced in four places for four different feedthroughs. Two of these are straight tubes ending in a 1.33" flange. These have been included for the sake of future flexibility, but have not been used; they end in blanks. The other two piercings are each small diameter tubes that skew-loft up to a 2.75" flange. Being larger, these flanges can take more variable feedthroughs. Initially, we used instrumentation feedthroughs. Assembling the connectors proved tiresome and error-prone, so the latest iteration makes use of c-sub connectors. Both in vacuum and regular c-sub cable assemblies are easily ordered from Accu-Glass, and so allow assembly without needing to crimp wires. The only downside is a lower (but still acceptable) maximum voltage. The tube is skew-lofted rather than a standard concentric loft so that the total height of the custom flange is minimized. This allows keeping the upper optical breadboard as low as possible, making alignment easier. The flange base is pierced, initially with five distinct holes, and later with a cruciform pattern to allow lasers to propagate vertically without limiting numerical aperture and to allow instrumentation cables to travel from the feedthroughs above to the cavity structure below. Finally, an interior thin tube is included to guide instrumentation cables. We were concerned that cables making the downward 90 degree turn from the feedthrough flange to the cavity structure would protrude inward and block optical access. To prevent this, the thin tube extends from the flange base upwards to above the level of the vertical tube piercings. In the most recent version of the custom flange, this tube has semicircular holes cut out that match up with the cruciform hole in the flange base. This ensures that the c-sub connector can fit through, as we wanted to use pre-assembled cables rather than crimping our own.

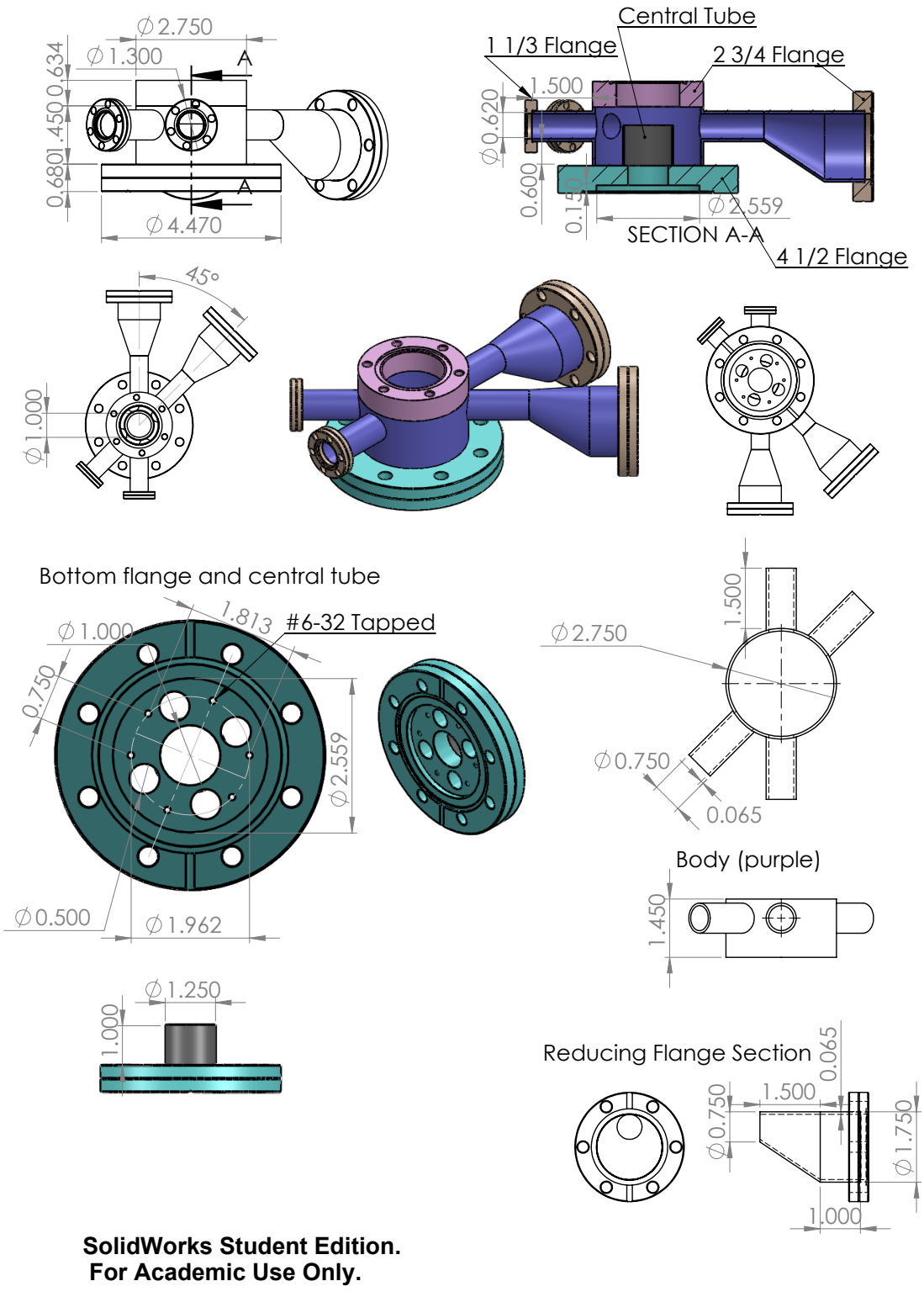

Figure B.2.1: Custom flange machine drawing.

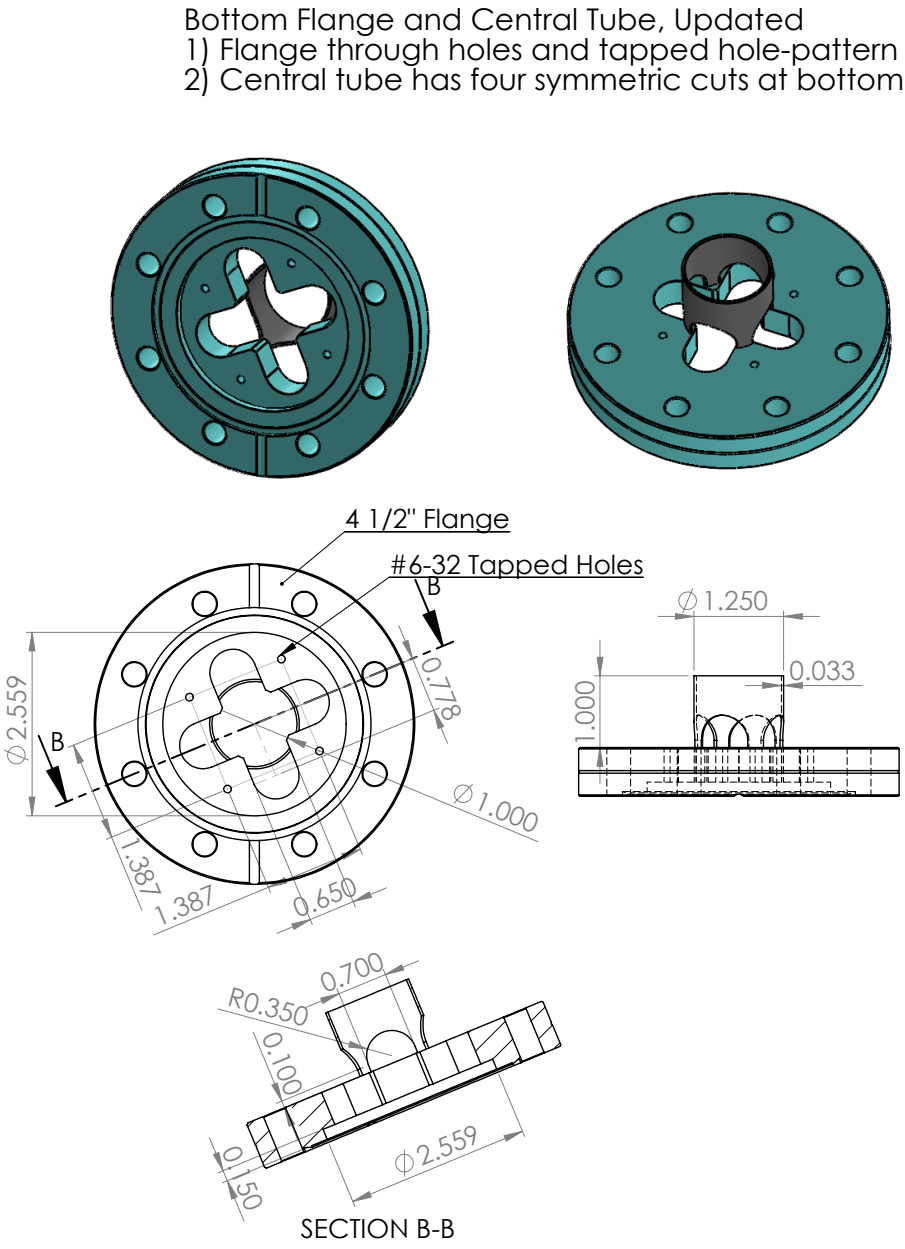

Figure B.2.2: Custom flange machine drawing, focused view.

B.3 Dispenser Mount

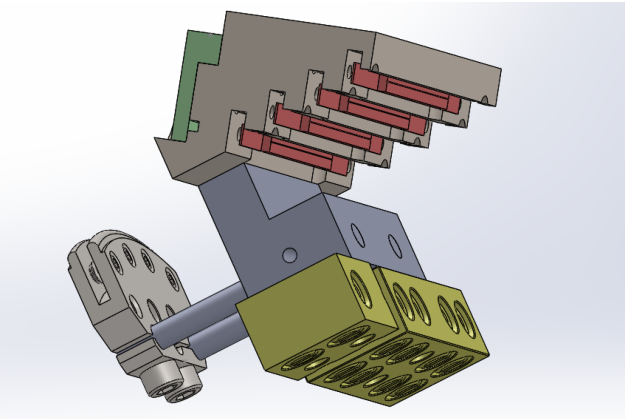

Figure B.3.1: **The Dispenser Assembly** consists of the main Macor ceramic structure that hold the four Rubidium dispensers (red). Screw heads hold the dispenser ends in place and make electrical contact. One screw from each attaches to the common ground plate nut (green) while the other screw is attached to an individual wire. All five wires go to the PEEK terminal blocks (yellow). The whole assembly is held together by a steel adapter that attaches to a groove grabber mounting system.

The Rubidium dispensers used in our experiments are activated by running between 2.5 and 3.5 amps through them. They also have finite lifetime, so we wish to mount several of them in the vacuum chamber. As such, we designed a mounting structure to be made of Macor ceramic that would hold four dispensers. We furthermore wanted to prevent Rubidium buildup on the side of the cavity structure, as electrode pins are exposed and are isolated from the steel cavity structure by small Macor washers. Potential buildup of Rubidium could short out these connection and halt our experiments. As such, the dispenser mount also includes thin flanges that stick down to block all directions of emission that aim above the MOT region.

The dispensers are each secured by the heads of two long silver-coated #0-80 screws. As it was impossible to obtain slotted versions of these screws, the through-holes for these are vented by additional slots in the Macor structure. One screw of each of the dispensers is screwed into a common ground plate nut, while the other screw of each of the dispensers is attached to a wire (clamped between two nuts on the backside of the structure). These four wires, plus a wire connected to the common ground plate nut go to PEEK terminal blocks

which connect them to five wires that go to an instrumentation feedthrough. We use the in vacuum terminal blocks so the dispenser assembly may relatively easily be removed to replace empty dispensers.

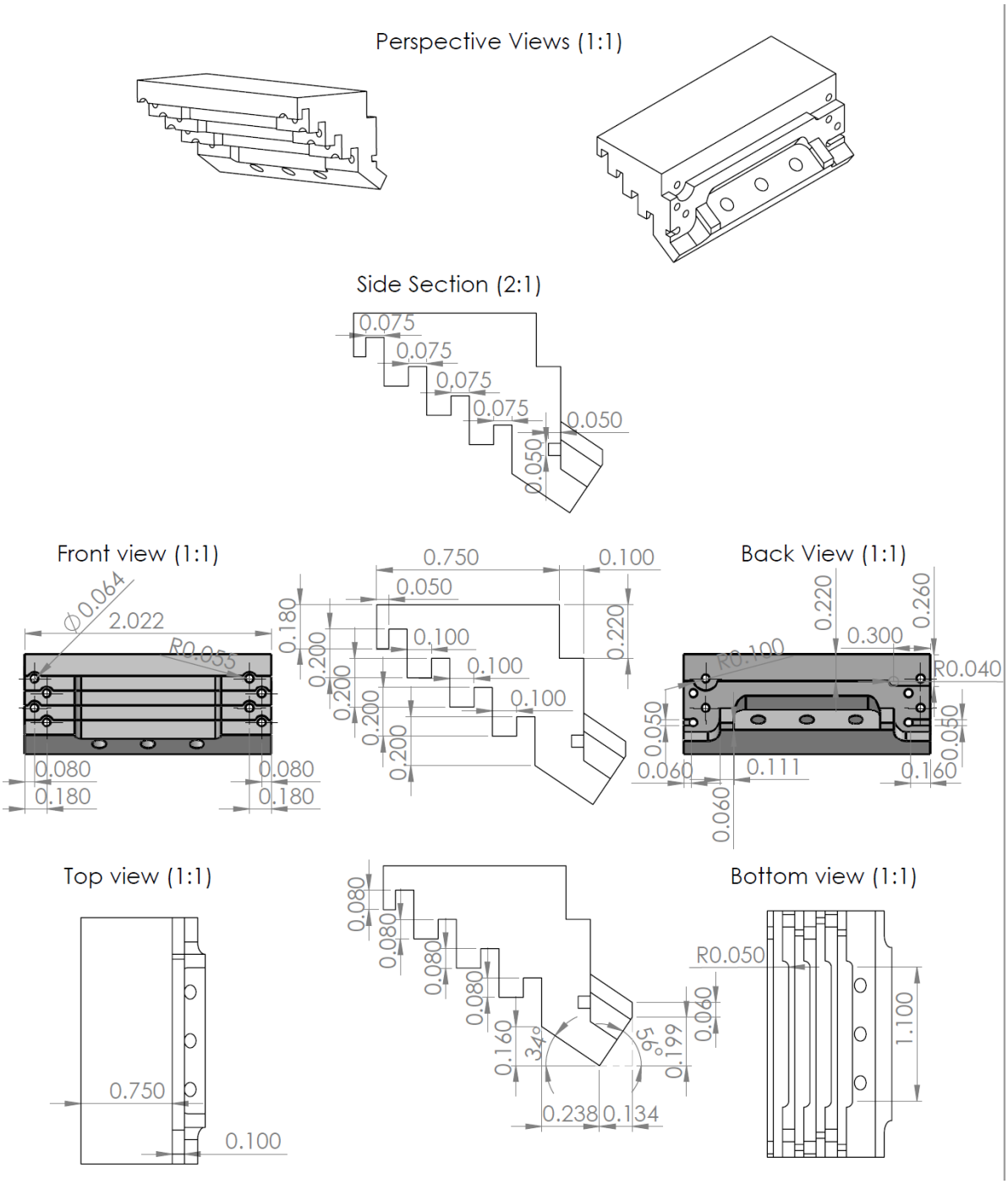

Figure B.3.2: Dispenser macor mount machine drawings.

APPENDIX C

A HIGH CURRENT HIGH VOLTAGE PIEZO DRIVER

This appendix details the design process and resulting circuit for a high current high voltage amplifier, for use with high capacitance stack piezos. By reducing its output impedance, the amplifier can drive a correspondingly higher capacitive load without unacceptable bandwidth limitations. The first two sections offer background and initial design considerations and improvements. Many readers may wish to skip to Section C.3 to learn about the final design. Additionally, a final section introduces a negative voltage variation of this circuit that works in two stages.

C.1 Background

Most of the optical cavities employed throughout the work described in this thesis required that their length be controlled to maintain resonance with a laser. This means that a voltage must needs control the position of a mirror to better than $\frac{\lambda}{2\mathcal{F}}$, where λ is the wavelength of the laser probing the cavity, and $\mathcal{F}$ is the finesse of the cavity. This is typically quitea small length, e.g. 10s of picometers. The other main requirement is that maximum change in the position of the mirror should cover several — certainly at least one — free spectral range of the cavity, i.e. the *throw* of the mirror actuator should be greater than $\lambda/2$.

While we have explored other options, the standard and best way to meet these requirements is by using a piezoelectric actuator, typically in a ring shape so that light may propagate into or out of the mirror which is actuated by the piezo. These devices are made of a material which experiences a mechanical strain in response to an electric field. In cylindrical piezos, the outer cylindrical surface of the piezo is held at an electric potential relative to the inner cylindrical surface, generating a radial electric field, which in turn generates an axial strain.

This is a relatively simple way to allow the throw of the piezo to be increased while keeping the necessary voltages reasonable — the necessary voltage depends only on the *thickness* of the ring, not the length. While simple and therefore cheap, these piezos typically need to be ~ 1 cm long with ~ 1 kV applied in order to create an $\sim \lambda$ throw. At this point, we needed a high voltage amplifier that could drive the several nanofarad capacitive load of the piezo. The development of this amplifier is described in the first section of this appendix. As we became more concerned about the stability of our optical cavities, we decided that having a mirror glued to the end of a piezo cylinder was perhaps causing additional mechanical modes to limit locking bandwidth, and so we explored other piezo options.

It is possible to stack layers of piezoelectric material between interleaved electrodes so that the strain may be parallel to the applied electric field. In these piezo stacks, the electromechanical coupling is typically a factor of two larger, and the layer thickness may be made smaller so that the same electric field is obtained by a smaller voltage. We have moved to using these piezos as a throw of several μm may be achieved using only $200V$ on a stack piezo 2 mm long. The central downside to these devices is that the capacitance of the piezo is dramatically increased, up to hundreds of nanofarads.

A greater piezo capacitance decreases the bandwidth with which the piezo may be driven. This does not affect the lock bandwidth of the cavity, as the PI lockbox corner frequency must simply be adjusted to match to piezo corner frequency. However, we found that our standard piezo driver only had ~ 1 Hz of bandwidth, making simply driving the piezo to see a cavity spectrum tiresome. We will conclude this appendix with a description of the changes to the circuit that increased the bandwidth of our piezo driver by three orders of magnitude.

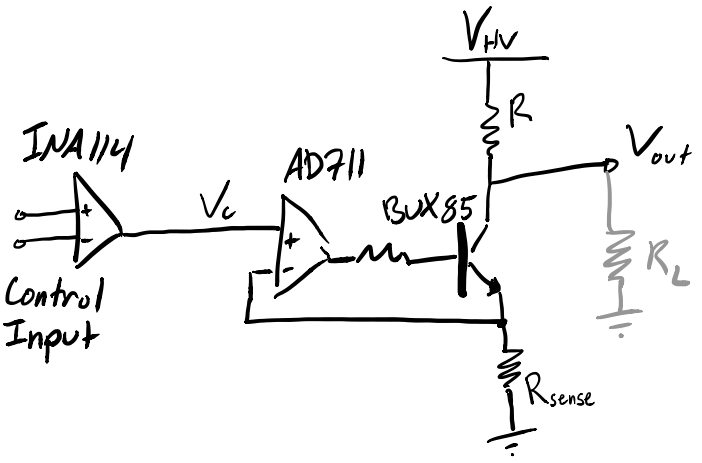

Figure C.1: The original piezo driver circuit.

C.2 Initial Improvements

The original design for a high voltage amplifier in use in the Simon lab is shown (schematically) in Fig. C.1. This design uses a control voltage V_c to determine the current through a sense resistor R_{sense}. This is the same current as flows through the main resistor R, so the output voltage is given by $V_{out} = V_{HV} - IR$. Since the voltage above R_{sense} is V_c (which varies between 0 and 10 volts) evidently $V_{out} = V_{HV} - V_c \frac{R}{R_{sense}}$.

In thinking of this a voltage source, it is useful to compute the Thevenin (output) resistance. A lower Thevenin resistance means that the actual voltage output is closer to the desired output given a finite load resistance. The Thevenin current is the current through the output when it is shorted to ground: $I_{th} = V_{HV}/R$, while the Thevenin voltage is the open circuit output voltage, which was calculated above. Therefore the Thevenin resistance is

$$R_{th} = R - \frac{V_c}{V_{HV}} \frac{R^2}{R_{sense}} \tag{C.1}$$

Now we need to understand the choice of R and R_{sense}. With $V_c = 0$, no current flows, so there is no voltage drop across resistor R, so $V_{out} = V_{HV}$. When $V_c = V_c^{max} = 10V$, we want

$V_{out} \approx 0V$, so we choose $R_{sense} = R\frac{V_c^{max}}{V_{HV}}$. For this design, 0 to 10 volts controlling 0 to 1kV, this means the ratio of output to control voltage (ignoring the inversion) is 100, so the ratio of R to R_{sense} should be 100. The behavior of the circuit is improved by reducing R, as this sets the scale of the output impedance. There are two factors that limit the reduction of R. First, the transistor and resistors must be able to handle the power dissipated, which increases as R is reduced, and second, the high voltage power supply must be able to source the current. The second condition was our limit, as we had only a 1 mA kilovolt supply, determining our choice of $R = 1\text{M}\Omega$ and thus $R_{sense} = 10k\Omega$.

Plugging this into equation (C.1) yields an output impedance that varies from R (when $V_c = 0$ and $V_{out} = V_{HV}$) all the way to 0 (when $V_c = V_c^{max}$ and $V_{out} = 0$)! This variation is not good. Perhaps relatedly, we found that the gain of the driver was lower for V_c near V_c^{max}. After optimizing the cavity lock in this regime, we changed the lock point to an intermediate value and found that the lock oscillates.

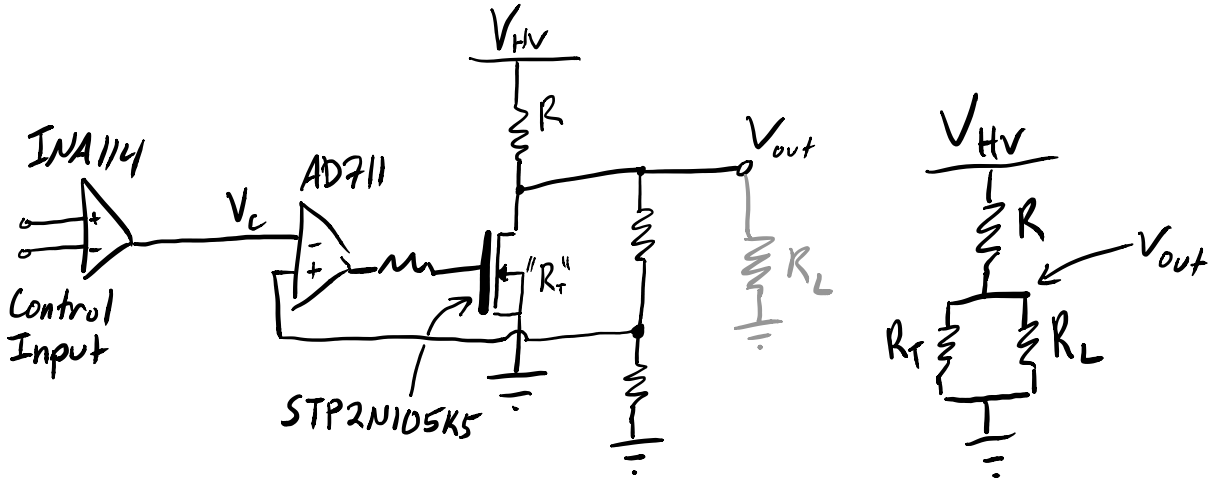

Figure C.2: (a) An improved piezo driver circuit. (b) The effective voltage divider circuit

The most obvious improvement to make is to feedback on the output voltage directly rather than setting a current. We have replaced the transistor with a MOSFET, which basically doesn't change anything. We will think of it as a voltage controlled resistor R_T. You can see that a voltage divider on the output provides the feedback point. The component values for

this divider are chosen so that the feedback point is at $V_{out}/100$ and no current flows (total resistance $> 10\text{M}\Omega$). This allows us to think of the feedback as directly setting $V_{out} = 100V_c$, by varying R_T until this is true. (This works as long as the sign of the feedback is correct!)

We think of this system as a voltage divider on V_{HV} with the upper resistor being R, and the bottom resistor being R_T and R_L in parallel. The output voltage should be given by $V_{out} = \alpha V_{HV}$ for $\alpha = V_c/V_c^{max}$. This fixes R_T, as $\alpha = \frac{R_{eff}}{R+R_{eff}}$ where $R_{eff} = \frac{R_L R_T}{R_L+R_T}$. For large R_L, as is the case for piezos, the feedback finds an R_T to set the output correctly; however, for $R_L \leq R\frac{\alpha}{1-\alpha}$, R_T would have to be negative. Since this is impossible, R_T goes to 0 and the output saturates at $V_{out} = \frac{R_L}{R+R_L}V_{HV}$

The great advantage of this design is that as the control voltage is tuned, the output voltage is precisely determined by V_c no matter R_L up to some cutoff, after which the output is saturated. The value of this cutoff is given by $\alpha^* = \frac{1}{1+R/R_L}$, so we want a large load impedance or a small R. As before, the value of R is determined by the maximum current that the high voltage supply can source as well as the total power that can be dissipated by the resistor.

C.3 Final Design

The circuit schematic of Fig. C.2(a) forms the basis of the final design, although numerous additional resistors and filters are necessary to make the circuit actually behave. In particular, the AD711 op amp will oscillate even with the correct sign of feedback. This is stabilized by a several nanofarad capacitor bridging the output and the *inverting* input. The circuit is designed to be compatible with a low resistance primary resistor R, so this element and the MOSFET appear on the board as Molex headers. The primary resistor is set as a kilohm power resistor while the MOSFET is an IXYS IXFN140N20P; both of these may be attached to a water cooled plate and connected to the board via Molex headers. The HV

power supply used with this is an Acopian L150MC100A2B19D2G3H5.

To reduce the number of water cooled plates necessary in the lab, the board includes two channels. To protect the lab in case the amplifier remains on while the water cooling is shut down (or the water cooling fails), the board also implements a temperature interlock based on a comparison of a standard $10k\Omega$ thermistor, which is attached to the water cooled plate, with reference resistor, implemented as a potentiometer so that the threshold is easily changed. The interlock controls a power relay (Potter and Brumfield T9GS5L14-12) in the high voltage line so that no high voltage current may flow if water cooling stops. Since the AD711 op amp cannot source enough current to switch the relay, the AD711 drives the base of a transistor which closes a circuit applying 15 volts through a current limiting 50Ω resistor to the control pins of the relay. As the switching current of the power relay is quite significant, a separate 15 V regulator is dedicated to driving the relay.

The full schematic and board layout are included below:

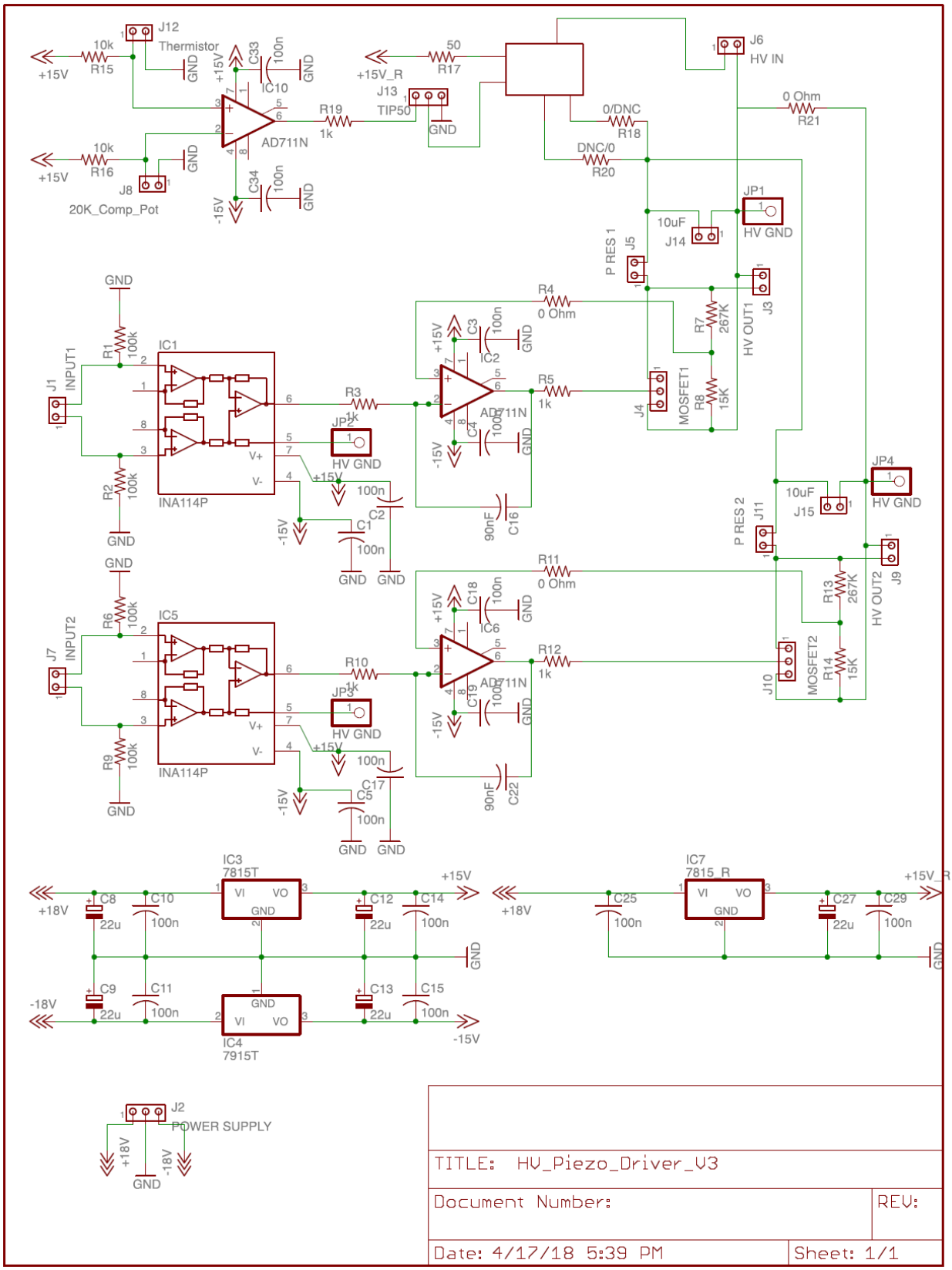

Figure C.1: Piezo driver schematic.

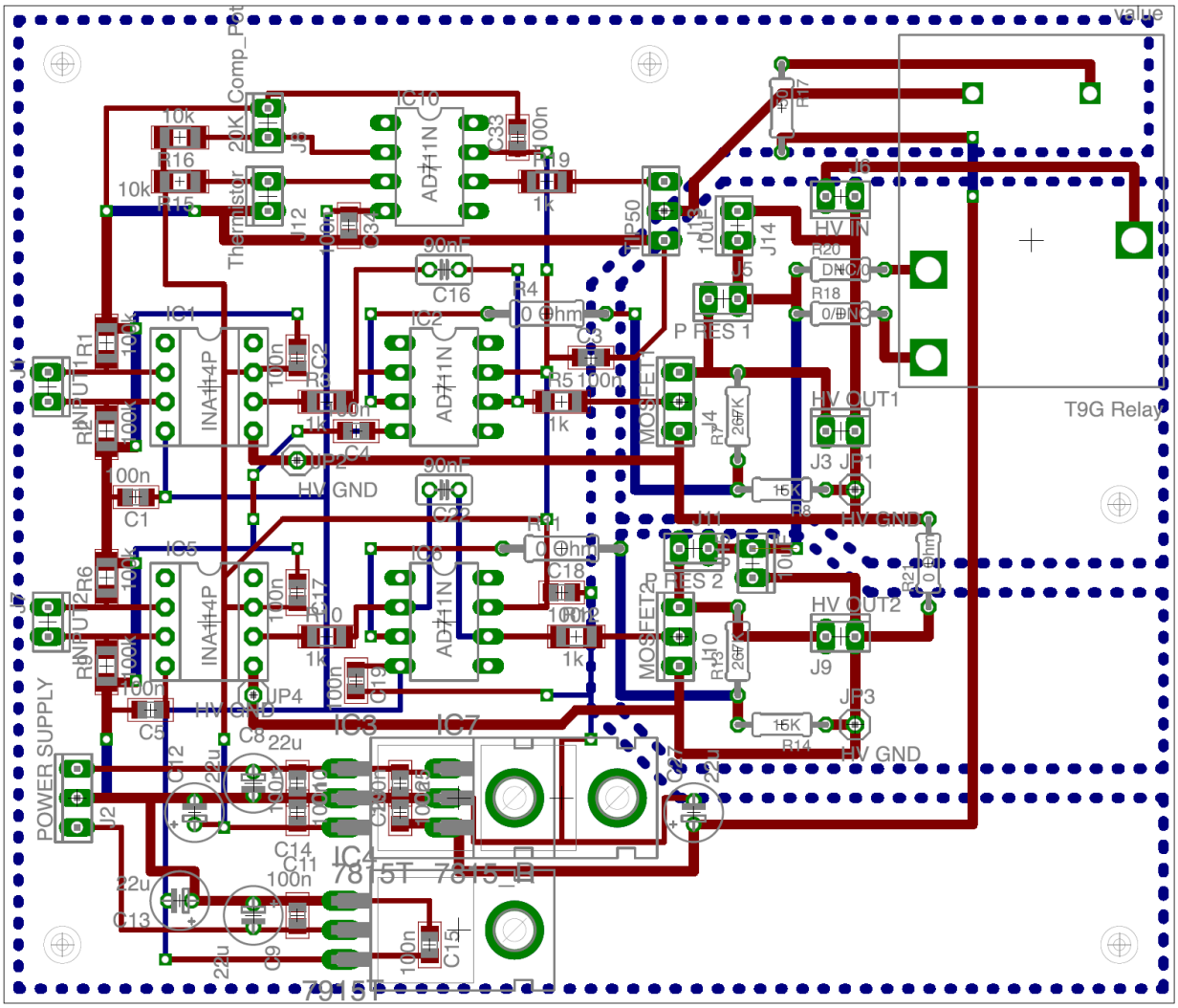

Figure C.2: Piezo driver board layout.

C.4 Negative Voltage Amplifier

At various points, it has been desired to use a large negative voltage to drive a peizo, rather than a positive voltage. This typically occurs because we are concerned that the large voltage on the cavity piezo surface is producing an electric field that perturbs the atoms. This can be tested and potentially fixed by setting the positive side of the piezo at ground, while setting the negative side of the piezo to a large negative voltage. For instance, for the polaritonic quantum dot experimental cavity, finite element analysis predicted an electric field gradient magnitude of 15 mV/cm at +800 V in the normal configuration (+800 on inner surface of piezo cylinder, GND on outer surface). By flipping this to GND and -800V, the high voltage is significantly shielded by the surrounding metal structure, having much less line-of-sight to the atoms. This is reflected in this configuration's finite element analysis prediction of 40 μV/cm electric field gradient, an improvement by a factor of 375!

For relatively low voltage piezos, e.g. most stacks, it is enough to switch the sign of the high voltage power supply and replace the NPN transistor or N-channel MOSFET with a PNP transistor or P-channel MOSFET, respectively. However, the largest breakdown voltages for PNP transistors devices seem to be collector-emitter voltages of $\sim$ 600 V.

To maintain the desired kilovolt range, we redesigned the circuit to have the large voltage drop step down across multiple 500 V PNP transistors (ZTX560). As before, we feedback on the output voltage divided by 100. The difference now is that we need to control the voltage applied to the upper stage transistor to ensure that half the voltage drop occurs there. This is accomplished by using the same output voltage divider chain to send half the output voltage into the base of the upper stage. This enforces that the voltage between the two transistor stages will be half the output voltage minus a (negligible) diode drop.

One complication arises in that the primary resistor is still limited to 1 MΩ by the 1 mA kilovolt supply. We need the voltage divider chain to have a large total resistance compared

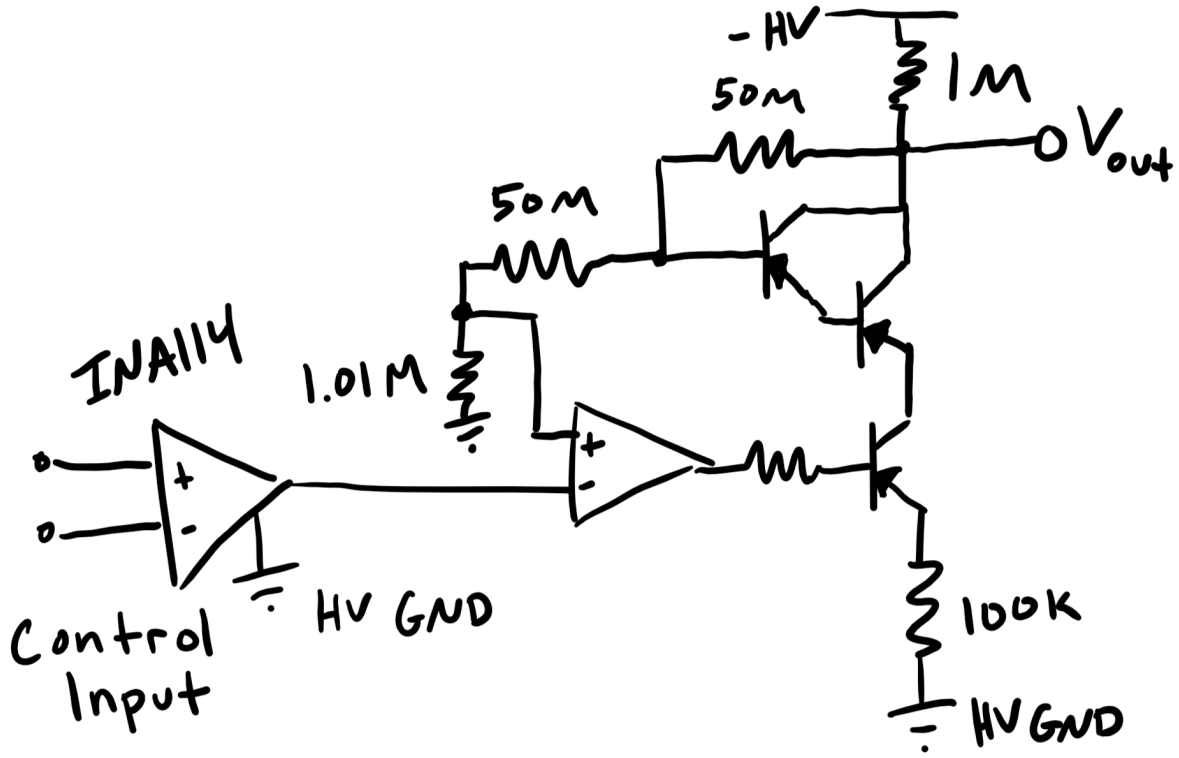

Figure C.1: A two-stage negative voltage amplifier.

to this, so we use a total of ~ 100 MΩ. However, we need this divider chain to provide constant division that is not affected by the variable base-emitter current of the upper stage. To ensure that this current is truly negligible, we configure the upper stage transistor into a Darlington pair, resulting in the schematic shown in Figure C.1.

It is worth noting that this basic idea for stepping down a voltage across multiple transistors could be extended significantly to make higher voltage amplifiers.

APPENDIX D

A FOUR CHANNEL COMPUTER CONTROLLED DIRECT DIGITAL SYNTHESIS BOX

Real-time computer controlled frequency synthesizers are an integral part of our experiments. Any time our experimental sequence calls for sweeping a laser frequency, this is implemented by referencing the laser to a sweeping rf tone produced by direct digital synthesis. We use AD9914 evaluation boards in their parallel data port modulation mode. The boards each receive a 3.5 GHz reference for the system clock and a 32 bit number called a frequency tuning word (FTW) that can vary between 0 and $2^{31} - 1$ (up to the Nyquist frequency). The AD9914 then outputs a frequency given by

$$f_{out} = \frac{FTW}{2^{32}} * f_{sysclk} \tag{D.1}$$

The great utility of this configuration is that the frequency tuning word can change quickly: at the SYNC_CLK rate which runs at $f_{syncclk} = \frac{1}{24} f_{sysclk}$, or equivalently, every 7 ns. We provide the rapidly updating 32 bit FTW with an FPGA (Opal Kelly XEM6001) which takes in a list of frequency-time endpoints via USB communication from the control computer and converts those waypoints into a smooth, real-time, and triggerable ramp of FTWs. DDS specific IOUPDATE control allows multiplexing multiple DDS boards onto the same FPGA at the expense of individual board update rate. Taking into account the FPGA finite state machine speed with four DDS boards, we end up with individual board frequency update rates of approximately 1 MHz.

The bill of materials and construction directions for a single four-channel box is included below:

4 Channel DDS Box Instructions

List of materials:

Line	Supplier	Item	QTY	Description	Notes
1	Analog Devices	AD9914 Evaluation Board	4	Contains DDS chip, includes IO support	Buy from Analog via credit card
2	Opal Kelly	XEM6001	1	FPGA + USB interface	Buy from Opal Kelly via credit card
3	Mini-Circuits	ZB4PD-42-S+	1	4-way power splitter	
4	SL Power Electronics	HN12-5.1-A+	1	12V AC-DC converter power supply	Digi-key part no. 271-2048-ND
5		Breakout board	1	Connect FPGA output to DDSs, supply 1.8V power	See schematic below; Dropbox/Simonlab Shared/Lindsay's Eagle Stuff/AdapterV2
6	TDK-Lambda	KMS40-3P3	1	3.3V AC-DC converter	Digi-key part no. 285-1783-ND
7	XP Power	SR10S1V8	4	1.8V regulator	Digi-key part no. 1470-2251-5-ND
8	Bud Industries	RM14214	1	Chassis; 19x17.187x8.718 in	Allied Electronics part no. 70148841
9	Bud Industries	TBC-14252	2	Top/bottom cover	Allied Electronics part no. 70148355
10	Analog Devices	ADCMP603	1	Comparator Board	Mouser
11			6	SMA-SMA chassis mount	e.g. L-com BA21
12			2	SMA- pins chassis mount	e.g. L-com BAC16
13			1	BNC-pins chassis mount, insulated	e.g. L-com BAC1503
14			1	SMA Tee	e.g. L-com BA19
15			4	SMA 50 Ohm term., male	e.g. L-com BTS5M
16			9	SMA-SMA cables 6-18” long	
17				Molex connectors	
18			1	Power entry switch	
19			4	12 pin ribbon cable	Amazon
20			8	12 pin female IDC header	Amazon
21			4	12 pin male IDC header	Amazon
22			4	64 pin ribbon cable	Amazon
23			8	64 pin female IDC header	Amazon
24			4	64 pin male IDC header	Amazon
25			1	20 pin ribbon cable	Amazon
26			2	20 pin female IDC header	Amazon
27			2	20 pin male IDC header	Amazon
28			1	50 pin ribbon cable	Amazon
29			2	50 pin female IDC header	Amazon
30			3	50 pin male IDC header	Amazon
31			8	10uF Capacitor	
32			8	0.1uF Capacitor	

It is preferable to purchase preassembled ribbon cables rather than the parts, as we have found the home-built ribbon cables to be a common source of error and instability.

Construction directions

1. Solder dual row male headers to appropriate PCBs
    a. Breakout board,
    b. FPGA board (JP1, JP2, JP3)
2. Solder on components of breakout board (capacitors, 1.8V regulator, Molex connectors)
3. Configure the four DDS boards:
    a. Jumpers across
        i. CTL-BUF -> GND
        ii. OSK-BUF -> GND
        iii. RESET-BUF -> GND ******(MAYBE NOT)*******
        iv. DRHOLD-BUF -> GND
        v. P102-DRCTL-BUF -> GND
        vi. PS0-BUF -> GND
        vii. PS1-BUF -> GND
        viii. PS2-BUF -> GND
        ix. ENABLE CLK INPUT
        x. P204 -> Disable
        xi. P203 -> Disable
        xii. P205 -> Disable
        xiii. P202
    b. 50 Ohm terminator on SYNC-IN
    c. remove any other jumpers, e.g. on IOCFG pins, MPI pins
    d. cut the following rows of pins (all three: GND, Signal, 3.3V)
        i. SYNC_IO-BUF
        ii. Unlabeled row between SYNC_IO-BUF and MPI31
4. Construct the chassis, and lay out locations of boards (see suggested layout below). Note that the FPGA (JP3 pin 47) needs to be within 6 inches of the OUT+ SMA connector of the comparator board. Drill all holes as necessary. (four standoffs per board, appropriate mounting for components mounted to sides, rectangular hole for power entry. Note that the USB hole must pass the large USB-B style head through.)
5. Mount the 4DDSs, breakout board, AC/DC converters, power entry switch, FPGA, comparator, and 4 way splitter.
6. Solder thick wire in twisted pairs from power entry switch to
    a. 12 V AC-DC converter
    b. 3.3V AC-DC converter
7. Connect 12V output to the input power of breakout board
8. Connect twisted pairs of wires from 1.8 V outputs of breakout board and from 3.3V output of the AC-DC converter to each of the DDS boards (see labeling on DDSs).

9. Connect 3.3V power to both power inputs of the comparator board via banana cables (cut in half). Ground the three grounds of the comparator board to the ground output of the 3.3V regulator.
10. Unless preassembled ribbon cables were purchased, assemble the ribbon cable connectors, measuring lengths to be sufficiently long with relatively little extra length. (4x 12 pin, 4x 64 pin, 1x 50 pin, 1x 20 pin). Headers should face same side. Be very careful to clamp solidly, without breaking the header.
11. Connect the following: (with handedness of connections same as in previous box)
    a. 50 pin ribbon cable from FPGA JP2, ribbon cable center crossing board, to breakout board, ribbon cable center crossing board.
    b. 20 pin ribbon cable from FPGA JP 1, ribbon cable center away from board, to breakout board, ribbon cable center crossing board.
    c. 12 pin ribbon cables from breakout board, ribbon cable center away from 20 pin header, to each DDS, ribbon cable center away from board.
    d. 64 pin ribbon cables from breakout board, ribbon cable center away from 50 pin header, to each DDS, ribbon cable center away from board.
12. Attach chassis-mount/bulkhead adapters
    a. SMA-SMA for 4 outputs and 3.5 GHz DDS clock input
    b. SMA-SMA for FPGA clock
    c. BNC-pins (insulated ground) for FPGA trigger
13. Connect SMA-tee to the IN- SMA of the comparator board, and 50-Ohm terminate one side. 50-Ohm terminate the IN+ SMA of the comparator board. Solder a 200kOhm(?) resistor from the pin to ground of an SMA-to-pins chassis mount, and connect to the LE-HYS SMA of the comparator board. Leave the shutdown, OUT-, and optional green banana cable connector all unconnected.
14. Connect SMA cables
    a. From 3.5 GHz clock input SMA chassis mount to the S side of the 4 way power splitter
    b. From each output of the 4 way power splitter to the clock input of the DDS boards
    c. From the output of each DDS board to the SMA output chassis mount.
    d. From FPGA 100 MHz clk SMA chassis mount to the unconnected port of the SMA-tee on the IN- SMA of the comparator board.
15. Using twisted pair with two pin female header or two pin female molex on one end, connect center pin of FPGA trigger to JP3 pin 3 and ground of FPGA trigger to JP3 pin 1.
16. Take a (short) SMA cable and cut it 6 inches away from one connector. Peel back the sheath to expose several millimeters of the center wire surrounded by white plastic. Twist the metal ground wires together. Strip 1mm of the white plastic insulation off of the center wire, making sure that the center pin and ground wires cannot short to each other. Solder the center pin and the twisted ground wires to a two pin female header. Connect this cable between the OUT+ SMA of the comparator board and the FPGA board such that the center pin goes to JP3 pin 47 and the ground goes to JP3 pin 49.

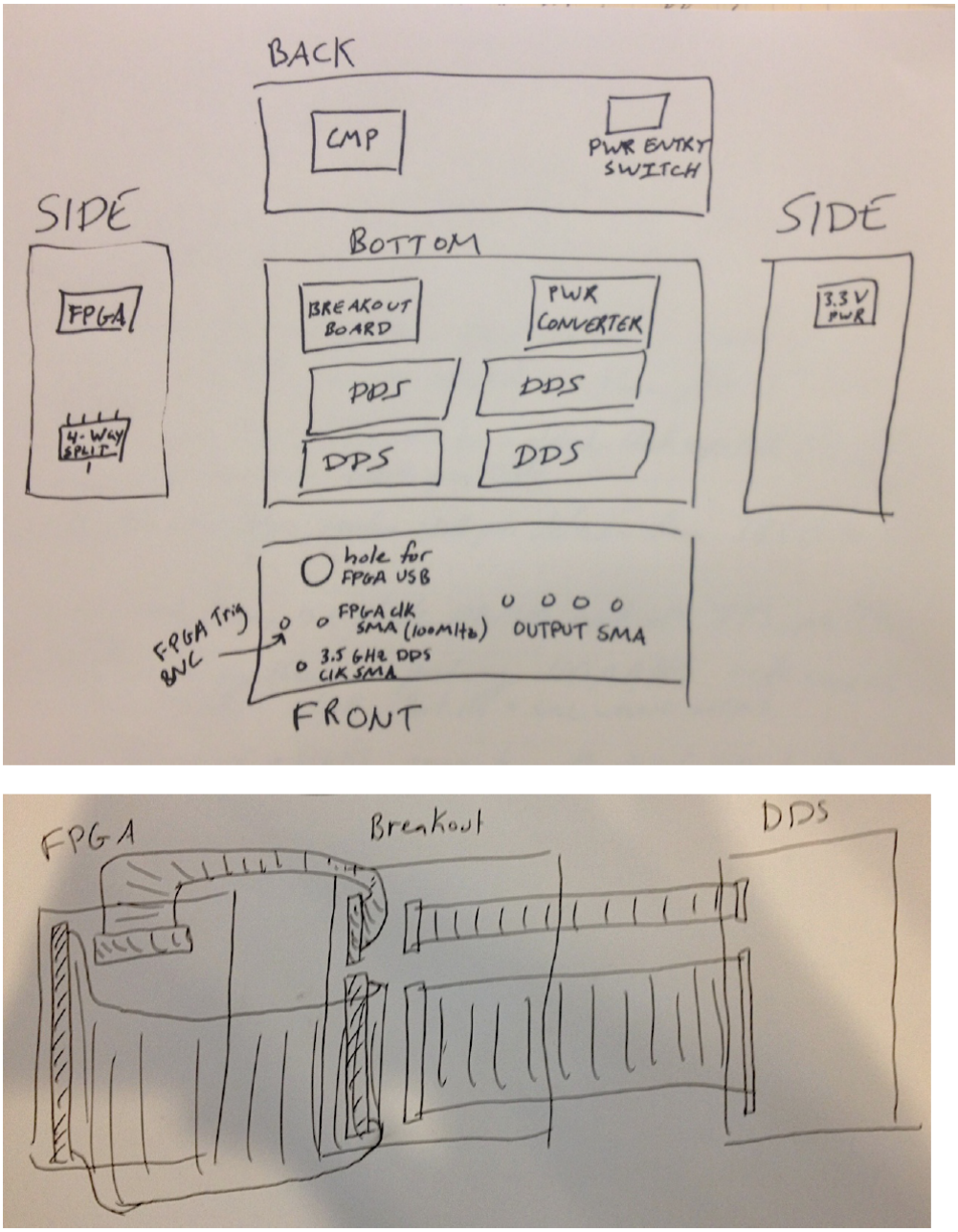

Figure D.1: Layout of DDS boards.

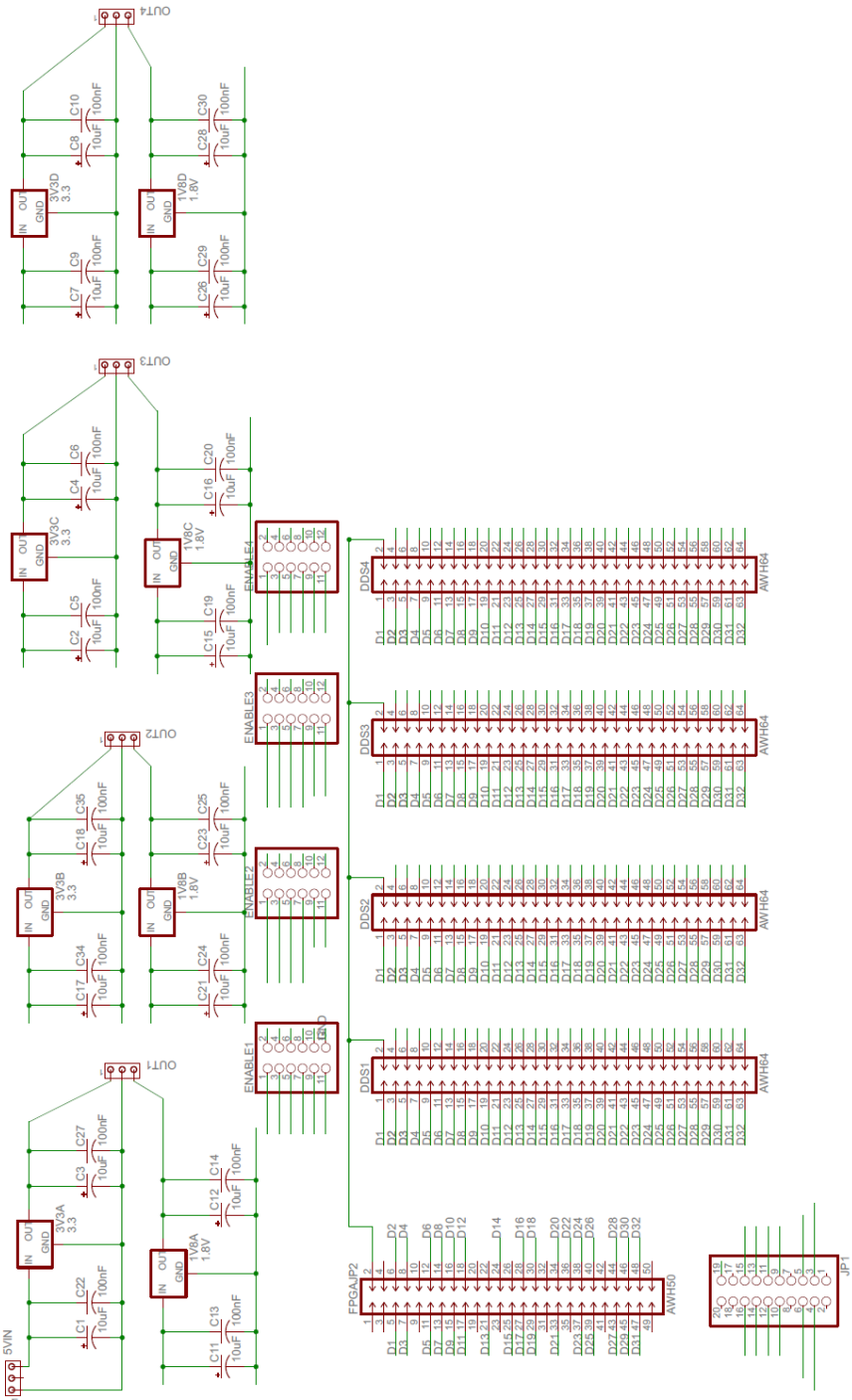

Figure D.2: Breakout board schematic.

APPENDIX E

TAPERED LASER DESIGN AND CHARACTERIZATION

We wished to obtain a new tunable diode laser at 1011 nm with an output of at least 1 W for the formation of a magic lattice to trap Rydberg polaritons. Near 1011 nm, the ground state polarizability due to the D1 and D2 lines becomes equal to the Rydberg state polarizability due to the Rydberg to $6P$ state; equal polarizabilities removes inhomogeneous broadening while trapping Rydberg polaritons in a lattice. A laser system from e.g. Toptica would cost $\sim$ \$50,000, while the standard home-built method would involve building an external cavity diode laser, locking and stabilizing it, and using that laser to seed a tapered amplifier. In an effort to reduce the complexity of this system, we designed and built a tapered laser. This laser design uses a DILAS TAL-1010-2000-CM, essentially a tapered amplifier chip as the gain medium, the only difference being that the output facet is not anti-reflection coated as in a tapered amplifier. The idea is then to take the amplified spontaneous emission (ASE, or equivalently, the superluminescence) that exits the *input* facet and retroreflect it in a cats-eye configuration to form a laser cavity. An intracavity frequency selective element would make the laser tunable over the full gain spectrum of the chip, and a piezo actuator on the retroreflecting mirror would provide fast frequency control over approximately the free spectral range of the laser cavity (several GHz). The intracavity frequency selective element was chosen to be a pair of Semrock MaxLine (LL01-1030) bandpass filters. These are 4 nm wide filters centered at 1030 nm. Tilting them causes the pass-band to move to lower wavelength. The filter transmission profile is flat topped, so two filters may be placed in series at slightly different angles so that the total pass-band is set only by the steepness of the transmission edge. This is optimized to a total transmission bandwidth of 1.2 nm, FWHM, at the cost of reducing the power transmission to $\sim 50\%$.

To improve the feedback bandwidth of the piezo, we also wished to implement a new design

from the group of Jun Ye [203]. This design improves the locking bandwidth by pushing the internal piezo resonances to high frequency by using a small, light, and stiff piezo with a small light mirror, which is glued together under high pressure to reduce the thickness of the (relatively soft) glue. The limiting factor is then coupling of the piezo-mirror system to so called 'mount-resonances': somewhere in the mounting structure, an element has a resonance at a low frequency, and the driven piezo pushes against its mount which in turn excites this other resonance. It is substantially impossible to eliminate these resonances, so the strategy is to dramatically reduce the coupling of the piezo-mirror system to these resonances. Several tactics are employed. First the block that the piezo-mirror system is attached to is made to be heavy and to not support high-Q resonances through which (off-resonantly) the mount resonances may be excited. This is done by making the mount out of a hollow copper cone, which is then filled with lead. The copper-lead interface has a significant acoustic impedance mismatch which helps to scatter acoustic waves; the interface is conical so that the waves scatter in different directions and do not directly retroreflect onto the piezo-mirror system. The lead is also ideal because it is soft, making it relatively lossy for acoustic modes, and has a low melting point, so it can easily be poured into the machined copper mount. Additionally, the two surfaces of the piezo are lightly sanded so that no acoustic etalon is formed. Finally, we attach the copper-lead mount to a heavy stainless steel block before mounting that block to a standard kinematic stage which might harbor the relevant resonances we wish to isolate.

The design of the laser as initially assembled is shown in figure E.1. There are several issues with the design which were addressed after initial construction.

- The intracavity filters' transmission edge is polarization dependent once tilted. The steepest edge is for S polarization. Given the horizontal polarization of the ASE, it is necessary to tilt the filters *vertically*, rather than horizontally to maintain the narrowest transmission feature.

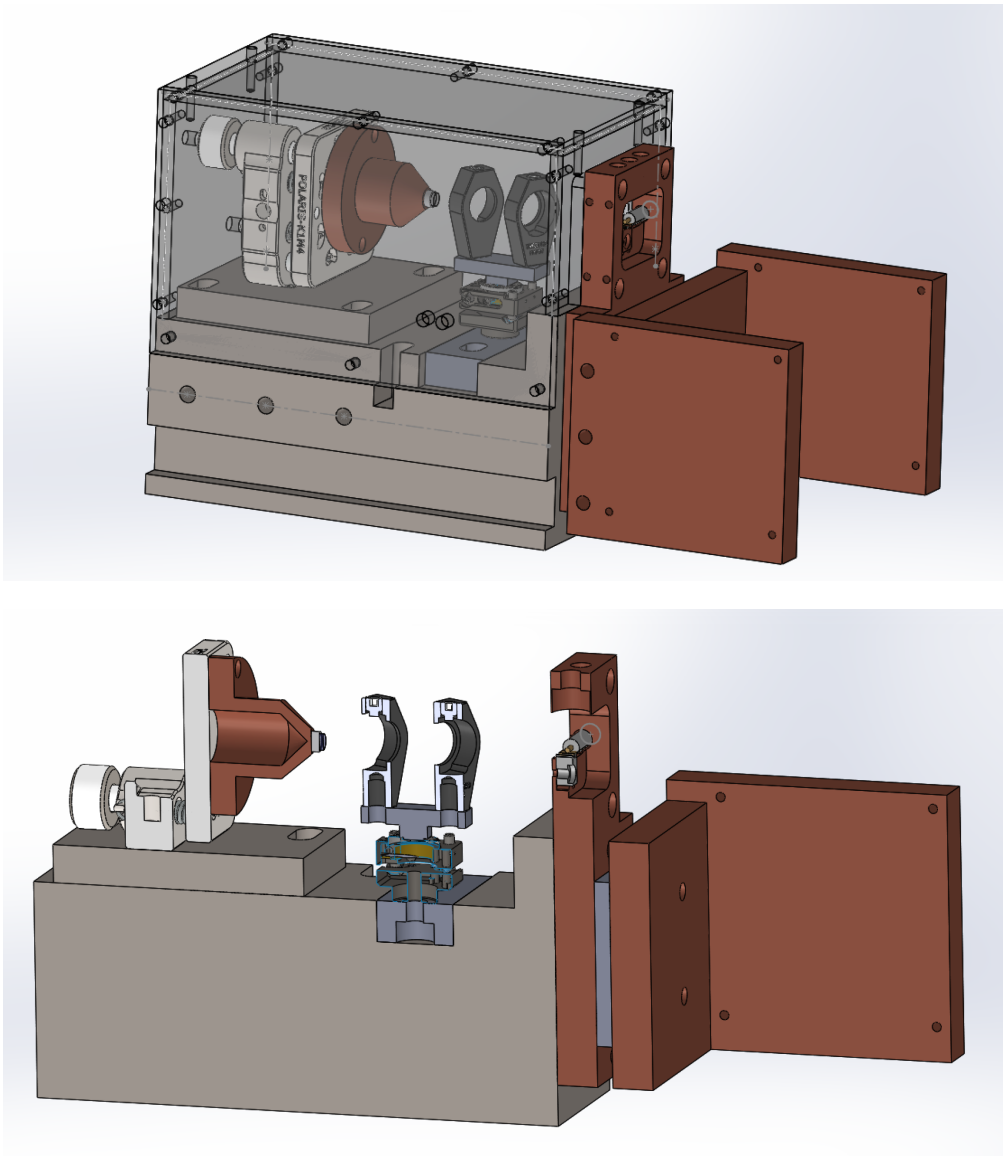

Figure E.1: **Tapered Laser Design.** The full Solidworks assembly **(a)** and its section **(b)** for the tapered laser is shown. The upright copper structure holds the c-mount packaged TPA, with output to the right. The chip and copper sandwich indium foil for good thermal contact. An SMA antenna provides the laser diode current. The upright copper structure is attached to the Invar laser cavity base, and is temperature stabilized by a 75 W Peltier module, which is backed by an additional copper structure that mounts two large copper heatsinks (Aavid 342946 not shown). The Invar base mounts two intracavity filters on a rotation stage as well as the retroreflector assembly, which consists of the mirror, piezo, copper mount (internal cavity filled with lead) and kinematic stage.

- After initial construction, the laser frequently mode hopped due to vibrations, both through the optical breadboard and the air. Enclosure in a box improved performance, but not enough. Performance was greatly improved by significantly shortening the laser cavity by inserting a stainless steel block between the copper mount and the kinematic mount. Halving the laser cavity length doubled the free spectral range, making the total feedback profile more selectively pick a single longitudinal mode. The steel block also served to better isolate the piezo-mirror system from mount resonances as described above.

Ultimately, we built a laser that output 1 W and which could be narrowed to somewhat less than 1 MHz, using both slow (piezo voltage) and fast (diode current) feedback based on a Pound-Drever-Hall error signal from the stable reference cavity (Finesse 200 at this wavelength). This represented a linewidth reduction from the free running laser, but was still significantly limited by the fast feedback bandwidth of 100 kHz, set by the modulation bandwidth of our Newport (Model 560B) laser diode current source. Our typical method of improving fast feedback bandwidth would be to modulate the laser current directly using a home-built MOSFET-based circuit. However, because of the high, 6 A laser current, this circuit needed to be redesigned and water cooled in order to function.

Finally, we discovered that the remaining mode hops of the laser were not just longitudinal modes but also transverse modes, looking like a transverse displacement of the output beam by a couple waists. At this point, we decided to stop pushing on this laser, as we had other options for accomplishing the same goal. We now assemble a list of design considerations for future laser building projects.

- Fundamentally, combining the laser source with the amplification is not a particularly useful thing to do. Building our own free-space TA system would be comparatively easy, and would enable using our standard low noise, high modulation bandwidth laser

diode current source system. Ideally, moving forward, we would purchase a Toptica DLpro at the desired wavelength since that laser is very stable and nice to work with. Engineering the ECDL to be easy to work with and stable is the hardest and most valuable part of the laser system. We can then build the rest of the laser system ourselves to save money.

- If we wished to improve the tapered laser design, the first thing to do would be to have a shorter cavity and more selective intracavity filter. A promising direction for this is reflective volume Bragg gratings. These filters can be several orders of magnitude narrower than the transmissive filters used in this laser.

- Special care should be taken to ensure that the collimating aspheres are well aligned. Perhaps we should even switch to objectives. Laser instability was made worse by poor feedback efficiency. Certainly, the 50% one-way efficiency of the intracavity filters should improved, but poor spatial overlap between the retroreflected ASE and the chip waveguide due to incorrect lens position could be significantly more limiting.

REFERENCES

[1] Doyle, M. *Beautiful Lego* (No Starch Press, 2013).

[2] Anderson, P. W. More is different. *Science* **177**, 393–396 (1972).

[3] Landau, L. D. On the theory of phase transitions. In ter Harr, D. (ed.) *English Translation: Collected Papers of Landau, L.D.* (Pergamon Press, 1965).

[4] Landau, L. & Lifshitz, E. Statistical Physics (Course of Theoretical Physics vol 5) (1958).

[5] Kadanoff, L. P. More is the same; phase transitions and mean field theories. *Journal of Statistical Physics* **137**, 777 (2009).

[6] Senthil, T. Quantum matters: Physics beyond Landau's paradigms. *International Journal of Modern Physics B* **20**, 2603–2611 (2006).

[7] Eisenstein, J. & Stormer, H. The fractional quantum Hall effect. *Science* **248**, 1510–1516 (1990).

[8] The Nobel prize in physics 1998. *NobelPrize.org* (1998). URL `https://www.nobelprize.org/prizes/physics/1998/press-release/`.

[9] Klitzing, K. v., Dorda, G. & Pepper, M. New method for high-accuracy determination of the fine-structure constant based on quantized Hall resistance. *Physical Review Letters* **45**, 494–497 (1980).

[10] Tsui, D. C., Stormer, H. L. & Gossard, A. C. Two-dimensional magnetotransport in the extreme quantum limit. *Physical Review Letters* **48**, 1559–1562 (1982).

[11] Thouless, D. J., Kohmoto, M., Nightingale, M. P. & den Nijs, M. Quantized Hall Conductance in a Two-Dimensional Periodic Potential. *Physical Review Letters* **49**, 405–408 (1982).

[12] Hatsugai, Y. Chern number and edge states in the integer quantum Hall effect. *Physical Review Letters* **71**, 3697–3700 (1993).

[13] Chen, X., Gu, Z.-C. & Wen, X.-G. Local unitary transformation, long-range quantum entanglement, wave function renormalization, and topological order. *Physical Review B* **82**, 155138 (2010).

[14] Nayak, C., Simon, S. H., Stern, A., Freedman, M. & Das Sarma, S. Non-Abelian anyons and topological quantum computation. *Reviews of Modern Physics* **80**, 1083–1159 (2008).

[15] Laughlin, R. B. Anomalous quantum Hall effect: an incompressible quantum fluid with fractionally charged excitations. *Physical Review Letters* **50**, 1395 (1983).

[16] Jain, J. K. Composite-fermion approach for the fractional quantum Hall effect. *Physical Review Letters* **63**, 199 (1989).

[17] Goldman, V. & Su, B. Resonant tunneling in the quantum Hall regime: measurement of fractional charge. *Science* **267**, 1010–1012 (1995).

[18] Saminadayar, L., Glattli, D., Jin, Y. & Etienne, B. c.-m. Observation of the e/3 fractionally charged Laughlin quasiparticle. *Physical Review Letters* **79**, 2526 (1997).

[19] De-Picciotto, R., Reznikov, M., Heiblum, M., Umansky, V., Bunin, G. & Mahalu, D. Direct observation of a fractional charge. *Physica B: Condensed Matter* **249**, 395–400 (1998).

[20] Reznikov, M., De Picciotto, R., Griffiths, T., Heiblum, M. & Umansky, V. Observation of quasiparticles with one-fifth of an electron's charge. *Nature* **399**, 238 (1999).

[21] Camino, F., Zhou, W. & Goldman, V. Realization of a Laughlin quasiparticle interferometer: Observation of fractional statistics. *Physical Review B* **72**, 075342 (2005).

[22] Dolev, M., Heiblum, M., Umansky, V., Stern, A. & Mahalu, D. Observation of a quarter of an electron charge at the ν= 5/2 quantum Hall state. *Nature* **452**, 829 (2008).

[23] Willett, R. L., Pfeiffer, L. N. & West, K. Measurement of filling factor 5/2 quasiparticle interference with observation of charge e/4 and e/2 period oscillations. *Proceedings of the National Academy of Sciences* **106**, 8853–8858 (2009).

[24] An, S., Jiang, P., Choi, H., Kang, W., Simon, S., Pfeiffer, L., West, K. & Baldwin, K. Braiding of Abelian and non-Abelian anyons in the fractional quantum Hall effect. *arXiv preprint arXiv:1112.3400* (2011).

[25] Spanton, E. M., Zibrov, A. A., Zhou, H., Taniguchi, T., Watanabe, K., Zaletel, M. P. & Young, A. F. Observation of fractional Chern insulators in a van der Waals heterostructure. *Science* **360**, 62–66 (2018).

[26] Yoshioka, D. *The quantum Hall effect*, vol. 133 (Springer Science & Business Media, 2013).

[27] Leinaas, J. M. & Myrheim, J. On the theory of identical particles. *Il Nuovo Cimento B (1971-1996)* **37**, 1–23 (1977).

[28] Wilczek, F. Quantum mechanics of fractional-spin particles. *Physical Review Letters* **49**, 957 (1982).

[29] Haldane, F. D. M. Fractional quantization of the Hall effect: a hierarchy of incompressible quantum fluid states. *Physical Review Letters* **51**, 605 (1983).

[30] Willett, R., Eisenstein, J., Störmer, H., Tsui, D., Gossard, A. & English, J. Observation of an even-denominator quantum number in the fractional quantum Hall effect. *Physical Review Letters* **59**, 1776 (1987).

[31] Moore, G. & Read, N. Nonabelions in the fractional quantum Hall effect. *Nuclear Physics B* **360**, 362–396 (1991).

[32] Read, N. & Rezayi, E. Beyond paired quantum Hall states: Parafermions and incompressible states in the first excited Landau level. *Physical Review B* **59**, 8084 (1999).

[33] Rezayi, E. & Read, N. Non-Abelian quantized Hall states of electrons at filling factors 12/5 and 13/5 in the first excited Landau level. *Physical Review B* **79**, 075306 (2009).

[34] Haldane, F. D. M. Model for a quantum Hall effect without Landau levels: Condensed-matter realization of the" parity anomaly". *Physical Review Letters* **61**, 2015 (1988).

[35] Kalmeyer, V. & Laughlin, R. Theory of the spin liquid state of the Heisenberg antiferromagnet. *Physical Review B* **39**, 11879 (1989).

[36] Yang, K., Warman, L. & Girvin, S. Possible spin-liquid states on the triangular and kagomé lattices. *Physical Review Letters* **70**, 2641 (1993).

[37] Kitaev, A. Fault-tolerant quantum computation by anyons. *Annals of Physics* **303**, 2–30 (2003).

[38] Levin, M. A. & Wen, X.-G. String-net condensation: A physical mechanism for topological phases. *Physical Review B* **71**, 045110 (2005).

[39] Karzig, T., Knapp, C., Lutchyn, R. M., Bonderson, P., Hastings, M. B., Nayak, C., Alicea, J., Flensberg, K., Plugge, S., Oreg, Y. *et al.* Scalable designs for quasiparticle-poisoning-protected topological quantum computation with Majorana zero modes. *Physical Review B* **95**, 235305 (2017).

[40] Kane, C. L. & Mele, E. J. Z 2 topological order and the quantum spin Hall effect. *Physical Review Letters* **95**, 146802 (2005).

[41] Fu, L., Kane, C. L. & Mele, E. J. Topological insulators in three dimensions. *Physical Review Letters* **98**, 106803 (2007).

[42] Moore, J. E. The birth of topological insulators. *Nature* **464**, 194–198 (2010).

[43] Hasan, M. Z. & Kane, C. L. Colloquium: Topological insulators. *Reviews of Modern Physics* **82**, 3045–3067 (2010).

[44] Fu, L. Topological crystalline insulators. *Physical Review Letters* **106**, 106802 (2011).

[45] Gu, Z.-C. & Wen, X.-G. Tensor-entanglement-filtering renormalization approach and symmetry-protected topological order. *Physical Review B* **80**, 155131 (2009).

[46] Armitage, N., Mele, E. & Vishwanath, A. Weyl and Dirac semimetals in three-dimensional solids. *Reviews of Modern Physics* **90**, 015001 (2018).

[47] Sato, M. & Ando, Y. Topological superconductors: a review. *Reports on Progress in Physics* **80**, 076501 (2017).

[48] Kosterlitz, J. M. & Thouless, D. J. Ordering, metastability and phase transitions in two-dimensional systems. *Journal of Physics C: Solid State Physics* **6**, 1181 (1973).

[49] Kosterlitz, J. The critical properties of the two-dimensional xy model. *Journal of Physics C: Solid State Physics* **7**, 1046 (1974).

[50] Su, W., Schrieffer, J. & Heeger, A. J. Solitons in polyacetylene. *Physical Review Letters* **42**, 1698 (1979).

[51] Rice, M. J. Charged π-phase kinks in lightly doped polyacetylene. *Physics Letters A* **71**, 152–154 (1979).

[52] Barkeshli, M. & Wen, X.-G. Bilayer quantum Hall phase transitions and the orbifold non-abelian fractional quantum Hall states. *Physical Review B* **84**, 115121 (2011).

[53] Maher, P., Wang, L., Gao, Y., Forsythe, C., Taniguchi, T., Watanabe, K., Abanin, D., Papić, Z., Cadden-Zimansky, P., Hone, J. *et al.* Tunable fractional quantum Hall phases in bilayer graphene. *Science* **345**, 61–64 (2014).

[54] Dean, C. R., Wang, L., Maher, P., Forsythe, C., Ghahari, F., Gao, Y., Katoch, J., Ishigami, M., Moon, P., Koshino, M. *et al.* Hofstadter's butterfly and the fractal quantum Hall effect in moiré superlattices. *Nature* **497**, 598 (2013).

[55] Bloch, I., Dalibard, J. & Zwerger, W. Many-body physics with ultracold gases. *Reviews of modern physics* **80**, 885 (2008).

[56] Keimer, B., Kivelson, S. A., Norman, M. R., Uchida, S. & Zaanen, J. From quantum matter to high-temperature superconductivity in copper oxides. *Nature* **518**, 179 (2015).

[57] Cao, Y., Fatemi, V., Fang, S., Watanabe, K., Taniguchi, T., Kaxiras, E. & Jarillo-Herrero, P. Unconventional superconductivity in magic-angle graphene superlattices. *Nature* **556**, 43 (2018).

[58] Boll, M., Hilker, T. A., Salomon, G., Omran, A., Nespolo, J., Pollet, L., Bloch, I. & Gross, C. Spin- and density-resolved microscopy of antiferromagnetic correlations in Fermi-Hubbard chains. *Science* **353**, 1257–1260 (2016).

[59] Chiu, C. S., Ji, G., Bohrdt, A., Xu, M., Knap, M., Demler, E., Grusdt, F., Greiner, M. & Greif, D. String patterns in the doped Hubbard model. *Science* **365**, 251 (2019).

[60] Brown, P. T., Mitra, D., Guardado-Sanchez, E., Nourafkan, R., Reymbaut, A., Hébert, C.-D., Bergeron, S., Tremblay, A.-M. S., Kokalj, J., Huse, D. A., Schauß, P. & Bakr, W. S. Bad metallic transport in a cold atom Fermi-Hubbard system. *Science* **363**, 379–382 (2019).

[61] Cooper, N. R. Rapidly rotating atomic gases. *Advances in Physics* **57**, 539–616 (2008).

[62] Fetter, A. L. Rotating trapped Bose-Einstein condensates. *Reviews of Modern Physics* **81**, 647–691 (2009).

[63] Schweikhard, V., Coddington, I., Engels, P., Mogendorff, V. P. & Cornell, E. A. Rapidly rotating Bose-Einstein condensates in and near the lowest Landau level. *Physical Review Letters* **92**, 040404 (2004).

[64] Goldman, J. C. B., Nathan & Zoller, P. Topological quantum matter with ultracold gases in optical lattices. *Nature Physics* 639 (2016).

[65] Gemelke, N., Sarajlic, E. & Chu, S. Rotating few-body atomic systems in the fractional quantum Hall regime. *arXiv preprint arXiv:1007.2677* (2010).

[66] Tai, E., Lukin, A., Rispoli, M., Schittko, R., Menke, T., Borgnia, D., Preiss, P., Grusdt, F., Kaufman, A. & Greiner, M. Microscopy of the interacting Harper–Hofstadter model in the two-body limit. *Nature* 519–523.

[67] Ozawa, T., Price, H. M., Amo, A., Goldman, N., Hafezi, M., Lu, L., Rechtsman, M. C., Schuster, D., Simon, J., Zilberberg, O. *et al.* Topological photonics. *Reviews of Modern Physics* **91**, 015006 (2019).

[68] Kasprzak, J., Richard, M., Kundermann, S., Baas, A., Jeambrun, P., Keeling, J., Marchetti, F., Szymańska, M., André, R., Staehli, J. *et al.* Bose–Einstein condensation of exciton polaritons. *Nature* **443**, 409 (2006).

[69] Balili, R., Hartwell, V., Snoke, D., Pfeiffer, L. & West, K. Bose-Einstein condensation of microcavity polaritons in a trap. *Science* **316**, 1007–1010 (2007).

[70] Winger, M., Badolato, A., Hennessy, K. J., Hu, E. L. & Imamoğlu, A. Quantum dot spectroscopy using cavity quantum electrodynamics. *Physical Review Letters* **101**, 226808 (2008).

[71] Smolka, S., Wuester, W., Haupt, F., Faelt, S., Wegscheider, W. & Imamoglu, A. Cavity quantum electrodynamics with many-body states of a two-dimensional electron gas. *Science* **346**, 332–335 (2014).

[72] Byrnes, T., Kim, N. Y. & Yamamoto, Y. Exciton-polariton condensates. *Nature Physics* **10**, 803–813 (2014).

[73] Klaers, J., Schmitt, J., Vewinger, F. & Weitz, M. Bose-Einstein condensation of photons in an optical microcavity. *Nature* **468**, 545–548 (2010).

[74] Carusotto, I. & Ciuti, C. Quantum fluids of light. *Reviews of Modern Physics* **85**, 299 (2013).

[75] Delteil, A., Fink, T., Schade, A., Höfling, S., Schneider, C. & İmamoğlu, A. Towards polariton blockade of confined exciton–polaritons. *Nature Materials* **18**, 219 (2019).

[76] Muñoz-Matutano, G., Wood, A., Johnsson, M., Vidal, X., Baragiola, B. Q., Reinhard, A., Lemaître, A., Bloch, J., Amo, A., Nogues, G., Besga, B., Richard, M. & Volz, T. Emergence of quantum correlations from interacting fibre-cavity polaritons. *Nature Materials* **18**, 213 (2019).

[77] Schuster, D. I. *Circuit quantum electrodynamics* (Yale University, 2007).

[78] Devoret, M. H. & Schoelkopf, R. J. Superconducting circuits for quantum information: an outlook. *Science* **339**, 1169–1174 (2013).

[79] Wendin, G. Quantum information processing with superconducting circuits: a review. *Reports on Progress in Physics* **80**, 106001 (2017).

[80] Roushan, P. *et al.* Observation of topological transitions in interacting quantum circuits. *Nature* 241–244.

[81] Owens, C., LaChapelle, A., Saxberg, B., Anderson, B. M., Ma, R., Simon, J. & Schuster, D. I. Quarter-flux Hofstadter lattice in a qubit-compatible microwave cavity array. *Physical Review A* **97**, 013818 (2018).

[82] Houck, A. A., Tureci, H. E. & Koch, J. On-chip quantum simulation with superconducting circuits. *Nature Physics* 292–299.

[83] Ma, R., Saxberg, B., Owens, C., Leung, N., Lu, Y., Simon, J. & Schuster, D. I. A dissipatively stabilized Mott insulator of photons. *Nature* **566**, 51 (2019).

[84] Birnbaum, K. M., Boca, A., Miller, R., Boozer, A. D., Northup, T. E. & Kimble, H. J. Photon blockade in an optical cavity with one trapped atom. *Nature* **436**, 87 (2005).

[85] Peyronel, T., Firstenberg, O., Liang, Q.-Y., Hofferberth, S., Gorshkov, A. V., Pohl, T., Lukin, M. D. & Vuletić, V. Quantum nonlinear optics with single photons enabled by strongly interacting atoms. *Nature* **488**, 57–60 (2012).

[86] Duan, L., Lukin, M. D., Cirac, J. I. & Zoller, P. Long-distance quantum communication with atomic ensembles and linear optics. *Nature* **414**, 413–418 (2001).

[87] Han, Y., He, B., Heshami, K., Li, C.-Z. & Simon, C. Quantum repeaters based on Rydberg-blockade-coupled atomic ensembles. *Physical Review A* **81**, 052311 (2010).

[88] Zhao, B., Müller, M., Hammerer, K. & Zoller, P. Efficient quantum repeater based on deterministic Rydberg gates. *Physical Review A* **81**, 052329 (2010).

[89] Brion, E., Carlier, F., Akulin, V. & Mølmer, K. Quantum repeater with Rydberg-blocked atomic ensembles in fiber-coupled cavities. *Physical Review A* **85**, 042324 (2012).

[90] Azuma, K., Tamaki, K. & Lo, H.-K. All-photonic quantum repeaters. *Nature Communications* **6**, 6787 (2015).

[91] Zwerger, M., Pirker, A., Dunjko, V., Briegel, H. J. & Dür, W. Long-range big quantum-data transmission. *Physical Review Letters* **120**, 030503 (2018).

[92] Li, Z.-D., Zhang, R., Yin, X.-F., Liu, L.-Z., Hu, Y., Fang, Y.-Q., Fei, Y.-Y., Jiang, X., Zhang, J., Li, L. *et al.* Experimental quantum repeater without quantum memory. *Nature Photonics* 1 (2019).

[93] Chang, D. E., Sørensen, A. S., Demler, E. A. & Lukin, M. D. A single-photon transistor using nanoscale surface plasmons. *Nature Physics* **3**, 807 (2007).

[94] Chen, W., Beck, K. M., Bücker, R., Gullans, M., Lukin, M. D., Tanji-Suzuki, H. & Vuletić, V. All-optical switch and transistor gated by one stored photon. *Science* **341**, 768–770 (2013).

[95] Gorniaczyk, H., Tresp, C., Schmidt, J., Fedder, H. & Hofferberth, S. Single-photon transistor mediated by interstate Rydberg interactions. *Physical Review Letters* **113**, 053601 (2014).

[96] Tiarks, D., Baur, S., Schneider, K., Dürr, S. & Rempe, G. Single-photon transistor using a Förster resonance. *Physical Review Letters* **113**, 053602 (2014).

[97] Lukin, M., Fleischhauer, M., Cote, R., Duan, L., Jaksch, D., Cirac, J. & Zoller, P. Dipole blockade and quantum information processing in mesoscopic atomic ensembles. *Physical Review Letters* **87**, 037901 (2001).

[98] Petrosyan, D. & Fleischhauer, M. Quantum information processing with single photons and atomic ensembles in microwave coplanar waveguide resonators. *Physical Review Letters* **100**, 170501 (2008).

[99] Saffman, M., Walker, T. G. & Mølmer, K. Quantum information with Rydberg atoms. *Reviews of Modern Physics* **82**, 2313–2363 (2010).

[100] Gorshkov, A. V., Otterbach, J., Fleischhauer, M., Pohl, T. & Lukin, M. D. Photon-photon interactions via Rydberg blockade. *Physical Review Letters* **107**, 133602 (2011).

[101] Shahmoon, E., Kurizki, G., Fleischhauer, M. & Petrosyan, D. Strongly interacting photons in hollow-core waveguides. *Physical Review A* **83**, 033806 (2011).

[102] Maxwell, D., Szwer, D., Paredes-Barato, D., Busche, H., Pritchard, J. D., Gauguet, A., Weatherill, K. J., Jones, M. & Adams, C. S. Storage and control of optical photons using Rydberg polaritons. *Physical Review Letters* **110**, 103001 (2013).

[103] Paredes-Barato, D. & Adams, C. All-optical quantum information processing using Rydberg gates. *Physical Review Letters* **112**, 040501 (2014).

[104] Schwarzkopf, A., Sapiro, R. & Raithel, G. Imaging spatial correlations of Rydberg excitations in cold atom clouds. *Physical Review Letters* **107**, 103001 (2011).

[105] Günter, G., Schempp, H., Robert-de Saint-Vincent, M., Gavryusev, V., Helmrich, S., Hofmann, C., Whitlock, S. & Weidemüller, M. Observing the dynamics of dipole-mediated energy transport by interaction-enhanced imaging. *Science* **342**, 954–956 (2013).

[106] Kuhn, A., Hennrich, M. & Rempe, G. Deterministic single-photon source for distributed quantum networking. *Physical Review Letters* **89**, 067901 (2002).

[107] Greentree, A. D., Tahan, C., Cole, J. H. & Hollenberg, L. C. Quantum phase transitions of light. *Nature Physics* **2**, 856 (2006).

[108] Angelakis, D. G., Santos, M. F. & Bose, S. Photon-blockade-induced Mott transitions and XY spin models in coupled cavity arrays. *Physical Review A* **76**, 031805 (2007).

[109] Chang, D. E., Gritsev, V., Morigi, G., Vuletic, V., Lukin, M. D. & Demler, E. A. Crystallization of strongly interacting photons in a nonlinear optical fibre. *Nature Physics* **4**, 884–889 (2008).

[110] Cho, J., Angelakis, D. G. & Bose, S. Fractional quantum Hall state in coupled cavities. *Physical Review Letters* **101**, 246809 (2008).

[111] Gerace, D., Türeci, H. E., Imamoglu, A., Giovannetti, V. & Fazio, R. The quantum-optical Josephson interferometer. *Nature Physics* **5**, 281 (2009).

[112] Weimer, H., Müller, M., Lesanovsky, I., Zoller, P. & Büchler, H. P. A Rydberg quantum simulator. *Nature Physics* **6**, 382 (2010).

[113] Nunnenkamp, A., Koch, J. & Girvin, S. Synthetic gauge fields and homodyne transmission in Jaynes–Cummings lattices. *New Journal of Physics* **13**, 095008 (2011).

[114] Zhang, X.-F., Sun, Q., Wen, Y.-C., Liu, W.-M., Eggert, S., Ji, A.-C. *et al.* Rydberg polaritons in a cavity: A superradiant solid. *Physical Review Letters* **110**, 090402 (2013).

[115] Otterbach, J., Moos, M., Muth, D. & Fleischhauer, M. Wigner crystallization of single photons in cold Rydberg ensembles. *Physical Review Letters* **111**, 113001 (2013).

[116] Sommer, A., Büchler, H. P. & Simon, J. Quantum crystals and Laughlin droplets of cavity Rydberg polaritons. *arXiv preprint arXiv:1506.00341* (2015).

[117] Hartmann, M. J., Brandao, F. G. & Plenio, M. B. Strongly interacting polaritons in coupled arrays of cavities. *Nature Physics* **2**, 849–855 (2006).

[118] Hayward, A. L., Martin, A. M. & Greentree, A. D. Fractional quantum hall physics in Jaynes-Cummings-Hubbard lattices. *Physical Review Letters* **108**, 223602 (2012).

[119] Umucalılar, R. O., Wouters, M. & Carusotto, I. Probing few-particle Laughlin states of photons via correlation measurements. *Physical Review A* **89**, 023803 (2014).

[120] Karzig, T., Bardyn, C.-E., Lindner, N. H. & Refael, G. Topological Polaritons. *Physical Review X* **5**, 031001 (2015).

[121] Clark, L. W., Schine, N., Baum, C., Jia, N. & Simon, J. Observation of Laughlin states made of light. *arXiv preprint arXiv:1907.05872* (2019).

[122] Walker, T. G. & Saffman, M. Consequences of Zeeman degeneracy for the van der Waals blockade between Rydberg atoms. *Physical Review A* **77**, 032723 (2008).

[123] Tanasittikosol, M., Pritchard, J., Maxwell, D., Gauguet, A., Weatherill, K., Potvliege, R. & Adams, C. Microwave dressing of Rydberg dark states. *Journal of Physics B: Atomic, Molecular and Optical Physics* **44**, 184020 (2011).

[124] Aad, G., Abbott, B., Abbott, D. C. *et al.* Observation of light-by-light scattering in ultraperipheral Pb + Pb collisions with the ATLAS detector. *Physical Review Letters* **123**, 052001 (2019).

[125] Scully, M. & Zubairy, M. *Quantum Optics* (Cambridge University Press).

[126] Tanji-Suzuki, H., Leroux, I. D., Schleier-Smith, M. H., Cetina, M., Grier, A. T., Simon, J. & Vuletić, V. Interaction between atomic ensembles and optical resonators: Classical description. In *Advances in atomic, molecular, and optical physics*, vol. 60, 201–237 (Elsevier, 2011).

[127] Kockum, A. F., Miranowicz, A., De Liberato, S., Savasta, S. & Nori, F. Ultrastrong coupling between light and matter. *Nature Reviews Physics* **1**, 19 (2019).

[128] Forn-Díaz, P., Lamata, L., Rico, E., Kono, J. & Solano, E. Ultrastrong coupling regimes of light-matter interaction. *Reviews of Modern Physics* **91**, 025005 (2019).

[129] Jaynes, E. T. & Cummings, F. W. Comparison of quantum and semiclassical radiation theories with application to the beam maser. *Proceedings of the IEEE* **51**, 89–109 (1963).

[130] Shore, B. W. & Knight, P. L. The Jaynes-Cummings model. *Journal of Modern Optics* **40**, 1195–1238 (1993).

[131] Tavis, M. & Cummings, F. W. Exact solution for an N-molecule—radiation-field Hamiltonian. *Physical Review* **170**, 379 (1968).

[132] Brune, M., Schmidt-Kaler, F., Maali, A., Dreyer, J., Hagley, E., Raimond, J. & Haroche, S. Quantum Rabi oscillation: A direct test of field quantization in a cavity. *Physical Review Letters* **76**, 1800 (1996).

[133] Kimble, H. J. The quantum internet. *Nature* **453**, 1023 (2008).

[134] Schuster, I., Kubanek, A., Fuhrmanek, A., Puppe, T., Pinkse, P. W., Murr, K. & Rempe, G. Nonlinear spectroscopy of photons bound to one atom. *Nature Physics* **4**, 382 (2008).

[135] Tanji-Suzuki, Haruka, Chen, W., Landig, R., Simon, J. & Vuletic, V. Vacuum-Induced Transparency. *Science* **333**, 1266–1269 (2011).

[136] Schuster, D., Houck, A. A., Schreier, J., Wallraff, A., Gambetta, J., Blais, A., Frunzio, L., Majer, J., Johnson, B., Devoret, M. *et al.* Resolving photon number states in a superconducting circuit. *Nature* **445**, 515 (2007).

[137] Fink, J., Göppl, M., Baur, M., Bianchetti, R., Leek, P., Blais, A. & Wallraff, A. Climbing the Jaynes–Cummings ladder and observing its nonlinearity in a cavity QED system. *Nature* **454**, 315 (2008).

[138] Salathé, Y., Mondal, M., Oppliger, M., Heinsoo, J., Kurpiers, P., Potočnik, A., Mezzacapo, A., Las Heras, U., Lamata, L., Solano, E. *et al.* Digital quantum simulation of spin models with circuit quantum electrodynamics. *Physical Review X* **5**, 021027 (2015).

[139] Barends, R., Lamata, L., Kelly, J., García-Álvarez, L., Fowler, A., Megrant, A., Jeffrey, E., White, T., Sank, D., Mutus, J. *et al.* Digital quantum simulation of fermionic models with a superconducting circuit. *Nature Communications* **6**, 7654 (2015).

[140] O'Malley, P. J., Babbush, R., Kivlichan, I. D., Romero, J., McClean, J. R., Barends, R., Kelly, J., Roushan, P., Tranter, A., Ding, N. *et al.* Scalable quantum simulation of molecular energies. *Physical Review X* **6**, 031007 (2016).

[141] Kandala, A., Mezzacapo, A., Temme, K., Takita, M., Brink, M., Chow, J. M. & Gambetta, J. M. Hardware-efficient variational quantum eigensolver for small molecules and quantum magnets. *Nature* **549**, 242 (2017).

[142] Santori, C., Fattal, D., Vuckovic, J., Solomon, G. S. & Yamamoto, Y. Indistinguishable photons from a single-photon device. *Nature* **419**, 594–597 (2002).

[143] Fushman, I., Englund, D., Faraon, A., Stoltz, N., Petroff, P. & Vučković, J. Controlled phase shifts with a single quantum dot. *science* **320**, 769–772 (2008).

[144] Kasprzak, J., Reitzenstein, S., Muljarov, E. A., Kistner, C., Schneider, C., Strauss, M., Höfling, S., Forchel, A. & Langbein, W. Up on the Jaynes–Cummings ladder of a quantum-dot/microcavity system. *Nature materials* **9**, 304 (2010).

[145] Volz, T., Reinhard, A., Winger, M., Badolato, A., Hennessy, K. J., Hu, E. L. & Imamoğlu, A. Ultrafast all-optical switching by single photons. *Nature Photonics* **6**, 605 (2012).

[146] Strekalov, D. V., Marquardt, C., Matsko, A. B., Schwefel, H. G. & Leuchs, G. Nonlinear and quantum optics with whispering gallery resonators. *Journal of Optics* **18**, 123002 (2016).

[147] Noh, C. & Angelakis, D. G. Quantum simulations and many-body physics with light. *Reports on Progress in Physics* **80**, 016401 (2016).

[148] Hartmann, M. J. Quantum simulation with interacting photons. *Journal of Optics* **18**, 104005 (2016).

[149] Dicke, R. H. Coherence in Spontaneous Radiation Processes. *Physical Review* **93**, 99 (1954).

[150] Parigi, V., Bimbard, E., Stanojevic, J., Hilliard, A. J., Nogrette, F., Tualle-Brouri, R., Ourjoumtsev, A. & Grangier, P. Observation and measurement of interaction-induced dispersive optical nonlinearities in an ensemble of cold Rydberg atoms. *Physical Review Letters* **109**, 233602 (2012).

[151] Maghrebi, M., Gullans, M., Bienias, P., Choi, S., Martin, I., Firstenberg, O., Lukin, M. D., Büchler, H. & Gorshkov, A. V. Coulomb bound states of strongly interacting photons. *Physical Review Letters* **115**, 123601 (2015).

[152] Bienias, P. Few-body quantum physics with strongly interacting Rydberg polaritons. *The European Physical Journal Special Topics* **225**, 2957–2976 (2016).

[153] Jia, N., Schine, N., Georgakopoulos, A., Ryou, A., Clark, L. W., Sommer, A. & Simon, J. A strongly interacting polaritonic quantum dot. *Nature Physics* **14**, 550–554 (2018). URL `https://doi.org/10.1038/s41567-018-0071-6`.

[154] Simon, J. *Cavity QED with atomic ensembles* (2010).

[155] Fleischhauer, M. & Lukin, M. D. Dark-state polaritons in electromagnetically induced transparency. *Physical Review Letters* **84**, 5094 (2000).

[156] Fleischhauer, M., Imamoglu, A. & Marangos, J. P. Electromagnetically induced transparency: Optics in coherent media. *Reviews of modern physics* **77**, 633 (2005).

[157] Mohapatra, A. K., Jackson, T. R. & Adams, C. S. Coherent optical detection of highly excited Rydberg states using electromagnetically induced transparency. *Physical Review Letters* **98**, 113003 (2007).

[158] Ningyuan, J., Georgakopoulos, A., Ryou, A., Schine, N., Sommer, A. & Simon, J. Observation and characterization of cavity Rydberg polaritons. *Physical Review A* **93**, 041802 (2016).

[159] Boddeda, R., Usmani, I., Bimbard, E., Grankin, A., Ourjoumtsev, A., Brion, E. & Grangier, P. Rydberg-induced optical nonlinearities from a cold atomic ensemble trapped inside a cavity. *Journal of Physics B: Atomic, Molecular and Optical Physics* **49**, 084005 (2016).

[160] Sheng, J., Chao, Y., Kumar, S., Fan, H., Sedlacek, J. & Shaffer, J. P. Intracavity Rydberg-atom electromagnetically induced transparency using a high-finesse optical cavity. *Physical Review A* **96**, 033813 (2017).

[161] Georgakopoulos, A., Sommer, A. & Simon, J. Theory of interacting cavity Rydberg polaritons. *Quantum Science and Technology* **4**, 014005 (2018).

[162] Grankin, A., Brion, E., Boddeda, R., Ćuk, S., Usmani, I., Ourjoumtsev, A. & Grangier, P. Inelastic photon scattering via the intracavity Rydberg blockade. *Physical Review Letters* **117**, 253602 (2016).

[163] Raimond, J., Vitrant, G. & Haroche, S. Spectral line broadening due to the interaction between very excited atoms: 'the dense Rydberg gas'. *Journal of Physics B: Atomic and Molecular Physics* **14**, L655 (1981).

[164] Urban, E., Johnson, T. A., Henage, T., Isenhower, L., Yavuz, D. D., Walker, T. G. & Saffman, M. Observation of Rydberg blockade between two atoms. *Nature Physics* **5**, 110 (2009).

[165] Gaetan, A., Miroshnychenko, Y., Wilk, T., Chotia, A., Viteau, M., Comparat, D., Pillet, P., Browaeys, A. & Grangier, P. Observation of collective excitation of two individual atoms in the Rydberg blockade regime. *Nature Physics* **5**, 115–118 (2009).

[166] Schauss, P., Cheneau, M., Endres, M., Fukuhara, T., Hild, S., Omran, A., Pohl, T., Gross, C., Kuhr, S. & Bloch, I. Observation of spatially ordered structures in a two-dimensional Rydberg gas. *Nature* **491**, 87–91 (2012).

[167] Dudin, Y. O. & Kuzmich, A. Strongly interacting Rydberg excitations of a cold atomic gas. *Science* **336**, 887–889 (2012).

[168] Beguin, L., Vernier, A., Chicireanu, R., Lahaye, T. & Browaeys, A. Direct measurement of the van der Waals interaction between two Rydberg atoms. *Physical Review Letters* **110**, 263201 (2013).

[169] Liang, Q.-Y., Venkatramani, A. V., Cantu, S. H., Nicholson, T. L., Gullans, M. J., Gorshkov, A. V., Thompson, J. D., Chin, C., Lukin, M. D. & Vuletić, V. Observation of three-photon bound states in a quantum nonlinear medium. *Science* **359**, 783–786 (2018).

[170] Li, L., Dudin, Y. & Kuzmich, A. Entanglement between light and an optical atomic excitation. *Nature* **498**, 466 (2013).

[171] Firstenberg, O., Adams, C. S. & Hofferberth, S. Nonlinear quantum optics mediated by Rydberg interactions. *Journal of Physics B: Atomic, Molecular and Optical Physics* **49**, 152003 (2016).

[172] Das, S., Grankin, A., Iakoupov, I., Brion, E., Borregaard, J., Boddeda, R., Usmani, I., Ourjoumtsev, A., Grangier, P. & Sørensen, A. S. Photonic controlled-phase gates through Rydberg blockade in optical cavities. *Physical Review A* **93**, 040303 (2016).

[173] Labuhn, H., Barredo, D., Ravets, S., De Léséleuc, S., Macrì, T., Lahaye, T. & Browaeys, A. Tunable two-dimensional arrays of single Rydberg atoms for realizing quantum Ising models. *Nature* **534**, 667 (2016).

[174] Li, L. & Kuzmich, A. Quantum memory with strong and controllable Rydberg-level interactions. *Nature Communications* **7**, 13618 (2016).

[175] Bernien, H., Schwartz, S., Keesling, A., Levine, H., Omran, A., Pichler, H., Choi, S., Zibrov, A. S., Endres, M., Greiner, M., Vuletić, V. & Lukin, M. D. Probing many-body dynamics on a 51-atom quantum simulator. *Nature* **551**, 579 (2017).

[176] Omran, A., Levine, H., Keesling, A., Semeghini, G., Wang, T. T., Ebadi, S., Bernien, H., Zibrov, A. S., Pichler, H., Choi, S. *et al.* Generation and manipulation of Schrödinger cat states in Rydberg atom arrays. *arXiv preprint arXiv:1905.05721* (2019).

[177] Keesling, A., Omran, A., Levine, H., Bernien, H., Pichler, H., Choi, S., Samajdar, R., Schwartz, S., Silvi, P., Sachdev, S., Zoller, P., Endres, M., Greiner, M., Vuletić, V. & Lukin, M. D. Quantum Kibble–Zurek mechanism and critical dynamics on a programmable Rydberg simulator. *Nature* **568**, 207 (2019).

[178] Beenakker, C. Theory of Coulomb-blockade oscillations in the conductance of a quantum dot. *Physical Review B* **44**, 1646 (1991).

[179] Leobandung, E., Guo, L., Wang, Y. & Chou, S. Y. Observation of quantum effects and Coulomb blockade in silicon quantum-dot transistors at temperatures over 100 K. *Applied physics letters* **67**, 938–940 (1995).

[180] Schoonveld, W., Wildeman, J., Fichou, D., Bobbert, P., Van Wees, B. & Klapwijk, T. Coulomb-blockade transport in single-crystal organic thin-film transistors. *Nature* **404**, 977 (2000).

[181] Sommer, A. & Simon, J. Engineering photonic Floquet Hamiltonians through Fabry–Pérot resonators. *New Journal of Physics* **18**, 035008 (2016).

[182] Schine, N., Ryou, A., Gromov, A., Sommer, A. & Simon, J. Synthetic Landau levels for photons. *Nature* **534**, 671–675 (2016). Letter.

[183] Barkeshli, M. & Qi, X.-L. Topological nematic states and non-abelian lattice dislocations. *Physical Review X* **2**, 031013 (2012).

[184] Jachymski, K., Bienias, P. & Büchler, H. P. Three-body interaction of Rydberg slow-light polaritons. *Physical Review Letters* **117**, 053601 (2016).

[185] Gullans, M., Diehl, S., Rittenhouse, S., Ruzic, B., D'Incao, J., Julienne, P., Gorshkov, A. & Taylor, J. Efimov states of strongly interacting photons. *Physical Review Letters* **119**, 233601 (2017).

[186] Roncaglia, M., Rizzi, M. & Cirac, J. I. Pfaffian state generation by strong three-body dissipation. *Physical Review Letters* **104**, 096803 (2010).

[187] Hafezi, M., Adhikari, P. & Taylor, J. Chemical potential for light by parametric coupling. *Physical Review B* **92**, 174305 (2015).

[188] Habraken, S. J. M. & Nienhuis, G. Modes of a twisted optical cavity. *Physical Review A* **75**, 033819 (2007).

[189] Berry, M. The geometric phase. *Scientific American* **259**, 46–55 (1988).

[190] Yuan, J., Long, X., Liang, L., Zhang, B., Wang, F. & Zhao, H. Nonplanar ring resonator modes: generalized Gaussian beams. *Applied Optics* **46**, 2980–2989 (2007).

[191] Kane, T. J. & Byer, R. L. Solid-state non-planar internally reflecting ring laser (1986). US Patent 4,578,793.

[192] Jia, N., Schine, N., Georgakopoulos, A., Ryou, A., Sommer, A. & Simon, J. Photons and polaritons in a broken-time-reversal nonplanar resonator. *Physical Review A* **97**, 013802 (2018).

[193] Siegman, A. E. Laser beams and resonators: beyond the 1960s. *IEEE Journal of selected topics in quantum electronics* **6**, 1389–1399 (2000).

[194] Chow, W., Gea-Banacloche, J., Pedrotti, L., Sanders, V., Schleich, W. & Scully, M. The ring laser gyro. *Reviews of Modern Physics* **57**, 61 (1985).

[195] Martin, G. J. Compact three-axis ring laser gyroscope (1998). US Patent 5,757,490.

[196] Noack, A., Bogan, C. & Willke, B. Higher-order Laguerre–Gauss modes in (non-) planar four-mirror cavities for future gravitational wave detectors. *Optics Letters* **42**, 751–754 (2017).

[197] Black, E. D. An introduction to Pound–Drever–Hall laser frequency stabilization. *American journal of physics* **69**, 79–87 (2001).

[198] Fox, R. W., Oates, C. W. & Hollberg, L. W. 1. Stabilizing diode lasers to high-finesse cavities. In *Experimental methods in the physical sciences*, vol. 40, 1–46 (Elsevier, 2003).

[199] Drever, R., Hall, J. L., Kowalski, F., Hough, J., Ford, G., Munley, A. & Ward, H. Laser phase and frequency stabilization using an optical resonator. *Applied Physics B* **31**, 97–105 (1983).

[200] Audoin, C. Frequency metrology. In *Metrology and fundamental costants* (1980).

[201] Bechhoefer, J. Feedback for physicists: A tutorial essay on control. *Reviews of Modern Physics* **77**, 783 (2005).

[202] Aström, K. J. & Murray, R. M. *Feedback systems: an introduction for scientists and engineers* (Princeton university press, 2010).

[203] Briles, T. C., Yost, D. C., Cingöz, A., Ye, J. & Schibli, T. R. Simple piezoelectric-actuated mirror with 180 kHz servo bandwidth. *Optics Express* **18**, 9739–9746 (2010).

[204] Poirson, J., Bretenaker, F., Vallet, M. & Le Floch, A. Analytical and experimental study of ringing effects in a Fabry–Perot cavity. Application to the measurement of high finesses. *JOSA B* **14**, 2811–2817 (1997).

[205] Zupancic, P., Preiss, P. M., Ma, R., Lukin, A., Tai, M. E., Rispoli, M., Islam, R. & Greiner, M. Ultra-precise holographic beam shaping for microscopic quantum control. *Optics Express* **24**, 13881–13893 (2016).

[206] Kerman, A. J., Vuletić, V., Chin, C. & Chu, S. Beyond optical molasses: 3D Raman sideband cooling of atomic cesium to high phase-space density. *Physical Review Letters* **84**, 439 (2000).

[207] Clark, L. W., Jia, N., Schine, N., Baum, C., Georgakopoulos, A. & Simon, J. Interacting Floquet polaritons. *Nature* (2019).

[208] Schine, N., Chalupnik, M., Can, T., Gromov, A. & Simon, J. Electromagnetic and gravitational responses of photonic Landau levels. *Nature* **565**, 173 (2019).

[209] High, A. A., Devlin, R. C., Dibos, A., Polking, M., Wild, D. S., Perczel, J., Leon, N. P. d., Lukin, M. D. & Park, H. Visible-frequency hyperbolic metasurface. *Nature* **522**, 192–196 (2015).

[210] Gopalakrishnan, S., Lev, B. L. & Goldbart, P. M. Emergent crystallinity and frustration with Bose–Einstein condensates in multimode cavities. *Nature Physics* **5**, 845–850 (2009).

[211] Baumann, K., Guerlin, C., Brennecke, F. & Esslinger, T. Dicke quantum phase transition with a superfluid gas in an optical cavity. *Nature* **464**, 1301–1306 (2010).

[212] Cooper, N. R. & Dalibard, J. Reaching Fractional Quantum Hall States with Optical Flux Lattices. *Physical Review Letters* **110**, 185301 (2013).

[213] Hafezi, M., Lukin, M. D. & Taylor, J. M. Non-equilibrium fractional quantum Hall state of light. *New Journal of Physics* 063001.

[214] Ningyuan, J., Owens, C., Sommer, A., Schuster, D. & Simon, J. Time-and site-resolved dynamics in a topological circuit. *Physical Review X* **5**, 021031 (2015).

[215] Otterbach, J., Ruseckas, J., Unanyan, R., Juzeliūnas, G. & Fleischhauer, M. Effective magnetic fields for stationary light. *Physical Review Letters* **104**, 033903 (2010).

[216] Wang, Z., Chong, Y., Joannopoulos, J. & Soljačić, M. Observation of unidirectional backscattering-immune topological electromagnetic states. *Nature* **461**, 772–775 (2009).

[217] Schneider, U., Hackermuller, L., Will, S., Best, T., Bloch, I., Costi, T. A., Helmes, R. W., Rasch, D. & Rosch, A. Metallic and insulating phases of repulsively interacting Fermions in a 3D optical lattice. *Science* **322**, 1520 –1525 (2008).

[218] Wen, X. G. & Zee, A. Shift and spin vector: New topological quantum numbers for the Hall fluids. *Physical Review Letters* **69**, 953–956 (1992).

[219] Hoyos, C. & Son, D. T. Hall Viscosity and Electromagnetic Response. *Physical Review Letters* **108**, 066805 (2012).

[220] Abanov, A. G. & Gromov, A. Electromagnetic and gravitational responses of two-dimensional noninteracting electrons in a background magnetic field. *Physical Review B* **90**, 014435 (2014).

[221] Can, T., Laskin, M. & Wiegmann, P. Fractional quantum Hall effect in a curved space: gravitational anomaly and electromagnetic response. *Physical Review Letters* **113**, 046803 (2014).

[222] Paredes, B., Fedichev, P., Cirac, J. I. & Zoller, P. 1/2 anyons in small atomic Bose-Einstein condensates. *Physical Review Letters* **87**, 010402 (2001).

[223] Umucalılar, R. & Carusotto, I. Many-body braiding phases in a rotating strongly correlated photon gas. *Physics Letters A* **377**, 2074–2078 (2013).

[224] Rechtsman, M. C., Zeuner, J. M., Plotnik, Y., Lumer, Y., Podolsky, D., Dreisow, F., Nolte, S., Segev, M. & Szameit, A. Photonic Floquet topological insulators. *Nature* **496**, 196–200 (2013).

[225] Hafezi, M., Mittal, S., Fan, J., Migdall, A. & Taylor, J. Imaging topological edge states in silicon photonics. *Nature Photonics* **7**, 1001–1005 (2013).

[226] Rechtsman, M. C., Zeuner, J. M., Tunnermann, A., Nolte, S., Segev, M. & Szameit, A. Strain-induced pseudomagnetic field and photonic Landau levels in dielectric structures. *Nat Photon* **7**, 153–158 (2013).

[227] Longhi, S. Synthetic gauge fields for light beams in optical resonators. *Optics Letters* **40**, 2941–2944 (2015).

[228] Chen, Y., Analytis, J. G., Chu, J.-H., Liu, Z., Mo, S.-K., Qi, X., Zhang, H., Lu, D., Dai, X., Fang, Z., Zhang, S., Fisher, I., Hussain, Z. & Z.-X., S. Experimental realization of a three-dimensional topological insulator, Bi2Te3. *Science* **325**, 178–181 (2009).

[229] Bradlyn, B., Elcoro, L., Cano, J., Vergniory, M., Wang, Z., Felser, C., Aroyo, M. & Bernevig, B. A. Topological quantum chemistry. *Nature* **547**, 298 (2017).

[230] Haldane, F. D. M. Nobel Lecture: Topological quantum matter. *Reviews of Modern Physics* **89**, 040502 (2017).

[231] Chiu, C.-K., Teo, J. C. Y., Schnyder, A. P. & Ryu, S. Classification of topological quantum matter with symmetries. *Reviews of Modern Physics* **88**, 035005 (2016).

[232] Avron, J. Odd viscosity. *Journal of statistical physics* **92**, 543–557 (1998).

[233] Avron, J. E., Seiler, R. & Zograf, P. G. Viscosity of quantum Hall fluids. *Physical Review Letters* **75**, 697–700 (1995).

[234] Klevtsov, S. & Wiegmann, P. Geometric adiabatic transport in quantum Hall states. *Physical Review Letters* **115**, 086801 (2015).

[235] Can, T., Chiu, Y., Laskin, M. & Wiegmann, P. Emergent conformal symmetry and geometric transport properties of quantum Hall states on singular surfaces. *Physical Review Letters* **117**, 266803 (2016).

[236] Niu, Q., Thouless, D. J. & Wu, Y.-S. Quantized Hall conductance as a topological invariant. *Physical Review B* **31**, 3372–3377 (1985).

[237] Jotzu, G., Messer, M., Desbuquois, R., Lebrat, M., Uehlinger, T., Greif, D. & Esslinger, T. Experimental realization of the topological Haldane model with ultracold fermions. *Nature* 237–240.

[238] Duca, L., Li, T., Reitter, M., Bloch, I., Schleier-Smith, M. & Schneider, U. An Aharonov-Bohm interferometer for determining Bloch band topology **347**, 288–292 (2015).

[239] Fläschner, N., Rem, B. S., Tarnowski, M., Vogel, D., Lühmann, D.-S., Sengstock, K. & Weitenberg, C. Experimental reconstruction of the Berry curvature in a Floquet Bloch band **352**, 1091–1094 (2016).

[240] Li, T., Duca, L., Reitter, M., Grusdt, F., Demler, E., Endres, M., Schleier-Smith, M., Bloch, I. & Schneider, U. Bloch state tomography using Wilson lines. *Science* **352**, 1094–1097 (2016).

[241] Aidelsburger, M., Lohse, M., Schweizer, C., Atala, M., Barreiro, J. T., Nascimbene, S., Cooper, N. R., Bloch, I. & Goldman, N. Measuring the Chern number of Hofstadter bands with ultracold bosonic atoms. *Nature Physics* **11**, 162–166 (2015).

[242] Thouless, D. J. Quantization of particle transport. *Physical Review B* **27**, 6083–6087 (1983).

[243] Nakajima, S., Tomita, T., Taie, S., Ichinose, T., Ozawa, H., Wang, L., Troyer, M. & Takahashi, Y. Topological Thouless pumping of ultracold fermions. *Nature Physics* **12**, 296–300 (2016).

[244] Lohse, M., Schweizer, C., Zilberberg, O., Aidelsburger, M. & Bloch, I. A Thouless quantum pump with ultracold bosonic atoms in an optical superlattice. *Nature Physics* **12**, 350–354 (2016).

[245] Tarnowski, M., Ünal, F. N., Fläschner, N., Rem, B. S., Eckardt, A., Sengstock, K. & Weitenberg, C. Measuring topology from dynamics by obtaining the Chern number from a linking number. *Nature Communications* **10**, 1728 (2019).

[246] Banerjee, M., Heiblum, M., Rosenblatt, A., Oreg, Y., Feldman, D. E., Stern, A. & Umansky, V. Observed quantization of anyonic heat flow. *Nature* **545**, 75–79 (2017).

[247] Mittal, S., Ganeshan, S., Fan, J., Vaezi, A. & Hafezi, M. Measurement of topological invariants in a 2D photonic system. *Nature Photonics* **10**, 180–183 (2016).

[248] Roushan, P., Neill, C., Megrant, A., Chen, Y., Babbush, R., Barends, R., Campbell, B., Chen, Z., Chiaro, B., Dunsworth, A. *et al.* Chiral ground-state currents of interacting photons in a synthetic magnetic field. *Nature Physics* **13**, 146–151 (2017).

[249] Stuhl, B., Lu, H.-I., Aycock, L., Genkina, D. & Spielman, I. Visualizing edge states with an atomic Bose gas in the quantum Hall regime. *Science* **349**, 1514–1518 (2015).

[250] Ma, R., Owens, C., LaChapelle, A., Schuster, D. I. & Simon, J. Hamiltonian tomography of photonic lattices. *Physical Review A* **95**, 062120 (2017).

[251] Lim, H.-T., Togan, E., Kroner, M., Miguel-Sanchez, J. & Imamoğlu, A. Electrically tunable artificial gauge potential for polaritons. *Nature Communications* **8**, 14540 (2017).

[252] Kitaev, A. Anyons in an exactly solved model and beyond. *Annals of Physics* **321**, 54–55 (2006).

[253] Bianco, R. & Resta, R. Mapping topological order in coordinate space. *Physical Review B* **84**, 241106 (2011).

[254] Caio, M. D., Möller, G., Cooper, N. R. & Bhaseen, M. Topological marker currents in Chern insulators. *Nature Physics* **15**, 257 (2019).

[255] Zaletel, M. P., Mong, R. S. & Pollmann, F. Topological characterization of fractional quantum Hall ground states from microscopic hamiltonians. *Physical Review Letters* **110**, 236801 (2013).

[256] Kane, C. & Fisher, M. Quantized thermal transport in the fractional quantum Hall effect. *Physical Review B* **55**, 15832–15837 (1997).

[257] Read, N. & Green, D. Paired states of fermions in two dimensions with breaking of parity and time-reversal symmetries and the fractional quantum Hall effect. *Physical Review B* **61**, 10267–10297 (2000).

[258] Gromov, A., Cho, G. Y., You, Y., Abanov, A. G. & Fradkin, E. Framing anomaly in the effective theory of the fractional quantum Hall effect. *Physical Review Letters* **114**, 016805 (2015).

[259] Mitchell, N., Nash, L., Hexner, D., Turner, A. & Irvine, W. Amorphous topological insulators constructed from random point sets. *Nature Physics* **14**, 380–385 (2018).

[260] Kohmoto, M. Topological invariant and the quantization of the Hall conductance. *Annals of Physics* **160**, 343–354.

[261] Brouder, C., Panati, G., Calandra, M., Mourougane, C. & Marzari, N. Exponential localization of Wannier functions in insulators. *Physical Review Letters* **98**, 046402 (2007).

[262] Wen, X. G. Chiral Luttinger liquid and the edge excitations in the fractional quantum Hall states. *Physical Review B* **41**, 12838–12844 (1990).

[263] Wen, X. G. & Zee, A. Shift and spin vector: New topological quantum numbers for the Hall fluids. *Physical Review Letters* **69**, 953–956 (1992).

[264] Klevtsov, S. Random normal matrices, Bergman kernel and projective embeddings. *Journal of High Energy Physics* **2014**, 133 (2014).

[265] Wu, Y.-H., Tu, H.-H. & Sreejith, G. J. Fractional quantum Hall states of bosons on cones. *Physical Review A* **96**, 033622 (2017).

[266] Klevtsov, S. Lowest Landau level on a cone and zeta determinants. *Journal of Physics A: Mathematical and Theoretical* **50**, 234003 (2017).

[267] Umucalılar, R. & Carusotto, I. Generation and spectroscopic signatures of a fractional quantum Hall liquid of photons in an incoherently pumped optical cavity. *Physical Review A* **96**, 053808 (2017).

[268] Chen, K.-H. *Creating extended Landau levels of large degeneracy with photons*. Ph.D. thesis, The Ohio State University (2018).

[269] Ivanov, P. A., Letscher, F., Simon, J. & Fleischhauer, M. Adiabatic flux insertion and growing of Laughlin states of cavity Rydberg polaritons. *Physical Review A* **98**, 013847 (2018).

[270] Dutta, S. & Mueller, E. J. Coherent generation of photonic fractional quantum Hall states in a cavity and the search for anyonic quasiparticles. *Physical Review A* **97**, 033825 (2018).

[271] Banerjee, M., Heiblum, M., Umansky, V., Feldman, D. E., Oreg, Y. & Stern, A. Observation of half-integer thermal Hall conductance. *Nature* **559**, 205–210 (2018). URL `https://doi.org/10.1038/s41586-018-0184-1`.

[272] Simon, S. H. Interpretation of thermal conductance of the $\nu = 5/2$ edge. *Physical Review B* **97**, 121406 (2018).

[273] Cooper, N. R., Wilkin, N. K. & Gunn, J. M. F. Quantum phases of vortices in rotating Bose-Einstein condensates. *Physical Review Letters* **87**, 120405 (2001).

[274] Regnault, N. & Jolicoeur, T. Quantum Hall fractions in rotating Bose-Einstein condensates. *Physical Review Letters* **91**, 030402 (2003).

[275] Umucalilar, R. O. & Carusotto, I. Fractional quantum Hall states of photons in an array of dissipative coupled cavities. *Physical Review Letters* **108**, 206809 (2012).

[276] Grusdt, F., Letscher, F., Hafezi, M. & Fleischhauer, M. Topological growing of Laughlin states in synthetic gauge fields. *Physical Review Letters* **113**, 155301 (2014).

[277] Kapit, E., Hafezi, M. & Simon, S. H. Induced self-stabilization in fractional quantum Hall states of light. *Physical Review X* **4**, 031039 (2014).

[278] Lebreuilly, J., Biella, A., Storme, F., Rossini, D., Fazio, R., Ciuti, C. & Carusotto, I. Stabilizing strongly correlated photon fluids with non-Markovian reservoirs. *Physical Review A* **96**, 033828 (2017).

[279] Oshikawa, M., Kim, Y. B., Shtengel, K., Nayak, C. & Tewari, S. Topological degeneracy of non-Abelian states for dummies. *Annals of Physics* **322**, 1477–1498 (2007).

[280] Deng, H., Haug, H. & Yamamoto, Y. Exciton-polariton Bose-Einstein condensation. *Reviews of Modern Physics* **82**, 1489–1537 (2010).

[281] Douglas, J. S., Habibian, H., Hung, C.-L., Gorshkov, A., Kimble, H. J. & Chang, D. E. Quantum many-body models with cold atoms coupled to photonic crystals. *Nature Photonics* **9**, 326–331 (2015).

[282] Haldane, F. & Raghu, S. Possible realization of directional optical waveguides in photonic crystals with broken time-reversal symmetry. *Physical Review Letters* **100**, 013904 (2008).

[283] Kollár, A. J., Papageorge, A. T., Vaidya, V. D., Guo, Y., Keeling, J. & Lev, B. L. Supermode-density-wave-polariton condensation with a Bose–Einstein condensate in a multimode cavity. *Nature Communications* **8**, 14386 (2017).

[284] Purdy, T. P., Brooks, D., Botter, T., Brahms, N., Ma, Z.-Y. & Stamper-Kurn, D. M. Tunable cavity optomechanics with ultracold atoms. *Physical Review Letters* **105**, 133602 (2010).

[285] Thompson, J., Tiecke, T., de Leon, N., Feist, J., Akimov, A., Gullans, M., Zibrov, A., Vuletić, V. & Lukin, M. Coupling a single trapped atom to a nanoscale optical cavity. *Science* **340**, 1202–1205 (2013).

[286] Goban, A., Hung, C.-L., Hood, J., Yu, S.-P., Muniz, J., Painter, O. & Kimble, H. Superradiance for atoms trapped along a photonic crystal waveguide. *Physical Review Letters* **115**, 063601 (2015).

[287] Pritchard, J., Maxwell, D., Gauguet, A., Weatherill, K., Jones, M. & Adams, C. Cooperative atom-light interaction in a blockaded Rydberg ensemble. *Physical Review Letters* **105**, 193603 (2010).

[288] Guerlin, C., Brion, E., Esslinger, T. & Mølmer, K. Cavity quantum electrodynamics with a Rydberg-blocked atomic ensemble. *Physical Review A* **82**, 053832 (2010).

[289] Kouwenhoven, L. P., Marcus, C. M., McEuen, P. L., Tarucha, S., Westervelt, R. M. & Wingreen, N. S. Electron transport in quantum dots. In *Mesoscopic electron transport*, 105–214 (Springer, 1997).

[290] Verger, A., Ciuti, C. & Carusotto, I. Polariton quantum blockade in a photonic dot. *Physical Review B* **73**, 193306 (2006).

[291] Günter, G., Robert-de Saint-Vincent, M., Schempp, H., Hofmann, C., Whitlock, S. & Weidemüller, M. Interaction enhanced imaging of individual Rydberg atoms in dense gases. *Physical Review Letters* **108**, 013002 (2012).

[292] Grusdt, F. & Fleischhauer, M. Fractional quantum Hall physics with ultracold Rydberg gases in artificial gauge fields. *Physical Review A* **87**, 043628 (2013).

[293] Grusdt, F., Yao, N. Y., Abanin, D., Fleischhauer, M. & Demler, E. Interferometric measurements of many-body topological invariants using mobile impurities. *Nature Communications* **7** (2016).

[294] Umucalılar, R., Macaluso, E., Comparin, T. & Carusotto, I. Time-of-flight measurements as a possible method to observe anyonic statistics. *Physical Review Letters* **120**, 230403 (2018).

[295] Macaluso, E., Comparin, T., Mazza, L. & Carusotto, I. Fusion channels of non-Abelian anyons from angular-momentum and density-profile measurements. *arXiv preprint arXiv:1903.03011* (2019).

[296] Aoki, T., Dayan, B., Wilcut, E., Bowen, W. P., Parkins, A. S., Kippenberg, T., Vahala, K. & Kimble, H. Observation of strong coupling between one atom and a monolithic microresonator. *Nature* **443**, 671 (2006).

[297] Silveri, M., Tuorila, J., Thuneberg, E. & Paraoanu, G. Quantum systems under frequency modulation. *Reports on Progress in Physics* **80**, 056002 (2017).

[298] Eckardt, A. Colloquium: Atomic quantum gases in periodically driven optical lattices. *Reviews of Modern Physics* **89**, 011004 (2017).

[299] Ma, R., Tai, M. E., Preiss, P. M., Bakr, W. S., Simon, J. & Greiner, M. Photon-assisted tunneling in a biased strongly correlated Bose gas. *Physical Review Letters* **107**, 095301 (2011).

[300] Parker, C. V., Ha, L.-C. & Chin, C. Direct observation of effective ferromagnetic domains of cold atoms in a shaken optical lattice. *Nature Physics* **9**, 769 (2013).

[301] Clark, L. W., Feng, L. & Chin, C. Universal space-time scaling symmetry in the dynamics of bosons across a quantum phase transition. *Science* **354**, 606–610 (2016).

[302] Daley, A. J. & Simon, J. Effective three-body interactions via photon-assisted tunneling in an optical lattice. *Physical Review A* **89**, 053619 (2014).

[303] Meinert, F., Mark, M. J., Lauber, K., Daley, A. J. & Nägerl, H.-C. Floquet engineering of correlated tunneling in the Bose-Hubbard model with ultracold atoms. *Physical Review Letters* **116**, 205301 (2016).

[304] Clark, L. W., Gaj, A., Feng, L. & Chin, C. Collective emission of matter-wave jets from driven Bose–Einstein condensates. *Nature* **551**, 356 (2017).

[305] Lignier, H., Sias, C., Ciampini, D., Singh, Y., Zenesini, A., Morsch, O. & Arimondo, E. Dynamical control of matter-wave tunneling in periodic potentials. *Physical Review Letters* **99**, 220403 (2007).

[306] Struck, J., Ölschläger, C., Weinberg, M., Hauke, P., Simonet, J., Eckardt, A., Lewenstein, M., Sengstock, K. & Windpassinger, P. Tunable gauge potential for neutral and spinless particles in driven optical lattices. *Physical Review Letters* **108**, 225304 (2012).

[307] Aidelsburger, M., Atala, M., Lohse, M., Barreiro, J. T., Paredes, B. & Bloch, I. Realization of the Hofstadter Hamiltonian with ultracold atoms in optical lattices. *Physical Review Letters* **111**, 185301 (2013).

[308] Miyake, H., Siviloglou, G. A., Kennedy, C. J., Burton, W. C. & Ketterle, W. Realizing the Harper Hamiltonian with laser-assisted tunneling in optical lattices. *Physical Review Letters* **111**, 185302 (2013).

[309] Clark, L. W., Anderson, B. M., Feng, L., Gaj, A., Levin, K. & Chin, C. Observation of density-dependent gauge fields in a Bose-Einstein condensate based on micromotion control in a shaken two-dimensional lattice. *Physical Review Letters* **121**, 030402 (2018).

[310] Jotzu, G., Messer, M., Desbuquois, R., Lebrat, M., Uehlinger, T., Greif, D. & Esslinger, T. Experimental realization of the topological Haldane model with ultracold fermions. *Nature* **515**, 237 (2014).

[311] Fläschner, N., Vogel, D., Tarnowski, M., Rem, B., Lühmann, D.-S., Heyl, M., Budich, J., Mathey, L., Sengstock, K. & Weitenberg, C. Observation of dynamical vortices after quenches in a system with topology. *Nature Physics* **14**, 265 (2018).

[312] Haykin, S. *Communication systems* (John Wiley & Sons, 2008).

[313] Strand, J., Ware, M., Beaudoin, F., Ohki, T., Johnson, B., Blais, A. & Plourde, B. First-order sideband transitions with flux-driven asymmetric transmon qubits. *Physical Review B* **87**, 220505 (2013).

[314] Naik, R., Leung, N., Chakram, S., Groszkowski, P., Lu, Y., Earnest, N., McKay, D., Koch, J. & Schuster, D. Random access quantum information processors using multimode circuit quantum electrodynamics. *Nature Communications* **8**, 1904 (2017).

[315] Beaudoin, F., da Silva, M. P., Dutton, Z. & Blais, A. First-order sidebands in circuit QED using qubit frequency modulation. *Physical Review A* **86**, 022305 (2012).

[316] Thompson, S. T., Hodby, E. & Wieman, C. E. Ultracold molecule production via a resonant oscillating magnetic field. *Physical Review Letters* **95**, 190404 (2005).

[317] Beaufils, Q., Crubellier, A., Zanon, T., Laburthe-Tolra, B., Maréchal, É., Vernac, L. & Gorceix, O. Radio-frequency association of molecules: an assisted Feshbach resonance. *The European Physical Journal D* **56**, 99 (2010).

[318] Chou, C., Polyakov, S., Kuzmich, A. & Kimble, H. Single-photon generation from stored excitation in an atomic ensemble. *Physical Review Letters* **92**, 213601 (2004).

[319] Thompson, J. K., Simon, J., Loh, H. & Vuletić, V. A high-brightness source of narrowband, identical-photon pairs. *Science* **313**, 74–77 (2006).

[320] Zeuthen, E., Gullans, M. J., Maghrebi, M. F. & Gorshkov, A. V. Correlated photon dynamics in dissipative Rydberg media. *Physical Review Letters* **119**, 043602 (2017).

[321] Thompson, J. D., Nicholson, T. L., Liang, Q.-Y., Cantu, S. H., Venkatramani, A. V., Choi, S., Fedorov, I. A., Viscor, D., Pohl, T., Lukin, M. D. *et al.* Symmetry-protected collisions between strongly interacting photons. *Nature* **542**, 206 (2017).

[322] Norcia, M. A., Cline, J. R., Bartolotta, J. P., Holland, M. J. & Thompson, J. K. Narrow-line laser cooling by adiabatic transfer. *New Journal of Physics* **20**, 023021 (2018).

[323] Hasan, M. & Kane, C. Colloquium: Topological insulators. *Reviews of Modern Physics* **82**, 3045–3067 (2010).

[324] Stern, A. Anyons and the quantum Hall effect—A pedagogical review. *Annals of Physics* **323**, 204 – 249 (2008). January Special Issue 2008.

[325] Du, X., Skachko, I., Duerr, F., Luican, A. & Andrei, E. Y. Fractional quantum Hall effect and insulating phase of Dirac electrons in graphene. *Nature* **462**, 192 (2009).

[326] Bolotin, K. I., Ghahari, F., Shulman, M. D., Stormer, H. L. & Kim, P. Observation of the fractional quantum Hall effect in graphene. *Nature* **462**, 196 (2009).

[327] Cooper, N., Dalibard, J. & Spielman, I. Topological bands for ultracold atoms. *Reviews of Modern Physics* **91**, 015005 (2019).

[328] Wickenbrock, A., Hemmerling, M., Robb, G. R., Emary, C. & Renzoni, F. Collective strong coupling in multimode cavity QED. *Physical Review A* **87**, 043817 (2013).

[329] Ritsch, H., Domokos, P., Brennecke, F. & Esslinger, T. Cold atoms in cavity-generated dynamical optical potentials. *Reviews of Modern Physics* **85**, 553 (2013).

[330] Léonard, J., Morales, A., Zupancic, P., Esslinger, T. & Donner, T. Supersolid formation in a quantum gas breaking a continuous translational symmetry. *Nature* **543**, 87 (2017).

[331] Vaidya, V. D., Guo, Y., Kroeze, R. M., Ballantine, K. E., Kollár, A. J., Keeling, J. & Lev, B. L. Tunable-range, photon-mediated atomic interactions in multimode cavity QED. *Physical Review X* **8**, 011002 (2018).

[332] Wallraff, A., Schuster, D. I., Blais, A., Frunzio, L., Huang, R.-S., Majer, J., Kumar, S., Girvin, S. M. & Schoelkopf, R. J. Strong coupling of a single photon to a superconducting qubit using circuit quantum electrodynamics. *Nature* **431**, 162–167 (2004).

[333] Barik, S., Karasahin, A., Flower, C., Cai, T., Miyake, H., DeGottardi, W., Hafezi, M. & Waks, E. A topological quantum optics interface. *Science* **359**, 666–668 (2018).

[334] Regnault, N. & Jolicoeur, T. Quantum Hall fractions for spinless bosons. *Physical Review B* **69**, 235309 (2004).

[335] Muller, A., Flagg, E. B., Lawall, J. R. & Solomon, G. S. Ultrahigh-finesse, low-mode-volume Fabry–Perot microcavity. *Optics Letters* **35**, 2293–2295 (2010).

[336] Hunger, D., Steinmetz, T., Colombe, Y., Deutsch, C., Hänsch, T. W. & Reichel, J. A fiber Fabry–Perot cavity with high finesse. *New Journal of Physics* **12**, 065038 (2010).

[337] Tiecke, T., Thompson, J. D., de Leon, N. P., Liu, L., Vuletić, V. & Lukin, M. D. Nanophotonic quantum phase switch with a single atom. *Nature* **508**, 241–244 (2014).

[338] Chang, T.-H., Fields, B., Kim, M. E. & Hung, C.-L. Microring resonators on a membrane optical circuit for atom-light interactions. *arXiv preprint arXiv:1905.10978* (2019).

[339] Sipahigil, A., Evans, R. E., Sukachev, D. D., Burek, M. J., Borregaard, J., Bhaskar, M. K., Nguyen, C. T., Pacheco, J. L., Atikian, H. A., Meuwly, C. *et al.* An integrated diamond nanophotonics platform for quantum-optical networks. *Science* **354**, 847–850 (2016).

[340] Dibos, A., Raha, M., Phenicie, C. & Thompson, J. D. Atomic source of single photons in the telecom band. *Physical Review Letters* **120**, 243601 (2018).

[341] Weber, S., Tresp, C., Menke, H., Urvoy, A., Firstenberg, O., Büchler, H. P. & Hofferberth, S. Tutorial: Calculation of Rydberg interaction potentials. *Journal of Physics B: Atomic, Molecular and Optical Physics* **50**, 133001 (2017). URL `https://doi.org/10.1088/1361-6455/aa743a`.

[342] Verstraete, F., Wolf, M. M. & Cirac, J. I. Quantum computation and quantum-state engineering driven by dissipation. *Nature Physics* **5**, 633–636 (2009).

[343] Shankar, S., Hatridge, M., Leghtas, Z., Sliwa, K., Narla, A., Vool, U., Girvin, S. M., Frunzio, L., Mirrahimi, M. & Devoret, M. H. Autonomously stabilized entanglement between two superconducting quantum bits. *Nature* **504**, 419–422 (2013).

[344] Ma, R., Owens, C., Houck, A., Schuster, D. I. & Simon, J. Autonomous stabilizer for incompressible photon fluids and solids. *Physical Review A* **95**, 043811 (2017).

[345] Cian, Z.-P., Zhu, G., Chu, S.-K., Seif, A., DeGottardi, W., Jiang, L. & Hafezi, M. Photon pair condensation by engineered dissipation. *arXiv preprint arXiv:1904.00016* (2019).

[346] Grimm, A., Frattini, N. E., Puri, S., Mundhada, S. O., Touzard, S., Mirrahimi, M., Girvin, S. M., Shankar, S. & Devoret, M. H. The Kerr-Cat Qubit: Stabilization, Readout, and Gates. *arXiv preprint arXiv:1907.12131* (2019).

[347] Gong, Z.-X., Xu, M., Foss-Feig, M., Thompson, J. K., Rey, A. M., Holland, M. & Gorshkov, A. V. Steady-state superradiance with Rydberg polaritons. *arXiv preprint arXiv:1611.00797* (2016).

[348] Lebreuilly, J., Wouters, M. & Carusotto, I. Towards strongly correlated photons in arrays of dissipative nonlinear cavities under a frequency-dependent incoherent pumping. *Comptes Rendus Physique* **17**, 836–860 (2016).

[349] Wang, C.-H., Gullans, M., Porto, J. V., Phillips, W. D. & Taylor, J. M. Photon thermalization via laser cooling of atoms. *Physical Review A* **98**, 013834 (2018).

[350] Wang, C.-H., Gullans, M., Porto, J., Phillips, W. D. & Taylor, J. M. Theory of Bose condensation of light via laser cooling of atoms. *Physical Review A* **99**, 031801 (2019).

[351] Guerlin, C., Bernu, J., Deleglise, S., Sayrin, C., Gleyzes, S., Kuhr, S., Brune, M., Raimond, J. & Haroche, S. Progressive field-state collapse and quantum non-demolition photon counting. *Nature* **448**, 889–893 (2007).

[352] Reiserer, A., Ritter, S. & Rempe, G. Nondestructive detection of an optical photon. *Science* **342**, 1349–1351 (2013).

[353] Wang, B. & Duan, L.-M. Engineering superpositions of coherent states in coherent optical pulses through cavity-assisted interaction. *Physical Review A* **72**, 022320 (2005).

[354] Leroux, I. D., Schleier-Smith, M. H. & Vuletić, V. Orientation-dependent entanglement lifetime in a squeezed atomic clock. *Physical Review Letters* **104**, 250801 (2010).

[355] Louchet-Chauvet, A., Appel, J., Renema, J. J., Oblak, D., Kjaergaard, N. & Polzik, E. S. Entanglement-assisted atomic clock beyond the projection noise limit. *New Journal of Physics* **12**, 065032 (2010).

[356] Leibfried, D., Barrett, M. D., Schaetz, T., Britton, J., Chiaverini, J., Itano, W. M., Jost, J. D., Langer, C. & Wineland, D. J. Toward Heisenberg-limited spectroscopy with multiparticle entangled states. *Science* **304**, 1476–1478 (2004).

[357] Kitagawa, M. & Ueda, M. Squeezed spin states. *Physical Review A* **47**, 5138 (1993).

[358] Law, C., Ng, H. & Leung, P. Coherent control of spin squeezing. *Physical Review A* **63**, 055601 (2001).

[359] Shen, C. & Duan, L.-M. Efficient spin squeezing with optimized pulse sequences. *Physical Review A* **87**, 051801 (2013).

[360] Gil, L., Mukherjee, R., Bridge, E., Jones, M. & Pohl, T. Spin squeezing in a Rydberg lattice clock. *Physical Review Letters* **112**, 103601 (2014).

[361] Norcia, M. A., Young, A. W., Eckner, W. J., Oelker, E., Ye, J. & Kaufman, A. M. Seconds-scale coherence in a tweezer-array optical clock. *arXiv preprint arXiv:1904.10934* (2019).

[362] Briegel, H.-J., Dür, W., Cirac, J. I. & Zoller, P. Quantum repeaters: the role of imperfect local operations in quantum communication. *Physical Review Letters* **81**, 5932 (1998).

[363] Pan, J.-W., Chen, Z.-B., Lu, C.-Y., Weinfurter, H., Zeilinger, A. & Żukowski, M. Multiphoton entanglement and interferometry. *Reviews of Modern Physics* **84**, 777 (2012).

[364] Pan, J.-W., Bouwmeester, D., Weinfurter, H. & Zeilinger, A. Experimental entanglement swapping: entangling photons that never interacted. *Physical Review Letters* **80**, 3891 (1998).

[365] Macaluso, E. & Carusotto, I. Ring-shaped fractional quantum Hall liquids with hard-wall potentials. *Physical Review A* **98**, 013605 (2018).

[366] Macaluso, E. & Carusotto, I. Hard-wall confinement of a fractional quantum Hall liquid. *Physical Review A* **96**, 043607 (2017).

[367] Girvin, S. M. The quantum Hall effect: novel excitations and broken symmetries. In *Aspects topologiques de la physique en basse dimension. Topological aspects of low dimensional systems*, 53–175 (Springer, 1999).

[368] Hofstadter, D. R. Energy levels and wave functions of Bloch electrons in rational and irrational magnetic fields. *Physical Review B* **14**, 2239–2249 (1976).

[369] Lin, Y., Compton, R. L., Jimenez-Garcia, K., Porto, J. V. & Spielman, I. B. Synthetic magnetic fields for ultracold neutral atoms. *Nature* **462**, 628–632 (2009).

[370] Abo-Shaeer, J., Raman, C., Vogels, J. & Ketterle, W. Observation of vortex lattices in Bose-Einstein condensates. *Science* **292**, 476–479 (2001).

[371] Yarmchuk, E., Gordon, M. & Packard, R. Observation of stationary vortex arrays in rotating superfluid helium. *Physical Review Letters* **43**, 214 (1979).

[372] Goldstein, H., Poole, C. & Safko, J. Classical mechanics (2002).

[373] Ho, T.-L. Bose-Einstein condensates with large number of vortices. *Physical Review Letters* **87**, 060403 (2001).

[374] Siegman, A. *Lasers*. University Science Bks (University Science Books, 1986).

[375] Wald, R. *General Relativity* (University of Chicago Press, 1984).

[376] Bernevig, B. A. & Haldane, F. Model fractional quantum Hall states and Jack polynomials. *Physical Review Letters* **100**, 246802 (2008).

[377] Wen, X.-G. Topological orders and edge excitations in fractional quantum Hall states. *Advances in Physics* **44**, 405–473 (1995).

[378] Douglas, M. R. & Klevtsov, S. Bergman kernel from path integral. *Communications in Mathematical Physics* **293**, 205 (2010).

[379] Schade, N. B., Schuster, D. I. & Nagel, S. R. A nonlinear, geometric Hall effect without magnetic field. *arXiv preprint arXiv:1902.03445* (2019).

[380] Read, N. Non-Abelian adiabatic statistics and Hall viscosity in quantum Hall states and $p_x + ip_y$ paired superfluids. *Physical Review B* **79**, 045308 (2009).

[381] Haldane, F. Geometrical description of the fractional quantum Hall effect. *Physical Review Letters* **107**, 116801 (2011).

[382] Bellissard, J., van Elst, A. & Schulz-Baldes, H. The noncommutative geometry of the quantum Hall effect. *Journal of Mathematical Physics* **35**, 5373–5451 (1994).

[383] Gromov, A. Geometric defects in quantum Hall states. *Physical Review B* **94**, 085116 (2016).

[384] Can, T. & Wiegmann, P. Quantum Hall states and conformal field theory on a singular surface. *Journal of Physics A: Mathematical and Theoretical* **50**, 494003 (2017).

[385] Ferrari, F. & Klevtsov, S. FQHE on curved backgrounds, free fields and large N. *Journal of High Energy Physics* **2014**, 86 (2014).

[386] Bradlyn, B. & Read, N. Topological central charge from Berry curvature: Gravitational anomalies in trial wave functions for topological phases. *Physical Review B* **91**, 165306 (2015).

[387] Mirgorodskiy, I., Christaller, F., Braun, C., Paris-Mandoki, A., Tresp, C. & Hofferberth, S. Electromagnetically induced transparency of ultra-long-range Rydberg molecules. *Physical Review A* **96**, 011402 (2017).

[388] Walls, D. F. & Milburn, G. J. *Quantum optics* (Springer Science & Business Media, 2007).

[389] Beijersbergen, M. W., Allen, L., Van der Veen, H. & Woerdman, J. Astigmatic laser mode converters and transfer of orbital angular momentum. *Optics Communications* **96**, 123–132 (1993).

[390] Eckardt, A. & Anisimovas, E. High-frequency approximation for periodically driven quantum systems from a Floquet-space perspective. *New Journal of Physics* **17**, 093039 (2015).

[391] Gangloff, D., Shi, M., Wu, T., Bylinskii, A., Braverman, B., Gutierrez, M., Nichols, R., Li, J., Aichholz, K., Cetina, M., Karpa, L., Jelenković, B., Chuang, I. & Vuletić, V. Preventing and reversing vacuum-induced optical losses in high-finesse tantalum (V) oxide mirror coatings. *Optics Express* **23**, 18014–18028 (2015).